CISM International Centre fo
Courses and Lectures

Roberto Camussi
*Editor*

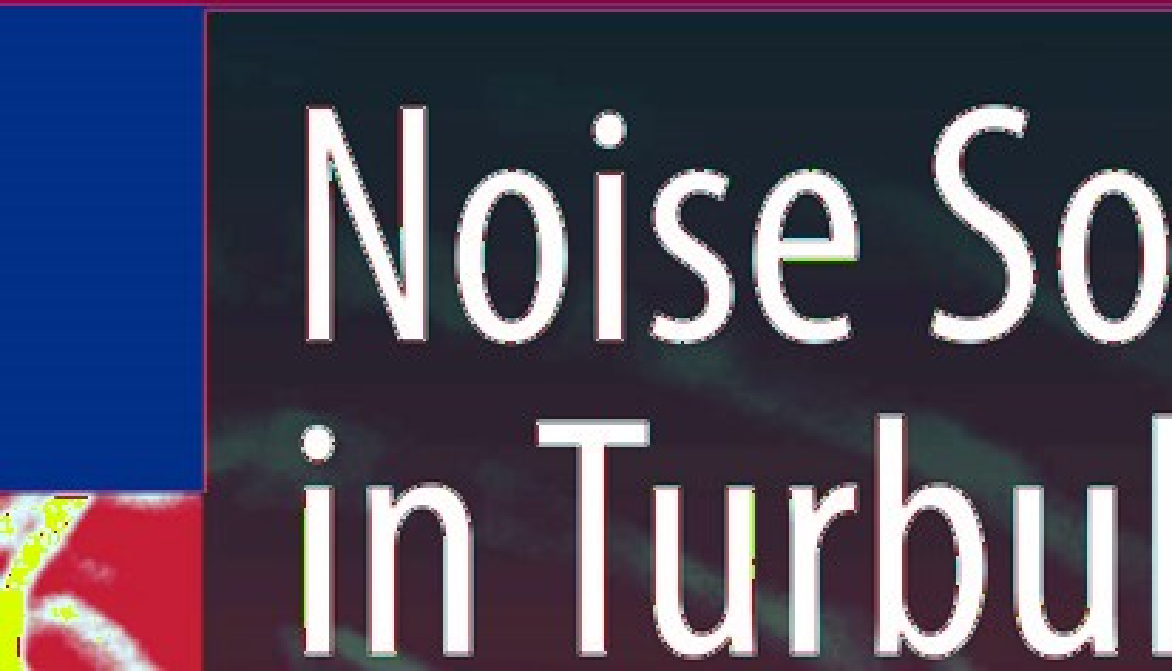

# Noise So
# in Turbul

# CISM Courses and Lectures

Series Editors:

The Rectors
Friedrich Pfeiffer - Munich
Franz G. Rammerstorfer - Wien
Jean Salençon - Palaiseau

The Secretary General
Bernhard Schrefler - Padua

Executive Editor
Paolo Serafini - Udine


The series presents lecture notes, monographs, edited works and proceedings in the field of Mechanics, Engineering, Computer Science and Applied Mathematics.
Purpose of the series is to make known in the international scientific and technical community results obtained in some of the activities organized by CISM, the International Centre for Mechanical Sciences.

# International Centre for Mechanical Sciences

## Courses and Lectures Vol. 545

For further volumes:
www.springer.com/series/76

*Roberto Camussi*
*Editor*

# Noise Sources in Turbulent Shear Flows: Fundamentals and Applications

Springer

*Editor*

Roberto Camussi
Università di Roma Tre
Roma, Italy

ISSN 0254-1971
ISBN 978-3-7091-1457-5 ISBN 978-3-7091-1458-2 (eBook)
DOI 10.1007/978-3-7091-1458-2
Springer Wien Heidelberg New York Dordrecht London



All contributions have been typeset by the authors
Printed in Italy

Printed on acid-free paper

Springer is part of Springer Science+Business Media (www.springer.com)

# *PREFACE*

*The knowledge of the physical mechanisms underlying the generation of noise in turbulent shear flows remains a challenging task despite over 50 years of intensive research in the field. The interest in this topic is considerable because turbulent shear flows originating noise are encountered in many engineering applications, such as flows in pipes, compressible and incompressible jets, turbulent boundary layers over rigid or elastic surfaces, wakes generated behind streamlined or bluff bodies.*

*Recent developments in terms of our capacity to both numerically and experimentally analyze the physics of turbulent shear flows have opened up new possibilities to improve our knowledge about noise generation and propagation mechanisms. These understandings lead, for example, to the development of flow/noise manipulation techniques and address the design of noise suppression devices.*

*The scope of this volume is to present a state-of-the-art review of on-going activities in noise prediction, modeling and measurement and to indicate current research directions. This book is partially based on class notes provided during the course 'Noise sources in turbulent shear flows', given at CISM on April 2011.*

*Introductory chapters on fundamentals topics will be followed by up-to-date reviews of arguments of specific interest for engineering applications.*

*The first part of the volume is denoted as 'Fundamentals' and contains two chapters. The first one covers general concepts of aeroacoustics, from the basic equations of fluid dynamics to the theoretical description of self-sustained oscillations in internal flows including the vortex sound theory. The second chapter illustrates more deeply the acoustic analogies in account also of the presence of solid surfaces. The flow features involved in sound generation are also highlighted by means of suitable dimensional analyses.*

*In the second part of the volume, denoted as 'Applications', particular emphasis is put into arguments of interest for engineers and relevant for aircraft design. An important topic included in this part is jet noise, which is treated from both an experimental and an analytical viewpoint. A comprehensive review of literature results as well*

*as a description of present understandings of noise generation and its predictions is presented.*

*A second chapter is devoted to describing airfoil broadband noise and its analytical modeling with emphasis on trailing edge noise and rotating blades.*

*The boundary layer noise is treated in another chapter that is divided into two parts. In the first one noise generation mechanisms are described. In the second, the problem of the interior noise and some basic approaches used for its control are presented.*

*As a fundamental completion of the state-of-the-art knowledge, a chapter is devoted to clarifying the concept of noise sources, their theoretical modeling and the techniques used for their identification in turbulent flows.*

*All these arguments are treated extensively with the inclusion of many practical examples and references to engineering applications.*

*For the purpose of optimizing the convenience of this book, the chapters are conceived to be self-contained. Readers may concentrate on the topic they are more interested in, with no need of consulting other chapters. The disadvantage of this approach lies in the repetition of some basic notions, such as the Lighthill's analogy or the Green's function formalism, which can be found replicated in more than one chapter. Indeed, scientists may use the same mathematical tool in a different but efficient way, depending on the purpose of their analysis.*

*To my opinion, these reiterations do not represent a shortcoming. On the contrary I consider this approach to be a quite instructive way for young researchers to discover and appreciate the amazing strength and effectiveness of theories, models and mathematical formalisms that provide the foundations of aeroacoustics.*

*Roberto Camussi*

**CONTENTS**

# Part 1: Fundamentals

# Introduction to Aeroacoustics and Self-Sustained Oscillations of Internal Flows

Avraham Hirschberg
Mesoscopic Transport Phenomena
Eindhoven University of Technology
Chapter in CISM Lecture Series: Noise Sources in Turbulent Shear Flows
18-22 April 2011 Udine, Italy

**Abstract** After a review of basic equations of fluid dynamics, the *Aeroacoustic analogy* of Lighthill is derived. This analogy describes the sound field generated by a complex flow from the point of view of a listener immerged in a uniform stagnant fluid. The concept of monopole, dipole and quadrupole are introduced. The scaling of the sound power generated by a subsonic free jet is explained, providing an example of the use of the integral formulation of the analogy. The influence of the Doppler Effect on the radiation of sound by a moving source is explained. By considering the noise generated by a free jet in a bubbly liquid, we illustrate the importance of the choice of the aeroacoustic variable in an aeroacoustic analogy. This provides some insight into the usefulness of alternative formulations, such as the *Vortex Sound Theory*. The energy corrolary of Howe based on the Vortex Sound Theory appears to be the most suitable theory to understand various aspects of self-sustained oscillation due to the coupling of vortex shedding with acoustic standing waves in a resonator. This approach is used to analyse the convective energy losses at an open pipe termination, human whistling, flow instabilities in diffusers, pulsations in pipe systems with deep closed side branches and the whistling of corrugated pipes.

## 1 Introduction

Due to the essential non-linearity of the governing equations it is difficult to predict accurately fluid flows under conditions at which they do produce sound. This is typical for high speeds with non-linear inertial terms in the equation of motion much larger than the viscous terms (high Reynolds numbers). Direct simulation of such flows is very difficult. When the flow velocity remains low compared to the speed of sound waves (low Mach numbers) the sound production is a minute fraction of the energy in the flow,

R. Camussi (Ed.), *Noise Sources in Turbulent Shear Flows: Fundamentals and Applications*, CISM International Centre for Mechanical Sciences, DOI 10.1007/978-3-7091-1458-2_1,

making numerical simulation even more difficult. It is not even obvious how one should define the acoustic field in the presence of flows. Aeroacoustics does provide such definitions. The acoustic field is defined as an extrapolation of an ideal reference flow. The difference between the actual flow and this reference flow is identified as source of sound. Using Lighthill's terminology, we call this an "analogy" [Lighthill (1952-54)].

In free field conditions the sound intensity produced by flows is usually so small that we can neglect the effect of acoustics on the flow. Furthermore, the listener is usually immerged in a uniform stagnant fluid. In such cases the convenient reference flow is the linear inviscid perturbation of this stagnant, uniform fluid. It is convenient to use an integral formulation of the aero-acoustical analogy. This integral equation is a convolution of the sound source by the Green function: the response of the reference state to a localized impulsive source. The advantage of the integral formulation is that random errors in the source term average out. One therefore often uses such an integral formulation to extract acoustic information from direct numerical simulations of the flow which are too rough to directly predict the acoustic field. Such an approach is used so as to obtain scaling laws for sound production by turbulent flows when only global information is available about the flow. When flow dimensions are small compared to the acoustical wave length (compact flow) we can locally neglect the effect of wave propagation within the source region. Here the analogy of Lighthill provides again a procedure which guarantees that we keep the leading order term where brute force would predict no sound production at all or would dramatically overestimate it [Crighton et al. (1992)]. In compact flows at low Mach numbers the flow is most efficiently described in terms of vortex dynamics, allowing a more detailed study of the sound production by nonlinear convective effects.

Walls have a dramatic effect on the production of sound because it becomes much easier compressing the fluid than in free space. In internal flows acoustic energy can accumulate into standing waves, which correspond to resonances. Even at low Mach numbers acoustical particle velocities of the order of magnitude of the main flow velocity can be reached when hydrodynamic flow instabilities couple with the acoustic standing waves. This relatively high amplitude facilitates numerical simulations considerably. Such self-sustained oscillations are best described qualitatively in terms of vortex dynamics.

In a pipe the main flow does not necessarily vanish when travelling

away from the source region. For these reasons another analogy should be used, called the Vortex-Sound Theory. Whilst Powell (1964) initially developed this theory for free space, Howe generalised it for internal flows [Howe (1975), Howe (1984), Howe (1998), Howe (2002)]. In Howe's approach the acoustic field is defined as the unsteady irrotational component of the flow, which again stresses the fact that vortices are the main sources of sound in isentropic flows. An integral formulation can also be used in this case.

When considering self-sustained oscillations, one is interested in conditions at which they appear and the amplitude they reach. While a linear theory provides information on the conditions under which self-sustained oscillation appears, the amplitude is determined by essentially non-linear saturation mechanisms. We will show that when ever the relevant non-linear mechanism is identified, the order of magnitude of steady self-sustained pulsation amplitude can be easily obtained. A balance between the acoustic power produced by the source and the dissipated power will be used.

A summary of the equations of fluid dynamics is given in (section 2). In Section 3 we introduce the acoustic field by means of Lighthill's analogy, followed by basic concepts of the acoustics of a stagnant uniform fluid, such as elementary solutions of the wave equation, acoustic energy, the Green function, multipole expansion, Doppler effect and convective effects due to a uniform main flow (section 4). We use the analogy of Lighthill to derive the scaling law for sound production by a subsonic isothermal free jet. The influence of the difference in speed of sound between the source region and the listener is discussed by using the example of bubbly liquids (section 5). We then introduce the acoustics of pipes, derive the low frequency limit of acoustic properties of a pipe discontinuity and of an open pipe termination (with and without main flow). In Section 6 we introduce the concepts of resonators and discuss closed-side branch and Helmholtz resonators. In section 7 we introduce vortex sound theory and apply it to the analysis of whistling, from human whistling to whistling of corrugated pipes. Some aspects introduced here are discussed in depth in the following chapters.

Our discussion is inspired by the book of Dowling and Ffowcs Williams (1983), which is an excellent introductory course. Basic acoustics is discussed in the books of Morse and Ingard (1968), Pierce (1990), Kinsler et al. (1982), Temkin (2001), Blackstock (2000) and Bruneau (2006). Aeroacoustics is treated in the books of Goldstein (1976), Blake (1986), Crighton et al. (1992), Howe (1998)and Howe (2002). In this introduction

we ignore the effect of wall vibration [Junger and Feit (1986), Cremer and Heckl (1988) and Norton (1989)]. Acoustics of musical instruments is discussed by Fletcher and Rossing (1998) and Chaigne and Kergomard (2008). In an earlier course Hirschberg et al. (1995) and a review paper [Fabre et al. (2012)] we discussed the aeroacoustics of woodwinds. In the Lecture notes of Rienstra and Hirschberg (1999) provide more details on the mathematical aspects.

## 2 Fluid dynamics

### 2.1 Conservation laws

The conservation of mass for an infinitesimal material element of density $\rho$ and volume $V$ is given in the continuum approximation by [Batchelor (1967), Landau and Lifchitz (1987), Kundu (1990)]:

$$\frac{D\rho V}{Dt} = 0 \tag{1}$$

where the convective time derivative is defined by:

$$\frac{D\rho}{Dt} = \frac{\partial \rho}{\partial t} + (\vec{v} \cdot \nabla)\, \rho \tag{2}$$

in vector notation. In the index notation we have:

$$\frac{D\rho}{Dt} = \frac{\partial \rho}{\partial t} + v_i \frac{\partial \rho}{\partial x_i} \ . \tag{3}$$

Following the convention of Einstein, a summation is assumed in equation (3) over the repeated index $i = 1, 2, 3$. The dilation rate of a fluid particle is given by:

$$\frac{1}{V}\frac{DV}{Dt} = \nabla \cdot \vec{v} = \frac{\partial v_i}{\partial x_i} \tag{4}$$

Hence, the mass conservation law (1) can be written in the conservation form:

$$\frac{\partial \rho}{\partial t} + \nabla \cdot (\rho \vec{v}) = \frac{\partial \rho}{\partial t} + \frac{\partial \rho v_i}{\partial x_i} = 0 \ . \tag{5}$$

In integral form this equation becomes:

$$\frac{d}{dt}\int_V \rho dV + \int_S \rho\, (\vec{v} \cdot \vec{n})\, dS = 0 \tag{6}$$

in which, $V$ is a fixed control volume delimited by the surface $S$ with outer unit normal $\vec{n}$ (Figure 1). The second law of Newton applied to an infinites-

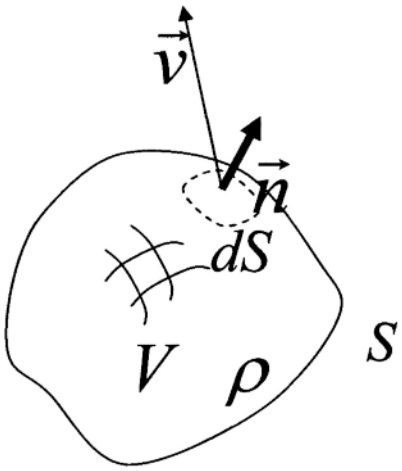


**Figure 1.** Control volume used to establish the integral conservation laws.

imal material element is:

$$\rho \frac{D\vec{v}}{Dt} = -\nabla \cdot \vec{\vec{P}} + \vec{f} \tag{7}$$

where $\vec{f}$ is the density of a force field acting on the bulk of the fluid and $\vec{\vec{P}}$ is the stress tensor representing the surface interaction between the particle and its surroundings. Using the definition of the convective derivative (2) and the mass conservation law (5) we obtain the conservation form of the momentum equation:

$$\frac{\partial \rho \vec{v}}{\partial t} + \nabla \cdot (\rho \vec{v} \vec{v}) = -\nabla \cdot \vec{\vec{P}} + \vec{f} \tag{8}$$

or in index notation:

$$\frac{\partial \rho v_i}{\partial t} + \frac{\partial \rho v_i v_j}{\partial x_j} = -\frac{\partial P_{ij}}{\partial x_j} + f_i \tag{9}$$

and integral form:

$$\frac{d}{dt} \int_V \rho \vec{v} dV + \int_S \rho \vec{v} \left( \vec{v} \cdot \vec{n} \right) dS = -\int_S \vec{\vec{P}} \cdot \vec{n} dS + \int_V \vec{f} dV \ . \tag{10}$$

The energy conservation law is, in differential form:

$$\frac{D\rho(e + v^2/2)}{Dt} = -\nabla \cdot \vec{q} - \nabla \cdot \left( \vec{\vec{P}} \cdot \vec{v} \right) + \vec{f} \cdot \vec{v} + Q_w \tag{11}$$

where $e$ is the internal energy of the fluid per unit of mass, $v = |\vec{v}|$, $\vec{q}$ the heat flux and $Q_w$ the energy production per unit volume.

### 2.2 Constitutive equations

The conservation laws are complemented by empirical constitutive equations. For simplicity we assume that the fluid is locally in a state close to thermodynamic equilibrium, so that we can express the internal energy in terms of two other state variables:

$$e = e(\rho, s) \tag{12}$$

where $s$ is the entropy per unit of mass. Using the thermodynamic equation:

$$de = Tds - pd\left(\frac{1}{\rho}\right) \tag{13}$$

we get the equations of state:

$$p = \rho^2 \left(\frac{\partial e}{\partial \rho}\right)_s \tag{14}$$

and

$$T = \left(\frac{\partial e}{\partial s}\right)_\rho . \tag{15}$$

As we also have $p = p(\rho, s)$ we can write:

$$dp = \left(\frac{\partial p}{\partial \rho}\right)_s d\rho + \left(\frac{\partial p}{\partial s}\right)_\rho ds . \tag{16}$$

The speed of sound $c$ is defined by:

$$c = \sqrt{\left(\frac{\partial p}{\partial \rho}\right)_s} . \tag{17}$$

In most applications we will consider an ideal gas for which:

$$de = c_v dT \tag{18}$$

with $c_v$ the specific heat capacity at constant volume. For an ideal gas this is a function of the temperature only. This further implies:

$$p = \rho RT \tag{19}$$

and

$$c = \sqrt{\gamma RT} = \sqrt{\frac{\gamma p}{\rho}} \tag{20}$$

with $R = c_p - c_v$ the specific gas constant, $\gamma = c_p/c_v$ the Poisson ratio and $c_p$ is the specific heat capacity at constant pressure. By definition:

$$c_v = \left(\frac{\partial e}{\partial T}\right)_\rho \tag{21}$$

and

$$c_p = \left(\frac{\partial i}{\partial T}\right)_p \tag{22}$$

where the specific enthalpy is defined by:

$$i = e + \frac{p}{\rho} \ . \tag{23}$$

Assuming local thermodynamic equilibrium, fluxes are linear functions of the flow variables. For the heat flux we use the law of Fourier:

$$\vec{q} = -K\nabla T \ , \tag{24}$$

where $K$ is the heat conductivity. The viscous stress tensor is defined by:

$$\tau_{ij} = p\delta_{ij} - P_{ij} \tag{25}$$

with $\delta_{ij}$ the Kronecker delta, equal to unity for $i = j$ and otherwise zero. The viscous stress tensor is described for a so-called Newtonian fluid in terms of the dynamic viscosity $\eta$ and the bulk viscosity $\mu$:

$$\tau_{ij} = 2\eta\left(D_{ij} - \tfrac{1}{3}D_{kk}\delta_{ij}\right) + \mu D_{kk}\delta_{ij} \tag{26}$$

with

$$D_{ij} = \frac{1}{2}\left(\frac{\partial v_i}{\partial x_j} + \frac{\partial v_j}{\partial x_i}\right) \ . \tag{27}$$

### 2.3 Boundary conditions

The boundary conditions corresponding to the continuum assumption and the local thermodynamic equilibrium are, for a solid impermeable wall with velocity $\vec{v}_w$ and temperature $T_w$ : $\vec{v} = \vec{v}_w$ and $T = T_w$.

### 2.4 Approximations

Sound production by flows occurs at relatively high Reynolds numbers. When considering wave propagation in air at audio frequencies, we can neglect friction and heat transfer over distances of the order of the wave length. Neglecting friction, heat transfer and heat production, the energy equation (11) becomes:

$$\frac{Ds}{Dt} = 0 \; . \tag{28}$$

The momentum equation (7) reduces to the Euler equation:

$$\rho \frac{D\vec{v}}{Dt} = -\nabla p + \vec{f} \; . \tag{29}$$

In terms of the vorticity $\vec{\omega} = \nabla \times \vec{v}$ the convective acceleration can be written as:

$$(\vec{v} \cdot \nabla)\, \vec{v} = \nabla \left( \frac{v^2}{2} \right) + \vec{\omega} \times \vec{v} \; . \tag{30}$$

For homentropic flows $\nabla s = 0$ we have furthermore $\nabla p/\rho = \nabla i$, so that the Euler equation can be written in the form of Crocco:

$$\frac{\partial \vec{v}}{\partial t} + \nabla B = -\left(\vec{\omega} \times \vec{v}\right) + \frac{\vec{f}}{\rho} \tag{31}$$

with the total enthalpy:

$$B = i + v^2/2 \; . \tag{32}$$

For irrotational flow $\vec{\omega} = 0$ we can introduce a velocity potential such that:

$$\vec{v} = \nabla \varphi \tag{33}$$

or:

$$\varphi = \int \vec{v} \cdot d\vec{x} \; . \tag{34}$$

In the absence of an external force field, the integration of the Euler equation yields the unsteady compressible Bernoulli equation:

$$\frac{\partial \varphi}{\partial t} + B = g(t) \tag{35}$$

in which the function $g(t)$ is determined by the boundary conditions.

In this isentropic flow approximation $dQ = 0$, so that it follows from the first law of thermodynamics:

$$dQ = de + pd\left(\frac{1}{\rho}\right) = di - \frac{1}{\rho}dp \tag{36}$$

and

$$i = \int \frac{dp}{\rho} \ . \tag{37}$$

## 3 Analogy of Lighthill

The key idea of Lighthill's analogy [Lighthill (1952-54)] is to derive a wave equation starting from the exact mass conservation equation (5) and the momentum equation (9):

$$\frac{\partial \rho}{\partial t} + \frac{\partial \rho v_i}{\partial x_i} = 0 \tag{5}$$

and

$$\frac{\partial \rho v_i}{\partial t} + \frac{\partial \rho v_i v_j}{\partial x_j} = -\frac{\partial p}{\partial x_i} + \frac{\partial \tau_{ij}}{\partial x_j} + f_i \ . \tag{9}$$

Taking the time derivative of (5) and subtracting from it, the divergence of (9) we obtain the exact equation:

$$\frac{\partial^2 \rho}{\partial t^2} - \frac{\partial^2 \rho v_i v_j}{\partial x_i \partial x_j} = \frac{\partial^2 p}{\partial x_i^2} - \frac{\partial^2 \tau_{ij}}{\partial x_i \partial x_j} - \frac{\partial f_i}{\partial x_i} \tag{38}$$

which is quite meaningless. By adding $\frac{1}{c_0^2}\frac{\partial^2 p}{\partial t^2}$ on both sides and rearranging the terms, making use of the fact that we chose $c_0$ to be a constant, we can write (38) as a wave equation:

$$\frac{1}{c_0^2}\frac{\partial^2 p}{\partial t^2} - \frac{\partial^2 p}{\partial x_i^2} = \frac{\partial^2 \rho v_i v_j - \tau_{ij}}{\partial x_i \partial x_j} - \frac{\partial f_i}{\partial x_i} + \frac{\partial^2}{\partial t^2}\left(\frac{p}{c_0^2} - \rho\right) \ . \tag{39}$$

This equation is still exact and still generally meaningless. We could have chosen $c_0$ to be a millimetre per century or equal to the speed of light. In order to have a meaningful equation we now assume that we consider sound production by a flow bounded by a fluid displaying small perturbations from a uniform stagnant state with speed of sound equal to $c_0$ (Figure 2). We furthermore define the perturbations in the pressure $p' = p - p_0$ and density $\rho' = \rho - \rho_0$ as deviations from the state $(p_0, \rho_0)$ of this reference uniform

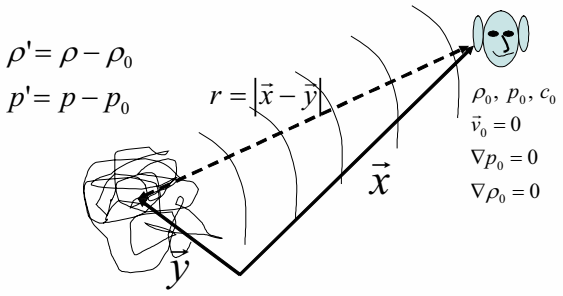


**Figure 2.** Sound sources and listener in the analogy of Lighthill

stagnant reference fluid. As the reference state is constant and uniform we can write (39) as:

$$\frac{1}{c_0^2}\frac{\partial^2 p'}{\partial t^2} - \frac{\partial^2 p'}{\partial x_i^2} = \frac{\partial^2 \rho v_i v_j - \tau_{ij}}{\partial x_i \partial x_j} - \frac{\partial f_i}{\partial x_i} + \frac{\partial^2}{\partial t^2}\left(\frac{p'}{c_0^2} - \rho'\right) . \qquad (40)$$

We will see (section 4) that this equation describes the propagation of acoustic waves in the uniform stagnant fluid when the right hand side of the equation (40) is negligible. In regions where the right hand side is not negligible, it describes the generation of sound. However, because the equation of Lighthill is a single exact equation for many unknowns, we will not obtain any result without approximations. Lighthill has shown that these approximations can best be introduced into an integral formulation of (40). We will now consider basic acoustic wave propagation allowing to understand some elementary aspects of the problem and to derive the integral formulation.

An interesting aspect of the analogy is that the sound source we find depends on the choice of the acoustic variable. Until now we have chosen pressure fluctuations $p'$ to describe the acoustic field. We could also have followed a similar procedure to obtain a wave equation for the density fluctuations $\rho'$. Starting from (38) we now subtract from both sides of the equation the term $c_0^2 \nabla^2 \rho'$ to find:

$$\frac{\partial^2 \rho'}{\partial t^2} - c_0^2 \frac{\partial^2 \rho'}{\partial x_i^2} = \frac{\partial^2 \rho v_i v_j - \tau_{ij}}{\partial x_i \partial x_j} - \frac{\partial f_i}{\partial x_i} + \frac{\partial^2}{\partial x_i^2}\left(p' - c_0^2 \rho'\right) . \qquad (41)$$

In principle equations (40) and (41) are identical. However the pressure formulation (40) is most convenient when considering sound production by combustion processes in which the time-dependent combustion yields time-dependent fluctuations in the entropy. In contrast, when considering a flow in spatially non-uniform fluids with large variations in speed of sound the density formulation (41) will be the most suitable. An example of this is the sound generation by turbulence in bubbly liquids (section 5.2). In this case the sound production appears to be dominated by the effect of differences in the speed of sound.

Equation (41) is often written for convenience in terms of the stress tensor of Lighthill :

$$\frac{\partial^2 \rho'}{\partial t^2} - c_0^2 \frac{\partial^2 \rho'}{\partial x_i^2} = \frac{\partial^2 T_{ij}}{\partial x_i \partial x_j} - \frac{\partial f_i}{\partial x_i} \tag{42}$$

where the stress tensor $\tau_{ij}$ is defined by:

$$T_{ij} = \rho v_i v_j - \tau_{ij} + \left(p' - c_0^2 \rho'\right) \delta_{ij} \ . \tag{43}$$

# 4 Acoustics of a uniform stagnant fluid

## 4.1 Wave equation

Looking at small perturbations $(p', \rho', \vec{v}')$ of a uniform stagnant state $(p_0, \rho_0)$ and neglecting friction and heat transfer, we find, for linear perturbations:

$$\frac{\partial \rho'}{\partial t} + \rho_0 \nabla \cdot \vec{v}' = 0 \ , \tag{44}$$

$$\rho_0 \frac{\partial \vec{v}'}{\partial t} + \nabla p' = \vec{f} \tag{45}$$

and

$$\frac{\partial s'}{\partial t} = \frac{Q_w}{\rho_0 T_0} \ . \tag{46}$$

The corresponding linearized equation of state is:

$$p' = c_0^2 \rho' + \left( \frac{\partial p}{\partial s} \right)_\rho s' \ . \tag{47}$$

Taking the time derivative of (44), subtracting the divergence of (45) and using (46) and (47) in order to eliminate $\rho'$ and $s'$, we obtain the wave equation for pressure perturbations:

$$\frac{1}{c_0^2} \frac{\partial^2 p'}{\partial t^2} - \nabla^2 p' = \frac{1}{T_0 \rho_0 c_0^2} \left( \frac{\partial p}{\partial s} \right)_\rho \frac{\partial Q_w}{\partial t} - \nabla \cdot \vec{f} \ . \tag{48}$$

As can be seen from this equation, the unsteady heat production is a source of sound, which is due to the dilatation of the fluid. This is in line with our common experience that turbulent flames are noisy. Also an unsteady non-uniform force field appears to be a source of sound. This is the sound source when considering the whistling of a cylinder placed with its axis normal to a uniform flow. Due to hydrodynamic instability, the wave behind the cylinder breaks down into a vortex street of alternating rotation direction. This periodic vortex shedding induces an unsteady force of the flow on the cylinder. The reaction force from the cylinder on the fluid is the source of sound. The so-called Aelonian tone will be discussed in section 7.2.

The next sections will focus on wave propagation and hence assume that $Q_w = 0$ and $\vec{f} = 0$. We therefore consider solutions of the homogeneous wave equation of d'Alembert

$$\frac{1}{c_0^2} \frac{\partial^2 p'}{\partial t^2} - \nabla^2 p' = 0 \ . \tag{49}$$

As the flow is isentropic the equation of state (16) reduces to $p' = c_0^2 \rho'$.

### 4.2 Elementary solutions

The homogeneous scalar wave equation (49) satisfies the plane wave solution:

$$p' = F\left(\vec{n}\cdot\vec{x} - c_0 t\right) \tag{50}$$

with $\vec{n}$ as the unit vector in the direction of propagation. This can easily be verified for $\vec{n} = (1,0,0)$, in which case the wave equation (45) reduces to:

$$\frac{1}{c_0^2}\frac{\partial^2 p'}{\partial t^2} - \frac{\partial^2 p'}{\partial x^2} = 0\ . \tag{51}$$

Using the chain rule we can verify that $p' = F(x - c_0 t)$ is a solution. The function $F(x)$ is determined by initial and boundary conditions. Also $p' = G(x + c_0 t)$ is a solution, representing a wave propagating in the opposite direction $\vec{n} = (-1,0,0)$. For harmonic waves with a frequency $f$ we can write this solution with the complex notation as:

$$p' = A\exp\left[i\omega\left(t - \frac{\vec{n}\cdot\vec{x}}{c_0}\right)\right] = A\exp\left[i\left(\omega t - \vec{k}\cdot\vec{x}\right)\right] \tag{52}$$

where $A$ is the complex amplitude, $\vec{k} = (\omega/c_0)\vec{n}$ the wave vector and $\omega = 2\pi f$. Substitution of the plane wave solution into the momentum equation (45)with $\vec{f} = 0$ yields:

$$\vec{u}' = \frac{p'}{\rho_0 c_0}\vec{n}\ . \tag{53}$$

Another elementary solution is obtained by considering spherical symmetric waves emanating from a point at source $\vec{y}$. The pressure field is then only a function of time and of distance $r = |\vec{x} - \vec{y}|$ between the source position $\vec{y}$ and the observer's position $\vec{x}$. The mass conservation law and momentum equation reduce to:

$$\frac{\partial \rho'}{\partial t} + \frac{\rho_0}{r^2}\frac{\partial}{\partial r}\left(r^2\frac{\partial v_r'}{\partial r}\right) = 0 \tag{54}$$

and

$$\rho_0\frac{\partial v_r'}{\partial t} + \frac{\partial p'}{\partial r} = 0 \tag{55}$$

where $v_r'$ is the fluid velocity in the radial direction. Eliminating the velocity and the density $\rho' = p'/c_0^2$ yields:

$$\frac{1}{c_0^2}\frac{\partial^2 r p'}{\partial t^2} - \frac{\partial^2 r p'}{\partial r^2} = 0 \tag{56}$$

which is satisfied by the one-dimensional d'Alembert solution for the product of pressure $p'$ and distance $r$:

$$p' = \frac{1}{r} F(r - c_0 t) \ . \tag{57}$$

By using this equation, we actually assume "free field" conditions. We assume that there are only outgoing waves and no incoming (or reflected) waves converging towards the source. For harmonic waves equation (57) becomes in complex notation:

$$p' = \frac{A}{r} \exp\left[i(\omega t - kr)\right] \tag{58}$$

with $k = \omega/c_0$. The corresponding radial velocity is found by substitution in the momentum equation:

$$v_r' = \frac{p'}{\rho_0 c_0} \left[1 + \frac{1}{ikr}\right] \ . \tag{59}$$

We observe that for large distances compared to the wave length $kr >> 1$, the solution can locally be approximated by a plane wave with: $p' = \rho_0 c_0 v_r'$. In this so-called "far field" approximation we have:

$$\frac{\partial p'}{\partial r} \approx -\frac{1}{c_0} \frac{\partial p'}{\partial t} \ . \tag{60}$$

In the opposite limit of near field $kr << 1$ the velocity varies quadratically with the distance $r$, which is typical for the incompressible flow from a point volume source. Whenever characteristic flow dimensions are small compared to the wave length we can neglect wave propagation. Such a flow is called a "compact" flow.

Using these results (58-59) we can now consider the sound radiated by a pulsating sphere of radius

$$a = a_0 + \widehat{a} \exp(i\omega t) \tag{61}$$

where $\widehat{a}/a_0 << 1$ and $\omega\widehat{a}/c_0 << 1$. Substituting (61) into (59) and using (58) we find:

$$i\omega\widehat{a} = \frac{A \exp(-ika_0)}{\rho_0 c_0 a_0} \left(1 + \frac{1}{ika_0}\right) \tag{62}$$

and

$$p' = -\frac{\rho_0 \omega^2 a_0 \widehat{a}}{(1 + (ka_0)^2)} (1 - ika_0) \left(\frac{a_0}{r}\right) \exp\left[i(\omega t - k(r - a_0))\right] \ . \tag{63}$$

This result shows that in the limit $ka_0 << 1$ for a given volume flux amplitude $4\pi a_0^2 \omega \widehat{a}$, the amplitude of the radiated sound wave increases linearly with the frequency. At low frequency the pulsating sphere is compact and is a very inefficient source of sound. In the opposite limit $ka_0 >> 1$ the radiated amplitude is independent of the frequency.

### 4.3 Acoustic energy

For further reference we now consider the acoustic energy. Following the original approach of Kirchhoff, we start from the linearized mass and momentum equations:

$$\frac{1}{c_0^2}\frac{\partial p'}{\partial t} + \rho_0 \nabla \cdot \vec{v}' = \frac{1}{T_0 \rho_0 c_0^2}\left(\frac{\partial p}{\partial s}\right)_\rho Q_w \tag{64}$$

and

$$\rho_0 \frac{\partial \vec{v}'}{\partial t} + \nabla p' = \vec{f}\,. \tag{65}$$

Then we multiply the mass conservation law by $p'/\rho_0$ and add the in-product of the momentum equation with the velocity $\vec{v}'$, to find:

$$\frac{\partial E}{\partial t} + \nabla \cdot \vec{I} = \frac{1}{(\rho_0 c_0)^2 T_0}\left(\frac{\partial p}{\partial s}\right)_\rho p' Q_w + \vec{v}' \cdot \vec{f} \tag{66}$$

with the acoustic energy density $E$ defined by :

$$E = \frac{1}{2}\rho_0 |\vec{v}'|^2 + \frac{(p')^2}{2\rho_0 c_0^2} \tag{67}$$

and the intensity $I$ defined by:

$$\vec{I} = p'\vec{v}'\,. \tag{68}$$

It should be noted that this derivation assumes that we did not neglect any relevant quadratic terms when using the linear approximation for the mass and momentum equation. This approach appears to be valid only for the case considered, i.e. of a uniform stagnant reference state [Morfey (1971), Landau and Lifchitz (1987), Pierce (1990), Myers (1991)].

Equation (66) clearly shows generating acoustic energy requires that a volume source should be placed at a position with a large acoustic pressure. A force needs an acoustic velocity to generate acoustic energy.

Considering a compact pulsating sphere near a rigid plane wave $kh << 1$ (Figure 3), we observe that due to reflection at the wall the amplitude of waves reaching an observer in the far field is roughly double the amplitude we would find in free space. Hence, the intensity is four times larger than in free space. However, the source only radiates into a half space, so that the time averaged power $< P >$ generated by the source is doubled. This result can also be understood as a result of the doubling of the pressure fluctuations surrounding the source, due to reflection at the wall, which, following our energy corollary doubles the generated power. This implies

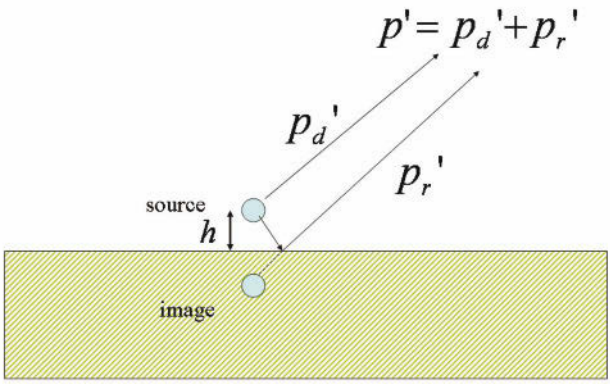


**Figure 3.** Influence of a rigid plane wall on the radiation of a compact sphere placed near the wall: $p' = p'_d + p'_r \approx 2p'_d \Rightarrow < P >= \frac{1}{2} 4\pi r^2 < I_r >= 2 \times 4\pi r^2 < \frac{(p'_d)^2}{\rho_0 c_0} >$

that the radiated power is doubled compared to free field conditions. This example stresses the fact that the sound power does not only depend on the source but also on the surroundings of the source.

### 4.4 Free space Green's function and integral formulation

Using the superposition principle we obtain an integral formulation of the wave equation for free space conditions. We first consider the sound generated by a pulse from a point source. This implies a localization in time and space, obtained by using the delta function. The delta function $\delta(t)$ is a generalized function defined by [Chrighton (1992)]:

$$\int_{-\infty}^{\infty} \delta(t) f(t) dt = f(0) \ . \tag{69}$$

For any well behaving function $f(t)$ and:

$$\int_{-\infty}^{\infty} \delta(t) dt = 1 \ . \tag{70}$$

The delta function has no meaning outside an integral. The free-field Green function $G_0(\vec{x}, t|\vec{y}, \tau)$ is the solution of the wave equation:

$$\frac{1}{c_0^2} \frac{\partial^2 G_0}{\partial t^2} - \nabla^2 G_0 = \delta(t - \tau)\delta(\vec{x} - \vec{y}) \tag{71}$$

where $\delta(\vec{x} - \vec{y}) = \delta(x_1 - y_1)\delta(x_2 - y_2)\delta(x_3 - y_3)$, for free-field boundary conditions and for the initial conditions:

$$G_0(\vec{x}, t|\vec{y}, \tau) = 0, \quad t \leq \tau \tag{72}$$

and

$$\frac{\partial}{\partial t} G_0(\vec{x}, t|\vec{y}, \tau) = 0, \quad t \leq \tau \tag{73}$$

corresponding to the causality condition that a wave cannot reach an observer before it has been emitted. In order to determine $G_0(\vec{x}, t|\vec{y}, \tau)$ we use the Fourier transform $\widehat{G}_0$ defined by:

$$G_0(\vec{x}, t|\vec{y}, \tau) = \int_{-\infty}^{\infty} \widehat{G}_0(\omega, \vec{x}|\vec{y}) \exp(i\omega t) d\omega \tag{74}$$

and

$$\widehat{G}_0(\omega, \vec{x}|\vec{y}) = \frac{1}{2\pi} \int_{-\infty}^{\infty} G_0(\vec{x}, t|\vec{y}, \tau) \exp(-i\omega t) dt \ . \tag{75}$$

As we consider the field generated by a point source in free-field conditions we know that the Fourier transform of the Green function is given by:

$$\widehat{G}_0(\omega, \vec{x}|\vec{y}) = \frac{A}{r} \exp(-ikr) \tag{76}$$

where $A$ is an amplitude which will be determined by using the properties of the delta function. We take the Fourier transform of the wave equation (71). Using the property (69) of the delta function:

$$\begin{aligned} &\tfrac{1}{2\pi}\int_{-\infty}^{\infty}\delta(t-\tau)\exp(-i\omega t)dt = \\ &= \tfrac{1}{2\pi}\int_{-\infty-\tau}^{\infty-\tau}\delta(t-\tau)\exp(-i\omega(t-\tau)-i\omega\tau)d(t-\tau) = \tfrac{\exp(-i\omega\tau)}{2\pi} \end{aligned} \tag{77}$$

we find:

$$-(k^2+\nabla^2)\widehat{G}_0 = \frac{\exp(-i\omega\tau)}{2\pi}\ . \tag{78}$$

We integrate this equation over a spherical volume $V$ of radius $R$ enclosing the source:

$$-\int_V (k^2+\nabla^2)\widehat{G}_0 dV = \frac{\exp(-i\omega\tau)}{2\pi}\ . \tag{79}$$

By taking the limit of a compact control volume $kR << 1$ and using the Gaussian Theorem we find:

$$-\int_s \frac{\partial\widehat{G}_0}{\partial r}dS = -4\pi R^2\ \frac{\partial\widehat{G}_0}{\partial r}\bigg|_{r=R} = 4\pi R^2\frac{A}{R^2} = \frac{\exp(-i\omega\tau)}{2\pi} \tag{80}$$

which yields the amplitude $A$. Substituting $A$ in (76) and transforming back to the time domain yields:

$$G_0(\vec{x},t|\vec{y},\tau) = \frac{\delta(\tau-t_e)}{4\pi r} \tag{81}$$

where the emission (retarded) time $t_e$ is defined by:

$$t_e = t - \frac{r}{c_0}\ . \tag{82}$$

Because Green's function in free-space only depends on the distance $r$ and time difference $(t-\tau)$, rather than on the source and observer's coordinates $(\vec{x},t)$ and $(\vec{y},\tau)$ separately, it satisfies the important symmetry properties:

$$G_0(\vec{x},t|\vec{y},\tau) = G_0(\vec{y},-\tau|\vec{x},-t) \tag{83}$$

and

$$\frac{\partial G_0}{\partial t} = -\frac{\partial G_0}{\partial \tau} \tag{84}$$

and

$$\frac{\partial G_0}{\partial x_i} = -\frac{\partial G_0}{\partial y_i}\ . \tag{85}$$

Equation (83) is the so-called reciprocity relation, which is also valid for Green's functions in the presence of walls.

We can now use the Green function to build the free-field solution of the non-homogeneous wave equation:

$$\frac{1}{c_0^2}\frac{\partial^2 p'}{\partial t^2} - \nabla^2 p' = q(\vec{x},t) \tag{86}$$

by using the superposition principle:

$$p'(\vec{x},t) = \int_{-\infty}^{t}\int_V q(\vec{y},\tau)G_0(\vec{x},t|\vec{y},\tau)dV_y d\tau = \int_V \frac{q(\vec{y},t_e)}{4\pi r}dV_y \tag{87}$$

where $dV_y = dy_1 dy_2 dy_3$.

Substitution of (87) into (86) and using the definition (71) of Green's function we can verify the validity of this solution.

In the presence of walls, we can still use the same free-field Green function. However, now the solution of the wave equation will include surface integrals representing the effect of reflections of waves at the walls. Using Green's theorem we have:

$$\begin{aligned} p'(\vec{x},t) = \quad & \int_{-\infty}^{t}\int_V q(\vec{y},\tau)G_0(\vec{x},t|\vec{y},\tau)dV_y d\tau \\ & - \int_{-\infty}^{t}\int_S \left[p'\nabla_y G_0 - G_0\nabla_y p'\right]\cdot\vec{n}dS_y d\tau \ . \end{aligned} \tag{88}$$

This integral formulation, in combination with Lighthill's analogy, yields the integral formulation of Curle (1955). The control volume is chosen such that it encloses the observation point $\vec{x}$. Note that in the literature the sign of the unit normal $\vec{n}$ is often chosen to be the opposite of the sign chosen here [Goldstein (1976), Dowling and Ffowcs Williams (1983)].

An alternative approach is the use of a so-called tailored Green function [Dowling and Ffowcs Williams (1983)]. This is a Green function defined by the wave equation (71) and the same (locally reacting linear) boundary conditions as the acoustic field under consideration. In that case the surface integrals of (88) vanish. An example of such a Green function for the trailing edge of a plate will be discussed in later chapters, Part 2.

### 4.5 Monopole, dipole and quadrupole

We consider radiation of a spatially limited source-region under free field conditions. Whenever the source region ($q(\vec{x},t) \neq 0$) is compact, we can neglect variations in the retarded time $t_e$ in the integral of equation (87).

Choosing the origin within the source region we get at distances large compared to the source region:

$$r = |\vec{x} - \vec{y}| \approx |\vec{x}| \tag{89}$$

and

$$t_e \approx t - \frac{|\vec{x}|}{c_0} \tag{90}$$

so that we have:

$$p'(\vec{x}, t) \approx \frac{1}{4\pi|\vec{x}|} \int_V q\left(\vec{y}, t - \frac{|\vec{x}|}{c_0}\right) dV_y \ . \tag{91}$$

We call the integral $\int_V q\left(\vec{y}, t - \frac{|\vec{x}|}{c_0}\right) dV_y$ the monopole strength of the source region. Whenever the source is the divergence of a force field $q(\vec{x}, t) = -\nabla \cdot \vec{f}$ integral (91) taken over a volume including the source region will vanish because the surface integral of the flux of the force field $\int_S \vec{f} \cdot \vec{n} dS_y = 0$ vanishes because $\vec{f} = 0$ on the surface. The surface, including the control volume, is outside the source region so that the force is either uniform or zero. By partial integration and using the symmetry property (83) we can write the formal solution of the wave equation as:

$$\begin{aligned} p'(\vec{x}, t) &= -\int_{-\infty}^{t} \int_V (\nabla_y \cdot \vec{f}(\vec{y}, \tau)) G_0(\vec{x}, t|\vec{y}, \tau) dV_y d\tau = \\ &= -\int_{-\infty}^{t} \int_V \vec{f}(\vec{y}, \tau) \nabla_x G_0(\vec{x}, t|\vec{y}, \tau) dV_y d\tau \ . \end{aligned} \tag{92}$$

As the integration over the source coordinates $\vec{y}$ does not interfere with the derivation by observer's coordinates $\vec{x}$ we have:

$$p'(\vec{x}, t) = -\nabla_x \cdot \int_{-\infty}^{t} \int_V \vec{f}(\vec{y}, \tau) G_0(\vec{x}, t|\vec{y}, \tau) dV_y d\tau \ . \tag{93}$$

For a compact source ($k|\vec{y}| << 1$ and distances large compared to the dimension of the source region ($|\vec{x}| >> |\vec{y}|$), we have a dipole field:

$$p'(\vec{x}, t) \approx -\nabla_x \cdot \left( \frac{1}{4\pi|\vec{x}|} \int_V \vec{f}\left(\vec{y}, t - \frac{|\vec{x}|}{c_0}\right) dV_y \right) \tag{94}$$

where $\left(\int_V \vec{f}\left(\vec{y}, t - \frac{|\vec{x}|}{c_0}\right) dV_y\right)$ is the dipole strength.
An alternative way to find this expression is to consider the solution $\phi_i$ of the wave equation:

$$\frac{1}{c_o^2} \frac{\partial^2 \phi_i}{\partial t^2} - \nabla^2 \phi_i = -f_i \tag{95}$$

following (87) this is simply:

$$\phi_i(\vec{x},t) = -\int_{-\infty}^{t}\int_V f_i(\vec{y},\tau)G_0(\vec{x},t|\vec{y},\tau)dV_y d\tau \ . \tag{96}$$

Obviously taking the divergence of equation 95 we also have:

$$\frac{1}{c_0^2}\frac{\partial^2(\partial\phi_i/\partial x_i)}{\partial t^2} - \nabla^2(\partial\phi_i/\partial x_i) = -\frac{\partial f_i}{\partial x_i} \tag{97}$$

which leads to equation (93) because $p'(\vec{x},t) = -\nabla\cdot\vec{\phi}$.

While a monopole can be represented as a pulsating compact sphere, a dipole field is generated by a compact translating sphere. In a similar way we can obtain for the sound source $\frac{\partial^2\rho v_i v_j}{\partial x_i \partial x_j}$ found in the analogy of Lighthill:

$$p'(\vec{x},t) = \frac{\partial^2}{\partial x_i \partial x_j}\int_{-\infty}^{t}\int_V \rho v_i v_j G_0(\vec{x},t|\vec{y},t)dV_y d\tau \ . \tag{98}$$

In a compact source region this is a so-called quadrupole field.

An alternative approach to the multipole expansion of the source [Goldstein (1976)] is to use a Taylor series expansion of the free space Green function around $\vec{y}=0$ in the general solution (87):

$$\begin{aligned} p'(\vec{x},t) = \textstyle\int_{-\infty}^{t}\int_V q(\vec{y},\tau)\Big[ & G_0(\vec{x},t\ 0,\tau) + \left(\tfrac{\partial G_0}{\partial y_i}\right)_{\vec{y}=0} y_i + \\ & + \tfrac{1}{2}\left(\tfrac{\partial^2 G_0}{\partial y_i \partial y_j}\right)_{\vec{y}=0} y_i y_j + ...\Big] dV_y d\tau \ . \end{aligned} \tag{99}$$

which, using the symmetry properties (85) of the Green's function and the far field approximation, yields:

$$\begin{aligned} & p'(\vec{x},t) \approx \tfrac{1}{4\pi|\vec{x}|}\textstyle\int_V q\left(\vec{y},t-\frac{|\vec{x}|}{c_0}\right)dV_y + \tfrac{x_i\partial}{4\pi|\vec{x}|^2 c_0\partial t}\int_V y_i q(\vec{y},t-\tfrac{|\vec{x}|}{c_0})dV_y + \\ & + \tfrac{x_i x_j}{4\pi|\vec{x}|^3}\tfrac{\partial^2}{c_0^2\partial t^2}\textstyle\int_V \frac{1}{2}y_i y_j q\left(\vec{y},t-\frac{|\vec{x}|}{c_0}\right)dV_y + ... \end{aligned} \tag{100}$$

An intuitive interpretation of monopole, diopole and quadrupole on surface water waves is provided in Figure 4. Due to the oscillating momentum in the region between the two monopoles forming a dipole it is obvious that a dipole cannot exist without any force acting on the fluid. This force is needed to change the momentum. Thus, unsteady force induces a dipole radiation and a dipole radiation cannot exist without a force acting on the fluid.

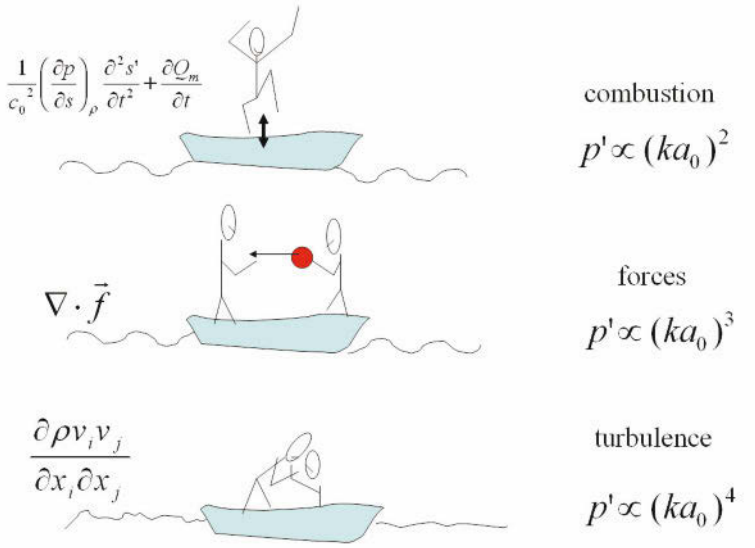


**Figure 4.** Intuitive interpretation of monopole, diopole and quadrupole on surface water waves. We provide a qualitative interpretation of physical realisations of monopole, dipole and quadrupole. Mass exchange between two monopoles with opposite phase implies an oscillating momentum. This is impossible without external force.

### 4.6 Analogy of Curle

The analogy of Curle (1955) is the integral formulation (88) applied to Lighthill's analogy (42) in terms of density fluctuations:

$$p'(\vec{x},t) = c_0^2 \rho'(\vec{x},t) = \int_{-\infty}^{t} \int_V \left( \frac{\partial^2 T_{ij}}{\partial y_i \partial y_j} - \frac{\partial f_i}{\partial y_i} \right) G_0(\vec{x},t|\vec{y},\tau) dV_y d\tau \\ -c_0^2 \int_{-\infty}^{t} \int_S \left[ \rho' \frac{\partial G_0}{\partial y_i} - G_0 \frac{\partial \rho'}{\partial y_i} \right] n_i dS_y d\tau \ . \tag{101}$$

The observer is placed within the control volume $V$ over which we carry out the integration. This equation is based on the assumption that at the listener's position $p' = c_0^2 \rho'$. We will further ignore the contribution from the external force field ($\vec{f} = 0$). By means of partial integration we move

the space derivatives from the source terms towards the Green function:

$$\begin{aligned} p'(\vec{x},t) = c_0^2 p' = \int_{-\infty}^{t} \int_V T_{ij} \frac{\partial^2 G_0}{\partial y_i \partial y_j} dV_y d\tau + \\ + \int_{-\infty}^{t} \int_S \left[ G_0 \frac{\partial T_{ij}}{\partial y_i} n_j - T_{ij} \frac{\partial G_0}{\partial y_j} n_i \right] dS_y d\tau - \\ - c_0^2 \int_{-\infty}^{t} \int_S \left[ \rho' \frac{\partial G_0}{\partial y_i} - G_0 \frac{\partial \rho'}{\partial y_i} \right] n_i dS_y d\tau \ . \end{aligned} \tag{102}$$

Using the definition of the viscous stress tensor (26) and the momentum equation (9) we can write (102) in the form:

$$\begin{aligned} p'(\vec{x},t) = c_0^2 p' = \int_{-\infty}^{t} \int_V T_{ij} \frac{\partial^2 G_0}{\partial y_i \partial y_j} dV_y d\tau + \int_{-\infty}^{\infty} \int_S G_0 \frac{\partial \rho v_i}{\partial t} n_i dS_y d\tau \\ - \int_{-\infty}^{t} \int_S \left( P_{ij} + \rho v_i v_j \right) \frac{\partial G_0}{\partial y_j} n_i dS_y d\tau + \int_{-\infty}^{t} \int_S \left( p' - c_0^2 \rho' \right) \frac{\partial G_0}{\partial y_i} n_i dS_y d\tau \ . \end{aligned} \tag{103}$$

Furthermore we neglect entropy fluctuations on the surface $S$.

By means of partial integration we move the time derivative in the second integral from the momentum flux to the Green's function. Using the symmetry relations of the free field derivative with respect to space (85) and time derivatives (84), we find in the far field approximation (60):

$$\begin{aligned} p'(\vec{x},t) = -\tfrac{1}{4\pi} \frac{\partial}{\partial t} \int_S \left[ \tfrac{\rho v_i}{r} \right]_{\tau = t_e} n_i dS_y - \\ - \tfrac{x_j}{4\pi |\vec{x}| c_0} \frac{\partial}{\partial t} \int_S \left[ \tfrac{P_{ij} + \rho v_i v_j}{r} \right]_{\tau = t_e} n_i dS_y + \\ + \tfrac{x_i x_j}{4\pi |\vec{x}|^2 c_0^2} \frac{\partial^2}{\partial t^2} \int_V \left[ \tfrac{T_{ij}}{r} \right]_{\tau = t} dV_y \ . \end{aligned} \tag{104}$$

In (104) we recognize the monopole sound production due to the volume flux leaving the surface (first integral), the dipole field generated by the force acting on the surfaces and the quadrupole field generated by fluctuations of the Reynolds stress tensor in the volume.

### 4.7 Doppler Effect

In Curle's formulation (section 4.6) we restricted ourselves to fixed control volumes. When considering sound produced by moving objects such as fan blades, it is more convenient to use a moving control volume. Ffowcs Williams and Hawkings (1969b) use generalized functions to take into account the motion of the sources, the result being a generalization of Curle's equation in which Doppler factors appear. In a further step Ffowcs Williams and Hawking [Goldstein (1976), Dowling and Ffowcs Williams (1983), Crighton et al. (1992)] introduce the boundaries of the control volume in the equation of motion, see next chapter. We now focus on the derivation

of the Doppler effect for point sources.
A moving point source is described by:

$$q(\vec{x},t) = Q(t)\delta(\vec{x} - \vec{x}_s(t)) \tag{105}$$

where $\vec{x}_s(t)$ is the position of the source. For free-field conditions we have:

$$p'(\vec{x},t) = \int_{-\infty}^{t}\int_{V} \frac{Q(\tau)\delta(\vec{y} - \vec{x}_s(\tau))\delta(\tau - t_e)}{4\pi r} dV_y d\tau \tag{106}$$

where $t_e = t - \frac{r}{c_0}$ and $r = |\vec{x} - \vec{y}|$. Using the properties of the delta function we get after spatial integration:

$$p'(\vec{x},t) = \int_{-\infty}^{t} \frac{Q(\tau)\delta\left(t - \tau - \frac{|\vec{x} - \vec{x}_s(\tau)|}{c_0}\right)}{4\pi|\vec{x} - \vec{x}_s(\tau)|} d\tau \tag{107}$$

This is an integral of the type:

$$\int_{-\infty}^{\infty} F(\tau)\delta(H(\tau))d\tau = \Sigma_i \frac{F(t_i)}{|\frac{dH}{d\tau}|_{\tau=t_i}} \tag{108}$$

with $H(t_i) = 0$. In the present case we have:

$$H(\tau) = t - \tau\frac{|\vec{x} - \vec{x}_s(\tau)|}{c_0} \tag{109}$$

so that:

$$\frac{dH}{d\tau} = -1 + \frac{\vec{x} - \vec{x}_s}{c_0|\vec{x} - \vec{x}_s(\tau)|} \cdot \frac{d\vec{x}_s}{d\tau} = -1 + M_r \tag{110}$$

where $M_r$ is the ratio of the source velocity component in the direction of the observer and the speed of sound. The sound field is given by:

$$p'(\vec{x},t) = \frac{Q(t_e)}{4\pi|1 - M_r||\vec{x} - \vec{x}_s(t_e)|} \tag{111}$$

where the emission time is the root of:

$$c_0(t - t_e) = |\vec{x} - \vec{x}_s(t_e)| \ . \tag{112}$$

For subsonic velocities there is only one root ($\tau = t_e$) of $H(\tau) = 0$. For a harmonically oscillating sound source with constant frequency $\omega$, the frequency of the signal reaching the observer is:

$$\frac{d\omega t_e}{dt} = \frac{\omega}{1 - M_r(t_e)} \tag{113}$$

because $\frac{dt_e}{dt} = \frac{1}{1-M_r(t_e)}$.

A further discussion of the Doppler Effect is provided in the next chapter, where it is shown that for supersonic Mach numbers, the sound source will have a strong radiation for directions such that $M_r = 1$. An example of such a radiation occurs when elastic bending waves in a plate propagate supersonically with respect to the surrounding fluid. As the velocity of propagation of bending waves increases with the frequency this occurs typically above a critical frequency $f_c$, which is called the coincidence frequency. This explains why we hear a high pitch when we hit a glass window.

From equation (111) we observe that in addition to the change in frequency we have an effect of the source motion on the amplitude reaching the observer. This effect can be understood as a result of the change in ratio of source size to acoustic wave length. From equation (63) we know that with increasing Helmholtz numbers the radiate sound amplitude of a compact object increases. In the direction of motion of the source, the emitted acoustic wave length is shorter by a factor $1 - M_r$, with an increased effective Helmholtz number as a result. In figure 5 we provide an intuitive interpretation of the Doppler shift in frequency.

Furthermore we note that for a moving object of volume $V$ the sound source is $q(\vec{x}, t) = \rho_0 \frac{d^2V}{dt^2} \delta(\vec{x} - \vec{x}_s(t))$. Hence we have:

$$p'(\vec{x}, t) = \rho_0 \frac{\partial^2}{\partial t^2} \left( \frac{V(t_e)}{4\pi |1 - M_r||\vec{x} - \vec{x}_s(t_e)|} \right) . \tag{114}$$

It shows that due to the time dependency of the retarded time $\partial t_e / \partial t$ an object of constant volume will radiate sound if its velocity varies. This is the so called thickness noise $p'_{th}$, which is very important in aircraft fans. In the far field approximation for a rigid of volume $V$ body moving at subsonic speed, we have:

$$p'_{th}(\vec{x}, t) \approx \rho_0 V \left( \frac{|1 - M_r| \frac{d^2 M_r}{dt_e^2} + 3 \frac{dM_r}{dt_e}}{4\pi |1 - M_r|^3 (1 - M_r)^2} \right) \frac{1}{|\vec{x} - \vec{x}_s(t_e)|} . \tag{115}$$

Another example is the sound radiated by a moving point force:

$$\vec{f} = \vec{F}(t) \delta(\vec{x} - \vec{x}_s(t)) \tag{116}$$

which is given by:

$$p'(\vec{x}, t) = -\nabla \cdot \left( \frac{\vec{F}(t_e)}{4\pi |\vec{x} - \vec{x}_s(t_e)||1 - M_r|} \right) . \tag{117}$$

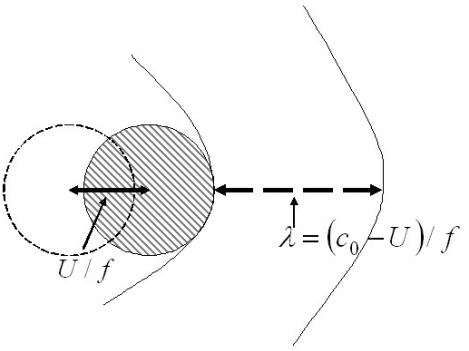


**Figure 5.** Intuitive interpretation of Doppler effect as a change in wave length $\lambda = \frac{c_0 - U}{f}$ of radiated wave due to the movement of the source with a velocity $U$ in the direction of the listener. The wave-length is reduced in the direction of the movement. This implies a reduction of the compactness of the source and leads to an increased radiation power.

In the far-field approximation we have:

$$p'(\vec{x},t) = -\frac{1}{1-M_r}\frac{(\vec{x}-\vec{x}_s(t_e))}{|(\vec{x}-\vec{x}_s(t_e))|}\cdot\frac{\partial}{\partial t_e}\left(\frac{\vec{F}(t_e)}{4\pi|\vec{x}-\vec{x}_s(t_e)||1-M_r(t_e)|}\right). \tag{118}$$

### 4.8 Influence of speed of sound gradient and of convective effects

Whenever a source of sound is compact we can separate the sound generation from the wave propagation. Even with this simplification the wave propagation remains extremely complex.

In the presence of flow and gradients in the speed of sound, acoustic

waves display complex propagation behaviour [Dowling 1983, Pierce 1990, Rienstra 1999]. An example of this is the sound propagation in the atmosphere. As a result of the non-uniformity of the temperature in the atmosphere waves are deflected from the straight path assumed in the elementary solutions for uniform stagnant fluid. An example being that a gun shot or thunder heard at large distances can be repeated multiple times, which yields a roll sound. This is due to the fact that sound can reach our ears along multiple paths.

We now consider a very basic problem of a plane wave that is reflected at the interface (shear layer) between two uniform media $a$ and $b$ with each having uniform flow speeds respectively $\vec{U}_a = (U_a, 0, 0)$ and $\vec{U}_b = (U_b, 0, 0)$ and speeds of sound $c_a$ and $c_b$ respectively.

In presence of a uniform flow the plane wave solution (52) becomes:

$$p'(\vec{x}, t) = A \exp\left(i\omega\left(t - \frac{\vec{x}\cdot\vec{n}}{c_0 + \vec{n}\cdot\vec{U}}\right)\right) = A \exp\left(i\left(\omega t - \vec{k}\cdot\vec{x}\right)\right) \quad (119)$$

with $\vec{n} = (\cos\theta, \sin\theta, 0)$ and $\vec{k} = \omega\vec{n}/(c_0 + \vec{n}\cdot\vec{U})$.

We assume an incident wave with amplitude $I$ and wave number $\vec{k}_I = \frac{\omega\vec{n}}{c_a + \vec{n}_I\cdot\vec{U}_a}$ in region $a$. This induces a reflected wave with amplitude $R$ and wave number $\vec{k}_R = \frac{\omega\vec{n}_R}{c_a + \vec{n}_R\cdot\vec{U}_a}$ and a transmitted wave with amplitude $T$ and wave number $\vec{k}_T = \frac{\omega\vec{n}_T}{c_b + \vec{n}_T\cdot\vec{U}_b}$ (Figure 6).

At the interface $x_2 = 0$ we have continuity of pressure so that for $x_2 = 0$ we have:

$$\begin{aligned} &I \exp\left(-\omega \tfrac{x_1 \cos\theta_I}{c_a + U_a \cos\theta_I}\right) + R \exp\left(-i\omega \tfrac{x_1 \cos\theta_R}{c_a + U_a \cos\theta_R}\right) = \\ &= T \exp\left(-i\omega \tfrac{x_1 \cos\theta_T}{c_b + U_b \cos\theta_T}\right) . \end{aligned} \quad (120)$$

As this equation should hold for any value of the coordinate $x_1$ (along the shear layer) the exponents should be identical:

$$\left(\frac{\cos\theta_I}{c_a + U_a\cos\theta_I}\right) = \left(\frac{\cos\theta_R}{c_a + U_a\cos\theta_R}\right) = \left(\frac{\cos\theta_T}{c_b + U_b\cos\theta_T}\right) . \quad (121)$$

The first equality of (121) implies that $\cos\theta_1 = \cos\theta_R$, so that the reflection angle is equal to the incidence angle $\theta_R = -\theta_I$.
The second equality of (121) yields the modified Snelius law:

$$\frac{c_a}{\cos\theta_I} + U_a = \frac{c_b}{\cos\theta_T} + U_b \quad (122)$$

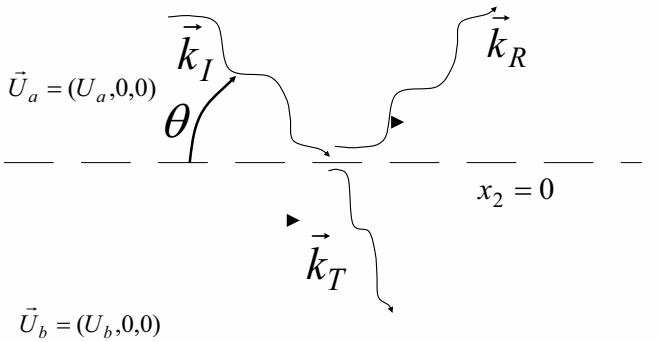


**Figure 6.** Reflection and refraction of a plane wave at a flat shear layer $x_2 = 0$ separating two uniform flows.

or:

$$\cos\theta_T = \frac{c_b \cos\theta_I}{c_a + (U_a - U_b)\cos\theta_I)} \ . \tag{123}$$

The maximum transmission angle is found for grazing incidence $\cos\theta_I = 1$: In the particular case of $c_a = c_b$ and $U_b = 0$ we find:

$$(\theta_T)_{max} = arcos\left(\frac{1}{1 + (U_a/c_a)}\right) \tag{124}$$

In high speed jets one does indeed observe a cone of silence along the axis of the jet, because the acoustic waves emitted along the main flow direction are bent away from the flow direction by the velocity gradient in the shear layers [Morfey (1978)].

The amplitude of the transmitted and reflected waves is calculated from the continuity of pressure at the interface $I + R = T$ complemented by the continuity of particle displacement at the interface.

# 5 Turbulence noise at low Mach numbers

## 5.1 Isothermal free jet

Considering the sound production of a turbulent free jet. This is the flow with a velocity $U_0$ at the outlet of a pipe of diameter $D$. Turbulence is an unsteady chaotic fluid motion which appears when viscous forces are small compared to non-linear convective forces. This corresponds to high Reynolds numbers $Re_D = U_0 D/\nu$. We limit ourselves to a low Mach number flow $M = U_0/c_0 \ll 1$ of an air jet surrounded by air with the same temperature as its surroundings. The prediction of the scaling rule between the power of this sound source and the Mach number was a major success of the theory of Lighthill (1952-54). As stressed by Powell (1990), the scaling law was predicted before it was corroborated by experiments. The steps taken by Lighthill were, however, quite intuitive and justification of some of these steps came only long after the original publication [Morfey (1973),(1976),(1978), Obermeier (1975)]. We now follow the Lighthill prodecure [1954].

Firstly Lighthill assumes that there are no external forces working on the flow and that the effect of walls can be neglected. In free field conditions equation (99) simplifies to:

$$\begin{aligned} p'(\vec{x},t) &= c_0^2 \rho' \int_{-\infty}^{t} \int_V T_{ij} \frac{\partial^2 G_0}{\partial y_i \partial y_j} dV_y d\tau = \\ &= \frac{\partial^2}{\partial x_i \partial x_j} \int_{-\infty}^{t} \int T_{ij} \frac{\delta\left(t-\tau-\frac{r}{c_0}\right)}{4\pi r} dV_y d\tau \ . \end{aligned} \tag{125}$$

This implies that the solution we are seeking for is, at most, a quadrupole field. In fact, we have imposed this by assuming that there are no external forces acting on the fluid and the potential monopole sources were neglected. Please note that in the analogy of Lighthill, $\rho'$ is used as aeroacoustical variable. In the next section we will discuss why this choice can be important. Carrying the time integration and using the far field approximation we find:

$$p'(\vec{x},t) = c_0^2 \rho' = \frac{x_i x_j}{|\vec{x}|^2 c_0^2} \frac{\partial^2}{\partial t^2} \int_V \frac{T_{ij}(\vec{y}, t - \frac{r}{c_0})}{4\pi r} dV_y \ . \tag{126}$$

The sound appears to be produced mainly by large coherent vortex structures with a length scale of the order of the pipe diameter $D$. For such scales the Reynolds number is large. We therefore expect the Reynolds stress tensor $\rho v_i v_j$ to be much larger than the viscous stress tensor $\tau_{ij}$ [Morfey (1976)]. Furthermore, at low Mach numbers variations in temperature and density are negligible [Morfey (1973), Morfey et al. (1978)], which implies that we

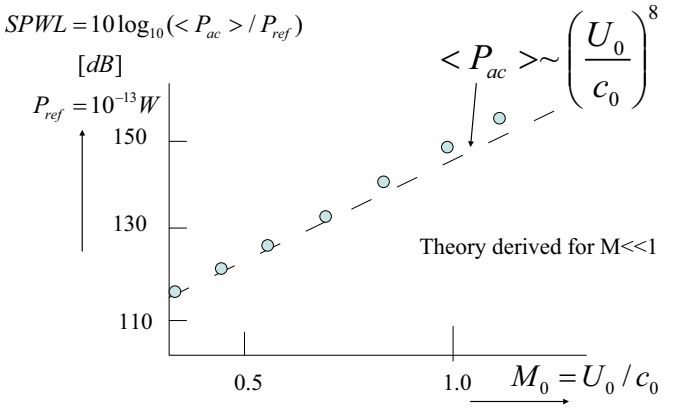


**Figure 7.** Overall acoustic sound power level (OAPWL) of the sound radiation from an isothermal free jet as a function of the jet Mach number: comparison of theory with experimental results [Fisher et al. (1973),Viswanathan (2009)].

can use the approximation proposed by Lighthill (1952-54):

$$T_{ij} \approx \rho_0 v_i v_j \ . \tag{127}$$

For a circular jet cross section the dominant frequency corresponds to a Strouhal number of unity. Hence the dominating frequency is $U_0/D$ and the corresponding acoustic wavelength is $D/M = Dc_0/U_0$. The sound source has a volume $V$ of the order of $D^3$. At low Mach numbers the sound source is small compared to the wave length. This implies that we can neglect variations of the retarded time in the integral (126): $r = |x - \vec{y}| \approx |\vec{x}|$. Summarizing we use the scaling rules:

$$\frac{\partial}{\partial t} \sim \frac{U_0}{D} \tag{128}$$

$$T_{ij} \sim \rho_0 U_0^2 \tag{129}$$

$$V \sim D^3 \ . \tag{130}$$

Substitution in (126) yields:

$$p' \sim \frac{\rho_0 U_0^4}{c_0^2} \left( \frac{D}{r} \right) \ . \tag{131}$$

In terms of sound source power $< P >= 4\pi r^2 \frac{(p')^2}{\rho_0 c_0}$ we have:

$$\frac{< P >}{\frac{1}{2}\rho_0 U_0^3 \frac{\pi D^2}{4}} \sim 32 M^5 \tag{132}$$

where we assumed an isotropic radiation pattern. This famous global scaling rule of Lighthill (1952-54) appears to be valid up to Mach numbers of order unity. At these high Mach numbers the radiation pattern has a high forward directivity due to the Doppler effect and, due to refraction of sound by the shear layers, it displays a cone of silence around the axis. The fact that the theory remains valid up to relatively high Mach numbers can be partially explained by the fact that the convection velocity $U_c$ of the vortices in the jet is only a fraction of the main flow velocity [Crighton et al. (1992)]. Typically we have $U_c/U_0 \approx 0.3$. Recent discussions on jet noise are Morris and Farassat (2002) and Viswanathan (2009) as well as the discussion in Part 2.

Obviously, by increasing the Mach number, the scaling law of Lighthill fails simply because the radiated power would become larger than the available jet power $\frac{1}{2}\rho U_0^3 \frac{\pi D^2}{4}$. Also the sound production mechanism changes drastically. The sound radiation from supersonic jets above $M = 3$ is largely due to hydrodynamic shear waves which display highly directional radiation patterns. Entropy effects due to temperature differences in the flow also become very important. In a supersonic flow the temperature typically varies from the stagnation temperature $T_t$ to the isentropic expansion temperature $T = T_t/(1 + (\gamma - 1)M^2/2)$. Starting from room temperature $T_t \approx 300K$ in the reservoir, $M = 3$ implies a main flow temperature $T \approx 100K$. Obviously, such a flow is not isothermal and we can use many different definitions of the temperature or Mach numbers to characterize the flow [Viswanathan (2009)].

Finally, most supersonic jet are either over- or underexpanded, and therefore display standing shock structures, which interact with vortices (turbulence) that give strong sound radiation. In some cases, this leads to spectacular self-sustained oscillation (jet screetch).

Note that approximation (128) is based on the fact that in a circular jet the characteristic Strouhal number for the sound production is of order unity $Sr_D = Df/U = 0(1)$. In a planar jet of thickness $H$ we find

$Sr_H = Hf/U = 0(10^{-1})$, which again stresses that the assumptions are not trivial [Bjørnø et al. (1984)].

Turbulence noise is essential because, when all other sound sources have been suppressed, this will always remain as the minimum remaining noise production which we can achieve. Lighthill's scaling law indicates that the most efficient way to reduce this noise is to reduce the flow velocity. The result derived for free-field conditions remains valid for confined flow. In the absence of resonances, one finds at low frequencies in a pipe $p' \sim \rho_0 U_0^3/c_0$ and $< P > \sim M^6$.

It is important to stress again that the analogy of Lighthill does not impose the quadrupole character of the source. Because we neglected the monopoles (no heat sources and negligible variation in density) and the dipoles (no external force acting on the "free" jet), the source has at most, a quadrupole character. Based on the integral formulation (126) the procedure imposes this assumed quadrupole character on the solution. So even if the applied model predicting the stress tensor $T_{ij}$ does involve density fluctuations and external forces, the formulation ensures that these contributions are ignored. This explains the success of such analogies [Schram and Hirschberg (2003)]. They filter out spurious sound sources due to errors in the estimation of the stress tensor $T_{ij}$.

### 5.2 Bubbly liquids

In the previous sections we used the analogy of Lighthill (1952-54) to obtain a scaling law for sound production by subsonic isothermal free jets. One of the choices in this derivation is to express the analogy in terms of fluctuations of density $\rho'$ (equation 40). As an alternative, we could have also used the fluctuations of pressure $p'$ (equation 39). In principle both formulations are equivalent as long as no approximations are involved. However, an analogy is only meaningful if we do use approximations. Depending on the choice of the aero-acoustic variable some approximations will appear naturally. For example using the pressure formulation, the entropy noise source term has the form $\partial^2(p'/c_0^2 - \rho')/\partial t^2$. This is a monopole sound source, to be understood as the time dependent volume expansion due to unsteady combustion. A more detailed analysis of thermal effects is provided by Morfey et al. (1978) and Dowling [in, Crighton et al. (1992)]). Using the density formulation, the entropy sound source term is a spatial derivative $\partial^2(p' - c_0^2\rho')/\partial x_i^2$. We will now explain the physical meaning of this apparently obscure sound source term. For this we consider the sound

produced by a turbulent free jet in a bubbly liquid, as observed by a listener immerged in the pure liquid. In such a case the speed of sound $c$ in the source region is much lower than the speed of sound $c_0$ of the fluid surrounding the listener.

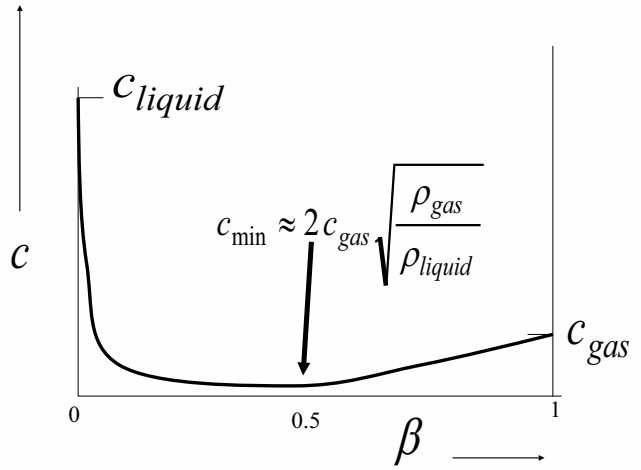


**Figure 8.** Low frequency limit of the speed of sound in a bubbly liquid as a function of the gas volume fraction [Crighton et al. (1992)].

Considering the low frequency limit of the behaviour of a mixture of gas bubbles and a liquid (Figure 8). We find that low frequency implies that gas density $\rho_g$ and fluid density $\rho_l$ are both uniform so that the mixture density $\rho$ is given by [Crighton et al. (1992)]:

$$\rho = \beta\rho_g + (1-\beta)\rho_l \tag{133}$$

where $\beta$ is the volume fraction of gas in the mixture. Assuming a quasi-steady behaviour, the pressure is uniform. Thus, we can add the compressibility of the two phases to obtain the compressibility of the mixture:

$$\frac{1}{\rho c^2} = \frac{\beta}{\rho_g c_g^2} + \frac{(1-\beta)}{\rho_l c_l^2} \tag{134}$$

where $c_g$ is the speed of sound in gas and $c_l$ is the speed of sound in liquid.

Eliminating the density by multiplying (133) by (134) yields:

$$c^2 = \frac{1}{[\beta\rho_g + (1-\beta)\rho_l]\left[\frac{\beta}{\rho_g c_g^2} + \frac{(1-\beta)}{\rho_l c_l^2}\right]} \ . \tag{135}$$

For air/water mixtures at neither too small or too large a value of $\beta$ we can neglect both the contribution of air to the mass density and the contribution of water to the compressibility. We then get:

$$c^2 \approx \frac{1}{[(1-\beta)\rho_l]\left[\frac{\beta}{\rho_g c_g^2}\right]} = c_g^2 \left(\frac{\rho_g}{\rho_l}\right) \frac{1}{\beta(1-\beta)} \ . \tag{136}$$

For air with ($\rho_g = 1.2kg/m, c_g = 340m/s$) and water with ($\rho_l = 1000kg/m$, $c_l = 1500m/s$) we get a minimal speed of sound $c_{min} \approx 20m/s$ at $\beta = 0.5$ . The entropy term in the analogy of Lighthill for an isentropic flow can be written as follows:

$$\frac{\partial^2}{\partial x_i^2}(p' - c_0^2\rho') = \frac{\partial^2}{\partial x_i^2} p' \left(1 - \frac{c_0^2}{c^2}\right) \ . \tag{137}$$

The pressure fluctuations in the source region are of the same order as the fluctuations in the Reynolds stress tensor: $p' \sim \rho U^2$. Hence, compared to a free jet of water surrounded by water, the bubbly liquid turbulence sound is enhanced by a factor $|(1 - c_0^2/c^2)| = 5 \times 10^3$, which is 74 dB. Infact, taking a shower in a bath tub, we observe that the water jet impinging on the water surface is much noisier than the jet immerged in the water, as we can understand qualitatively in terms of the analogy of Lighthill. According to Morfey (1973) and Powell (1990) this entropy term can be understood as the sound produced by the unsteady force exerted on the mixture as a result of the "buoyancy" force due to the difference in density between the two phases undergoing a pressure gradient. This corresponds to a slip between the two phases. Obviously, as there are no net external forces, this sound source must be a quadrupole, the force of the gas on the liquid being balanced by the reaction force of the liquid on the gas.

Similar effects, though much weaker can be found in non-isothermal gas free jets. Contrary to earlier literature predicting a dipole [Morfey (1973), Obermeier (1975)], recent studies indicate that the overall acoustic power level radiated by hot jets is also in line with the height power law of Lighthill [Viswanathan (2009)], which actually confirms that this sound source is also a quadrupole. In the early literature it was also suggested that next to convection effects due to density differences, the heat transfer between a hot

gas free jet and its surroundings would generate a monpole sound source. In cases with ideal gasses and a uniform constant Poisson ratio $\gamma$, this does not occur due to the jet contraction by cooling compensating exactly expansion of the surroundings due to heating [Morfey and Wright (2007)]. Monopole sound sources do occur as a result of combustion or phase transition (moisture condensation).

Bubble resonance can induce an even larger amplification of turbulent sound production [Dowling and Ffowcs Williams (1983)]. Yet, it is argued by Crighton (1975) that typical turbulent eddies corresponding to frequencies close to resonance frequencies of bubbles are much smaller than the bubbles and can therefore not excite the bubbles coherently. He therefore uses the low frequency approximation described above.

## 6 Waves in pipes

### 6.1 Pipes modes

We are considering propagation of harmonic waves $p' = \hat{p}\exp(i\omega t)$ in a duct with a uniform rectangular cross section, with the duct axis is in the $x_3$ direction. The duct is delimited by rigid walls in the planes: $x_1 = 0, x_1 = h_1, x_2 = 0, x_2 = h_2$ (Figure 9). For such harmonic waves the wave equation

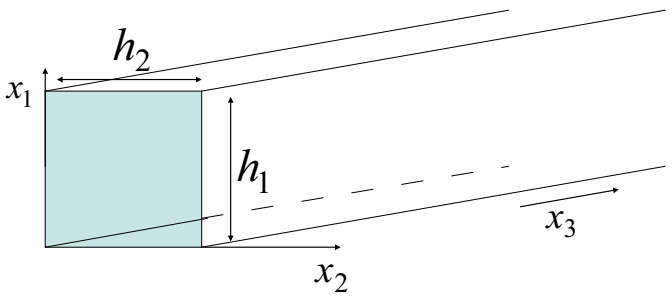


**Figure 9.** Duct with rectangular cross section.

(47) can be written as:

$$\left[k_0^2 + \frac{\partial^2}{\partial x_1^2} + \frac{\partial^2}{\partial x_2^2} + \frac{\partial^2}{\partial x_3^2}\right] \hat{p} = 0 \ . \tag{138}$$

This is the Helmholtz equation.
Seeking a solution by using the method of separation of variables:

$$\hat{p} = F(x_1)G(x_2)H(x_3) \ . \tag{139}$$

and substituting (139) in (138) we get:

$$k_0^2 + \frac{1}{F}\frac{d^2F}{dx_1^2} + \frac{1}{G}\frac{d^2G}{dx_2^2} + \frac{1}{H}\frac{d^2H}{dx_3^2} = 0 \ . \tag{140}$$

As this equation should be valid for any value of $\vec{x} = (x_1, x_2, x_3)$ each factor in (140) should be constant:

$$\frac{1}{F}\frac{d^2F}{dx_1^2} = -\alpha^2 \ . \tag{141}$$

$$\frac{1}{G}\frac{d^2G}{dx_2^2} = -\beta^2 \tag{142}$$

and

$$\frac{1}{H}\frac{d^2H}{dx_1^2} = -\left[k_0^2 - \alpha^2 - \beta^2\right] \ . \tag{143}$$

The constants $\alpha$ and $\beta$ are determined by the boundary conditions of zero normal velocity at the rigid walls. The normal component of the pressure gradient, which is proportional to this normal velocity, vanishes at the walls:

$$\left(\frac{dF}{dx_1}\right)_{x_1=0} = \left(\frac{dF}{dx_1}\right)_{x_1=h_1} = 0 \tag{144}$$

and

$$\left(\frac{dG}{dx_2}\right)_{x_2=0} = \left(\frac{dG}{dx_2}\right)_{x_2=h_2} = 0 \tag{145}$$

From this we can conclude that the possible solutions for $F$ and $G$ have the form:

$$F_m = \cos(\alpha_m x_1) \ \ ; \ \ \alpha_m = \frac{m\pi}{h_1} \ \ ; \ \ m = 0, 1, 2, 3, ... \tag{146}$$

and

$$G_n = \cos(\beta_n x_2) \ \ ; \ \ \beta_n = \frac{n\pi}{h_2} \ \ ; \ \ n = 0, 1, 2, 3, ... \tag{147}$$

Substitution in equation (143) yields:

$$\frac{1}{H_{mn}}\frac{d^2H_{mn}}{dx_1^2} = -\left[k_0^2 - \alpha_m^2 - \beta_n^2\right] = -k_{mn}^2 \ . \tag{148}$$

There are two types of solution, depending on the sign of $k_{mn}^2$. For positive values we have propagating wave modes:

$$\hat{p}_{mn}^{\pm} = \cos\left(\frac{m\pi}{h_1}x_1\right)\cos\left(\frac{n\pi}{h_2}x_2\right)\exp(\mp i|k_{mn}|x_3) \tag{149}$$

and for negative values we have evanescent modes:

$$\hat{p}_{mn}^{\pm} = \cos\left(\frac{m\pi}{h_1}x_1\right)\cos\left(\frac{n\pi}{h_2}x_2\right)\exp(\mp|k_{mn}|x_3) \tag{150}$$

with

$$|k_{mn}| = \left|\sqrt{k_0^2 - \left(\frac{m\pi}{h_1}\right)^2 - \left(\frac{n\pi}{h_2}\right)^2}\right| \tag{151}$$

The solution we are looking for is a linear superposition of these modes:

$$p' = \left(\sum_{m=0}^{\infty}\sum_{n=0}^{\infty}\left(A_{mn}^{+}\hat{p}_{mn}^{+} + A_{mn}^{-}\hat{p}_{mn}^{-}\right)\right)\exp(i\omega t) \tag{152}$$

where the amplitudes of the modes are determined by the boundary conditions at the boundaries of the duct in the $x_3$ direction. For each mode there is a cut off frequency $(\omega_{mn})_c$ below which the mode is evanescent. For example for the mode $\hat{p}_{10}$ we have:

$$(\omega_{10})_c = \frac{\pi c_0}{h_1} \ . \tag{153}$$

The duct width should be larger than half the wave length to allow propagation of this first higher-order mode. The mode $\hat{p}_{00}$ is the plane wave mode and will always propagate.

Evanescent waves do not propagate energy. They decay exponentionally with the distance along the duct. In the low frequency limit $\omega \ll (\omega_{mn})_c$ the pressure perturbation due to an evanescent mode will decay faster than $\exp\left(-\frac{m\pi}{h_1}x_1\right)$. For mode (1,0) a distance $h_1$ is sufficient for a decay by a factor $\exp(\pi) \approx 23$. All other higher-order modes will decay even faster.

Hence, the acoustic field will be dominated by plane waves in the low frequency limit for distances larger than the duct width away from discontinuities . This result will be applied in the following sections.

In this discussion we have neglected damping. In ducts damping due to visco-thermal losses at the walls is usually dominant. These effects on acoustical wave propagation are discussed in Pierce (1990), Bruneau (2006) and Rienstra and Hirschberg (1999). Damping, in presence of flow, has been extensively studied by Ronneberger and Ahrens (1977), Peters et al. (1993), Howe (1998) and Allam and Abom (2005).

### 6.2 Reflection at pipe discontinuities at low frequencies

We are looking at the reflection and transmission of plane acoustic waves at an abrupt transition at $x = 0$ between a pipe with uniform cross-section $S_1(x < 0)$ and another with uniform cross-section $S_2(x > 0)$ (Figure 10). Assuming that small perturbations of a stagnant fluid, as described by the

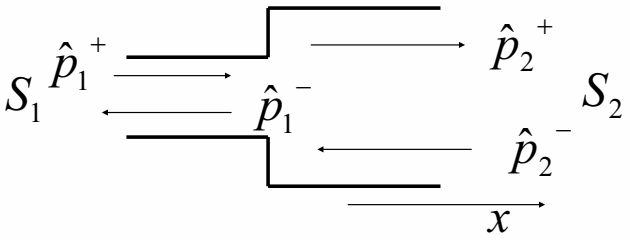


**Figure 10.** Reflection and transmission of waves at a pipe discontinuity.

linearized mass and momentum equations (44 and 45), the integral formu-

lation of the mass equation can be applied:

$$\frac{d}{dt}\int_V \rho' dV + \int_S \rho_0 \vec{v}' \cdot \vec{n} dS = 0 \tag{154}$$

to a volume $V$ enclosed by the fixed surface $S$ with outer unit normal vector $\vec{n}$. The surface $S$ is chosen to enclose the pipe discontinuity and cut the pipes at a distance of the order of the pipe diameter from the discontinuity. As explained in the previous section, the acoustic field in the pipes is dominated at low frequences by the plane travelling waves. This implies that the acoustic field is given by:

$$p'_i = p_i^+ \exp(-ik_0 x) + p_i^- \exp(ik_0 x) \tag{155}$$

where the index $i = 1$ corresponds to the $x < 0$ and $i = 2$ to $x > 0$. Using equation (53) we have:

$$S_1(p_1^+ - p_1^-) - S_2(p_2^+ - p_2^-) \sim \left(\frac{\omega}{c_0}\frac{V}{S_1}(p_1^+ + p_1^-)\right) \tag{156}$$

At low frequency the volume flux across the pipe discontinuity is constant and the flow is locally incompressible.
Assuming, $\vec{f} = 0$ and integrating the momentum equation (45) along the x-axis, we get the linearized Bernoulli equation:

$$\rho_0 \frac{d}{dt}\int_{x_1}^{x_2} v'_x dx = p'(x_1) - p'(x_2) \ . \tag{157}$$

In terms of plane waves we have:

$$p_1^+ + p_1^- - (p_2^+ + p_2^-) \sim \left(\frac{\omega}{c_0}\frac{V}{S_1}(p_1^+ - p_1^-)\right) \tag{158}$$

which implies that, at low frequencies $\omega V/(c_0 S_1) << 1$, the pressure is continuous across the pipe discontinuity.
Thus, we have:

$$S_1(p_1^+ - p_1^-) = S_2(p_2^+ - p_2^-) \tag{159}$$

and

$$p_1^+ + p_1^- = p_2^+ + p_2^- \ . \tag{160}$$

In the form of a scattering matrix we get:

$$\begin{bmatrix} p_1^- \\ p_2^+ \end{bmatrix} = \frac{1}{S_1 + S_2}\begin{bmatrix} S_1 - S_2 & 2S_2 \\ 2S_1 & S_2 - S_1 \end{bmatrix}\begin{bmatrix} p_1^+ \\ p_2^- \end{bmatrix} \ . \tag{161}$$

For an anechoic (non-reflecting) pipe termination of segment 2 ($p_2^- = 0$) we have a reflection coefficient $R = p_1^-/p_1^+ = (S_1 - S_2)/(S_1 + S_2)$ and a transmission coefficient $T = p_2^+/p_1^+ = 2S_1/(S_1 + S_2)$. For the limit $S_2 \gg S_1$ we find the ideal open-end behaviour $R = -1$ and $T = 0$. The acoustic flow from pipe segment 1 cannot change the pressure in the much wider pipe segment 2, so that $p_1^+ + p_1^- = 0$. The outflow corresponding to a positive incoming pressure wave produces an under-pressure at the pipe outlet which propagates into the pipe as a reflected wave with negative amplitude wave. In the opposite limit $S_2 \ll S_1$, $R = 1$ because the acoustic flux meets a closed pipe termination causing into a positive wave travelling back $p_1^+ - p_1^- = 0$, the result being that the pressure at the end of section 1 is twice as high. Hence, the transmission coefficient is $T = 2$. One can check by using the energy equation that this transmitted wave does not carry any energy in the limit $S_2/S_1 \Rightarrow 0$.

### 6.3 Open pipe termination in quiescent fluid

In the ideal open pipe termination limit discussed in the previous section, the radiation of sound from the open pipe termination was ignored.
This is the very low frequency limit. With increasing the frequency we get deviations. Firstly the inertia of the oscillating acoustic flow outside the pipe, around the open end, which implies that there is a finite pressure at the outlet of the pipe supplying the force needed for the acceleration of the fluid. As discovered by Bernoulli, this effect can be accounted for by assuming that the wave reflection occurs at a small distance $\delta$ outside the pipe. This is called the end correction [Rayleigh (1954), Pierce (1990), Dowling and Ffowcs Williams (1983)]. The exact value of this end correction depends strongly on the geometry of the pipe termination. Whilst we get in the low frequency limit $\delta = 0.61a$ [Levine and Schwinger (1948)] for a pipe with a radius $a$ and infinitely thin walls (unflanged pipe) we get $\delta = 0.82a$ for a flanged pipe (pipe end flush with a flat wall) [Morse and Ingard (1968), Peters et al. (1993)]. The order of magnitude of this end correction can be estimated by considering the pulsation of a sphere of radius $a_0$. The end correction corresponds to the part of the solution (63) for the pressure field which does not carry energy (not in phase with $i\omega\hat{a}$):

$$p' = -\frac{\rho_0\omega^2 a_0\hat{a}(1 - ika_0)}{(1 + (ka_0)^2)}\left(\frac{a_0}{r}\right)\exp\left[i(\omega t - k(r - a_0))\right] \ . \tag{162}$$

We find $\delta = a_0$. Another way to look at this is to consider the incompressible part of the acoustic velocity ($v_r = i\omega\hat{a}(a_0/r)^2\exp(i\omega t)$) associated with the pulsation of the sphere and to integrate the radial component of the

momentum ($\rho_0(\partial v_r'/\partial t = -(\partial p'/\partial r)$) to calculate the associated pressure on the surface of the sphere $\hat{p}(a_0) = \int_{a_0}^{\infty} \rho_0\omega^2\hat{a}(a_0/r)^2 dr = \rho_0\omega^2\hat{a}a_0$. It shows that for a 3-D radial flow the end correction is determined by the near field, which is incompressible.

This does not apply to a two-dimensional flow through a slit. Assuming an incompressible flow would result in an infinite large end correction, the near field is essentially compressible [Lesser and Lewis (1972)]. This illustrates the complexity of two-dimensional acoustic fields, as is discussed in Dowling and Ffowcs Williams (1983). In practice, this means that the use of a two-dimensional model for an unbounded flow can lead to unrealistically large radiation losses.

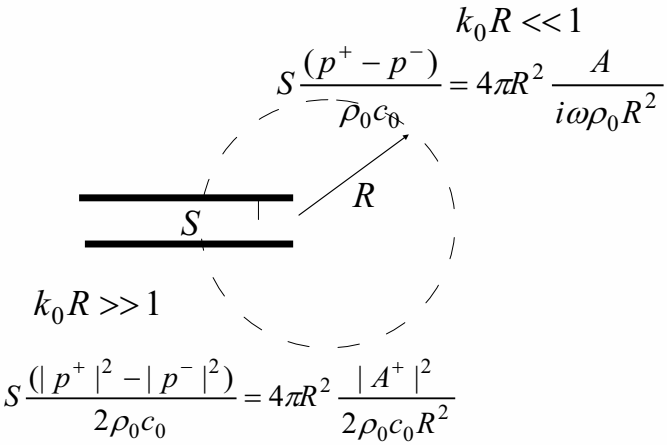


**Figure 11.** Sound radiation from a compact open unflanged pipe termination.

The fact that we hear music generated by a wind instrument is a clear demonstration that waves are radiated by the open pipe terminations (Figure 11). We now estimate the amplitude of these waves by coupling a plane wave propagation model in the pipe with a spherical wave emerging from the pipe termination. We assume that the frequency is so low that one can neglect compressibility in the region of the transition from plane waves to spherical waves.

In this case the mass conservation law implies:

$$S_p v'_x = 4\pi R^2 v'_r \tag{163}$$

where $S_p$ is the pipe cross sectional area and $R$ is the distance chosen such that it is small compared to the acoustic wave length, but large compared to the pipe radius ($R > \sqrt{S_p}$). In terms of plane waves amplitude and spherical wave amplitude we have:

$$S_p(p_1^+ - p_1^-) = 4\pi R^2 \frac{A}{R}\left(1 + \frac{1}{ik_0R}\right)\exp(-ik_0R) \approx -i4\pi\frac{A}{k_0} \ . \tag{164}$$

The conservation of acoustic energy over the same control volume yields:

$$S_p(|p_1^+|^2 - |p_1^-|^2) \approx 4\pi\frac{|A|^2}{k_0^2} \tag{165}$$

neglecting the phase of the waves and combined with (164) this implies:

$$\frac{Z_r}{\rho_0 c_0} = \frac{1-R}{1+R} = \frac{(k_0 a)^2}{4} \ . \tag{166}$$

For a flanged pipe termination we have :

$$\frac{Z_r}{\rho_0 c_0} = \frac{1-R}{1+R} = \frac{(k_0 a)^2}{2} \ . \tag{167}$$

Reflections on the flange (wall) double the radiation power (Figure 3).

### 6.4 Convective effects on reflection from an open pipe termination

Until now it was assumed that the fluid in the pipe is stagnant. Now we will consider the influence of a uniform, steady outgoing flow $U_p$ in the pipe on the acoustic response of the pipe termination. For plane waves the convected d'Alembert solution is:

$$p' = p^+ \exp\left(i\omega\left(t - \frac{x}{c_0 + U_p}\right)\right) + p^- \exp\left(i\omega\left(t + \frac{x}{c_0 - U_p}\right)\right) \ . \tag{168}$$

Through substitution in the linearized momentum equation:

$$\rho_0\left(\frac{\partial u'}{\partial t} + U_p\frac{\partial u'}{\partial x}\right) = -\frac{\partial p'}{\partial x} \tag{169}$$

we get:

$$u' = \frac{p^+}{\rho_0 c_0} \exp\left(i\omega\left(t - \frac{x}{c_0 + U_p}\right)\right) - \frac{p^-}{\rho_0 c_0} \exp\left(i\omega\left(t + \frac{x}{c_0 - U_p}\right)\right) \quad (170)$$

Looking at a pipe of a uniform cross section $S_p$, terminated by an orifice plate with opening $S_0$. The flow leaves the pipe through the orifice forming a free jet downstream of the pipe, which contracts slightly after leaving the orifice to reach a minimum cross section $S_j$ before mixing with the surrounding air. The pressure at the minimum cross section in the jet is equal to the pressure of the surroundings. Typically, the contraction factor is $S_j/S_0 = 0.7$ for a thin orifice plate with sharp edges. In the low frequency limit we can describe the flow by using the integral mass conservation law:

$$\rho_p U_p S_p = \rho_j U_j S_j \ . \quad (171)$$

The integration of the momentum equation in the quasi-static approximation, neglecting friction and heat transfer and assuming an irrotational flow (equations 35 and 37) yields:

$$\frac{U_2^2}{2} + \int_p \frac{dp}{\rho} = \frac{U_j^2}{2} + \int_j \frac{dp}{\rho} \ . \quad (172)$$

Introducing perturbations in these equations shows in linear approximation, assuming $p'_j = 0$:

$$\rho'_p U_{p0} S_p + \rho_{p0} u'_p S_p = \rho_{j0} u'_j S_j \quad (173)$$

and

$$U_{p0} u'_p + \frac{p'_p}{\rho_{p0}} = U_{j0} u'_j \ . \quad (174)$$

Using the equation of state $p'_p = c_{p0}^2 \rho'_p$ we have:

$$S_p \left[p_p^+ (1 + M_p) - p_p^- (1 - M_p)\right] = S_j \rho_{j0} c_{p0} u'_j \quad (175)$$

and

$$p_p^+ (1 + M_p) + p_p^- (1 - M_p) = \rho_{j0} U_{j0} u'_j \ . \quad (176)$$

Elimination of the jet velocity fluctuations yields:

$$R = \frac{p_p^-}{p_p^+} = \left[\frac{1 + M_p}{1 - M_p}\right] \left[\frac{M_p \left(U_{j0}/U_{p0}\right)^2 - 1}{M_p \left(U_{j0}/U_{p0}\right)^2 + 1}\right] \ . \quad (177)$$

We observe that the pipe termination is anechoic ($R = 0$) for $M_p = U_{p0}/c_{p0} = \left(U_{p0}/U_{j0}\right)^2 \simeq \left(S_j/S_p\right)^2$ (figure 12). This particular behaviour

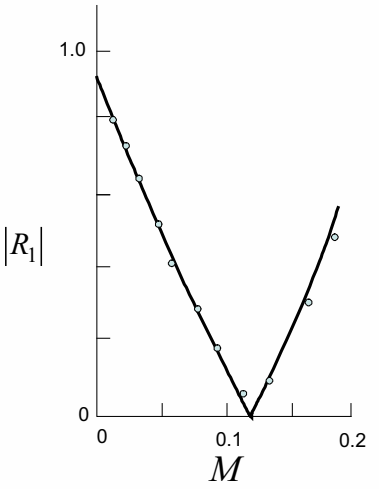


**Figure 12.** Convective effects on the reflection and transmission at an orifice in a pipe (measurements [Hofmans et al. (2000)]). The upstream reflection coefficient $|R_1|$ displays a sharp minimum at a critical Mach number, as predicted by the theory (theory, 0 experiments).

was first observed and explained by Bechert [1980]. It is a consequence of sound absorption by vortex shedding (modulation of the shear layers of the jet). While the model does not explicitly take the effect of viscosity into account, the assumption that $p'_j = 0$ can only be explained by the presence of a free jet, which is a consequence of flow separation due to viscosity. Also we assume implicitly that all the kinetic energy in this jet is dissipated by turbulence without any pressure recovery.

Note that in the presence of flow the acoustical intensity is given by [Morfey (1971)]:

$$I' = m'B' = (\rho' U + \rho_0 u')\left(u' U + \tfrac{p'}{\rho_0}\right) = \tfrac{1}{\rho_0 c_0}\left[[p^+(1+M)]^2 - [p^-(1-M)]^2\right] . \tag{178}$$

Where $m'$ is the fluctuation in mass flux:

$$m = \rho u \tag{179}$$

and $B'$ is the fluctuation in the total enthalpy:

$$B = i + \frac{v^2}{2} \ . \tag{180}$$

Consequently a reflection coefficient $R = -1$ indicates energy losses. This is the limit found when $U_{j0} = U_{p0}$.

### 6.5 Resonators in duct systems

Acoustic energy can accumulate in parts of a duct system delimited by strongly reflecting boundaries, an example of this being an expansion chamber of length $L$ and cross section $S_m$ along a pipe of cross section $S_p << S_m$. Such an expansion chamber can also be used as muffler, to reflect waves generated by an engine. Maximum transmission losses are found in cases where the expansion chamber length matches an odd number of quarter wave-length of the incoming waves (figure 13). Other obvious examples of resonators are pipe segments terminated either by open or closed pipe terminations.

The flute can be approximated as an open-open pipe with uniform cross section displaying resonances when an integer number of half wave length matches the pipe length. Since the mouth opening of the flute is smaller than the pipe cross section, the end correction of the mouth opening is quite large. This implies an important inertia, which would detune the pipe resonances if it was not combined with a compliance approaching that of a pipe segment of the length of the end correction. For this reason the mouth of the flute is not at the pipe termination. The volume in the dead end between the closed pipe termination and the mouth opening is adjusted by means of a movable piston (cork) so that the first resonances of the pipe are exactly multiples of the fundamental. This strongly enriches the sound produced by the instrument [Chaigne and Kergomard (2008)].

The close-open pipe of a uniform cross-section is a model for the clarinet. It displays resonances when the length of the pipe matches an odd number of quarter wave-length. This promotes odd harmonics of the fundamental, giving the sound a particular character. The use of a conical close-open pipe, such as the oboe or the saxophone, provides a series of resonances at frequencies that are a multiple of half wave length matching the pipe

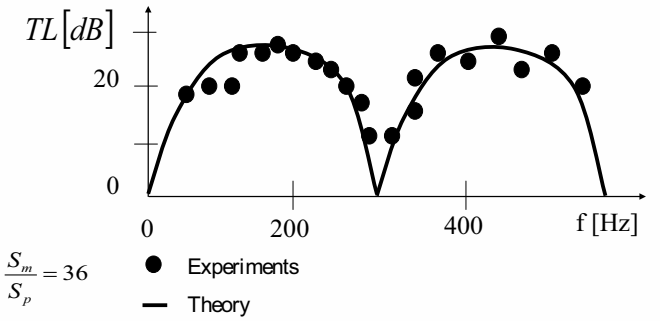


**Figure 13.** Comparison between measurement [Davis 1954] and theory [Dowling 1983] for transmission losses of a simple expansion chamber along a pipe with an anechoic termination. The transmission losses are defined by: $TL = 20log(I/T)$, with $I$ the amplitude of the incident wave and $T$ the amplitude of the transmitted wave. Maxima of transmission losses correspond to a length equal to an odd number of quarter wave-length. Minima correspond to an integer number of half wave-length.

length. In conical pipes the acoustic field is dominated by spherical waves rather than plane waves. Consequently the radiation efficiency of the sound source (reed) increases at low frequences linearily with the frequency, as demonstrated by equation (63). Thus, contrary to the clarinet, the lowest resonance frequency does not correspond to the strongest impedance in conical pipe instruments [Chaigne and Kergomard (2008)].

A pipe system can display localized acoustic standing waves, captured between two reflectors. A typical reflector is a closed side branch and the closed end of it imposes a standing wave within the side branch [Bruggeman et al. (1991), Ziada and Bühlmann (1992), Tonon et al. (2011)]. The incoming and reflected waves have equal amplitudes as imposed by the closed pipe termination $R = 1$. Whenever the closed side-branch length corresponds to

an odd number of quarter wave-length the standing wave imposes a pressure node at the junction of the closed side branch with the main pipe. At low frequencies the pressure is continuous over the junction and this imposes a pressure node in the main pipe (equation 157). Thus, this pressure node acts as an ideal open pipe termination with $R = -1$. When two closed side branches with equal resonance frequency are placed at a distance corresponding to an integer number of half a wave length, we obtain an acoustically perfectly closed system [Bruggeman et al. (1991), Ziada and Bühlmann (1992), Tonon et al. (2011)]. Paradoxically enough, this system is open for the flow [Hein and Koch (2008)]. The most spectacular resonances are obtained when considering two opposite closed side-branches forming a cross configuration with the main pipe [Keller (1984), Kriesels et al. (1995), Dequand et al. (2003c), Slaton and Zeegers (2005)]. This will be discussed in more detail in the next chapter.

A series of closed side branches of equal length can display strong acoustical resonances even if the side-branches are placed at arbitrary distances from each other. A system of deep closed side branches of random depth can also display Anderson localization [Dépolier et al. (1986)].

Another example of strong localization of a resonant acoustic field in an apparently open system is the Beta Parker mode in a pipe system with a splitter plate [Welsh and Stokes (1984),Stokes and Welsh (1986)]. When the longitudinal splitter plate (separating the pipe in two equally wide parallel ducts) is longer than the pipe width, there is a resonance for which the half wave length is longer than the pipe width. Hence, at this frequency only plane waves propagate along the main pipe. If the two pipe segments separated by the splitter plate are oscillating in opposite phases, the system will not radiate any plane waves and actually does not radiate at all. This type of resonance has been observed in ventilation ducts (due to guiding vanes at bends), turbines (stator or rotor) [Welsh and Stokes (1984), Stokes and Welsh (1986)] and even protection grid in building (ventilators, roof) [Spruyt (1972)].

### 6.6 The Helmholtz resonator

The bottle or Helmholtz resonator is an elementary acoustical resonator [Dowling and Ffowcs Williams (1983), Pierce (1990), Rienstra and Hirschberg (1999)]. It is an acoustical mass-spring system, because the volume of the bottle acts as a spring, while the inertia of the flow (mass) is concentrated in the neck (Figure 6.6). If the neck has a uniform cross section $S$ and a

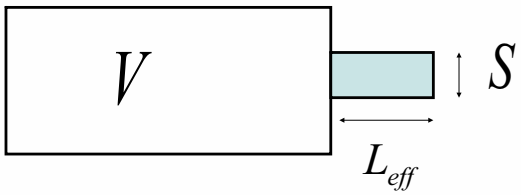


**Figure 14.** The Helmholtz resonator as an acoustical mass spring system.

length $L$ the mass obviously is:

$$M = \rho_0 S(L + 2\delta) \tag{181}$$

where $\delta$ is the end correction at one end of the neck (section 6.3). The spring constant of the system is obtained by starting from the mass conservation law, assuming a uniform density within the volume:

$$\frac{\Delta\rho}{\rho_0} = -\frac{\Delta V}{V} = -\frac{S\Delta x}{V} \tag{182}$$

where $\Delta x$ is the acoustic fluid displacement in the neck. The uniform density assumption is actually in agreement with the fact that we neglect inertia in the volume of the bottle, implying a uniform pressure. This is exactly the same assumption as for a massless spring, which implies that the tension is uniform over the spring. Assuming an adiabatic compression we have: $\Delta p = c_0^2 \Delta\rho$. The force acting on the fluid in the neck is therefore:

$$\Delta F = S\Delta p = -S\rho_0 c_0^2 \frac{S\Delta x}{V} \ . \tag{183}$$

From this we deduce that the spring constant $K$ of the system is:

$$K = \rho_0 c_0^2 \frac{S^2}{V} \tag{184}$$

and the resonance frequency of the resonator is given by:

$$\omega_0 = \sqrt{\frac{K}{M}} = c_0 \sqrt{\frac{S}{VL}} \ . \tag{185}$$

It is interesting to note that for an ideal gas $\rho_0 c_0^2 = \gamma p_0$ where $\gamma$ is the Poisson ratio of specific heats at constant pressure and volume respectively. When considering an oven or furnace with an open door, the gas density in the neck of the system is close to that of the surrounding air at room temperature, while the average pressure $p_0$ in the volume is atmospheric. Hence, the resonance frequency depends only weakly on the temperature in the oven.

A bottle of cider or champagne has a neck with a non-uniform cross section $S(x)$. In order to calculate its resonance frequency we need a more sophisticated approach [Cummings (1972)]. We start again by applying the integral mass conservation law on the volume, assuming a uniform density in the volume:

$$V \frac{d\rho'}{dt} = \frac{V}{c_0^2} \frac{dp'}{dt} = -\rho_0 u' S(L) \tag{186}$$

where $u'$ is the acoustic velocity at the pipe opening $x = L$. Furthermore, we use the integral of the momentum equation (45) over the neck of the bottle:

$$\rho_0 \frac{d}{dt} \int_0^L u' \frac{S(L)}{S(x)} dx = \rho_0 \int_0^L \frac{S(L)}{S(x)} dx \frac{du'}{dt} = p'(0) - p'(L) \tag{187}$$

where we assumed the flow in the neck to be incompressible. Elimination of $u'$ yields a second-order harmonic equation corresponding to the resonance frequency:

$$\omega_0 = c_0 \sqrt{\frac{S(L)}{VL_{eff}}} \tag{188}$$

with:

$$L_{eff} = \int_0^L \frac{S(L)}{S(x)} dx \ . \tag{189}$$

# 7 Vortex sound theory and whistling

## 7.1 Powell/Howe analogy

The quantitative relationship between vortex shedding and sound production was first established by Powell (1964). His approach was limited

to free field conditions and low Mach numbers. Howe [Howe (1975), Howe (1998), Howe (2002)] proposed a generalization of this approach to arbitrary Mach numbers, which is valid for confined flows. In its most general form it implies a numerical solution of a complex convective wave equation [Doak (1995), Musafir (1997)] and it is mostly used at low Mach numbers. In most cases it is used for the analysis of the sound production based on an energy corollary, which we are looking at.

In section (5.2) we have seen that the choice of variable is important in an analogy, because it determines the approximations that are intuitively reasonable. In section (6.4) we have seen that in the presence of a frictionless mean flow, the total enthalpy fluctuation is a natural variable. Following equation (31):

$$\frac{\partial \vec{v}}{\partial t} + \nabla B = -(\vec{\omega} + \vec{v}) + \frac{\vec{f}}{\rho} \tag{190}$$

we see that the Corriolis acceleration $(\vec{\omega} \times \vec{v})$ acts as a source of sound if we define the acoustic velocity $\vec{u}'$ as the time-dependent part of the potential flow in a Helmholtz decomposition of the flow velocity:

$$\vec{v} = \nabla(\varphi_0 + \varphi') + \nabla \times \vec{\psi} \; . \tag{191}$$

This yields the definition proposed by Howe (1984) for the acoustic velocity:

$$\vec{u}' = \nabla \varphi' \; . \tag{192}$$

For low Mach number flows Howe (1984) proposes the use of the following approximation for the time average acoustic power $< P >$ produced by a flow:

$$< P >= -\rho_0 < \int_V (\vec{\omega} \times \vec{v}) \cdot \vec{u}' dV > \; . \tag{193}$$

This corresponds to the use of the energy corollary (64) assuming $\vec{f} = -\rho_0(\vec{\omega} \times \vec{v})$. This intuitive statement gives an excellent insight into the sound production associated with vortex shedding in low Mach number flows, which is due to the fact that vorticity is a conserved quantity in 2-D frictionless flows. We therefore have an intuition for the dynamics of vortices in such flows [Prandtl (1934), Milne-Thomson (1952), Paterson (1983), Saffman (1992)].

A drawback of the vortex sound theory is that it stresses the dipole character of the sound source: $\nabla \cdot (\vec{\omega} \times \vec{v})$. Unlike the analogy of Lighthill, it does not impose a quadrupole character to the sound field. Thus, in order

to apply this analogy to flows, such as a free jet, one has to use analogies as proposed by Möhring (1978) or Schram and Hirschberg (2003), which do take this aspect into account. In our discussions we limit ourselves to applications with a dominant dipole source term. In such cases the formulation of Howe (1984), as given in equation (193) can be used.

### 7.2 Aeolian tone

For Reynolds numbers $Re_D = UD/\nu$ above 50 the wake of a cylinder of diameter $D$ placed with its axis normal to a uniform flow (velocity $U$, kinematic viscosity $\nu$) is unstable with periodic vortex shedding occurring. Vortices have alternating vorticity signs, which results in an oscillating lift force (normal to the flow direction). The force of this flow on the cylinder comes from a reaction force $\vec{F}$ of the cylinder on the flow. This reaction force acts as a source of sound. For low Mach numbers the cylinder is compact so that we can neglect variation of the retarded time over the source region. Equation (94) can be written in the following form:

$$p'(\vec{t},t) \approx \frac{x_i}{4\pi c_0 |\vec{x}|^2} \frac{\partial F_i}{\partial t} \ . \tag{194}$$

The lift force scales with $\rho U^2 DL$ where $L$ is the length of the cylinder over which the vortex shedding is coherent. The oscillation frequency corresponds to a Strouhal number which is somewhat dependent on the Reynolds number $Sr_D = fD/U \approx 0.2$. This was already observed by Strouhal (1878) (Figure 15). The most important conclusions that can be drawn from this experience is:

- the cylinder does not need to vibrate or oscillate in order to generate the whistling tone,
- the vortices shed by the cylinder do not impinge on any surface or edge.

The first statement contradicts our intuition that sound is produced by wall vibrations. Oscillation of the cylinder can occur and can strongly affect the frequency. This occurs when the mechanical oscillation frequency is close to the natural vortex shedding frequency. One can then observe a strong increase in coherence length of the vortex shedding [Blake (1986)].

The second statement contradicts the intuition that sound is produced upon impingement of vortices on edges. In early work [Rockwell (1983)] this assumption is generally accepted, although it is a rather misleading assumption, as the following examples show.

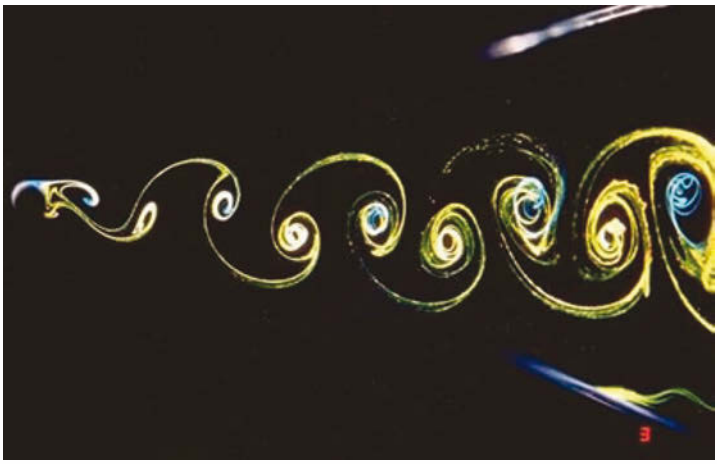

**Figure 15.** Von Karman vortex street behind a cylinder (copyright Onera, The French Aerospace Lab).

### 7.3 Human whistling

As we have seen in section (6.4) convective effects induce acoustical energy absorption upon reflection at an open pipe termination with outflow. The ratio of reflected and incoming acoustic intensity is, following equation (178) and with $R = -1$:

$$R_E = \frac{I^-}{I^+} = \frac{1-M}{1+M} \ . \tag{195}$$

This is a consequence of the losses in total enthalpy $\Delta B' = Uu'$ in the free jet formed by flow separation at the pipe exit. This corresponds to the modulation of the kinetic energy in the jet. This kinetic energy is dissipated by turbulence in the jet with negligible pressure recovery ($p' = 0$).

We now analyse the same phenomenon by using the energy corollary of Howe (193). As a first step we consider the spatial distribution of the acoustic velocity field $\vec{u}'$ at the pipe exit. A potential flow such as the acoustic field $\vec{u}' = \nabla\varphi'$ does not separate from sharp edges. This flow follows

the walls smoothly. The acoustic streamlines around the edges of the open pipe termination are curved. Which implies that there should be a pressure gradient directed towards the inner side of the bend which provides the centripetal force bending the streamlines. Following the Bernoulli equation (36) this decrease in pressure implies an increase of velocity towards the interior of the bend. Actually, this also follows directly from the condition that the acoustic flow should be irrotational $\nabla \times \vec{u}' = \nabla \times \nabla\varphi' \equiv 0$. Rotation due to the bending of streamlines should be compensated by a gradient in the radial direction of the tangential component of the velocity. In terms of forces the radial pressure gradient balances the centrifugal force. As the velocity increases and the radius of curvature of the streamlines decreases as we approach the interior of the bend, the centrifugal force increases dramatically. Obviously for a sharp edge we have a singularity in a potential flow [Prandtl (1934), Milne-Thomson (1952), Paterson (1983)]. As we approach the edge, the magnitude of the acoustic velocity becomes infinitely large. However, moving away from the edge in the direction of the pipe axis, causes rapid decrease of the amplitude of the acoustic field. The direction of the acoustic velocity also turns gradually from normal to the pipe axis towards the direction of the pipe axis (Figure 16). A harmonically oscillating acoustic field implies that the acoustic flux is directed pipe-outward during half the oscillation period and is directed pipe-inward during the next half period.

The next step in our analysis is to consider the vortex shedding. Vortex shedding is the result of viscous effects in the boundary layers of the flow. In these boundary layers the flow velocity $|\vec{v}|$ decreases from the bulk flow velocity down to the zero velocity imposed by the no-slip boundary condition $\vec{v} = 0$ at the wall. At high Reynolds numbers the boundary layers are thin. The flow in these boundary layers is mainly directed along the wall and this implies that the pressure in the boundary layer is equal to the pressure imposed by the bulk flow at the outer edge of the boundary layer. In the bulk of the flow there is an equilibrium between inertia and pressure gradient (as the viscous forces are negligible for high Reynolds numbers). An increase in pressure is compensated by a reduction of velocity. This allows fluid particles to move against an adverse pressure gradient. In the viscous boundary layer, the fluid has lost much of its kinetic energy and cannot use its inertia to overcome an adverse pressure gradient. Viscous drag of the fluid in the boundary layer by the bulk flow can allow to overcome a small pressure gradient. However, in a steady flow with bulk velocity $U$ there will be back flow along the wall, when the characteristic time for momentum diffusion across the boundary layer $\theta^2/\nu$ (with $\theta$ the momentum thickness

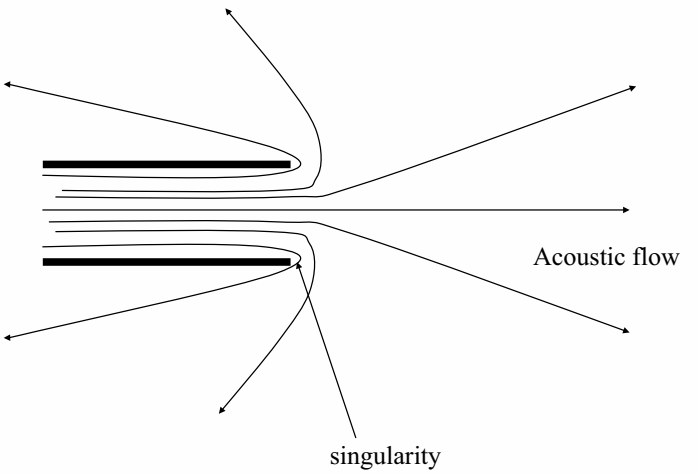


**Figure 16.** Acoustic streamlines at an unflanged pipe termination.

of the boundary layer) becomes larger than the characteristic deformation time $(\partial U/\partial x)^{-1}$. As a consequence the flow will separate from the wall. As the flow passes a sharp edge at the end of an unflanged open pipe, the flow will certainly separate from the wall. This implies that the flow continues tangentially to the wall (along the direction of the axis of the pipe) rather than following the bend, as does the potential flow. A shear layer is formed separating the main flow from a dead water region around the free jet. In this shear layer there is vorticity $\vec{\omega}$. Due to the instability of the shear layer this vorticity concentrates in coherent vortical structures (vortices). Each time the acoustic field turns from pipe inward to pipe outward a new vortex is formed at the edge of the pipe termination. This vortex accumulates most of the vorticty shed at the sharp edge while travelling at almost constant velocity $U_c \approx U/2$ in the direction of the pipe axis. The strength of the vortex is measured by the circulation $\Gamma \equiv \oint_C \vec{v} \cdot d\vec{x} = \int_S \vec{\omega} \cdot d\vec{S}$ taken along a contour $C$ enclosing the vortex. The circulation is the flux of the vorticity vector through a surface sustained by the contour. In first approximation, with the acoustic velocity considerably smaller than the bulk flow velocity, we have $d\Gamma/dt = -UU_c$, as illustrated in Figure 17 [Nelson et al. (1983)]. After an oscillation period a new vortex is shed from the pipe edges and the

old vortex continues to travel at almost constant speed. Further downstream these vortex rings are eventually dissipated by turbulence.

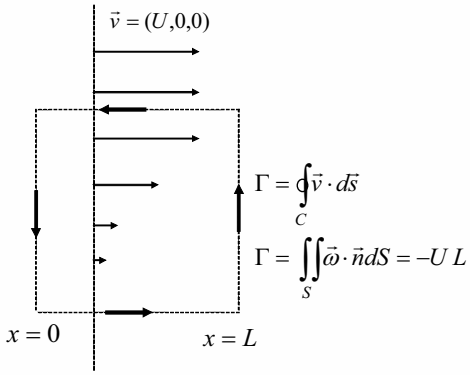


**Figure 17.** Vorticity and circulation of a shear layer.

Considering a new vortex shed at the edges of the pipe, we can see that the vector $\vec{\omega} \times \vec{v}$ is directed normal to the pipe axis in the direction away from this axis. In first approximation the convection velocity is $\vec{v} \approx (U_c, 0, 0)$. At this point in time the acoustic velocity $\vec{u}'$ is oriented in the same direction and locally very large due to the singularity of the acoustic flow at the edge. Hence the triple product $-\rho_0(\vec{\omega} \times \vec{v}) \cdot \vec{u}'$ is very large and negative. The formation of a new vortex by acoustic excitation of the shear layer implies sound absorption, which seems quite logical. The less trivial message from the theory of Howe, is that, after half a period, the same vortex will start to generate sound, because the sign of the acoustic velocity changes while those of the rotation $\vec{\omega}$ and of the convection velocity $\vec{v}$ do not change. The power produced in the second half period is much lower than the initial sound absorption because the growth in the vortex circulation is not able to compensate for the decrease in acoustic velocity amplitude and its rotation in the direction of the pipe axis (Figure 18). We obtained a result similar to the predicted sound absorption found when using the quasi-steady model.

The major gain is the understanding that there is a possibility of net

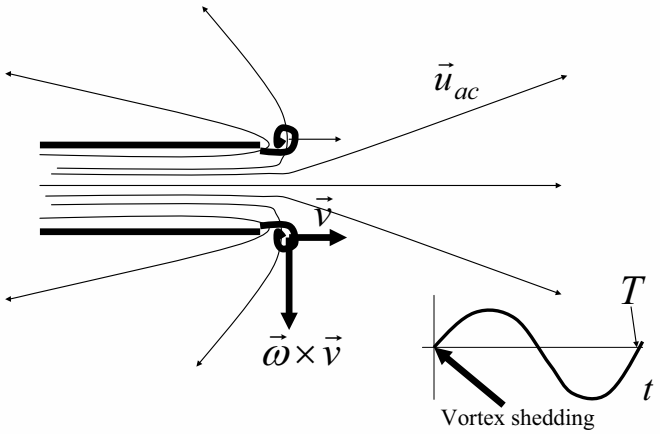


**Figure 18.** Sound absorption as a result of a strong initial absorption.

sound production by the vortex shedding, if we can reduce the initial absorption and enhance production. This is exactly what occurs when we whistle with our lips. Flow separation at our lips occurs actually almost at the neck of the channel formed by our lips. This implies that there is a strong reduction of the singularity of the acoustic velocity, because the lips are rounded rather than sharp and the acoustic velocity is almost parallel to the axis of the flow. Moreover, if we ensure that the vortex travels over the radius of curvature $R$ of our lips within half an oscillation period, it will start producing sound. As the acoustic field has not expanded in free space its amplitude is still large and the direction reasonably normal to the main flow axis. This particularly favourable condition is met when the Strouhal number $Sr_R = fR/U = (fR/U_c)(U_c/U) \approx 0.25$. The frequency $f$ is imposed by the Helmholtz resonance of our mouth cavity in combination with the neck formed by our lips (Figure 19) [Wilson et al. (1971), Hirschberg et al. (1995)]. Once we have adjusted this geometry we should tune the flow velocity to match the Strouhal number condition. This explains why a child, that is blowing too hard will never be able to whistle by blowing harder and harder.

This simple experiment confirms that we do not need any impingement of vortices on an edge to generate sound. It furthermore indicates that sharp

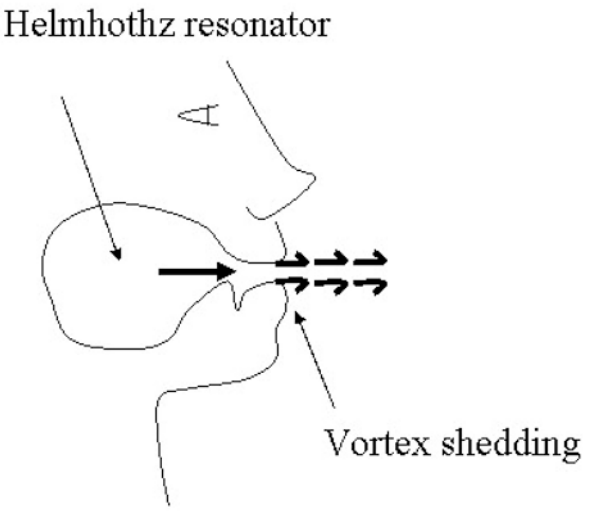


**Figure 19.** Human whistling [Wilson et al. (1971)].

edges are not necessary for vortices to be shed. Finally, it indicates that sharp edges at the flow separation point actually tend to reduce sound due to vortex shedding. We should note, however, that sharp edges will strongly enhance broadband noise production. This effect is clear when we consider the sound produced by blowing hard trough our lips in comparison with the sound produced by blowing along our teeth (as we do when we generate a fricative sound such as an [s]).

A related configuration is that of a pipe terminated by a diffuser, which is a conical expansion from the pipe cross section $S_p$ to the outlet cross section $S_0$. This allows reducing the loss of energy by dissipation of kinetic energy in the free jet at the outlet. This works only typically if the increase in cross section is not much larger than a factor 2. Furthermore, the opening angle of the diffuser cone should be less than 8 degrees. This would imply very long diffusers. In practice one uses therefore opening angles of about 20 to 25 degrees. In this case the flow partially separates from the wall within the diffuser. Considering the steady flow performance the losses due to this flow separation is rather marginal. However, it has a spectacular consequence on the energy reflection coefficient for acoustic waves travelling in the pipe towards the open end. Measurements of $R_E = I^-/I^+$ appear to be larger than unity for two ranges of Strouhal numbers (Figure 20). This implies

sound generation and potentially whistling of the pipe system too. The lowest Strouhal number corresponds roughly to a travel time of the vortices through the diffuser half that of the oscillation period. The second higher Strouhal number corresponds to a travel time of one and a half periods. This means that there are two co-existing vortices within the diffuser. These two flow conditions are called hydrodynamic modes or stages Howe (1998). The same type of behaviour can be observed with another configuration in the next section.

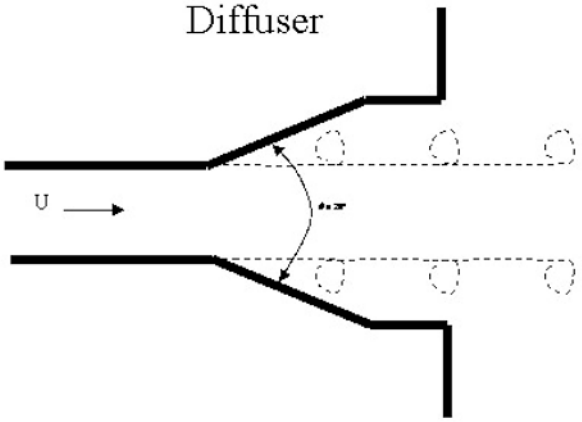


**Figure 20.** Low separation in diffuser at pipe termination.

### 7.4 Flow induced instabilities in pipe systems with closed side branches

As explained in section 6.5, closed side branches are almost perfect reflectors at frequencies such that the length corresponds to an odd number of quarter wave-length. Early quantitative research on the self-sustained oscillation of this type of closed side-branch resonators has been carried out by Bruggeman et al. (1991) and Ziada and Bühlmann (1992). A literature review on this subject is provided by Tonon et al. (2011). The simplest configuration is a set of two side branches of equal length $L$ and diameter $D$ placed opposite each other, forming a cross with the main pipe of diameter $D_p$. Figure 22a shows the amplitude of pressure fluctuations $p'$ measured at the closed side-branch termination as a function of the average flow velocity $U$ along the main pipe. It also shows the corresponding frequency $f$. With increasing flow velocity $U$ we observe successively the

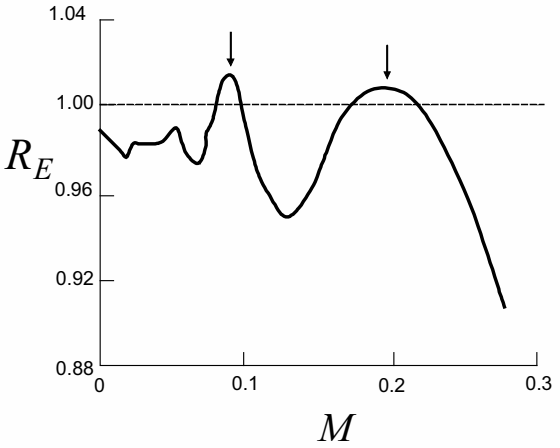


**Figure 21.** Measurement of energy reflection coefficient $R_E$ demonstrating the whistling of a diffuser [Van Lier et al. (2001)]. Arrows indicate acoustic energy production.

first three acoustic modes of the system with: $He_L = fL/c_0 \approx \frac{1}{4}; \frac{3}{4}$ and $\frac{5}{4}$. For each of these acoustic modes we observe two critical Strouhal numbers (two hydrodynamic modes)for optimal whistling: $Sr_D = fD/U \approx 0.5$ and 1.0. They correspond to a travel time of the vortices across the opening of the side-branches of one period and two periods respectively.

Figure 22b shows flow visualization for these two hydrodynamic modes. In this case, the acoustic velocity is mainly normal to the convection velocity of the vortices. If the edges of the T-junctions between the main pipe and the side-branches are rounded, the acoustic velocity amplitude is, in first approximation, spatially uniform over the path of the vortices. The increase in circulation of the vortex during the first oscillation period, whilst traveling from the upstream edge towards the downstream edge explains the net sound production in the system.

It should be noted that for the prediction of the oscillation amplitude we consider self-sustained oscillations. The instability of the shear layer acts

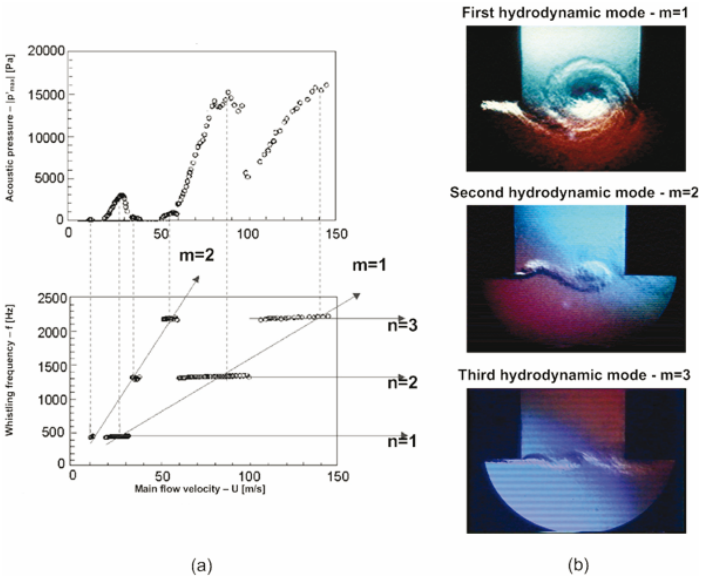


**Figure 22.** Whistling of a cross configuration with two opposite closed side-branches [Kriesels et al. (1995)]. Figure a: Amplitude of pressure pulsations and whistling frequency. The hydrodynamic modes $m = 1$ and $m = 2$ correspond to $Sr = fD/U = 0.5$ and 1.0, respectively. Figure b: Flow visualization of the first three hydrodynamic modes in a cross junction (pictures Olivier Schneider and Bram Wijnands). The main pipe is horizontal. The flow is from left to right.

as an amplifier in this feedback loop, transferring energy from the main flow to the acoustic field. The acoustic resonator selects oscillations close to the resonance frequency. It is a filter. The acoustic oscillation induces new vorticity perturbations at the upstream edge, where the flow separates from the wall. If all these elements in the feedback loop were linear the system would be either stable, neutrally stable or unstable. In stable conditions perturbations decay exponentionally to zero. In unstable conditions the amplitude increases indefinitely. In neutrally stable conditions, the amplitude is the amplitude imposed at the initial conditions, and can have any value. We cannot predict a stable limit cycle oscillation with finite amplitude on the basis of linear theory [Bruggeman et al. (1991), Tonon et al. (2011)]. The non-linear phenomenon which limits the pulsation amplitude depends on the amplitude of the oscillations. For moderate pulsation amplitudes

($|u'/U| = |p'|/\rho_0 c_0 U \leq 0.1$), the main non-linearity is the saturation of the shear layer amplification due to the concentration of the vorticity into discrete vortices. Once the shear layer has rolled-up to form a discrete vortex we have reached a maximum perturbation. Actually, because the amount of vorticity shed is almost independent of the amplitude $d\Gamma/dt \approx -UU_c$ and the path of the vortex almost straight (from the upstream edge to the downstream edge), the product $\rho_0(\omega \vec{\times} \vec{v})$ is mainly determined by the mean flow. It scales with $\rho_0 U^2$. The power generated by this source is at a fixed Strouhal number proportional to the acoustic amplitude $|\vec{u}'|/U$. The losses due to friction and radiation are proportional to the square of the amplitude $|\vec{u}'|^2/U^2$. A finite amplitude is found by balancing the power generated by the source and the power related to friction and radiation losses [Tonon et al. (2011)]. When $|\vec{u}'|/U \geq 1$ vortex shedding and path become dependent on the amplitude. Furthermore, additional vortex shedding from the downstream edge of the T-junction induces additional losses which are scaling with $(|\vec{u}'|/U)^3$. As a consequence $|\vec{u}'|/U = 0(1)$ is a kind of maximum of the pulsation amplitude which is reached when friction and radiation losses are negligible.

The exact value of the maximum pulsation amplitude depends on the details of geometry. For a cross configuration with rounded edges one can reach $|\vec{u}'|/U \simeq 2$ [Slaton and Zeegers (2005)]. At such large pulsation amplitudes shock waves are formed in the side branches due to non-linear wave steepening. For sharp edges one finds $|\vec{u}'|/U \leq 0.8$ [Kriesels et al. (1995)]. In a Helmholtz resonator under grazing flow with rounded edges one finds $|\vec{u}'|/U \leq 0.6$ [Dequand et al. (2003a)]. In flue instruments such as a recorder flute or a flute one typically finds $|\vec{u}'|/U \leq 0.3$ [Verge et al. (1997), Dequand et al. (2003b)].

An interesting aspect of this discussion is that in contrast to turbulence noise produced by flows in free field conditions, the acoustic flow due to whistling is not a small perturbation of the flow. This implies that numerical simulation of the flow is not impossible. In following section an example of such a successful numerical simulation is given.

### 7.5 The "Voice of the Dragon"

Corrugated pipes (Figure 23) are locally rigid and globally flexible. This makes them very useful for many applications ranging from vacuum cleaner tubes to risers for offshore natural gas production. A problem is, however, that flow through such pipe can cause severe whistling. Actually, a plastic

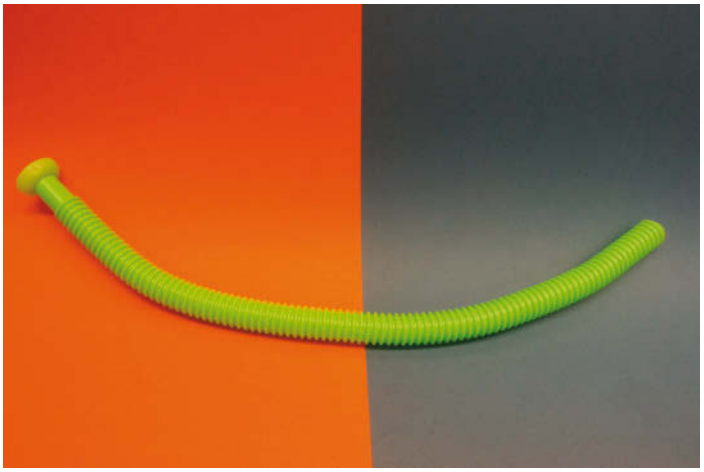

**Figure 23.** Corrugated pipe used as musical toy.

corrugated pipe of a length of $L = 80\ cm$ and an inner diameter $D = 3\ cm$ is commonly used as a musical toy called: hummer [Silverman and Cushman (1989)]. In musical applications this toy is called: the "Voice of the Dragon" [Silverman and Cushman (1989)]. Holding one open end of the tube in the hand and swirling the tube above the head produces a melodic sound with increasing pitch as the angular rotation velocity $\Omega$ increases. This tube is actually a centrifugal pump. Due to centrifugal acceleration $\Omega^2 r$ there is a pressure gradient $\partial p/\partial r = -\rho_0 \Omega^2 r$ along the tube, where $r$ is the distance from the (non moving) open end. At the moving open end of the tube the outflow forms a free jet due to viscous flow separation. This free jet implies that the pressure at this open end is close to the atmospheric pressure $p_0$. Hence the pressure at the opposite (non moving) open end is $p(0) = p_0 - \frac{1}{2}\rho_0 \Omega^2 L^2$. In the inflow from the surrounding to the fixed inlet, we can apply the Bernoulli equation $p(0) + \frac{1}{2}\rho_0 U^2 = p_0$ from which we conclude that in first order approximation $U = \Omega L$ [Nakiboglu et al. (2012)].

The flow along the corrugations can be seen as a grazing flow along a shallow cavity. The cavity depth $H$ is so small (order of a few millimetres) that we can in first approximation neglect the compressibility of the air in the cavity. The shear layer formed along the opening of the cavity is unstable. The whistling is caused by coupling this instability to a longitudinal acoustic wave along the pipe. The acoustic modes of the pipe have frequencies predicted by $f_n = n(c_{eff}/2L)$ $(n = 1, 2, 3)$ where the effective speed of

sound along the pipe is:

$$c_{eff} = c_0 \sqrt{\frac{V_{in}}{V_{tot}}} \ . \tag{196}$$

Were $V_{in} = \pi D^2 L/4$ is the inner volume excluding the cavities of the corrugations and $V_{tot}$ is the total volume of the tube including the cavities.

The critical Strouhal number $Sr_W = f(W + r_{up})$ for whistling based on the cavity width $W$ plus the upstream edge radius of the cavities $r_{up}$ appears to be a function of W/D. As shown in figure 25 $Sr_W$ varies from

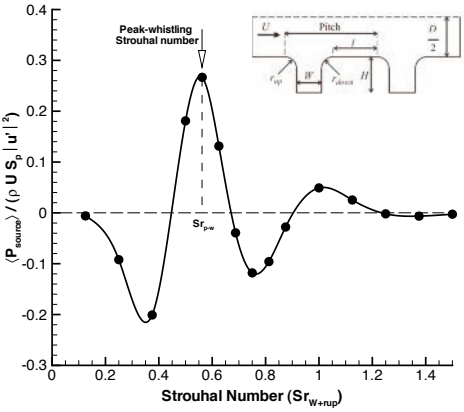


**Figure 24.** Sound power produced by a cavity in a corrugated tube as a function of the Strouhal number [Nakiboglu et al. (2011)].

0.8 to 0.3 as $W/D$ varies from 1 to 0.05. In an attempt to explain this variation Nakiboglu et al. (2011) considered incompressible 2-D axial symmetric flow simulations of a single cavity along a tube. These simulations have been carried out with a commercial code. In the model Nakiboglu et al. (2011) imposes, at a distance $D/2$ upstream of the cavity, a steady flow profile corresponding to the time average of the fully developed turbulent flow profile through a corrugated pipe. This can be calculated by using a steady RANS (Reynolds Average Navier Stokes) calculation or it can be measured. A harmonically oscillating uniform (over the cross section) velocity representing the acoustic plane wave is superposed on this time average profile. The fluctuation in the difference in total enthalpy $\Delta B'$ over the cavity is calculated. The difference of total enthalpy $\Delta B'_{ref}$ calculated for the same boundary conditions across a reference straight tube segment is

subtracted $\Delta B' - \Delta B'_{ref}$. The acoustic power generated by the cavity is then calculated by using vortex sound theory:

$$< P >=< \rho_0(\Delta B' - \Delta B'_{ref})u' > \quad . \tag{197}$$

Figure 24 shows the results obtained for this acoustic power at fixed am-

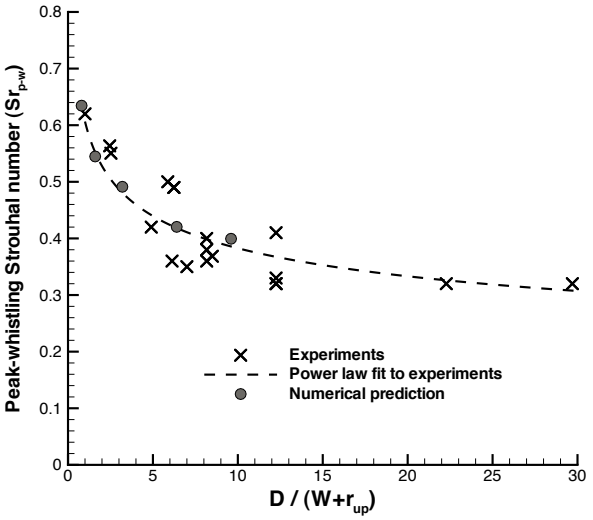


**Figure 25.** Predicted and measured Strouhal number for corrugated pipes as a function of the ratio $D/W$ of pipe diameter to cavity width [Nakiboglu et al. (2012)].

plitude $|\vec{u}'|/U$ as a function of $Sr_W = f(W + r_{up})/U$. The maximum of the predicted power is assumed to correspond to the critical whistling Strouhal number (Figure 25). As explained by Nakiboglu et al. (2011) the decrease of $Sr_W$ with increasing $D/(W + r_{up})$ is acually due to the change in ratio of boundary layer thickness and cavity width. The same effect has been reported by Golliard (2002), Kooijman et al. (2008) and Ma Ruolong et al. (2009).

We observe an almost perfect agreement between theory and experiments (Figure 25). The prediction of the whistling amplitude using this model appears to be less successful [Nakiboglu et al. (2011)]. The model overestimates the source power by about a factor of two.

Another interesting fact is that a laminar model was used to predict the dynamic response of a turbulent flow to acoustic forcing. This approach has already been used in many papers such as the work of Michalke (1965) and Méry and Casalis (2008). However, we do provide at this point any explanations for the success of the quasi-laminar method. This calls for further research.

## Bibliography

S. Allam, M. Abom, *Investigation of damping and radiation using full plane wave decomposition in ducts*, In *J. Sound. Vib. 292*, pages 519-534, 2005.

D.J. Acheson, *Elementary Fluid Dynamics*, Clarendon Press, Oxford, 1990.

A.B.C. Anderson, *Metastable jet-tone states of jets from sharp-edged, circular, pipe like orifices*, In *J. Acoust. Soc. Am. 27*, pages 13-21, 1955.

G.K. Batchelor, *An introduction to Fluid dynamics*, Cambridge University Press, Cambridge, UK, 1967.

D.W. Bechert, *Sound absorption caused by vorticity shedding, demonstrated with a jet flow.*, in *J. Sound Vib. 70*, pages 389-405, 1980.

L. Bjørnø, P.N. Larsen, *Noise of air jets from rectangular slits*, in *Acustica 54*, pages 247–256, 1984.

D.T. Blackstock, *Fundamentals of physical acoustics*, Wiley-Interscience, NY, 2000.

W.K. Blake, *Mechanics of Flow-Induced Sound and Vibration, Vol. I and II*, Academic Press, Orlando, 1986.

J.C. Bruggeman, A. Hirschberg, M.E.H. van Dongen, A.P.J. Wijnands, *Self-sustained aero-acoustic pulsations in gas transport systems: experimental study of the influence of closed side branches*, in *J. Sound Vib. 150*, pages 371–393, 1991.

M. Bruneau, *Fundamentals of Acoustics*, ISTE Ltd, London (2006).

A. Chaigne, J. Kergomard, *Acoustique des instruments de musique*, Paris: Berlin, 2008.

L. Cremer, M. Heckl, *Structure-Borne Sound, second edition*, Springer-Verlag, Berlin, 1988.

D.G. Crighton, *Basic principles of aerodynamic noise generation*, in *Prog. Aerospace Sci. 16*, pages 31–96, 1975.

D.G. Crighton, *The Kutta condition in unsteady flow*, in *Ann Rev. Fluid Mech. 17*, pages 411–445, 1985.

D.G. Crighton, A.P. Dowling, J.E. Ffwocs Williams, M. Heckl, F.G. Leppington, *Modern methods in analytical acoustics*, Lecture notes, Springer-Verlag, London, 1992.

A. Cummings, *Acoustics of a ciderbottle* in *Applied Acoustics 5*, pages 161–170, 1972.

N. Curle, *The influence of solid boundaries upon aerodynamic sound*, in *Proc. Roy. Soc. A 231*, pages 505–514, 1955.

C. Dépollier, J. Kergomard, F. Laloe, *Localisation d'Anderson des ondes dans les réseaux acoustiques unidimensionnels aléatoires*, in *Annales de Physique 11*, pages 457–492, 1986.

S. Dequand, X. Luo, J. Willems, A. Hirschberg, *Helmolz-like resonator self-sustained oscillations, part 1: Acoustical measurements and analytical models*, in *AIAA Journal 41*, pages 408–415, 2003.

S. Dequand, J.F.H. Willems, M. Leroux, R. Vullings, M. van Weert, C. Thieulot, A. Hirschberg, *Simplified models of flue instruments: Influence of mouth geometry on the sound source*, in *J. Acoust. Soc. Am. 113*, pages 1724–1735, 2003.

S. Dequand, S.Hulshoff, A.Hirschberg, *Self-sustained oscillations in a closed side branch system*, in *J. Sound Vib. 265*, pages 359–386, 2003.

P.E. Doak, *Fluctuating total enthalpy as a generalized Field*, in *Acoust. Phys. 44*, pages 677–685, 1995.

A.P. Dowling, J.E. Ffowcs Williams, *Sound and sources of sound*, Ellis Horwood Publisher, Chichester, 1983.

B. Fabre, A. Hirschberg, A.P.J. Wijnands, *Vortex shedding in steady oscillations of a flue organ pipe*, in *Acta Acustica 82*, pages 863–877, 1996.

B. Fabre, J. Gilbert, A. Hirschberg, X. Pelorson, *Aero-Acoustics of musical instruments*, in *Ann. Rev. Fluid Mech. 44*, in press, 2012.

N.H. Fletcher, T. Rossing, *The physics of musical instruments, Second edition*, Springer-Verlag, NY, 1998.

M.J. Fisher, P.A. Lush, M. Harper Bourne, *Jet noise*, in *J. Sound and Vib. 28*, pages 563–585, 1973.

J.E. Ffowcs Williams, *Hydrodynamic noise*, in *Ann. Rev. Fluid Mechanics 1*, pages 197–222, 1969.

J.E. Ffowcs Williams, D.L. Hawkings, *Sound generation by turbulence and surfaces in arbitrary motion*, in *Phil. Trans. Roy. Soc. (London) Ser. A, 264*, pages 321–342, 1969.

M. Goldstein, *Aero-Acoustics*, McGraw-Hill, NY, 1976.

J. Golliard, *Noise of Helmholtz-resonator like cavities excited by a low Mach-number Turbulent Flow*, PhD-thesis, l'Université de Poitiers, Fr, 2002, ISBN 90-6743-964-9.

S. Hein,W. Koch, *Acoustic resonances and trapped modes in pipes and tunnels*, in *Journal of Fluid Mechanics 605*, pages 401–428, 2008.

A. Hirschberg, J. Kergomard, G. Weinreich, (edts), *Mechanics of Musical Instruments*, Springer Verlag, Wien, 1995.

A. Hirschberg, J. Gilbert, A.P.J. Wijnands, R. Msallam, *Shock waves in trombones*, in *J. Acoust. Soc. Am. 99*, pages 1754–1758, 1996.

G.C.J. Hofmans, *Vortex sound in confined flows*, PhD thesis, Technische Universiteit Eindhoven, 1998.

G.C.J. Hofmans, R.J.J. Boot, P.P.J.M. Durrieu, Y. Auregan, A. Hirschberg, *Aeroacoustic response of a slit-shaped diaphragm in a pipe at low Helmholtz number: quasi-steady results*, in *J. Sound Vib. 244*, pages 35–56, 2001.

M.S. Howe, *Contribution to the theory of aerodynamic sound, with application to excess jet noise and the theory of the flute*, in *J. Fluid Mech. 71*, pages 625–673, 1975.

M.S. Howe, *On the absorption of sound by turbulence and other hydrodynamic flows*, in *IMA J. Applied Math. 32*, pages 187–209, 1984.

M.S. Howe, *Acoustics of Fluid-Structure Interactions*, Cambridge University Press, Cambridge, UK, 1998.

M.S. Howe, *Theory of Vortex Sound*, Cambridge University Press, Cambridge, UK, 2002.

M.C. Junger, D. Feit, *Sound, Structures and Their Interaction, second edition*, MIT Press, 1986.

J.J. Keller, *Non-linear self-excited acoustic oscillations in cavities*, in *J. Sound Vib. 94*, pages 397–409, 1984.

L.E. Kinsler, A.R. Frey, A.B. Coppens, J.V. Sanders, *Fundamentals of Acoustics, third edition*, in *John Wiley, NY* 1982.

G. Kooijman, A. Hirschberg, J. Golliard, *Acoustical response of orifices under grazing flow: Effect of boundary layer profile and edge geometry*, in *J. Sound Vib. 315*, pages 849–874, 2008.

P.C. Kriesels, M.C.A.M. Peters, A. Hirschberg, J.C. Bruggeman, A.P.J Wijnands, *High amplitude vortex induced pulsations in a gas transport system*, in *J. Sound Vib. 184*, pages 343–368, 1995.

P.K. Kundu, *Fluid mechanics*, Academic Press, Harcourt, 1990.

L.D. Landau, E.M. Lifshitz, *Fluid Mechanics, Second edition*, Pergamon Press, Oxford, 1987.

M.B. Lesser and J.A. Lewis, *Applications of Matched Asymptotic Expansion Methods to Acoustics. II. The Open-Ended Duct*, in *Acoust. Soc. Am 52*, pages 1406–1410, 1972.

H. Levine, J. Schwinger, *On the radiation of sound from a unchanged circular pipe*, in *Physical Review 73*, pages 383-406, 1948.

L. Lier van, S. Dequand, A. Hirschberg, *Aeroacoustics of diffusers: An experimental study of typical industrial diffusers at Reynolds of O(105)*, in *J. Acoust. Soc. Am. 109*, pages 108–115, 2001.

Lighthill, M.J., *On sound generated aerodynamically I & II*, in *Proceedings of the Royal Society of London Series A 21*, pages 564–587, 1952 and 222, pages 1–32, 1954.

P. Martinez-Lera, C. Schram, S. Föller, R. Kaess & W. Polifke, *Identification of the aeroacoustic response of a low Mach number flow through a T-joint*, in *J. Acoust. Soc. Am. 126*, pages 582–586, 2009.

F. Méry, G. Casalis, *Global instability of an inviscid compressible flow over a cavity*, in *Am. Inst. Phys. Conf. Proc. 1040*, page 810, 2008.

A. Michalke, *On spatially growing disturbances in an inviscid shear layer*, in *J. Fluid Mech. 23*, pages 521–544, 1965.

L.M. Milne-Thomson, *Theoretical Aerodynamics*, Macmillan, London, 1952.

W. Möhring, *On vortex sound at low Mach number*, in *J. Fluid Mech. 85*, pages 685–691, 1978.

C.L. Morfey, *Acoustic energy in non-uniform flow*, in *J. Sound Vib. 14*, pages 159–170, 1971.

C.L. Morfey, *Amplification of aerodynamic sound by convected flow inhomogeneities*, in *J. Sound Vib. 31*, pages 391–397, 1973.

C.L. Morfey, *Sound radiation due to unsteady dissipation in turbulent flows*, in *J. Sound Vib. 48*, pages 95–111, 1976.

C.L. Morfey, V.M. Szewczyk, B.J. Tester, *New Scaling Laws for Hot and Cold jet mixing noise based on a geometric Acoustics Model*, in *J. Sound Vib. 61*, pages 255–292, 1978.

C.L. Morfey, M.C.M. Wright, *Extensions of Lighthill's acoustic analogy with application to computational aeroacoutics*, in *Proc. R. Soc. A, Math. Phys. Eng. Sci 463*, pages 2101-2127, 2007.

P.J. Morris, F. Farassat, *Acoustic analogy and alternative theories for jet noise prediction*, in *AIAA Journal 40*, pages 671–680, 2002.

P.M. Morse, K.U. Ingard, *Theoretical acoustics*, Princeton University Press, Princeton, N, 1968.

M.K. Myers, *Transport of energy by disturbances in arbitrary flows*, in *J. Fluid Mech. 226*, 383–400, 1991.

R.E. Musafir, *A discussion on the structure of aeroacoustic wave equations*, in *Proceedings of 4th French Congress on Acoustics, Marseille , Teknea, Toulouse, France*, pages 923–926, 1997.

G. Nakiboglu, S.P.C. Belfroid, J.F.H. Willems A. Hirschberg, *Whistling behavior of periodic systems: Corrugated pipes and multiple side branch system*, in *Int. J. Mech. Sci. 52*, pages 1458–1470, 2010.

G. Nakiboglu, S.P.C. Belfroid, J.Golliard, A. Hirschberg, *On the whistling of corrugated pipes: effect of pipe length and flow profile* in *J. Fluid Mech. 672*, pages 78–108, 2011.

G. Nakiboglu, O. Rudenko, A. Hirschberg, *Aero-Acoustics of the swinging corrugated tube: Voice of the Dragon*, in *J. Acoust. Soc. Am. 131*, pages 749–765, 2012.

P.A. Nelson, N.A. Halliwell, P.E. Doak, *Fluid dynamics of a flow excited resonance,part 2: theory*, in *J. Sound Vib. 91*, pages 375–402, 19983.

M.P. Norton, *Fundamental of noise and vibration analysis for engineers*, Cambridge University Press, Cambridge, UK, 1989.

F. Obermeier, *Sound generation by heated subsonic jets*, in *J. Sound Vib. 41*, pages 463–472, 1975.

A.R. Paterson, *A first course in Fluid dynamics*, Cambridge University Press, Cambridge, UK, 1983.

M.C.A.M. Peters, A. Hirschberg, A.J. Reijnen, A.P.J. Wijnands, *Damping and reflection coefficient measurements for an open pipe at low Mach and low Helmholtz numbers*, in *J. Fluid Mech. 256*, pages 499–534, 1993.

A.D. Pierce, *Acoustics*, McGraw-Hill, NY (1981), presently available from Acoustical Society of America, NY, 1990.

A. Powell, *Vortex sound theory*, in *J. Acoust. Soc. Am. 36*, pages 177–195, 1964.

A. Powell, *Some aspects of Aero-Acoustics from Rayleigh until today*, in *J. Vib. Acoust. 112*, pages 145–159, 1990.

L.Prandtl, *Fundamentals of hydro- and aerodynamics*, Dover Pub., NY, 1934.

J.W.S. Rayleigh, *The theory of sound (1894)*, Dover reprint,1954.

S.W. Rienstra, A. Hirschberg, *An introduction to Acoustics, Report IWDE 99-02*, Instituut Wiskundige Dienstverlening, TU Eindhoven, 1999.

D. Rockwell, *Oscillations of impinging shear layers*, in *AIAA Journal 21*, pages 645–664, 1983.

D. Ronneberger, C. Ahrens, *Wall shear stress caused by small amplitude perturbations of turbulent boundary-layer flow: an experimental investigation*, in *J. Fluid Mech. 83*, pages 433–464, 1977.

Ma Ruolong, P.E. Slaboch, S.C. Morris, *Fluid Mechanics of the flow excited Helmholtz resonator* in *J. Fluid Mech. 623*, pages 1–26, 2009.

P.G. Saffman, *Vortex dynamics*, Cambridge University Press, Cambridge, UK, 1992.

C. Schram, A. Hirschberg, *Application of vortex sound theory to vortex-pairing noise: sensitivity to errors in flow data*, in *J. Sound Vib. 266*, pages 1079–1098, 2003.

M.P. Silverman, G.M. Cushman, *Voice of the dragon: the rotating corrugated resonator*, in *Eur. J. Phys. 10*, pages 298–304, 1989.

W.V. Slaton, J.C.H. Zeegers, *Acoustic power measurements of a damped aeroacoustically driven resonator*, in *J. Acoust. Soc. Am. 118*, pages 83–91, 2005.

A.G. Spruyt, *Stromings-geïnduceerde akoestische resonanties in de industrie*, in *Nederlandse Akoestisch Genootschap, NAG Journaal 22*, pages 1–12, 1972.

A.N. Stokes, M.C. Welsh, *Flow resonant sound interaction in a duct containing a plate, 2: square leading edge*, in *J. Sound Vib. 104*, pages 55–73, 1986.

V. Strouhal, *Über eine besondere Art der Tonerregung*, in *Annalen der Physik 241*, pages 216–251, 1878.

S. Temkin, *Elements of Acoustics*. in *Acoustical Society of America*, NY, 2001, Reprint.

D. Tonon, B.J.T. Landry, S.P.C. Belfroid, J.F.H. Willems, G.C.J. Hofmans, A.Hirschberg, *Whistling of a pipe system with multiple side branches: Comparison with corrugated pipes*. in *J. Sound Vib. 329*, pages 1007–10024, 2010.

D. Tonon, A. Hirschberg, J. Golliard, S. Ziada, *Aero-Acoustics of pipe systems with closed branches*, in *Int. J. Aero-Acoustics 10*, pages 201–276, 2011.

M.P. Verge, B. Fabre, A. Hirschberg, A.P.J. Wijnands, *Sound production in recorderlike instruments. I. Dimensionless amplitude of the internal acoustic field*, in *J. Acoust. Soc Am. 101*, pages 2914-2924, 1997.

K. Viswanathan, *Mechanisms of jet noise generation: classical theories and recent developments*, in *Int. J. Aero-Acoustics 8*, pages 355–408, 2009.

M.C. Welsh, A.N. Stokes, *Flow-resonant sound interaction in a duct containing a plate, part I: Semi-circular leading edge*, in *J. Sound Vib. 95*, 1984.

T.A. Wilson, G.S. Beavers, M.A. De Coster, D.K. Holger, D. Regenfuss, *Experiments on the fluid mechanics of whistling*, in *J. Acoust. Soc. Am. 50*, pages 366–372, 1971.

S. Ziada, E.T. Bühlmann, *Self-excited resonances of two side-branches in close proximity*, in *J. Fluids Struct. 6*, pages 583–601, 1992.

# Sound Radiation by Moving Surfaces and the Green's Functions Technique

Michel Roger
Ecole Centrale de Lyon

**Abstract**

The present chapter is dealing with some fundamentals of sound radiation from rigid moving bodies or bodies in a flow. The theoretical background of the analogy is reminded in a first part. According to Ffowcs Williams & Hawkings' formulation the problem of sound generation by unsteady flows in the presence of solid surfaces is restated as a problem of linear acoustics with equivalent moving sources. Therefore the solving procedure is based on standard Green's function technique. This procedure is detailed in the second part as a necessary background and source motion is considered a key feature of the radiation. Aspects inherent to the wave operator and specific aspects of acoustic sources on the one hand, and source physics and source motion on the other hand, are addressed separately for the sake of physical understanding. In the third part formal developments and dimensional analysis of Ffowcs Williams & Hawkings' equation are proposed, both to highlight the flow features involved in sound generation and to point out the effects of motion. Some introductory topics have been presented in chapter 1 and are re-addressed for specific purposes.

## 1 Aerodynamic Noise Generation - Reminder of Basic Principles

### 1.1 Introduction

Aerodynamic noise radiation from an unsteady flow is a dissipation mechanism by which a tiny part of the mechanical energy of the flow is converted into sound. The particularity of this acoustic dissipation in open-air aeroacoustic problems is that it propagates at large distances and contaminates the environment. Moreover the acoustic dissipation rate of aerodynamic noise is a very rapidly increasing function of the characteristic Mach number. Yet it is at a much lower order of magnitude than other forms of

R. Camussi (Ed.), *Noise Sources in Turbulent Shear Flows: Fundamentals and Applications*, CISM International Centre for Mechanical Sciences, DOI 10.1007/978-3-7091-1458-2_2,

dissipation such as viscous losses. This makes the points of view of Fluid Dynamics and of Aeroacoustics differ. In absence of acoustic back-reaction, a flow can be most often described ignoring its acoustic dissipation, for what enters the scope of mechanical efficiency, losses, fuel consumption, and so on. In contrast describing the acoustic field requires a much higher level of accuracy. This remark holds for all unsteady flows encountered in aeronautics, turbomachinery, heating and ventilating engineering and ground transportation. More precisely the scope of this book reduces to the basic sound generating mechanisms which develop around bodies in translating motion because of some unsteadiness in the flow, provided by turbulence or instabilities.

As mentioned in chapter 1, the pioneering work of Sir M.J. Lighthill in the fifties (1952) addressing the problem of turbulence noise is generally considered the starting point for the investigation of aerodynamic noise. This work was next extended by Ffowcs Williams & Hawkings (1969) to include the presence of moving bodies in a flow. The basic idea is to define an acoustic analogy, by which the real problem involving a highly disturbed flow and moving solid surfaces is restated as a problem of linear acoustics in an unbounded uniform medium with some equivalent acoustic sources. The difficulty of solving exact, non-linear equations is then apparently avoided and replaced by the question of defining the equivalent sources. A crucial point is that there are different ways of deriving a wave equation from the equations of gas dynamics, leading to various analogies. Any analogy is based, first on the choice of the field variable the wave equation will govern, and secondly on the wave operator itself. Lighthill's formulation and subsequent developments resort to the classical wave operator acting on the fluctuating density recognized as the relevant acoustic variable. Other choices can be proposed, each leading to a different definition of the equivalent source terms. Anyway, the difficulty inherent to the equations of gas dynamics cannot be escaped by just writing the equations in another way. The pseudo-wave equation of the acoustic analogy cannot be solved exactly because generally the equivalent source terms still include contributions of the field variable to be determined : the equation and the source terms are said implicit. Therefore the advantage of the formalism is enlightened only if simplifying assumptions are accepted, for instance making the source terms explicit by removing the acoustic field variable from them. This has the effect of discarding some part of the physics. The resulting approach is an interpretation. It is fruitful whenever the neglected phenomena are of secondary importance and the dominant mechanism is preserved in the process. Furthermore the degree of simplification of the source terms can also be a matter of available means of describing the flow. Finally different

analogies are more suited in different practical problems, as already pointed in chapter 1. Because the interest of an acoustic analogy is to benefit from the formal simplicity of the standard Green's function solving procedure, the classical wave equation was preferred historically. Ffowcs Williams & Hawkings' formulation presented in this chapter and extensively applied in the aeroacoustic community obeys this strategy. But the idea of the analogy can be extended to more general propagation operators. Such extensions, more especially dealing with jet-noise applications, are described in subsequent chapters.

It must be stated clearly that the aim of an analogy is not essentially to provide very accurate results, but rather to infer general laws from the standard procedures associated with the classical wave equation. This may be sufficient to achieve low-noise design in engineering applications. However, a preliminary knowledge of the main flow features must be already available, either from experiments, Computational Fluid Dynamics (CFD) or theoretical considerations. What is the degree of required accuracy in the flow variables to get satisfactory acoustic results will be one of the key issues when applying the method. In other words tell me the flow I will tell you the sound.

### 1.2 Basic Mechanisms - External Flows

Major noise generating mechanisms from external wall-bounded flows are introduced and described shortly in this section. Phenomena associated with thermal conductivity are discarded so that the analysis is focused on mechanical aspects. Complementary developments should be considered for internal flows and/or combustion problems, as discussed in chapter 1. The different ways the mechanisms can be simulated or modeled for the sake of noise predictions in the far-field will be addressed in subsequent chapters.

The first fundamental principle to be retained from everyday life experience is that vortex dynamics makes sound. This implies two major mechanisms. First, sound is generated as free vortices interact mutually: this occurs in any turbulent mixing region such as a free jet or a turbulent boundary layer over a smooth boundary. Secondly, sound is generated as vortices interact directly with a geometrical singularity of a solid surface, such as a sharp edge, a corner, an excrescence or any accident. The second mechanism is much more efficient, as easily understood for instance by putting a knife blade in the jet of a pressure-cooker valve and hearing the difference in radiated sound level.

Examples shown is the chapter are just specific declinations of the same process. They are mostly related to a broadband noise signature since a

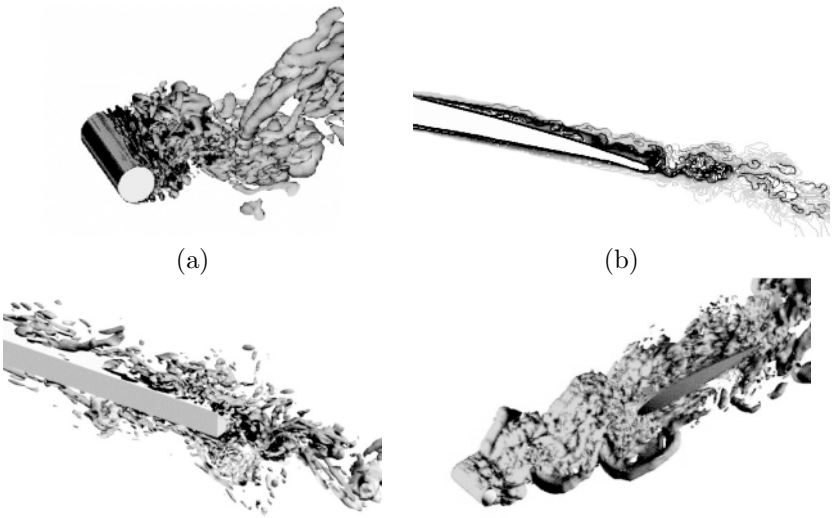


**Figure 1.** Generic turbulent flows responsible for broadband noise generation, illustrated by instantaneous 3D patterns (a, c, d) and 2D vortical trace (b). (a): vortex-shedding from a cylinder; (b): trailing-edge scattering of a turbulent boundary layer; (c): combined trailing-edge scattering and vortex shedding; (d): combined vortex-shedding and turbulence impingement on an airfoil. From Moon et al (2010) (a), Wang et al (2009) (b), Chang et al (2006) (c) and Jacob et al (2002).

turbulent flow is the origin of the sound generating process. Sound can also be radiated when a solid surface is moving through the air in an accelerated, periodic motion, as shown in section 5.4. This specific mechanism is typically involved in the tonal noise of rotating blades, not addressed in this book.

Typical unsteady vortical flows attached to solid surfaces and generating broadband or narrow-band noise at relatively moderate-to-large Reynolds numbers (in the sense that the flow regime is definitely turbulent) are illustrated in Fig. 1-a-to-d from Moon et al (2010), Wang et al (2009), Chang et al (2006) and Jacob et al (2002). All pictures are deduced from validated Large-Eddy Simulations (LES), either compressible or incompressible. They only illustrate the vortex dynamics responsible for sound production, not

the sound itself. The vortex-shedding mechanism (Fig. 1-a) produces the Aeolian tones heard when the wind is blowing on mechanical structures. The noise produced by trailing-edge scattering (Fig. 1-b) is important for all rotating-blade technologies, especially for wind turbines. Both may be produced together in the case of blunted trailing-edges (Fig. 1-c). The two-body configuration of Fig. 1-d is a first step toward the investigation of more complicated ones, such as the high-lift devices of an aircraft wing. In this case, the impingement of the vortical patterns shed from the first body onto the second one is generally much noisier than the vortex shedding itself. The first three cases are mechanisms of what is called the self-noise of a solid surface in a flow. The fourth one illustrates the turbulence-impingement noise of an airfoil. Both that noise and trailing-edge noise will be addressed specifically in chapter 5.

Going into the details, the faster the inertia variation in a vortical flow is, the more efficient is the acoustic dissipation. This makes sound production much stronger in the vicinity of singular points on a solid surface, such as leading or trailing edges of blades, slots or bumps on surfaces, and so on. For vortex-shedding noise, the dominant unsteady vortical motion takes place downstream in the very near wake. The rapid inertia variation is precisely in the formation of the vortices. As a result the source domain is the immediate vicinity of the cylinder. Trailing-edge noise is due to the rapid re-arrangement of boundary-layer turbulence as it is convected past the edge; this is why the efficient source region is a limited area around the trailing edge. The same holds in configuration (c) for both incriminated mechanisms. In case (d) the dominant source region is the more or less extended vicinity of the airfoil leading edge.

Previous examples refer to bodies of limited extent with respect to the acoustic or aerodynamic length scales. But boundary-layer flows developing on the walls of elongated bodies also generate sound. It is well accepted that a developed turbulent boundary layer over an extended and smooth surface such as a rigid flat plate is not an efficient sound generator because of its dominant quadrupole nature, as pointed out by Goldstein (1976). In contrast the aerodynamic sound is much higher if the surface exhibits a geometrical singularity. Therefore cavities, slits, excrescences or steps appear as localized sources of noise. This will be discussed in section 2.5.

Pictures of Fig. 1 together with aforementioned arguments stress that the dominant sources are quite localized around the surface edges and that vortex dynamics farther away in the wake is a minor contribution. With respect to a distant observer the unsteady flows act as equivalent moving sources radiating in the surrounding medium. The prediction methodology subsequently developed is in two steps; one is the description of the equiva-

lent sources, the other one is the description of the propagation itself. Both are detailed in next sections.

## 2 Ffowcs Williams & Hawkings' Formulation of the Acoustic Analogy

### 2.1 The Wave Equation

Lighthill's equation and alternative forms such as Powell-Howe's equation are reformulations of general gas dynamics equations which do not address specifically the question of physical boundaries. Yet aerodynamic noise from wall-bounded flows can be predicted from this general background by solving the wave equation together with relevant boundary conditions imposed on the wall surfaces. The needed material can be any code or software solving the wave equation, or the Helmholtz equation provided that a Fourier transform is performed to investigate single frequencies. This makes the sources of sound interpreted as distributed quadrupoles in Lighthill's analogy, and their radiation understood as just scattering by the surfaces. Such a view can be inconvenient if the character of the sources is fundamentally modified by the scattering. Furthermore the formal simplicity of the formalism, brought by the homogeneity of the propagation space, is partly lost because of the needed account of boundaries. Another interpretation is obtained when replacing the surfaces by additional equivalent sources supposed to radiate in free space, thus extending the original idea of the acoustic analogy. This is the essence of Ffowcs Williams & Hawkings' formulation (1969) presented now (Curle's analysis introduced in chapter 1 for a stationary surface can be considered included in this more general one).

The principle is as follows. The physical surfaces are removed and replaced by mathematical surfaces (Fig. 2). The corresponding inner volume is assumed to contain the same fluid at rest as in the distant propagating medium, whereas the surrounding flow is kept as such. In order to maintain the discontinuity between the inner volume and the real flow outside, additional sources of mass and momentum must be distributed on the surfaces. This is achieved by writing the equations in the sense of generalized functions. The continuity equation becomes

$$\frac{\partial \rho}{\partial t} + \frac{\partial}{\partial x_i}\left(\rho V_i\right) = \left[\rho\left(V_i - V_{si}\right)\right]_{(1)}^{(2)} \frac{\partial f}{\partial x_i}\,\delta(f)\,, \tag{1}$$

introducing the jump of a quantity $[\,]_{(1)}^{(2)}$ between both sides of the surfaces and specifying the kinematics of the surfaces by the equation $f(\mathbf{x}, t) = 0$.

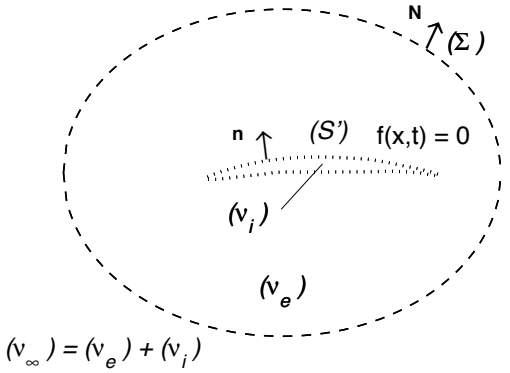


**Figure 2.** Mathematical surface definition in Ffowcs Williams & Hawkings' analogy. The outer surface ($\Sigma$) is rejected to infinity.

Here $\rho$ and $\mathbf{V}$ stand for the total density and velocity fields, and $\mathbf{V}_s$ is the body-surface velocity. The momentum equation reads

$$\frac{\partial}{\partial t}\left(\rho\, V_i\right) + \frac{\partial}{\partial x_j}\left(\rho\, V_i\, V_j - \sigma_{ij}\right) = \left[\rho\, V_i (V_j - V_{sj}) - \sigma_{ij}\right]_{(1)}^{(2)} \delta(f)\, \frac{\partial f}{\partial x_j} \quad (2)$$

with the same convention. In the inner volume the density reduces to $\rho_0$ and the fluid is at rest, whereas approaching the surface from outside the flow speed equals the body-surface velocity: $\mathbf{V} = \mathbf{V}_s$. The same algebra as for Lighthill's analogy yields the wave equation

$$\frac{\partial^2 \rho}{\partial t^2} - c_0^2\, \frac{\partial^2 \rho}{\partial x_i^2} = \frac{\partial^2}{\partial x_i\, \partial x_j}\left(\rho\, V_i\, V_j - \sigma'_{ij} - c_0^2\, \rho\, \delta_{ij}\right) \quad (3)$$
$$+ \frac{\partial}{\partial x_i}\left(\sigma'_{ij}\, \delta(f)\, \frac{\partial f}{\partial x_j}\right) + \frac{\partial}{\partial t}\left(\rho_0\, V_{si}\, \delta(f)\, \frac{\partial f}{\partial x_i}\right),$$

where Dirac's delta function is introduced. The first source term involves Lighthill's stress tensor $T_{ij} = \rho\, V_i\, V_j - \sigma'_{ij} - c_0^2\, \rho\, \delta_{ij}$ already discussed in

chapter 1 and involving the stress tensor $\sigma'_{ij}$. Furthermore if the function $f$ is properly scaled the normal unit vector on the surfaces is just $\nabla f = \mathbf{n}$ .

Equation (3) is exact, as a reformulation of the general equations of fluid dynamics. $\rho$ and $T_{ij}$ are understood in the sense of generalized functions: they are zero inside the mathematical surfaces and equal, respectively, to the density fluctuations and Lighthill's tensor of the flow outside. According to the new statement of the analogy the density fluctuations in the real fluid, in the presence of flow and rigid bodies, are those which would exist in an equivalent acoustic medium perfectly at rest and forced by three source distributions. The first term is responsible for the noise produced by virtue of flow mixing and distortions around the solid bodies. It is just the continuation of the quadrupole sources recognized by Lighthill. The second term is a surface distribution of dipoles (divergence of a vector field); it generates what is referred to as loading noise by reference to the aerodynamic loading of a surface in a flow. The third source term involving the time derivative of a scalar quantity is a distribution of monopoles. The resulting acoustic field will be called thickness noise.

The practical use of the formal result is subjected to the same need for simplifications of the source terms as for Lighthill's equation, if explicit solutions are expected from the general background of linear acoustics.The simplifications are summarized in next section.

### 2.2 Usual Approximations

Equation (3) is tractable in the usual way if the right-hand side is known independently of any acoustic consideration. The following approximations are generally retained; they can be partially released if the needed information is provided by a CFD code, for instance.

First the Reynolds number of the flow is assumed high and the fluctuating Mach number is assumed low. This leads to Lighthill's approximation $T_{ij} \simeq \rho_0 U_i U_j$ in which $\rho_0$ is the mean density and $\mathbf{U}$ stands for the aerodynamic velocity, cleaned of the acoustic motion. The second source term represents all contact forces, say $\mathbf{P}$, applied from the surfaces onto the fluid, and can be written $\nabla \cdot \mathbf{P}$. It involves both aerodynamic forces and acoustic pressure forces which represent sound scattering effects: $\mathbf{P} = \mathbf{P}^{aero} + p\,\mathbf{n}$. In many applications of interest, typically dealing with rotating-blade noise technology, the diffraction effects are ignored. This is accepted for convenience but only valid as long as the surfaces are acoustically compact. Any surface in a disturbed flow is both a source of sound and a scattering screen. Substantial errors can be generated if the surfaces are not compact anymore. The third term does not require any approximation, since it is

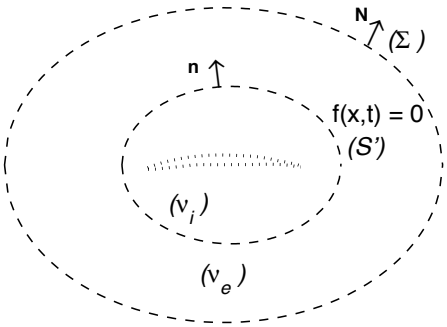


**Figure 3.** Permeable control surface definition in Ffowcs Williams & Hawkings' analogy. The outer surface ($\Sigma$) is rejected to infinity.

completely defined by the kinematics of the surfaces, assumed known.

### 2.3 Acoustic Analogy in a Moving Fluid

Invariance by any change of Galilean reference frame ensures that the equations of the acoustic analogies initially derived for a surrounding medium at rest naturally extend to the case of a uniformly moving medium of speed $\mathbf{V}_0$.The convected wave equation according to Ffowcs Williams & Hawkings' formulation, including Lighthill's as a special case, becomes

$$\frac{D^2\rho}{Dt^2} - c_0^2 \frac{\partial^2 \rho}{\partial x_i^2} = \frac{\partial^2}{\partial x_i \partial x_j} \left(\rho V_i' V_j' - \sigma_{ij}' - c_0^2 \rho \delta_{ij}\right) \tag{4}$$

$$+ \frac{\partial}{\partial x_i} \left(\sigma_{ij}' \delta(f) \frac{\partial f}{\partial x_j}\right) + \frac{D}{Dt} \left(\rho_0 (V_{si} - V_{0i}) \delta(f) \frac{\partial f}{\partial x_i}\right).$$

Lighthill's tensor is now defined by the relative velocity $\mathbf{V}' = \mathbf{V} - \mathbf{V}_0$, as well as the thickness-noise term involving the surface velocity vector $\mathbf{V}_s$. Furthermore time derivatives are accounting for convection by the mean flow : $D/Dt = \partial/\partial t + \mathbf{V}_0 \cdot \nabla$.

### 2.4 Penetrable Surfaces and the Extended Analogy

In all applications where the quadrupole term in eq. (3) is significant and must be calculated, which preferentially occurs at high speeds, the computations can be made cumbersome because the sources are distributed within a volume the boundaries of which are not precisely defined. In contrast, the surface source terms are much simpler to compute and clearly delimited. If CFD must be used in a limited domain surrounding the surfaces, and if the computations are able to reproduce the acoustic field in the vicinity of its sources, a more convenient way of solving the acoustic problem can be proposed by taking the information not on the physical surfaces but on a penetrable control surface that can be user-defined at some distance away. This generalized form of Ffowcs Williams & Hawkings' analogy is widely used in modern Computational Aero-Acoustics (CAA). The continuity and momentum equations are now written as

$$\frac{\partial \rho}{\partial t} + \frac{\partial}{\partial x_i}\left(\rho V_i\right) = \left\{\rho_0 V_{sn} + \rho\left(V_n - V_{sn}\right)\right\}\delta(f)\,,$$

$$\frac{\partial}{\partial t}\left(\rho V_i\right) + \frac{\partial}{\partial x_j}\left(\rho V_i V_j - \sigma'_{ij}\right) = \left\{\rho V_i\left(V_n - V_{sn}\right) - \sigma'_{ij}\, n_j\right\}\delta(f)\,,$$

where $\mathbf{n} = \nabla f$ stands for the normal to the control surface and where $V_{sn} = \mathbf{V}_s \cdot \nabla f$ and $V_n = \mathbf{V} \cdot \nabla f$ are normal velocities. The new expression of Ffowcs Williams & Hawkings' equation reads

$$\begin{aligned}\frac{\partial^2 \rho}{\partial t^2} - c_0^2 \frac{\partial^2 \rho}{\partial x_i^2} &= \frac{\partial^2}{\partial x_i\, \partial x_j}\left(\rho V_i V_j - \sigma'_{ij} - c_0^2\, \rho\, \delta_{ij}\right) \\ &- \frac{\partial}{\partial x_i}\left\{\left[\rho V_i (V_n - V_{sn}) - \sigma'_{ij}\, n_j\right]\delta(f)\right\} \\ &+ \frac{\partial}{\partial t}\left\{\left[\rho_0 V_{sn} + \rho\left(V_n - V_{sn}\right)\right]\delta(f)\right\}\end{aligned} \tag{5}$$

and all notations refer to the control surface, again of equation $f = 0$. Lighthill's tensor only needs being evaluated outside the surface. Therefore the latter can be chosen in such a way that the quadrupole contribution becomes negligible. In counterpart since the control surface is penetrable, the surface source terms are more complicated than in the standard form of Ffowcs Williams & Hawkings' equation.

As an example of the methodology, the sound radiated by a rotor operating in free field can be computed from a fixed control surface embedding the rotor, using eq. (5), which seems far simpler than the integration over the

moving blades. But the CFD code applied to get the complete field inside the control surface must reproduce accurately the sound waves generated by the blades or in the vicinity of the blades and their propagation up to the surface, in order to avoid numerical errors. This may be challenging. Finally, the benefit in the solving of the acoustic equation of the analogy is at the price of a bigger computational effort in the simulation of the flow inside the control surface. No way to escape the intrinsic difficulties.

An important corollary of Ffowcs Williams & Hawkings' formulation with penetrable surfaces is that it can take the non linear processes into account more easily. If sound is generated close to surfaces at a very high level, it propagates initially with significant non-linear aspects. Since the analogy written on the physical surfaces is exact when no approximation is made and since the wave equation is linear, the non-linear mechanisms must be all grouped in the equivalent quadrupole sources; if the latter are discarded from the analysis, the non linearity is ignored. In contrast, non-linear effects are treated implicitly by the CFD code used to solve the internal problem when resorting to a penetrable control surface.

### 2.5 Plurality of Interpretations

An acoustic analogy may be useless if no simplification is made. In contrast when simplifications are accepted to take advantage from the formal simplicity of linear acoustics, the analogy cannot be exact anymore and becomes an interpretation. In some circumstances the same configuration can be interpreted differently, resorting to either Lighthill's formalism or Ffowcs Williams & Hawkings'.

As an example consider the sketch of Fig. 4-(a) dealing with an excrescence attached to a plate of large dimensions, mimicking the side mirror of a car. Sound originates from the vicinity of the excrescence where intense vortex dynamics takes place. Lighthill's interpretation formulates the problem with distributed quadrupoles $T_{ij}$ assumed to radiate in a medium limited by the surfaces of the plate and of the body. Boundary conditions need being specified all over the surfaces. The tensor $T_{ij}$ must be deduced from a simulation of the flow. Because the Mach number is small in the case of the side-mirror, the only affordable effort is often incompressible LES. This is not an issue when post-processing the flow field with Lighthill's analogy, of course as long as there is no acoustic back-reaction on the flow. In principle the same configuration can be formulated with Ffowcs Williams & Hawkings' analogy. The surfaces are not considered as boundary conditions anymore but as distributed additional dipoles radiating as if the medium was unbounded. These sources are essentially wall-pressure fluctuations

if the Reynolds number of the flow is high enough, ensuring that inertial effects in the vortical motion dominate and that viscous terms may be neglected. The exact analogy states that the pressure includes the so-called hydrodynamic pressure associated with vorticity and the acoustic pressure associated with compressibility. If an incompressible simulation is used to feed the equation of the analogy with aerodynamic input data, the generation of sound by the surface is reproduced but the sound reflection by the surface is not. This is a significant source of error because the plate is larger than the acoustic wavelengths of interest. Furthermore sound radiates only in a half-space. In contrast, if accurate enough, a compressible simulation would account for the reflection.

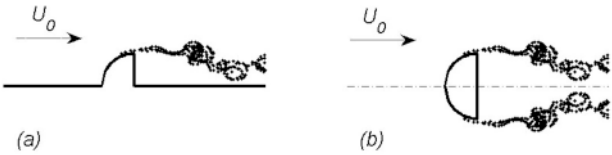


**Figure 4.** Excrescence on a flat wall. Real configuration (a) and best-suited image representation (b).

To cope with this issue, the problem can be stated by removing the plate and adding the symmetric images of both the flow and the excrescence (configuration (b)). The featured symmetric body is expectedly compact and now applying Ffowcs Williams & Hawkings' analogy with an incompressible description of the flow as input data makes sense. In configuration (b) the dominant sources should be dipoles distributed over the surfaces because at low Mach number quadrupoles are much less efficient; this accepted property results from the higher cancellations between constitutive elements of a quadrupole. But precisely the symmetry of the equivalent flow induces partial cancellation of opposite wall-normal forces. This features quadrupoles which combine with Lighthill's quadrupoles in the surrounding volume. In comparison the fluctuating forces parallel to the wall are doubled by the reflection. Again they are small at high Reynolds number, so that the quadrupole contribution can dominate, despite its intrinsic lower efficiency (Posson & Perrot (2006)). Introducing the image flow to account for the presence of a reflecting plane has been also discussed by Goldstein (1976) in connection with the noise generated by developed turbulent boundary layers over a flat plate. The net result is that, due to the cancellation of induced pressure forces, the sound remains fundamentally of quadrupole

nature. Again the viscous forces parallel to the plate are generally ignored because they are negligible at high Reynolds number. A different situation can be encountered if the viscous forces are made much larger by wall roughness.

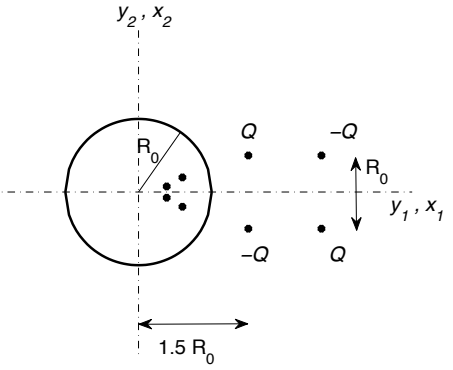


**Figure 5.** Academic exercise: scattering of a lateral quadrupole by a cylinder. Two-dimensional equivalent source distribution.

The different ways of posing a problem of aeroacoustics are typically illustrated next on the example of the vortex-shedding sound from a circular cylinder in a flow (Fig.1-(a)). For simplicity, the mechanism is described in two dimensions and the incriminated vortex dynamics is reproduced by an equivalent lateral quadrupole close to the cylinder in the near wake, in accordance with Lighthill's interpretation. The radiation process involves reflection or scattering of the quadrupole by the curved surface of the cylinder. At subsonic Mach numbers and in view of the vortex-shedding frequency $f_0 \simeq 0.2U_0/D$ where $U_0$ is the flow speed and $D$ is the diameter, the region embedding the cylinder section and the quadrupole is of small extent compared to the acoustic wavelength. The wave equation or the Helmholtz equation becomes locally equivalent to Laplace's equation. This means that the local acoustic motion can be assimilated to an incompressible potential flow. The sound field of a source close to the circle is obtained by removing the circle and adding two identical image sources : one at the center of the circle and the other one at distance $R_0^2/a$, where $a$ is the true distance of the source and $R_0$ the circle radius. The resulting configuration is shown in Fig. 5, where the image sources at the center are not shown because they exactly cancel each other. The natural field that would be radiated

by the isolated quadrupole in absence of the circle is shown in Fig. 6-(a), where the four expected lobes are clearly identified. Were the quadrupole close to a reflecting plane tangent to the circle, the field would be that of subplot (b), even less efficient. But the true sound as produced by the direct and image sources is much stronger and exhibits the two lobes of an equivalent dipole with orientation normal to the incident flow (subplot (c)). This is explained by the antisymmetric structure of the von Kármán vortex street, from which the assumption of a lateral quadrupole is justified. Nearly the same sound field is obtained by just ignoring the direct sources (subplot (d)); the radiating efficiency is explained by the image sources only, in other words by the scattering. The dipole-like behavior is due to the different partial cancellations between the source pairs closest to and farthest from the center. The two-lobed pattern is what would be similarly predicted by the dominant, loading-noise term of Ffowcs Williams & Hawkings' analogy. Indeed the dominant effect of vortex shedding is an oscillating induced lift on the cross-section of the rod, acting as a dipole. For this the equivalent source will be called a lift dipole. Both problem statements are found equivalent. Since the body is acoustically compact, the interpretation of Ffowcs Williams & Hawkings is better suited because it directly emphasizes the dipolar character of the sound field. Lighthill's approach in this case shows that the quadrupole behavior of the source is dramatically modified by the reflection on the cylinder. This is because the circular section is a compact body and because the source is very close to it in terms of wavelengths. This fundamental change is more deeply discussed by Howe (2003) using the formalism of compact Green's functions, not detailed here. It is worth noting that the case of the free-cylinder vortex shedding is very different from the side-mirror image flow. Changing from a symmetric to an antisymmetric flow pattern results in the excitation of a very efficient lift dipole.

Finally all classical statements of the acoustic analogy lead to the definition of equivalent moving sources in a linear wave equation. The sources can be monopoles, dipoles or quadrupoles. The formal solving of the wave equation and the effect of source motion on the radiated field are fundamental aspects, addressed in the next sections.

## 3 Green's Functions Technique - Moving Sources

The formal solution of the linear wave equation is provided by Green's function technique, fully described in many handbooks of acoustics and more specifically by Goldstein (1976). This background is shortly reminded here for the sake of completeness. The wave equation describes all prob-

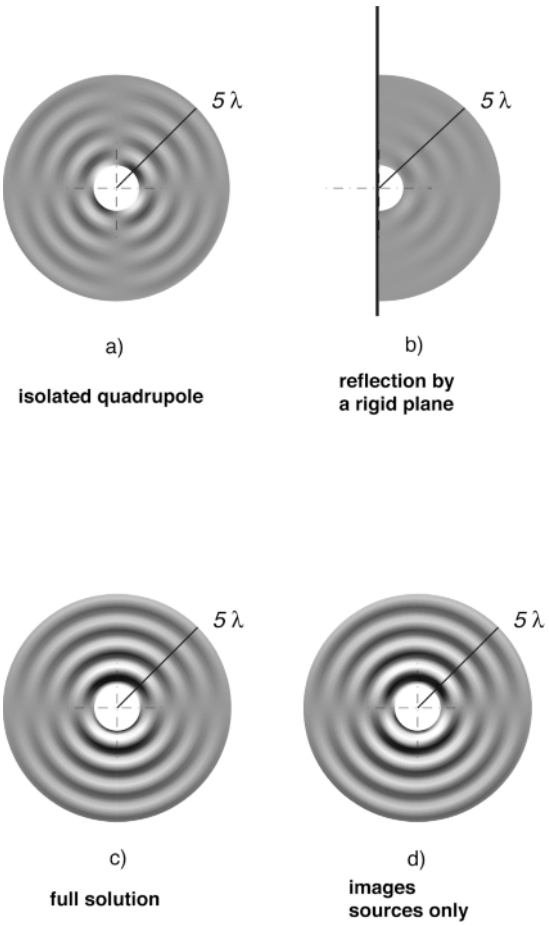


**Figure 6.** Academic exercise: scattering of a lateral quadrupole by a cylinder. Instantaneous pressure maps up to a distance of 5 wavelengths from the cylinder axis.

lems in mathematical physics in which the effect of some scalar quantity propagates with a finite speed. Aeroacoustics is just a special case in which the sources are related to unsteady flow features. Therefore source motion

is first analyzed here from the more general standpoint of the wave equation itself, and later specified to monopole, dipole and quadrupole acoustic sources. This will highlight the specific nature of acoustic sources.

### 3.1 General Solution

For the sake of generality, assume a prescribed source distribution $S(\mathbf{y}, t')$ radiating in a volume of space $\mathcal{V}(t')$ limited by possibly moving surfaces $\mathcal{S}(t')$. The local normal on the surfaces $\mathbf{n}$ is pointing outwards the volume. The wave equation for the scalar field variable $\varphi$ to be solved is written as

$$\Delta\varphi - \frac{1}{c_0^2}\frac{\partial^2\varphi}{\partial t'^2} = S\,.$$

Is called a Green's function for this equation and noted $G$ any solution in the case of an impulse point source, according to

$$\Delta G - \frac{1}{c_0^2}\frac{\partial^2 G}{\partial t'^2} = -\,\delta(\mathbf{x}-\mathbf{y})\,\delta(t-t')\,,$$

where $\delta$ is Dirac's delta function. $G$ depends on four variables and represents the field produced at point $\mathbf{x}$ and time $t$ by an elementary source at point $\mathbf{y}$ and time $t'$. If the effect of initial conditions is ignored, which is justified for periodic or stationary random processes, the formal solution for the scalar field follows as (Goldstein (1976))

$$\varphi(\mathbf{x},t) = -\int_{-\infty}^{\infty}\int_{\mathcal{V}(t')} G(\mathbf{x},t/\,\mathbf{y},t')\,S(\mathbf{y},t')\,d\mathbf{y}\,dt' \tag{6}$$

$$-\int_{-\infty}^{\infty}\int_{\mathcal{S}(t')}\left\{G\left(\frac{\partial}{\partial n}+\frac{V_n}{c_0^2}\frac{\partial}{\partial t'}\right)\varphi - \varphi\left(\frac{\partial}{\partial n}+\frac{V_n}{c_0^2}\frac{\partial}{\partial t'}\right)G\right\}d\mathcal{S}_y\,dt'\,.$$

The Green's function is not unique as long as no boundary condition is involved in its definition, but its expression must be known in order that explicit solutions are derived. The so-called tailored Green's function would provide the field produced at point $\mathbf{x}$ and time $t$ by an elementary source at point $\mathbf{y}$ and time $t'$ in the presence of the surfaces. If it can be known and introduced in the solution, then the surface integral vanishes. The corresponding explicit result generally leads to closed-form solutions. If another Green's function is used, the result is implicit and the formal solution is an integral equation. The simplest statement is obtained with the free-space Green's function $G_0$ for which the volume integral represents the direct field radiated by the source distribution and the surface integral represents all

effects of reflection and diffraction by the surfaces. The surface integral of course vanishes for sources radiating in free space, since no boundaries are present. This is assumed in the next and leads to the simplest solving procedure. Within the scope of the acoustic analogy, this formal simplicity is a great advantage of Ffowcs Williams & Hawkings' equation, obtained by considering the solid surfaces not as boundary conditions but rather as equivalent sources. The general free-field solution reads

$$\varphi(\mathbf{x},t) \;=\; -\int_{-\infty}^{\infty}\int_{\mathcal{V}(t')} G_0(\mathbf{x},t/\,\mathbf{y},t')\,S(\mathbf{y},t')\,d\mathbf{y}\,dt' \tag{7}$$

and the free-space Green's function has the fairly simple expression

$$G_0(\mathbf{x},t/\,\mathbf{y},t') \;=\; \frac{\delta(t'-t+R/c_0)}{4\,\pi\,R}\,,$$

with $R=|\mathbf{R}|=|\mathbf{x}-\mathbf{y}|$. Reduction of the time integral by the property of the delta-function leads to the formula of retarded potentials

$$\varphi(\mathbf{x},t) \;=\; -\int_{\mathcal{V}(t')} \frac{S(\mathbf{y},t+R/c_0)}{4\,\pi\,R}\,d\mathbf{y} \;=\; -\int_{\mathcal{V}(t')} \frac{[S]}{4\,\pi\,R}\,d\mathbf{y}\,. \tag{8}$$

The quantity $t_e=t-R/c_0$ is the retarded time or the emission time of the source at point $\mathbf{y}$, corresponding to a contribution at point $\mathbf{x}$ and time $t$. Conventionally, the evaluation of a quantity at the retarded time is denoted by squared brackets. The integral is to be performed over the actual, finite extent of the source distribution.

It is worth noting that for monochromatic fields of time dependence $e^{-i\,\omega\,t}$, the wave equation reduces to the Helmholtz equation, written below for the corresponding Green's function as

$$\left\{\Delta \;+\; k^2\right\}\,G_\omega \;=\; -\,\delta(\mathbf{x}-\mathbf{y})\,,$$

with $k=\omega/c_0$. The solution reads

$$G_\omega(\mathbf{x}/\mathbf{y}) \;=\; \frac{e^{i\,\omega\,R/c_0}}{4\,\pi\,R}\,.$$

It is seen that $G_0$ et $G_\omega\,e^{i\,\omega\,t'}$ are conjugate quantities by Fourier transform.

### 3.2 Moving Sources

Retarded-potential formula, eq. (8) is a description in terms of stationary sources. In order to address separately features related to source physics and source motion, going back to eq. (7) and specifying the motion in the source distribution $S$ is more appropriate. In this section, we consider an elementary point source of strength $q$ moving at constant speed $U_0 = |\mathbf{U}_0|$ in rectilinear motion (Fig. 7). Then $S(\mathbf{y}, t') = -q(t')\,\delta(\mathbf{y} - \mathbf{U}_0 t')$. Performing first the volume integral and then the time integral, and using properties of the delta-function (Jones (1972)) yields the simple expression

$$\varphi(\mathbf{x}, t) = \frac{1}{4\,\pi} \sum_j \frac{q(t_{ej})}{R_{ej}\,|1 - M_0\,\cos\theta_{ej}|}\,, \tag{9}$$

where the index $e$ refers to quantities evaluated at the emission time and where $M_0 = U_0/c_0$ is the Mach number. Indeed in a moving-source context the source continues its motion along its path during the propagation towards the observer. The received information at $(\mathbf{x}, t)$ is naturally expressed as a function, not only of the source strength at the corresponding emission time but also of the retarded location $\mathbf{y}_e = \mathbf{U}_0 t_e$, different from the current location $\mathbf{y} = \mathbf{U}_0 t$. The summation means that more than one retarded position is able to provide a contribution at $(\mathbf{x}, t)$ depending on the value of the Mach number. Using eq. (9) requires passage formulas between both sets of current and retarded coordinates. This is achieved by solving the retarded-time equation $t' = t_e(t)$ or equivalently by geometrical considerations on the sketch of Fig. 7. The result is

$$\frac{R_e(t)}{R(t)} = \frac{1}{\beta^2}\left(M_0\,\cos\theta(t) \pm \sqrt{M_0^2\,\cos^2\theta(t) + \beta^2}\right), \tag{10}$$

$$\cos\theta_e(t) = M_0 + \frac{R(t)}{R_e(t)}\,\cos\theta(t)\,, \tag{11}$$

with $\beta = \sqrt{1 - M_0^2}$.

Equations (9) to (11) imply key features of the radiation process. First the Doppler factor $1 - M_0\,\cos\theta_e$ in the denominator of eq.(9) causes anisotropy in the field, referred to as convective amplification. This is clearly understood from the instantaneous pattern of wavefronts emitted by the source at successive time steps, shown in Fig.8. For sub-critical motion ($M_0 < 1$) all wavefronts get closer to each other in front of the source and spread away from each other behind. The quantity delivered by the source in the forward (resp. rearward) direction distributes in a smaller

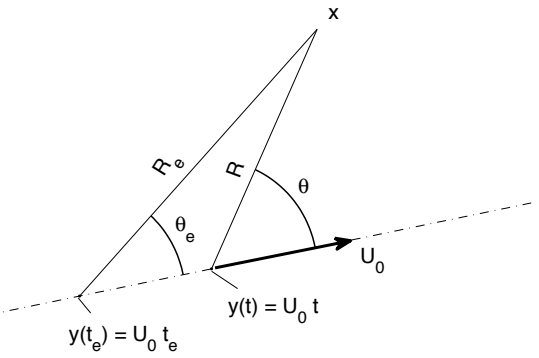


**Figure 7.** Retarded (emission) and current (reception) coordinates.

(resp. larger) volume between adjacent wavefronts, with respect to the case of a stationary source. The injection per unit volume is increased (resp. decreased), precisely in the ratio $1 - M_0 \cos\theta_e$.

Secondly, since $R_e(t)$ must be real and positive, the retarded-time equation always has a single root given by the sign + in the formula when $M_0 < 1$, and has zero or two roots depending on the angle $\theta$ for the supercritical regime $M_0 > 1$ because both signs are acceptable. In this case the series of wavefronts intersect each other with a conical envelope called the Mach cone (Fig.8-b). As long as the observer is external to the Mach cone he cannot receive any signal, whereas once inside he always receives two signals from two different retarded locations.

Finally, if the source function is assumed monochromatic with strength $q(t') = q_0\, e^{-i\,\omega_e\, t}$, the received signal cannot be monochromatic anymore. However performing a Taylor expansion of the solution around a reference time within a characteristic period of oscillation would restore an instantaneous frequency at observer $\omega = \omega_e/(1-M_0 \cos\theta_e)$. The received frequency is higher (resp. lower) than the emitted frequency for an approaching (resp. retreating) source. This frequency shift is known as Doppler effect. Again it is understood from Fig.8: an observer located in front of (resp. behind) the source receives wavefronts at a frequency higher (resp. lower) than the frequency emitted by the source, in the ratio of the Doppler factor.

For supercritical moving sources this factor has a singularity for the crit-

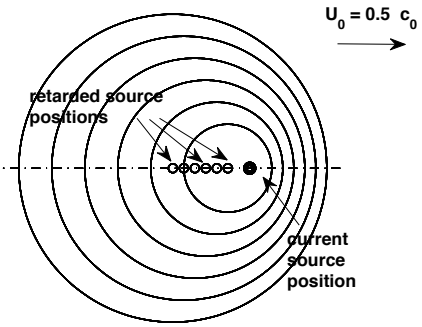


(a)

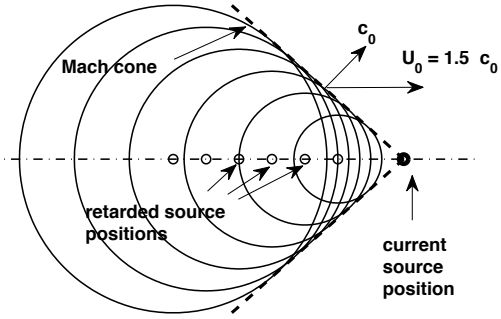


(b)

**Figure 8.** Wavefront structures featured by sub-critical (a) and supercritical (b) point sources. Motion from left to right.

ical angle $\theta_e = \sin^{-1}(1/M_0)$ encountered when the observer is exactly on the Mach cone attached to the source, at which the formalism breaks down. In order to give sense to the singularity, the supercritical moving elementary source can be simulated thanks to the identity with a linear distribution of stationary phased sources, provided that finite time and space scales are associated to the sources. This is illustrated in Fig. 9 in a discretized form with a series of impulses emitted by a linear array of sources, similarly to

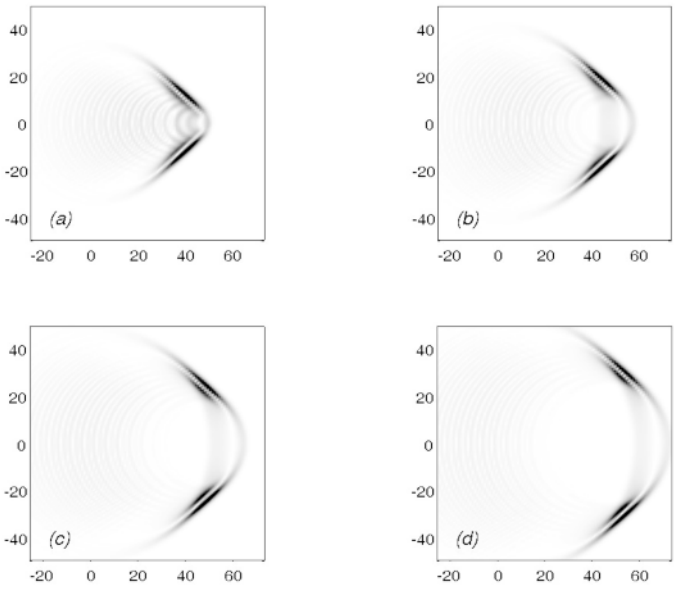


**Figure 9.** Formation of a focused wave on the Mach cone of a supercritical source, synthesized by 17 Gaussian spots. Simulated Mach number $M_0 = 2$, motion from left to right. From (a) to (d), successive time steps, gray scale updated for clarity.

what happens with Christmas electric garlands. Gaussian impulses which are solutions of the wave equation in spherical coordinates are used, according to the wave pattern $\varphi(r,t) = [(r - c_0\,t)/r]\,e^{-a^2\,(r-c_0\,t)^2}$, where $a$ is a parameter. Seventeen stationary sources are taken in the example to simulate a motion at Mach number 2 and the waves are superimposed at different time steps to produce the plots of the figure. The signal is found to focus as a spot on the Mach cone whereas it is rapidly attenuated in other directions. A closer look at the solution would exhibit a decay like the inverse square root of the propagation distance in the direction normal to the cone. Therefore the Doppler singularity is interpreted as a focused cylindrical wave in three-dimensional space (see Ffowcs Williams (1993)). When this happens with acoustic sources, sound propagates at much larger

distances than what is expected from simple spherical spreading. In aeroacoustics, such focused waves are encountered in supersonic jets because of supersonically convected quadrupoles. The mechanism is known as 'Mach-wave radiation'. Advancing blade tips of high-speed helicopter rotors also produce equivalent waves because of quadrupole sources onset within the air beyond the tip radius and moving supersonically.

It is worth noting that for a supersonically flying aircraft, the Mach cone of the acoustic sources is hidden by the shock wave structure attached to the aircraft. The shock wave is a non-linear, compressible aerodynamic feature, whereas the Mach cone is a linear wave envelope, but the both of them have the same angle.

All preceding features refer to the wave equation and can be observed as well in particle physics and in water waves. For instance the formation of a Mach cone for supercritical particles in the high atmosphere is known as the Cerenkov effect, and a similar pattern is generated when making ducks and drakes on water surface with a flat stone. Further aspects of source motion in aeroacoustics accounting for space and time correlation scales are discussed by Crighton (1975).

### 3.3 The Convected Wave Equation

Most problems in aeroacoustics involve stationary sources radiating in a uniformly moving medium instead of moving sources radiating in a medium at rest. This configuration is referred to as convection problem. The distinction has to be made because sound is always analyzed with the point of view of the observer. Noise radiated by helicopter rotors in forward flight by means of microphones embedded on an aircraft flying with the same velocity, aeolian tones emitted by wires in the wind and sound radiation by mock-ups in wind-tunnels are typical examples of convection problems. Because the source and observer are stationary in a moving medium of velocity $U_0 = |\mathbf{U}_0|$, the acoustic field is a solution of the convected wave equation:

$$\Delta\varphi - \frac{1}{c_0^2}\frac{D^2\varphi}{Dt^2} = S\,, \qquad \frac{D}{Dt} = \frac{\partial}{\partial t} + \mathbf{U}_0 \cdot \nabla \tag{12}$$

and by convention the first coordinate $x_1$ of unit vector $\mathbf{e}_1$ is in the direction of fluid motion, assumed lower than the propagation speed. The result can be deduced from the invariance of the general equations in a change of Galilean frame of reference, noting that the classical wave equation applies in a frame of reference moving with the propagating medium. The free-field Green's function for eq. (12), say $G_c$, differs from $G_0$. However, the

development of wavefronts in the convection problem is similar to that of a source moving with the same velocity $U_0$ in the opposite direction in a medium at rest. The source-to-observer relationship is depicted in Fig. 10 in terms of emission and reception coordinates, to be compared to Fig. 7. Due to wavefront convection, the exact (or geometrical) coordinates $(R, \theta)$ do not coincide with the coordinates of emission $(R_e, \theta_e)$. The latter are apparent coordinates for the observer. A geometrically equivalent configuration of moving source can be defined, in which the observer receives the same signal at time $t$ as if the source was at the retarded location $(R_e(t), \theta_e(t))$, whereas the actual location is the current one $(R(t), \theta(t))$. If this configuration is considered at that precise time when both sketches can be geometrically superimposed, the same relationship holds between $(R_e(t), \theta_e(t))$ and $(R(t), \theta(t))$, on the one hand, and between $(R_e, \theta_e)$ and $(R, \theta)$ on the other hand. Both the retarded coordinates in Fig. 7 and the apparent coordinates in Fig. 10 are emission coordinates; in the same way the current coordinates in Fig. 7 and the exact coordinates in Fig. 10 are reception coordinates. The passage formulas for the problem of convection are directly obtained from eqs. (10) and (11) as

$$\frac{R_e}{R} \;=\; \frac{1}{\beta^2}\left(M_0\,\cos\theta \;+\; \sqrt{M_0^2\,\cos^2\theta \;+\; \beta^2}\right)\,, \tag{13}$$

$$\cos\theta_e \;=\; M_0 \;+\; \frac{R}{R_e}\,\cos\theta\,. \tag{14}$$

The only difference with the case of the moving source is that eqs. (13) and (14) do not involve time as a parameter. Consequently, no Doppler effect occurs, so that the frequency at observer is exactly the same as the proper frequency of the source. This points two key features out. Doppler frequency shift occurs because of relative motion between source and observer. In contrast, convective amplification occurs in both problems, since it is a consequence of relative motion between source and propagating medium. This formal identity also provides a straightforward determination of the free-space Green's function for the convected wave equation by specifying an impulse source in the general retarded-potential formula. The expression follows as

$$G_c(\mathbf{x}, t/\mathbf{y}, t') \;=\; \frac{\delta(t' - t + R_e/c_0)}{4\pi\, R_s}\,, \tag{15}$$

with $R_s \;=\; R_e\,(1 - M_0\,\cos\theta_e) \;=\; R\,\sqrt{1 - M_0^2\,\sin^2\theta}$, $\theta$ being defined according to the sketch of Fig. 10. Changing for Cartesian coordinates in the

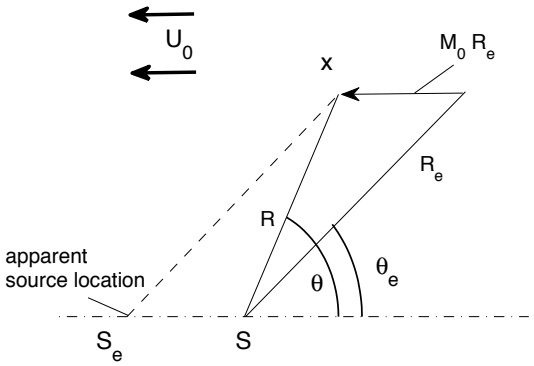


**Figure 10.** Stationary source radiating in a moving medium.

reference frame $(\mathbf{e}_1, \mathbf{e}_2, \mathbf{e}_3)$ and choosing $\mathbf{e}_1$ in the direction of the stream yields

$$R_s \;=\; \sqrt{(x_1 - y_1)^2 \;+\; \beta^2[(x_2 - y_2)^2 + (x_3 - y_3)^2]}\,,$$

$$R_t \;=\; \frac{1}{\beta^2}\,(R_s \;-\; M_0(x_1 - y_1))\,.$$

The retarded-potential formula in a moving medium follows as

$$\varphi(\mathbf{x}, t) \;=\; -\,\frac{1}{4\,\pi}\,\int_{\mathcal{V}_\infty} \frac{S(\mathbf{y}, t - R_t/c_0)}{R_s}\,d\mathbf{y}\,. \tag{16}$$

The formal identity also holds for the convected Helmholtz equation stating about harmonic signals. In this case the Green's function reads

$$G_\omega(\mathbf{x}/\mathbf{y}) \;=\; \frac{e^{i\,k\,R_t}}{4\,\pi\,R_s}\,.$$

It has been first addressed by Garrick & Watkins (1954).

### 3.4 Specific Properties of Acoustic Sources

Convective amplification and Doppler frequency shift associated with source motion have been introduced for an elementary point source specified

in the wave equation. They are characteristics of all waves fields, for instance also encountered in electromagnetism and water waves. Additional features are found when addressing acoustic sources, and more especially the source terms of the wave equation deduced from the acoustic analogy, rewritten symbolically as

$$\Delta p' - \frac{1}{c_0^2}\,\frac{\partial^2 p'}{\partial t^2} \;=\; -\rho_0\,\frac{\partial q}{\partial t} \;+\; \rho_0\,\frac{\partial F_i}{\partial x_i} \;+\; \rho_0\,\frac{\partial^2 Q_{ij}}{\partial x_i\,\partial x_j}\,.$$

This equation involves monopole, dipole and quadrupole-like source densities, so called because of the derivatives involved in their definition. The sources are moving in the applications but result from different fundamental mechanisms. Consider again the subsonic rectilinear motion as an illustrative example and the case of the monopole. Because the moving monopole is actually a moving source of mass as long as no combustion process associated with entropy variations is considered, the motion must be specified in the continuity equation, as

$$\frac{\partial \rho'}{\partial t} \;+\; \rho_0\,\frac{\partial v_i'}{\partial x_i} \;=\; \rho_0\,q(t)\,\delta(\mathbf{x} - \mathbf{U}_0\,t)\,,$$

yielding the corresponding wave equation for the acoustic pressure

$$\Delta p' - \frac{1}{c_0^2}\,\frac{\partial^2 p'}{\partial t^2} \;=\; -\rho_0\,\frac{\partial}{\partial t}\,\left[q(t)\,\delta(\mathbf{x} - \mathbf{U}_0\,t)\right]$$

different from the canonical form considered in previous section. Introducing the acoustic potential $\phi$ restores the canonical form for $\phi$ leading to eq. (9), from which the formal solution is derived for the acoustic pressure as now

$$p'(\mathbf{x},t) \;=\; \rho_0\,\frac{\partial}{\partial t}\,\sum_j\,\frac{q(t_{ej})}{4\,\pi\,R_{ej}\,|1 - M_0\,\cos\theta_{ej}|}\,.$$

The derivative of the denominator generates an extra factor $1/R_{ej}$ and corresponds to the near field of the moving monopole. As long as the acoustic far field is only of interest and the source is in subsonic motion, the solution reduces to

$$p'(\mathbf{x},t) \;=\; \frac{\rho_0}{4\,\pi}\,\frac{q'(t_e)}{R_e\,(1 - M_0\,\cos\theta_e)^2}\,, \tag{17}$$

where $q'$ stands for the time derivative of the mass injection. The Doppler

factor now appears twice in the denominator. In fact one factor arises from the shifted wavefront structure inherent to any source motion and the second one comes from the time derivative in the definition of the monopole. For this reason the monopole is better defined as different from the elementary source of mass, the former appearing as the time derivative of the latter.

The same procedure can be applied to sources of higher polar orders, by means of suited changes of variables. For a dipole of strength $F_j$ in the $\mathbf{e}_j$ direction, which is defined as two elementary sources of mass very close to each other and in phase opposition, the far-field pressure is found as

$$p'(\mathbf{x},t) \;=-\,\frac{\rho_0}{4\,\pi\,c_0}\,\frac{F_j'(t_e)\,[\mathbf{e}_j\cdot(\mathbf{R}/R)]}{R_e\,(1-M_0\,\cos\theta_e)^2}\,, \tag{18}$$

with no summation on $j$. Sound is again resulting from the time derivative of the source function. The convective amplification is the same but it has a different physical reason. One Doppler factor is due to the wavefront shift, and the other one is produced by virtue of a modified retarded-time difference between the two elementary sources of the dipole.

For a quadrupole of axes $\mathbf{e}_j$ and $\mathbf{e}_i$ the same procedure leads to the far-field term

$$p'(\mathbf{x},t) \;=\; \frac{\rho_0}{4\,\pi\,c_0^2}\,\frac{Q_{ij}''(t_e)\,[\mathbf{e}_i\cdot(\mathbf{R}/R)]\,[\mathbf{e}_j\cdot(\mathbf{R}/R)]}{R_e\,(1-M_0\,\cos\theta_e)^3} \tag{19}$$

involving the second time derivative of the quadrupole strength $Q_{ij}$, again without index summations. Convective amplification is found stronger for the quadrupole. This is important at high speeds and is determinant in the physics of mixing noise from jets. It is also noticeable that convective amplification induces additional directivity. Finally the nature of the moving acoustic sources cannot be ignored to analyze the far field.

Typical wave patterns of point dipoles are illustrated on the plots of Fig. 11, valid for both a moving source in a stationary medium and *vice versa* provided the reference frame is attached to the source. Convective amplification makes the radiation of a dipole parallel to the relative fluid motion stronger upstream (Fig. 11-b). Such a source will be called a drag dipole. The same holds for the case of a monopole, not shown here. In contrast radiation remains symmetrical for a lift dipole (Fig. 11-a). The total radiated power is enhanced for all types of sources, as shown below.

**Power criteria for moving point sources** Assessing the total acoustic power radiated by moving sources is made questionable by the need for

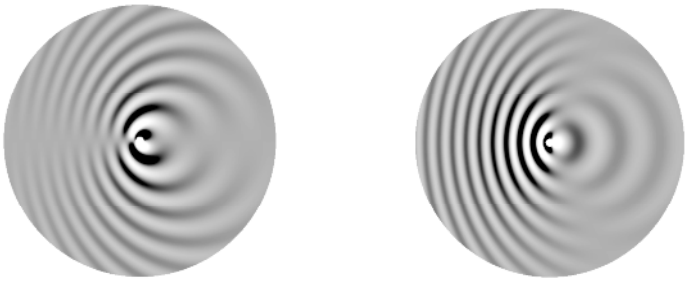

(a) (b)

**Figure 11.** Wavefront patterns of moving lift and drag dipoles, respectively normal (a) and parallel (b) to the relative flow direction, from left to right. Mach number $M_0 = 0.5$.

extending the usual definitions of acoustic intensity and power. For stationary sources the power is provided by integrating the instantaneous flux of the intensity vector over a control surface embedding the sources. If the surface is a sphere centered on the source, the intensity is of magnitude $I = < p'^2 > /(\rho_0 c_0)$ along the radial direction. But for a moving source issues are related to the different retarded positions of the source for reception of simultaneous signals at different points on the observation sphere. Equivalently the source and the control surface can be assumed stationary and the surrounding medium moving uniformly in the opposite direction. Now the only issues are related to the effect of fluid motion: the integration requires the extended definition of acoustic intensity in a uniformly moving fluid, which is a well-accepted notion (see for instance Goldstein (1976)).

As an alternative the far-field formulas derived for moving point sources and transposed to stationary sources in a moving medium by virtue of the equivalence discussed in section 3.3 can be used directly. Indeed they provide the acoustic intensity $I$ as a function of both the emission angle $\theta_e$ and the effective propagation distance $R_e$. Therefore integrating over all emission angles for a constant value of $R_e$ provides an acoustic-power indicator. When the expressions for the acoustic intensity are scaled by the source strength, the reduced expressions follow for a monopole, a parallel dipole and a perpendicular dipole, respectively, as

$$I_m(\theta_e) = \frac{1}{R_e^2 \, (1 - M_0 \cos\theta_e)^4} \, ,$$

$$I_{d1}(\theta_e) \;=\; \frac{\cos^2\theta_e}{R_e^2\,(1-M_0\cos\theta_e)^4}\,, \qquad I_{d2}(\theta_e,\phi) \;=\; \frac{\sin^2\theta_e\,\cos^2\phi}{R_e^2\,(1-M_0\cos\theta_e)^4}\,,$$

where $\phi$ is the complementary angle between the projection of the distance vector in the plane $\theta_e = 0$ and some direction normal to the relative flow direction. For the monopole and the parallel dipole the radiation is axisymmetrical and a simple integral over $\theta_e$ is performed with the sphere element $2\,\pi\,R_e^2\,\sin\theta_e\,d\theta_e$. The corresponding power criteria follow as

$$\Pi_m(M_0) \;=\; 4\,\pi\,\frac{1+M_0^2/3}{(1-M_0^2)^3}\,, \qquad \Pi_{d1}(M_0) \;=\; \frac{4\pi}{3}\,\frac{1+3M_0^2}{(1-M_0^2)^3}\,,$$

the factors $4\,\pi$ and $4\,\pi/3$ standing for the classical values of stationary monopoles and dipoles. A double integral is needed in the case of the perpendicular dipole, leading to

$$\Pi_{d2}(M_0) \;=\; \frac{4\pi}{3}\,\frac{1}{(1-M_0^2)^2}\,.$$

The result is substantially different for that dipole because it involves the squared amplification factor $(1-M_0)$ instead of the power 3 for the other two. Finally amplification rates are obtained by just forming the ratios of acoustic powers for the moving and stationary sources, as

$$T_m(M_0) \;=\; \frac{1+M_0^2/3}{(1-M_0^2)^3}\,, \qquad T_{d1}(M_0) \;=\; \frac{1+3M_0^2}{(1-M_0^2)^3}\,,$$

$$T_{d2}(M_0) \;=\; \frac{1}{(1-M_0^2)^2}\,.$$

These ratios characterize the effect of source motion assuming that the motion itself keeps the sources unchanged. They are plotted in Fig. 12 as functions of the source Mach number $M_0$. Obviously the lift (perpendicular) dipole is found much less sensitive to motion in the sense that its amplification is much weaker. This is essentially because the direction of motion relative to the fluid, for which the Doppler factor induces the strongest amplification, coincides with the extinction of the dipole radiation, whereas in the direction of maximum radiation the Doppler factor is just 1. For obstacles or bodies in a flow, the induced fluctuating aerodynamic forces are recognized as the dominant sources. They are precisely equivalent to quasi-perpendicular dipoles in most situations of interest, such as the circular cylinder in a flow (Fig. 1-a), thin airfoils with moderate camber and so on.

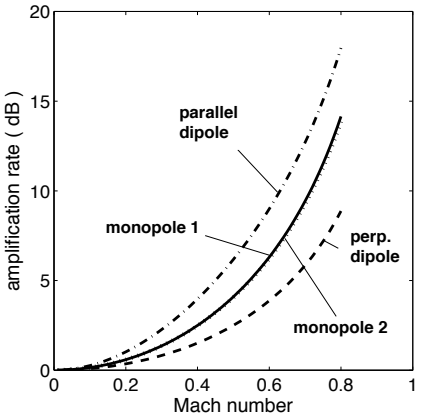


**Figure 12.** Acoustic power amplification rates as evaluated with the compact-monopole and dipole expressions. Second evaluation for the monopole plotted in dotted line.

Evaluating the acoustic power according to the aforementioned extended definition in a uniformly moving fluid requires quite tedious derivations, not detailed here. For instance, in the case of the monopole, the alternative expression of the amplification rate could be derived as

$$T_m \;=\; \frac{M_0^2}{(1-M_0^2)^3} \;+\; \frac{1}{2}\ln\left(\frac{1+M_0}{1-M_0}\right)\,\frac{1}{M_0\,(1-M_0^2)^2}\,.$$

Though mathematically different, the result is very close to the first evaluation for any reasonably subsonic Mach number, as shown in Fig. 12. It is found that globally source motion has a weak effect on sound power at Mach numbers typically below 0.3 or 0.5 depending on the source type, whereas the amplification is very significant at higher Mach numbers, characteristic of aeronautical applications.

It must be noted that the present simple developments do not hold anymore at source speeds approaching the speed of sound because the compactness needed for the definition of quasi-point sources cannot be ensured anymore.

## 4 Tailored Green's Functions - The Rigid Half-Plane

Exact tailored Green's functions which remain tractable for analytical modeling are very few in mathematical wave theory. Some of them can be generated from the free-space Green's function by the method of images, taking advantage of the fact that reflecting plates can be removed provided that the symmetric images of the primary sources are introduced (the principle has already been used in Fig. 4). The half-space bounded by an infinite, either soft or rigid wall, and the quarter-space defined by two perpendicular planes, can be treated this way. Similar is the case of the channel limited by two parallel planes, if the infinite set of sources corresponding to the successive reflections is considered. However the channel is better considered as a waveguide, and the Green's function expressed as a combination of the so-called acoustic modes of propagation (see for instance Goldstein (1976) for sound propagation in ducts). Other tailored Green's functions useful when formulating open-air radiation problems are also available for the space limited by a wedge of arbitrary angle, the half-plane being the special case of wedge with external angle $2\,\pi$ (Macdonald (1915)). Quite obviously, deriving tailored Green's functions for more complicated shapes can be as difficult as solving the full problem and is often accessible only through numerical implementations of the wave equation or of the Helmholtz equation. Therefore approximate Green's functions are an interesting alternative when they can be defined, for instance by removing the observer at very large distances. A class of such approximations, not discussed here, is provided by Howe's so-called compact Green's functions (Howe (2003)), often addressing sources very close to compact solid bodies and observers in the acoustic far field. Since the tailored Green's functions rely on source and/or observer distances scaled by the acoustic wavelength, they are more specifically associated with the Helmholtz equation and the frequency-domain approach.

### 4.1 The Half-Plane Green's Function

The emphasis is put here on the Green's function of the space limited by a rigid half-plane with zero thickness, known as the half-plane Green's function for the Helmholtz equation, because of its applications in aeroacoustics, for instance in the analytical modeling of trailing-edge noise or high-lift device noise. Initially derived by Macdonald (1915) in spherical coordinates for a stationary medium, the expression is easily transposed in cylindrical coordinates for a source point $\mathbf{x}_0 = (r_0, \theta_0, z_0)$ and an observer at point $\mathbf{x} = (r, \theta, z)$, with the $z$ axis along the edge and $\theta$ being $\pi$ along

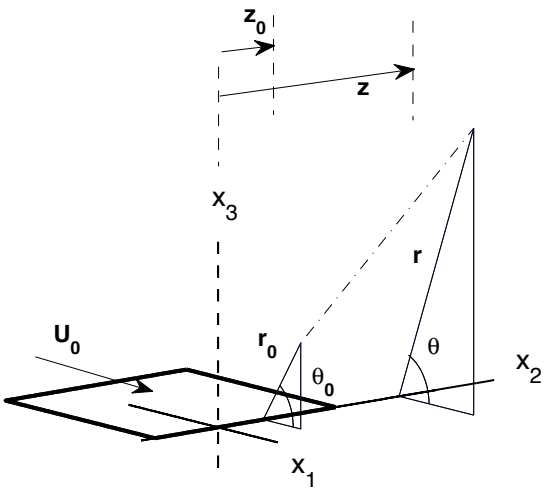


**Figure 13.** Half-plane set of coordinates for the definition of tailored Green's functions in the presence of uniform flow.

the half-plane and zero in its continuation (Fig. 13). It reads

$$G_\omega^{(1/2)}(\mathbf{x},\mathbf{y}) = \frac{-i\,k}{4\,\pi^2}\int_{-\infty}^{\xi_0} K_1^*\,(i\,kR\,\cosh\,\xi)\;d\xi \qquad (20)$$

$$+\,\frac{-i\,k}{4\,\pi^2}\int_{-\infty}^{\xi_1} K_1^*\,(i\,kR'\,\cosh\,\xi)\;d\xi\,,$$

where $K_1$ is the modified Bessel function of the first kind and where the upper bounds are given by

$$\sinh\,\xi_0 = \frac{2}{R}\,(r\,r_0)^{1/2}\,\cos\frac{\theta-\theta_0}{2}\,, \qquad \sinh\,\xi_1 = \frac{-2}{R'}\,(r\,r_0)^{1/2}\,\cos\frac{\theta+\theta_0}{2}\,.$$

R is the distance from the source to the observer $R = [r^2 + r_0^2 + (z - z_0)^2 - 2\,r\,r_0\,\cos(\theta-\theta_0)]^{1/2}$, and the similar expression for the distance from the image point to the observer $R'$ holds with $\cos(\theta+\theta_0)$. Equation (20) is the basis for deriving the radiated field of arbitrary source distributions accounting for the diffraction by the edge. The acoustic field of a point

dipole of force $\mathbf{P}$ is finally given by the scalar product $\mathbf{P}\cdot\nabla G_\omega^{(1/2)}$, and that of a quadrupole of strength $\mathbf{Q}$ by the double scalar product $\mathbf{Q}:\nabla\nabla G_\omega^{(1/2)}$.

Most reported applications, such as the trailing-edge noise analysis proposed by Ffowcs Williams & Hall (1970), are based on the asymptotic form of the Green's function for far-field observer and sources very close to the edge in terms of acoustic wavelengths. The asymptotic form reads

$$G_\omega^{(1/2)}(\mathbf{x},\mathbf{y}) \simeq \frac{e^{ik\bar{R}}}{\bar{R}}\left\{1+2\frac{e^{-i\pi/4}}{\sqrt{\pi}}\,(2kr_0\,\sin\phi)^{1/2}\,\sin\frac{\theta_0}{2}\,\sin\frac{\theta}{2}\right\}. \quad (21)$$

Because space derivatives of the Green's function are involved in the radiation by multi-pole sources, the term 1 in the brackets has no effect and factors $(kr_0)^{-1/2}$ and $(kr_0)^{-1}$ are produced, for dipoles and quadrupoles respectively. Since $kr_0$ is a small parameter, the net result is an amplification of the natural radiation by the sources. Furthermore the asymptotic directivity is determined by the factor $\sin\theta/2$ and features a cardioid pattern, no sound being radiated in the continuation of the half-plane and the maximum sound being radiated along the half-plane.

A two-dimensional version of the half-plane Green's function has been derived by Jones (1972), citing Macdonald, and re-addressed by Rienstra (1981) as

$$G_{\omega\,2D}^{(1/2)}(x_1,x_3,k) = \frac{1}{4\,\pi}\int_{-\infty}^{\xi_1}\frac{e^{i\,k\,r_1\,\sqrt{1+u^2}}}{\sqrt{1+u^2}}\,du + \frac{1}{4\,\pi}\int_{-\infty}^{\xi_2}\frac{e^{i\,k\,r_2\,\sqrt{1+u^2}}}{\sqrt{1+u^2}}\,du\,, \quad (22)$$

where the quantities $r_{1,2}$ and $\xi_{1,2}$ are just deduced from the equivalent parameters in eq. (20) by putting $z=z_0=0$.

A useful transformation can next be introduced to extend the preceding Green's functions in a stationary medium to the case of a uniformly moving medium, provided that the fluid motion is along $x_1$. The transposition formula reads

$$G_{M_0}^{(1/2)}(x_1,x_3,k) = \frac{1}{\beta}\,G_\omega^{(1/2)}(X_1,x_3,K)\,e^{-i\,K\,M_0\,(X_1-Y_1)}\,, \quad (23)$$

where $(X_1,Y_1) = (x_1,y_1)/\beta$, $K = k/\beta$ and where corrected angles accounting for flow convection are considered in original expressions. The transformation holds for two-dimensional and three-dimensional spaces, and

stretches the coordinate along the direction of the flow. In the two-dimensional case of a trailing edge, thus positive Mach number, a correction accounting for the Kutta condition has been proposed by Jones and re-addressed by Rienstra (1981). This condition has a noticeable effect at Mach numbers exceeding 0.5 and/or for sources located very close to the edge (see Roger & Moreau (2008)). It is ignored in the present discussion for conciseness.

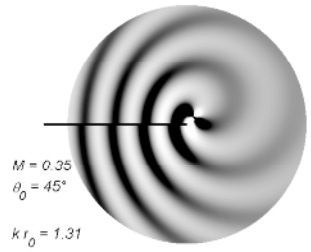


(a)

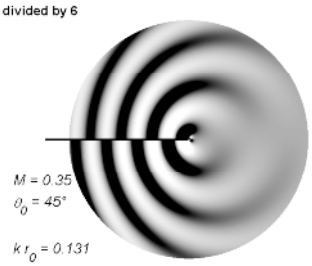


(b)

**Figure 14.** Sample wave patterns produced by the same point quadrupole either at some distance (a) or very close to a trailing edge (b), featuring the asymptotic regime. Source angle 45°, flow from left to right.

Exact two-dimensional radiation patterns obtained for the same point lateral quadrupole located at two different distances from a trailing edge are plotted in Fig. 14. The Mach number is 0.35, the source angle is $\theta_0 = 45°$ and no Kutta condition is applied. For the first plot (Fig. 14-a) the reduced distance to the edge is $kr_0 = 1.31$ and the same spiral pattern as in free field is recognized. At same distance but at $\theta_0 = 135°$, a shadow zone would be observed in the bottom part of the map because the half-

plane would act as a screen. For the second plot (Fig. 14-b) at the reduced distance $kr_0 = 0.131$ the asymptotic regime is reached and the radiation has the typical cardioid directivity imposed by the Green's function, with wavefronts in phase opposition on both sides. The same would be found for other source angles at the same distance. This regime is accompanied by a strong amplification since the gray-scale has been artificially damped by a factor 6 in order to make both plots comparable. An even stronger amplification would be found imposing a Kutta condition. The asymptotic regime is typical of trailing-edge noise from attached turbulent boundary-layers. Indeed Lighthill's interpretation followed by Ffowcs Williams & Hall (1970) involves quadrupoles remaining very close to the surface and the trailing edge in terms of acoustic wavelengths for all frequencies of interest. In contrast quadrupoles located farther away from the edge are amplification-free. From this fundamental result it is expected that attached turbulent flows over a trailing edge are much more efficient sound generators than small-scale vortical patterns developing, for instance, in the separated shear layers on stalled airfoils. According to Roger & Moreau (2008) the asymptotic regime is typically entered below $kr_0/\beta \simeq 0.4$ for quadrupoles and below $kr_0/\beta \simeq 0.2$ for dipoles. As a result turbulence convected along a wall far from a singularity must be a poor source of sound. More precisely, classical results about the relationship between trailing-edge noise and wall-pressure statistics (see chapter 5) make the cut-off frequency of the sound spectrum expected around $\omega\delta/U_0 \simeq 3$ for loaded airfoils, where $\delta$ is the boundary-layer thickness within which the quadrupole sources are distributed. A rough estimate of the condition for amplification associated with the asymptotic cardioid regime up to that frequency therefore reads $3\,(M_0/\beta)\,r_0/\delta < 0.4$. It appears that the condition is more easily satisfied at low speeds.

The asymptotic half-plane Green's function also explains the directivity of the vortex-shedding sound emitted as a von Kármán vortex street is formed in the near wake of a thin airfoil or plate with blunted trailing-edge. The roll-up of vortices features quadrupole sources that are scattered by the edge and the sound produced is again cardioid-like, with phase opposition on both sides of the plate. Because the shedding frequency is $0.2U_0/h$ where $h$ is the trailing-edge thickness and because the shorter expected edge-vortex distance is around $h$, now $kr_0/\beta \simeq 0.4\,\pi\,M_0/\beta$ is likely to be lower than 0.4 at low Mach numbers for the closest vortices. Despite the fact that they result from fundamentally different mechanisms, both trailing-edge noise and vortex-shedding noise have the same characteristic radiation properties imposed by the Green's function. Oppositely a laminar separation bubble at leading edge is sometimes observed on thin airfoils, triggering a turbulent

reattached flow. Since the bubble free shear layer is initially laminar, it is a possible source of noise only if its first oscillations take place at a leading-edge distance below the threshold $kr_0/\beta < 0.4$, and if the favorable condition is fulfilled by frequencies effectively covered by the instabilities.

## 5 Solution of Ffowcs Williams & Hawkings' Equation

### 5.1 Formal Solution

Since the solid surfaces responsible for sound generation are replaced by equivalent sources, the wave equation of the analogy as stated by Ffowcs Williams & Hawkings is solved in an unbounded medium at rest by making use of the free-space Green's function. The formal solution is described below for the standard application with integration on the solid surfaces. After making use of the general properties of convolution products and performing the change of variable $\mathbf{y} \to \eta$ where $\eta$ is the source coordinate vector in the reference frame attached to the surfaces, the acoustic pressure fluctuation at point $\mathbf{x}$ and time $t$ is expressed as

$$
\begin{aligned}
c_0^2\,\rho'(\mathbf{x},t) \;=\; & \frac{\partial^2}{\partial x_i\,\partial x_j}\int_{-\infty}^{+\infty}\int_{\mathcal{V}_\infty} T_{ij}(\eta,t')\frac{\delta(t'-t+R_\eta/c_0)}{4\,\pi\,R_\eta}\,d\eta\,dt' \qquad (24)\\
& + \frac{\partial}{\partial x_i}\int_{-\infty}^{+\infty}\int_{\mathcal{V}_\infty}\left(\sigma'_{ij}\,\delta(f)\frac{\partial f}{\partial y_j}\right)(\eta,t')\frac{\delta(t'-t+R_\eta/c_0)}{4\,\pi\,R_\eta}\,d\eta\,dt'\\
& + \frac{\partial}{\partial t}\int_{-\infty}^{+\infty}\int_{\mathcal{V}_\infty}\rho_0\left(V_{si}\delta(f)\frac{\partial f}{\partial y_i}\right)(\eta,t')\frac{\delta(t'-t+R_\eta/c_0)}{4\,\pi\,R_\eta}\,d\eta\,dt'\,,
\end{aligned}
$$

with $R_\eta = |\mathbf{x}-\mathbf{y}(\eta,t')|$. Note that the surfaces are assumed rigid.

Now use can be made of properties of the delta-function (Jones (1972)) to perform the time integrals, leading to the first form of Ffowcs Williams & Hawkings' solution

$$
\begin{aligned}
c_0^2\,\rho'(\mathbf{x},t) \;=\; & \frac{1}{4\,\pi}\frac{\partial^2}{\partial x_i\,\partial x_j}\int_{\mathcal{V}_e}\left[\frac{T_{ij}}{R|1-M_r|}\right]d\eta \qquad (25)\\
& -\frac{1}{4\,\pi}\frac{\partial}{\partial x_i}\int_{\mathcal{S}}\left[\frac{P_i}{R|1-M_r|}\right]d\mathcal{S}_\eta\\
& +\frac{1}{4\,\pi}\frac{\partial}{\partial t}\int_{\mathcal{S}}\left[\frac{\rho_0\,V_n}{R|1-M_r|}\right]dS_\eta
\end{aligned}
$$

expressed as integrals over the external volume $\mathcal{V}_e$ and the body surfaces

$\mathcal{S}$. Note that here the summation required for the two possible roots of the retarded-time equation in supersonic motion is not written for simplicity. In eq. (25) $\mathbf{P}$ is the net force on the fluid from each surface element, $V_n$ is the normal velocity field on the surfaces for a normal unit vector pointing inwards, $\mathbf{M}$ is the Mach number of the sources, corresponding to the velocity in the stationary frame of reference, $1 - M_r$ with $M_r = \mathbf{M} \cdot \mathbf{R}/R$ is the Doppler factor related to the projected motion on the line from the source to the observer, and the squared brackets mean that the embedded quantity is to be evaluated at the retarded time. Equation (25) clearly separates the contributions of source motion with respect to the stationary axes, and source physics described in the moving axes, leading to generality the simple arguments introduced with translating point sources in sections 3.2 and 3.4.

Though exact the result involves a surface distribution of monopoles whereas the total mass is constant for rigid surfaces. There is only fluid displacement induced by the passage of the surfaces. In fact the instantaneous balance of monopoles is exactly zero and sound is radiated only because of retarded-time differences between the monopoles. For this reason an alternative and mathematically equivalent form of the result has been proposed by Ffowcs Williams & Hawkings (1969) and Goldstein (1976) as

$$
\begin{aligned}
c_0^2\,\rho'(\mathbf{x},t) \;=\; & \frac{1}{4\,\pi}\,\frac{\partial^2}{\partial x_i\,\partial x_j}\int_{\mathcal{V}_e}\left[\frac{T_{ij}}{R|1-M_r|}\right]d\eta \\
& -\frac{1}{4\,\pi}\,\frac{\partial}{\partial x_i}\int_{\mathcal{S}}\left[\frac{P_i}{R|1-M_r|}\right]d\mathcal{S}_\eta \\
& -\frac{1}{4\,\pi}\,\frac{\partial}{\partial x_i}\int_{\mathcal{V}_i}\left[\frac{\rho_0\,\Gamma_i}{R|1-M_r|}\right]d\eta \;+\; \frac{\partial^2}{\partial x_i\,\partial x_j}\int_{\mathcal{V}_i}\left[\frac{\rho_0 V_i^{(0)} V_j^{(0)}}{R|1-M_r|}\right]d\eta\,,
\end{aligned}
\tag{26}
$$

introducing volume integrals of equivalent dipoles and quadrupoles over the inner volume $\mathcal{V}_i$ of the surfaces. Note that the volume and surface boundaries do not depend on time anymore. Notations $(\mathbf{V}^{(0)}, \Gamma)$ stand for the absolute velocity and acceleration fields defining the solid-body motion of the surfaces. All quantities are now defined in the sense of ordinary functions. Finally the noise radiated by flows and surfaces in arbitrary motion can be thought of as produced by dipoles and quadrupoles only. Moreover, when the inner volume of the surfaces tends to zero, as in the case of thin airfoils or blades of compressors, the noise from the third and fourth source terms in eq. (26) is expected negligibly small. This justifies the terminology of thickness noise. Both formulations are singular at the sonic radiation angle for which the denominator vanishes. The physical meaning of the singularity has been discussed in section 3.2. As shown by Ffowcs Williams &

Hawkings (1969) and Farassat (1983), it is removable at the price of other sophisticated solving procedures, not detailed here. The present expressions hold away from the singular condition, for either subsonic or supersonic regimes. For simplicity the subsonic regime is retained later on.

### 5.2 Far-Field Noise Radiation

In usual applications the observation point $\mathbf{x}$ is in the acoustic far-field, for which the general solution must be specified. This is achieved by applying commutation rules between the space derivatives and the retarded-time operator and only retaining the terms with the spherical attenuation (see Goldstein (1976) and Ffowcs Williams & Hawkings (1969)). Because the acoustic pressure is defined as $p' = c_0^2\,\rho'$ eq. (26) is changed in

$$\begin{aligned} p'(\mathbf{x},t) \;=\; & \frac{1}{4\,\pi}\int_{\mathcal{V}_e}\left[\frac{R_iR_j}{c_0^2\,R^3(1-M_r)}\frac{\partial}{\partial t'}\left(\frac{1}{1-M_r}\frac{\partial}{\partial t'}\left(\frac{T_{ij}}{1-M_r}\right)\right)\right]\,d\eta \\ & + \frac{1}{4\,\pi}\int_{\mathcal{S}}\left[\frac{R_i}{R^2\,c_0\,(1-M_r)}\left(\frac{\partial}{\partial t'}\left(\frac{P_i}{1-M_r}\right)\right)\right]\,d\mathcal{S}_\eta \\ & + \frac{1}{4\,\pi}\int_{\mathcal{V}_i}\left[\frac{R_i}{R^2\,c_0\,(1-M_r)}\left(\frac{\partial}{\partial t'}\left(\frac{\rho_0\Gamma_i}{1-M_r}\right)\right)\right]\,d\eta \\ & + \frac{1}{4\,\pi}\int_{\mathcal{V}_i}\left[\frac{R_iR_j}{c_0^2\,R^3(1-M_r)}\frac{\partial}{\partial t'}\left(\frac{1}{1-M_r}\frac{\partial}{\partial t'}\left(\frac{\rho_0V_i^{(0)}V_j^{(0)}}{1-M_r}\right)\right)\right]\,d\eta\,. \end{aligned} \tag{27}$$

This formula shows that unsteadiness is a necessary condition for noise to be heard in the far-field. Because dipoles are fundamentally more efficient sources than quadrupoles, on the one hand, and because thickness noise is expected of secondary importance for thin surfaces on the other hand, loading noise is very often dominant and never negligible. This is why the emphasis is put on the loading-noise term to highlight the role of unsteadiness. Writing

$$\frac{\partial}{\partial t'}\left(\frac{P_i}{1-M_r}\right) \;=\; \frac{1}{1-M_r}\frac{\partial P_i}{\partial t'} \;-\; \frac{P_i}{(1-M_r)^2}\frac{\partial(1-M_r)}{\partial t'}$$

indicates that far-field noise has two origins, namely the intrinsic unsteadiness of the source terms, considered in the moving frame of reference attached to the surface, and the unsteadiness due to source motion expressed by the Doppler factor. Furthermore,

$$\frac{\partial(1-M_r)}{\partial t'} \;=\; \frac{M_i}{R}\left(V_i^{(0)} - \frac{R_iR_j}{R^2}V_j^{(0)}\right) - \frac{R_i}{R\,c_0}\Gamma_i\,,$$

thus in turn the Doppler unsteadiness splits into two contributions. The second one results from the acceleration of the source; the first one also exists for non-accelerated motion but must be neglected as a near-field term in the far-field approximation. An important conclusion is that a steady force does produce sound if accelerated. This is a well-known contribution to the tonal noise radiated by high-speed rotating blades. In contrast a body in uniform translating motion produces sound in the far field only by virtue of unsteady aerodynamics, and variations of the denominator can be ignored to evaluate that noise.

When applied to the first term of Ffowcs Williams & Hawkings' equation the same analysis yields the simplified statement

$$p'(\mathbf{x},t) \;=\; \frac{1}{4\,\pi\,c_0}\int_{\mathcal{V}_e}\left[\frac{R_i R_j}{R^3(1-M_r)^3}\,\frac{\partial^2 T_{ij}}{\partial t'^2}\right]\,d\eta$$

useful for a preliminary understanding of the mixing noise from jets: far-field sound of translating quadrupoles arises from the second time derivatives of Lighthill's stress tensor. In fact the result is just an extended version of the point-quadrupole formula derived in section 3.4.

### 5.3 Compact Sources in Motion

For both numerical implementation issues and deeper insight into the general solution, the possibility of reducing the extended source region to a single point source or to a discretized set of sources involves the property of source compactness. A source region is said acoustically compact when retarded time variations over it are negligible in comparison with a characteristic period $T_\eta$. This condition is simple for stationary sources but more subtle for moving sources. It reads

$$T_\eta \;\gg\; \frac{L}{c_0\left[1-\overline{M}_r\right]}\,, \qquad\qquad \frac{L}{\left[1-\overline{M}_r\right]} \;\ll \lambda \tag{28}$$

where $L$ is the extent of the source region and $1-\overline{M}_r$ an average value of the Doppler factor.

A simple example is detailed below to illustrate this key notion. Consider an emitting segment of length $L$ moving at some subsonic speed $V_0 = M_0\,c_0$, as depicted in Fig. 15. At time $t$ the segment is between two points $(A,B)$ but the sound received at observer comes from retarded locations between the points $(A',B')$ that are the retarded locations of $(A,B)$ and that define the 'acoustic image' of the segment. Because the propagation distances from

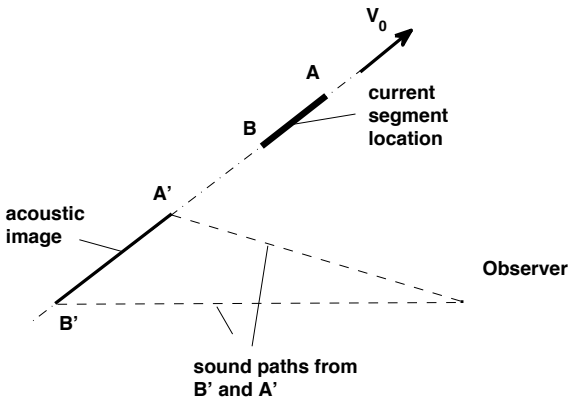


**Figure 15.** The moving segment.

all retarded locations are different, the length of the acoustic image differs from $L$. It is longer if the segment is approaching the observer and shorter if it is leaving. Motion artificially induces spatial stretching of any source distribution. Because compactness must be evaluated on the acoustic image, a given source region is more compact when leaving the observer and less compact when approaching. Assuming dipoles on the segment, the general expression of the acoustic pressure is provided for instance by the second term of Ffowcs Williams & Hawkings' solution specified as the line integral

$$p'(\mathbf{x},t) \,=\, \frac{1}{4\,\pi}\,\int_{-L/2}^{L/2}\left[\frac{R_i}{c_0\,(1-M-r)\,R^2}\,\frac{\partial}{\partial t'}\,\left(\frac{P_i}{1-M_r}\right)\right]\,d\eta\,.$$

For simplicity consider a uniform distribution of identical dipoles with axis aligned along the segment direction $\mathbf{e}_1$. The strength of the dipoles is $\mathbf{P} = P(t)\,\mathbf{e}_1 \,=\, A\,e^{-i\,\omega\,t}\,\mathbf{e}_1$. At the origin of time the center of the segment will be at observer's location, so that the times of interest are negative. The observer is assumed in the acoustical and geometrical far field, in front of the segment and on its trajectory. In these conditions the general formula reduces to

$$p'(\mathbf{x},t) \,=\, \frac{-i\,\omega\,A}{4\,\pi\,c_0\,(1-M_0)^2}\,\int_{-L/2}^{L/2}\left[\frac{e^{-i\,\omega\,t'}}{R(t')}\right]\,d\eta\,,$$

where the retarded time is a function of $(\mathbf{x}, \eta, t)$. At any time $t'$ the center of the segment is distant from the observer of $-M_0\, c_0\, t'$ and the element of the segment of coordinate $\eta$ is at distance $-(\eta + M_0\, c_0\, t')$ . Therefore $t_e(\eta) = (t+\eta/c_0)/(1-M_0)$. Furthermore in the far field $1/R_e(t) \simeq 1/R_0(t)$ where $R_0(t)$ is the retarded distance of the center of the segment. It is worth noting that the parameters involved in the far-field assumptions must be evaluated at the retarded time and position. Therefore the condition of geometrical far field reads $R_e(t) \gg L/(1 - M_0)$ and involves the length of the acoustic image of the segment. The acoustic pressure is finally written as

$$p'(\mathbf{x}, t) \simeq \frac{-i\, k\, A\, e^{-i\,\omega\, t/(1-M_0)}}{4\,\pi\,(1 - M_0)^2\, R_0(t)} \int_{-L/2}^{L/2} e^{-i\, k\, \eta/(1-M_0)}\, d\eta$$

$$= \frac{-i\, k\, A\, e^{-i\,\omega\, t/(1-M_0)}}{4\,\pi\,(1 - M_0)\, R_0(t)}\, \frac{L}{1 - M_0}\, \frac{\sin\left[kL/(2\,(1 - M_0))\right]}{kL/(2\,(1 - M_0))}\,.$$

The result for a stationary segment with the same source distribution would be obtained by putting $M_0 = 0$. The expression involves the sine-cardinal function which approaches 1 at very low frequencies such that $k\,L\,/(1 - M_0) \ll 1$. Under this condition the acoustic pressure is proportional to the length of the segment, because the distributed sources are identical and perfectly in phase in the example, and the whole segment is said compact. When the argument is a multiple of $\pi$, the function is exactly zero and no sound can be heard in the conditions of the example: all sources interfere in such a way to produce a complete cancellation. The crucial point associated with source motion is that the Mach number now enters the definition of the argument. Typically at $kL = \pi$ assuming source compactness for the stationary segment remains acceptable, whereas for the approaching segment at Mach number 0.5 the same frequency corresponds to a total extinction of the sound.

It is worth noting that the length of the acoustic image of the segment extends to infinity if the segment approaches the observer at exactly the speed of sound. In such conditions the solving procedure has been recognized as no longer valid. More generally the sonic singularity also means that any discretization cell of the source domain will not fulfill the compactness condition, leading to possible issues for numerical implementation.

Going back to the general result the assumed dominant loading-noise term for a compact surface in Ffowcs Williams & Hawkings' solution simplifies to

$$\frac{1}{4\,\pi} \int_{\mathcal{S}} \left[ \frac{R_i}{c_0\, R^2 (1 - M_r)}\, \frac{\partial}{\partial t'} \left( \frac{P_i}{1 - M_r} \right) \right] d\mathcal{S}_\eta$$

$$\simeq -\frac{1}{4\,\pi}\left[\frac{\overline{R}_i}{c_0\,\overline{R}^2}\,\frac{\partial}{\partial t'}\left(\frac{F_i}{1-\overline{M}_r}\right)\right], \qquad F_i = -\int_{\mathcal{S}} P_i\,d\mathcal{S}_\eta\,,$$

where the total aerodynamic force induced by the fluid on the surface $\mathbf{F}$ is introduced and where the over-bar, omitted in the following, stands for an average value over the surface. This simplified expression is the basis of the dimensional analysis proposed in the next section.

### 5.4 Dimensional Analysis

A rapid analysis is proposed in this section to assess both parts of the loading-noise term for a compact segment of lifting surface, keeping in mind that similar principles could be applied to other source terms. The kinematics of interest is that of a blade segment rotating at constant speed $\Omega$ at some radius $R_0$, so that the characteristic velocity scale is $U_0 = \Omega\,R_0$. The corresponding centripetal acceleration is $\Gamma_i = U_0^2/R_0$. The chord length is $c$ and the spanwise extent is assumed of the same order of magnitude. Steady-loading noise involves the steady-state aerodynamic force which scales according to $F_0 \simeq C_L\,c^2\,\rho_0\,U_0^2\,/2$ (see chapter 5 for justifications). In contrast the fluctuations around the mean value $F_0$ arise from time variations of the relative flow velocity on the segment; the velocity disturbances of amplitude $w$ are in most cases proportional to the mean-flow speed, leading to some disturbance rate $w/U_0$ which is assumed constant in the present analysis. According to simple unsteady aerodynamic arguments, typically Sears' theory outlined in chapter 5, the fluctuating force amplitude is evaluated as $\tilde{F} \simeq \pi\,\rho_0\,c^2\,w\,U_0$ and its time derivative as

$$\left|\frac{\partial F}{\partial t'}\right| \propto n\,\rho_0\,c^2\,w\,U_0^2/R_0\,,$$

where $n$ stands for a multiple of the rotational frequency ($R_0/U_0$ is taken as the relevant time scale). Furthermore $\partial M_r/\partial t' \propto U_0^2/(c_0\,R_0)$. Finally, introducing the acoustic far-field intensities $I_S$ and $I_U$ associated with steady-loading noise and unsteady-loading noise respectively leads to the dimensional evaluations

$$I_S \propto \frac{\rho_0\,c^4\,U_0^8}{R_0^2\,c_0^5\,R^2\,(1-M_0)^6}\,, \qquad I_U \propto n^2\,\frac{\rho_0\,(w/U_0)^2\,c^4\,U_0^6}{R_0^2\,c_0^3\,R^2\,(1-M_0)^4}\,,$$

$M_0 = U_0/c_0$ being the characteristic Mach number and $R$ the distance to the observer. This is made irrespective of possibly different constant scaling factors. Unsteady-loading noise intensity is found to scale with the sixth

power of a characteristic flow speed and to include the fourth power of the Doppler factor in the denominator. This is typical of dipoles in translating motion and is generally retained as the scaling law of dipole sources in aeroacoustics. In contrast steady-loading noise scales like the eighth power of flow speeds with the sixth power of the Doppler factor in the denominator, similarly to what is obtained for translating quadrupoles (see section 3.4). Comparing both contributions is achieved by forming the ratio

$$\frac{I_S}{I_U} \propto \frac{1}{n^2} \left(\frac{U_0}{w}\right)^2 \left(\frac{M_0}{1-M_0}\right)^2$$

to be considered with the rate of unsteadiness $w/U_0$ as parameter. It appears that the flow Mach number strongly determines which contribution dominates. At low to moderately subsonic Mach numbers and for a significantly disturbed oncoming flow, steady-loading noise can be neglected. The fluctuating forces on the moving bodies are the most efficient sound sources. This holds especially at higher frequencies. Conversely, at high Mach numbers, and more precisely at lower frequencies, steady-loading noise is the dominant mechanism, even with effective unsteadiness in the flow. But unsteady-loading noise must be considered anyway.

For constant rotating motion thus constant centripetal acceleration, the dipole part of thickness noise in eq. (27) would be found to behave like steady-loading noise. Without going further into the details, the same simple developments also suggest that quadrupole sources associated with flows around a body become efficient at transonic speeds.

Finally the dimensional analysis justifies that preferred attention is paid to unsteady loading noise in most applications. This is not only true for the broadband noise of bodies in translating motion but also for subsonic rotating blade segments. As a consequence all predictions methods developed in chapter 5 will hold for low-speed fans as well, even though the rotating motion will not be explicitly taken into account. Now once recognized as the primary source of sound, the unsteady loads on moving surfaces must be known as a first step to enable any prediction of the radiated sound field based on the acoustic analogy. This makes aeroacoustic predictions generally more challenging than classical aerodynamic predictions for engineering applications. Simulating steady-state aerodynamics is clearly affordable with modern computational tools; but it is more specifically related to the performances and mechanical efficiency of a system (fan, propeller, turbofan engine...). Acoustic predictions require the description of all kinds of unsteadiness in the flow, which is a much more demanding task in terms of resources. Moreover flow unsteadiness is often not intrinsic to the system

but rather depending on the environment or the installation of the system.

## 6 Concluding Remarks

The acoustic analogy has been presented in this chapter as a theoretical background for the analysis of aerodynamically generated sound. Once the equations of gas dynamics are reformulated as a linear wave equation, all flow features responsible for sound production are grouped in equivalent source terms. This mathematical statement makes the radiated sound field easily expressed from the sources, provided that the latter are previously determined accepting some simplifications. In that sense the analogy is an indirect approach. The flow must be first described assuming that it develops independently of its acoustic signature, and the sound calculation appears as a post-processing step. The equivalent sources are moving with respect to the observer and/or the surrounding medium. Therefore attention has been paid to emphasize all effects of motion in the formal solution, classically expressed by the Green's function technique. The most crucial point for practical sound predictions is the description of the sources. Applications to lifting surfaces are presented in chapter 5.

## Bibliography

K. W. Chang, J. H. Seo, Y. J. Moon & M. Roger, *Prediction of Flat Plate Self Noise*, 12th AIAA/CEAS Aeroacoustics Conference, paper 2006-2513, Cambridge MA, 2006

D.G. Crighton, *Basic principles of aerodynamic noise generation*, Prog. Aerosp. Sciences, 16(1),1975

F. Farassat, *The prediction of the noise of supersonic propellers in time domain; new theoretical results*, AIAA 8th. Aeroacoustics Conference, paper AIAA 83-0743, Atlanta, 1983.

J.E. Ffowcs Williams & L.H. Hall, *Aerodynamic sound generation by turbulent flow in the vicinity of a scattering half-plane*, J. Fluid Mech., vol.40, pp. 657–670, 1970.

J.E. Ffowcs Williams & D.L. Hawkings, *Sound generated by turbulence and surfaces in arbitrary motion*, Phil. Trans. Roy. Soc., A 264, 1969.

J.E. Ffowcs Williams, *Supersonic Sources make Focussed Waves* in Symposium on Aerodynamics & Aeroacoustics, Tucson AR, 1993. Published by K.Y. Fung, World Scientific 1994.

I.E. Garrick & C.E. Watkins, *A Theoretical Study of the Effect of Forward Speed on the Free-Space Sound-Pressure Field Around Propellers*, NACA Report 1198, 1954.

M.E. Goldstein, *Aeroacoustics*, McGraw-Hill, NY, 1976.

M.S. Howe, *Theory of Vortex Sound*, Cambridge Univ. Press, Cambridge, 2003.

M. Jacob, J. Boudet, D. Casalino & M. Michard, *A rod-airfoil experiment as benchmark for broadband noise modeling*, J. Theo. Comp. Fluid Dyn., 26 pages, on line, DOI: 10.1007/s00162-004-0108-6 2002

D.S. Jones, *Generalised functions*, MacGraw Hill, 1966.

D.S. Jones, *Aerodynamic Sound due to a Source Near a Half-Plane*, J. Inst. Maths Applics, vol. 9, pp. 114122, 1972.

H.M. Macdonald, *A Class of Diffraction Problems*, Proc. London Math. Soc. vol. 2(14), 1915.

Y.J. Moon, J.H Seo, Y.M. Bae, M. Roger & S. Becker, *A hybrid prediction method for low-subsonic turbulent flow noise*, Comput. & Fluids, vol. 39, pp. 1125-1135, 2010

H. Posson & F. Perrot, *Far-field evaluation of the noise radiated by a side-mirror using LES and acoustic analogy*, 12th AIAA/CEAS Aeroacoustics Conference, paper 2006-2719, Cambridge MA, 2006.

S.W. Rienstra, *Sound diffraction at a trailing edge*, J. Fluid Mech., vol. 108, pp. 443460, 1981.

M. Roger & S. Moreau, *Edge scattering of distributed sources - application to high-lift device noise*, 14th AIAA/CEAS Aeroacoustics Conference, AIAA Paper 2008-2866, Vancouver, Canada, 2008.

M. Wang, S. Moreau, G. Iaccarino & M. Roger, *LES prediction of wall-pressure fluctuations and noise of a low-speed airfoil*, Int. J. of Aeroacoustics, vol. 8(3), pp.177-198, 2009.

# Part 2: Applications

# Jet Noise

Philip J. Morris* and K. Viswanathan†

* Department of Aerospace Engineering, The Pennsylvania State University, University Park, PA 16802, USA

† The Boeing Company, Seattle, WA 98124, USA

**Abstract** This chapter provides an overview of the present understanding of jet noise from both an experimental and analytical viewpoint. First, a general review of experimental observations is provided. Only single axisymmetric jets are considered. Then a historical review of theoretical contributions to jet noise understanding and prediction is provided. The emphasis is on both the assumptions and shortcomings of the approaches, in addition to their successes. The present understanding of jet noise generation mechanisms and noise predictions is then presented. It is shown that there remain two competing explanations of many observed phenomena. The ability of the different approaches to predict jet noise is assessed. Both subsonic and supersonic jets are considered. Finally, recent prediction methods and experimental observations are described.

## 1 Introduction

The advent of the jet engine as the preferred propulsion system, first for military aircraft and then for commercial aircraft, highlighted the problem of jet noise. The extremely high noise levels of the small military jets of the Second World War needed to be reduced significantly before larger jet-powered aircraft could be introduced into civilian service. In the early 1950's letters began appearing in the Times of London complaining about "the screaming of jet fighters" at seaside towns in England on the weekends and a Presidential Commission identified noise as the "principal nuisance factor," for people who live near airports (see Bolt (1953)). Initially, research was experimental. In England, jet noise studies were being conducted at Cranfield by Westley and Lilley (1952) and in Southampton by Powell (1953a). In the United States, von Gierke (1953) at Wright-Patterson Air Force Base and Hubbard and Lassiter (1953) at Langley Field were also conducting jet and propeller noise measurements. Powell (1954) provided a survey of jet

R. Camussi (Ed.), *Noise Sources in Turbulent Shear Flows: Fundamentals and Applications*, CISM International Centre for Mechanical Sciences, DOI 10.1007/978-3-7091-1458-2_3,

noise experiments conducted to that time. The seminal theoretical contributions were made by Lighthill (1952), Lighthill (1954). In addition, the introduction of his *Acoustic Analogy* provided a framework for the correlation of experimental data. For example, the theory resulted in scaling laws such as the "eighth power law" for the radiated power as well as the high and low frequency dependencies of the spectrum. A review of this theory and its subsequent extensions is given in Section 3.1.

These notes are not intended to be a comprehensive review of jet noise research over the last fifty years. There have been several excellent reviews during this period. These include (among others); Lighthill (1963), Ribner (1964), Goldstein (1976), Ffowcs Williams (1977), Lilley (1995), Goldstein (1995) and Tam (1995a). A good reference for an overview of aircraft noise is given by Smith (1989). Here we have emphasized key theoretical and experimental studies and the latest developments. These notes represent our opinions, not always unanimous, and we apologize in advance for any omissions.

## 2 Experimentally Observed Characteristics of Jet Noise

There are three principal jet noise components. These are the turbulent mixing noise, broadband shock-associated noise, and screech tones. The latter two components are present only for supersonic jets and only when the nozzle is operated at off-design conditions. The relative importance of the three components is strongly dependent on the noise radiation direction. Turbulent mixing noise is dominant in the aft direction, while the shock noise is dominant in the forward direction for round nozzles. Most commercial jet engines have fixed nozzle geometry, with the jet Mach number being subsonic during takeoff. During climb and at cruise, the ambient pressure is much lower than at sea level and the nozzle is often operated at supersonic conditions, generating shock noise. Several experimental studies since the seventies have investigated the characteristics of the three noise components. First the salient experimental results are presented.

### 2.1 Turbulent Mixing Noise

The noise from a high-speed jet is intimately related to the turbulence characteristics of the jet. Both fine-scale turbulence and large-scale turbulence generate noise. It is important to note here that the terms fine-scale and large-scale turbulence noise are very imprecise and confusing. As discussed in Section 3.3, the terms are used in these notes to distinguish

between different noise generation mechanisms. The fine-scale turbulence mechanism is taken to be associated with relatively compact sources and involves the propagation of the sound, once generated, through the moving, sheared mean flow. Thus mean flow/acoustic interaction effects such as refraction, described in Section 3.1, are important for this noise source. The large-scale noise mechanism is associated with a direct connection between the turbulent structures in the jet shear layer and the acoustic field. An example is given by the instability wave model discussed in Section 3.2. Both mechanisms are broadband in nature, though the large-scale noise radiation is expected to dominate at low frequencies and small angles to the jet downstream axis. The relative contributions of these two noise mechanisms depend on the jet Mach number, jet temperature, and the radiation angle. For subsonic jets, especially at low and moderate temperatures, the large turbulence structures propagate downstream at subsonic speeds relative to the ambient speed of sound. For these jets, the fine-scale turbulence is probably the dominant noise source at most angles. However, at angles close to the jet axis, including the peak noise radiation angles, the contribution from large-scale structures could be significant. For supersonic jets, and subsonic jets at high temperatures, as in practical jet engine applications, the large-scale structures convect downstream at supersonic speeds relative to the ambient speed of sound. As such, they are efficient generators of noise and constitute the dominant noise sources, especially in the downstream direction.

Jet noise depends on the jet operating conditions: Nozzle Pressure Ratio (NPR) $p_t/P_a$ and Total Temperature Ratio (TTR) $T_t/T_a$, the nozzle exit area (related to the fully expanded jet diameter $D_j$), the distance of the observer from the nozzle exit, ambient conditions, and the polar direction of radiation $\psi$. [1] Usually, the origin of the reference coordinate system is located at the center of the nozzle exit, with *the noise emission angle measured from the inlet axis.* Unless otherwise stated, this convention is followed throughout this set of class notes. However, theoretical analysis usually uses the angle $\theta$, which is the polar angle measured from the jet downstream axis. Jet noise was typically measured in 1/3-octave bands until the late nineteen eighties. The bandwidth that corresponds to a particular 1/3-octave band center frequency, increases as frequency increases. In the last few decades, high quality narrow band spectra have been measured. These narrow band data shed more light on the noise characteristics and have been used by researchers in the development of noise prediction

[1] For noncircular jets the noise is also a function of the azimuthal location, though this effect is generally small unless the aspect ratio of the nozzle is very large.

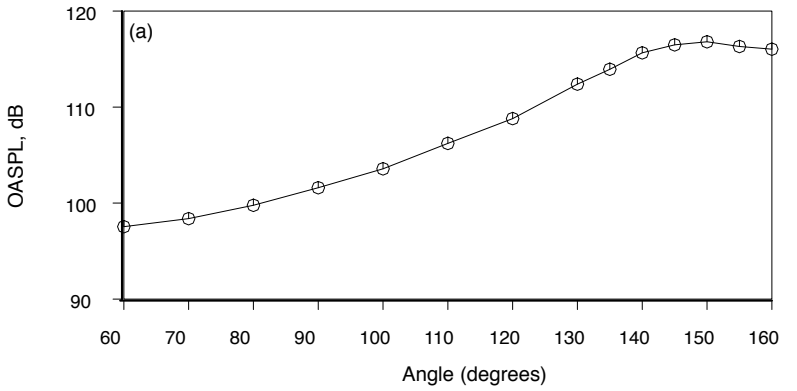


**Figure 1.** Overall Sound Pressure Level of typical mixing noise from a round nozzle corrected to a polar distance of 100 diameters. $D$ = 8.79 cm, $M_j$ = 0.86, $T_t$ = 811K.

methods. However, the metric for the calculation of aircraft or engine noise is the effective perceived noise level (EPNL), which is based on octave or 1/3-octave spectra. In computing the EPNL, the measured spectrum at each observer angle is converted to a single number based on a set of formulae or a table, with the octave band center frequencies weighted differently. The heaviest weighting is given to frequency bands to which the average human listener is most sensitive. For aircraft certification, the computed perceived noise level at each angle (or time) is integrated to account for the duration effect, and an effective perceived noise level is calculated. The approved procedure for noise certification has been established by the Federal Aviation Authority, see code of federal regulations, part 36. The procedure for aircraft noise certification is described by Peart et al. (1995). It is clear from the above description that these regulations have profound implications for noise reduction strategies. Though it would be desirable to reduce the noise level at all frequencies, any noise reduction concept should target those frequencies that reduce the perceived noise level.

Figure 1 shows the typical noise characteristics of a hot subsonic jet with $M_j$ = 0.86 and $T_t$ = 811 K at a polar distance of 100 diameters. The Overall Sound Pressure Level (OASPL) increases gradually with observer angle from the inlet and reaches a peak at approximately 150 degrees. The spectra at 90 degrees to the jet are shown in Figure 2 from Viswanathan (2004). This figure also shows the effect of increasing Mach number. It should be noticed

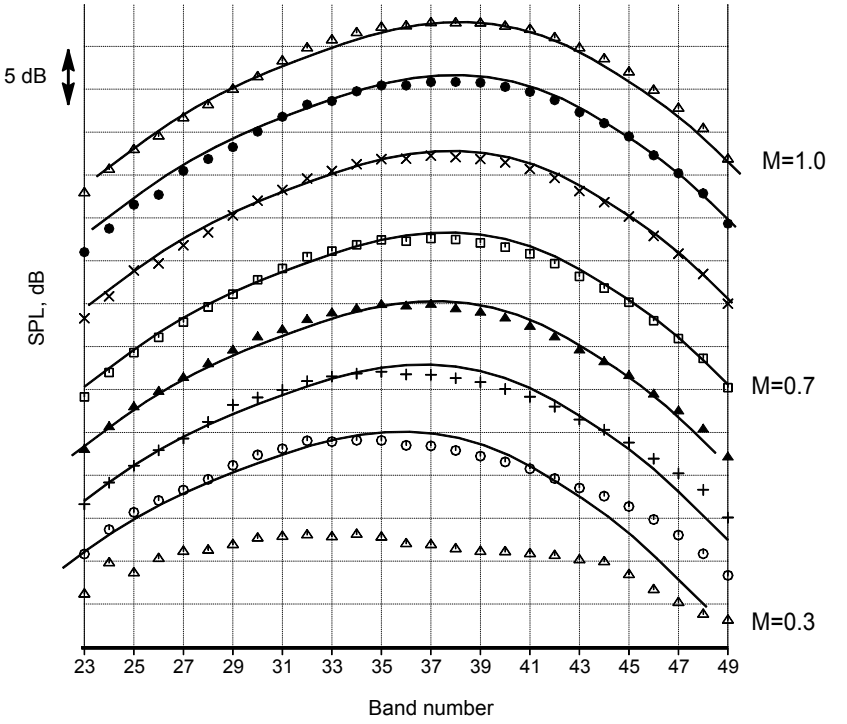


**Figure 2.** Comparison of spectra from unheated jets. $D$ = 1.5 in., inlet angle = $90^o$. Symbols: $M$ = 0:3; 0:4; 0:5; 0:6; 0:7; 0:8; 0:9; 1:0. Lines: FSS spectrum. (From Viswanathan (2004), with permission)

that all the spectra have the same broad, flat shape, which is characterized by the fine-scale similarity (FSS) spectrum of Tam et al. (1996). This is discussed in more detail in Section 3.3 below. At the lowest Mach number the jet noise spectra are contaminated by facility noise and do not conform to the FSS spectral shape. The spectral shape at larger inlet angles is much more peaked with a faster roll-off at both high and low frequencies. This is shown in Figure 3 from Viswanathan (2004) for several subsonic Mach numbers and an unheated jet at 160 degrees. Also shown in the figure are curves representing the Large Scale Similarity (LSS) spectrum from Tam et al. (1996): see Section 3.3. The agreement is very good. Also notice that the peak frequency is independent of jet Mach number.

The acoustic analogy by Lighthill (1954) provides a scaling formula for

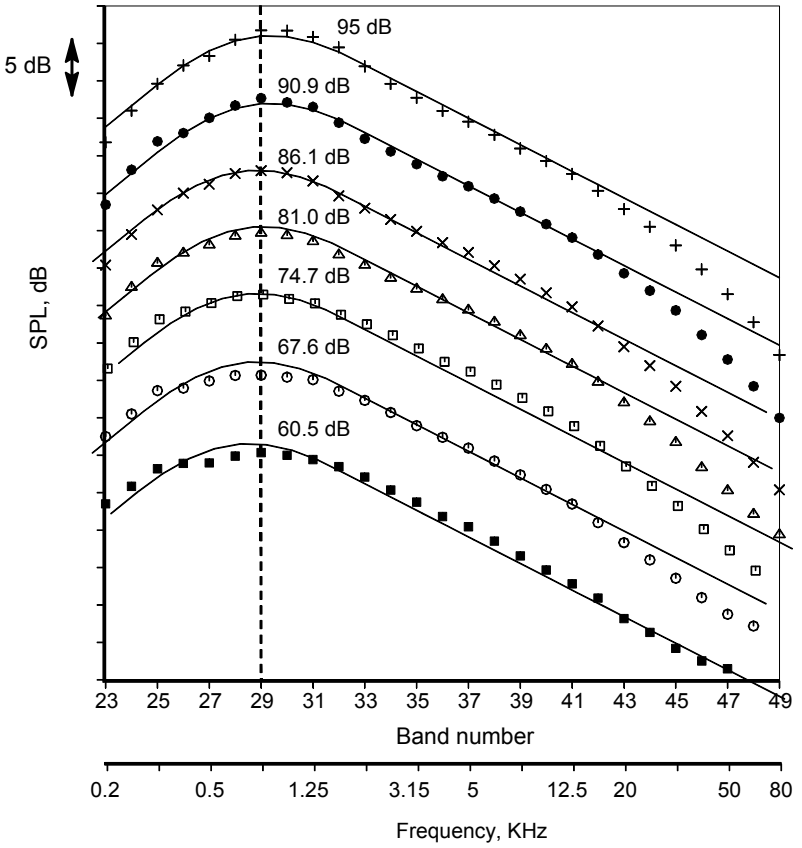


**Figure 3.** Comparison of spectra from unheated jets. $D$ = 2.45 in., inlet angle = 160$^o$. Symbols: ■, $M$ = 0.4; ○, 0.5; □, 0.6; △, 0.7; ×, 0.8; •, 0.9; +, 1.0. Lines: LSS spectrum. (From Viswanathan (2004), with permission)

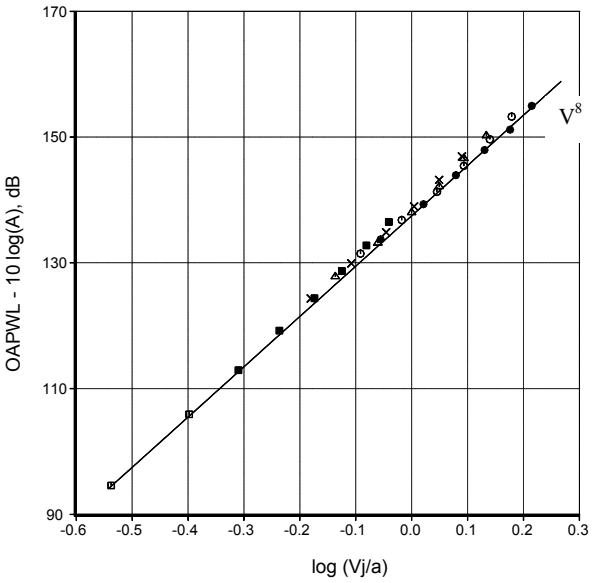


**Figure 4.** Comparison of spectra from unheated jets. $D$=2.45 in. Symbols: $V^8$,□. ■, $T_t/T_a$ = 1.0; ×, 1.8; △, 2.2; ○, 2.7; •, 3.2. (From Viswanathan (2004), with permission)

the power radiated by a low Mach number, unheated jet that varies as the eighth power of velocity (see Section 3.1). The variation of the Overall Power Level (OAPWL)for a range of jet Mach numbers from 0.5 to 1.0 and total temperature ratios of 1.0 (unheated) to 3.2 is shown in Figure 4 from Viswanathan (2004). Also shown is a line representing the $V^8$ variation. The agreement is good. However, as shown by Viswanathan (2004) a closer look at the effect of temperature shows that each total temperature ratio follows its own power curve with a slightly different exponent for each temperature. This is shown in Figure 5 from Viswanathan (2004). Notice that the unheated jet has an exponent that is very close to the eighth power scaling.

Viswanathan (2004) also showed that the effect of heating on jet noise at a fixed jet velocity was different for lower velocity jets than at higher velocities. At lower velocities, heating at a fixed velocity increased the noise and at higher velocities, heating decreased the levels. The transition occurs

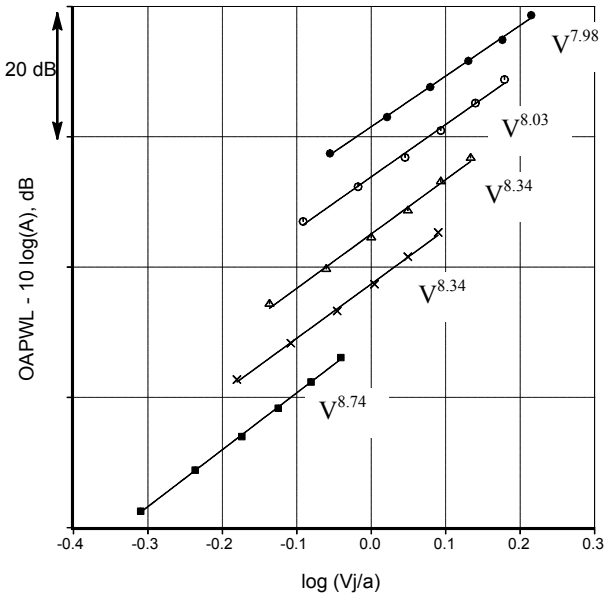


**Figure 5.** Variation of OAPWL with jet velocity, $D = 2.45$ in. ■, $T_t/T_a = 1.0$; ×, 1.8; △, 2.2; ○, 2.7; •, 3.2. (From Viswanathan (2004), with permission)

at an acoustic Mach number $V_j/a$ of approximately 0.8. The variation of OASPL at different angles was also shown to depend differently above and below this acoustic velocity. For example, Figure 6 shows the variation of OASPL at an inlet angle of $160^o$ for different acoustic Mach numbers and temperature ratios. The value of the velocity exponent decreases from 9.67 for the unheated case to 7.67 for the highest temperature case. Note that the data fall in clusters with the highest temperature giving the lowest level at the higher acoustic velocities. On the basis of the database generated in the Boeing Low Speed Aeroacoustic Facility (LSAF) Viswanathan (2006) developed scaling laws to identify the different components of jet noise. He argued that the jet total temperature was an important parameter and that,

$$\text{Sound power} \propto \left(\frac{V_j}{a}\right)^n, \; n = n\left(\frac{T_t}{T_a}\right). \tag{1}$$

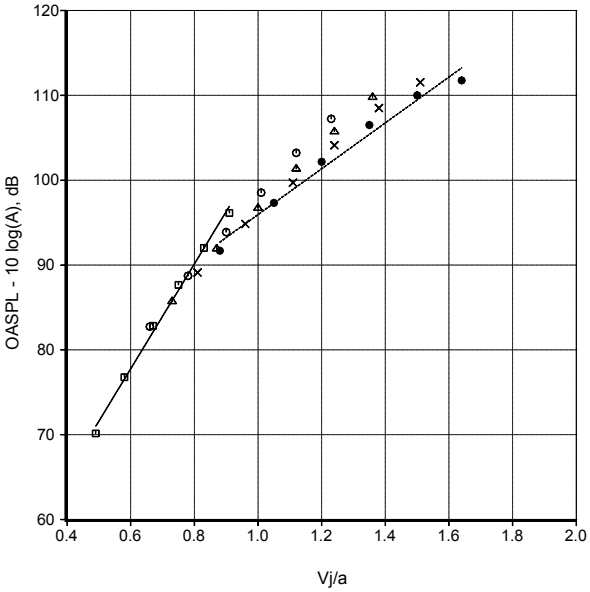


**Figure 6.** Variation of OASPL with jet velocity, $D = 2.45$ in. Inlet angle $= 160^o$. □, $T_t/T_a$ = 1:0; ○, 1.8; △, 2.2; ×, 2.7; •, 3.2. (From Viswanathan (2004), with permission)

In addition, the OASPL can be scaled by,

$$\text{OASPL} \propto \left(\frac{V_j}{a}\right)^n,\ n = n\left(\theta, \frac{T_t}{T_a}\right). \tag{2}$$

The variation of the velocity exponent with inlet angle and temperature ratio is shown in Figure 7 from Viswanathan (2006). The exponent is relatively uniform for lower inlet angles and then rises rapidly in the peak noise radiation direction. At $90^o$ the exponent falls monotonically with increase in temperature ratio, being approximately 5.6 for the highest temperature. An example of the collapse of the spectra at $90^o$ is shown in Figure 8 from Viswanathan (2006)). All the spectra for the subsonic cases collapse very well. The lines show the spectra for supersonic cases where broadband shock-associated noise becomes evident (See Section 2.2). If it assumed that the mixing noise spectra would also continue to collapse if the supersonic cases were ideally expanded, then the scaling laws and spectral shapes not only provide a method for noise prediction (see Viswanathan (2007)), they

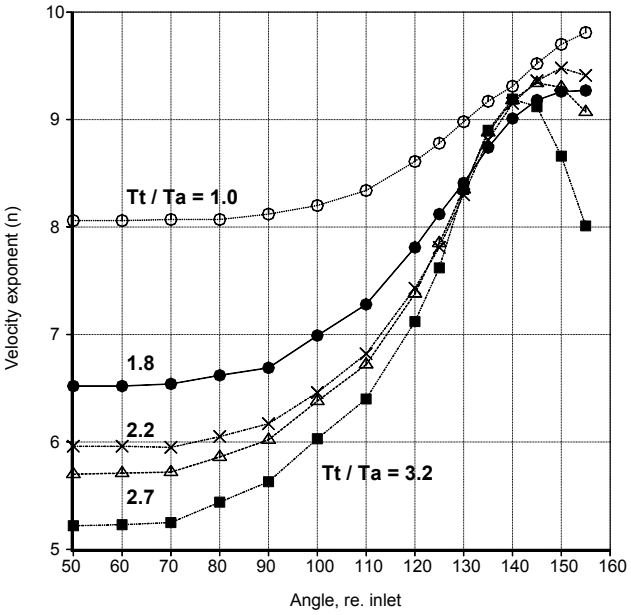


**Figure 7.** Velocity exponent for various angles and jet stagnation temperature ratios. (From Viswanathan (2006))

also provide a means for the separation of mixing and broadband shock-associated noise. An example is shown in Figure 9 from Viswanathan (2006). The mixing noise dominates at lower frequencies and is of the same order of magnitude as the shock noise at high frequencies. In the mid-frequencies, the spectrum is dominated by broadband shock-associated noise. Shock noise is described in the next section.

### 2.2 Broadband Shock-Associated Noise

A convergent nozzle operated at supercritical pressure ratios always produces expansions and shocks in the plume. This results in the appearance of shock-associated noise. The same situation occurs when a convergent-divergent (C-D) nozzle is operated at off-design conditions. Shock-associated noise generally consists of discrete tones and broadband components. Though it is possible to design a shock-free C-D nozzle for laboratory investigation, C-D nozzles in commercial and military applications are usually constructed with straight conical sections, so some level of shock noise is present even at

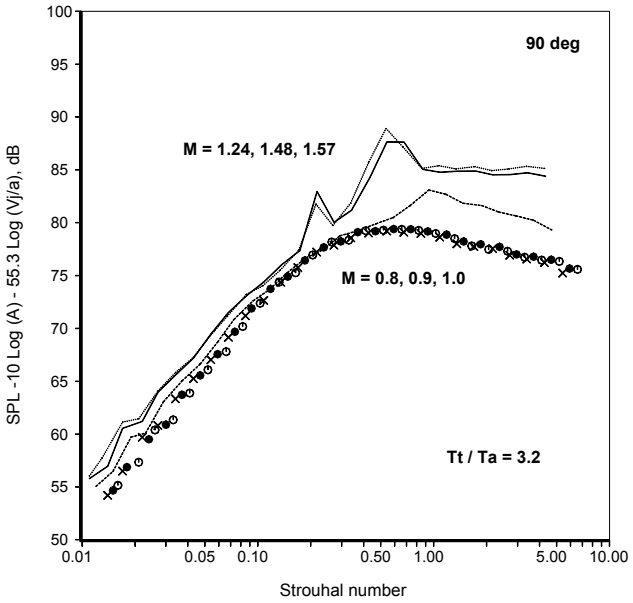


**Figure 8.** Normalized spectra from heated jets at $90^o$. $T_t/T_a = 3.2$, $D = 1.5$ in. Symbols: subsonic Mach numbers; lines: supersonic Mach numbers. Velocity exponent n = 5.53. (From Viswanathan (2006))

the supposed design conditions. Harper-Bourne and Fisher (1974) were the first to provide a comprehensive experimental study and model of broadband shock-associated noise. They operated a convergent nozzle at supercritical pressure ratios and at ambient reservoir temperatures, and observed a dramatic increase in noise in the forward quadrant. They identified this noise source as being associated with the quasi-periodic shock cell structure in the jet plume. From an examination of their cold data, together with hot jet data from Rolls-Royce, they showed that the intensity of shock noise is only a function of nozzle pressure ratio and is nearly independent of jet reservoir temperature and hence jet velocity. Subsequently, Tanna (1977), Seiner and Norum (1979), Seiner and Norum (1980), Norum and Seiner (1982a), Norum and Seiner (1982b), Tam and Tanna (1982), Seiner (1984), Seiner and Yu (1984), Yamamoto et al. (1984) and, more recently, Viswanathan et al. (2009) have carried out extensive studies that have formed the basis for our understanding of shock-associated noise.

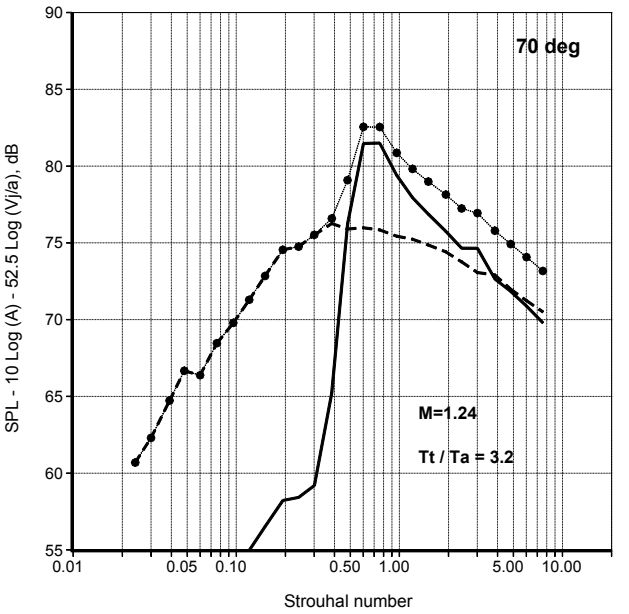


**Figure 9.** Extracted components of turbulent mixing noise and broadband shock-associated noise from total measured noise. $M = 1.24$, $T_t/T_a = 3.2$, inlet angle = $70^o$. Solid: shock noise; dashed: mixing noise; symbols and dotted line: total noise. (From Viswanathan (2006))

The experiments conducted at NASA Langley Research Center by Seiner, Norum and Yu included measurements of the aerodynamic characteristics, as well as the near and far field acoustics of shock containing plumes in order to uncover the physical mechanisms responsible for the generation of shock noise. Both convergent and C-D nozzles were tested. Whereas a convergent nozzle can only be operated supersonically at underexpanded conditions ($p_e/p_a > 1$), where $p_e$ and $p_a$ are the exit and ambient pressures respectively, a C-D nozzle can be operated at either overexpanded ($p_e/p_a < 1$) or underexpanded conditions.

Figure 10 from Norum and Seiner (1982a) shows typical narrowband noise spectra from a C-D nozzle with design Mach number of 1.5 at a fully expanded Mach number of 1.8 (NPR=4.72), and unheated. Several spectra are shown that cover polar angles from 30° to 120°. Also shown are predictions by Tam (1987): see Section 4.3. This figure displays all the three

noise components. A screech tone is clearly visible in all the spectra, with its amplitude more than 10 dB above the broadband noise in the forward angles. The distinct peak to the right of the screech tone is the broadband shock-associated noise. The broadband noise contains one dominant peak, with a secondary peak sometimes evident, and the peak frequency of the radiation increases with angle from the inlet. The half-width of the broadband spectral peak widens as the radiation angle increases and in the aft quadrant the peak is very broad. The broadband shock noise component is dominant in the forward quadrant. The peak to the left of the screech tone is the turbulent mixing noise, which is most easily identified at 120°. The peak frequency of the broadband shock noise increases with angle. The spectral level of the shock noise is nearly unaffected by jet temperature at a fixed Mach number. Though recent experiments by Viswanathan et al. (2009) and Kuo et al. (2011) show that the addition of small amounts of heating increases the peak levels, but then the levels become effectively independent of jet temperature.

The intensity of shock noise depends on the degree of mismatch between the design Mach number, $M_d$ and the fully expanded Mach number, $M_j$. Figure 11, from Seiner and Yu (1981), shows the variation of noise intensity obtained with a C-D nozzle of design Mach number 1.5 operated over a range of fully expanded Mach numbers. The jet was operated unheated and the radiation angle shown is 30°. Also shown on this plot (denoted by dark circles and solid line) is the turbulent mixing noise obtained by operating the three nozzles at their design Mach numbers of 1.0, 1.5 and 2.0. The difference between the open circles (and dashed line) and the dark circles (and solid line) is an estimate of the shock noise contribution. When the Mach number of a C-D nozzle is progressively increased from subsonic to slightly supersonic conditions, the flow is highly overexpanded with strong shocks in the plume. Depending on the degree of overexpansion, a Mach disc may be present in the plume. The total noise of the jet in the forward quadrant increases with contributions from shock noise. As the Mach number is increased from unity, the noise level increases until the Mach disc disappears. This Mach number is denoted by point C. At higher Mach numbers, there is a decrease in noise due to the weakening of the shock strength and the minimum noise occurs at the design point A. With a further increase in Mach number, the nozzle is operated at underexpanded conditions and the shock noise again begins to increase following the trend AB. When the flow is highly underexpanded, normal shocks appear again and a Mach disc is formed, point B. The spectral level reaches a peak at approximately this condition and any further increase in Mach number results in a slight decrease initially and then no further change in the noise level. The diameter

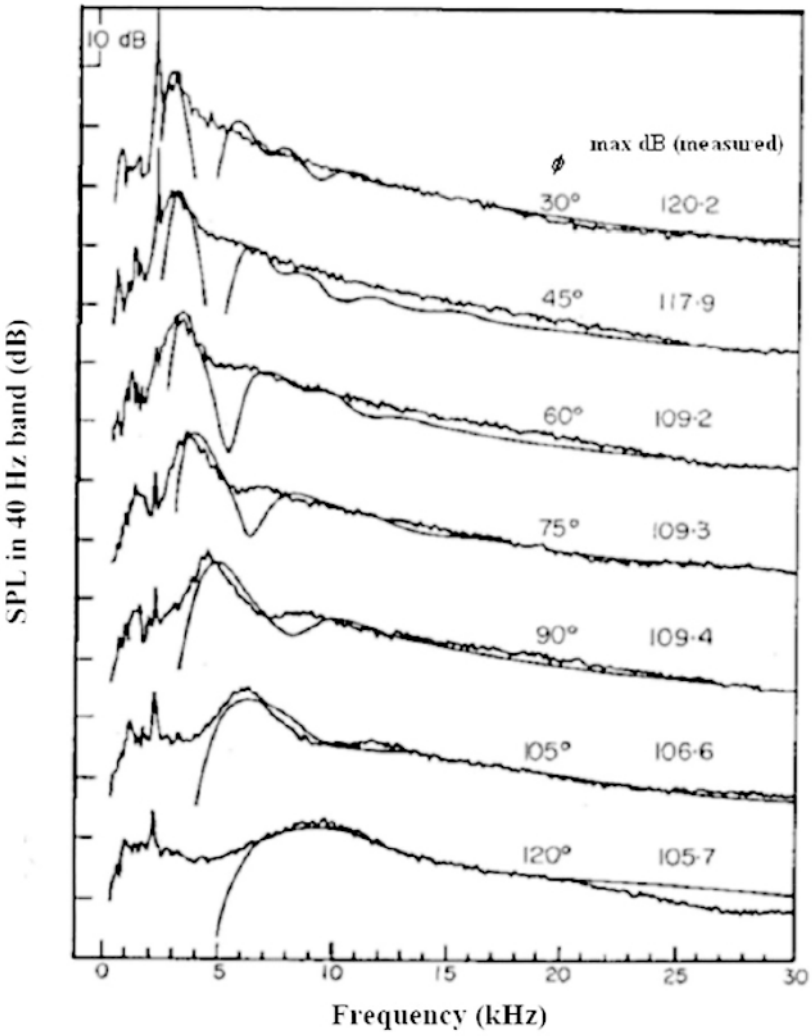


**Figure 10.** Narrow band noise spectra for a convergent-divergent nozzle operated at Mach numbers of 1.67. Design Mach number = 1.5. $D$ = 5.08 cm. (Adapted from Norum and Seiner (1982a) and Tam (1987)).

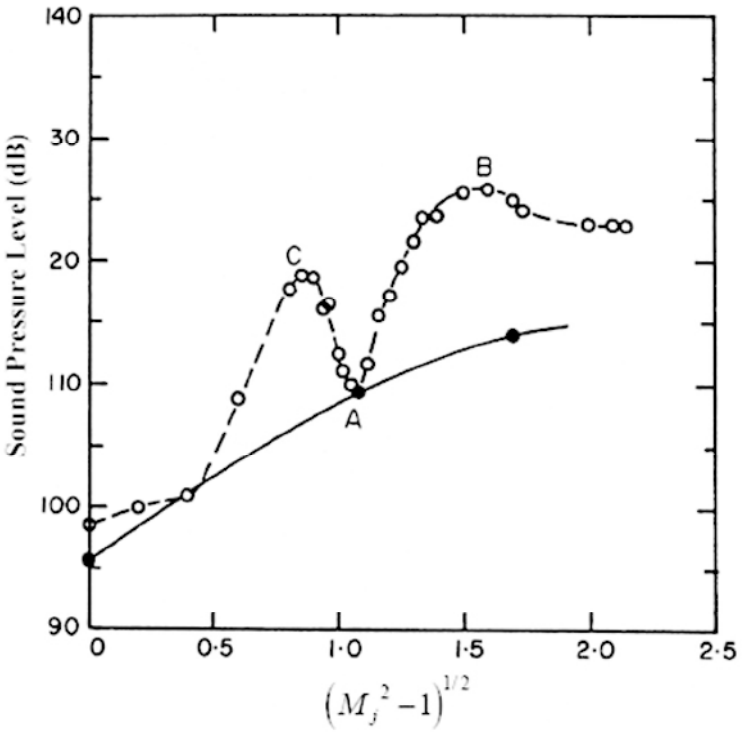


**Figure 11.** Variation of noise intensity with Mach number at $30^o$ to the inlet axis. Design Mach number = 1.5. ○, Imperfectly expanded jet; •, perfectly expanded jet. (Adapted from Seiner and Yu (1981)).

and the downstream location of the Mach disc increases with the degree of underexpansion. Seiner and Norum (1980) recommended that a distinction should be made between plumes with strong shocks and plumes with weak expansion and compression waves. In the latter case the flow is supersonic while in the former case there are mixed supersonic and subsonic flow regimes, due to the presence of the normal shocks. These strong shocks reduce the extent of the supersonic flow and weaken the strength of the downstream shocks.

These experiments also showed that though the first shock cell has the greatest strength, the downstream shocks are responsible for shock noise production. The main region of shock noise production was found to occur near the end of the potential core for both underexpanded and overexpanded

supersonic jets. Flow and near-field acoustic correlations indicated a spatial coherence of several shock wavelengths, with the shock noise appearing to originate from the vicinity of each oblique shock wave. These results suggested strongly that broadband shock noise is produced by the interaction of turbulent flow structures with the periodic shock cell system.

The relative importance of broadband shock-associated noise and turbulent mixing noise is a strong function of radiation angle and jet operating conditions. For a fixed Mach number, the turbulent mixing noise level increases as the jet temperature is increased, while the amplitude of the broadband shock noise remains nearly unaltered. Hence, the magnitude of the shock noise over the mixing noise is a maximum for cold jets, as seen in Figure 10. The shock noise radiation is fairly omnidirectional, whereas the mixing noise radiates principally in the aft directions. The jet temperature then sets the relative levels of the two components. Figure 12 shows the effect of total temperature ratio on the OASPL from a convergent nozzle operated at a fully-expanded Mach number of 1.36 (underexpanded). The shock noise is see to be relatively omindirectional for each temperature ratio. The increase at some angles near 90 degrees in the unheated case is due to the presence of screech tones. The mixing noise is highly directional and dominates the shock noise in level for large angles to the inlet axis. In the unheated case, the peak levels of the shock and mixing noise are similar (within 5 dB when the screech tones are neglected). At the highest temperature ratio the peak mixing noise OASPL is approximately 15 dB higher than the shock noise.

### 2.3 Screech Tones

Powell (1953b), Powell (1953c) was the first to perform detailed investigations of screech tones from model scale supersonic jets. Powell's experiments from convergent nozzles revealed that the wavelengths of the screech tones increased with increasing NPR and that the tone radiated preferentially in the upstream direction. A two-dimensional nozzle exhibited a smooth variation of screech wavelengths with pressure ratio, while an axisymmetric nozzle had discontinuous frequency (and corresponding wavelength) jumps with increasing NPR. He attributed the tone generation phenomenon to a feedback mechanism. Davies and Oldfield (1962) showed that the various screech modes of an axisymmetric nozzle were not disjoint but actually overlapped, indicating that several modes could co-exist or that the preference for a particular mode switched randomly back and forth. Many investigators have studied the screech phenomenon since then. For example, Hammitt (1961), Westley and Woolley (1969), Westley and

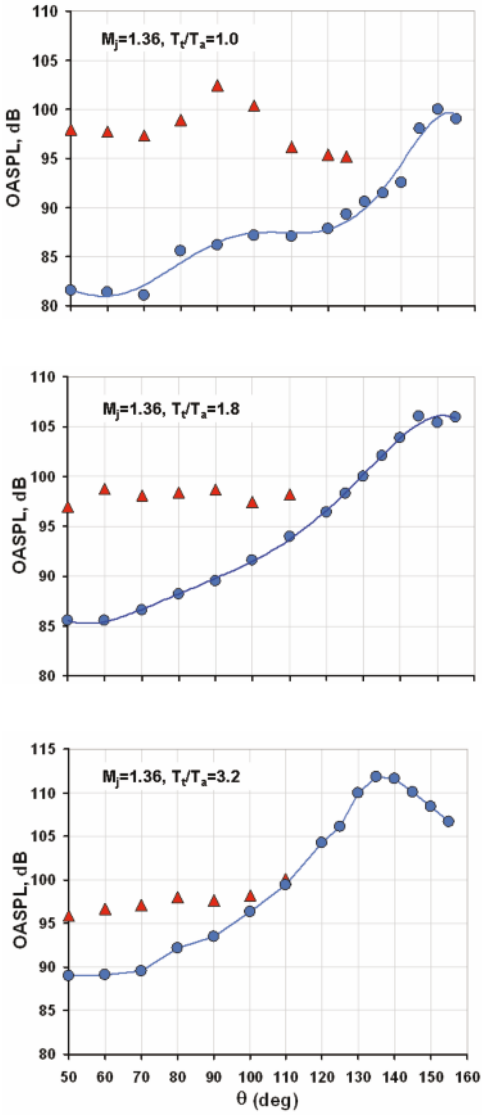


**Figure 12.** Directivity of the mixing and shock components at different temperature ratios. Convergent nozzle; $M_j$ = 1.36. ▲, shock noise; •, mixing noise. (From Viswanathan et al. (2009)).

Woolley (1975), Rosfjord and Toms (1975), Sherman et al. (1976), and researchers at the NASA Langley Research Center, including Norum (1983) and Seiner (1984), are just a few references. Raman (1998), Raman (1999) has provided an extensive list of references.

The discrete screech tones can be of high intensity depending on the nozzle operating conditions and geometry. Usually, these tones are more pronounced for cold jets, with the amplitude of screech decreasing with increasing jet temperature. As the jet temperature is increased at a fixed Mach number, the screech frequency increases. The frequency of screech is independent of observer angle, indicating that the source of screech is spatially stationary. Simultaneous multiple screech modes are generally observed at most jet operating conditions. Figure 13, from Seiner (1984), shows the screech modes as a function of jet Mach number. This figure is a compilation of various experimental measurements of screech tones obtained with a convergent nozzle and an unheated jet. The round jet exhibits a staging phenomenon when the Mach number is increased, with jumps in the screech frequency. Optical observations have revealed that the different screech modes are associated with different oscillatory modes of the jet plume. These are either toroidal or helical mode instabilities. At lower Mach numbers, the toroidal large-scale instabilities are dominant, while the helical modes become dominant above a Mach number of approximately 1.3. Flow visualizations by Seiner et al. (1986), among others, have shown that the left and right hand helical disturbances are excited simultaneously, causing the jet to flap up and down. However, the azimuthal orientation of the flapping plane is not constant and has been found to precess for as yet unknown reasons. As seen in Figure 13, more than one mode may be present at a given Mach number. However, these tones are not harmonics of each other. As the jet Mach number is increased, the wavelength of the screech increases until a critical value is reached, beyond which a marked jump in wavelength occurs. For the Mach number range of 1.1 to 1.8, more than five modes or stages, labeled A1, A2, B, C, D and E in Figure 13 have been observed. These tones are very sensitive to the details of the experimental facility and not all modes are observed in any individual facility.

In summary, the screech generation mechanism is strongly dependent on upstream geometry. In commercial engines, the nozzle geometry is seldom perfectly axisymmetric. For realistic hot engine flows, screech is not considered to be a problem at all. However, high tone levels have been measured in military aircraft with closely spaced engines. For such aircraft (F-15 and the B1-B), sonic fatigue and structural failure of upstream aircraft components is a concern. The early work of Hay and Rose (1970) showed clearly that significant noise amplitudes around the screech frequency could

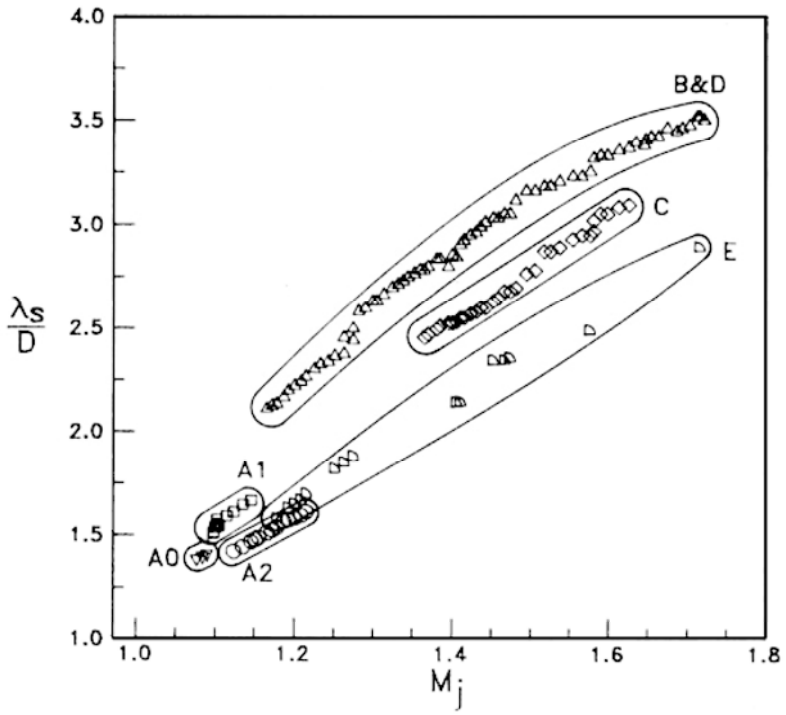


**Figure 13.** Variation of fundamental screech tone wavelength with Mach number for various stages of screech. Convergent nozzle and unheated flow. (From Seiner (1984), with permission).

be present for some engine conditions and geometries. As the flight altitude increased, the nozzle operated at supersonic conditions due to the decrease in ambient static pressure. Consequently, high tone levels were observed at cruise. Prolonged exposure to the high dynamic loads, when there was a matching of the screech frequency and that of the structural modes caused structural damage. Seiner et al. (1987) investigated the screech characteristics and the plume dynamics of twin supersonic jets using axisymmetric C-D and rectangular nozzles. The study revealed that when two adjacent supersonic nozzles have a centerline spacing less than two nozzle diameters, the axial evolution of each nozzle plume's preferred shear layer instability wave was coupled. This coupling process stimulated an axially synchronized and enhanced growth of each plume's preferred spatial instability. Under these conditions, the dynamic pressure in the inter-nozzle region was found

to be significantly higher than would be expected from two uncoupled supersonic jets. In some instances, the amplitude was found to exceed the design loads for the structure. This study also showed that the staging phenomenon observed for the convergent nozzle was not as prevalent as for the single C-D nozzle. Even when several modes existed simultaneously, only one mode was dominant, with a significantly higher amplitude. At lower Mach numbers, when the nozzle was operated in an overexpanded state, the axisymmetric screech mode was dominant. In the underexpanded state (higher Mach numbers), the helical mode was found to be dominant.

### 2.4 Forward Flight Effects

The effects of forward flight on aircraft noise are difficult to quantify for a variety of reasons. Even the measurement of this effect poses a significant challenge; validated predictions of the effects of flight are consequently harder. Flight testing of aircraft is very expensive and time-consuming. Several factors such as multiple engine noise sources, multiple engine configurations, engine installation effects and non-uniform flow around the engines, atmospheric propagation effects, varying weather conditions over very long propagation distances, ground reflection, and ground absorption at shallow grazing angles render even the interpretation of the measured data very difficult. Given this level of complexity, it is not surprising that there is no consensus on what constitutes a flight effect for individual engine noise components. Since the early seventies, many experimental techniques have been developed that attempt to simulate a real aircraft flyover. These have consisted of a jet embedded in a wind tunnel, a jet mounted on tracked vehicles on land, a jet mounted on a whirling rotor arm, and taxiing aircraft. Crighton et al. (1976) provide a critical evaluation of the different techniques and the advantages and disadvantages associated with each. They highlighted some fundamental issues regarding the necessity to preserve the dimensionless parameters at the model-scale and the importance of the detailed nature of the noise source and its acoustic environment, in evaluating the direct effect of flight on source strength.

Nowadays, flight effects are usually assessed by embedding a jet simulator in a free jet wind tunnel of much larger diameter, in a large anechoic chamber. Von Glahn et al. (1973), Cocking and Bryce (1975), Bushell (1975), Packman et al. (1975), and Tanna and Morris (1977) carried out some of the earliest studies. In wind tunnel tests, the microphones are located either in the tunnel flow or in the static environment outside the tunnel flow. The latter case of out-of-flow measurements are the easiest to perform and true far field measurements can be made. However, correc-

tions are needed for the propagation of sound through the tunnel jet shear layer. Some of the factors that need to be considered in the development of these corrections are: the finite thickness of the tunnel shear layer; the axial spreading of the tunnel shear layer in the downstream direction; multiple reflections of sound waves between the jet and tunnel shear layers; the scattering of sound by turbulence in the tunnel shear layer; the background noise of the tunnel shear layer; any near field interaction of the jet and tunnel shear layers if the wind tunnel is not large enough; and a few other issues such as the possible excitation of the tunnel flow by the jet. The other major issue concerns the distributed nature of the jet sources. If there is a rapid variation of the correction factor with angle, it is necessary to place the microphones at a large distance from the tunnel shear layer so as to be able to invoke the assumption that the jet acts as a point source. The conflicting requirements of a very large wind tunnel to prevent the interaction of the jet flow with the simulator shear layer and a large anechoic chamber to ensure far field observer locations pose a tremendous problem and these requirements are not met by many facilities.

In-flow measurements avoid problems with propagation through the tunnel shear layer. However, the tunnel may not be perfectly anechoic. The problem of the tunnel flow over the microphones is also an issue. However, the biggest concern is the requirement for a very large tunnel to ensure that the microphones are in the far field, especially for a large source region.

Out-of-flow measurements are generally favored. Many of the issues mentioned above with this type of arrangement have been investigated. Amiet (1975) developed analytical expressions for the calculation of the refraction from the shear layer assuming that the tunnel shear layer could be represented by a vortex sheet. Morfey and Szewczyk (1977a) examined the various issues and recommended some guidelines for the proper choice of tunnel size, jet and tunnel operating conditions, to assure good quality of data. The scattering of sound by the turbulence of the tunnel shear layer was shown to be negligible. This proposed correction procedure was used by Tanna and Morris (1977) to interpret their data. Amiet (1978) evaluated the various correction procedures and the validity of the assumptions made in their derivations. All these methodologies attempt to convert the measured wind tunnel data to equivalent flyover conditions. Based on these ideas, the aircraft and engine companies have developed procedures to extrapolate the wind-on model scale data to full-scale flyover conditions. One of the biggest differences in these methods is the prescription of the source location for a given frequency. Empirical relations for source distributions have been derived based on theoretical considerations, acoustic mirror measurements, microphones located at multiple sideline arrays, and a combina-

tion of in-flow and out-of-flow microphones. In the multiple sideline array technique, data from each array are extrapolated to a common larger distance, with an assumed source distribution. Through proper modification of the source locations, the difference between the two sets of extrapolated data is driven to an acceptable tolerance. However, when a novel suppressor nozzle is tested, this process has to be repeated since the source distributions could be very different. Not unexpectedly, the same data processed by different procedures yield slightly different noise estimates. This is not to say that there are fundamental problems with these methods; rather, that the complexities are addressed and treated in different ways.

Norum and Shearin (1988) made extensive measurements of the far field acoustic characteristics and the plume fields of supersonic jets in an open wind tunnel with a tunnel Mach number range of 0.0-0.4. Their study indicated that there were three effects of flight on broadband shock noise. There was a lowering of the peak frequency with flight Mach number. Also, the spectral peak became narrower and several higher-order peaks became prominent with increasing flight speed. Norum and Brown (1993) extended the range of tunnel Mach number by using a free jet of diameter 0.30 m, and performed detailed aerodynamic and acoustic measurements from small convergent and C-D nozzles ($D_j$ = 1.90 cm). The Mach number of the free jet was as high as 0.9. They noticed that the plume characteristics could be altered significantly when the free jet Mach number was increased to higher values. Even for the C-D nozzle at its design Mach number, weak shocks were observed at a flight Mach number of 0.6. With further increase in freestream Mach number, the strength and extent of the shock-containing region increased dramatically. Norum and Brown attempted to isolate the effects of source strength modification, convection due to the freestream and refraction by the shear layer as the flight speed was increased. They reported that the change in source strength for the shock noise was minimal, while the convection effect was very strong. A decrease in peak frequency of broadband shock noise was also observed with increasing flight Mach number. Finally, the effect of flight on turbulent mixing noise showed a monotonic decrease in amplitude with increasing flight Mach number at all frequencies.

The effects of forward flight on the OASPL is usually characterized in terms of the flight velocity parameter $k = 10\log_{10}\left[V_j/\left(V_j - V_t\right)\right]$ where $V_j$ is the jet velocity and $V_t$ is the tunnel or flight velocity. Early studies by Tanna and Morris (1977) and Michalke and Michel (1979) suggest an exponent of 5 to 5.5, especially at 90 degrees. This was argued by Tanna and Morris (1977) to be consistent with the reduction of the turbulence intensity with forward flight as measured by Morris (1976). This value has been

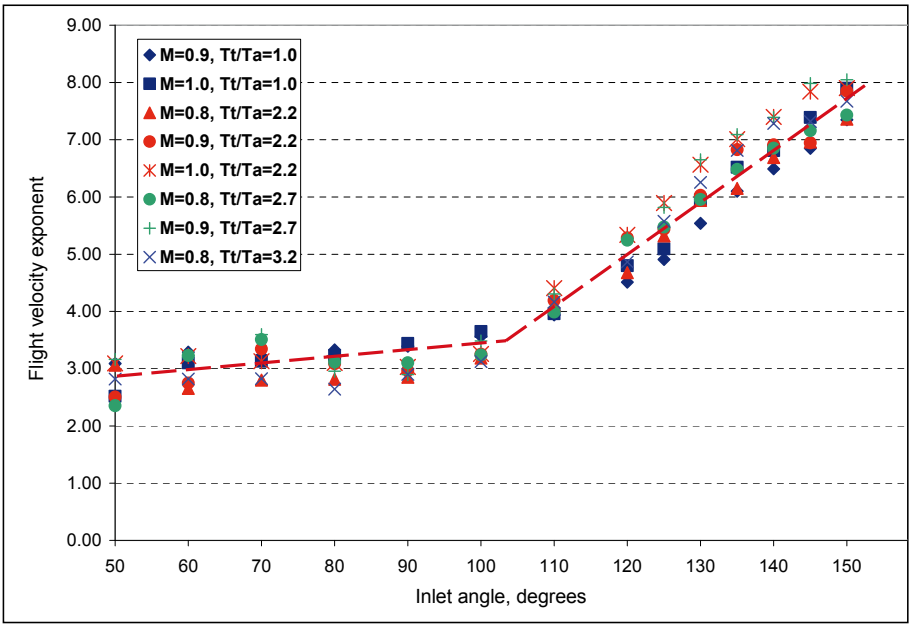


**Figure 14.** Variation of the relative velocity exponent with radiation angle; various jet conditions (From Viswanathan and Czech (2011)).

used in noise prediction methods to account for the effect of forward flight: for example the ARP876 by SAE (1994). However, recent measurements by Viswanathan and Czech (2011) show a lower value of velocity exponent at sideline angles with a steadily increasing value from inlet angles of 110 degrees. Figure 14 shows this variation of velocity exponent with radiation angle for various jet operating conditions. The reason for this difference could be contamination by the free jet noise and facility noise in the previous experiments: particularly at low jet exit velocities. Viswanathan and Czech (2011) removed any spectra that showed evidence of these effects in determining the velocity exponent. However, this lower exponent is not consistent with the measured reductions in turbulence intensities with forward flight. This remains a question to be resolved by both measurements and simulations.

## 3 Turbulent Mixing Noise

Experiments and analysis of turbulent mixing noise have been ongoing for fifty years. For most of this period, the *acoustic analogy*, proposed by Lighthill (1952), Lighthill (1954), and its extensions, have dominated analysis and predictions. In the 1970's, it was recognized that large-scale turbulent structures in the jet mixing layer are very efficient noise radiators in high-speed jets. In addition, with recent increases in computational power, Direct Numerical Simulations (DNS) and Large Eddy Simulations (LES) have shown their potential to provide a complete three-dimensional, time-dependent prediction of both the flow and noise of jets.

In Section 3.1 the early acoustic analogy models and their subsequent extensions to include the effects of source convection and mean flow refraction are described. Jet noise prediction schemes based on the acoustic analogy are also introduced. Section 3.2 describes the mechanism of noise generation by large-scale turbulent structures, modeled as instability waves. The associated analytical and numerical predictions are also introduced. A recent empirical correlation of turbulent mixing noise directivity and spectra is described in Section 3.3. Finally, the model of Tam and Auriault (1999) for noise generation and radiation by fine-scale turbulence, as well as more recent improvements in acoustic analogy-based models, are described in Section 3.4.

### 3.1 Lighthill's Acoustic Analogy

A general theory for sound generated aerodynamically was developed by Lighthill (1952). He chose to formulate the problem by comparing the full equations of motion with the equations governing density fluctuations in a uniform acoustic medium at rest. The differences were considered to be the effect of a fluctuating force field, acting on the uniform acoustic medium, which would be known *if the flow were known*. Such an approach has been called an *acoustic analogy*, as it replaces the physical noise sources by a distribution of equivalent sources. Lighthill's equation was introduced in Chapter 1. Here it is written as,

$$\frac{\partial^2 \rho}{\partial t^2} - a_o^2 \frac{\partial^2 \rho}{\partial x_i \partial x_i} = \frac{\partial^2 T_{ij}}{\partial x_i \partial x_j}. \tag{3}$$

$T_{ij}$, known as the *Lighthill stress tensor*, is the instantaneous applied stress at any point given by,

$$T_{ij} = \rho v_i v_j + p_{ij} - a_o^2 \rho \delta_{ij}, \tag{4}$$

where $p_{ij}$ is the compressive stress tensor, given for a Stokesian gas by

$$p_{ij} = p\delta_{ij} - \mu\left[\frac{\partial v_i}{\partial x_j} + \frac{\partial v_j}{\partial x_i} - \frac{2}{3}\left(\frac{\partial v_k}{\partial x_k}\right)\delta_{ij}\right] \tag{5}$$

$\mu$ is the coefficient of viscosity and $p$ is the thermodynamic pressure.

For low Mach number, unheated flows, Lighthill argued that $T_{ij} \simeq \rho_o v_i v_j$ where $\rho_o$ is the constant mean density of the medium. It should be noted that the equivalent source term, $\partial^2 T_{ij}/\partial x_i \partial x_j$ contains all physical effects such as convection and refraction. It is also important to note that $v_i$ is the instantaneous velocity: not a perturbation about a mean value. To overcome this problem to some extent it is possible to write the equations of motion in a frame of reference moving with the mean axial velocity, with the time derivatives replaced with convective derivatives and where the velocities are perturbations about the mean velocity. Then the Lighthill stress tensor is nonlinear in the fluctuations. This generalization of Lighthill's acoustic analogy for sources embedded in a uniform mean flow is described by Dowling et al. (1978). Alternatively, the average of the equation can be subtracted from its instantaneous form. This approach has been used in more recent acoustic analogies.

In any event, the solution to Eqn. (3) can be obtained using the free space Green's function for the wave equation,

$$\rho(\mathbf{x},t) - \rho_o = \rho'(\mathbf{x},t) = \frac{1}{4\pi a_o^2}\frac{\partial^2}{\partial x_i \partial x_j}\int T_{ij}(\mathbf{y},\tau_1)\frac{d\mathbf{y}}{|\mathbf{x}-\mathbf{y}|} \tag{6}$$

where $\tau_1$ is the retarded time,

$$\tau_1 = t - |\mathbf{x}-\mathbf{y}|/a_o \tag{7}$$

In the far field where $x = |\mathbf{x}| >> |\mathbf{y}|$, Eqn. (6) becomes

$$\rho'(\mathbf{x},t) = \frac{1}{4\pi a_o^4}\int \frac{x_i x_j}{x^3}\frac{\partial^2 T_{ij}}{\partial \tau_1^2}(\mathbf{y},\tau_1)\,d\mathbf{y} \tag{8}$$

If it is assumed that the velocity scales with the jet exit velocity $V_j$ and that the time rate of change of the source term varies as $V_j/\ell$ where $\ell$ is a characteristic length scale, it is readily shown that

$$\rho'(\mathbf{x},t) \sim \rho_o\left(\frac{V_j}{a_o}\right)^4\frac{d_j}{x} \tag{9}$$

where it has been assumed that $\ell$ scales with the jet exit diameter $d_j$ and $x \simeq |\mathbf{x}-\mathbf{y}|$ in the far field. The far field intensity $I(\mathbf{x})$, defined as the

acoustic energy flux per unit area, is given by

$$I(\mathbf{x}) = \frac{a_o^3}{\rho_o}\left\langle \left(\rho'(\mathbf{x},t)\right)^2 \right\rangle \sim \rho_o V_j^3 M_a^5 \left(\frac{d_j}{x}\right)^2 \tag{10}$$

where $\langle\ \rangle$ denotes the time average value and $M_a$ is the acoustic Mach number: the ratio of the jet exit velocity to the ambient speed of sound. This gives Lighthill's famous eighth power law, that the total acoustic power output is proportional to

$$\rho_o V_j^3 M_a^5 d_j^2 \tag{11}$$

Since the total mechanical power of the jet is proportional to $\rho_o V_j^3 d_j^2$, the acoustic efficiency is approximately

$$\eta \propto M_a^5 \tag{12}$$

The constant of proportionality can be estimated to be very small (of the order $10^{-4}$) so, fortunately, the acoustic efficiency is very low.

Lighthill (1954) applied his general theory to the sound generated by turbulence. He related the sound intensity in the far field to the statistical properties of the turbulent sources. To account for the effects of convection of the turbulent eddies in the jet, the statistical properties were described in a moving reference frame. Ffowcs Williams (1963) provided a more complete analysis of the effects of convection as well as the effect of the relative motion of the jet exhaust and the observer. He also showed how to remove an apparently singular result that occurs when the sources convect at the speed of sound in the direction of the observer. These results are most clearly developed in terms of the source wavenumber frequency spectrum. To see this, following Proudman (1952), the source component in the direction of the observer is introduced such that

$$T_{xx} = \frac{(x_i - y_i)(x_j - y_j)}{|\mathbf{x}-\mathbf{y}|^2} T_{ij} \tag{13}$$

This form is appropriate for isotropic turbulence. For statistically stationary turbulence the intensity can be obtained from the autocorrelation of the far field density in the form,

$$\begin{aligned} I(\mathbf{x},\tau^*) &= \frac{a_o^3}{\rho_o}\left\langle \rho'(\mathbf{x},t)\,\rho'(\mathbf{x},t+\tau^*)\right\rangle \\ &= \frac{1}{16\pi^2\rho_o a_o^5 x^2}\int\int \frac{\partial^4}{\partial\tau^4} R^f(\mathbf{y},\boldsymbol{\Delta},\tau)\,d\boldsymbol{\Delta}d\mathbf{y} \end{aligned} \tag{14}$$

where the integrand is to be evaluated at

$$\tau = \tau^* + \frac{|\mathbf{x}-\mathbf{y}| - |\mathbf{x}-\mathbf{y}-\boldsymbol{\Delta}|}{a_o} \simeq \tau^* + \frac{\boldsymbol{\Delta}\cdot\mathbf{x}}{a_o x} \quad \text{for} \quad |\mathbf{x}| >> |\mathbf{y}| \tag{15}$$

$R^f(\mathbf{y},\boldsymbol{\Delta},\tau)$ is the cross correlation of the Lighthill stress tensor, given by

$$R^f(\mathbf{y},\boldsymbol{\Delta},\tau) = \langle T_{xx}(\mathbf{y},\tau_1)\, T_{xx}(\mathbf{y}+\boldsymbol{\Delta},\tau_1+\tau)\rangle \tag{16}$$

where $\Delta$ is the separation distance between the two source locations. The superscript $f$ indicates that the correlation is performed in a fixed reference frame. The wavenumber frequency spectrum of the sources is defined as the Fourier transform of the cross correlation function. That is,

$$H^f(\mathbf{y},\mathbf{k},\omega) = \frac{1}{(2\pi)^4}\int\int R^f(\mathbf{y},\boldsymbol{\Delta},\tau)\exp\left[-i(\omega\tau+\mathbf{k}\cdot\boldsymbol{\Delta})\right] d\boldsymbol{\Delta}\, d\tau \tag{17}$$

here, $\mathbf{k}$ and $\omega$ are a wavenumber vector and radian frequency respectively. Also, the spectral density of the intensity at the observer $S(\mathbf{x},\gamma)$, where $\gamma$ is the observer frequency, is given by the Fourier transform of the intensity,

$$S(\mathbf{x},\gamma) = \frac{1}{2\pi}\int I(\mathbf{x},\tau^*)\exp\left(-i\gamma\tau^*\right) d\tau^* \tag{18}$$

Then, it is readily shown that,

$$S(\mathbf{x},\gamma) = \frac{\pi}{2\rho_o a_o^5 x^2}\int \gamma^4 H^f\left(\mathbf{y}, -\frac{\gamma\mathbf{x}}{a_o x}, \gamma\right) d\mathbf{y} \tag{19}$$

Equation (19) shows that the spectral density depends on an integral over the source volume of the frequency–weighted source wavenumber frequency spectrum. It is important to note that, for a given observer frequency $\gamma$, only the wavenumber component of the source spectrum that has a sonic phase velocity in the direction of the observer contributes to the radiated noise. As discussed by Ffowcs Williams (1963), Crighton (1975) and Goldstein (1984), among others, this means that only a small fraction of the wavenumbers present in the turbulence can contribute to the noise radiation for convectively subsonic jets ($M_a \lessapprox 1.4$).

In the practically important case where the convection is in the axial direction, a new coordinate is introduced such that

$$\boldsymbol{\delta} = \boldsymbol{\Delta} - U_c\tau\mathbf{i} \tag{20}$$

where $\mathbf{i}$ is the unit vector in the $x_1$, axial, direction. Then the far field autocorrelation for the intensity is given by

$$I(\mathbf{x},\tau^*) = \frac{1}{16\pi^2\rho_o a_o^5}\int\int |1-M_c\cos\theta|^{-5}\frac{\partial^4}{\partial\tau^4}R^m(\mathbf{y},\boldsymbol{\delta},\tau)\, d\boldsymbol{\delta}\, d\mathbf{y} \tag{21}$$

where

$$R^f(\mathbf{y}, \boldsymbol{\Delta}, \tau) = R^m(\mathbf{y}, \boldsymbol{\delta}, \tau) \tag{22}$$

The superscript $m$ refers to a correlation in the moving reference frame and $\theta$ is the polar angle of the observer relative to the downstream jet axis. The integrand in Eqn. (21) is to be evaluated at

$$\tau = \frac{\boldsymbol{\delta} \cdot \mathbf{x}/x + a_o \tau^*}{a_o (1 - M_c \cos\theta)} \tag{23}$$

and $M_c = U_c/a_o$. If the wavenumber frequency spectrum in the moving reference frame is defined by

$$H^m(\mathbf{y}, \mathbf{k}, \omega) = \frac{1}{(2\pi)^4} \int \int R^m(\mathbf{y}, \boldsymbol{\delta}, \tau) \exp\left[-i(\omega\tau + \mathbf{k} \cdot \boldsymbol{\delta})\right] d\boldsymbol{\delta} d\tau \tag{24}$$

then the spectral density is given by

$$S(\mathbf{x}, \gamma) = \frac{\pi}{2\rho_o a_o^5 x^2} \int \gamma^4 H^m\left(\mathbf{y}, -\frac{\gamma \mathbf{x}}{a_o x}, \omega\right) d\mathbf{y} \tag{25}$$

with

$$\omega = \gamma(1 - M_c \cos\theta) \tag{26}$$

It is important to remember that $\boldsymbol{\delta} = \boldsymbol{\delta}(\tau)$ in the differentiation in the integrand of Eqn. (21): see Ffowcs Williams (1963). Again the radiated noise is at a wavenumber that gives a sonic phase velocity in the direction of the observer at the frequency $\gamma$: but, the source spectrum is now evaluated at a Doppler shifted frequency, $\omega$ given by Eqn. (26).

**Source Cross Correlation Function** In order to make any noise predictions, based on the preceding formulas for the spectral density, it is necessary to provide a model for the source cross correlation function. In addition, though the introduction of the Proudman (1952) form of the correlation in Eqn. (13) simplifies the algebra, it conceals the individual contributions of the different components of $T_{ij}$. Ribner (1969) derived expressions for the relative weightings of the individual source correlations to the far field intensity for an axisymmetric jet. He assumed that the correlation involving the velocity fluctuations had a joint normal probability. This enabled $\langle u_i' u_j' u_k' u_l' \rangle$ to be written in terms of the second moments $\langle u_i' u_j' \rangle$, etc.

Models for the source correlation function have been based on an assumption of isotropic turbulence (for example, Ribner (1969), Balsa and Gliebe (1977), Lilley (1995) and Lilley (1996)), axisymmetric turbulence (Khavaran (1999)), on measured two-point velocity correlations such as

those obtained by Davies et al. (1963) and Chu (1966), or based on Large Eddy Simulations (Karabasov et al. (2010)). For example, consider a source correlation in the moving reference frame with a Gaussian form[2]. That is,

$$R^m(\mathbf{y},\delta,\tau) = \rho_s^2 u_s^4 \exp\left[-\left(\frac{\delta_1^2}{\ell_1^2}+\frac{\delta_2^2}{\ell_2^2}+\frac{\delta_3^2}{\ell_3^2}+\omega_s^2\tau^2\right)\right] \tag{27}$$

$\rho_s$, $u_s$, and $\omega_s$ are density, velocity fluctuation, and frequency scales in the source region. $\ell_i$ are the source length scales in the $y_i$ directions. All these scales are functions of the source location $\mathbf{y}$. It should be noted that this form is chosen for simplicity and is only a crude approximation to the actual cross correlation. So it should only be used to obtain estimates for the overall sound power radiated rather than detailed spectral densities and directivities. Lilley (1995) has argued that, though there may be large negative values in the longitudinal correlation in the fixed reference frame, the moving frame correlation is likely to be positive except at large separations. The wavenumber frequency spectrum corresponding to the correlation in Eqn. (27) is readily obtained and then Eqn. (25) yields the far field spectral density,

$$S(\mathbf{x},\gamma) = \frac{1}{32\pi\rho_o a_o^5 x^2}\int \ell_1\ell_2\ell_3\rho_s^2 u_s^4\omega_s^3\left(\frac{\gamma}{\omega_s}\right)^4 \exp\left(-\frac{\gamma C_\theta^2}{4\omega_s^2}\right)d\mathbf{y} \tag{28}$$

where $C_\theta$ is referred to as the *modified Doppler factor* given by,

$$C_\theta = \left[(1-M_c\cos\theta)^2 + \frac{\omega_s^2}{a_o^2}\left(\ell_1^2\cos^2\theta+\ell_2^2\sin^2\theta\right)\right]^{1/2} \tag{29}$$

The overall intensity is obtained by integration of Eqn. (28) with respect to $\gamma$ giving

$$I(x) = \frac{3}{4\sqrt{\pi}\rho_o a_o^5 x^2}\int \frac{\ell_1\ell_2\ell_3\rho_s^2 u_s^4\omega_s^4}{C_\theta^5}d\mathbf{y} \tag{30}$$

The source strength in the denominator of the integrand in Eqn. (30) is weighted by five inverse powers of the modified Doppler factor. This is called the *convective amplification* effect. In general terms, this results in an increased intensity for observer locations closer to the downstream jet axis. However, this directivity is modified by mean flow–acoustic interaction effects. These are described in the next section.

[2]Identical results are obtained if the analysis is performed in the fixed reference frame if the fixed reference frame cross correlation is obtained by a coordinate transformation from the moving frame as given by Eqn. (22). (See Morris et al. (2002)).

**Mean Flow–Acoustic Interaction Effects** Lighthill's simplification of his equivalent source term to $\rho_o v_i v_j$ is valid for low Mach number unheated jets. Detailed measurements of jet noise spectra and directivity over a range of operating conditions by Lush (1971) and Ahuja and Bushell (1973), indicated that the theoretical predictions embodied in Eqns. (28) and (30) did not match the experiments: particularly at angles close to the downstream jet axis and at high frequencies. Atvars et al. (1965) had performed experiments with point sources embedded in a jet flow and showed that refraction effects by the jet flow were important. These experimental observations complemented attempts to extend Lighthill's acoustic analogy to include the effects associated with the equivalent sources being surrounded by a moving, sheared flow. Phillips (1960) developed an acoustic analogy that included the effects of a uniform mean flow. However, it was Lilley (1972), Lilley (1973) who argued that the Phillips' acoustic analogy still included mean flow acoustic interaction effects in its equivalent source term. Lilley developed an acoustic analogy such that the equivalent sources acted on a parallel shear flow. Lilley (1972), Lilley (1973) originally followed Phillips (1960) by first developing a convected wave equation for the logarithm of the pressure.

The equations of continuity, momentum and energy, and the equation of state for a perfect gas can be rearranged in the form

$$\frac{D\pi}{Dt} = -\frac{\partial v_i}{\partial x_i}, \tag{31}$$

and

$$\frac{Dv_i}{Dt} = -a^2 \frac{\partial \pi}{\partial x_i}, \tag{32}$$

where,

$$\pi = \frac{1}{\gamma} \ln\left(\frac{p}{p_o}\right), \tag{33}$$

and

$$\frac{D}{Dt} \equiv \frac{\partial}{\partial t} + v_j \frac{\partial}{\partial x_j}. \tag{34}$$

$p_o$ is the mean static pressure that is assumed to be constant and $a$ is the speed of sound that may vary. Phillips' equation is obtained by elimination of the divergence of the velocity from Eqns. (31) and (32), giving

$$\frac{D^2\pi}{Dt^2} + \frac{\partial}{\partial x_i}\left(a^2 \frac{\partial \pi}{\partial x_i}\right) = -\frac{\partial v_j}{\partial x_i}\frac{\partial v_i}{\partial x_j}. \tag{35}$$

If the variables in Eqn. (35) are decomposed into fluctuations about the mean thermodynamic properties and a parallel mean flow of the form $\overline{u}_i =$

$V(x_2, x_3)\,\delta_{i1}$ is introduced, where the overbar denotes a time average, the term on the right hand side of Eqn. (35) is found to contain terms that are linear in the perturbations. Lilley (1972), Lilley (1973) argued that only terms that are second order in the fluctuations should be considered as equivalent sources, as linear terms describe propagation effects. If the convective derivative operator, Eqn. (34) is applied to Eqn. (35), the variables are again decomposed, and only linear terms are retained on the left hand side, Lilley's equation is obtained,

$$\frac{D_o}{Dt}\left[\frac{D^2\pi'}{Dt^2} - \frac{\partial}{\partial x_i}\left(\overline{a^2}\frac{\partial \pi'}{\partial x_i}\right)\right] + 2\overline{a^2}\left[\frac{\partial V}{\partial x_\alpha}\frac{\partial^2 \pi'}{\partial x_1 \partial x_\alpha}\right] = \Gamma, \tag{36}$$

where $\alpha = 2, 3$, and

$$\frac{D_o}{Dt} \equiv \frac{\partial}{\partial t} + V\frac{\partial}{\partial x_1}. \tag{37}$$

The source term $\Gamma$ is at least second order in fluctuations of velocity and temperature and some terms are multiplied by the mean shear and temperature gradients. In the limit of infinitesimal fluctuations, the equation reduces to a homogeneous form first derived by Pridmore-Brown (1958) to describe sound propagation in a duct containing a nonuniform mean flow. It is also known as the *compressible Rayleigh equation.*

In general, solutions of Lilley's equation must be obtained numerically. However, asymptotic solutions at low frequency were developed by Mani (1976) who used a vortex sheet approximation for the jet. A solution for a cylindrical vortex sheet representation of the jet mean flow was also given by Dowling et al. (1978). High frequency solutions have been obtained by Balsa (1976) and Goldstein (1982). Solutions based on ray acoustics are given by Durbin (1983).

The general characteristics of solutions to Lilley's equation are explained most simply by considering a two–dimensional mean flow with $V = V(y)$ as discussed by Lilley (1972). For simplicity, the speed of sound is assumed to be constant. If solutions of the form[3]

$$\pi' \sim f(y)\,(1 - \kappa M)\exp\left[ik\,(\kappa x - a_o t)\right], \tag{38}$$

are introduced into Lilley's equation, where $M = V/a_o$, the equation takes the form

$$\frac{d^2 f}{dy^2} + q(y)\,f = r(y), \tag{39}$$

[3]The inclusion of $(1 - \kappa M)$ eliminates the first derivative from the differential operator in the resulting equation.

where,

$$q(y) = k^2\left[\kappa^2 - (1-\kappa M)^2\right] - \frac{\kappa}{(1-\kappa M)}\left[\frac{d^2M}{dy^2} + 2\kappa\left(\frac{dM}{dy}\right)^2\right], \tag{40}$$

and $r(y)$ is representative of the source distribution. The turning points of Eqn. (39) correspond to $q(y_c) = 0$. For $q(y) > 0$ the general solutions are periodic and propagation will occur. For $q(y) < 0$ the solutions decay exponentially. At high frequencies $q(y)$ is dominated by the first term. Now, $\kappa = k_1/k = \cos\theta$ is the angle of radiation relative to the downstream jet axis. It is readily shown that the turning points correspond to

$$\theta_c = 1/(1+M) \tag{41}$$

For $\theta < \theta_c$ the sound experiences exponential decay away from the source while for $\theta > \theta_c$ the sound waves are able to propagate. $\theta_c$ is the boundary of the *zone of silence* of geometric acoustics. This is equivalent to Snell's law in optics.

Since, in a real jet, the flow is not truly parallel, but develops slowly in the axial direction, $\theta_c$ also changes with axial distance. Also, a sound wave may only experience exponential decay for a portion of its propagation path before radiating. Finally, the simple result of Eqn. (41) is only true at very high frequencies. All these factors result in a zone of silence that is not completely silent. The greatest attenuation and refraction occurs for the highest frequencies and low frequencies are relatively unaffected.

**Noise Prediction Models Based on the Acoustic Analogy** In spite of the considerable effort expended on theoretical developments arising from the acoustic analogy, actual noise prediction methods are scarce. At the simplest level some general scaling laws have been developed. These are well summarized by Ribner (1964) and Lilley (1995). An example is the 'slice-of-the-jet' method in which contributions to the overall radiated power from axial slices of the jet are estimated. For example, Eqn. (30) can be integrated over all angles, with the convective amplification effects neglected for simplicity, to give the radiated power from a volume element of the jet as,

$$dP \sim \frac{\rho_o u_s^8}{a_o^5 \ell_s} dV \tag{42}$$

Here, it has been assumed that the source length scales are all proportional to $\ell_s$, that the source density is equal to the ambient density, and that $\omega_s \sim u_s/\ell_s$. In the annular mixing region of the jet, $u_s \sim U_j$, $dV \sim D_j x dx$,

and $\ell_s \sim x$. In the developed region of the jet, $u_s \sim U_j D_j/x$, $dV \sim x^2 dx$, and $\ell_s \sim x$. So that,

$$\frac{dP}{dx} \sim \begin{cases} \left(\rho_o U_j^8 D_j / a_o^5\right) & \text{in the annular mixing region} \\ \left(\rho_o U_j^8 D_j / a_o^5\right)(x/D_j)^{-7} & \text{in the developed jet} \end{cases} \tag{43}$$

Thus, the contribution to the radiated power from each axial slice of the jet is constant in the annular mixing and then decays rapidly beyond the end of the potential core. If these expressions are integrated with respect to $x$, the eighth power law given by Eqn. (11) is obtained. Since $\omega_s \sim u_s/\ell_s$, the characteristic source frequency scales as $U_j/x$ in the annular mixing region and as $U_j D_j/x^2$ in the developed jet. Then the spectral density of the acoustic power is given by,

$$\frac{dP}{df} = \frac{dP}{dx}\left|\frac{dx}{df}\right| \sim \begin{cases} \left(\rho_o U_j^9 D_j / a_o^5\right) f^{-2} & \text{in the annular mixing region} \\ \left(\rho_o U_j^5 D_j^5 / a_o^5\right) f^{2} & \text{in the developed jet} \end{cases} \tag{44}$$

Thus, the acoustic power spectrum is predicted to scale as $f^2$ at low frequencies (generated predominantly in the developed jet) and $f^{-2}$ at high frequencies(generated near the jet exit in the annular mixing region). These results give an indication of the regions of the jet responsible for sound generation and provide an overall picture of jet noise scaling and are useful for preliminary design estimates. But they do not predict absolute amplitude and mean flow/acoustic interaction effects are not included.

The first method to attempt to predict both the aerodynamic and acoustic properties of jets was the Mani-Gliebe-Balsa (MGB) prediction scheme (see Balsa et al. (1978)). In this method the jet aerodynamics were predicted using the turbulence model of Reichardt (1941) in which the jet plume is synthesized by a summation of elemental jets each with a Gaussian velocity profile. Comparisons of the aerodynamic predictions with measurements are given by Gliebe and Balsa (1978) as well as Gliebe et al. (1995). To obtain the characteristic frequency and length scales needed to describe the acoustic sources, such as those in Eqn. (28), two models were used. Balsa and Gliebe (1977) assumed that $\omega \sim (\tau/\rho)^{1/2}/\ell$ with $\ell \sim (x/\bar{u})(\tau/\rho)^{1/2}$. Here, $\tau$ is the magnitude of the Reynolds shear stress that is given by Reichardt's turbulence model and $\bar{u}$ is the mean axial velocity. Gliebe and Balsa (1978) assumed that $\omega$ was proportional to the local mean velocity gradient and $\ell \sim u'/\omega$, where $u'$ is the local turbulence intensity. Mean flow acoustic interaction effects were modeled using solutions to Lilley's equation [Eqn. (36)] with the multistream jets modeled as cylindrical vortex sheets. Similar solutions had been obtained by Mani (1976) and Balsa (1975). The

relative contributions from the individual components of the source term were based on the quadrupole correlations developed by Ribner (1969) that assumed isotropic turbulence in a moving reference frame. Some comparisons between predictions and measurements are given by Balsa and Gliebe (1977) and Gliebe and Balsa (1978). The agreement between predictions and measurements is generally reasonable, though significant discrepancies are evident in the directivities at higher frequencies and the individual 1/3 octave spectra at different angles.

A different prediction methodology developed from the noise source and propagation model is described by Tester and Morfey (1976). The emphasis of this study was on the prediction of the mean flow/acoustic interaction effects on the sources described by Lilley's equation. They derived both high frequency (Geometric Acoustics) and low frequency solutions to Lilley's equation. This analysis led to the notion that if the noise spectra at 90 degrees to the jet axis were known then the noise spectra at any other angle could be predicted using their acoustic model. Morfey and Szewczyk (1977a), Morfey and Szewczyk (1977b) used a large database of experimental data and removed all amplitude scaling factors and mean flow/acoustic interaction effects as described by a high frequency solution to Lilley's equation. This enabled them to construct two *master spectra* representing the spectral shapes at 90 degrees to the jet axis. They needed two spectra to be able to correlate the spectra for hot, low speed jets, where sources associated with the temperature fluctuations in the jet were argued to be important. However, as discussed by Viswanathan (2004), and shown in Figure 15, the change in spectral shape at low Mach numbers can be associated with a Reynolds number effect. Morfey and Szewczyk (1978) give a summary of their predictions for noise radiation outside the zone of silence. Predictions within the zone of silence, described by Morfey and Szewczyk (1977b) were less satisfactory, particularly for very high speed jets. However, no account of the noise radiation by the large-scale structures was included in their model, so this result is perhaps not surprising. It should be emphasized that this model was purely acoustic in that it didn't attempt to predict any turbulence properties to be used to model the noise source characteristics. Any changes in the jet turbulence, perhaps by the addition of a noise reduction device, would not be reflected in the noise predictions as the *master spectra* were developed for an unmodified single jet. Morris and Tanna (1985) were able to adapt the model to predict the noise radiated by coannular jets with the core stream faster than the fan stream. They did this by dividing the jet into three equivalent jets to represent the inner and outer shear layers and the developed region of the jet. Good agreement with experiment was obtained using reasonable assumptions for the properties of

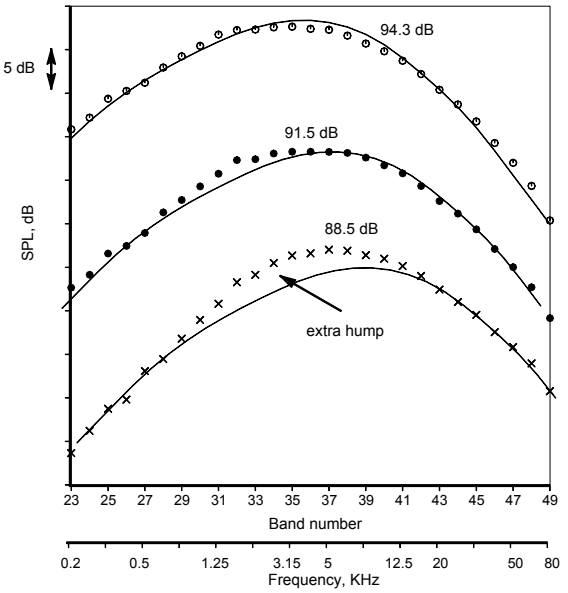


**Figure 15.** Comparison of measured spectra with fine-scale similarity spectrum. $M = 0.7$, $T_t/T_a = 3.2$, $\phi = 90$ degrees. $\times$, $D = 3.81$ cm; $\bullet$, $D = 6.22$ cm; $\circ$, $D = 8.79$ cm.(From Viswanathan (2004), with permission).

the separate jets.

In an effort to improve the generality of the aerodynamic component of the MGB code, Khavaran et al. (1994) replaced Reichardt's turbulence model with a $k - \varepsilon$ model. This revision and its extensions are known as the MGB-Khavaran (MGBK) model. The acoustic formulation in terms of source description was unchanged but the mean flow/acoustic interaction effects were based on high frequency solutions of Lilley's equation by Balsa (1976). The length and frequency scales required to define the source spectral characteristics were written in terms of $k$ and $\varepsilon$ such that $\ell \sim k^{3/2}/\varepsilon$ and $\omega \sim \varepsilon/k$. Flow and noise predictions were made for a single C-D nozzle with $M_j$ = 1.4 and $T_t/T_a$ = 3.3 The variation of overall SPL was predicted reasonably well: but 1/3 octave spectra predictions, particularly away from the peak noise direction, were less satisfactory. Two additional changes were reported by Khavaran (1999). Firstly, rather than using an isotropic description of the acoustic sources, an axisymmetric turbulence model was

incorporated. In such a model, the axial turbulence intensity is assumed to be greater than the other two components that are equal. This is a better representation of the measured anisotropic properties of the turbulence in the jet. Noise and flow predictions were made for a dual stream nozzle. The primary and secondary Mach numbers and total temperature ratios were $M_p \sim 1.0$, $T_{tp}/T_a = 2.7$ and $M_s \sim 1.0$, $T_{ts}/T_o \sim 1.0$. Khavaran examined the effects of the ratio of the axial and lateral turbulence intensities on the radiated noise as well as the contributions of "self" and "shear" noise. The predictions showed an improvement over the previous ones ( Khavaran et al. (1994)), particularly for the 1/3 octave spectra. However, the revisions in the source description permitted two more empirical factors to be assigned: the ratios of the turbulence intensities and the length scales in the axial and lateral directions.

Viswanathan (2001) describes a comparison of predictions of single stream jet noise with measurements, using both the MGBK method and the fine-scale turbulence mixing noise model by Tam and Auriault (1999). This latter model, as well as additional recent prediction models, is described in Section 3.4 below. The predictions were made without any prior access to the experimental data. In general, the spectral predictions with the Tam and Auriault model were superior to those made with the MGBK method. However, as discussed further in Section 3.4, the fine-scale turbulence model does not provide predictions in the peak noise direction. Tam and Auriault (1999) argue that the noise radiation in this direction is dominated by noise from the large-scale turbulent structures. The mechanism by which this noise generation and radiation process occurs and its modeling are described in the next section.

### 3.2 Large Scale Structures and Instability Wave Model Theory

It is now generally recognized that the noise radiation from high speed jets in the peak noise direction is dominated by the noise generated by the large scale turbulent structures in the jet. Tam (1995a) provides an extensive review of the role played by the large scale structures in jet noise. Beginning with the experiments by McLaughlin and his research team at Oklahoma State University ( McLaughlin et al. (1975), McLaughlin et al. (1977)) numerous experimental observations of large-scale structures in both subsonic and supersonic jets at both high and low Reynolds number have been made.

The key observation of the large-scale turbulent structures in a high Reynolds number jet is that, though they occur in a non-deterministic fashion in space and time, any single occurrence is in the form of a train of

structures of gradually increasing scale in the axial direction. The growth of the jet upstream of the end of the potential core, as in the case of the two-dimensional shear layer, is associated with the engulfment of ambient fluid and the ejection of high speed jet fluid induced by the large-scale structures. The fact that the large-scale structures appear as a slowly-developing sequence suggests that they may be modeled in both a physical and mathematical sense by a train of waves of gradually varying wavelength. If the growth and decay of the instability wave is included the large-scale structures can be modeled as wavepackets. Tam (1971) was the first to demonstrate a direct link between the instability waves in the thin shear layers close to the jet exit and a radiating wave pattern. Chan and Westley (1973) also demonstrated the connection between the directional acoustic radiation from high speed jets and predictions based on a spatial stability analysis using a vortex sheet approximation to the jet flow. They showed good agreement between the computed and measured wavelengths and phase velocities of waves in the near fields of high speed helium jets.

In order to extend these ideas to jets with finite thickness, realistic jet profiles, several researchers used ideas originally proposed by Ko et al. (1970) who examined the development of finite amplitude instabilities in wakes. Chan (1974a), Chan (1974b), Chan (1975), Morris (1974), Morris (1977), Liu (1974) and Tam (1975) predicted the evolution of fixed frequency instability waves in jet flows. Tam and Morris (1985) also used this general formulation to predict the development of tone-excited jets. The mean momentum and energy integral equations, with an eddy viscosity model to describe the dissipative action of the small-scale turbulence, were solved to describe the mean jet flow development. The local radial variation of the instability wave properties was obtained from a linear, inviscid instability analysis, and the amplitude of the instability wave was determined by the integral kinetic energy equation for the wave.

Tam and Morris (1980) and Morris and Tam (1979) showed how the development of an instability wave could be coupled to the near and far sound fields of a two-dimensional shear layer and a jet respectively. The range of validity of these analyses was subsequently extended by Tam and Burton (1984). The local stability analysis of the jet flow that is used to describe the evolution of the instability waves, can be based either on a parallel mean flow approximation or some account can be taken of the effects of the relatively slow axial variation of the mean flow. The method of multiple scales (see Nayfeh (1973)) can be used for the latter purpose. In the method of multiple scales a series expansion is developed for the perturbations developing in the non-parallel mean flow. The expansion parameter $\varepsilon$ is a measure of the relative rate of change of the mean flow

in the axial to the cross stream directions. In a jet, $\varepsilon \sim d\delta/dx$ where $\delta$ is a measure of the jet shear layer thickness. All the terms in the series expansion are required to have vanishing amplitude at large radial distances. However, Tam and Morris (1980) showed that the multiple scales expansion is not uniformly valid at large radial distances. A complete description of the unsteady field associated with the instability waves, including their acoustic radiation, can be obtained by the method of matched asymptotic expansions. The inner solution is given by the multiple scales solution. This solution involves an uneven stretching of the axial and radial coordinates to allow for the slow axial variation of the jet mean flow. However, there is no such preferred stretching required in the acoustic field. This implies that the coordinates should be stretched equally. The resulting series solution of the linearized equations of motion provides the outer solution. The matching of the two series solutions takes place in an intermediate region where both solutions can be used. For the jet case, the matching procedure is described by Tam and Burton (1984) and complete details are given by Dahl (1994). To lowest order, the pressure outside the jet is given by,

$$p(r,x,\phi,t) = \int_{-\infty}^{\infty} g(k)\, H_n^{(1)}[i\lambda(k)\, r] \exp[i(kx + n\phi - \omega t)]\, dk, \tag{45}$$

where,

$$g(k) = \frac{1}{2\pi} \int_{-\infty}^{\infty} A_o(\varepsilon x) \exp[i\Theta(\varepsilon x)/\varepsilon - ikx]\, dx. \tag{46}$$

$A_o(\varepsilon x)$ is the slowly axially varying amplitude of the leading order term in the inner solution, $\Theta(\varepsilon x)/\varepsilon$ provides the corresponding rapid phase variation, $k$ is an axial wavenumber and $g(k)$ represents the Fourier transform of the axial variation of the inner instability wave solution. $n$ is the azimuthal wavenumber, $\omega$ is the instability wave radian frequency, and $H_n^{(1)}[\ ]$ is the Hankel function of the first kind and order $n$.

$$\lambda(k) = \left(k^2 - \bar{\rho}_o M_j^2 \omega^2\right)^{1/2} \text{ with } 0 \le \arg(\lambda) < \pi/2 \tag{47}$$

where $\bar{\rho}_o$ is the ambient density nondimensionalized by the jet exit mean density. The pressure in the far field can be obtained by replacing the Hankel function in Eqn. (45) by its asymptotic form for large argument, introducing spherical polar coordinates centered on the jet exit with the polar axis aligned with the jet axis, and evaluating the resulting integral by the method of stationary phase (see Tam and Morris (1980)). The

stationary point is given by

$$k_s = \bar{\rho}_o^{1/2} M_j \omega \cos\theta \tag{48}$$

where $\theta$ is the polar angle. The mean square pressure in the far field is then given by

$$D(\theta) = R^2 |p|^2_{R\to\infty} = 4 |g(k_s)|^2 \tag{49}$$

Thus, the far field directivity is determined by the magnitude of the component of the instability wave's axial wavenumber spectrum that has a sonic phase velocity in the direction of the far field observer. This condition applies in general and must be met by any source spectrum for noise radiation to occur.

Equation (49) is sufficiently simple that it provides an opportunity to examine the effect of the instability wave's phase velocity and amplitude growth and decay on the far field directivity. Detailed calculations of the amplitude and phase evolution of a single frequency instability (see Tam and Burton (1984)) suggest that,

$$A_o(\varepsilon x) \exp\left[i\Theta(\varepsilon x)/\varepsilon\right] \sim A \exp\left[-\alpha^2 (x - x_o)^2\right] \exp(i\omega x/c) \tag{50}$$

where $A$ and $\alpha$ control the amplitude and its growth and decay rate respectively, $x_o$ is an arbitrary axial location for the wave's maximum amplitude, and $c$ is the nondimensional instability wave phase velocity (assumed to be constant). Then, from Eqn. (49) the far field directivity is given by,

$$D(\theta) = \frac{A}{\pi\alpha^2} \exp\left[-\frac{\omega^2}{2\alpha^2 c^2} (1 - M_c \cos\theta)^2\right], \tag{51}$$

where, $M_c = cU_j/a_o$. If the instability wave's phase velocity is supersonic with respect to the ambient speed of sound $a_o$, that is, $M_c \geq 1$, the far field directivity will have its peak amplitude at,

$$\theta_{\text{peak}} = \cos^{-1}(1/M_c). \tag{52}$$

However, even if the instability wave travels at a subsonic phase velocity, relative to the ambient speed of sound, the instability wave or wavepacket can still radiate to the far field. In this case, the peak radiation direction will occur at $\Theta = 0$. The amplitude is controlled by the value of $\alpha$: the growth or decay factor of the wave amplitude. If $\alpha >> 1$, $D(\theta)$ varies slowly with $\Theta$. This is the case where either the growth or decay of the instability wave amplitude is very rapid. However, if $\alpha << 1$, and the wave's amplitude variation is slow, the far field sound pressure level would fall very rapidly with increasing $\theta$. Tam and Morris (1980) showed that if the growth and

decay of the instability wave is determined by linear theory, $\alpha$ is relatively small and the decrease in noise radiation levels with decrease in (shear layer) Mach number is very rapid. This suggests that the instability waves or large-scale structures are very inefficient noise radiators at convectively subsonic conditions. However, if the amplitude variation, most likely the decay of the large-scale structures, is controlled by a nonlinear process, then a rapid decay is possible and the radiation efficiency of the large scale structures would be significant. This issue is discussed again in Section 3.3.

So far, only a single frequency instability wave has been considered. At low to moderate Reynolds numbers, such as in the experiments by McLaughlin et al. (1975), McLaughlin et al. (1977), a single frequency or azimuthal mode number can be excited easily. At high Reynolds numbers the jet turbulence has a broadband spectrum. Tam and Chen (1979) developed a stochastic model for the large-scale turbulent structures in a two-dimensional shear layer in terms of a random superposition of the shear layer instability waves. The spectrum and two-point statistics were shown to be dominated by the most unstable mode. As described in Section 4.3 below, Tam (1987) used this stochastic description of the turbulence to develop a prediction scheme for broadband shock-associated noise. Morris et al. (1990) also used a broadband excitation of instability waves in a shear layer to simulate the axial evolution of the shear layer growth rate and the turbulence spectrum. This model was able to predict the absolute value of the shear layer growth rate for a wide range of velocity ratios and Mach numbers, without the need to specify any empirical model constants. These ideas were extended to jets by Viswanathan and Morris (1992). All these models demonstrate that the turbulence spectrum at the largest scales is controlled by the large-scale structures. In addition, the models are weakly nonlinear: that is, there is no significant interaction between different frequency and azimuthal mode number components. Thus, the broadband noise spectrum can be considered as a random superposition of the contributions of individual frequency and azimuthal mode number components. In closing this discussion it is important to note that the noise radiation by the large-scale structures or instability waves is broadband, though its peak will be at relatively low frequencies, so it is not readily distinguished from the noise radiation by the fine-scale turbulence. However, the two mechanisms do generate different spectral shapes in the far field. This is discussed further in the next section.

### 3.3 Similarity Spectra and the Two Mechanisms of Turbulent Mixing Noise

Two mechanisms have been recognized in the generation of turbulent mixing noise. The first is associated with the large-scale structures in the jet. The second is related to the more random spatial and temporal behavior of the smaller turbulent scales. The prediction of jet noise radiation by the large scales can be determined within the framework of an instability wave model as described in Section 3.2. In very high speed jets there is a direct weakly nonlinear coupling between the flow disturbances created by the large-scale structures and the acoustic field they generate. At lower jet velocities, a strong nonlinear mechanism is likely to be needed for the spatial and temporal behavior of the large-scale structures to generate the wavenumbers necessary for noise radiation. However, at this time, no first principles theory exists for noise radiation by large-scale structures in convectively subsonic jets. On the other hand, the smaller-scale turbulence, when viewed in terms of its wavenumber and frequency content, is able to generate radiating components. But the energy-containing components of the turbulence are not efficient noise radiators in convectively subsonic jets. The theoretical description of this noise generation process is the one found in almost all models based on the acoustic analogy, described in Section 3.1, as well as the model proposed by Tam and Auriault (1999), to be described in the next section.

Since the radiation by the large-scale structures involves a direct connection between the jet turbulence and the acoustic field, this process does not experience mean flow/acoustic interaction effects. On the other hand, noise from fine-scale turbulence, being a more local process within the turbulent jet plume, is subject to refraction as the generated sound propagates through the sheared mean flow. Both mechanisms generate sound over a broad range of frequencies, though the large-scale structure noise is strongest at low frequencies and in directions close to the downstream jet axis.

In the mixing layer of a high Reynolds number turbulent jet, there is no intrinsic length scale. Furthermore, molecular viscosity is not important, except as an energy sink at the smallest scales. So high Reynolds number jets exhibit a dynamic, inviscid behavior. Hence, there is also no intrinsic time scale in this region of the jet. Experimental measurements have shown that the mean flow as well as the turbulence statistics exhibit self-similarity. Tam et al. (1996) contended that the noise from the fine scale turbulence is also generated in the same region of the jet, where the flow properties are similar. Based on these observations, they proposed that the noise spectra of both the large and small scale noise components should also exhibit self-similarity. They reasoned further that the absence of a time (or frequency)

scale implied that the frequency $f$ must be scaled by $f_L$, the peak frequency of the large turbulent structures noise spectrum or $f_F$ the peak frequency of the fine-scale turbulence noise spectrum.

Tam et al. (1996) expressed the jet noise spectrum $S$ as a sum of the two independent noise components, in the following similarity form,

$$S = \left[AF\left(\frac{f}{f_L}\right) + BG\left(\frac{f}{f_F}\right)\right]\left(\frac{D_j}{r}\right)^2 \tag{53}$$

$F(f/f_L)$ and $G(f/f_F)$ are the similarity spectra associated with the large-scale and fine-scale turbulence, respectively and $r$ is the radial distance to the observer from the jet exit. These spectrum functions have been normalized such that $F(1) = G(1) = 1$. $A$ and $B$, the amplitudes of the two spectra, and the peak frequencies $f_L$ and $f_F$ are functions of the jet operating conditions and direction of radiation.

Tam et al. (1996) also recast this equation in decibel form as,

$$10\log\left(\frac{S}{p_{\text{ref}}^2}\right) = 10\log\left(\frac{A}{p_{\text{ref}}^2}F\left(\frac{f}{f_L}\right) + \frac{B}{p_{\text{ref}}^2}G\left(\frac{f}{f_F}\right)\right) - 20\log\left(\frac{r}{D_j}\right) \tag{54}$$

where $p_{\text{ref}}$ is the standard reference pressure ($2\times10^{-5}$ N/m$^2$) of the decibel scale. If this hypothesis is true, then this equation would be valid for any jet operating condition and radiation angle. At large aft angles where the large-scale structure noise is dominant, and in the forward quadrant where the fine scale structure is dominant, the above equation reduces to a simpler form with the measured spectra characterized by either the large-scale or fine-scale component, $F$ or $G$.

Tam et al. (1996) investigated the jet noise database acquired with round nozzles, operated at supersonic Mach numbers, at NASA Langley's Jet Noise Laboratory (JNL). This database consisted of narrow-band data with a 122 Hz bandwidth that covered a Mach number range of 1.37 to 2.24 and a total temperature ratio range of 1.0 to 4.9. From a selected subset of this database, they developed two empirical similarity spectrum functions and determined that the empirical spectra fitted the measured spectra over the entire range of Mach numbers and temperature ratios. Figure 16 shows the shape of these two similarity spectra, $10\log F$ and $10\log G$, plotted on a decibel scale as a function of $\log(f/f_{\text{peak}})$. The shapes of the two similarity spectra are very different. The spectrum associated with the large-scale structures ($10\log F$) has a narrow peak and drops off linearly, while the spectral shape associated with the fine-scale turbulence ($10\log G$) has a broader peak and a more gradual roll off away from the peak. The correct

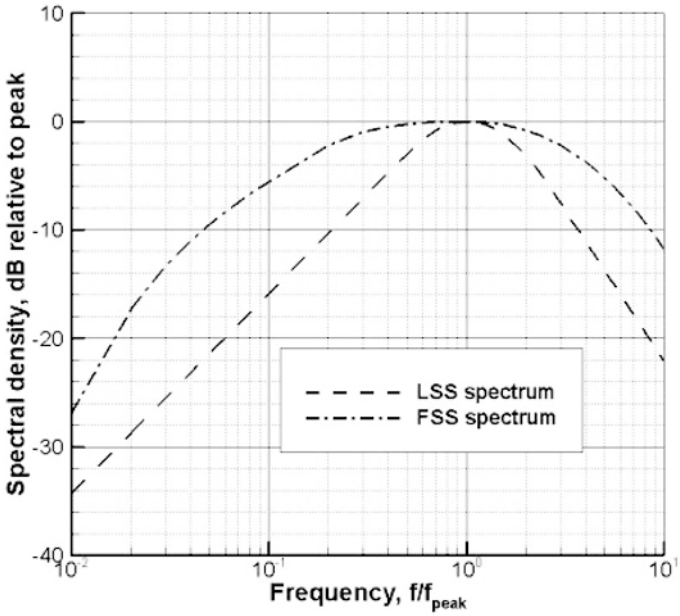


**Figure 16.** Similarity spectra for the two components of turbulent mixing noise. ———-, Large turbulent structure noise; — – —, fine-scale turbulence noise. (Adapted from and inspired by Tam et al. (1996))

analytical expressions for the two master spectra can be found in Tam and Zaman (2000).

Tam (1998a) also examined the supersonic noise data of Yamamoto et al. (1984) from a variety of round nozzles: convergent, C-D, convergent with a plug, C-D with a plug, and a 20-chute C-D suppressor. Good agreement between the similarity spectra and measurements for both static and wind-on conditions, was found. This study indicates that the turbulent mixing noise of supersonic jets from not-too-complex nozzle geometries consist of two components. In addition, the shapes of the noise spectra of supersonic jets are very similar regardless of the nozzle geometry.

More recently, Tam and Zaman (2000) carried out some simple experiments and measured noise from elliptic (AR=3.0) and rectangular (AR=3.0, 8.0) nozzles, a circular nozzle with 2 and 4 tabs, and a six-lobed mixer nozzle. All the test points were restricted to unheated jets at subsonic Mach numbers. The results showed that, in general, turbulent mixing noise from

non-circular subsonic jets can also be described by the two similarity components. However, it should be borne in mind that the quality of this data set is questionable. One interesting result of this study is that the noise field of the lobed mixer was very different from those from the other simpler geometries. The lobed mixer, designed to enhance perimeter mixing with the ambient fluid, divides the main jet into many thin sheets at the nozzle exit. As such, flow from this geometry does not apparently support large-scale structures comparable in scale to the equivalent circular diameter. The test results indicated that the noise spectrum at large aft angles, where the large-scale structure noise typically dominates, fitted the spectrum associated with fine-scale turbulence. Tam and Zaman (2000) concluded that the nozzle geometry, by suppressing the development of large-scale structures, effectively eliminated the noise associated with this component. In the absence of this component, the fine-scale noise component becomes dominant at all radiation angles.

In summary, there is strong evidence that two self-similar spectra can be used to characterize the radiated noise spectra for a wide range of jet operating conditions. This applies to supersonic jets, from both circular and other simple non-circular nozzle geometries as well as cold subsonic jets. The spectra at lower angles to the jet inlet from heated subsonic jets can also be characterized by the fine-scale similarity spectrum. At angles close to the jet downstream axis, the spectral shape changes at higher temperatures, as noted by Viswanathan (2004). An important point to remember is that all these experimental data are restricted to single stream nozzles. However, in closing this section, it should be noted that other explanations for the different spectral shapes between the sideline and large aft angles are available. For example, it has been argued that a combination of convective amplification, Doppler frequency shift, and mean flow/acoustic interaction effects, could result in the observed spectral changes with angle. This hypothesis is the basis for the jet noise model developed by Morfey and Szewczyk (1978) as well as the MGB and MGBK methods discussed in Section 3.1. It remains to be determined whether one or other of these descriptions of turbulent mixing noise generation, or a combination of the two, are valid.

### 3.4 Noise from Fine-Scale Turbulence

Traditional theories of aerodynamic noise and the development of their mathematical foundations were described in Section 3.1. These methods require a detailed knowledge of turbulence, which is then used as input for noise calculations. Therein lies the fundamental difficulty in these ap-

proaches. Despite nearly a century of turbulence research, our understanding of turbulence and the development of accurate models for the turbulence statistics are still remote. Given this situation, it is perhaps not surprising that most existing methods[4], which make use of some model for the statistical properties of the turbulence, fail to capture the spectral characteristics of jet noise at all angles.

Tam (1995b) and Tam (1998b) have provided a different perspective on jet noise. As described in Section 3.2, Tam and Morris, among others, have had success in predicting the large-scale structure noise of circular and non-circular jets using an instability wave model. Following the arguments presented in the previous section that the turbulent mixing noise consists of two components. Tam and Auriault (1999) proposed a model, not formulated as an acoustic analogy, for the fine-scale noise component. Drawing an analogy with the kinetic theory of gases, they reasoned that the fine-scale turbulence exerts a pressure on its surroundings, which must be balanced by the pressure and momentum flux of the surrounding fluid. Since this pressure fluctuates in time, it will lead to compressions and rarefactions in the fluid, resulting in acoustic disturbances. They argued that the time rate of change of this pressure in the moving frame of the fluid would constitute the source of the fine-scale turbulence noise. They also argued that the propagation of the resulting sound waves through the jet flow can be described by the Euler equations linearized about the jet mean flow. It should be noted that, if the mean flow is taken to be parallel, the linearized Euler equations are equivalent to the propagator provided by Lilley's equation. Tam and Auriault (1999) obtained the Green's functions for the linearized Euler equations in terms of their adjoint solutions. Details of the use of the adjoint solution to calculate refraction effects in sheared mean flows are given by Tam and Auriault (1998). The method is quite novel, though it is not without difficulties. The cause of the difficulties is the presence of Kelvin-Helmholtz (K-H) instabilities. Both the physical problem and its adjoint have these convective instabilities. It is possible for these unstable solutions to dominate over and obscure the part of the solution associated with sound wave propagation. Tam and Auriault (1998) acknowledged their presence and, in order to avoid these instabilities, they introduced damping functions and damping regions to suppress them. Agarwal et al. (2004) have shown how the instability can be suppressed if a frequency domain formulation is used for the adjoint Green's function.

Tam and Auriault (1999) showed how the pressure fluctuation outside the jet could be related to the convolution of the adjoint pressure and the

[4]There are some exceptions to this statement. These cases are described in Section 6.1

convective derivative of their source term. The formula for the pressure fluctuation is given by,

$$p(\mathbf{x},t) = \int_{-\infty}^{\infty} \cdots \int_{-\infty}^{\infty} \left\{ \int_{-\infty}^{\infty} p_a(\mathbf{x}_1,\mathbf{x},\omega) \exp\left[-i\omega(t-t_1)\right] d\omega \right\} \frac{Dq_s(\mathbf{x}_1,t_1)}{Dt_1} dt_1 d\mathbf{x}_1 \tag{55}$$

where $p_a(\mathbf{x}_1,\mathbf{x},\omega)$ is the time harmonic adjoint pressure, $q_s = 2\rho k_s/2$, and $k_s$ is the turbulent kinetic energy of the fine-scale turbulence per unit mass. An expression for the autocorrelation of the intensity can then be obtained and the far field spectral density is obtained using Eqn. (19).

As in noise prediction models based on the acoustic analogy, it is necessary to specify a mathematical expression for the noise source space-time correlation function. Tam and Auriault (1999) assumed that the source correlation had the same characteristics as the measured two-point space-time correlation of the fluctuating axial velocity in a jet. Morris and Farassat (2002) have shown that there is no essential difference between models based on the acoustic analogy and the predictive model developed by Tam and Auriault (1999) [5]. The key difference in the resulting prediction formulas lies in the model used to describe the two-point space-time correlation of the source function. Tam and Auriault (1999) showed that the spectral density can be written,

$$S(\mathbf{x},\omega) = 4\pi \left(\frac{\pi}{\ln 2}\right)^{3/2} \int_{-\infty}^{\infty}\int_{-\infty}^{\infty}\int_{-\infty}^{\infty} \frac{A^2 \hat{q}_s^2 \ell_s^3}{\tau_s} \left|p_a(\mathbf{x}_2,\mathbf{x},\omega)\right|^2 \frac{\exp\left[-\omega^2\ell_s^2/\left\{\bar{u}^2(4\ln 2)\right\}\right]}{\left[1+\omega^2\tau_s^2\left(1-\frac{\bar{u}}{a_o}\cos\theta\right)^2\right]} d\mathbf{x}_2 \tag{56}$$

where $\bar{u}$ is the local mean velocity and $\theta$ is the polar angle relative to the downstream jet axis. This formula contains three parameters associated with the fine scale turbulence: a typical length scale $\ell_s$, a time scale $\tau_s$, and a measure of the intensity of the fluctuating kinetic energy $A^2q^2$, where $q = \frac{2}{3}\bar{\rho}k$, $\bar{\rho}$ is the mean density and $k$ is the turbulent kinetic energy per unit mass. Tam and Auriault (1999) used the modified $k-\varepsilon$ model of Thies and Tam (1996) to obtain these three characteristic parameters. Since the $k-\varepsilon$ model also includes the contributions from the large-scale turbulence, they proposed to extract the fine-scale turbulence contribution through the use of constants with values of less than unity. That is,

$$\ell_s = c_\ell\left(k^{3/2}/\varepsilon\right), \quad \tau_s = c_\tau\left(k/\varepsilon\right): \quad c_\ell = 0.256, \quad c_\tau = 0.233 \tag{57}$$

[5] Though the modeling philosophy and details of the analysis are different.

where $\varepsilon$ is the viscous dissipation rate. The values of these constants, and a third constant to set the absolute level, were determined by a best fit of the predicted noise to measured data.

There are three major steps involved in this prediction method. First, the jet mean flow field and the turbulence properties $k$ and $\varepsilon$, are computed. In the second step, the adjoint Green's function is evaluated using the jet mean flow field. Finally, the radiated noise is calculated by adding the noise contributions from each volume element in the computational grid.

Tam and Auriault (1999) show good agreement of the predicted noise spectra with measured data for cold jets at both subsonic and supersonic Mach numbers: however, there are some discrepancies at the very high frequencies. The ability of the model to predict the spectral variations with radiation angle for a Mach 2.0 isothermal jet is also demonstrated. This model also captures the effect of jet temperature on radiated noise. Finally, they show good comparisons of the peak spectral levels for a wide range of jet operating conditions. Tam et al. (2001) show additional test cases for cold jets embedded in a freestream, with good predictive capability. It should be emphasized that this theory makes absolute noise predictions; intensity, directivity, as well as the spectral characteristics of the measured data are reproduced. Of course this is a semi-empirical theory because of the three new constants in addition to the empirical constants inherent in the $k - \varepsilon$ turbulence model. Importantly, it should be noted that Tam and Auriault (1999) limit their predictions to angles close to 90° to the jet axis. They argue that noise at other angles, particularly in the peak noise direction at small angles to the jet downstream axis, depend on noise from the large-scale structures. So, fine-scale turbulence noise predictions would not be relevant at other angles. Similar findings were obtained by Morris and Farassat (2002) and Morris and Boluriaan (2004) using an acoustic analogy based on the linearized Euler equations.

This model is not without critics. Ribner (2000) questions the validity of the two similarity components and the approach adopted by Tam and Auriault (1999). However, it should be noted that there is a vast amount of experimental data that has established the presence of large-scale structures and their Mach wave radiation. In addition, examination of the expression for the spectral density, Eqn. (56), shows that the jet temperature does not appear explicitly in the integrand. Fisher (38) pointed out that since the dipole term that occurs in classical approaches based on the acoustic analogy is not included, this model should not be able to predict the noise from hot jets.

It should also be noted that there is no convective amplification of the fine-scale turbulence noise in the model of Tam and Auriault (1999). This is

not a result of the use of the fixed frame of reference description of the source statistics. The result is independent of the reference frame for consistent source descriptions. Morris et al. (2002) show that if a Gaussian model is used to describe the source correlation in the Tam and Auriualt model, convective amplification appears: but, with only three inverse powers of the modified Doppler factor, rather than the five appearing in models based on the acoustic analogy, such as given by Eqn. (31).

## 4 Broadband Shock-Associated Noise

The characteristics of shock-associated noise were described in Section 2.2 Harper-Bourne and Fisher (1974) proposed a simple model, consisting of phased sources at regular intervals to represent the turbulence/shock cell system interaction. They inferred that the interaction of the spatially coherent turbulence with the quasi-periodic point sources would be necessary to produce the observed noise characteristics in the far field. Tam (1995a) stressed that any shock noise model must incorporate these features and points out that prior and later studies on sound generation by the interaction of random turbulence with a single shock wave do not represent the generation mechanism of broadband shock-associated noise. This section describes the broadband shock-associated noise generation mechanism as well as models to predict its radiated noise.

### 4.1 The Noise Generation Mechanism

It is now well established that broadband shock-associated noise is generated by the interaction of the large-scale structures that propagate downstream and the quasi-periodic shock cell structure. The point-source array model proposed by Harper-Bourne and Fisher Harper-Bourne and Fisher (1974) was successful in explaining many of the observed noise characteristics. Tam and Tanna (1982) proposed an alternate theory based on the observed properties of the large-scale turbulence structures, which possess the important characteristics of being coherent and spatially quasi-periodic over several jet diameters. Thus the large-scale structures are wave-like when viewed as a whole. As these structures propagate downstream, they interact with the shock cell system established in the jet plume of an imperfectly expanded supersonic jet. Tam and Tanna (1982) proposed a simple analytical model to explain the noise generation mechanism. They first expressed the pressure perturbation associated with the shock cells as a summation of the waveguide modes. Such a first order shock solution had been developed by Pack (1950), based on the work of Prandtl (1904).

In a cylindrical polar coordinate system centered at the nozzle exit, any perturbation associated with the shock cells can be expressed as,

$$u_s = \sum_{n=1}^{\infty} A_n \phi_n (r) \cos (k_n x) = \frac{1}{2} \sum_{n=1}^{\infty} A_n \phi_n (r) \left( e^{ik_n x} + e^{-ik_n x} \right), \tag{58}$$

where $A_n$, $\phi_n(r)$ and $k_n$ are the amplitude, the eigenfunction, and the axial wavenumber of the $n$-th mode, respectively. The fundamental shock cell spacing $L_1 = 2\pi/k_1$.

The large-scale turbulent structures can be represented by a linear superposition of the normal wave modes of the flow with random amplitude functions. For a frequency $f = \omega/2\pi$, the corresponding disturbance quantity can be expressed as

$$u_t = \Re \{ B (x) \psi (r) \exp [i (kx - \omega t + m\phi)] \}, \tag{59}$$

where $B(x)$, $\psi(r)$, $k$, and $m$ are the amplitude, the eigenfunction or radial distribution, the axial wavenumber, and the azimuthal mode number of the traveling instability wave, respectively. The wavenumber and frequency are related by $u_c = \omega/k$, where $u_c$ is the convection or phase velocity of the large-scale turbulent structure or instability wave.

The perturbations created by a weak interaction between the instability waves or large scale structures and the shock cell structure are given by the product of the Eqns. (58) and (59). The expression for the shock cell structure involves two summations corresponding to the different signs of the exponent. Tam and Tanna (1982) noted that the phase velocities of the terms associated with the shock cell component with the positive exponent, given by $\omega/(k + k_n)$, are less than those of the instability wave alone. They are usually subsonic relative to the ambient speed of sound and do not radiate. For the term involving the product with the component with the negative exponent, the interaction quantity is given by

$$\Re \left\{ \frac{1}{2} B (x) \psi (r) A_n \phi_n (r) \exp [i(k - k_n)x - i\omega t] \right\}. \tag{60}$$

This expression represents a traveling wave with wavenumber $(k - k_n)$ and phase velocity equal to $\omega/(k - k_n)$, if any amplitude variation $B(x)$ is ignored. If $k_n$ is slightly larger than $k$, then the phase velocity is negative. This phase velocity could be supersonic relative to the ambient speed of sound even if the convection velocity of the large-scale structures themselves, given by $\omega/k$, is subsonic. These supersonic components would generate Mach wave radiation mainly in the upstream direction. The direction

of radiation can be related to the phase velocity and ambient speed of sound by

$$a_o = \left(\frac{\omega}{k - k_n}\right) \cos(\pi - \phi) \tag{61}$$

where $\phi$ is measured from the jet inlet direction. This relation can be rewritten as an expression for the frequency as a function of angle as,

$$f_n = \frac{u_c}{L_n(1 + M_c \cos\phi)}, \quad n = 1, 2, 3, \ldots \tag{62}$$

where $M_c = u_c/a$ is the convection Mach number of the large scale structures relative to the ambient speed of sound and $L_n$ is the wavelength of the $n$-th Fourier mode of the shock cell structure. $L_1$ is the fundamental shock cell spacing. The peak frequency for a given angle of radiation would be close to but not exactly that given by Eqn. (62). The axial variation of the instability wave amplitude $B(x)$, broadens the wavenumber spectrum, as shown by Tam and Morris (1980) and discussed in Section 3.2. This broadening produces a band of components with different supersonic phase velocities at frequency $f$. These components radiate at different angles, producing the observed directivity pattern at this frequency.

Since the shock cell system is composed of several waveguide modes, with different wavelengths, the interaction effects of the different waveguide modes are different. The principal direction of radiation and the spectral content of the noise are different for each mode. Thus, the far field noise that is made up of the superposition of the contributions from all the modes should exhibit multiple peaks and directional dependencies. These are precisely the characteristics observed experimentally as shown in Figure 10. Since the amplitude of the broadband shock noise is directly proportional to the amplitude of the waveguide modes, and the amplitudes decrease rapidly with mode number, the spectral levels associated with the higher order modes are smaller than that of the fundamental. Even though multiple peaks are possible, they may not be easily observed. This explains why only a single dominant peak is often observed in the measured spectra.

Tam and Tanna (1982) also developed an expression for the intensity of broadband shock associated noise for jets operated at slightly off-design conditions $\left|M_j^2 - M_d^2\right| \leq 1$, where $M_d$ and $M_j$ are the design and fully-expanded Mach numbers of the jet respectively. The intensity is given by,

$$I_s \propto \left(M_j^2 - M_d^2\right)^2. \tag{63}$$

This expression, which is valid for both convergent and C-D nozzles, was shown to provide excellent agreement with measured data for both cold and

hot jets, and for over- and under-expanded modes of operation for the C-D nozzle. This expression is not valid when a strong shock, such as a Mach disc, is present in the plume.

### 4.2 Models for the Shock Cell Structure

From the model described in the previous section, it is clear that an accurate representation of the shock cell structure as well as the large scale turbulence structures is necessary for the prediction of broadband shock noise. When a supersonic jet is operated at an under-expanded condition, $p_e/p_o > 1$, where $p_e$ and $p_o$ are the exit and ambient pressures respectively, expansion waves occur at the nozzle exit so that the pressures inside and outside the jet can come into balance. In the overexpanded mode, oblique shock waves are set up in the plume. Tam and Tanna (1982) derived an expression for the fully expanded jet diameter $D_j$, which is larger than the physical nozzle diameter for the under-expanded case and smaller for the over-expanded case. Pack (1950), following Prandtl (1904), first provided a complete shock cell solution using a vortex sheet approximation to represent the jet shear layer. This solution is valid only for slightly imperfectly expanded jets, and only close to the nozzle exit where the shear layer is thin. However, experimental evidence shows that the region of importance for shock noise generation is close to the end of the potential core, where the shear layer is no longer thin. Further, the effect of turbulence in reducing the shock strength and smoothing sharp discontinuities must be taken into account. Tam et al. (1985) extended Pack's linear solution to account for the slowly diverging mean flow using the method of multiple scales. The effect of turbulence was simulated through the inclusion of eddy viscosity terms. The most suitable value for the turbulent Reynolds number was determined by comparison of predictions with experimental data. They evaluated the contributions of the higher order terms to the non-parallel correction and concluded that only the first order correction term was significant. Thus, the simpler locally parallel assumption was shown to be adequate for the calculation of the shock cell structure.

Tam et al. (1985) demonstrated very good agreement between their predictions and measured data for a variety of jet operating conditions. Both the axial and radial variations of the pressure field, in terms of shock cell spacing and shock amplitude were well predicted for both over- and under-expanded jets. Morris et al. (1989) extended Tam's vortex sheet shock cell model for jets of arbitrary geometry using a boundary element technique. Examples for circular, elliptic and rectangular jets were given. Bhat et al. (1990) included the effects of finite jet shear layer thickness and

the dissipative effects of the fine-scale turbulence in a shock cell model for elliptic jets. They also concluded that the fundamental waveguide mode could be used as a good approximation for the shock spacing at the end of the potential core and that the higher order modes only contributed to the fine structure of the shock cells near the jet nozzle exit.

The linear shock cell model is valid only for weakly imperfectly expanded jets, with $\left|M_j^2 - M_d^2\right| \leq 1$. Extensive plume surveys carried out at NASA Langley Research Center and reported by Norum and Seiner (1982a) indicated that as the degree of mismatch between the design and fully expanded Mach numbers increased, there was a dramatic change in the shock cell structure. At highly off-design conditions, the strength of the first shock cell increased tremendously while the rest of the shock cells remained regular and quasi-periodic. That is, downstream of the first shock, the shock cell structure for the strongly off-design conditions resembled that of the slightly imperfectly expanded jet. Based on this observation and the fact that the first shock plays only a negligible role in noise generation as noted by Seiner and Norum (1980), Tam (1990) suggested that the linear solution, suitably modified, could be used to model the shock cell structure of even moderately imperfectly expanded jets. Tam (1990) also developed a semi-empirical formula to estimate the initial amplitude of the linear shock cells for this situation.

### 4.3 Broadband Shock-Associated Noise Prediction

A good representation of the large-scale turbulence structures is the next required step in the development of predictions for broadband shock-associated noise. Tam (1987) proposed a formal mathematical theory starting from the equations of motion. Tam and Chen (1979), in their study of plane mixing layers, had developed a stochastic model to describe the large-scale turbulence structures. In this approach, the large structures are represented by a superposition of the instability wave modes of the flow, with the amplitudes of the instability waves represented by stochastic random functions possessing similarity properties. In the initial mixing region of the axisymmetric jet, self-similarity applies and hence the same argument can be invoked. Here, only a general description of the stochastic theory is provided. Complete details are given by Tam (1987) and Tam (1995a).

Tam (1987) decomposed the flow variables into four parts, consisting of the time-averaged mean, perturbations associated with the turbulence structures, perturbations associated with the shock cell structure and the time-dependent disturbances that are generated as a consequence of the interactions between the large structures and the quasi-periodic shock struc-

tures. These interaction terms, which are responsible for shock noise generation, can be determined from the solution of a boundary value problem. Tam developed expressions for the noise power spectrum, both for the near and far fields. The complete formal solution requires extensive computations, which renders it impractical. So, Tam introduced a similarity source model for the interaction terms and developed a semi-empirical theory with four empirical constants. The values of the empirical constants were chosen by comparison with the measurements of Norum and Seiner (1982a).

Tam (1987) showed good agreement with experiment for both the spectral levels and directivity of broadband shock-associated noise for both under- and over-expanded supersonic jets. A sample comparison at several radiation angles was shown in Figure 10. There is good overall agreement, with the predicted peak frequencies at all angles following the measured trend. The calculated spectra also reproduce the reduction in the half-width of the dominant peak, as the observer angle moves towards the jet inlet. Tam also showed good comparisons of the near-field OASPL with experiments. For practical airplane applications, such as the prediction of the impinging shock noise on the fuselage, this capability is very valuable.

Tam (1990) extended his theory for slightly imperfectly expanded jets to moderately imperfectly expanded Mach numbers. Based on the measurements of Norum and Seiner (1982a), as shown in Fig. 11, Tam noted that the dependence of broadband shock noise on jet Mach number for underexpanded jets is quite different from that for overexpanded jets. The expression for the intensity of shock-associated noise, given by the slightly imperfectly expanded theory, $I_s \propto \left(M_j^2 - M_d^2\right)^2$, is strictly valid only for small deviations of the fully expanded Mach number from the design Mach number. To increase the range of applicability of the theory for a broader Mach number range, for Mach numbers slightly less than that of local maximum point C to slightly greater than point B in Fig. 11, Tam (1990) made modifications to the stochastic theory. Primarily, this approach involved the proper prescription of the shock cell strength, since the turbulence spectrum and the shock cell wavelength are not affected significantly by the degree of imperfect expansion. He noted that the effect on spectral shape was consequently unimportant and that the degree of imperfect expansion only affected the spectral level. Suitable expressions for the broadband shock-associated noise, for both cold and hot jets, were shown to provide very good agreement with measured spectra for jets operated at strongly off-design conditions.

Tam (1991) included the effects of flight on broadband shock-associated noise, through additional considerations of changes in the noise source as well as the effect of flight on the convection speed of the large scale struc-

tures. He argued that due to the thick boundary layer on the nozzle external surface, the shock cell strength would not be modified to a great extent and hence could be approximated by that for the static case: especially for low flight Mach numbers. Further, he assumed that the same similarity source spectrum adopted for the static case, with account taken of the increased shock-cell spacing and increased convection speed for the large-scale structures due to the co-flowing stream, would be valid. He developed modified expressions for the noise power spectrum and peak frequency for the flight case. This formulation provided the correct trends of a reduction in peak frequency, a narrowing of the spectral peak, and the appearance of higher order peaks with increasing flight speed. Tam (1992), through a transformation of the co-ordinate system, developed expressions for the calculation of broadband shock noise as measured by a ground observer in a typical fly-over noise test. This expression contains a term in the form of the familiar Doppler shift, but without a high power of convective amplification factor.

Tam and Reddy (1996) adapted the stochastic noise theory for the prediction of broadband shock noise from rectangular nozzles. The flow and shock cell structure of supersonic rectangular jets is different from those of round jets. As noted out by Tam (1988), for rectangular nozzles with straight sidewalls, two different shock cell systems are set up in the flow. One is the familiar system formed outside the nozzle and the other one originates inside the nozzle, close to the nozzle throat. Because of the second shock cell system, broadband shock noise is generated even at the so-called design Mach number of the nozzle. So, an additional term was added to the expression for the shock cell strength, to account for the second shock cell system. Tam (1988) had already developed a vortex sheet model for the description of the shock cell spacing from elliptic and rectangular jets. This expression was modified empirically to account for the finite thickness of the mixing layer. Furthermore, the convection velocity of the large-scale structures was changed to be $0.55U_j$, instead of the typical value of $0.7U_j$ used for circular jets. With these modifications, good agreement with the measurements of Ponton et al. (1986) was shown for rectangular nozzles with different aspect ratios.

The primary difficulty with the stochastic broadband shock noise theory is that it does not provide a connection to the flow. So, calculations for different geometries requires a reformulation of the model parameters. To overcome this difficulty, Morris and Miller (2010) developed a broadband shock-associated noise (BBSAN) model that uses input from RANS CFD calculations to provide the properties of the shock cell structure and the characteristic scales of the turbulence. The model is formulated as an acoustic analogy based on the linearized Euler equations. The far field pres-

sure is determined from a convolution of the equivalent source terms and the vector Green's function for the linearized Euler equations. In the first version of the model the effects of mean flow refraction were neglected, since BBSAN radiation occurs primarily towards smaller inlet angles or towards the sideline. The evaluation of the spectral density depends on a model for the shock cell structure and the second order two-point velocity correlation of the turbulence. Note that it is the fourth order cross correlation of the velocity that is needed for the source modeling of fine-scale turbulence noise in the traditional acoustic analogy framework. In addition, the shock cell structure is represented by its axial wavenumber spectrum. In this way the model has much in common with Tam (1987).

Calculations were presented by Morris and Miller (2010) for circular and rectangular jets using the same empirical parameters for all cases. Figure 17 shows a prediction for a circular convergent nozzle with $M_j = 1.5$ and $T_t/T_a = 1.0$. The observer is at an inlet angle of $60^o$ at $R/D = 100$. The total BBSAN prediction is shown with the black line and compares well with measurements - especially in the peak BBSAN frequency range. Curves are also shown for the contribution to the total spectrum from the turbulence interaction with different peaks in the shock cell wavenumber spectrum. These interactions give multiple smaller peaks at higher frequencies, which are also seen in the measurements. The same parameters are used to predict the BBSAN for a rectangular jet with aspect ratio 1.75. This is shown in Figure 18. The agreement is very good. Note how the mixing noise overwhelms the BBSAN at small angles to the jet downstream axis in this case. This model has been extended to dual stream jets. In this case, the presence of the outer high speed fan stream does give rise to propagation effects. Miller and Morris (2011) consider dual stream jets operating off-design and include adjoint solutions to the vector Green's function to account for refraction effects. It should be noted that Tam et al. (2009) has extended his model for the BBSAN peak frequencies for a dual stream jet.

## 5 Jet Screech Tones

Experimental measurements have shown that screech tones are very sensitive to upstream conditions, as discussed in Section 2.3. The amplitude of the tone could be altered by as much as 10 dB, just by changing the nozzle lip thickness. It is not surprising then, that the prediction of screech amplitude is very difficult and no method for its prediction existed until recently. Shen and Tam (1998), Shen and Tam (2000), Shen and Tam (2002) have provided the first direct numerical simulations of axisymmetric and three-dimensional screech tones. The simulations use a finite difference

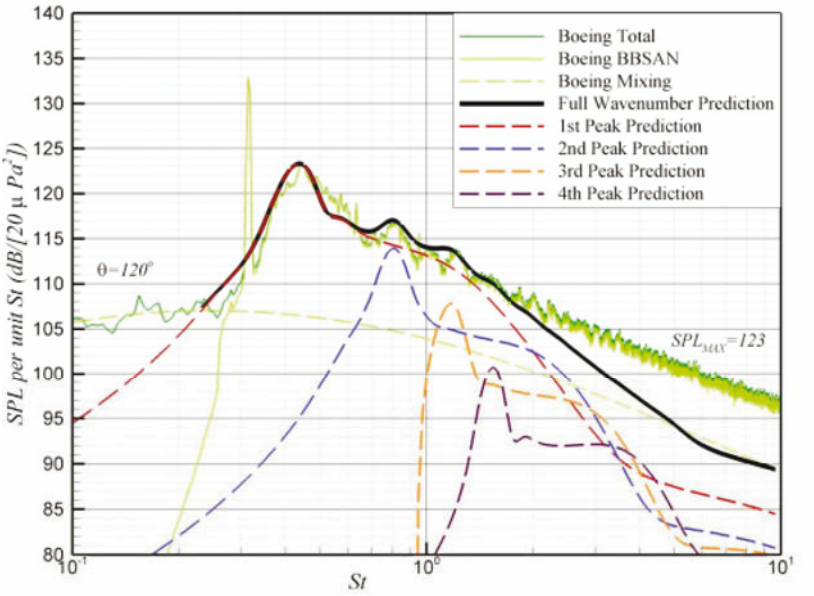


**Figure 17.** Total BBSAN prediction and the accompanying contributions from selective integrations over contributing wavenumbers of the shock cell structure wavenumber spectrum. $M_d = 1.0$, $M_j = 1.5$, $T_t/T_a = 1.0$, $R/D = 100$, inlet angle = $60^o$. (From Morris and Miller (2010)).

methodology with optimized algorithms used for both space and time discretizations. The effects of the fine-scale turbulence are included through the use of a $k - \varepsilon$ model. Comparisons of screech frequency, mode staging, and amplitude are made with experiments. Good agreement is obtained for all these phenomena. However, the calculations are computationally very expensive, even though three-dimensional effects are included in a simplified fashion. Thus, much work remains to be done in this area. On the other hand, several formulas for the prediction of the screech frequency have been developed over the years, based on different theoretical models.

### 5.1 Prediction of Screech Tone Frequency

The screech tone generation mechanism is very similar to the mechanism of broadband shock noise generation. For the generation of tones, a single excited instability wave is responsible, while for the generation of broadband

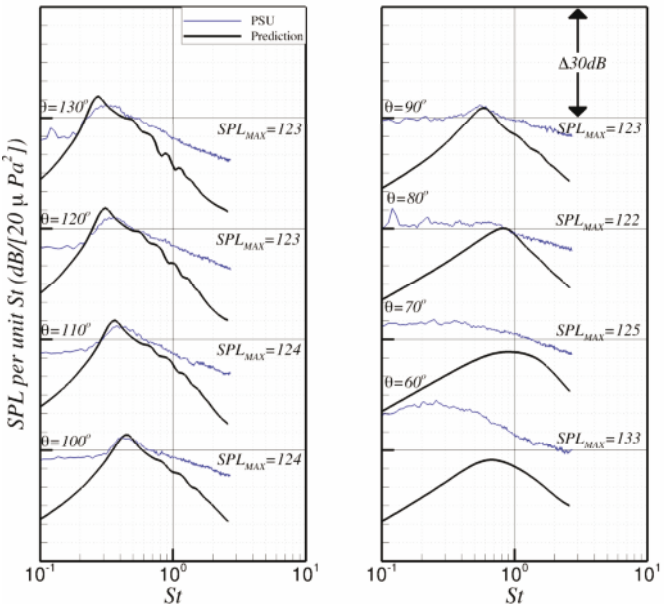


**Figure 18.** Comparison of BBSAN predictions with experiments for an AR = 1.75 rectangular jet. $M_d = 1.50$, $M_j = 1.70$, $T_t/T_a = 2.20$, and $R/D_e = 100$, in the minor axis direction. (From Morris and Miller (2010)).

shock noise, a spectrum of instability waves is involved. Tam et al. (1986) examined the relationship between the two shock noise components and provided experimental and theoretical evidence that the two are indeed related. From the shock noise data of Norum and Seiner (1982a), they observed that the fundamental screech frequency was always at a lower value than the peak frequency of broadband shock noise and that the half-width of the broadband shock noise spectrum decreased rapidly as the observer position moved towards the jet inlet. They also showed that only a narrow band of frequencies are radiated in the upstream direction when acoustic waves are generated by the interaction mechanism. Based on their analysis and experimental observations, they suggested that the screech frequency could be regarded as the limiting case of broadband shock noise as the observer angle approaches the nozzle inlet, $\phi = 0^o$. The decrease in the spectrum half-width and peak frequency, and the approach of the broadband shock noise spectrum peak frequency to the screech frequency, is evident in

Figure 10.

Tam et al. (1986) also noted that the feedback mechanism was not similar to that for the generation of cavity tones or impingement tones since there was no constraining geometric feature that would set the feedback path length for a shock containing jet and thus set the frequency of the tone. They proposed that the screech frequency is determined by the weakest link of the feedback loop, which is the connection between the outer and inner parts of the loop at the nozzle exit. This connection is responsible for triggering the instability waves. Therefore, sound waves of sufficient strength must reach the nozzle exit in order to excite an instability wave of large enough amplitude, so as to maintain the feedback loop. However, the interaction mechanism generates only a narrow band of frequencies with high intensity that travel in the upstream direction. Hence if the feedback loop is to be self-sustaining, then the fundamental screech frequency must be confined to this upstream propagating narrow band of frequencies. The weakest link hypothesis also explains why a good approximation for the screech frequency is obtained by setting $\phi = 0$ in the equation for the broadband shock noise peak frequency; Eqn. (62).

In order to use the expression for the peak frequency of broadband shock noise and screech, the value of the convection velocity $u_c$ and the shock cell wave number $k_n$ are required. As in the interaction theory, the source of broadband shock noise would occur near the axial location at which the instability wave attains its maximum amplitude, consistent with the observations of Seiner and Yu (1984). Thus, the phase velocity and shock cell wavenumber must be evaluated at the location where the amplitude of the instability wave is maximum. This axial location can be determined if a locally parallel assumption for the mean flow is used in a stability analysis. Tam et al. (1986) describe an iterative procedure for the calculation of the fundamental screech frequency. This methodology requires no empirical inputs and the screech frequencies are calculated from first principles. However, this methodology involves extensive computations. In order to develop a simple formula for the estimation of screech frequencies, they adopted some simplifying assumptions. First, on the basis of experimental observations, the convection velocity was assumed to be 70% of the fully expanded jet velocity $U_j$. Secondly, the value of the lowest order shock cell wave number, $k_1$ was obtained using a vortex sheet model for the shear layer. Additionally, to account for the finite thickness of the jet shear layer, the shock cell spacing near the end of the potential core was estimated to be 20% less than that given by the vortex sheet model. Using values based on these assumptions and the isentropic relationships, Tam et al. (1986) developed the following semi-empirical expression for the fundamental screech

frequency,

$$\frac{f_s D_j}{U_j} = 0.67\left(M_j^2 - 1\right)^{-1/2}\left[1 + 0.7M_j\left(1 + \frac{\gamma - 1}{2}M_j^2\right)^{-1/2}\left(\frac{T_t}{T_o}\right)^{1/2}\right]^{-1} \quad (64)$$

In this expression, $D_j$ is the fully-expanded jet diameter, which, as shown by Tam and Tanna (1982), is related to the nozzle geometric diameter $D$ by,

$$\frac{D_j}{D} = \left[\left(1 + \frac{\gamma - 1}{2}M_j^2\right)\Big/\left(1 + \frac{\gamma - 1}{2}M_d^2\right)\right]^{\left[\frac{\gamma+1}{4(\gamma-1)}\right]}\left(\frac{M_d}{M_j}\right)^{1/2} \quad (65)$$

This formula was shown to provide good agreement with measured screech frequencies. Figure 19 from Tam et al. (1986) illustrates that Eqn. 64 provides a good match with data obtained by Rosfjord and Toms (1975) using a convergent nozzle for both cold and heated jets. The agreement is better at higher nozzle pressure ratios. In the development of Eqn. (64), a helical instability wave mode was assumed to be dominant. It is known that for for a convergent nozzle and $M_j < 1.3$ the toroidal instability mode is dominant. Thus, it is perhaps not surprising that the agreement is not as good at the lower Mach numbers. Tam (1988) extended these concepts to jets of non-axisymmetric cross-sections and developed a formula for the calculation of screech tones from rectangular jets. Again, he demonstrated good agreement with measured frequencies. Morris et al. (1989) also used their shock cell model for arbitrary geometry jets to predict the screech frequencies for rectangular jets and obtained good agreement with measurements. Tam (1995a) developed an expression that accounted for the effect of forward flight on the peak frequency of radiation.

Recently, Panda (1998), Panda (1999) carried out detailed experiments on the screech generation mechanism of choked axisymmetric jets. He found a partial interference of the downstream-propagating instability waves and the upstream-propagating acoustic waves along the jet boundary, resulting in a standing wave pattern. A corresponding length scale, identical to that of the standing wavelength, was also observed in the jet shear layer. The new length scale was found to be approximately 80% of the shock cell spacing. This new length scale correlated the measured screech frequencies well. Interestingly, Tam et al. (1986) selected the same modifications to the shock cell length based on entirely different reasoning (the effects of growth of the jet shear layer on the shock spacing) in the development of the semi-empirical formula, Eqn. (64). However, it should be noted that the complete analysis by Tam et al. (1986), in which the shock cell spacing is determined by a multiple scales analysis, does not involve this assumption.

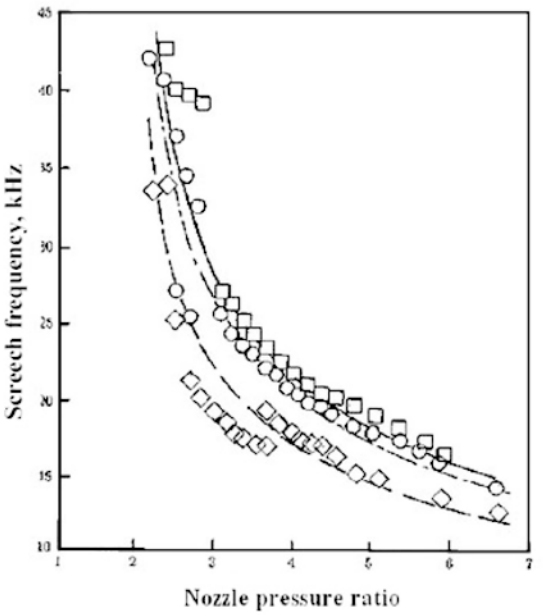


**Figure 19.** Predictions of screech frequency for hot and cold jets from a round convergent nozzle at different nozzle pressure ratios. Measurements shown by symbols and predictions shown by lines. ◇, ———, $T_t$ = 291 K; ○, — – —, $T_t$ = 596 K; □, — — —, $T_t$ = 803 K. (From Tam et al. (1986), with permission)

### 5.2 Intensity and Directivity Prediction

The prediction of the screech tone intensity remains a challenging problem. The phenomenon of mode switching or staging adds an additional layer of complication, which makes the development of a prediction method even more intimidating. Numerical simulations, with detailed specification of the entire upstream geometry, could provide a means for computing the intensity of the screech tone for a particular geometry. Such simulations using computational aeroacoustics methods have been attempted for simple geometries. Shen and Tam (1998) carried out such a simulation for a low supersonic Mach number jet for which the toroidal instability mode is dominant. This axisymmetric numerical simulation provided good qualitative details of the screech phenomenon. Features such as mode switching and the principal radiation lobes of the fundamental and second harmonics were

reproduced in this study. The predicted screech intensities were close to the values measured on a large reflecting surface placed upstream of the nozzle exit. Shen and Tam (2000) have also examined the effects of jet temperature and nozzle-lip thickness on the screech tone intensity. The results of their simulations were in agreement with the experimental observations.

It has been observed that the intensity of the screech tones decreases with increasing jet temperature. The reasons for this observed change in intensity appear to be understood. In the previous section it was shown that, in the weakest link theory, the frequency of screech is determined by the characteristics of the feedback acoustic waves. Tam et al. (1994) examined the role of the other two factors responsible for screech generation; that is, the instability waves and the shock cell structure. They suggested that the characteristics of the instability waves dictated the intensity and occurrence of screech tones. By carrying out a hydrodynamic stability analysis, they examined the evolution of the instability waves for a variety of Mach numbers and jet temperatures. This study revealed that the axisymmetric or toroidal modes have the highest total amplification at lower supersonic Mach numbers. Above a Mach number of approximately 1.3, the helical or flapping mode becomes dominant. Since the feedback mechanism is driven by the instability waves, which function as the energy source, the observed switching or staging of screech mode from toroidal to flapping at about this Mach number can be attributed to the change in the dominant instability wave mode. Secondly, the Strouhal number of the most amplified instability wave decreases with increases in jet temperature and jet Mach number. In terms of frequency, even though the jet velocity increases as $\sqrt{T_t}$, the decrease in Strouhal number is greater than $1/\sqrt{T_t}$. Hence, the frequency of the most amplified instability wave decreases with increasing temperature. The measured screech frequencies, on the other hand, increase as the jet temperature increases. The implication is that the feedback mechanism is not driven by the most amplified instability waves, thereby leading to a reduction in tone intensity. At elevated temperatures, these tones may not be easily observed above the background noise. Tam et al. (1994) summarized that the observed reduction in tone intensity or the non-occurrence of the tone is the direct result of the mismatch between the screech tone frequencies and the band of the most amplified instability waves. As mentioned earlier, screech tones are not considered to be important in most real engine applications. The non-symmetric geometric features of installed engines and the reduction of screech intensity with increase in temperature, provide an explanation of this observation.

## 6 Recent Developments

Research in jet noise prediction is an ongoing activity. Significant progress has been made in recent years in the direct simulation of the jet flow and the noise it radiates. An example of such a computation is the work by Shur et al. (2005). These authors used a hybrid RANS/LES method and then propagated the near field solution to the far field using a permeable surface Ffowcs Williams - Hawkings equation solution (see Ffowcs Williams and Hawkings (1969), Brentner and Farassat (1998)). In this section, three additional topics will be covered very briefly: new acoustic analogy prediction methods; new views on the role of large-scale structures; and nonlinear propagation.

### 6.1 New Acoustic Analogies

As noted in Section 3.1 little success has been achieved with the prediction of the noise spectra in the peak radiation direction based on acoustic analogies. Two recent approaches appear to have overcome some these earlier problems. Goldstein and Leib (2008) and Karabasov et al. (2010) have extended earlier approaches and achieved some success. However, it should be noted that both studies were limited to convectively subsonic, unheated jets. The work by Goldstein and Leib (2008) builds on the generalized acoustic analogy developed by Goldstein (2003). Goldstein and Leib (2008) rearranged the equations of continuity, momentum, and energy for an ideal gas into a system of five formally linear equations. The equivalent sources on the right hand sides of the system of equations have zero time average. The problem is split into two parts: first, find the vector Green's function for the system of equations, and then model the statistical properties of the noise sources. Goldstein and Leib (2008) stress the importance of accounting for the slow divergence of the jet flow in the Green's function. They base their statistical model for the sources on their expected symmetry properties as well as experimental measurements. Predictions are presented for unheated jets with Mach numbers 0.5, 0.9 and 1.4 and the comparisons with measurements are very encouraging. Karabasov et al. (2010) take a slightly different approach. They also used the generalized acoustic analogy of Goldstein (2003), but they calculate the vector Green's function numerically using an adjoint approach (see Tam (1998a)). In addition, they use a companion Large Eddy Simulation (LES) to provide source statistics, including the general shape of the two-point space-time cross correlations as well as the relative amplitude of the different components. However, they choose to use very simple Gaussian functions to model the correlations. They present results for an unheated jet with Mach

number 0.75 and compare with noise measurements. Again, the agreement is quite good. The authors argue that the important effects to be included are; the divergence of the mean flow, the use of non-isotropic source models, the inclusion of the radial variation of the Green's function, and the use of the same observer location as in the experiments. A careful examination of these two works indicates that different assumptions are made in order to achieve similar agreement with measurements. The two studies do agree on the importance of including the mean flow divergence in the propagation calculation and the need for an anisotropic source model. The other differences have yet to be reconciled.

### 6.2 The Role of Large Scale Structures in Jet Noise

In Section 3.2 the role of large scale turbulent structures and their modeling as instability waves was discussed. In addition, in Section 3.3 the ability of two similarity spectra to successfully collapse the measured noise spectra at all angles was described. This is only a part of a growing body of experimental evidence that there are two noise generation mechanisms - though this remains a very contentious issue. At issue is the role played by the large scale turbulent structures in subsonic or convectively subsonic jets. Excellent discussions of recent experimental evidence are given by Tam et al. (2008) and Viswanathan (2009). In particular it is noted that the noise characteristics at small angles to the jet downstream axis, including the peak noise directions, and that at larger angles to the downstream axis are very different. In addition, these differences are observed, whether the flow is subsonic or supersonic. For example, Figure 20 from Tam et al. (2008) shows the variation of the OASPL with inlet angle. The levels are determined by fitting the FSS and LSS spectral shapes to the measured data. So at some angles, for example 120-140 degrees, both spectra are used to match the data. The FSS levels vary very slowly with angle, whereas the LSS levels increase rapidly with increase in inlet angle. Note that the effects are similar whether the flow is unheated or heated, except that in the heated case (higher exit velocity) the LSS dominates at more angles. A similar trend is observed in terms of the peak Strouhal number. This is shown in Figure 21 from Tam et al. (2008). The peak Strouhal number for the FSS noise increases slowly with increase in inlet angle, whereas the LSS peak Strouhal number decreases rapidly. Additional evidence of the differences associated with noise radiation in the two regions comes in the form of the correlations between fluctuations of velocity and density in the jet and the radiated pressure. For example, Figure 22 from Tam et al. (2008) shows the directivity of the normalized correlation between density fluctuations in

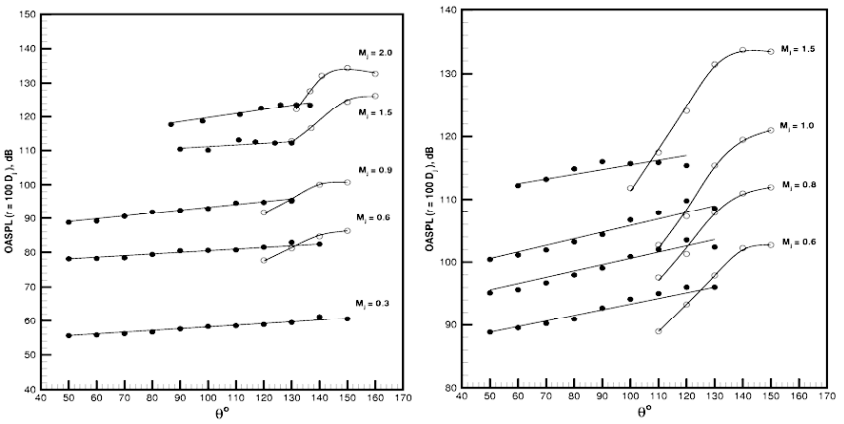


**Figure 20.** Variation of OASPL with inlet angle. (a) $T_t/T_a = 1.0$, (b) $T_t/T_a$ =2.2. (From Tam et al. (2008), with permission).

the jet and the far field pressure as a function of jet operating conditions and inlet angle. Again there is a clear demarcation of two regions: one of very low correlation at smaller inlet angles and one of very high correlation at large inlet angles. Tam et al. (2008) argue that the flow measurement, using Rayleigh scattering, is for a very small probe volume. For small or fine scale turbulent blobs, the probe will only sense the contribution from a single blob and so the correlation would be expected to be very low as many blobs would contribute to the total radiated noise. This explains the very low correlations at smaller inlet angles where the fine-scale mechanism dominates. However, though a single point measurement, the flow probe signal would be representative of larger turbulent structures that are coherent over a larger volume of the turbulence. The strong correlations at the larger inlet angles are consistent with the noise at these angles being radiated by these large scale structures. Also, though the correlation levels do decrease with at lower Mach numbers, there is still a significant correlation in the subsonic case.

As noted in Section 3.2, the large scale structures can be represented by instability waves or wave packets. There have been several recent studies that have used this concept. For example, Reba et al. (2010) developed a wavepacket model and determined the parameters needed to define the wavepacket (amplitude, phase velocity, and growth and decay rates) from microphone measurements on a conical cage array of near field micro-

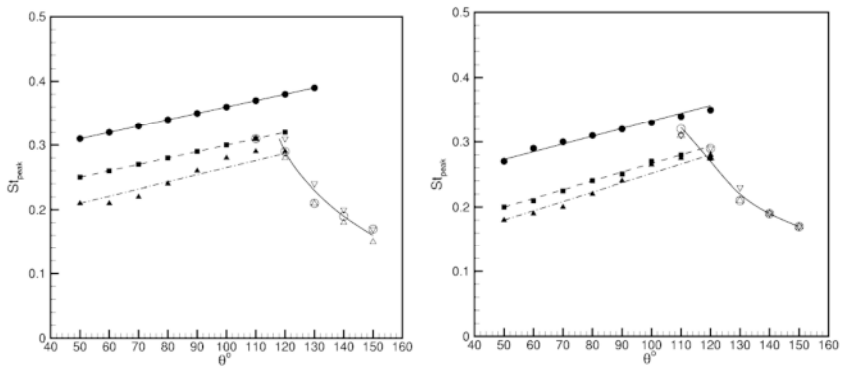


**Figure 21.** ; Variation of peak Strouhal number with inlet angle. (a) $M_j$ =0.6; •, ▽, $T_t/T_a$ =1.0, ■, ○, $T_t/T_a$ =1.8, ▲, △, $T_t/T_a$ =2.7. (b) $M_j$ =1.0; •, ▽, $T_t/T_a$ =1.0, ■, ○, $T_t/T_a$ =2.2, ▲, △, $T_t/T_a$ =3.2. (From Tam et al. (2008), with permission).

phones. They then projected the noise associated with the wavepacket to the far field and compared with measurements. The measurements show good agreement at large inlet angles in the peak noise direction. Morris (2009) examined large-scale mixing noise generation. He used the LSS spectrum to extract only the large-scale mixing noise from measured far field spectra for both subsonic and supersonic jets. From the directivities for different Strouhal numbers he was able to project back to a cylindrical surface around the jet and determine the axial wavenumber spectrum of the pressure fluctuations on the surface. He showed that the shape of the spectrum for all the jet operating conditions was consistent with that produced by wavepackets. However, only the lowest wavenumbers (the ones that give a sonic phase velocity to a far field observer) were able to radiate in the subsonic cases. This provides further evidence that the noise radiation in the peak noise direction is controlled by the large-scale turbulent structures.

### 6.3 Nonlinear Propagation

The noise generated by high performance military aircraft engines is so intense that the propagation of the sound to the far field observer is no longer linear. The earliest evidence of nonlinearity in jet noise was provided by the Olympus engines for the Concorde. Ffowcs Williams et al. (1975) observed a phenomenon they called "crackle." These were intermittent "intense spasmodic short-duration compressive elements of the wave form." Though these

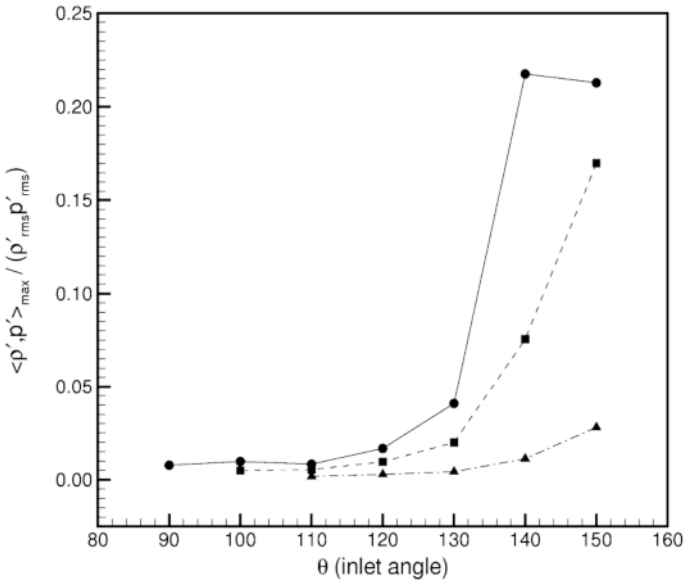


**Figure 22.** Directivity of normalized $\langle \rho', p' \rangle_{\max}$ correlation. Laser probe locations are at $r/D = 0$, $x/D = 12$ (Mach 1.8), 10 (Mach 1.4 and Mach 0.95), •, $M$ =1.8; ■, $M$ =1.4; ▲, $M$ =0.95. (From Tam et al. (2008), with permission).

are not easily characterized by a change in the spectral shape, the skewness increases and the sound is very annoying. Ffowcs Williams et al. (1975) argued that the source of this change in the signal was associated with wave steepening at the source rather than from nonlinear propagation. However, though the character of the time history is set at the source, nonlinear propagation occurs and does maintain the skewed and annoying nature of the sound into far field.

Methods to predict the nonlinear propagation of jet noise have used the Burgers equation (see Morfey and Howell (1981), Gee (2005), Saxena et al. (2009) and Lee et al. (2010)) and the one-dimensional Navier-Stokes equations (see Wochner et al. (2005)). Morfey and Howell (1981) introduced a nonlinearity parameter that indicates those regions of the spectrum where nonlinear effects are either increasing or decreasing the intensity. However, their solution was based on a knowledge of the spectrum of the noise in the near field rather than the time history, so the propagation results were not

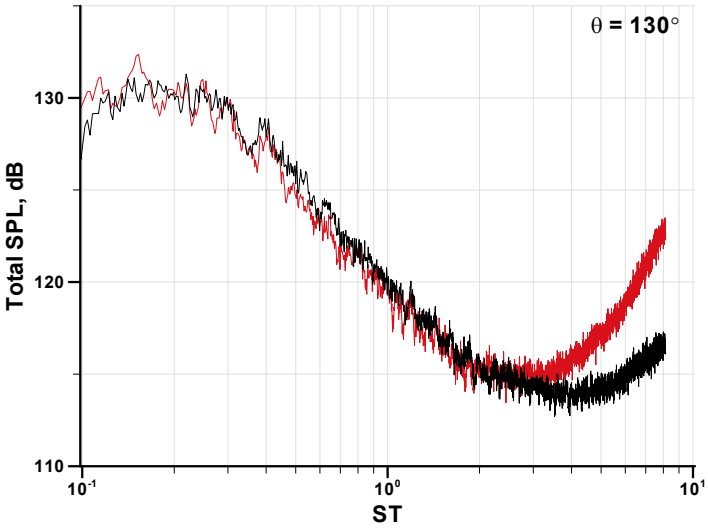


**Figure 23.** Comparison of spectra from sideline microphones at different locations normalized to a fixed distance; $M$ =1.72, and $T_t/T_a$ =2.7. Gray: 25-ft polar, and black: 15-ft constant sideline. (From Viswanathan (2009)).

satisfactory. The more recent studies make use of the measured time history and then propagate this wave form, using solutions to the Burgers equation, in the same way that sonic boom propagation is calculated. The algorithm used by Gee (2005) is based on the "Anderson algorithm" (see Anderson (1974)). The nonlinear steepening is calculated in the time domain using the "Earnshaw" solution ( Earnshaw (1860)) and the atmospheric absorption effects are calculated in the frequency domain. The calculations by Saxena et al. (2009) and Lee et al. (2010) determine both the nonlinear and atmospheric absorption effects in the frequency domain. This has computational and accuracy advantages as shown by Lee et al. (2010). The effects of nonlinear propagation are best seen when the experimental data are represented in lossless or standard day form and propagated linearly to a common observer location. A good example is shown in Figure 23 from Viswanathan et al. (2009). Here, measurements in a jet with $M$ =1.72 and $T_t/T_a$ =2.7 are shown for a microphone distances of 15 and 25 feet. If linear propagation were present at all frequencies then the curves would fall on top of each other (assuming that the measurements are in the far field). However, it

is clear that at high frequencies the curves don't collapse. This is evidence on the presence of nonlinear propagation. Care should be taken not to assume that the spectra shown are "as-measured" spectra. The lift at high frequencies is purely because the data have been made lossless assuming linear propagation. The "as-measured" spectra would still show a roll-off at high frequencies, but it would be less rapid if nonlinear propagation were present.

## 7 Acknowledgements

These notes are based on a earlier version written by the authors that was intended to be part of a book on high speed jets. We have added some new material and some topics have been removed to prevent excessive length. For example; jet noise reduction, dual-stream jets, and non-circular jets are not discussed. The authors plan to add these topics to a future publication that emphasizes progress in jet noise modeling, prediction and experiments in the last ten years. The original version was reviewed by Prof. Geoffrey M. Lilley who, as always, offered some valuable and insightful criticism.

## Bibliography

A. Agarwal, P. J. Morris, and R. Mani. The calculation of sound propagation in nonuniform flows: Suppression of instability waves. *AIAA Journal*, 42(1):80–88, 2004.

K. K. Ahuja and K. W. Bushell. An experimental study of subsonic jet noise and comparison with theory. *Journal of Sound and Vibration*, 30 (3):317–341, 1973.

R. K. Amiet. Correction of open jet wind tunnel measurements for shear layer refraction. AIAA Paper 75-532, 1975.

R. K. Amiet. Refraction of sound by a shear layer. *Journal of Sound and Vibration*, 58(4):467–482, 1978.

M. O. Anderson. Propagation of a spherical N wave in an absorbing medium and its diffraction for a circular aperture. ARL-TR 74-25, Applied Research Laboratories, University of Texas at Austin, Austin, TX, 1974.

J. Atvars, L. K. Schubert, and H. S. Ribner. Refraction of sound from a point source placed in an air jet. *Journal of the Acoustical Society of America*, 37:168–170, 1965.

T. F. Balsa. Fluid shielding of low frequency convected sources by arbitrary jets. *Journal of Fluid Mechanics*, 70:17–36, 1975.

T. F. Balsa. The far field of high frequency convected singularities in sheared flows, with application to jet-noise prediction. *Journal of Fluid Mechanics*, 74:193–208, 1976.

T. F. Balsa and P. R. Gliebe. Aerodynamics and noise of coaxial jets. *AIAA Journal*, 15(11):1550–1558, 1977.

T. F. Balsa, P. R. Gliebe, R. A. Kantola, R. Mani, E. J. Stringas, and J. C. F. Wang. High velocity jet noise source location and reduction. Task 2 - theoretical developments and basic experiments. RD 76-79 Vol. 2, FAA, (Available from DTIC as AD A094291), 1978.

T. R. S. Bhat, P. J. Morris, and R. S. Baty. A linear shock cell model of non-circular jets using conformal mapping with a pseudo-spectral hybrid scheme. AIAA Paper 90-3960, 1990.

R. H. Bolt. The aircraft noise problem. *Journal of the Acoustical Society of America*, 25(3):363–366, 1953.

K. S. Brentner and F. Farassat. Analytical comparison of acoustic analogy and Kirchhoff formulation for moving surfaces. *AIAA Journal*, 36(8): 1379–1386, 1998.

K. W. Bushell. Measurement and prediction of jet noise in flight. AIAA Paper 75-461, 1975.

Y. Y. Chan. Spatial waves in turbulent jets. *Physics of Fluids*, 17(1):46–53, 1974a.

Y. Y. Chan. Spatial waves in turbulent jets. Part II. *Physics of Fluids*, 17 (9):1667–1670, 1974b.

Y. Y. Chan. Nonlinear spatial wave development in an axisymmetrical turbulent jet. Aeronautical report LR-585, National Research Council Canada, 1975.

Y. Y. Chan and R. Westley. Directional acoustic radiation generated by spatial jet instability. *C.A.S.I. Transactions*, 6(1):36–41, 1973.

W. T. Chu. Turbulence measurements relevant to jet noise. UTIAS Report 119, Institute for Aerospace Studies, University of Toronto, ON, Canada, 1966.

B. J. Cocking and W. D. Bryce. Subsonic jet noise in flight based on some recent wind tunnel results. AIAA Paper 75-462, 1975.

D. G. Crighton. Basic principles of aerodynamic noise generation. *Progress in Aerospace Sciences*, 16(1):31–95, 1975.

D. G. Crighton, J. E. Ffowcs Williams, and I. C. Cheeseman. The outlook for simulation of forward flight effects on aircraft noise. AIAA Paper 76-530, 1976.

M. D. Dahl. *The Aeroacoustics of Supersonic Coaxial Jets*. PhD thesis, Department of Aerospace Engineering, Penn State University, 1994.

M. G. Davies and D. E. S. Oldfield. Tones from a choked axisymmetric jet. II. The self-excited loop and mode of oscillation. *Acustica*, 12:267–277, 1962.

P. O. A. L. Davies, M. J. Fisher, and M. J. Barratt. The characteristics of the turbulence in the mixing region of a round jet. *Journal of Fluid Mechanics*, 15:337–367, 1963.

A. P. Dowling, J. E. Ffowcs Williams, and M. E. Goldstein. Sound production in a moving stream. *Philosophical Transactions of the Royal Society of London*, A288:321–349, 1978.

P. A. Durbin. High frequency green function for aerodynamic noise in moving media. part i: General theory. Part II: Noise from a spreading jet. *Journal of Sound and Vibration*, 91(4):519–538, 1983.

S. Earnshaw. On the mathematical theory of sound. *Philosophical Transactions of the Royal Society of London, Series A*, 50:133–148, 1860.

J. E. Ffowcs Williams. The noise from turbulence convected at high-speed. *Philosophical Transactions of the Royal Society of London, Series A*, 255: 469–503, 1963.

J. E. Ffowcs Williams. Aeroacoustics. *Annual Review of Fluid Mechanics*, 9:447–468, 1977.

J. E. Ffowcs Williams and D. L. Hawkings. Sound generation by turbulence and surfaces in arbitrary motion. *Philosophical Transactions of the Royal Society of London, Series A*, 264:321–342, 1969.

J. E. Ffowcs Williams, J. Simson, and V. J. Virchis. Crackle: an annoying component of jet noise. *Journal of Fluid Mechanics*, 71(2):251–271, 1975.

M. J. Fisher. Comment on "jet mixing noise from fine-scale turbulence". *AIAA Journal*, 2(379), 38.

K. L. Gee. *Prediction of nonlinear jet noise propagation*. PhD thesis, Graduate Program in Acoustics, Penn State University, 2005.

P. R. Gliebe and T. F Balsa. Aeroacoustics of axisymmetric single- and dual-flow exhaust nozzles. *Journal of Aircraft*, 15(11):743–749, 1978.

P. R. Gliebe, J. F. Brausch, R. K. Majjigi, and R. Lee. *Aeroacoustics of Flight Vehicles: Theory and Practice, Volume 2: Noise Control*, chapter Jet Noise Suppression, pages 207–269. The Acoustical Society of America, Woodbury, NY, 1995.

M. E. Goldstein. *Aeroacoustics*. McGraw-Hill, New York, NY, 1976.

M. E. Goldstein. High frequency sound emission from moving point multipole sources embedded in arbitrary transversely sheared mean flows. *Journal of Sound and Vibration*, 80(4):499–522, 1982.

M. E. Goldstein. Aeroacoustics of turbulent shear flows. *Annual Review of Fluid Mechanics*, 16:263–285, 1984.

M. E. Goldstein. *Aeroacoustics of Flight Vehicles: Theory and Practice, Volume 1: Noise Sources*, chapter Noise From Turbulent Shear Flows, pages 291–310. The Acoustical Society of America, Woodbury, NY, 1995.

M. E. Goldstein. A generalized acoustic analogy. *Journal of Fluid Mechanics*, 488:315–333, 2003.

M. E. Goldstein and S. J. Leib. The aeroacoustics of slowly diverging supersonic jets. *Journal of Fluid Mechanics*, 600:291–337, 2008.

A. G. Hammitt. The oscillation and noise of an overpressure sonic jet. *Journal of Aerospace Sciences*, 28:673–680, 1961.

M. Harper-Bourne and M. J. Fisher. The noise from shock waves in supersonic jets. In *Noise Mechanisms*, AGARD-CP-131, pages 1–13, 1974.

J. A. Hay and E. G. Rose. In-flight shock cell noise. *Journal of Sound and Vibration*, 11(4):411–420, 1970.

H. H. Hubbard and J. W. Lassiter. Experimental studies of jet noise. *Journal of the Acoustical Society of America*, 25(3):381–384, 1953.

S.A. Karabasov, M.Z. Afsar, A.P. Hynes, T.P. andDowling, W.A. McMullan, C.D. Pokora, G.J. Page, and McGuirk J.J. Jet noise - acoustic analogy informed by large eddy simulation. *AIAA Journal*, 48(7):1312–1325, 2010.

A. Khavaran. Role of anisotropy in turbulent mixing noise. *AIAA Journal*, 37(7):832–841, 1999.

A. Khavaran, E. A. Krejsa, and C. M. Kim. Computation of supersonic jet mixing noise for an axisymmetric convergent-divergent nozzle. *Journal of Aircraft*, 31(3):603–609, 1994.

D. R. S. Ko, T. Kubota, and L. Lees. Finite disturbance effect on the stability of a laminar incompressible wake behind a flat plate. *Journal of Fluid Mechanics*, 40:315–341, 1970.

C. Kuo, D. K. McLaughlin, and P. J. Morris. Effects of supersonic jet conditions on broadband shock-associated noise. AIAA Paper 2011-1032, 2011.

S. Lee, P. J. Morris, and K. S. Brentner. Improved algorithm for nonlinear sound propagation with aircraft and helicopter noise applications. *AIAA Journal*, 48(11):2586–2595, 2010.

M. J. Lighthill. On sound generated aerodynamically: I. general theory. *Proceedings of the Royal Society of London, Series A:*, 211:564–581, 1952.

M. J. Lighthill. On sound generated aerodynamically: Ii. turbulence as a source of sound. *Proceedings of the Royal Society of London, Series A:*, 222:1–32, 1954.

M. J. Lighthill. Jet noise. *AIAA Journal*, 1(7):1507–1517, 1963.

G. M. Lilley. The generation and radiation of supersonic jet noise. IV. Theory of turbulence generated jet noise, noise radiation from upstream sources and combustion noise. TR-72-53, United States Air Force Aeropropulsion Laboratory, 1972.

G. M. Lilley. On the noise from air jets. In *Noise Mechanisms*, number 131 in AGARD-CP, pages 13.1–13.12, 1973.

G. M. Lilley. *Aeroacoustics of Flight Vehicles: Theory and Practice, Volume 1: Noise Sources*, chapter Jet Noise Classical Theory and Experiments, pages 211–289. The Acoustical Society of America, Woodbury, NY, 1995.

G. M. Lilley. The radiated noise from isotropic turbulence with applications to the theory of jet noise. *Journal of Sound and Vibration*, 190(3):463–476, 1996.

J. T. C. Liu. Developing large-scale wavelike eddies and the near jet noise field. *Journal of Fluid Mechanics*, 62(3):437–464, 1974.

P. A. Lush. Measurements of subsonic jet noise and comparison with theory. *Journal of Fluid Mechanics*, 46(3):477–500, 1971.

R. Mani. The influence of jet flow on jet noise. Part 1. The noise of unheated jets. Part 2. The noise of heated jets,. *Journal of Fluid Mechanics*, 73 (4):753–793, 1976.

D. K. McLaughlin, G. L. Morrison, and T. R. Troutt. Experiments on the instability waves in a supersonic jet and their acoustic radiation. *Journal of Fluid Mechanics*, 69(1):73–95, 1975.

D. K. McLaughlin, G. L. Morrison, and T. R. Troutt. Reynolds number dependence in supersonic jet noise. *AIAA Journal*, 15:526–532, 1977.

A. Michalke and U. Michel. Prediction of jet noise in flight from static tests. *Journal of Sound and Vibration*, 67(3):341–367, 1979.

S. A. E. Miller and P. J. Morris. The prediction of broadband shock-associated noise including propagation effects. AIAA Paper 2011-2923, 2011.

C. L. Morfey and G. P. Howell. Nonlinear propagation of aircraft noise in the atmosphere. *AIAA Journal*, 19(8):986–992, 1981.

C. L. Morfey and V. M. Szewczyk. Jet noise modelling by geometric acoustics. Part I: Theory and prediction outside the cone of silence. ISVR Technical Report No. 91, University of Southampton, 1977a.

C. L. Morfey and V. M. Szewczyk. Jet noise modelling by geometric acoustics. Part II: Theory and prediction inside the cone of silence. ISVR Technical Report No. 91, University of Southampton, 1977b.

C. L. Morfey and V. M. Szewczyk. New scaling laws for hot and cold jet mixing noise based on a geometric acoustics model. *Journal of Sound and Vibration*, 73:255–292, 1978.

P. J. Morris. A model for the structure of jet turbulence as a source of noise. AIAA Paper 1974-0001, 1974.

P. J. Morris. Turbulence measurements in subsonic and supersonic jets in a parallel stream. *AIAA Journal*, 14(10):1468–1475, 1976.

P. J Morris. Flow characteristics of the large scale wave-like structure of a supersonic round jet. *Journal of Sound and Vibration*, 53(2):223–244, 1977.

P. J. Morris. A note on noise generation by large scale turbulent structures in subsonic and supersonic jets. *International Journal of Aeroacoustics*, 8(4):301–315, 2009.

P. J. Morris and S. Boluriaan. The prediction of jet noise from CFD data. AIAA Paper 2004-2977, 2004.

P. J. Morris and F. Farassat. The acoustic analogy and alternative theories for jet noise prediction. *AIAA Journal*, 40(4):671–680, 2002.

P. J. Morris and S. A. E. Miller. Prediction of broadband shock-associated noise using Reynolds-averaged Navier-Stokes computational fluid dynamics. *AIAA Journal*, 48(12):2931–2961, 2010.

P. J. Morris and C. K. W. Tam. *Mechanics of Sound Generation in Flows*, chapter On the Radiation of Sound by the Instability Waves of a Compressible Axisymmetric Jet, pages 55–61. Springer-Verlag, New York, NY, 1979.

P. J. Morris and H. K. Tanna. The noise from normal-velocity-profile coannular jets. *Journal of Sound and Vibration*, 98(2):213–234, 1985.

P. J. Morris, T. R. S. Bhat, and G Chen. A linear shock cell model for jets of arbitrary exit geometry. *Journal of Sound and Vibration*, 132: 199–211, 1989.

P. J. Morris, M. G. Giridharan, and G. M. Lilley. On the turbulent mixing of compressible free shear layers. *Proceedings of the Royal Society of London*, A431:219–243, 1990.

P. J. Morris, S. Boluriaan, G. M. Lilley, and L. N. Long. Two-point cross correlations of turbulence and noise predictions: Analysis and simulation. AIAA Paper 2002-0071, 2002.

A. H. Nayfeh. *Perturbation Methods*. John Wiley & Sons, Inc., New York, NY, 1973.

T. D. Norum. Screech suppression in supersonic jets. *AIAA Journal*, 21(2): 235–240, 1983.

T. D. Norum and M. C. Brown. Simulated high speed flight effects on supersonic jet noise. AIAA Paper 93-4388, 1993.

T. D. Norum and J. M. Seiner. Measurements of static pressure and far field acoustics of shock-containing supersonic jets. Technical report, NASA TM 84521, 1982a.

T. D. Norum and J. M. Seiner. Broadband shock noise from supersonic jets. *AIAA Journal*, 20:68–73, 1982b.

T. D. Norum and G. Shearin. Shock structure and noise of supersonic jets in simulated flight to Mach 0.4. Technical report, NASA TP 2785, 1988.

D. C. Pack. A note on Prandtl's formula for the wavelength of a supersonic gas jet. *Quarterly Journal of Mechanics and Applied Mathematics*, 3: 173–181, 1950.

A. B. Packman, K. W. Ng, and R. W. Paterson. Effect of simulated forward flight on subsonic jet exhaust noise. AIAA Paper 75-869, 1975.

J. Panda. Shock oscillation in underexpanded screeching jets. *Journal of Fluid Mechanics*, 363:173–198, 1998.

J. Panda. An experimental investigation of screech noise generation. *Journal of Fluid Mechanics*, 378:71–96, 1999.

N. A. Peart, M. J. T. Smith, B. Magliozzi, and H. Sternfeld. *Aeroacoustics of Flight Vehicles: Theory and Practice, Volume 2: Noise Control*, chapter Flyover-Noise Measurement and Prediction, pages 357–382. The Acoustical Society of America, Woodbury, NY, 1995.

O. M. Phillips. On the generation of sound by supersonic turbulent shear layers. *Journal of Fluid Mechanics*, 9:1–28, 1960.

M. K. Ponton, J. C. Manning, and J. M. Seiner. Far-field acoustics of supersonic rectangular nozzles with various throat aspect ratios. Technical report, NASA TM 89002, 1986.

A. Powell. The noise of choked jets. *Journal of the Acoustical Society of America*, 25(3):385–389, 1953a.

A. Powell. On the noise emanating from a two-dimensional jet above the critical pressure. *Aeronautical Quarterly*, IV:103–122, 1953b.

A. Powell. On the mechanism of choked jet noise. *Proceedings of the Physical Society of London*, B66:1039–1056, 1953c.

A. Powell. A survey of experiments on jet noise. *Aircraft Engineering*, 26 (299):2–9, 1954.

L. Prandtl. Über die stationaren Wellen in einem Gasstrahl. *Physikalische Zeitschrift*, 5:599–601, 1904.

D. C. Pridmore-Brown. Sound propagation in a fluid flowing through an attenuating duct. *Journal of Fluid Mechanics*, 4:393–406, 1958.

I. Proudman. The generation of noise by isotropic turbulence. *Proceedings of the Royal Society of London*, A214:119–132, 1952.

G. Raman. Advances in understanding supersonic jet screech: review and perspective. *Progress in Aerospace Sciences*, 34:45–106, 1998.

G. Raman. Supersonic jet screech: half-century from Powell to the present. *Journal of Sound and Vibration*, 225(3):543–571, 1999.

R. Reba, S. Narayanan, and T. Colonius. Wave-packet models for large-scale mixing noise. *International Journal of Aeroacoustics*, 9(4 & 5): 533–558, 2010.

H. Reichardt. Über eine neue Theorie der freien Turbulenz. *Zeitschrift für angewandte Mathematik und Mechanik*, 21:257–264, 1941.

H. S. Ribner. The generation of sound by turbulent jets. *Advances in Applied Mechanics*, 8:103–182, 1964.

H. S. Ribner. Quadrupole correlations governing the pattern of jet noise. *Journal of Fluid Mechanics*, 38(1):1–24, 1969.

H. S. Ribner. Comment on, "Jet mixing noise from fine-scale turbulence". *AIAA Journal*, 38(2):377–378, 2000.

T. J. Rosfjord and H. L. Toms. Recent observations including temperature dependence of axisymmetric jet screech. *AIAA Journal*, 13:1384–1386, 1975.

SAE. *Gas Turbine Jet Exhaust Noise Prediction, Revision D.* Number ARP876. Society of Automotive Engineers, A21, Aircraft Noise Measurement Committee, 1994.

S. Saxena, P. J. Morris, and K. Viswanathan. Algorithm for the nonlinear propagation of broadband jet noise. *AIAA Journal*, 47(1):186–194, 2009.

J. M. Seiner. Advances in high speed jet aeroacoustics. AIAA Paper 84-2275, 1984.

J. M. Seiner and T. D. Norum. Experiments on shock associated noise of supersonic jets. AIAA Paper 79-1526, 1979.

J. M. Seiner and T. D. Norum. Aerodynamic aspects of shock containing jet plumes. AIAA Paper 80-0965, 1980.

J. M. Seiner and J. C. Yu. Acoustic near field and local flow properties associated with broadband shock noise. AIAA Paper 81-1975, 1981.

J. M. Seiner and J. C. Yu. Acoustic near-field properties associated with broadband shock noise. *AIAA Journal*, 22:1207–1215, 1984.

J. M. Seiner, M. K. Ponton, and J. C Manning. The preferred spatial mode of instability for a Mach 2 jet. AIAA Paper 86-1942, 1986.

J. M. Seiner, M. K. Ponton, and J. C. Manning. Model and full scale study of twin supersonic plume resonance. AIAA Paper 87-0244, 1987.

H. Shen and C. K. W. Tam. Numerical simulation of the generation of axisymmetric mode jet screech tones. *AIAA Journal*, 36(10):1801–1807, 1998.

H. Shen and C. K. W. Tam. Effects of jet temperature and nozzle-lip thickness on screech tones. *AIAA Journal*, 38(5):762–767, 2000.

H. Shen and C. K. W. Tam. Three-dimensional numerical simulation of the jet screech phenomenon. *AIAA Journal*, 40(1):33–41, 2002.

P. M. Sherman, D. R. Glass, and K. G. Duleep. Jet flow field during screech. *Applied Science Research*, 32:282–303, 1976.

M. L. Shur, P. R. Spalart, and M. Kh. Strelets. Noise prediction for increasingly complex jets. Part I: methods and tests. Part II applications. *International Journal of Aeroacoustics*, 4(3& 4):213–266, 2005.

M. J. T. Smith. *Aircraft Noise.* Cambridge University Press, Cambridge, UK, 1989.

C. K. W. Tam. Directional acoustic radiation from a supersonic jet generated by shear layer instability. *Journal of Fluid Mechanics*, 46(4): 757–768, 1971.

C. K. W. Tam. Supersonic noise generated by large scale disturbances. *Journal of Sound and Vibration*, 38(1):51–79, 1975.

C. K. W. Tam. Stochastic model theory of broadband shock associated noise from supersonic jets. *Journal of Sound and Vibration*, 116:265–302, 1987.

C. K. W. Tam. The shock-cell structures and screech tone frequencies of rectangular and non-axisymmetric supersonic jets. *Journal of Sound and Vibration*, 121(1):135–147, 1988.

C. K. W. Tam. Broadband shock-associated noise of moderately imperfectly expanded supersonic jets. *Journal of Sound and Vibration*, 140(1):55–71, 1990.

C. K. W. Tam. Broadband shock associated noise from supersonic jets in flight. *Journal of Sound and Vibration*, 151:131–147, 1991.

C. K. W. Tam. Broadband shock associated noise from supersonic jets measured by a ground observer. *AIAA Journal*, 30:2395–2401, 1992.

C. K. W. Tam. *Aeroacoustics of Flight Vehicles: Theory and Practice, Volume 1: Noise Sources*, chapter Noise generated by Large-Scale Coherent Motion, pages 311–390. The Acoustical Society of America, Woodbury, NY, 1995a.

C. K. W. Tam. Supersonic jet noise. *Annual Review of Fluid Mechanics*, 27:17–43, 1995b.

C. K. W. Tam. Influence of nozzle geometry on the noise of high-speed jets. *AIAA Journal*, 36(8):1396–1400, 1998a.

C. K. W. Tam. Jet noise: since 1952. *Theoretical and Computational Fluid Dynamics*, 10:393–405, 1998b.

C. K. W. Tam and L. Auriault. Mean flow refraction effects on sound radiated from localized sources in a jet. *Journal of Fluid Mechanics*, 370:149–174, 1998.

C. K. W. Tam and L. Auriault. Jet mixing noise from fine-scale turbulence. *AIAA Journal*, 37(2):145–153, 1999.

C. K. W. Tam and D. E. Burton. Sound generated by instability waves of supersonic flows. Part 1. Two-dimensional mixing layers; Part 2. Axisymmetric jets. *Journal of Fluid Mechanics*, 138:249–295, 1984.

C. K. W. Tam and K. C. Chen. A statistical model of turbulence in two-dimensional mixing layers. *Journal of Fluid Mechanics*, 92:303–326, 1979.

C. K. W. Tam and P. J. Morris. The radiation of sound by the instability waves of a compressible plane turbulent shear layer. *Journal of Fluid Mechanics*, 98:349–381, 1980.

C. K. W. Tam and P. J. Morris. Tone excited jets, Part V: a theoretical model and comparison with experiment. *Journal of Sound and Vibration*, 102(1):119–151, 1985.

C. K. W. Tam and N. N. Reddy. Prediction method for broadband shock-associated noise from supersonic rectangular jets. *Journal of Aircraft*, 33 (2):298–303, 1996.

C. K. W. Tam and H. K. Tanna. Shock associated noise of supersonic jets from convergent-divergent nozzles. *Journal of Sound and Vibration*, 81 (3):337–358, 1982.

C. K. W. Tam and K. B. M. Q. Zaman. Subsonic jet noise from nonaxisymmetric and tabbed nozzles. *AIAA Journal*, 38(4):592–599, 2000.

C. K. W. Tam, J. A. Jackson, and J. M. Seiner. A multiple-scales model of the shock-cell structure of imperfectly expanded supersonic jets. *Journal of Fluid Mechanics*, 153:123–149, 1985.

C. K. W. Tam, J. M. Seiner, and J. C. Yu. Proposed relationship between broadband shock associated noise and screech tones. *Journal of Sound and Vibration*, 110(2):309–321, 1986.

C. K. W. Tam, K. K. Ahuja, and R. R. Jones. Screech tones from free and ducted supersonic jets. *AIAA Journal*, 32(5):917–922, 1994.

C. K. W. Tam, M. Golebiowski, and J. M. Seiner. On the two components of turbulent mixing noise from supersonic jets. AIAA Paper 96-1716, 1996.

C. K. W. Tam, N. Pastouchenko, and L. Auriault. Effects of forward flight on jet mixing noise from fine-scale turbulence. *AIAA Journal*, 39(7): 1261–1269, 2001.

C. K. W. Tam, K. Viswanathan, K. K. Ahuja, and J. Panda. The sources of jet noise: experimental evidence. *Journal of Fluid Mechanics*, 615: 253–292, 2008.

C. K. W. Tam, N. N. Pastouchenko, and K. Viswanathan. Broadband shock-cell noise from dual stream jets. *Journal of Sound and Vibration*, 324:861–891, 2009.

H. K. Tanna. An experimental study of jet noise. Part I. Turbulent mixing noise; Part II. Shock associated noise. *Journal of Sound and Vibration*, 50(3):405–444, 1977.

H. K. Tanna and P. J. Morris. In-flight simulation experiments on turbulent jet mixing noise. *Journal of Sound and Vibration*, 53(3):389–405, 1977.

B. J. Tester and C. L. Morfey. Developments in jet noise modelling - Theoretical predicitons and comparisons with measured data. *Journal of Sound and Vibration*, 46(1):79–103, 1976.

A. T. Thies and C. K. W. Tam. Computation of turbulent axisymmetric and non-axisymmetric jet flows using the $k - \varepsilon$ model. *AIAA Journal*, 34(2):309–316, 1996.

K. Viswanathan. Assessment of jet noise theory/prediction methods. In *Proceedings of the Jet Noise Workshop*, NASA-CP 2001-211152, pages 979–1010, 2001.

K. Viswanathan. Aeroacoustics of hot jets. *Journal of Fluid Mechanics*, 516:39–82, 2004.

K. Viswanathan. Scaling laws and a method for identifying components of jet noise. *AIAA Journal*, 44(10):2274–2285, 2006.

K. Viswanathan. Improved method for the prediction of noise from single jets. *AIAA Journal*, 45(1):151–161, 2007.

K. Viswanathan. Mechanisms of jet noise generation: classical theories and recent developments. *International Journal of Aeroacoustics*, 8(4): 355–408, 2009.

K. Viswanathan and M. J. Czech. Measurement and modeling of effect of forward flight on jet noise. *AIAA Journal*, 49(1):216–234, 2011.

K. Viswanathan and P. J. Morris. Predictions of turbulent mixing in axisymmetric compressible shear layers. *AIAA Journal*, 30(6):1529–1536, 1992.

K. Viswanathan, M. B. Alkislar, and M. J. Czech. Characteristics of the shock noise component of jet noise. *AIAA Journal*, 48(1):25–46, 2009.

H. E. von Gierke. Physical characteristics of aircraft noise sources. *Journal of the Acoustical Society of America*, 25(3):367–378, 1953.

U. Von Glahn, D. Groesbeck, and J. Goodykoontz. Velocity decay and acoustic characteristics of various nozzle geometries in forward flight. AIAA Paper 73-629, 1973.

R. Westley and G. M. Lilley. An investigation of the noise from a small jet and methods for its reduction. Report 53, College of Aeronautics, Cranfield, 1952.

R. Westley and J. H. Woolley. The nearfield sound pressures of a choked jet during a screech cycle. In *Aircraft Engine Noise and Sonic Boom*, number 42 in AGARD-CP, pages 23.1–23.13, 1969.

R. Westley and J. H. Woolley. The near field sound pressures of a choked jet when oscillating in the spinning mode. AIAA Paper 75-479, 1975.

M. S. Wochner, A. A. Atchley, and V. W. Sparrow. Numerical simulation of finite amplitude wave propagation in air using a realistic atmospheric absorption model. *Journal of the Acoustical Society of America*, 118(5): 2891–2898, 2005.

K. Yamamoto, J. F. Brausch, B. A. Janardan, D. J. Hoerst, A. O. Price, and P. R. Knott. Experimental investigation of shock-cell noise reduction for single-stream nozzles in simulated flight. Test nozzles and acoustic data, comprehensive data report, Vol. 1, NACA CR-168234, 1984.

# Analysis techniques for aeroacoustics: noise source identification

P. Jordan
Institut Pprime, UPR-CNRS-3346,
Université de Poitiers, ENSMA, France

## 1 Introduction

Aeroacoustic analysis is concerned with the problem of *sound source mechanism identification*. Let us consider for a moment what we mean by this, because, depending on the context, the same terminology can be interpreted differently. Two different contexts for the analysis of an aeroacoustic system, or indeed a fluid flow system in general, are: (1) the *kinematic* context; and, (2) the *dynamic* context.

When we are interested in kinematics, we are concerned with description of the space-time structure of a fluid flow, and perhaps with phenomenological explanations *vis-à-vis* our observation of that structure: *this vortical structure interacted with that one to produce this or that result*. Such kinematic descriptions will very often be with regard to some observable; in aeroacoustics that observable is the radiated sound field: *this vortical structure interacted with that one to produce this or that property of the sound field*.

Aeroacoustic theory was constructed from such a kinematic standpoint. Lighthill (1952) states on the second page of his seminal paper that he wishes to provide "...a general procedure for estimating the *intensity* of the sound produced in terms of the details of the fluid flow...". He makes it clear that the search for sound source mechanisms, as he intends it, "is concerned with uncovering the mechanism of conversion of energy between...the kinetic energy of fluctuating shearing motions and the acoustic energy of fluctuating longitudinal motions.". The "details of the fluid flow", the "fluctuating shearing motions", are considered as given.

However, if we are to consider more broadly the problem of source mechanism identification, we realise that, in order to be able to speak clearly about source mechanisms we need to be able to speak clearly about fluid

R. Camussi (Ed.), *Noise Sources in Turbulent Shear Flows: Fundamentals and Applications*, CISM International Centre for Mechanical Sciences, DOI 10.1007/978-3-7091-1458-2_4,

dynamics mechanisms, and it is difficult to do so without placing ourselves in the context of dynamics: we would like to be able to explain ***why*** *this vortical structure interacted with that one to produce this or that property of the sound field*; i.e. we wish to discern the dynamic law that underpins the observed interactions, *where sound production is concerned*. Of course there is one very simple, correct, but not terribly useful, reply to such an inquiry: the Navier-Stokes equations constitute the underlying dynamic law, both of the "fluctuating shearing motions" of the turbulence and the "fluctuating longitudinal motions" of the sound field. But for high Reynolds number turbulence this law, and the space-time flow structure that it engenders, are—from the point of view of perspicacious phenomenological description, flow-state prediction, or design guidance—invariably too complex to be useful; we are thus forced to seek simplified models.

Lighthill (1952) provided us with a tool that allows the "fluctuating longitudinal motions" of the sound field to be modelled more simply, and then connected to the "fluctuating shearing motions" of the turbulence; but the same tool does not provide an analogous clarification with regard to how the latter should be modelled. His theory and its descendants are probably best thought of as means by which *the connection* between the two kinds of motion can be modelled; and by virtue of this connection-model, some insight can be provided regarding the kinematic structure of the underlying flow motions. However, these theories cannot inform with regard to the dynamic law of the "fluctuating shearing motions" that underpin sound radiation.

These lectures are concerned with the exposition of an analysis methodology which, while it uses aeroacoustic theory as a central tool, attempts to take the problem of source mechanism identification beyond the kinematic limits imposed by that theory. The methodology, whose objective is source mechanism identification on both kinematic and dynamic levels (implicit is assumption is that the Navier-Stokes dynamics can be modelled in a simplified manner, that simplification being specifically tailored with respect to the acoustic observable), is largely an exercise in system reduction, and relies both on theoretical considerations and signal-processing tools. The document has therefore been organised as follows. In the next section, §2, an overview of aeroacoustic theory is provided; we focus on the earliest (Lighthill (1952)) and most recent theoretical developments (Goldstein (2003), Goldstein (2005), Sinayoko et al. (2011)). This is followed by a discussion, in section §3, of the source modelling problem, the bulk of the attention being focused on 'coherent structures'. It is in this section that the analysis methodology evoked above is outlined. Example implementations of the methodology are presented in section §4, where two specific case

studies are considered. The various signal processing tools used to support the analysis methodology, and which are implemented in section §4 without detailed explanation, form the basis of section §5. Finally, a brief outline of two reduced-order dynamical modelling approaches is given in section §6.

**Acknowledgements**

I would like to acknowledge Laurent Cordier, Joël Delville, Yves Gervais and Bernd Noack, all of whom have contributed to the development of the ideas contained in this document. Anurag Agarwal, Tim Colonius and Jonathan Freund, who continue to stimulate and enrich my general appreciation of aeroacoustics, also deserve to be mentioned. Finally, very special thanks are due to André Cavalieri and Franck Kerhervé, on whose research a good deal of the material contained herein is based.

## 2 Aeroacoustic theory

In this section we provide a brief presentation of the basic mathematical constructs necessary for an understanding of aeroacoustic theory: the wave equation and its integral solution by means of the free-space Green's function. This is followed by a detailed exposition of the theory of Lighthill (1952), where its dimensional, statistical and instantaneous representations are used to illustrate some aspects of the relationship between turbulence and sound. The first theoretical evolutions of Lighthill's theory, due to Phillips (1960) and Lilley (1974), are then evoked, more briefly, followed by a presentation of the most recent theoretical developments, due to Goldstein (2003) and Goldstein (2005), and which amount to a generalisation of the earlier acoustic analogies. Our exposition of Goldstein's generalised theory follows the slightly modified formulation proposed by Sinayoko et al. (2011), and we use a model problem computed by these authors in order to illustrate some of the essential aspects of aeroacoustic theory as it pertains to subsonic jets.

### 2.1 The wave equation

The motion of a viscous, compressible, heat-conducting fluid continuum is governed by the equations of mass, momentum and energy conservation, and the equation of state, which are, respectively:

$$\frac{\partial \rho}{\partial t} + \nabla \cdot (\rho \boldsymbol{u}) = m \tag{1}$$

$$\frac{\partial \rho \boldsymbol{u}}{\partial t} + \nabla \cdot \rho \boldsymbol{u}\boldsymbol{u} + \nabla \cdot \boldsymbol{P} = f \tag{2}$$

$$\rho T\big(\frac{\partial s}{\partial t} + \boldsymbol{u} \cdot \nabla s\big) = -\nabla \cdot \boldsymbol{q} + \boldsymbol{\tau} : \nabla \boldsymbol{u} \tag{3}$$

$$\mathrm{d}p = c^2 \mathrm{d}\rho + \big(\frac{\partial p}{\partial s}\big)_\rho \mathrm{d}s, \tag{4}$$

where

$$\boldsymbol{P} = p\boldsymbol{I} - \boldsymbol{\tau} \tag{5}$$

represents fluid stresses associated with the thermodynamic pressure, $p$, and the viscous stresses, $\boldsymbol{\tau}$; $\boldsymbol{q}$ is the heat flux due to conduction, given by Fourier's law, $\boldsymbol{q} = -K\nabla T$; $T$ is the temperature, $s$ is the entropy, and

$$c^2 = \big(\frac{\partial p}{\partial \rho}\big)_s. \tag{6}$$

Taken together, these equations constitute a closed system of differential equations that governs all classes of motion of a fluid continuum. The

mechanisms that underpin the generation of propagative acoustic energy are contained within this system. However, due to the non-linear nature of the equations, general solutions are not available; and, furthermore, in the general case it is not clear how to: (1) classify motions as turbulent, thermal and acoustic—this classification being possible only in certain limited cases, as shown by Chu and Kovásznay (1958); and, (2) identify clear relationships of cause and effect between different regions of a fluid in motion, or between different kinds of fluctuation of that motion (between velocity and pressure for example).

In acoustics, the situation is considerably simplified, as we focus on one particular class of fluid motion: that which is characterised by small amplitude fluctuations of a potential nature. In this case it is legitimate to linearise the equations of motion, which reduce, in the case of a quiescent fluid medium, and in the absence of external sources of mass or momentum, to

$$\frac{\partial \rho'}{\partial t} + \rho_o \nabla \cdot \boldsymbol{u}' = 0 \tag{7}$$

$$\rho_o \frac{\partial \boldsymbol{u}'}{\partial t} + \nabla p' = 0 \tag{8}$$

$$\frac{\partial s'}{\partial t} = 0 \tag{9}$$

$$p' = c_o^2 \rho'. \tag{10}$$

The velocity perturbation, $\boldsymbol{u}'$, can be eliminated by subtracting the time derivative of the mass conservation equation from the divergence of the momentum conservation equation, giving:

$$\frac{\partial^2 \rho'}{\partial t^2} - \Delta p' = 0. \tag{11}$$

$p'$ and/or $\rho'$ can then be eliminated, by means of the constitutive equation $p' = c_o^2 \rho'$, to give wave equations in either the density or the pressure:

$$\begin{aligned} \frac{\partial^2 p'}{\partial t^2} - c_o^2 \Delta p' &= 0 \\ \frac{\partial^2 \rho'}{\partial t^2} - c_o^2 \Delta \rho' &= 0. \end{aligned} \tag{12}$$

### 2.2 Green's functions

So, what do these wave equations represent? Well, simply stated: they describe propagative wave-like fluctuations of the density or pressure in a

quiescent fluid medium[1]. Such wave-like motion will only be sustained by the medium for space-time scales that satisfy the balance expressed by the equation. A Fourier transform of the wave equation can help illustrate this:

$$\begin{aligned} \omega^2 p' &= c_o^2 |\boldsymbol{\kappa}|^2 p', \\ \omega p' &= c_o |\boldsymbol{\kappa}| p'. \end{aligned} \tag{13}$$

This is known as the dispersion relation for the wave equation, and what it states is that for propagation to be supported in the quiescent, homogeneous fluid medium considered, the time scales of the motion, $\omega^{-1}$, must be matched with the space scales, $\boldsymbol{\kappa}^{-1}$, by the speed of sound, $c_o$. When such a system is excited by a disturbance that does not satisfy this criterion, the associated motions will not be supported as a propagating wave, and will tend, rather, to evanescence (very rapid decay). This concept is central to understanding the mechanisms by which a given source structure [2] generates a propagative energy flux, and these mechanisms can be most clearly seen by looking at integral solutions of the wave equation, which can be obtained by means of an appropriate Green's function.

The Green's function, $G(\boldsymbol{x}, t|\boldsymbol{y}, \tau)$, describes the wave-like *response* (as described by the wave equation) of the quiescent fluid medium to an impulse localised at $\boldsymbol{x} = \boldsymbol{y}$ and at time $t = \tau$. Where the free-field Green's function is concerned, a single clap of your hands in a large open space is an approximate equivalent of this. Mathematically, this can be expressed as:

$$\frac{\partial^2 G}{\partial t^2} - c_o^2 \Delta G = \delta(\boldsymbol{x} - \boldsymbol{y})\delta(t - \tau). \tag{14}$$

Once we have found the Green's function we are equipped with a filter which, when convolved with a given source, will extract the space-time scales of the source structure that *match* the balance expressed by the propagation operator ($\frac{\partial^2 p'}{\partial t^2} = c_o^2 \Delta p'$), and which are therefore capable of producing a propagating wave. For example, consider the physical problem described by

$$\frac{\partial^2 p'}{\partial t^2} - c_o^2 \Delta p' = q(\boldsymbol{x}, t), \tag{15}$$

where $q(\boldsymbol{x}, t)$ is some (known) source (this could be an unsteady, spatially-distributed force field, or an unsteady, spatially-distributed, addition of

[1] In fact the wave equation can, alternatively, be expressed in terms of a velocity potential, $\phi$, from which density ($\rho = \frac{1}{c_o^2}\frac{\partial \phi}{\partial t}$), pressure ($p = \frac{\partial \phi}{\partial t}$) and velocity ($\mathbf{u} = \vec{\nabla}\phi$) can all be derived.

[2] In what follows we will see that the flow equations can be manipulated such that this source represents the turbulent jet.

mass), that drives sound waves in a quiescent medium. Multiplying equation 14 by $p'$, equation 15 by $G$, integrating in both space and time (neglecting the effect of initial conditions), and subtracting the former from the latter, we get, provided there are no solid boundaries, and after a little manipulation

$$p'(\boldsymbol{x},t) = \int_{t_o}^{t} \int_{V} q(\boldsymbol{y},\tau) G(\boldsymbol{x},t|\boldsymbol{y},\tau) d\boldsymbol{y} d\tau. \tag{16}$$

The right hand side of this equation describes the filtering of $q(\boldsymbol{y},\tau)$ by $G(\boldsymbol{x},t|\boldsymbol{y},\tau)$: $G(\boldsymbol{x},t|\boldsymbol{y},\tau)$ allows us to extract, from the heart of what might be an extremely complex, and largely (acoustically) ineffective, source structure, $q(\boldsymbol{y},\tau)$, only those scales that are acoustically-matched.

This is the key to analysing and understanding aeroacoustic systems, experimentally, numerically or theoretically. It is necessary to identify the space-time scales (or flow behaviour that leads to the generation of such scales) that are actually efficient in the generation of sound waves—the vast majority are not. In the context of Lighthill's acoustic analogy the problem is exactly that described here, insofar as the wave equation used has the same form as 15. For the more sophisticated acoustic analogies, while the wave equations and source descriptions change, conceptually we are dealing with the same scenario: the dispersion-relations and Green's functions will change, and this will modify the criterion by which we identify the pertinent space-time scales of the 'source' quantity (which it is then necessary to relate to the turbulence characteristics of the jet). Further discussion on this point is provided in the next section.

### 2.3 Lighthill's acoustic analogy

Lighthill's acoustic analogy is a peculiar kind of object: it amounts to a model representation of the jet-noise problem, but one which is described by an exact fluid dynamics equation (nothing less than the Navier-Stokes equations is stated). This dual quality constitutes both the elegance of, and the crux of the interpretational difficulties associated with, the acoustic analogy formulations in general.

Lighthill sought to rearrange the equations of mass and momentum conservation—taken in their full, non-linear form—such that the wave operator would appear. In order to do so, he followed the same basic steps used in the derivation of the wave equation, but without performing the linearisation. Taking the time derivative of the mass conservation equation, the divergence of the momentum conservation equation, and combined the

two gives, after a little manipulation, [3]

$$\frac{\partial^2 \rho'}{\partial t^2} - c_o^2 \Delta \rho' = \nabla \cdot \nabla \cdot (\rho \boldsymbol{uu} - \boldsymbol{\tau} + (p' - c_o^2 \rho') \boldsymbol{I}). \tag{17}$$

In terms of $p'$, the equation becomes

$$\frac{1}{c_0^2} \frac{\partial^2 p'}{\partial t^2} - \Delta p' = \nabla \cdot \nabla \cdot (\rho \boldsymbol{uu} - \boldsymbol{\tau}) + \frac{1}{c_0^2} \frac{\partial^2}{\partial t^2} (p' - c_o^2 \rho'). \tag{18}$$

These inhomogeneous wave equations can be interpreted in terms of a source term (the right hand side) that drives density or pressure fluctuations, as described by the left hand side.

We can now examine integral solutions to Lighthill's equation, and it is at this point that we make a first connection between radiated sound energy and the flow characteristics of a turbulent jet.

These solutions can be considered on three levels: that of (1) elementary dimensional analysis; (2) time-averaged (second and higher order) statistics; and, (3) space-time analysis. The third of these gives us the most direct insight, in so far as it allows a local (in space and time) grasp of the sound production mechanisms; it is most useful for highly organised flows, and/or for understanding the organised component of high Reynolds number flows ('coherent structures'). In the second approach, detailed understanding is hampered by time-averaging, and we are obliged to consider the connection between the radiated sound power and the jet flow via the second and higher order statistical moments of the unsteady flow; this kind of approach is most useful for the more random components of the flow unsteadiness. The first of the approaches is the most elementary of the three, where very little physical insight is provided regarding the underlying mechanisms. In section §3 we will revisit these representations when we discuss the role played by coherent structures in the generation of sound.

Integral solutions to equations 17 and 18 can be obtained using the Green's function formalism outlined earlier. Henceforth we will change to tensor notation, we will only consider the equation expressed in terms of $p'$, and we will consider the simplified source quantity

$$\frac{\partial^2 \rho u_i u_j}{\partial y_i \partial y_j}(\boldsymbol{y}, t) : \tag{19}$$

the term associated with viscous effects $\boldsymbol{\tau}$ can be neglected for most flows of interest, and the third term on the right hand side of equation 18 is believed

[3] See Lighthill (1952) for full details.

to correspond to the effect of temperature fluctuations (this is often referred to as the entropy source term). This is probably an oversimplification, as in high Mach number flows there is evidence to suggest that the first and third terms on the right hand side of equation 18 are correlated (cf. Bodony and Lele (2005)). However, as our objective in this lecture is to make as clear as possible, and in as simple a manner as possible, the essential workings of acoustic analogies, we will continue to use this simplified scenario. Once the reasoning has been clearly understood in terms of the simplified source term, it is conceptually straightforward to extend to more complex source terms.

The free-field Green's function is $G_o = \frac{\delta}{4\pi|\boldsymbol{x}-\boldsymbol{y}|}$, and so solution to Lighthill's equation can be written as follows:

$$\begin{aligned} p'(\boldsymbol{x},t) &= \int_{\infty}^{\infty}\int_{V_y} \frac{\partial^2 \rho u_i u_j}{\partial y_i \partial y_j}(\boldsymbol{y},t)\delta\Big(t-\tau-\frac{|\boldsymbol{x}-\boldsymbol{y}|}{c_o}\Big)\frac{\mathrm{d}V_y \mathrm{d}\tau}{4\pi|\boldsymbol{x}-\boldsymbol{y}|} \\ &= \int_{V_y} \frac{\partial^2 \rho u_i u_j}{\partial y_i \partial y_j}\Big(\boldsymbol{y},t-\frac{|\boldsymbol{x}-\boldsymbol{y}|}{c_o}\Big)\frac{\mathrm{d}V_y}{4\pi|\boldsymbol{x}-\boldsymbol{y}|}. \end{aligned} \tag{20}$$

From equation 20 we can proceed in two ways: (1) we can do the most basic kind of dimensional analysis, which will lead to the simplest expressions of the relationship between radiated sound power and flow characteristics; or, (2) we can take things from the statistical standpoint. We will here do both.

First, however, we introduce two simplifications that are frequently used. The first exploits the reciprocity property of the Green's function, which means that source and observer can be interchanged. This allows the double divergence in equation 20, which is in terms of the source coordinates $\boldsymbol{y}$, to be expressed in terms of the observer coordinates, $\boldsymbol{x}$, at which point it can be taken outside the volume integral:

$$p'(\boldsymbol{x},t) = \frac{1}{4\pi}\frac{\partial^2}{\partial x_i \partial x_j}\int_{V_y} \rho u_i u_j\Big(\boldsymbol{y},t-\frac{|\boldsymbol{x}-\boldsymbol{y}|}{c_o}\Big)\frac{\mathrm{d}V_y}{|\boldsymbol{x}-\boldsymbol{y}|}. \tag{21}$$

Now that differentiation is being performed in the observer frame (assumed to be in the farfield), where fluctuations are entirely acoustic, the spatial derivatives are related to temporal derivatives through

$$\frac{\partial}{\partial x_i} = -\frac{x_i}{|\boldsymbol{x}|}\frac{1}{c_o}\frac{\partial}{\partial t}, \tag{22}$$

because we are dealing with a non-dispersive wavefield: if you want to know the spatial gradient of the waveform, rather than walk along the wave and measuring the slope as you go, you can simply stay put, letting the

wavefield pass you by, at the speed of sound; by then measuring its temporal rate of change, knowing it's propagation speed and considering that the sound waves are locally plane, you immediately have access to the spatial derivative. The solution can thus be written, because we are in the farfield ($|\boldsymbol{x}-\boldsymbol{y}| \approx |\boldsymbol{x}|$), in the following simplified form:

$$p'(\boldsymbol{x},t) = \frac{x_i x_j}{4\pi c_o^2 |\boldsymbol{x}|^3} \frac{\partial^2}{\partial t^2} \int_{V_y} \rho u_i u_j \Big(\boldsymbol{y}, t - \frac{|\boldsymbol{x}|}{c_o}\Big) \mathrm{d}V_y. \tag{23}$$

**Dimensional analysis** Let us consider the problem of the subsonic propulsive jet, which is the system that Lighthill's analogy was first used to assess. If we consider that a characteristic eddy dimension in the turbulent jet plume is of the order of the jet diameter, $D$, which corresponds, approximately, to the vorticity thickness of the mixing-layer at the end of the potential core of a subsonic jet[4], a characteristic frequency is $f = U_o/D$, where $U_o$ is the exit velocity of the jet, and $Df/c_o = U_o/c_o = M$, where $M$ is the Mach number (a measure of compressibility). This means that

$$p' \sim \frac{f^2}{c_o^2} \rho_o U_o^2 \frac{D^3}{|\boldsymbol{x}|} \tag{24}$$

$$\sim \rho_o U_o^2 \frac{f^2}{c_o^2} \frac{M^2 c_o^2}{f^2} \frac{D}{|\boldsymbol{x}|} \tag{25}$$

$$\sim \rho_o U_o^2 M^2 \frac{D}{|\boldsymbol{x}|}, \tag{26}$$

and so the acoustic intensity, $I = \frac{\langle p'^2 \rangle}{\rho_o c_o}$, should scale as

$$I = \sim \rho U_o^3 M^5 \Big(\frac{D}{|\boldsymbol{x}|}\Big)^2 \sim U_o^8. \tag{27}$$

This very simple analysis immediately shows the very strong dependence of the sound power radiated on the velocity and Mach number of a jet. This was the first major result of Lighthill's theory. In terms of jet noise control, if we are to judge an analysis in terms of the impact it has had on the design of the application, it remains *the most significant* result to date: it was clear from this analysis that the jet velocity and Mach number would need to be reduced, and that moderate reductions could lead to significant reductions

[4] This region is now known to be one of the most important in terms of sound production, but was not known at the time of Lighthill's first estimates of the sound power radiated by a flow

in sound power. In order to do so, without losing thrust, larger diameter jets would be required: the introduction, and subsequent optimisation of, the (low and high) by-pass jet engine led, between 1950 and 2000, to a 20dB reduction in the sound power radiated by jets exhausts at take-off.

**Statistical analysis** We now consider the second way in which it is possible to relate radiated sound power to flow/source characteristics. Using equation 23, expressions for the autocorrelation of the farfield pressure (which is related to the power spectrum of the pressure by a Fourier transform) can be obtained; this can then be related to the turbulence through the term $\rho u_i u_j$. Assuming constant density in the source term ($\rho = \rho_o$), the autocorrelation function of the farfield pressure fluctuation is given by

$$\begin{aligned} C(\boldsymbol{x},\tau) &= \langle p'(\boldsymbol{x},t)p'(\boldsymbol{x},t+\tau)\rangle \\ &= \rho_o \frac{x_i x_j x_k x_l}{16\pi^2 c_o^4 |\boldsymbol{x}|^6} \int_{V_{y''}} \int_{V_{y'}} \Big\langle \frac{\partial^2 u_i u_j}{\partial t^2}\Big(\boldsymbol{y}', t - \frac{|\boldsymbol{x}-\boldsymbol{y}'|}{c_o}\Big) \\ &\qquad \frac{\partial^2 u_k u_l}{\partial t^2}\Big(\boldsymbol{y}'', t - \frac{|\boldsymbol{x}-\boldsymbol{y}''|}{c_o} + \tau\Big)\Big\rangle \mathrm{d}\boldsymbol{y}'\mathrm{d}\boldsymbol{y}''. \end{aligned} \tag{28}$$

And, if the turbulence is considered to be statistically stationary, the equation can be rewritten as

$$\begin{aligned} C(\boldsymbol{x},\tau) = \rho_o \frac{x_i x_j x_k x_l}{16\pi^2 c_o^4 |\boldsymbol{x}|^6} \int_{V_{y''}} \int_{V_{y'}} \frac{\partial^4}{\partial \tau^4} \Big\langle u_i u_j\Big(\boldsymbol{y}', t - \frac{|\boldsymbol{x}-\boldsymbol{y}'|}{c_o}\Big) \\ u_k u_l\Big(\boldsymbol{y}'', t - \frac{|\boldsymbol{x}-\boldsymbol{y}''|}{c_o} + \tau\Big)\Big\rangle \mathrm{d}\boldsymbol{y}'\mathrm{d}\boldsymbol{y}''. \end{aligned} \tag{29}$$

By virtue of this equation we now have a far more detailed description of how the sound power radiated by a jet flow is related to that flow: for a single observer in the farfield, at $\boldsymbol{x}$, the sound power, as a function of frequency,[5] is given by a volume integral, over the entire extent of the jet, of the two-point, two-time correlation of the Reynolds stress field.

**Instantaneous analysis** The two approaches presented above, both of which involve considerable data compression when compared to the full space-time fields from which they begin (and where mechanisms show themselves most exactly), necessarily hide a certain amount of information.[6]

[5] The power spectrum is given by taking the Fourier transform

[6] In 1952 measurement and computational capabilities were such that it was not possible to access full-field data; the two-point correlations were about the best that could be achieved.

Some kind of compression is of course indispensable: the formidable complexity of the full space-time structure of turbulence is such that useful assimilation and description is only possible at the expense of some such information loss. However, the ever-increasing capabilities of numerical simulation, experimental data acquisition and data post-processing, mean that new kinds of analysis and modelling methodologies, which deal more directly with the local space-time details of flow mechanisms, can be considered. Such methodologies and tools, which are outline sections §3, §5 and §6, are essential from the point of view of real-time, closed-loop control, towards which fluid dynamics research is headed. It is therefore useful to consider the space-time-local representation of the solution to Lighthill's equation 20.

As outlined above, the physical system described by an inhomogeneous wave equation, such as Lighthill's, involves a coupling between a source term—which in this sub-section we will simply refer to as $q(\boldsymbol{x}, t)$—and some base-flow medium that can sustain propagative, wavelike perturbations in accordance with the balance expressed by the wave equation. In the context of Lighthill's formulation, the mechanism by which a propagative wave is set up, in the quiescent medium, by the source, amounts to the acoustic matching described earlier. In order therefore to have access to what is happening in real time, we need to examine the integral solution in its most primitive form

$$p(\boldsymbol{x}, t) = \frac{1}{4\pi} \int_V \frac{q(\boldsymbol{y}, t - \frac{|\boldsymbol{x}-\boldsymbol{y}|}{c})}{|\boldsymbol{x} - \boldsymbol{y}|} d^3\boldsymbol{y}. \tag{30}$$

What this equation tells us is that if we consider the excitation field in a distorted space-time reference frame, $q(\boldsymbol{y}, t - \frac{|\boldsymbol{x}-\boldsymbol{y}|}{c})$, the farfield pressure is given by simply summing all the points of that distorted field. If the source field is considered in undistorted space-time, additional time-delays, corresponding to wave-propagation times, weight the summation. Physically, this summation corresponds to the time-delayed constructive and destructive interference phenomena that underpin, respectively, loud or quiet source activity. We will discuss this in the next section when we consider the antenna-like wavepacket radiation associated with 'coherent structures'.

### 2.4 Acoustic analogies of Phillips and Lilley

A difficulty with the Lighthill analogy, for the problem of jet noise, is that the wave equation describes propagation through a medium at rest. While this model is approximately correct outside the region of turbulent flow, it is not so within the turbulent jet. Two subsequent developments, due to Phillips (1960) and Lilley (1974), were aimed at improving this aspect of

the model. Both were motivated by the desire to explicitly describe effects associated with interactions between the sound field and the jet.

Phillips (1960) proposed an alternative rearrangement of the Navier-Stokes equations, leading to:

$$\frac{\mathrm{d}^{\,2}\pi}{\mathrm{d}t^2} - \frac{\partial}{\partial x_i}\Big(c^2\frac{\partial \pi}{\partial x_j}\Big) = \frac{\partial u_i}{\partial x_j}\frac{\partial u_j}{\partial x_i} - \frac{\partial}{\partial x_i}\Big(\frac{1}{\rho}\frac{\partial \tau_{ij}}{\partial x_j}\Big) + \frac{\mathrm{d}}{\mathrm{d}t}\Big(\frac{1}{C_p}\frac{\mathrm{d}s}{\mathrm{d}t}\Big), \tag{31}$$

where $\pi = \log(p)$. This equation comprises, explicitly, in the wave operator, some effects of the mean velocity (via the material derivative), in addition to the effects of variable speed of sound that can occur due to temperature or Mach number gradients. The right hand side, which again is considered a source term, comprises, as did Lighthill's source term, terms associated with non-linear momentum fluctuations, viscous stresses and a term due to entropy unsteadiness.

The modification due to Lilley (1974) comes about from recognising that if we linearise Phillips' equation about some mean flow, and we consider the fluctuation to be entirely acoustic, the source contains a term associated with flow-acoustic interaction in the form of refraction of the small-amplitude acoustic disturbances by mean shear. To see this, consider acoustic disturbances propagation in two-dimensional shear-flow with mean velocity profile $U(y)\cdot\vec{x}$. Linearising Phillip's equation about this mean flow, and neglecting thermal and viscous effects, the LHS reduces to

$$\frac{1}{c_o^2}\frac{\mathrm{d}^2 p}{\mathrm{d}t^2} - \frac{\partial^2 p}{\partial x_i^2}, \tag{32}$$

while the RHS reduces to

$$2\rho_o \frac{\partial v}{\partial x}\frac{\mathrm{d}U(y)}{\mathrm{d}y}. \tag{33}$$

When it is possible to verify that the perturbation about the mean flow is indeed an acoustic disturbance, this term describes the refraction of sound by the mean flow, and one can argue that it should appear on the LHS, in the wave operator.

With this in mind, Lilley took the material derivative of Phillips' equation:

$$\frac{\mathrm{d}}{\mathrm{d}t}\Big[\frac{\mathrm{d}^2\pi}{\mathrm{d}t^2} - \frac{\partial}{\partial x_i}\Big(c^2\frac{\partial \pi}{\partial x_j}\Big)\Big] + 2\frac{\partial v_j}{\partial x_i}\frac{\partial}{\partial x_j}\Big(c^2\frac{\partial \pi}{\partial x_i}\Big) = -2\frac{\partial v_j}{\partial x_i}\frac{\partial v_k}{\partial x_j}\frac{\partial v_i}{\partial x_k} + \Psi, \tag{34}$$

where

$$\Psi = 2\frac{\partial v_j}{\partial x_i}\frac{\partial}{\partial x_j}\Big(\frac{1}{\rho}\frac{\partial \tau_{ij}}{\partial x_k}\Big) - \frac{\mathrm{d}}{\partial t}\Big[\frac{\partial}{\partial x_i}\Big(\frac{1}{\rho}\frac{\partial \tau_{ij}}{\partial x_j}\Big)\Big] + \frac{\mathrm{d}^2}{\mathrm{d}t^2}\Big[\frac{1}{c_p}\frac{\mathrm{d}s}{\mathrm{d}t}\Big], \qquad (35)$$

and we see that by linearising this equation about a base-flow comprising mean shear, we obtain a wave operator that describes acoustic propagation in that shear-flow. It is important to point out however, that a Reynolds decomposition of the velocity field (into $U+u$), does not correspond to a split into hydrodynamic and acoustic disturbances, and so it is not clear that the linear term so obtained does indeed correspond to a refraction effect in the case of a turbulent jet, where the fluctuation about the time-averaged mean, within the jet, is largely hydrodynamic. This problem of decomposing a flow into acoustic and non-acoustic components lies at the heart of much of the controversy that surrounds acoustic analogy approaches for the description and study of aeroacoustic systems. The most recent attempt to address this difficulty has been proposed by Goldstein (2003) and Goldstein (2005).

### 2.5 The generalised acoustic analogy

Goldstein (2003, 2005) has shown how the formulations typified by the efforts of Phillips (1960) and Lilley (1974) amount to particular cases in a more general framework. In what follows we provide, firstly, a compact exposition of this generalised formulation, in order to facilitate description and interpretation. We then proceed to give a more complete presentation, following the work of Sinayoko et al. (2011). We end with an overview of a model problem, proposed by these authors, which serves as an instructive illustration of the differences between different acoustic analogy formulations.

**In a nutshell** Consider the Navier-Stokes equations, expressed in the compact form

$$\mathcal{N}(\boldsymbol{q}) = 0, \qquad (36)$$

where $\boldsymbol{q}$ is here a vector containing all of the dependent flow variables, and $\mathcal{N}$ represents the Navier-Stokes operator. Goldstein's generalisation of the acoustic analogy proceeds as follows.

The full solution is first decomposed into a (possibly unsteady) base-flow and a perturbation:

$$\boldsymbol{q} = \overline{\boldsymbol{q}}_D + \boldsymbol{q}_A, \qquad (37)$$

the subscript $D$ indicating non-linear fluid dynamics, as opposed to linear acoustic dynamics, which are denoted by the subscript $A$. From this

decomposition an equation of the following form can be written

$$\mathcal{L}_{\overline{\boldsymbol{q}}_D}(\boldsymbol{q}_A) = s(\overline{\boldsymbol{q}}_D), \tag{38}$$

where $\mathcal{L}_{\overline{\boldsymbol{q}}_D}$ is a linear operator describing the evolution of $\boldsymbol{q}_A$, a disturbance generated and carried by $\overline{\boldsymbol{q}}_D$. Let us consider this equation for a moment, as it has certain uses, but also some limitations.

A first difficulty associated with an equation constructed in this manner is that, if we are to interpret it in terms of a non-acoustic, causal, source, $s(\overline{\boldsymbol{q}}_D)$, that drives an acoustic effect, $\boldsymbol{q}_A$, we need to be sure that the full flow solution has been decomposed into acoustic and non-acoustic, or radiating and non-radiating, components: there is presently no consensus as to how such a decomposition might be unambiguously effected.

A second difficulty becomes apparent when we consider what has been gained by identifying $s(\overline{\boldsymbol{q}}_D)$ in this way. If we consider equation 38 to be physically pertinent—in other words we believe that we have successfully decomposed the flow solution into acoustic and non-acoustic components—at best we can consider the decomposition of equation 37 to provide us with the kinematic structure of the flow, $\overline{\boldsymbol{q}}_D$, that underpins sound radiation. However, as we will see in the following example, $\overline{\boldsymbol{q}}_D$ is almost identical to $\boldsymbol{q}$, the full flow solution, as one would expect given the large amplitude disparity between hydrodynamic and acoustic fluctuations at the heart of the flow; and so the question that arises is the following: in what way does the information provided by decomposition 37 and equation 38 enlighten us with regard to the physical flow mechanisms associated with sound production? The answer appears to be: it constitutes a powerful means by which the radiating flow structure can be *visualised* and probed. For instance, by superposing $s(\overline{\boldsymbol{q}}_D)$ and $\overline{\boldsymbol{q}}_D$, and studying, simultaneously, the space-time (or frequency-wavenumber) structure of the two, it may be possible to gain some insight regarding what it was about the flow motions $\overline{\boldsymbol{q}}_D$ that led to the radiating source structure $s(\overline{\boldsymbol{q}}_D)$: *this structure* ($\in \overline{\boldsymbol{q}}_D$) *interacted with that structure* ($\in \overline{\boldsymbol{q}}_D$) *to produce this or that aspect of the source field* ($\in s(\overline{\boldsymbol{q}}_D)$).

However, having clarified the kinematics in this way, it is then necessary to address the question of the dynamics, as the flow motions associated with the generation of sound can only be fully understood in the context of their underlying dynamic law. In the context of high Reynolds number turbulent jets, $\overline{\boldsymbol{q}}_D$ will be no less complex than $\boldsymbol{q}$, and thus the dynamic law of the source is approximately the Navier-Stokes operator; in which case we arrive at the conclusion that the sound-source mechanism is the turbulence! The point on which we insist is the same evoked in the introduction: while the acoustic analogies can provide simplified models for the propagation

and connection-to-turbulence parts of the problem, they do not directly provide any such simplification where the "fluctuating shearing motions" are concerned. These points will be further discussed in section §3.

**Full derivation** The following derivation, taken from Sinayoko et al. (2011), shows, in detail, how a generalised acoustic analogy, such as that evoked more compactly above, can be formulated for a homentropic fluid medium. The derivation is followed by the presentation and discussion of a model problem chosen by those authors; the problem considered constitutes a useful illustration of the differences between this and more conventional acoustic analogies; it also serves to illustrate the limitations of acoustic analogies in general.

*Unsteady, non-radiating base-flow*

The flow equations are written as:

$$\frac{\partial \rho}{\partial t} + \frac{\partial}{\partial x_j}\rho v_j = 0 \tag{39}$$

$$\frac{\partial}{\partial t}\rho v_i + \frac{\partial}{\partial x_j}\rho v_i v_j + \frac{\partial p}{\partial x_i} = \frac{\partial}{\partial x_j}\sigma_{ij} \tag{40}$$

$$\frac{\partial p}{\partial t} + v_j \frac{\partial p}{\partial x_j} + \gamma p \frac{\partial v_j}{\partial x_j} = 0. \tag{41}$$

Using a modified pressure variable $\pi = p^{1/\gamma}$, the momentum and energy equations can be rewritten as

$$\frac{\partial}{\partial t}\rho v_i + \frac{\partial}{\partial x_j}\rho v_i v_j + \frac{\partial}{\partial x_i}\pi^\gamma = 0 \tag{42}$$

$$\frac{\partial \pi}{\partial t} + \frac{\partial}{\partial x_j}\pi v_j = 0. \tag{43}$$

Note that the pressure equation now appears in conservative form.

For the moment consider that a filter capable of extracting acoustic, or radiating, disturbances, $\boldsymbol{q}'$, from the full flow variable, $\boldsymbol{q}$, exists: $\mathcal{L}' = \mathcal{I} - \mathcal{L}$.

Application of this filter to the conservation equations gives:

$$\frac{\partial \rho'}{\partial t} + \frac{\partial}{\partial x_j}(\rho v_j)' = 0 \tag{44}$$

$$\frac{\partial}{\partial t}(\rho v_i)' + \frac{\partial}{\partial x_j}(\rho v_i v_j)' + \frac{\partial}{\partial x_i}(\pi^\gamma)' = 0 \tag{45}$$

$$\frac{\partial (\pi)'}{\partial t} + \frac{\partial}{\partial x_j}(\pi v_j)' = 0. \tag{46}$$

The non-linear momentum flux term can be expanded as

$$\rho v_i v_j = \overline{\rho}\tilde{v_i}\tilde{v_j} + \tilde{v_j}(\rho v_i)' + \tilde{v_i}(\rho v_j)' - \tilde{v_i}\tilde{v_j}\rho' + O(\rho'^2), \tag{47}$$

where

$$\tilde{v_i} = \frac{\overline{(\rho v_i)}}{\overline{\rho}}. \tag{48}$$

$O(\rho'^2)$ terms, being quadratic in the radiating (acoustic variables), are several orders of magnitude smaller than radiating components, and can be neglected. Thus, application of the filter $\mathcal{L}'$ to the expanded momentum flux term gives

$$(\rho v_i v_j)' \approx \underbrace{(\overline{\rho}\tilde{v_i}\tilde{v_j})'}_{A} + \underbrace{(\tilde{v_j}(\rho v_i)' + \tilde{v_i}(\rho v_j)' - \tilde{v_i}\tilde{v_j}\rho')'}_{B}. \tag{49}$$

Term A is the acoustically-matched part of the non-linear momentum flux term, i.e. it comprises only those components of the triple correlation $\overline{\rho}\tilde{v_i}\tilde{v_j}$ that present radiation-capable space-time scales, and that can thereby couple with the sound field. The second group of terms, B, corresponds to acoustically-matched components of hydrodynamic-acoustic interaction terms: refraction, scattering, convective transport, etc.

Similarly the modified pressure term, which is also non-linear, can be expanded and filtered:

$$\pi^\gamma = (\overline{\pi} + \pi')^\gamma = \overline{\pi}^\gamma + \gamma\overline{\pi}^{\gamma-1}\pi' + O(\pi'^2), \tag{50}$$

$$(\pi^\gamma)' = \underbrace{(\overline{\pi}^\gamma)'}_{A} + \underbrace{(\gamma\overline{\pi}^{\gamma-1}\pi')'}_{B}. \tag{51}$$

On account of the homentropic character of the fluid medium, it can be shown (see Sinayoko et al. (2011) for details) that the radiating component

arising due to the non-linearity of the non-radiating pressure term, A, is equal to zero:

$$(\overline{\pi}^{\gamma})' = \frac{\pi_\infty}{\rho_\infty}(\overline{\rho}^{\gamma})' = \left(\frac{\rho_\infty}{\pi_\infty}\right)^{\gamma-1}(\overline{p})' = 0. \tag{52}$$

Similarly, the energy flux term, $(\pi v_j)'$, can be decomposed as follows

$$(\pi v_j)' \approx \underbrace{(\overline{\pi}\tilde{v_j})'}_{A} + \underbrace{(\frac{\overline{\pi}}{\overline{\rho}}(\rho v_j)' + \tilde{v_j}\pi' - \frac{\overline{\pi}}{\overline{\rho}}\tilde{v_j}\rho')'}_{B}, \tag{53}$$

and the radiating component of the non-linear part shown also to be equal to zero:

$$(\overline{\pi}\tilde{v_j})' = \frac{\pi_\infty}{\rho_\infty}(\overline{\rho}\tilde{v_j})' = \frac{\pi_\infty}{\rho_\infty}(\overline{\rho v_j})' = 0. \tag{54}$$

The filtered Navier Stokes equations can now be re-written, placing all of the non-zero sound source terms, A (which comprise radiating components of non-linear interactions of non-radiating components) on the right hand side, and the flow-acoustic interaction terms, B, on the left:

$$\frac{\partial \rho'}{\partial t} + \frac{\partial}{\partial x_j}(\rho v_j)' = 0, \tag{55}$$

$$\frac{\partial}{\partial t}(\rho v_i)' + \frac{\partial}{\partial x_j}(\tilde{v_j}(\rho v_i)' + \tilde{v_i}(\rho v_j)' - \tilde{v_i}\tilde{v_j}\rho')' + \gamma\frac{\partial}{\partial x_i}(\overline{\pi}^{\gamma-1}\pi')' = -\frac{\partial}{\partial x_j}(\overline{\rho}\,\tilde{v_i}\tilde{v_j})', \tag{56}$$

$$\frac{\partial \pi'}{\partial t} + \frac{\partial}{\partial x_j}\big(\frac{\overline{\pi}}{\overline{\rho}}((\rho v_j)' - \tilde{v_j}\rho') + \tilde{v_j}\pi'\big)' = 0. \tag{57}$$

This is a generalised acoustic analogy, the source and propagator components of which depend on how the filter, $\mathcal{L}'$ is defined.

*Time-averaged base-flow*

In order to compare the above formulation with more conventional approaches, Sinayoko et al. (2011) repeat the same derivation where the decomposition into base-flow and perturbation follows a simple Reynolds decomposition. The result leads to a formulation synonymous with the Linearised Euler Equations.

Base flow and perturbation are thus defined by

$$q = q_0 + q'', \tag{58}$$

where $q_0$ and $q''$ denote, respectively, the steady (time-averaged) and unsteady part of $q$. Following the previous procedure leads to

$$\frac{\partial \rho''}{\partial t} + \frac{\partial (\rho v_j)''}{\partial x_j} = 0, \tag{59}$$

$$\frac{\partial (\rho v_i)''}{\partial t} + \frac{\partial (\rho v_i v_j)''}{\partial x_j} + p_\infty \frac{\partial (\pi^\gamma)''}{\partial x_i} = 0, \tag{60}$$

$$\frac{\partial \pi''}{\partial t} + \gamma \frac{\partial (\pi v_j)''}{\partial x_j} = 0. \tag{61}$$

The term $\rho v_i v_j$ can be decomposed as

$$\rho v_i v_j = \frac{\rho v_i \, \rho v_j}{\rho}$$
$$= \begin{cases} (a) & \rho_0 \hat{v}_i \hat{v}_j + \\ (b) & \hat{v}_j (\rho v_i)'' + \hat{v}_i (\rho v_j)'' - \hat{v}_i \hat{v}_j \rho'' + \\ (c) & \dfrac{1}{\rho_0} (\rho v_i)'' \, (\rho v_j)'' - \dfrac{\hat{v}_j}{\rho_0} (\rho v_i)'' \rho'' - \dfrac{\hat{v}_i}{\rho_0} (\rho v_j)'' \rho'' + \dfrac{\hat{v}_i \, \hat{v}_j}{\rho_0} \rho''^2 + O(\rho''^3), \end{cases} \tag{62}$$

where

$$\hat{v}_i = \frac{(\rho v_i)_0}{\rho_0}, \tag{63}$$

which is analogous to $\tilde{v}_i$ but uses a steady base flow rather than a non-radiating base flow.

Term (a) is steady and so cannot contribute to sound production or propagation; term (b) is an interaction term, between the time-averaged mean flow and the fluctuation, although it is clearly incorrect to speak of flow-acoustic interaction, the fluctuation in this case being dominated by hydrodynamic unsteadiness (turbulence). Term (c) contains quadratic and higher order non-linearities dominated by hydrodynamic unsteadiness. It is terms of this kind that are referred to as 'source' in acoustic analogies that involve time-averaged base-flows, or Linearised Euler formulations.

The term $(\pi^\gamma)''$ is decomposed as:

$$\pi^\gamma = (\pi_0 + \pi'')^\gamma = \pi_0^\gamma + \gamma \pi_0^{\gamma-1} \pi'' + \frac{1}{2} \gamma (\gamma - 1) \pi_0^{\gamma-2} \pi''^2 + O(\pi''^3) \tag{64}$$

$$(\pi^\gamma)'' \approx \gamma \pi_0^{\gamma-1} \pi'' + \frac{1}{2} \gamma (\gamma - 1) \pi_0^{\gamma-2} (\pi''^2)''. \tag{65}$$

Finally, the term $\pi v_j$ is decomposed as follows:

$$\pi v_j = \frac{\pi \rho v_j}{\rho} = \begin{cases} (a) & \dfrac{\pi_0}{\rho_0}(\rho v_j)_0 \\ (b) & \dfrac{\pi_0}{\rho_0}(\rho v_j)'' + \hat{v_j}\pi'' - \dfrac{\pi_0}{\rho_0}\hat{v_j}\rho'' \\ (c) & \dfrac{1}{\rho_0}\pi''(\rho v_j)'' - \dfrac{\hat{v_j}}{\rho_0}\rho''\pi'' - \dfrac{\pi_0}{\rho_0^2}\rho''(\rho v_j)'' + \dfrac{\pi_0 \hat{v_j}}{\rho_0^2}\rho''^2 + O(\rho''^3), \end{cases} \tag{66}$$

where $(a)$ has no unsteady part, $(b)$ corresponds to interaction terms and $(c)$ to source terms; however, Sinayoko *et al.* show that term $(c)$ can be shown to be equal to zero.

Equations (59–61) are now re-written, the quadratic non-linear terms being placed on the right hand side, the interaction terms, between the mean-flow and the perturbation, being retained as 'propagation terms' on the left hand side:

$$\frac{\partial \rho''}{\partial t} + \frac{\partial}{\partial x_j}(\rho v_j)'' = 0, \tag{67}$$

$$\frac{\partial}{\partial t}(\rho v_i)'' + \frac{\partial}{\partial x_j}(\hat{v_j}(\rho v_i)'' + \hat{v_i}(\rho v_j)'' - \hat{v_i}\hat{v_j}\rho'') + \gamma \frac{\partial}{\partial x_i}\pi_0^{\gamma-1}\pi'' = f_{2i}, \tag{68}$$

$$\frac{\partial \pi''}{\partial t} + \frac{\partial}{\partial x_j}\left(\frac{\pi_0}{\rho_0}(\rho v_j)'' + \hat{v_j}\pi'' - \frac{\pi_0}{\rho_0}\hat{v_j}\rho''\right) = 0, \tag{69}$$

where the momentum equation source term $f_{2i}$ is defined as

$$f_{2i} \equiv -\frac{\partial}{\partial x_j}\left(\frac{1}{\rho_0}(\rho v_i)''(\rho v_j)'' - \frac{\hat{v_j}}{\rho_0}(\rho v_i)''\rho'' - \frac{\hat{v_i}}{\rho_0}(\rho v_j)''\rho'' + \frac{\hat{v_i}\,\hat{v_j}}{\rho_0}\rho''^2\right) - \frac{1}{2}\gamma(\gamma-1)\frac{\partial}{\partial x_i}(\pi_0^{\gamma-2}(\pi)^{"2})''. \tag{70}$$

Application of the two foregoing formulations to a model flow, where the flow is manipulated in such away that the sound-production mechanisms are clear, will help to more fully appreciate what the two formulations involve.

**Application to a model problem** We here provide a brief exposition of the model problem and main results. For more complete details the reader should refer to Sinayoko et al. (2011).

A Direct Numerical Simulation is performed wherein a laminar, axisymmetric jet is driven at the inflow by two different frequencies. The response of the jet comprises the growth of two hydrodynamic instabilities; these

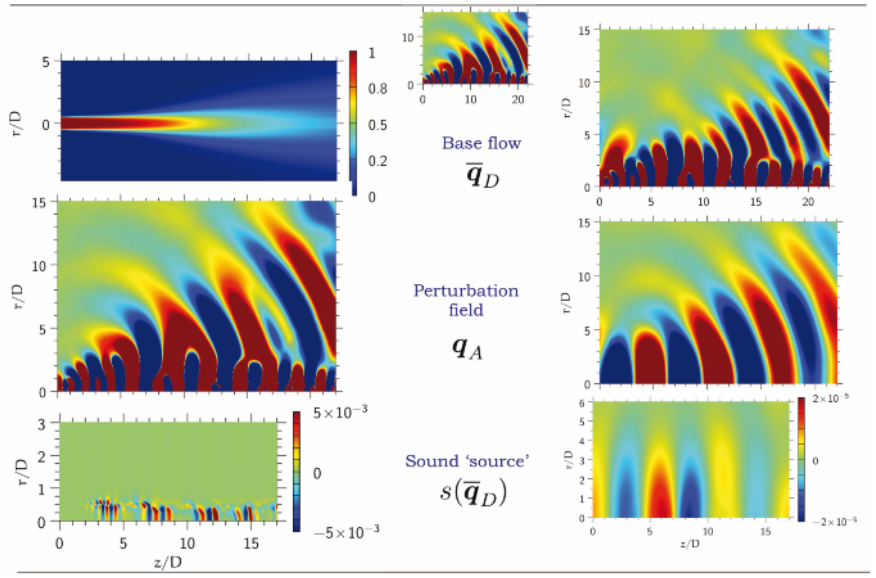


**Figure 1.** Top center: full flow solution; Left and right columns show, from top to bottom: base flow, perturbation and sound source corresponding to the two flow decompositions; left column :$\boldsymbol{q}_0 + \boldsymbol{q}''$; right column: $\overline{\boldsymbol{q}}_D + \boldsymbol{q}_A$.

undergo a non-linear interaction which results in a difference wave, and it is this difference wave that dominates the generation of sound waves. The instability waves each couple directly with the sound field, but this linear mechanism is weaker than that of the non-linear interaction.

The full solution of the model problem is shown in figure 1. The filtering operation used to separate 'radiating' and 'non-radiating' components of the flow is based on the free-space Green's function, and in this particular implementation the 'perturbation' is defined as the radiating component of the flow *at the dominant radiation frequency only.* It is for this reason that some radiating components remain in the base flow, $\overline{\boldsymbol{q}}_D$.

The considerable differences between what is referred to as 'base flow', 'perturbation' and, consequently, 'source' are illustrative of the degree to which different acoustic analogies will yield different interpretational frameworks: the mechanisms that we infer from the equations can differ as widely as the decompositions, base-flows, perturbations and sources with which they are associated. Much contemporary debate regarding the true physics

of sound production is fueled by this lack of universality.

We here draw attention to one importance difference in particular. In the case of the time-averaged base flow (which is what is used in Lilley or Linearised Euler formulations), the fluctuation is largely dominated, as stated earlier, by hydrodynamic unsteadiness, whereas the radiating fluctuation obtained by means of an acoustic filter is mainly acoustic. The difference in both amplitude and space-time structure between the two attests to this. As seen in figure 1, when a time-averaged base-flow is considered, the perturbation within the jet is dominated by hydrodynamic, convective scales. When the radiating/non-radiating decomposition is used, the perturbation shows an acoustic (radiating) scale throughout the jet. A corresponding difference in amplitude between the two perturbations (not shown in the figure, where colour scales are saturated) is also observed. This illustrates the extent to which it is incorrect to think of interactions terms of the kind $\boldsymbol{q}_0\boldsymbol{q}''$ as corresponding to mean-flow/acoustic interaction; the correct interpretation is that these terms are dominated by mean-flow/turbulence interactions, as is the interpretation attributed to such terms by students of incompressible turbulence (cf. George et al. (1984)), where such terms are referred to as slow-pressure terms.

Finally, Sinayoko et al. (2011) verify that when the time-averaged base flow is driven by the two source terms, the correct result is obtained in the acoustic field. Figure 2 shows this.

### 2.6 Conclusion

Two things are worth pointing out with regard to the results of the model problem considered above. The first is the difference between the two source terms; it clearly cannot be correct to refer to both of these as the 'source of sound'. Furthermore, because in this model problem the flow has been carefully manipulated so that the fluid dynamics and acoustic mechanisms are clear, we know that the dominant source mechanism comprises a non-linear interaction between two hydrodynamic instabilities; this interaction creates an acoustically-matched difference wave. The source identified by the formulation based on the decomposition into a predominantly non-radiating unsteady base-flow and a monochromatic, purely radiating disturbance resembles such a difference wave. The source obtained using a time-averaged base flow and corresponding disturbance does not. The former system does therefore appear to constitute a more physically pertinent description of the problem than the latter. The causal reading of the problem, as a one way transmission of fluctuation energy from 'source' to 'sound', also appears to be more justified by the former formulation. As evoked earlier,

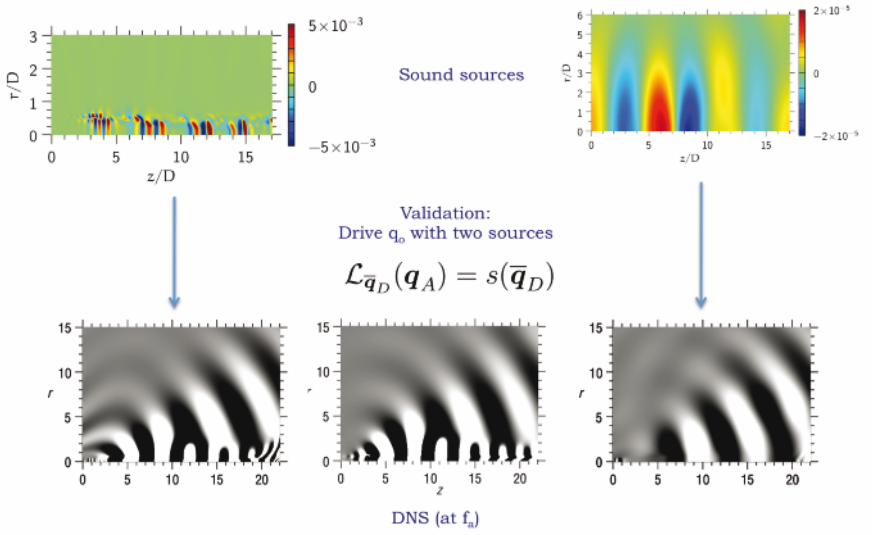


**Figure 2.** Result of driving the time-averaged base flow by both sources. Result is compared with the DNS result at the peak acoustic frequency. While the source term constructed from the non-radiating, unsteady base flow elicits a purely acoustic response, the source term associated with the time-averaged base flow causes the mean-flow to respond with both hydrodynamic and acoustic components. Both give the correct result in the acoustic field.

this improved consistency is also manifest in the response of the base-flow to excitation by the two sources; in the former case the response is purely acoustic, consistent with what has been denoted 'perturbation', whereas in the latter case the response is dominated, within the flow, by hydrodynamics: we therefore have a case in the latter situation where the cause is part of the effect and *vice versa*; this is clearly problematic. It should also be noted, however, that in both cases the correct solution is obtained in the sound field. This shows, as has been borne out over the past 10 years or so by means of numerical simulation, that all acoustic analogies are capable of providing a link between turbulence and sound; however, the differences illustrated by the foregoing study shows that we need to be careful with regard to the physical interpretations that we infer from analysis based on

acoustic analogies.

Where the question of the relationship between $\overline{\boldsymbol{q}}_D$ and $s(\overline{\boldsymbol{q}}_D)$ is concerned, further visualisation and analysis will always be necessary. The same is true with regard to the question of the dynamic law that underpins $\overline{\boldsymbol{q}}_D$. These observations constitute useful departure points for the experimental approach, and the remainder of these lectures will be concerned with outlining methodologies and tools that can be useful in this regard.

# 3 The modelling challenge

## 3.1 Introduction

As outlined in the previous section, estimation of the sound radiation from a turbulent flow, using an acoustic analogy, requires the solution of a propagation equation given a corresponding source term. If the source is not known exactly (such exact knowledge implies knowledge of the full Navier Stokes solution) it must be modelled, and the question of how best to construct this model arises.

Regardless of the acoustic analogy used, the source is a function of the flow turbulence, and so the question of source modelling is inseparable from that of turbulence modelling. In this section we consider the turbulent jet, and the link between this and sound sources. The way turbulence is perceived and modelled has changed considerably in the last fifty years, as has, correspondingly, our understanding of the jet as a source of sound. We therefore briefly trace out these evolutions, providing examples of some recent developments where the source modelling question is concerned.

## 3.2 A systematic approach to modelling

Analysis of aeroacoustic systems is, like that of most of complex fluid systems, largely an exercise in system reduction. We are interested in discerning the essential aspects of the fluid system with regard to the quantity (observable) that interests us (the radiated sound in the present case), our end objective being to come up with a simplified model of the flow (both *kinematically* and *dynamically*). And, of course, it is a prerequisite that this simplified model provide as accurate as possible a prediction of the radiated sound field: how best to model the flow turbulence as a sound source. The acoustic analogy can be useful as an aid, but, as we saw in the previous section, used in isolation it is not sufficient.

The information neglected in a simplified model of an aeroacoustic system can be seen as an error, and the success or failure of that model will be reflected by the degree to which the acoustic analogy considered is sensitive to that error. Note, however, that such errors can arise, or be perceived, in two quite different contexts. The errors might be due to there being incomplete flow information available to us. Or, alternatively, the 'error' might be something that we intentionally introduce, through the removal of flow information that we consider non-essential where the sound production problem is concerned. In the latter case, the missing information is something that we are required to consider and choose carefully. An analysis methodology is outlined in this section, concerned with such a *considered*

*removal of non-essential information*: we intentionally introduce considered and calculated 'errors'.

The sensitivity issue has been studied in an *ad hoc* manner by Samanta et al. (2006) with the former idea in mind: how sensitive are acoustic analogies to unwanted errors? The authors considered a DNS of a two-dimensional mixing layer, which they used in conjunction with a number of acoustic analogy formulations (Lighthill-like and Lilley-like formulations were assessed); the sound fields computed by all analogies showed good agreement with the DNS, consistent with the results of the model problem considered in the previous section. The full solution of the DNS was then artificially modified so as to introduce an error, which we here denote $\delta s(\mathbf{q})$. This error was produced through a manipulation of the coefficients of the POD modes [7] of the full solution. The sound field was then recomputed, by means of the different acoustic analogies, using the contaminated flow data, and the error in the sound field so computed was assessed in each case.

Different kinds of source error were explored: effects analogous to low-pass filtering, and the reduction of energy in narrow frequency bands, are two examples. In many cases the resultant error in the sound field was found to be similar for all of the acoustic analogies considered. For one particular case, however, where the error corresponds to a division of the first POD mode coefficient by 2 (this amounts to a significant reduction of the low frequency fluctuation energy of the flow), the Lighthill-like formulation showed greater sensitivity than the other formulations.

The problem can be thought about as follows. Consider an acoustic analogy, written in the general form $\mathcal{L}p = s(\mathbf{q})$. The parameter space of the source, $s(\mathbf{q})$, can be expressed in terms of an orthonormal basis, to which there corresponds an inner product; such is the case, for instance, for the POD basis of Samanta et al. (2006). If we now consider the eventual impact of the introduction of a small disturbance (which simulates a modelling error) to the source, $\delta s(\mathbf{q})$ (as per Samanta et al. (2006)), we are interested in the impact that this will have on the acoustic field, i.e. $\delta p$. The problem comes down to the following situation: if $\delta s(\mathbf{q}) \parallel \nabla\mathcal{L}$ then the sound field will be sensitive to small perturbations in the source, $\delta s(\mathbf{q})$. $\delta s(\mathbf{q})$ is in this case aligned with the direction of maximum sensitivity of the propagation operator $\mathcal{L}$ in the parameter space considered. If, on the other hand, $\delta s(\mathbf{q}) \perp \nabla\mathcal{L}$, then changes in $s(\mathbf{q})$ will have no impact on the sound field, $p$. [8]

This way of viewing the aeroacoustic problem means that the modelling

[7] see section 5 for an exposition of POD

[8] This shows that the arbitrary introduction of disturbances to, and subsequent comparison of, two different analogies cannot provide an unambiguous assessment, in an absolute sense, of the relative robustness of the two formulations. For, if the gradients

problem can be formulated in the following way: beginning with full flow information $\mathbf{q}$, from a numerical simulation for example, we are required to find the directions (in a suitably chosen parameter space) of the flow solution that can be eliminated without adversely affecting the quality of sound prediction. We must identify the 'errors' $\delta\mathbf{q}$, such that we obtain a simplified flow field, $\hat{\mathbf{q}} = \mathbf{q} - \delta\mathbf{q}$; the source computed from this simplified flow field, $s(\hat{\mathbf{q}})$, has an associated error, and this error must be such that the component of $s(\hat{\mathbf{q}})$ aligned with the propagation operator is unaffected.

The following analysis methodology, based on the above reasoning, is intended as a guide for the analysis of complex aeroacoustic systems, from the point of view of source mechanism identification and the design of simplified models (from both kinematic and dynamic standpoints).

*Analysis methodology*

1. Obtain full or partial information associated with the complete flow solution, $\mathbf{q}$ (whose dynamic law we know: the Navier-Stokes operator, $\mathcal{N}(\mathbf{q}) = 0$); this data could be provided by experimental measurements or from a numerical simulation;
2. Identify and extract, from $\mathbf{q}$, the observable of interest: the radiated sound in our case, $\mathbf{q}_A$;
3. Construct an observable-based filter, $\mathcal{F}_{\mathbf{q}_A}$, which, applied to the full solution removes information not associated with sound production, and thereby provides a reduced-complexity sound-producing flow skeleton (*kinematics*), $\hat{\mathbf{q}}_D = \mathcal{F}_{\mathbf{q}_A}(\mathbf{q})$;
4. Analyse $\hat{\mathbf{q}}_D$ with a view to postulating a simplified *ansatz* for the source, $s(\hat{\mathbf{q}}_D)$;
5. Using an acoustic analogy, compute $\hat{\mathbf{q}}_A = \mathcal{L}^{-1}s(\hat{\mathbf{q}}_D)$, and verify that $\min||\mathbf{q}_A - \hat{\mathbf{q}}_A||$;
6. Determine a reduced-complexity dynamic law, $\hat{\mathcal{N}}(\hat{\mathbf{q}}_D) = 0$, that governs the evolution of $\hat{\mathbf{q}}_D$.

Let us consider step 3 for a moment, as the observable-based filter, $\mathcal{F}_{\mathbf{q}_A}$, can be defined with varying degrees of rigour. The following are some possible scenarios. (i) In some situations the application of $\mathcal{F}_{\mathbf{q}_A}$ might be quite heuristic, e.g. no more than the simple observation of the flow—we see with relative ease that *this structure interacted with that to produce this aspect of the sound field*, whence we propose a model. (ii) Alternatively,

$\nabla\mathcal{L}_1$ and $\nabla L_2$ (where the subscripts 1 and 2 indicate the two analogies) have different directions in the parameter space, one will always be able to find a perturbation that causes one operator to appear less robust than the other.

it could comprise a more sophisticated flow visualisation, or perhaps a series of measurements giving quantitative access to the flow solution, from which a simplified model might be proposed, provided the essential mechanisms show themselves clearly in this data. However, in the context of high Reynolds number turbulent flows, it is frequently necessary to approach the design of $\mathcal{F}_{\mathbf{q}_A}$ in a more rigorous, methodological and objective, manner. Two further avenues can be pursued in this regard: (iii) it may be possible, using a purely theoretical deduction, to identify flow (or source) information that can be safely removed (examples are provided in what follows); and, (iv) signal processing tools can be used to decompose the complex system into more easily manageable 'building blocks', whose relative importance for sound production can then be tested.

Early analysis in aeroacoustics (1950s-1980s) was largely undertaken in contexts (i) and (iii), due to the limited capabilities of measurement and signal-processing. With the progressive improvement of the two latter disciplines, analysis in contexts (ii) and (iv) has become more common. In what follows we will show how a complete analysis will generally involve a combination of (i)-(iv).

In the following, we provide a short historical sketch (contexts (i) and (iii) are preponderant) outlining how the complexity of the turbulent jet was observed, considered, discerned and finally modelled with respect to both its internal turbulence mechanisms and the associated sound sources.

### 3.3 Turbulence: as a space-time chaos

When Lighthill first provided us with a theoretical foundation from which to model, study and understand jet noise, turbulence, both generally and in the specific case of the round jet, was considered to comprise a space-time chaos, devoid of any underlying order. The standard at that time for the kinematic description of turbulence structure could be found in turbulence theories such as that of Batchelor (1953): attempts to understand and model turbulence were based on the Reynolds Averaged Navier-Stokes (RANS) equations, where the only conceptual constructs invoked, aside from those expressed in the conservation equations, are those required for closure (Boussinesq's notion of eddy viscosity, for instance) on one hand, and, on the other, the flow entities supposed to participate in the physical processes associated with the various terms that appear in the RANS equations: fluctuation energy is 'produced', 'transported', 'dissipated' by virtue of interactions between stochastic flow 'scales' or 'eddies'.

Figure 3(a), which shows a schlieren photograph of a turbulent jet, gives a visual sense of this stochastic character. Source terms in acoustic analogies

were constructed in accordance with this conceptual picture of turbulence. Lighthill (1952) assumed a statistical distribution of uncorrelated eddies throughout the source region, and this led to the well known $U^8$ power law for the isothermal turbulent jet. However, predictions based on Lighthill's analogy, using such kinematic models for the turbulence, do not explain all of the features of subsonic jet noise: at low emission angles (with respect to the downstream jet axis), for example, the $U^8$ power law does not hold, and the narrower spectral shape is generally not well predicted. Something is missing from this combination of acoustic-analogy formulation and source representation.

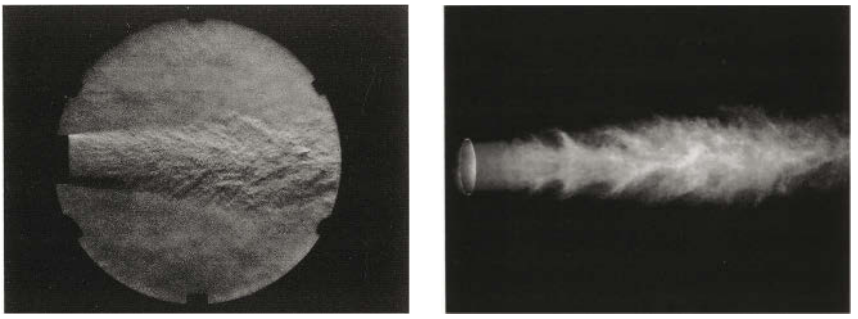

(a) (b)

**Figure 3.** Different visualisation techniques of jets at similar Reynolds number, taken from Crow and Champagne (1971). (a) Schlieren photography; $Re = 1.06 \times 10^5$; (b) $CO_2$ fog visualisation using sheet illumination; $Re = 7.5 \times 10^4$.

### 3.4 Turbulence and 'coherent structures'

Soon after the first attempts by Lighthill and his successors to predict the sound radiated by turbulent jets a change occurred in the way turbulence is perceived. Turbulent flows were observed to be more ordered than had previously been believed, and a new conceptual flow entity was born, sometimes referred to as a 'coherent structure', or, alternatively, a 'wave-packet'. Mollo-Christensen (1967) was one of the first to report such order in the case of the round jet: "...although the velocity signal is random, one should expect to see intermittently a rather regular spatial structure in the shear layer.". A series of papers followed, confirming these observations and postulating on the nature of this order (Crow and Champagne (1971), Brown

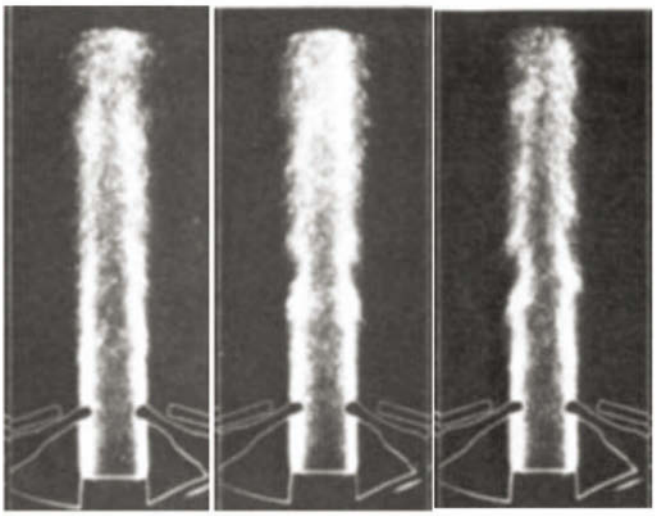

**Figure 4.** Flash Schlieren images of jets ($Re = 5 \times 10^5$; $M = 0.83$), taken from Moore (1977). Left: random ensemble average; middle: conditional average using axisymmetric nearfield pressure signature as trigger; right: conditional average using a single nearfield microphone as trigger (this educes the antisymmetric organisation).

and Roshko (1974) and Moore (1977) to cite just a few). Figure 3(b), taken from Crow and Champagne (1971), provides a visual sense of this underlying order: by changing visualisation technique, using sheet illumination and carbon dioxide fog, rather than the fine grained patterns revealed by the schlieren technique, an axially-aligned waveform with wavelength of the order of the jet diameter is observed.

A further illustration of the underlying organisation present in high Reynolds number jets is shown in figure 4, which shows the difference between time-averaged and conditionally-averaged images of round jets at high Reynolds and Mach numbers. We will discuss conditional averaging techniques later in more detail.

### *Order in chaos*

The following series of citations gives a sense of the impression that this

discovery made on researchers working in the field of both turbulence and aeroacoustics.

"The apparently intimate connexion between jet stability and noise generation appears worthy of further investigation" – Mollo-Christensen and Narasimha (1960)

"[jet noise] is of interest as a problem in fluid dynamics in the class of problems which involve the interaction between instability, turbulence and wave emission" – Mollo-Christensen (1963)

"There appear to be at least two distinguishable types of emitted sound, one dominating at very low frequencies and another dominating at high frequencies. A relation which gives a smooth interpolation between these asymptotic ranges would prove useful, if one could be invented." – Mollo-Christensen (1963)

"The data suggest that one may perhaps represent the fluctuating [hydrodynamic] pressure field in terms of rather simple functions. For example, one may consider the jet as a...semi-infinite antenna for sound..." – Mollo-Christensen (1967)

"...although the velocity signal is random, one should expect to see intermittently a rather regular spatial structure in the shear layer." – Mollo-Christensen (1967)

"We therefore decided to stress measurements near and in the jets, hoping to discern some of the simpler features of the turbulent field. We also did measure for field pressures, and intended to see if we could not connect the two sets of observations somehow, using the equations of sound propagation." – Mollo-Christensen (1967)

"It is suggested that turbulence, at least as far as some of the lower order statistical measures are concerned, may be more regular than we may think it is, if we could only find a new way of looking at it." – Mollo-Christensen (1967)

"The mechanics of turbulence remains obscure, so that it comes as a matter of some relief to find that the motions which now interest us are coherent on a large scale...Such large eddies might be readily recognisable as a coherent transverse motion more in the category of a complicated laminar

flow than chaotic turbulence. In any event the eddies generating the noise seem to be much bigger than those eddies which have been the subject of intense turbulence study. They are very likely those large eddies which derive their energy from an instability of the mean motion..." – Bishop et al. (1971)

"These [measurements] suggest that hidden in the apparently random fluctuations in the mixing layer region is perhaps a very regular and ordered pattern of flow which has not been detected yet" – Fuchs (1972)

"Whether one views these structures as waves or vortices is, to some extent, a matter of viewpoint." – Brown and Roshko (1974)

"All this evidence suggests that the turbulence in the mixing layer of the jet behaves like a train similar to the hydrodynamic stability waves propagating in the shear flow." – Chan (1974)

"The dominant role of the dynamics and interaction of the large structure in the overall mechanism that eventually brings the two fluids into intimate contact becomes apparent. It is clear that any theoretical attempts to model the complex mixing process in the shear layer must take this ubiquitous large structure into account." – Dimotakis and Brown (1976)

"Turbulence research has advanced rapidly in the last decade with the widespread recognition of orderly large-scale structure in many kinds of turbulent shear flows...some measure of agreement seems to have been reached among investigators on the general properties of the coherent motions." – Crighton and Gaster (1976)

"...the turbulence establishes an equivalent laminar flow profile as far as large-scale modes are concerned." – Crighton and Gaster (1976)

"In the last years our understanding of turbulence, especially in jets, has changed rather dramatically. The reason is that jet turbulence has been found to be more regular than had been thought before." – Michalke (1977)

"This 'new-look' in shear-flow turbulence, contrary to the classical notion of essentially complete chaos and randomness, has engendered an unusually high contemporary interest in the large-scale structures." – Hussain and Zaman (1981)

"The last twenty years of research on turbulence have seen a growing

realisation that the transport properties of most turbulence shear flows are dominated by large-scale vortex motions that are not random." – Cantwell (1981)

"Suddenly it was feasible and reasonable to draw a picture of turbulence! The hand, the eye, and the mind were brought into a new relationship that had never quite existed before; cartooning became an integral part of the study of turbulence." – Cantwell (1981)

As we see from many of the above citations, stability theory is frequently evoked as a possible theoretical framework for the dynamical modelling of the flow behaviour described above. However, a full treatment of hydrodynamic stability is beyond the scope of this lecture, and so we will simply list, briefly, a few of the different kinds of stability frameworks that are sometimes used to model the organised component of turbulent shear flows. We would also point out that the application of stability theory to turbulent flows, where the stability of a time-averaged mean-flow is considered, is not entirely rigorous (hydrodynamic stability analysis is self-consistent only when applied to laminar flows), involving a number of assumptions: one of these is that there exists a scale-separation between a large-scale organised component of the flow and a finer-grained, stochastic, 'background' component; the latter establishes a mean-flow profile that can sustain large-scale instabilities, and acts, furthermore, as a kind of eddy viscosity that damps the large-scale instabilities.

The first stability calculations with respect to the round jet were performed by Batchelor and Gill (1962) who studied the temporal stability problem for a plug flow. Michalke and Timme (1967) looked at the temporal instability of a finite-thickness, two-dimensional shear layer, while Michalke (1971) considered the spatial instability of a finite thickness axisymmetric shear-layer. Crighton & Gaster (1976) took account of the slow axial variation of the shear-layer thickness. Mankbadi and Liu (1984) made an attempt to include the effect of non-linearities. Tam and Morris (1980) used matched asymptotic expansions to obtain the acoustic field of a two-dimensional compressible mixing-layer; Tam and Burton (1984) then extending this effort to the case of a round jet. More recent approaches have been based on linear and non-linear Parabolised Stability Equations, as used by Colonius et al. (2010) for example, and Global Stability approaches, applied for instance to the problem of heated jets by Lesshafft et al. (2010).

### 3.5 Coherent structures as a sound source

We now turn our attention to the mechanisms by which such coherent structures may be active as sound sources. We will work in the context of Lighthill's acoustic analogy, whence by means of theoretical considerations it will be possible to gain some insight regarding pertinent simplifications. We are, therefore, in what follows, working in the context of steps 3, 4 and 5 of the analysis methodology outlined earlier; and with regard to the filtering operation, $\mathcal{F}_{\mathbf{q}_A}$, we are in context (iii).

**The wavepacket source *ansatz*** Mollo-Christensen (1967) appears to have been first to propose a mechanism by which coherent structures might be active as a source of sound. Observing that the nearfield pressure signature of the subsonic jet presents a surprising degree of organisation in the $(y_1, \tau)$ plane, he suggested that such organisation could result in the jet behaving as a 'semi-infinite antenna for sound'. Where this kind of sound production is concerned, a convected wavepacket constitutes a pertinent model for the organised component of the flow. Such a model, first explored by Michalke (1971) and Crow (1972), continues to be widely used by researchers today, even if there is probably some disagreement with regard to the salient sound-producing features and dynamic law of such wavepackets.

Our presentation of the wavepacket sound source is organised as follows:

- We begin by introducing the basic wavepacket source *ansatz*, as proposed by Michalke (1971), Crow (1972) (see also Crighton (1975)),
- We then outline some of the arguments used to justify its simple line-source form: the elimination of the radial dimension is a good example of observable-based simplification,
- We next present a comparison of experimentally obtained acoustic data with the sound field characteristics of the wavepacket model,
- We then discuss, in greater detail, the radiation mechanism associated with wavepackets, exploring a number of different kinds of behaviour which lead to its being enhanced:
  1. Spatial modulation,
  2. Temporal modulation,
  3. Temporally-localised wavepacket truncation,
  4. Space-time 'jitter'.
- Finally, we present, in section §4, two case studies, in which a number of numerical databases (obtained both by Large Eddy Simulation and by Direct Numerical Simulation) are analysed, following the methodology outlined earlier, and the salient sound-producing features of wavepackets thereby educed.

**The basic wavepacket model** First attempts to explore the wavepacket *ansatz* as a kinematic model for the organised component of the jet were made by Michalke (1971), Crow (1972) (see also Crighton (1975)). The physical problem considered is that of small amplitude acoustic disturbances propagating through a quiescent, homogeneous medium, as a result of an externally-imposed source term:

$$\frac{1}{c_o^2}\frac{\partial^2 p(\boldsymbol{x},t)}{\partial t^2} - \nabla p(\boldsymbol{x},t) = s(\boldsymbol{y},t), \tag{71}$$

where the source takes the following form:

$$s(\boldsymbol{y},t) = \frac{\partial^2}{\partial y_1^2} 2\rho_0 U\tilde{u}\frac{\pi D^2}{4}\delta(y_2)\delta(y_3)\mathrm{e}^{(\omega t-\kappa_y y_1)}\mathrm{e}^{(-y_1^2/l^2)}. \tag{72}$$

The solution of the spherical wave equation to an externally-imposed excitation of this kind is:

$$p(\mathbf{x},t) = -\frac{\rho_0 U\tilde{u}M_c^2(kD)^2 L\sqrt{\pi}\cos^2\theta}{8|\mathbf{x}|}\mathrm{e}^{-\frac{L^2k^2(1-M_c\cos\theta)^2}{4}}\mathrm{e}^{\mathrm{i}\omega\left(t-\frac{|\mathbf{x}|}{c}\right)}, \tag{73}$$

where $M_c$ is the Mach number based on the phase velocity of the convected wave, $U_c$.

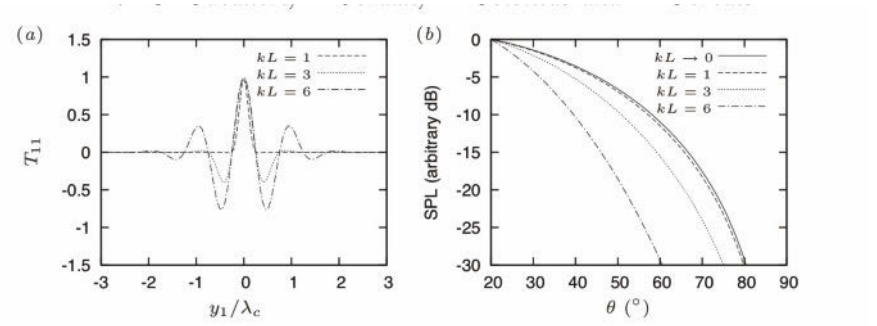


**Figure 5.** Effect of axial compactness parameter, $kL$, on directivity.

As outlined in section §2, equation 73 results from a convolution of the source *ansatz* with the free-space Green's function, this operation identifying the source characteristics to which the radiated sound field is sensitive.

One of these characteristics, visible in the solution, is the source compactness, $kL$. Figure 5 shows how for small values of $kL$ the source is compact, while for larger values it becomes non-compact, exhibiting numerous oscillations over its spatial extent. The corresponding dependence of the sound field directivity is shown in the right-hand figure: the less compact the source, the more the sound field is 'beamed', due to an antenna effect, to shallow axial angles. For $kL = 6$ the directivity pattern is close to exponential; sources exhibiting such exponential directivity are termed superdirective (Crighton and Huerre (1990)).

It can be seen in equation 72 that the source is concentrated on a line (by $\delta(y_2)\delta(y_3)$). This may seem strange considering that the turbulent region of a propulsive jet fills a volume that is approximately bounded by a conical surface. This simplification can be justified, however, by appealing to the radiation efficiency of different azimuthal modes of a cylindrical source (which is a slightly better approximation to the real dimensions of a jet, particularly when one considers the regions of maximal turbulence intensity: these lie on such a cylindrical surface). In the following section we outline this justification; this is an exercise in system reduction based purely on theoretical arguments: we use the Lighthill acoustic analogy formulation to demonstrate how certain 'directions' of the source system can be disregarded: the conclusion that we come to is that equation 72 is a reasonable approximation for the coherent structures where low-angle sound emission is concerned.

**Radiation efficiency of azimuthal modes** The following is taken from Cavalieri et al. (2010b) and Cavalieri et al. (2011a), similar analysis being found in Michalke (1970). Consider a source term of the form

$$T_{11}(\mathbf{y},\tau) = \rho_0 U \tilde{u} R \delta(r-R) \mathrm{e}^{\mathrm{i}(\omega\tau - k y_1)} \mathrm{e}^{-\frac{y_1^2}{L^2}} C_m \mathrm{e}^{\mathrm{i}m\phi}. \tag{74}$$

Where $m$ denotes azimuthal Fourier mode number, and $C_m$ the corresponding Fourier coefficient. The corresponding solution of the wave equation can be written

$$p(\mathbf{x},t) = \frac{\rho_0 U \tilde{u} R^2}{4\pi c^2 |\mathbf{x}|} \frac{\partial^2}{\partial t^2} \iint \mathrm{e}^{\mathrm{i}\left[\omega\left(t - \frac{|\mathbf{x}-\mathbf{y}|}{c}\right) - k y_1\right]} \mathrm{e}^{-\frac{y_1^2}{L^2}} C_m \mathrm{e}^{im\phi} \mathrm{d}\phi \mathrm{d}y_1. \tag{75}$$

We assume, without loss of generality, that the observer is at $\Phi = 0$ and $x_2 = 0$ in cartesian coordinates, where $\Phi = \tan^{-1}(x_2/x_3)$. The distance can be expressed, with a far-field assumption, as,

$$|\mathbf{x}-\mathbf{y}| \approx |\mathbf{x}| - y_1 \cos\theta - R\cos\phi\sin\theta, \tag{76}$$

where $\theta$ is the angle of $\mathbf{x}$ to the jet axis. The solution thus becomes

$$p(\mathbf{x},t) = \frac{\rho_0 U \tilde{u} R^2}{4\pi c^2 |\mathbf{x}|} \frac{\partial^2}{\partial t^2} \int\int \mathrm{e}^{\mathrm{i}\left[\omega\left(t-\frac{|\mathbf{x}|-y_1\cos\theta-R\cos\phi\sin\theta}{c}\right)-ky_1\right]} \mathrm{e}^{-\frac{y_1^2}{L^2}} C_m \mathrm{e}^{\mathrm{i}m\phi} \mathrm{d}\phi \mathrm{d}y_1, \tag{77}$$

which can be rearranged as

$$p(\mathbf{x},t) = \frac{\rho_0 U \tilde{u} R^2}{4\pi c^2 |\mathbf{x}|} \frac{\partial^2}{\partial t^2} \int_{-\infty}^{\infty} \mathrm{e}^{\mathrm{i}\left[\omega\left(t-\frac{|\mathbf{x}|-y_1\cos\theta}{c}\right)-ky_1\right]-\frac{y_1^2}{L^2}} \mathrm{d}y_1 \int_0^{2\pi} C_m \mathrm{e}^{\mathrm{i}\left(m\phi-\omega\frac{R\cos\phi\sin\theta}{c}\right)} \mathrm{d}\phi. \tag{78}$$

Evaluation of the azimuthal integral

$$I_1 = \int_0^{2\pi} \mathrm{e}^{\mathrm{i}\left(m\phi-\omega\frac{R\cos\phi\sin\theta}{c}\right)} \mathrm{d}\phi, \tag{79}$$

which can be expressed as

$$I_1 = \int_0^{2\pi} \mathrm{e}^{\mathrm{i}(m\phi)} \mathrm{e}^{(-\mathrm{i}\pi \mathrm{St} M\cos\phi\sin\theta)} \mathrm{d}\phi, \tag{80}$$

indicates the radiation efficiency of azimuthal mode $m$; i.e. the capacity of that azimuthal source mode to couple with the acoustic field.[9] This integral can be expressed in terms of Bessel functions $J_m$,

$$J_m(x) = \frac{1}{2\pi \mathrm{i}^m} \int_0^{2\pi} \mathrm{e}^{ix\cos\phi} \mathrm{e}^{\mathrm{i}m\phi} \mathrm{d}\phi, \tag{81}$$

giving

$$I_1 = (-\mathrm{i})^m 2\pi J_m(\pi \mathrm{St} M \sin\theta). \tag{82}$$

For $\mathrm{St}M\sin\theta = 0$ the $I_1$ integral yields $2\pi$ for $m = 0$, and 0 for all other values of $m$. This means that, if we neglect retarded time differences along the azimuthal direction, which is justified if this direction is acoustically compact (i.e., the acoustic wavelength is much larger than the azimuthal wavenumber, which being always smaller than the jet diameter, $D$, allows

[9] Or, stated otherwise, the extent to which that mode is aligned with the propagation operator. If we find that certain modes are not so aligned, this will be an indication that there neglect constitutes a pertinent modelling simplification.

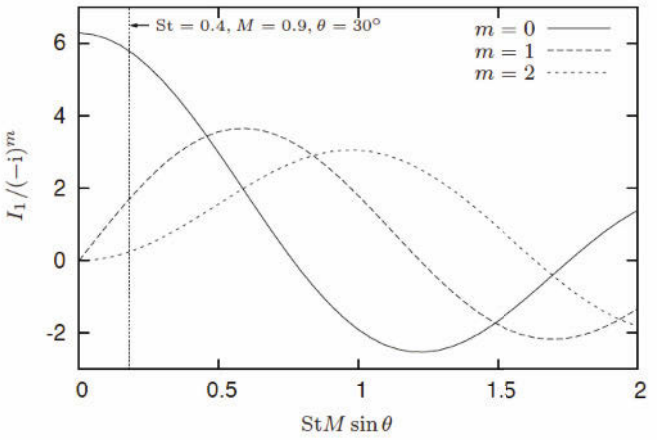


**Figure 6.** Results for the $I_1$ integral

the compactness criterion to be expressed in terms of the jet diameter: $D/\lambda = \mathrm{St}M$) only axisymmetric wave-packets can radiate. In other words, if the wave-packet diameter $D$ is compact, or, if the observation angle $\theta$ is small, only the axisymmetric wave-packet has significant radiation. This is always true for $\theta = 0$ and $\theta = \pi$, i.e. for an observer on the jet axis (Michalke (1970); Michalke and Fuchs (1975); Michel (2009)).

Figure 6 shows the $I_1$ integral, divided by $(-\mathrm{i})^m$ so as to yield a real quantity. We see that the integral of $m = 0$ decays from its compact value of $2\pi$, eventually goes to zero, and then oscillates. The integrals for the higher azimuthal modes are zero at the compact limit, as expected from the properties of the Bessel functions; they go from zero to a certain value, which is of the same order of the $m = 0$ integral, and then oscillate.

In order to appreciate the implications for a realistic jet flow, consider the sound radiation to low axial angles from a high Mach number subsonic jet. Taking $\theta = \pi/6$, $M = 0.9$ and $\mathrm{St} = 0.4$, we have $\mathrm{St}M\sin\theta = 0.18$, and in this case, as seen in fig. 6, we can, if we have similar amplitudes $C_m$ for the different $m$ values, neglect all modes $m > 0$ and consider the compact limit ($I_1 = 2\pi$ for $m = 0$) as a first approximation; the $I_1$ integral for $m = 1$ yields a sound intensity 10dB lower than that for $m = 0$, the integrals for higher $m$ modes being lower still. Suzuki and Colonius (2006) have provided experimental evidence showing that the peak amplitudes, $C_m$, for azimuthal modes $m = 0$ and $m = 1$ are similar, the amplitudes of mode $m = 2$ being

somewhat lower.

If we retain only the axisymmetric wave-packet and approximate $I_1$ as $2\pi$, we have

$$p(\mathbf{x},t) = \frac{\rho_0 U \tilde{u} R^2}{2c^2|\mathbf{x}|}\frac{\partial^2}{\partial t^2}\int C_0 \mathrm{e}^{\mathrm{i}\left[\omega\left(t-\frac{|\mathbf{x}|-y_1\cos\theta}{c}\right)-ky_1\right]}\mathrm{e}^{-\frac{y_1^2}{L^2}}\mathrm{d}y_1, \tag{83}$$

and integration gives

$$p(\mathbf{x},t) = -C_0\frac{\rho_0 U\tilde{u}M_c^2(kD)^2L\sqrt{\pi}\cos^2\theta}{8|\mathbf{x}|}\mathrm{e}^{-\frac{L^2k^2(1-M_c\cos\theta)^2}{4}}\mathrm{e}^{\mathrm{i}\omega\left(t-\frac{|\mathbf{x}|}{c}\right)} \tag{84}$$

which is the same result obtained using the line source in equations 71, 72 and 73. This means that for small values of the parameter $\mathrm{St}M\sin\theta$, the use of a wave-packet concentrated on a line leads to the same result as a surface wave-packet, justifying therefore the use of a line distribution for $T_{11}$, whose amplitude is that of the azimuthal mean of the $u$ fluctuation on the jet lipline. We will see, later, the extent to which this considerably simplified source model, and variants thereof, can mimic the sound-producing behaviour of a turbulent jet. In particular, we will be interested in some important additional modifications, identified thanks to the application of the analysis methodology outlined earlier, which are necessary in order that the *ansatz* be capable of producing quantitative agreement with the sound field radiated by the turbulent jet. First, however, let us examine some experimental data, comparing, qualitatively, with the basic wavepacket *ansatz* outlined above.

**Experimental evidence of wavepacket radiation** The following results are taken from Cavalieri et al. (2011b). The experiments were performed at the Bruit & Vent jet-noise facility of the Pprime Institute. The setup is shown in figure 7. The exit diameter of the jet is $D = 0.05m$, the flow is isothermal, and the exit velocity is varied over the Mach number range $0.3 < M < 06$; the corresponding Reynolds number range is $3.7\times10^5 < Re < 5.7\times10^5$, and the boundary layer is tripped in all cases so as to ensure that at the outlet it is fully turbulent. Acoustic measurements are performed by means of an azimuthal distribution of six microphones at a radial distance of $35D$, and the axial position of the ring array was variable. In this way the directivity of the sound field, decomposed into azimuthal Fourier modes, can be studied. These measurements can then be compared with the sound field of the wavepacket *ansatz* discussed above; in particular we focus on the axisymmetric component. Figure 7(b) shows the directivity in terms of both the overall SPL and the contributions from

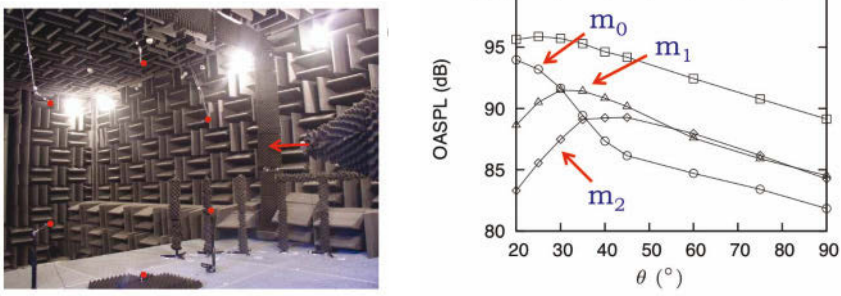


(a) (b)

**Figure 7.** (a) Jet noise experiment assessing azimuthal structure of the acoustic field radiated by moderate Mach number jets; $0.3 < M < 06$, $< Re <$. Red arrow shows direction of jet; red circles indicate the positions of the 6 azimuthally-distributed microphones; (b) OASPL: squares: total; contributions from azimuthal modes m=0, m=1 & m=2 indicated in figure. Note dominance of axisymmetric mode in downstream radiation.

each of the first three azimuthal Fourier modes, $m = 0$, $m = 1$ and $m = 2$. The axisymmetric component, $m = 0$, dominates the downstream radiation, sideline radiation comprising larger contributions from modes $m = 1$ and $m = 2$.

The dominance of the low-angle radiation by the axisymmetric mode is consistent with the foregoing analysis of the efficiency of azimuthal source modes, suggesting the existence of wavepacket radiation. By continuing to interrogate the experimental data with respect to the wavepacket model characteristics, we can evaluate the extent to which this model is pertinent.

Concentrating now on the lower emission angles, assessing the power spectral density as a function of emission angle and azimuthal Fourier mode, we obtain the result shown in figure 8. As we move from 40° to 20° we observe the progressive emergence of the axisymmetric component of the power spectrum, and we note that this emergence occurs over a relatively narrow spectral range, with peak frequency $St_D = 0.2$. The energy of the axisymmetric component of the sound field finds itself concentrated at low angles (highly directive) and across a relatively narrow range of frequency. At the lowest emission angles the peak of the overall spectrum is almost entirely axisymmetric, the energy of mode $m = 0$ being $10dB$ (that is one

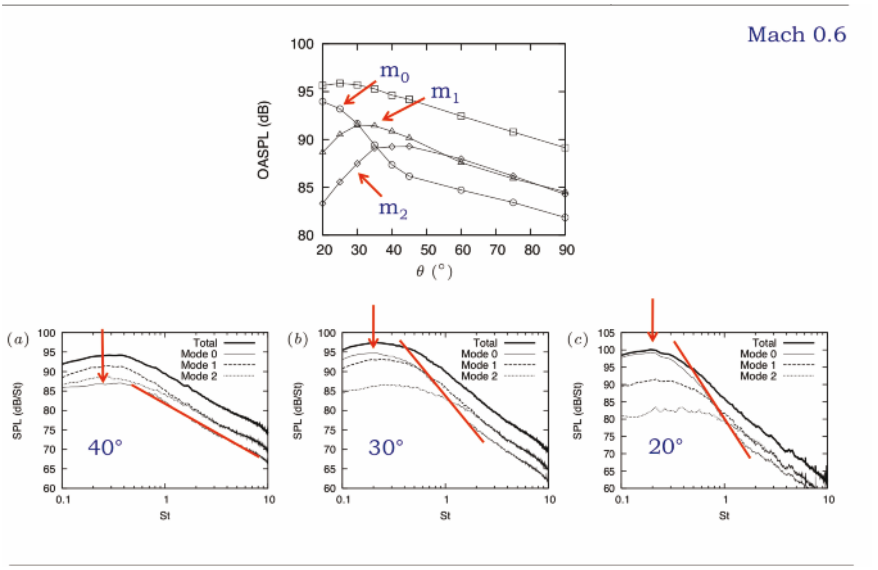


**Figure 8.** Power spectra of azimuthal modes 0, 1 & 2 at low emission angles.

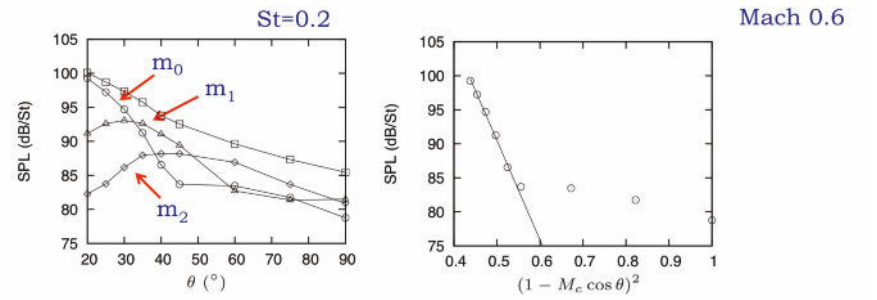


**Figure 9.** Narrowband-filtered (at $St_D = 0.2$) directivity of azimuthal modes and comparison of axisymmetric mode with wavepacket *ansatz*. Axisymmetric component of experimentally obtained sound field is superdirective (exponential polar decay) in agreement with the wavepacket model

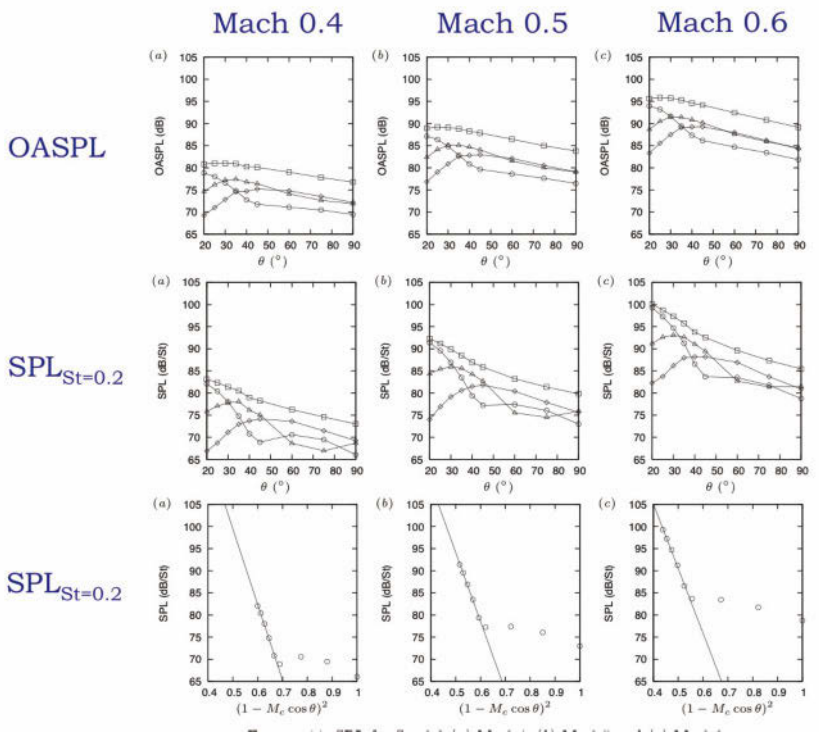


**Figure 10.** Azimuthal mode directivities as a function of Mach number. Axisymmetric mode is superdirective for all Mach numbers; indicates wavepacket radiation even at low Mach number

order of magnitude) greater than the next most energetic azimuthal mode, $m = 1$. The narrowband character of the emergence of the axismmetric mode, whose energy is concentrated at $St_D = 0.2$, justifies an assessment of the directivity of the SPL in a narrow frequency range centered at this frequency. The result is shown in figure 9(a), where the downstream directivity of the axisymmetric component at this frequency is even more marked. Comparison can now be made with the directivity factor of the wavepacket *ansatz*, $(1 - M_c \cos\theta)^2$; this is done in figure 9(b). The exponential character of the axisymmetric component of the sound field, when plotted as a function of this wavepacket directivity factor again suggests that the associated underlying source mechanism is associated with an axially extended

wavepacket of the kind modelled by equation 72. The term *superdirectivity* was coined by Crighton and Huerre (1990) to describe such directivity.

It is now of interest to study two further aspects of the experimental sound field: the Mach number dependence and the spectral scaling; both will allow further insight with regard to the possibility that the downstream radiation is underpinned by these relatively simply wavepacket source functions. Figure 10 shows the OASPL and narrowband-filtered SPL as a function of emission angle for the different azimuthal Fourier modes of the sound field, as a function of jet Mach number. The result shows that precisely the same behaviour observed at Mach 0.6 is also observed at lower Mach number, suggesting that wavepacket radiation is a dominant mechanism for low-angle emission, even at low Mach number.

Finally, we assess the scaling of spectra for the modes $m_0$ and $m_1$, as a function of Mach number, for emission angle $\theta = 30°$. The result is shown in figure 11, where both Strouhal ($St_D = fD/U_j$) and Helmholtz ($He = D/\lambda$) numbers are assessed. For the axisymmetric component of the sound field we find that Helmholtz scaling best collapses the sound spectra. As the Helmholtz number is the ratio of a characteristic flow scale to a characteristic scale of the sound field, the fact that this parameter collapses the axisymmetric component of the sound field suggests that the associated source is non-compact, as it suggests that this component of the sound field is sensitive to the ratio between flow scales and acoustic scales; this would not be so for a compact source, where a clear scale separation exists between acoustic waves and flow eddies.

By comparing the experimental data with the details of the wavepacket *ansatz*, it is possible to make a quantitative estimate of the wavepacket compacntess parameter, $kL$, which can be written as

$$Lk = \frac{2\pi}{M_c} He \frac{L}{D}. \tag{85}$$

Considering the jet at $M = 0.6$, we have, $M_c = 0.36$, $He = 0.12$ and $D = 0.05$. For the same jet the directivity of the axismmetric mode is characterised by a decrease of $15.6dB$ over the angular range $20° < \theta < 45°$, which allows us to estimate that the compactness parameter, $Lk = 6.5$. Comparison with figure 5, gives a sense of the corresponding wavepacket structure; this value, which suggests that the wavepacket extends over an axial region of about $6D$, is consistent with the analysis of Hussain and Zaman (1981), who educed coherent structures from low Mach number turbulent jets by means of conditional averaging of hotwire measurements.

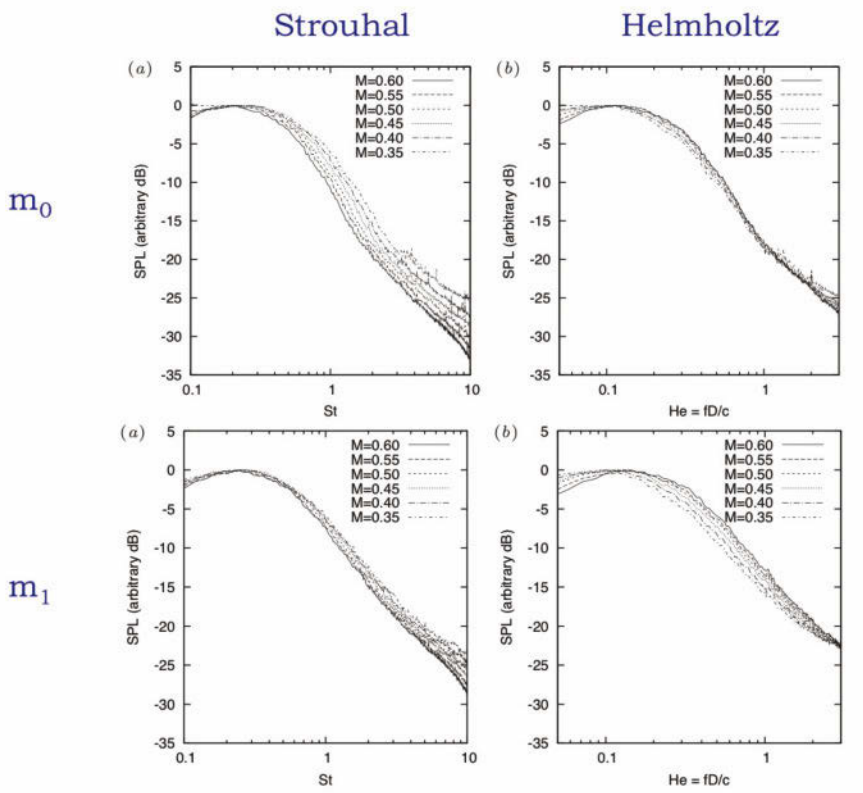


**Figure 11.** Scaling of azimuthal modes 0 and 1. Axisymmetric mode scales best with Helmholtz number, $He = D/\lambda$, suggesting that it is associated with a non-compact source. Substituting the experimental parameters into the wavepacket model we can deduce that $Lk = 6.5$; comparison with figure5 shows that this implies wavepacket with a spatial structure comprising about three oscillations, extended over approximately $6D$, i.e. from the jet exit to beyond the end of the potential core.

**The radiation mechanism** Let us now consider the details of the mechanism by which sound sources, and in particular, 'coherent structures', excite acoustic modes in turbulent flows. The mechanism can be understood by considering the acoustic analogy, written down either as a partial differential equation, or expressed in terms of its integral solution; time-domain,

frequency-domain and linear alebraïc formulations of both the inhomogeneous PDE and its integral solution can be helpful in understanding the essentials: the sound production mechanism can be thought about in three different ways; we can say that:

1. Space-time inhomogeneity of the source field is such that cancellation (in time-delayed coordinates) between regions of positive and negative stresses is incomplete; the fluid medium thus finds itself subjected to compressions and rarefactions that engender a propagative energy flux,
2. The propagation operator has an acoustic response to only those components of the source field that are acoustically-matched: those that satisfy the dispersion relation $\omega^2 = c_0^2|\boldsymbol{\kappa}|^2$; in terms of the integral solution we can say that the Green's function filters out, from the full range of source scales, only those that satisfy that dispersion relation,
3. In terms of linear algebra we can say that the propagator maps to the farfield those components of the source with which it is aligned: $\mathcal{L} \parallel s(\boldsymbol{q})$.

In the case of the wavepacket, these different scenarios can be represented schematically as in figure 12.

Let us now consider a number of different kinds of physical wavepacket behaviour that can lead to such radiation, before going on to explore data from turbulent jets. The following is taken from Cavalieri et al. (2011a) and Cavalieri et al. (2010b).

**Spatial modulation** The wavepacket characteristic most often referred to in the literature as important for the production of radiating sound energy is its spatial modulation. A subsonically-convected spatial sinusoid of constant amplitude and infinite spatial extent contains only non-radiating scales, because $\omega < k_x c$. However, any truncation or spatial modulation of the amplitude of that wavepacket will cause its axial wavenumber spectrum to broaden, and in this way some of the wavepacket energy will find itself in the acoustically-matched region of the spectrum. Figure 12 illustrates this: (a) shows non-radiating and radiating space-time structures; (b) shows the frequency-wavenumber spectrum of a radiating wavepacket—the tail of the spectrum that finds itself in the radiating sector causes sound radiation.

**Temporal modulation** A further feature of the unsteadiness associated with the orderly part of a turbulent jet is its intermittency. The earlier citations from Mollo-Christensen recognise this. A further citation from Crow

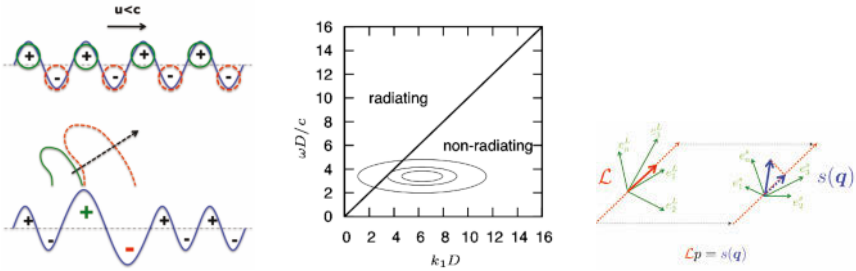


(a) (b) (c)

**Figure 12.** Different ways of thinking about the wavepacket radiation mechanism: (a) Space-time representation: amplitude inhomogeneities lead to incomplete cancellation, and associated compressions and rarefactions; (b) frequency-wavenumber representation; mechanism can be thought of as a filter that only passes the source components that satisfy $\omega^2 = c_0^2|\boldsymbol{\kappa}|^2$; (c) Representation in terms of linear algebra: mapping to the farfield of source by propagation operator: directions of the source, $s(\boldsymbol{q})$, that are parallel to the propagator, $\mathcal{L}$, get mapped to the farfield.

and Champagne (1971) is also relevant; they observed, by means of flow visualisation, the appearance of a train of coherent 'puffs' of turbulence. These were characterised by an average Strouhal number of 0.3, but the authors noted how "three or four puffs form and induct themselves downstream, an interval of confused flow ensues, several more puffs form, and so on".

The effect of such intermittency can considered in a number of ways. Ffowcs Williams and Kempton (1978) were the first to consider a kinematic model for such behaviour; this took the form of a random variation of the phase velocity of the convected wavepacket, as shown in equation 86. In this case the wave envelope remains time-invariant.

$$s(\boldsymbol{y},\tau) = \frac{\partial^2}{\partial y_1^2} 2\rho_0 U\tilde{u}\frac{\pi D^2}{4}\delta(y_2)\delta(y_3)\frac{[1+\epsilon(t-y_1/U)]}{U}\mathrm{e}^{(\omega t-\kappa_y y_1)}\mathrm{e}^{(-y_1^2/l^2)}. \tag{86}$$

Figure 13, which shows data taken from the DNS of Freund (2001) and the experimental measurements of Tinney and Jordan (2008), illustrates how intermittency is also manifest in an unsteadiness of the wavepacket envelope: a pattern of convected waves is observed from $x \approx D$ to $x \approx 6D$. These are characterised by some average frequency, but they undergo a modulation which is both spatial and temporal: the maximum amplitude of the wave

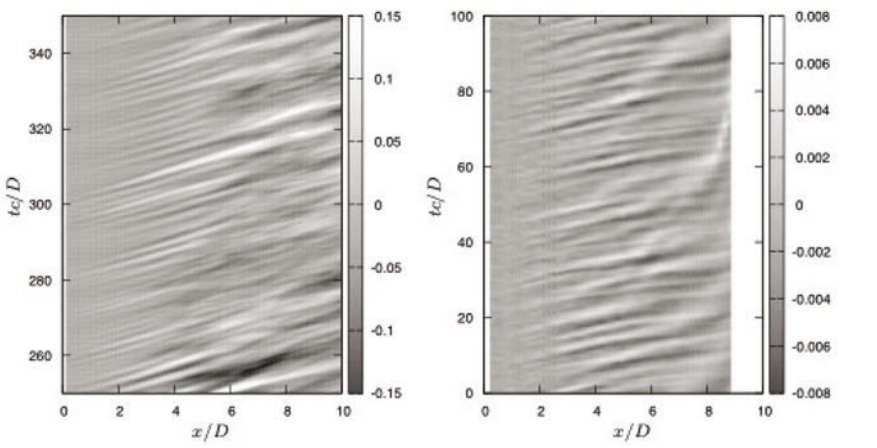


**Figure 13.** Left: axisymmetric axial velocity fluctuation at $r/D = 0.5$, from DNS of Freund (2001); $Re = 3600$. Right: nearfield pressure signature of jet at $Re = 5.10^6$, from measurements of Tinney and Jordan (2008). Note in both cases the time variation of wavepacket amplitudes and spatial extension.

changes in time, as does the position where it breaks down. A model for the former effect is

$$T_{11}(\mathbf{y},\tau) = 2\rho_0 U\tilde{u}\frac{\pi D^2}{4}\delta(y_2)\delta(y_3)\mathrm{e}^{\mathrm{i}(\omega\tau - ky_1)}\mathrm{e}^{-\frac{y_1^2}{L^2}}\mathrm{e}^{-\frac{\tau^2}{\tau_c^2}}. \tag{87}$$

Examples of this kind of space and time modulation are shown in figure 14 and this leads to a radiated sound pressure:

$$p(\mathbf{x},t) = \frac{\rho_0 U\tilde{u}D^2\cos^2\theta}{8c^2|\mathbf{x}|}\frac{\partial^2}{\partial t^2}\int_{-\infty}^{\infty}\left\{\mathrm{e}^{\mathrm{i}(\omega\tau-ky_1)}\mathrm{e}^{-\frac{y_1^2}{L^2}}\mathrm{e}^{-\frac{\tau^2}{\tau_c^2}}\right\}_{\tau=t-\frac{|\mathbf{x}-\mathbf{y}|}{c}}\mathrm{d}y_1, \tag{88}$$

where $c$ is the speed of sound in the undisturbed fluid and $\theta$ is the angle of $\mathbf{x}$ to the jet axis. Use of the far-field approximation $|\mathbf{x}-\mathbf{y}| \approx |\mathbf{x}| - y_1\cos\theta$ leads to

$$p(\mathbf{x},t) = \frac{\rho_0 U\tilde{u}D^2\cos^2\theta}{8c^2|\mathbf{x}|}\frac{\partial^2}{\partial t^2}\left\{\mathrm{e}^{\mathrm{i}\omega\left(t-\frac{|\mathbf{x}|}{c}\right)-\frac{\left(t-\frac{|\mathbf{x}|}{c}\right)^2}{\tau_c^2}}\int_{-\infty}^{\infty}f(y_1)\mathrm{d}y_1\right\} \tag{89}$$

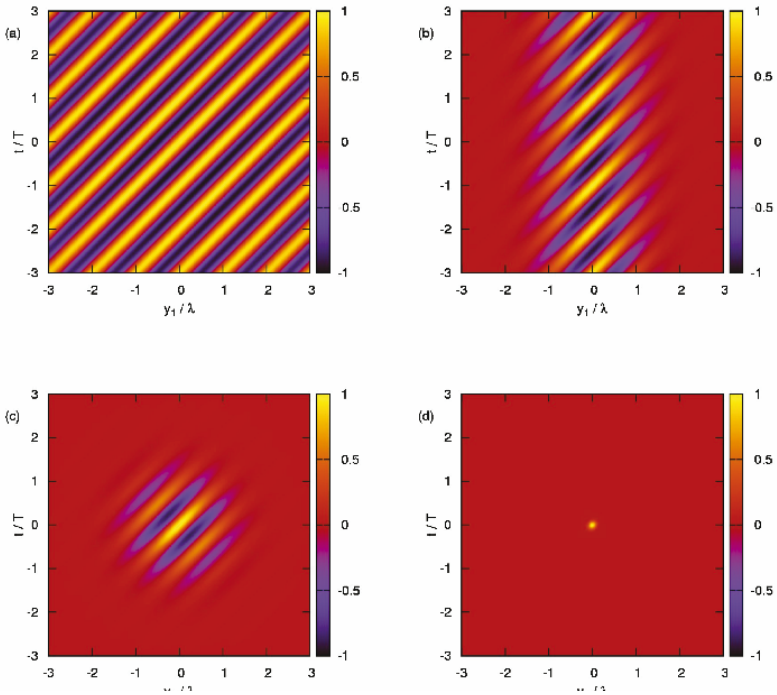


**Figure 14.** Space- and time-modulated wavepackets.

with

$$f(y_1) = \mathrm{e}^{\mathrm{i}\left(\frac{\omega y_1 \cos\theta}{c} - k y_1\right)} \mathrm{e}^{-\frac{y_1^2}{L^2} - \frac{(y_1 \cos\theta)^2}{c^2 \tau_c^2}} \mathrm{e}^{-\frac{2 y_1 \cos\theta \left(t - \frac{|\mathbf{x}|}{c}\right)}{c \tau_c^2}}, \tag{90}$$

where $c$ is the speed of sound in the undisturbed fluid and $\theta$ is the angle of $\mathbf{x}$ to the jet axis.

Evaluation of the integral of equation 90 leads to an analytical expression for the pressure in the far field:

$$p(\mathbf{x}, t) = PQ \mathrm{e}^{\mathrm{i}\omega t_r - \frac{t_r^2}{\tau_c^2} - \frac{L^2}{4\tau_c^2 \gamma^2}\left[(ck - \omega\cos\theta)\tau_c^2 - 2\mathrm{i}t_r \cos\theta\right]^2} \tag{91}$$

with

$$t_r = t - \frac{|\mathbf{x}|}{c}, \tag{92}$$

$$P = \frac{\rho_0 U \tilde{u} D^2 \tau_c c L \sqrt{\pi} \cos^2\theta}{4c^2 |\mathbf{x}| \gamma}, \tag{93}$$

$$Q = \left\{ \left[ \mathrm{i}\omega - 2\frac{t_r}{\tau_c^2} + \frac{\mathrm{i}L^2 \cos\theta}{\tau_c^2 \gamma^2} \left[ (ck - \omega\cos\theta)\tau_c^2 - 2\mathrm{i}t_r \cos\theta \right] \right]^2 - \frac{2c^2}{\gamma^2} \right\}, \tag{94}$$

and

$$\gamma = \sqrt{\tau_c^2 c^2 + L^2 \cos^2\theta}. \tag{95}$$

If we calculate the limit with $\tau_c \to \infty$ of eqs. (91)–(95), we have

$$\gamma \to \tau_c c \tag{96}$$

and

$$P \to \frac{\rho_0 U \tilde{u} D^2 L \sqrt{\pi} \cos^2\theta}{4c^2 |\mathbf{x}|}, \tag{97}$$

which, after substitution in eq. (91), leads, as expected, to the earlier result for a purely spatially modulated wavepacket,

$$p(\mathbf{x}, t) = -\frac{\rho_0 U \tilde{u} M_c^2 (kD)^2 L \sqrt{\pi} \cos^2\theta}{8|\mathbf{x}|} \mathrm{e}^{-\frac{L^2 k^2 (1 - M_c \cos\theta)^2}{4}} \mathrm{e}^{\mathrm{i}\omega\left(t - \frac{|\mathbf{x}|}{c}\right)}, \tag{98}$$

where $M_c$ is the convective Mach number given by $\omega/(kc)$.

We can define a source efficiency as the ratio between the acoustic energy,

$$E_A = \int_0^\infty \int_\Omega \frac{p^2}{\rho_0 c} \mathrm{d}S(\mathbf{x}) \mathrm{d}t, \tag{99}$$

with the surface integral calculated over a spherical surface $\Omega$ in the far field, and the turbulent kinetic energy, or "source" energy, given by

$$E_S = \frac{1}{T} \int_0^\infty \int_{V_S} \frac{\rho_0 u^2}{2} \mathrm{d}\mathbf{y} \mathrm{d}\tau. \tag{100}$$

This allows an evaluation of the impact of changes in the space and time scales of the wavepacket envelope on the acoustic efficiency. Figure 15 shows this dependence. Note that the colour scale is logarithmic: at high Mach number small reductions in either the spatial or temporal extent of the wavepacket can lead to considerably enhanced radiation efficiency; the space-time localisation of a wavepacket is thus an important source parameter: such behaviour in a jet comprises a flow 'direction' to which the wave operator is highly sensitive.

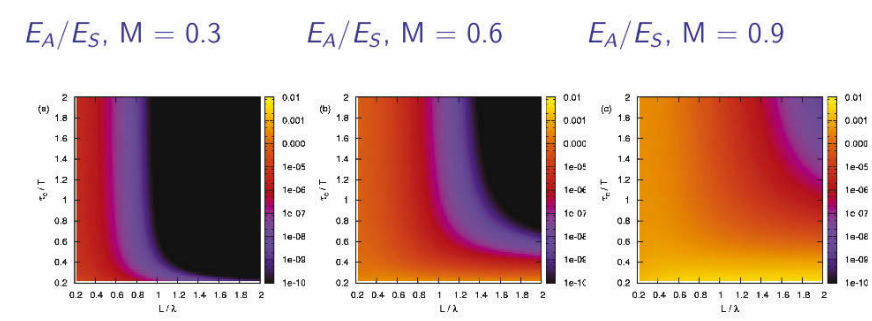


**Figure 15.** Wavepacket efficiency, as a function of space- and time-envelope scales, for different Mach numbers.

**Temporally-localised envelope truncation** In order to provide temporal changes in the spatial extent of the envelope function, in an effort to better model the wavepacket characteristics observed in figure 13, we can model $T_{11}$ as

$$T_{11}(\mathbf{y},\tau) = 2\rho_0 U\tilde{u}\frac{\pi D^2}{4}\delta(y_2)\delta(y_3)\mathrm{e}^{\mathrm{i}(\omega\tau - ky_1)}\mathrm{e}^{-\frac{y_1^2}{L^2(\tau)}}. \tag{101}$$

With this expression the peak amplitude of the convected wave is kept constant, but the characteristic length of the envelope, $L$, changes with time. We model the changes in $L$ as

$$L(\tau) = L_0 - \kappa\mathrm{e}^{-\frac{(\tau-\tau_0)^2}{\tau_L^2}}, \tag{102}$$

where $L_0$ is an initial envelope width and $\kappa$ is the maximum envelope reduction, which happens at $\tau = \tau_0$. This reduction of the envelope occurs over an interval characterised by the temporal scale $\tau_L$, and is modelled by a Gaussian function. Examples of this source behaviour are shown in fig. 16. The sound radiation is obtained in this case by numerical integration using this line source. A sample result is shown in figure 16: we note that the envelope truncation also leads to an enhancement of the sound radiation, again suggesting that this kind of unsteadiness, observed in the numerical and experimental data, may underpin the emission of high-amplitude acoustic perturbations to the far field of turbulent jets: again, in the spirit of the system reduction at the heart of the analysis methodology evoked earlier,

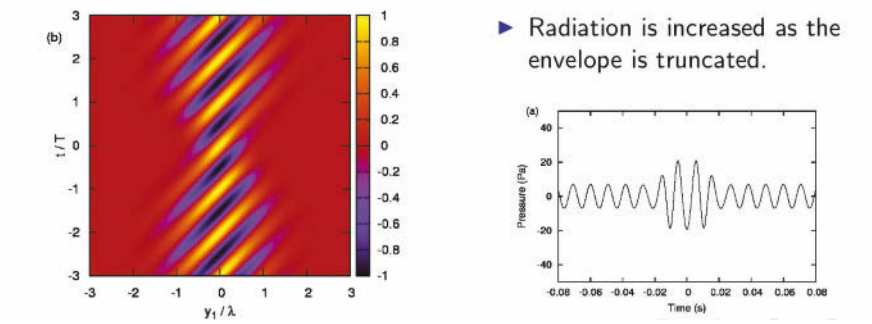


**Figure 16.** Space- and time-modulated wavepackets.

the propagation operator is sensitive to this kind of flow behaviour, and so such flow 'directions' should, again, be retained, i.e. explicitly modelled.

We now consider a final model, which takes us closer again to the behaviour we observe in the data shown in figure 13. We wish to mimic the space-time 'jitter' manifest in the data, we must therefore capture the time variation of the wavepacket envelope in terms of both its peak amplitude and its axial extent. This final model combines the effects modelled individually in the two previous models.

**Space-time 'jitter'** $T_{11}$ is now modelled as

$$T_{11}(\mathbf{y},\tau) = 2\rho_0 U\tilde{u}\frac{\pi D^2}{4}\delta(y_2)\delta(y_3)A(\tau)\mathrm{e}^{\mathrm{i}(\omega\tau - ky_1)}\mathrm{e}^{-\frac{y_1^2}{L^2(\tau)}}, \tag{103}$$

where we allow temporal variations of the amplitude $A$, and also temporal changes in $L$. This expression, used in conjunction with the far-field assumption, leads to:

$$p(\mathbf{x},t) = \frac{\rho_0 U\tilde{u}D^2\cos^2\theta}{8c^2|\mathbf{x}|}\frac{\partial^2}{\partial t^2}\int_{-\infty}^{\infty} A\left(t - \frac{|\mathbf{x}| - y_1\cos\theta}{c}\right) \mathrm{e}^{\mathrm{i}\left[\omega\left(t-\frac{|\mathbf{x}|-y_1\cos\theta}{c}\right)-ky_1\right]}\mathrm{e}^{-\frac{y_1^2}{L^2\left(t-\frac{|\mathbf{x}|-y_1\cos\theta}{c}\right)}}\mathrm{d}y_1. \tag{104}$$

If the amplitude $A$ and the characteristic length of the envelope, $L$, change slowly when evaluated at retarded-time differences ($y_1\cos\theta/c$) along

the wave-packet, we can consider axial compactness for these functions in the integration, such that

$$A\left(t-\frac{|\mathbf{x}|-y_1\cos\theta}{c}\right)\approx A\left(t-\frac{|\mathbf{x}|}{c}\right) \tag{105}$$

and

$$L\left(t-\frac{|\mathbf{x}|-y_1\cos\theta}{c}\right)\approx L\left(t-\frac{|\mathbf{x}|}{c}\right). \tag{106}$$

If $^*$ is used to denote a function evaluated at the retarded time $t-\frac{|\mathbf{x}|}{c}$, we have

$$p(\mathbf{x},t)=\frac{\rho_0 U\tilde{u}D^2\cos^2\theta}{8c^2|\mathbf{x}|}\frac{\partial^2}{\partial t^2}\left\{A^*\int \mathrm{e}^{\mathrm{i}\left[\omega\left(t-\frac{|\mathbf{x}|-y_1\cos\theta}{c}\right)-ky_1\right]}\mathrm{e}^{-\frac{y_1^2}{(L^*)^2}}\,\mathrm{d}y_1\right\} \tag{107}$$

Evaluation of this integral, considering that the temporal changes in $L$ and in $A$ are slower than those related to the harmonic oscillation in $\omega$, leads to

$$p(\mathbf{x},t)=-A^*\frac{\rho_0 U\tilde{u}M_c^2(kD)^2L^*\sqrt{\pi}\cos^2\theta}{8|\mathbf{x}|}\mathrm{e}^{-\frac{(L^*)^2k^2(1-M_c\cos\theta)^2}{4}}\mathrm{e}^{\mathrm{i}\omega\left(t-\frac{|\mathbf{x}|}{c}\right)} \tag{108}$$

This means that for sufficiently slow temporal changes in $A$ and in $L$, the radiated sound field at a given time $t$ is that of a wave-packet whose amplitude and envelope corresponds to the values $A^*$ and $L^*$, that is, *to the wave-packet at the retarded time* $t-|\mathbf{x}|/c$ (compare with eq. (98)).

In the spirit of the analysis methodology outlined earlier the models considered here will be used, in conjunction with an ensemble of data-processing/reduction techniques (outlined in section §5), to analyse data obtained using Large Eddy Simulation and Direct Numerical Simulation.

### 3.6 Conclusion

In this section we have considered the source modelling problem from the perspective of 'coherent structures'. It has been shown how considerable simplifications can be justified where the associated sound production mechanisms are concerned, these simplifications being for the most part derived from theoretical reasoning based on Lighthill's acoustic analogy. In what follows we will explore some numerical databases, from which we will endeavour to extract and evaluate the salient source features through the application of a number of different analysis tools. These analyses closely follow the methodology outlined at the beginning of this section; and a detailed exposition of the various analysis tools implemented are described in section §5.

## 4 Two case studies

In this section we provide two examples of applications of the analysis methodology outlined earlier, focusing on the organised component of the turbulent jet discussed in the previous section; we also make use of the wavepacket sound source models of that section.

Let us begin by briefly recalling the analysis methodology: (1) we equip ourselves with complete or partial data from full Navier-Stokes solution[10]; (2) we then identify the acoustic observable, $\mathbf{q}_A$, and design a corresponding filter, $\mathcal{F}_{\mathbf{q}_A}$[11], used to extract the radiating flow skeleton, $\hat{\mathbf{q}}_D$; (3) we construct a simplified kinematic source model, $s(\hat{\mathbf{q}}_D)$ (based on the models developed in section §3), and verify that solution of $\mathcal{L}\hat{\mathbf{q}}_A = s(\hat{\mathbf{q}}_D)$ is such that $|\mathbf{q}_A - \hat{\mathbf{q}}_A|$ be acceptably small. The final stage of the analysis methodology involves identifying the associated dynamic law; this aspect will be outlined briefly in section §6.

We use three different databases for the analysis, two LES and one DNS. The two LES use different numerical schemes, leading to one having higher space-time scale resolution than the other. We will refer to these as $LES_{MD}$ and $LES_{HR}$, the subscripts denoting, respectively, moderate and high resolution. The $DNS$ and $LES_{MR}$ therefore constitute databases where coherent structures are relatively easy to identify, on account, respectively, of the low Reynolds number and the moderate scale resolution. $LES_{HR}$ is more challenging, as it contains a broader range of turbulence scales, making the coherent structures more difficult to educe. In this case we are required to construct a filter based on Linear Stochastic Estimation (LSE).[12]

### 4.1 Case study 1. Moderate-resolution LES and DNS

We begin by performing a Large Eddy Simulation of a Mach 0.9, isothermal jet, with nominal Reynolds number, $Re = 400000$. The details of the computation can be found in Cavalieri et al. (2010a). An image of the flow solution is shown in figure 17, where the first stage in the analysis methodology is illustrated. We, of course, verify that the simulation shows good agreement with experimental results: at peak sound radiation frequencies

[10] It is true that the LES does not provide a full Navier Stokes solution, being based on filtered equations; we nonetheless consider that it provides a relatively complete representation of the behaviour of the larger structures, which are those we are interested in here.

[11] In the first study this filter is rather heuristic, being based simply on flow visualisation following the application of Fourier and wavelet transforms; in the second, the filter has a rigorous mathematical definition.

[12] A detalied presentation of LSE is provided in section §5.

the LES is within 2dB of experimentally observed values.

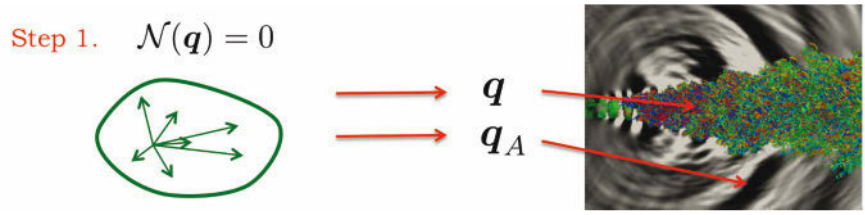


**Figure 17.** First stage of analysis: obtain Navier Stokes solution, $\mathbf{q}$, which contains the acoustic observable, $\mathbf{q}_A$.

The next stage is to analyse the observable, $\mathbf{q}_A$. To do so we implement the following signal processing: azimuthal Fourier decomposition is performed on the acoustic data on a cylindrical surface of radius, $r = 9D$, and which extends from $x/D = 0$ to $x/D = 20$; wavelet transforms are applied in the time direction, for each azimuthal Fourier mode. The reasons for this choice of data-processing can be found in the previous section: we saw in the experiment that the sound field is dominated by only three azimuthal Fourier modes; this being the case, it is legitimate and useful to break the sound field down into these building blocks. This will allow us to simplify the analysis. Also, we saw that coherent structures in jets display intermittency, and in peak radiation directions much of the overall sound energy arrives in temporally localised bursts. This suggests a link between the intermittency of coherent structures and peak sound radiation, and the models developed in the previous section illustrate how such source behaviour can indeed enhance the sound radiation efficiency of organised flow structures.

We can see in figure 18 that the downstream direction is, in agreement with what was observed experimentally, dominated by axisymmetric sound radiation. We will therefore focus on this component of the sound field, and see if we can ascertain the associated flow kinematics. Note the procedure that is being followed here: we are gradually eliminating flow information, thereby homing in progressively on the dominant aspects of the flow with regard to the acoustic observable. By doing so we simplify the task of analysing and later modelling the jet as a source of sound.

We now consider the temporal structure of the axisymmetric component of the sound field. Application of a wavelet transform[13] to the time history

[13]The wavelet transform is presented in section §5.

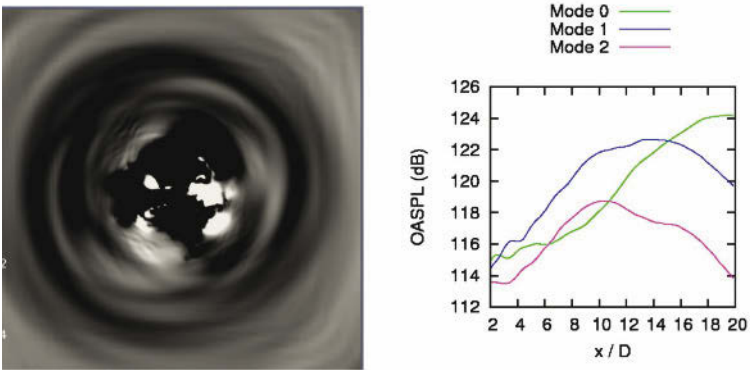


**Figure 18.** Left: instantaneous image of the jet, taken in a cross-section at $x/D = 7$; note the azimuthal organisation of the radiating pressure wave. Right: jet directivity as a function of azimuthal Fourier mode; note, consistent with image on the left, dominance of the axisymmetric mode in the downstream direction.

of the axisymmetric mode of the sound field at each axial station provides a corresponding scalogram. Figure 19 shows an example for the axial station, $x/D = 17$ (i.e. at low emission angle, $\theta \approx 30°$). A series of high-amplitude events, labelled A - H, stand out. By setting a threshold the scalogram can be filtered and the time signal reconstructed such that only the said events are retained. In what follows we concentrate on the first high-amplitude event. This filtering procedure is applied to the sensors at all axial stations and the result is shown in figure 20. We have here isolated one particular piece of the observable, $\mathbf{q}_A(m = 0\,;\, 19 < tc_0/D < 30)$, and from this filtered information we will now work our way back into the flow, $\mathbf{q}_D$, in order to analyse and understand the flow events that caused the high-amplitude sound pressure fluctuation.

Figure 21 shows the flow at four consecutive times during the production of the said fluctuation. The following behaviour is observed. At $t = 8.576$ (top left) we see an axisymmetric wavepacket extending out to about $x/D = 5$, downstream of which the structures are tilted into something closer to mode 1. As far as the axisymmetric component of the flow is concerned we therefore have a truncated wavepacket. We saw in section §3 how such behaviour can lead to enhanced acoustic efficiency, and, indeed, consistent with this, a high-amplitude depression is emitted from the flow

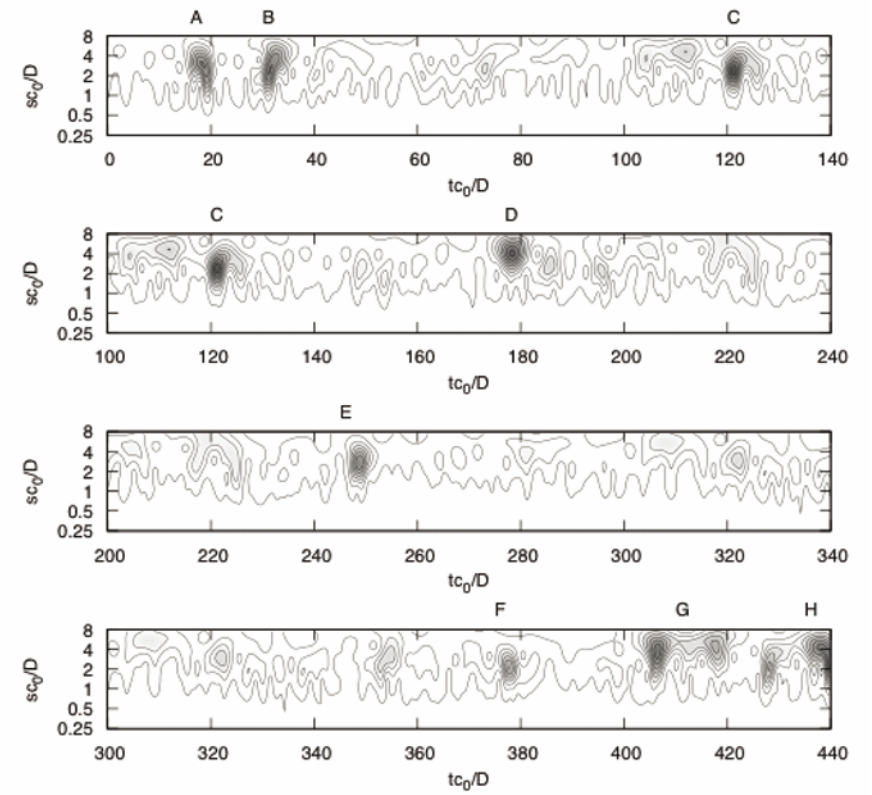


**Figure 19.** Scalogram computed from the time history of the axisymmetric acoustic mode at $r/D = 9$, $x/D = 17$

at this time. This propagating wave is the same observed in figure 20 at ($tc_0/D \approx 20\,;\, 15 < x/D < 20$). After the emission of this wavefront the axisymmetric wavepacket extends axially, as seen in figure 21 at $t = 9.514$, and then undergoes a second truncation, at both the upstream and downstream ends ($t = 12.596$), at which point a second wavefront is released from the flow: this corresponds to the second depression observed, after wavelet transform, in figure 20, at ($tc_0/D \approx 25\,;\, 15 < x/D < 20$). Finally, the axisymmetric wavepacket increases in both intensity and axial extent, as seen in figure 21 at $t = 16.48$, before collapsing a third time (not shown)

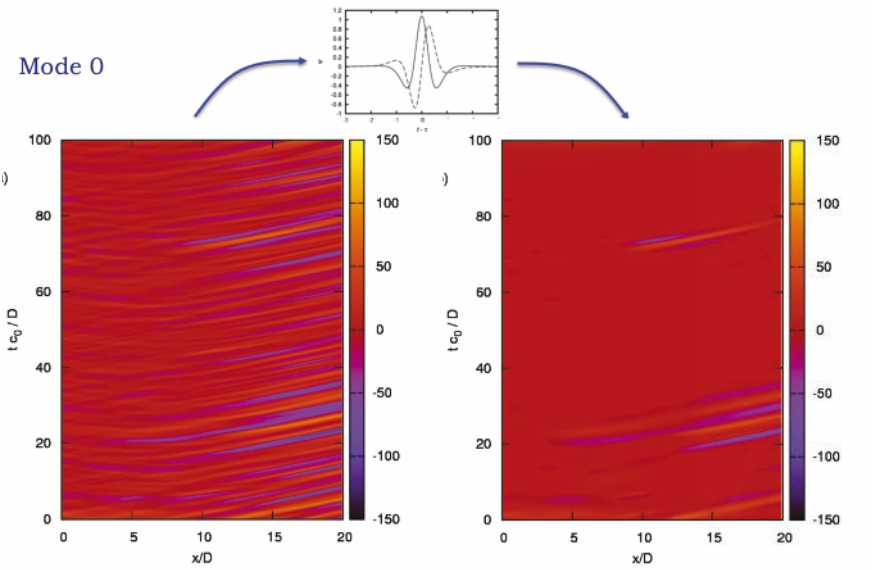


**Figure 20.** Left: space-time structure of axisymmetric component of sound field on cylindrical surface with $r/D = 9$. Right: same filed after application of wavelet filtering; this serves to isolate high amplitude bursts.

and thereby releasing the third wavefront observed in figure 20.

The flow kinematics associated with the high-amplitude axisymmetric acoustic wavepacket is thus seen to comprise a drifting of the flow in and out of axially-extended axisymmetry; i.e. we have space-time modulation, or 'jitter' of an axisymmetric wavepacket. This behaviour is reminiscent of the observation of Crow and Champagne (1971) cited earlier: "three or four puffs form and induct themselves downstream, an interval of confused flow ensues, several more puffs form, and so on". The third wavepacket *ansatz* proposed in section §3 would therefore appear to be appropriate. We recall the source model

$$T_{11}(\mathbf{y},\tau) = 2\rho_0 U \tilde{u} \frac{\pi D^2}{4} \delta(y_2)\delta(y_3) A(\tau) \mathrm{e}^{\mathrm{i}(\omega\tau - k y_1)} \mathrm{e}^{-\frac{y_1^2}{L^2(\tau)}}. \tag{109}$$

By application of a short-time Fourier series (figure 22), followed by the fitting of a Gaussian envelope function (figure 23), values of $A(\tau)$ and $L(\tau)$ are obtained. Inserting these into equation 109 and then solving the wave equation with this as source allows us to assess to what degree our kinematic

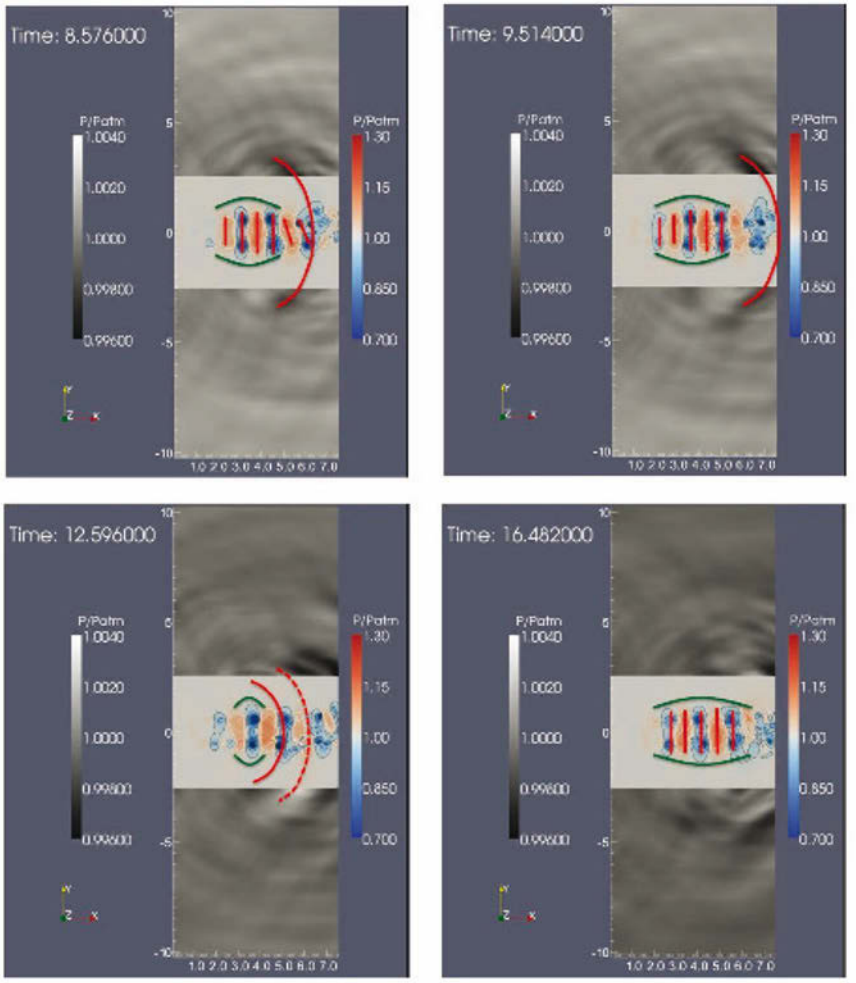


**Figure 21.** Visualisation of the hydrodynamic pressure within the jet at times corresponding to the acoustic wavepacket identified by wavelet transform in figure 20

source model, $s(\hat{\mathbf{q}}_D)$, reproduces a result, $\hat{\mathbf{q}}_A$, which is close to the acoustic observable $\mathbf{q}_A$. The result is shown in figure 24 , where the result of the model is compared with both the OASPL of the axisymmetric mode of

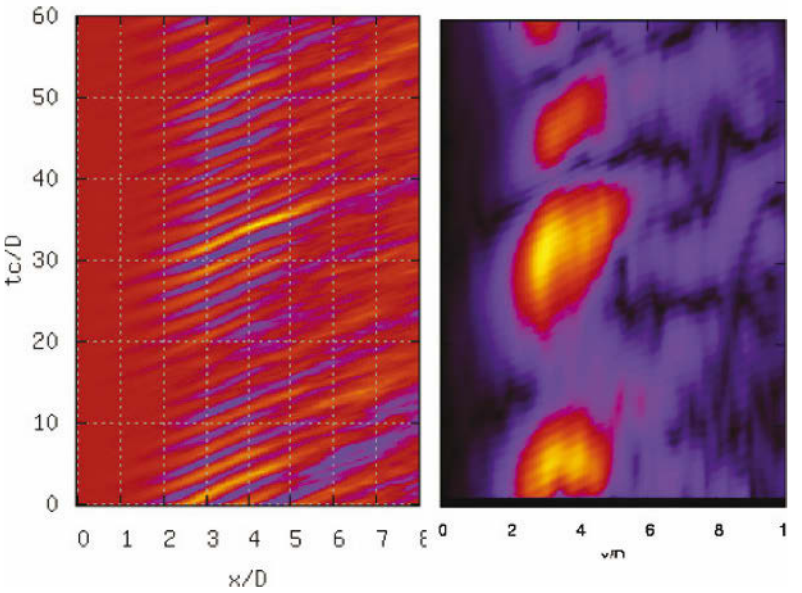


**Figure 22.** Left: space-time structure of axisymmetric component of axial velocity fluctuation at $r/D = 0.5$; right: short-time Fourier transform of the data in figure on the left.

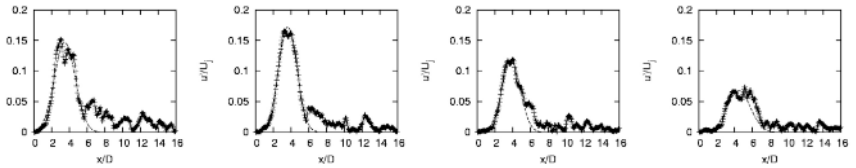

**Figure 23.** Gaussian functions are fitted to the result of projecting the flow data on the short-time Fourier series. In this way, values for the instantaneous wavepacket envelope amplitude, $A(\tau)$ and length scale, $L(\tau)$ can be obtained.

the LES, and a result obtained using a wavepacket *ansatz* where the time-averaged values of the $A(\tau)$ and $L(\tau)$ are used, i.e. a wavepacket that does not jitter. Whereas the non-jittering wavepacket shows a 12dB discrepancy

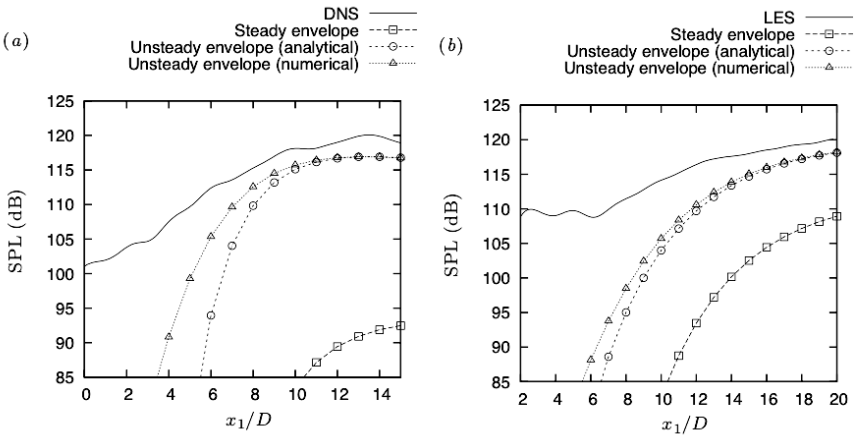


**Figure 24.** Comparison of the DNS and LES sound fields, left and right, respectively, with those obtained using simplified, jittering source models.

with the LES, showing it to be clearly incorrect, the jittering wavepacket is within 1.5dB, suggesting that this kinematic description is physically pertinent: this confirms that this behaviour comprises flow directions that are aligned with the propagation operator. The same procedure applied to the DNS database produced similar agreement, as can be seen in figure 24.

The next stage in the analysis methodology, which is work in progress, is to repeat the above analysis with respect to the other azimuthal Fourier modes of the sound field, in that way building up a composite, simplified kinematic description of the jet as a sound source, at which point it will be possible to address the question of the associated simplified dynamic law. Tools for reduced order dynamical modelling are outlined briefly in section §6.

### 4.2 Case study 2. High-resolution LES

The foregoing case study was considerably simplified by the relatively organised character of the flow solutions obtained using DNS and $LES_{MR}$. In this case study (taken from Kerhervé et al. (2010)) we consider a Large Eddy Simulation (Bogey et al. (2003)) with a higher order numerical scheme, which provides a flow solution with a broader range of turbulence scales in the noise producing region of the flow. This flow thus presents a greater

challenge in terms of flow feature eduction, and is in this respect a step closer to the high-Reynolds number experimental context.

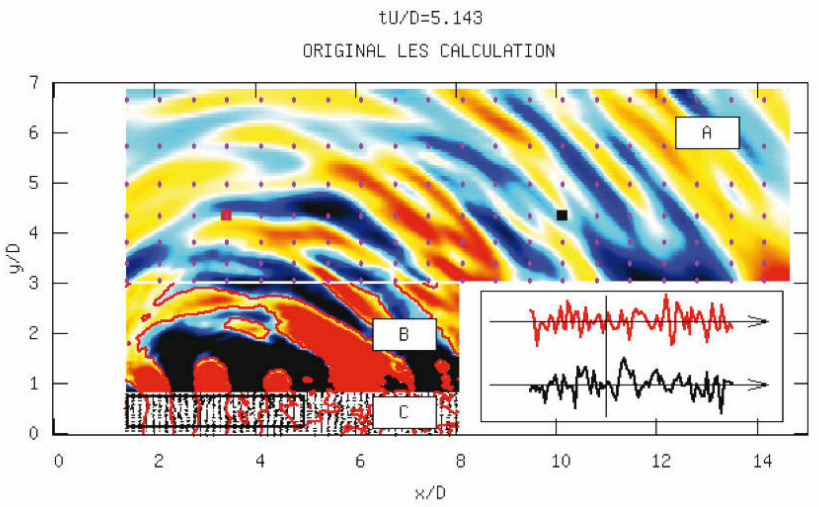


**Figure 25.** Large Eddy Simulation solution of Bogey et al. (2003), as used by Kerhervé et al. (2010). Zones $A$: linear acoustic region; zone $B$: nearfield, transition from non-linear hydrodynamics to linear acoustics; zone $C$: non-linear turbulent region.

A two-dimensional slice of the flow solution is shown in figure 25. Again, in the spirit of the analysis methodology outlined in section §3, we consider, separately, the acoustic region, where we define what is to be our observable, $\mathbf{q}_A$, and the flow region, where we are interested in reducing $\mathbf{q}_D$ down to $\hat{\mathbf{q}}_D$. As seen in figure 25, the flow zone has been further split into zones $B$ and $C$; the reason for this is that these zones present quite different behaviour. In zone $C$ the flow is turbulent, non-linear, dominated by confused vortical motion, whereas in zone $B$ fluctuations are predominantly irrotational, and a transition is observed, as we move radially through this region, the flow motions going from being dominated by hydrodynamics to being dominated by acoustics. It is often in this region of the flow, particularly in high Reynolds number experimental contexts, as the short historical note in section §3 outlined, that the signature of coherent structures is most easily observed.

Because of the greater complexity of both the flow and sound fields computed by this LES, we refine our definition of $\mathbf{q}_A$ by filtering the sound field so as to only retain fluctuations associated with low-angle emission, which is believed to be predominantly contributed to by coherent structures. A frequency-wavenumber transform and subsequent filtering allows this to be achieved. The procedure works as follows. For each $y-$ position in zone $A$, the pressure field is Fourier transformed from $(x,t)$ to $(\kappa_x,\omega)$:

$$\tilde{p}(k_x,y,\omega)=\iint p(x,y,t)e^{-j(\omega t+k_x x)}\,dt\,dx. \tag{110}$$

A bandpass filter is then applied, which, for a given frequency, retains wavenumbers in the range $\omega/c(\theta_1)<k_x<\omega/c(\theta_2)$ where $\mathrm{c}(\theta_i)=c_o/\cos(\theta_i)$ and $\theta_i$ denotes a given radiation direction. The bandpass filter is defined as

$$\Omega(\omega,k_x)=\begin{cases} 1 & \text{if } k_x<\omega/c(\theta_i) \\ \exp\left[-\frac{(k_x-|\omega|/c(\theta_i))^4}{\alpha^4}\right] & \text{otherwise} \end{cases}. \tag{111}$$

The filtered pressure is then recovered by inverse Fourier transform after application of the frequency-wavenumber filter,

$$p_f(x,y,t)=\iint \tilde{p}(k_x,y,\omega)\Omega(\omega,k_x)e^{j(\omega t-k_x x)}\,d\omega\,dk_x. \tag{112}$$

The results of the filtering are shown in figure 26. On the left the entire propagating field is shown in both frequency-wavenumber and physical space. The middle and right figures show, respectively, sound radiation in the angular sectors $0^\circ<\theta<60^\circ$ and $60^\circ<\theta<120^\circ$. The space-time field corresponding to the middle image is considered the acoustic observable, $\mathbf{q}_A$, and we now use this to construct a filter, $\mathcal{F}_{\mathbf{q}_A}$, by which we can eliminate, from the full flow solution, any information not directly associated with sound production. What remains is then considered the sound producing flow skeleton, which we can subsequently proceed to analyse and model.

**Linear Stochastic Estimation** The method used in order to perform the said filtering is based on Linear Stochastic Estimation, which provides a means by which an approximation of a conditional average

$$\hat{\mathbf{q}}(\mathbf{x},t)=<\mathbf{q}(\mathbf{x},t)|\mathbf{q}_A(\mathbf{x},t+\tau)> \tag{113}$$

can be obtained. For the specific case considered in this study, $\mathbf{q}$ will be either the hydrodynamic pressure or the turbulent velocity, associated with

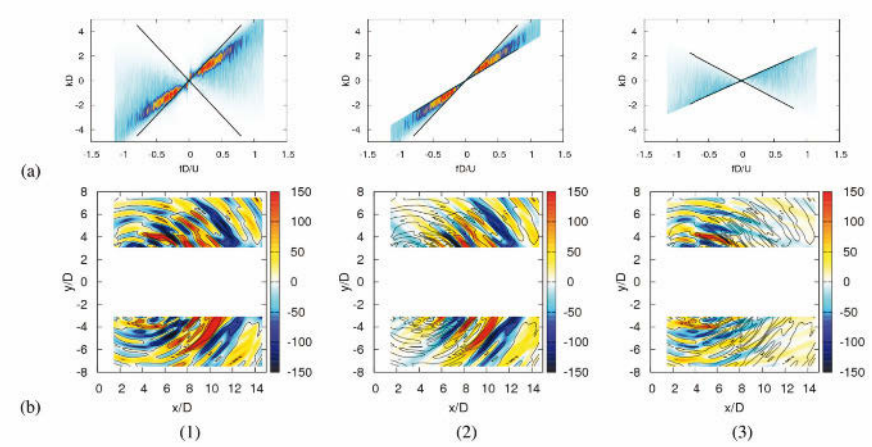


**Figure 26.** Top row: segments of frequency-wavenumber spectrum corresponding to radiation in different angular ranges; bottom row: corresponding instantaneous fields. Left column: $0° < \theta < 180°$; middle columne: $0° < \theta < 60°$; right columne: $60° < \theta < 120°$

the full LES solution, in zones $B$ and $C$; $\mathbf{q}_A$ is the acoustic pressure, filtered so as to only retain components radiating in the angular range, $0 < \theta < 60$. The approach is used to determine, independently, conditional averages (which are here a function of space and of time) of the turbulent velocity and the pressure in zones $B$ and $C$[14]:

$$\hat{\mathbf{u}}(\mathbf{x},t) =< \mathbf{u}(\mathbf{x},t)|p_A(\mathbf{y},t+\tau(\mathbf{x}|\mathbf{y})) > \tag{114}$$

$$\hat{p}(\mathbf{x},t) =< p(\mathbf{x},t)|p_A(\mathbf{y},t+\tau(\mathbf{x}|\mathbf{y})) >, \tag{115}$$

where the time delay $\tau(\mathbf{x}|\mathbf{y})$ corresponds to the propagation time between each flow point and each observer (obtained by means of ray-tracing).

As LSE is comprehensively dealt with in section §5 we here simply recall the main result, which is that the above conditional average can be

[14] where the pressure is concerned it is, in zone $C$, predominantly hydrodynamic, while in zone $B$ it contains a increasing proportion of acoustic fluctuation as we move radially away from the jet through zone $B$

approximated as

$$\hat{\mathbf{q}}(\mathbf{x},t) = \sum_{i=1}^{N} a(\mathbf{x},\mathbf{y_i}) p_A(\mathbf{y_i}, t+\tau(\mathbf{x}|\mathbf{y_i})); \tag{116}$$

i.e. the value of the the filtered (conditional) flow variable, $\hat{\mathbf{q}}(\mathbf{x},t)$, is obtained as the weighted linear combination of the values of the acoustic pressure, $p_A(\mathbf{y}_i, t+\tau(\mathbf{x}|\mathbf{y}_i))$; the acoustic domain, $\mathbf{y}$ is discretised into an ensemble of discrete sensors. The coefficients $a(\mathbf{x},\mathbf{y_i})$ are obtained by solving a linear system of equations of the form $\mathbf{Q} = \mathbf{P}\cdot\mathbf{A}$ where,

$$\mathbf{Q} = \begin{bmatrix} \overline{q(\mathbf{x},t)p_A(\mathbf{y}_1, t+\tau(\mathbf{x}|\mathbf{y_1}))} \\ \vdots \\ \overline{q(\mathbf{x},t)p_A(\mathbf{y}_N, t+\tau(\mathbf{x}|\mathbf{y_N}))} \end{bmatrix} \quad \mathbf{A} = \begin{bmatrix} a(\mathbf{x},\mathbf{y_1}) \\ \vdots \\ a(\mathbf{x},\mathbf{y_N}) \end{bmatrix} \tag{117}$$

$$\mathbf{P} = \begin{bmatrix} \overline{p_A(\mathbf{y_1},t)p_A(\mathbf{y_1},t)} & \cdots & \overline{p_A(\mathbf{y_N},t)p_A(\mathbf{y_1},t+\tau(\mathbf{x}|\mathbf{y_1})-\tau(\mathbf{x}|\mathbf{y_N}))} \\ \vdots & \ddots & \vdots \\ \overline{p_A(\mathbf{y_1},t)p_A(\mathbf{y_N},t+\tau(\mathbf{x}|\mathbf{y_N})-\tau(\mathbf{x}|\mathbf{y_1}))} & \cdots & \overline{p_A(\mathbf{y_N},t)p_A(\mathbf{y_N},t))} \end{bmatrix} \tag{118}$$

A sample of the result is shown in figure 27. Note the differences in flow field structure, in zones $B$ and $C$, between the full Large Eddy Simulation solution ($\mathbf{q}(\mathbf{x},t)$; figure on left) and the result obtained by Stochastic Estimation ($\hat{\mathbf{q}}(\mathbf{x},t)$; figure on right). The quantity shown in zone $B$ is pressure, while in zone $C$ both pressure and velocity are shown (the bottom part of the figure shows a zoom on the section of zone $C$ indicated by the black rectangle in the top part of the figure). In zone $C$, the velocity field is indicated by means of black arrows (showing the velocity vector in the plane), and the skeleton of the pressure field can be discerned by means of red iso-contours indicating $p(\mathbf{x},t) = 0$ or $\hat{p}(\mathbf{x},t) = 0$. In the case of $\hat{\mathbf{u}}(\mathbf{x},t)$ the gamma criterion has been used to colour the velocity field. This quantity, often used as a visual aid for the study of coherent structures (Graftieaux et al. (2001),) is defined as:

$$\Gamma(\mathrm{P}) = \frac{1}{S}\int_S \frac{\mathbf{P}M \wedge (\mathbf{U}_M - \mathbf{U}_P)]\cdot\overrightarrow{z}}{||\mathbf{P}M||\cdot||\mathbf{U}_M - \mathbf{U}_P||} dS \quad \text{with} \quad \mathbf{U}_P = \frac{1}{S}\int_S \mathbf{U}_M dS, \tag{119}$$

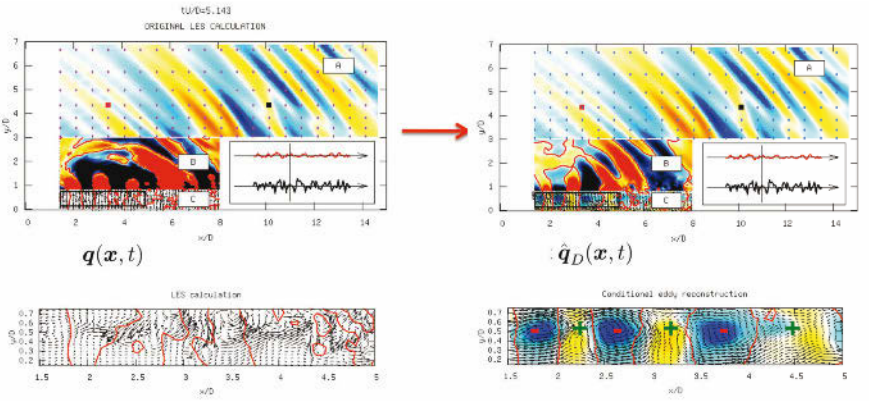


**Figure 27.** Left: Zone A: Low-angle filtered acoustic field; zones B and C: full LES solution. Right: Zone A Low-angle filtered acoustic field; zones B and C: conditional (filtered) flow, $\hat{\mathbf{q}}_D$

where $P$ is the point where the function is evaluated, $M$ lies in the region $S$ centered on $P$–generally chosen as a rectangular area, $\mathbf{z}$ is the unit vector normal to the measurement plane, $\mathbf{U}_M$ and $\mathbf{U}_P$ are the velocity vectors at point $M$ and $P$ respectively, and $N$ is the number of point in $S$.

The result shown in figure 27 suggests the kind of wavepacket radiation observed in the previous studies. In zone $C$ we observe a convected train of coherent vortical structures carrying a corresponding succession of positive and negative hydrodynamic pressures. The fact that the pressure and velocity fields are estimated independently, and yet produce a result that is, qualitatively, physically consistent (high and low hydrodynamic pressures carried, respectively, by vortical structures and saddle points ), justifies our thinking about the result, $\hat{\mathbf{q}}(\mathbf{x},t)$, as a sub-space of the flow.

We can now study this filtered field with a view to understanding what kind of simplified models might be appropriate where sound production is concerned. Two avenues appear worth pursuing: (1) We can decompose the field $\hat{\mathbf{q}}(\mathbf{x},t)$ into orthogonal building blocks by means of Proper Orthogonal Decomposition; (2) we can study $\hat{\mathbf{q}}(\mathbf{x},t)$ during periods of high-level sound emission in order to get a sense of what loud and quiet periods of flow activity look like. The first of these steps is of interest for two reasons. Firstly, the orthogonal building blocks constitute a basis that can help to characterise, and quantitively assess the degree of complexity (the number

of degrees of freedom) of, the flow *kinematics*. And, secondly, the same basis provides a possible framework within which to begin studying the *dynamics* of the reduced-complexity flow skeleton.

**Proper Orthogonal Decomposition** Proper Orthogonal Decomposition (POD) is presented in some detail in section §5, we therefore here simply recall the main equations and results, before applying it to the both the complete flow solution, $\mathbf{q}(\mathbf{x}, t)$, and the reduced-complexity, filtered flow, $\hat{\mathbf{q}}(\mathbf{x}, t)$.

The snapshot POD is used in this situation. The eigenvalues and eigen vectors of the two-time correlation function, $R(t, t')$, are first computed:

$$\int_T C(t, t')a^{(n)}(t')dt' = \lambda^{(n)}a^{(n)}(t) \tag{120}$$

where $a^{(n)}(t)$ are the eigen-vectors, $\lambda^{(n)}$ the eigenvalues and the two-time correlation function, $C(t, t')$, is defined as,

$$C(t, t') = \frac{1}{T}\iint_S \sum_{i=1}^{n_c} u_i(\mathbf{x}, t)u_i(\mathbf{x}, t')d\mathbf{x} \tag{121}$$

with $n_c = 3$ the number of components of the vector velocity field (when POD is effected on the pressure field, $n_c = 1$) and $T$ the duration of the data set. An associated set of spatial functions $\Phi_i^{(n)}(\mathbf{x})$ can be obtained by projection of $a^{(n)}(t)$ onto the velocity or pressure fields:

$$\Phi_i^{(n)}(\mathbf{x}) = \int_T a^{(n)}(t)u_i(\mathbf{x}, t)dt \quad \text{with } i = 1, .., n_c. \tag{122}$$

The result of the POD can provide two pieces of information. The convergence of the eigenspectrum, shown in figure 28, gives a sense of how many POD modes are required to represent the flow: if the convergence is rapid a large portion of the flow energy is captured with relatively few modes, if it is slow we require a large number of modes to capture the same energy. The former situation indicates that the flow is relatively organised, while the latter indicates a more disorganised flow. The spatial modes $\Phi_i^{(n)}$ give us a sense of the characteristic spatial structures that dominate the flow.

The eigenspectrum, shown in figure 28, shows that while the eigenspectrum associated with $\mathbf{q}$ has a slow convergence, 80 modes being required to capture 50% of the energy, that of $\hat{\mathbf{q}}$ is considerably more rapid, only 6 modes being necessary to represent the same percentage of the associated fluctuation energy.

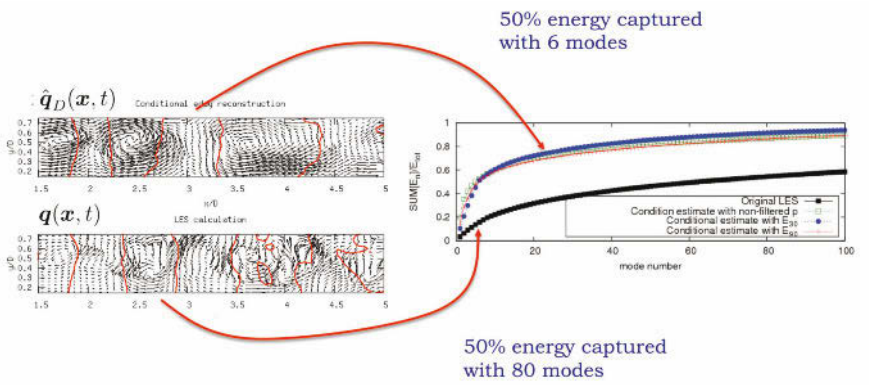


**Figure 28.** Eigenspectra associated with $\mathbf{q}$ and $\hat{\mathbf{q}}$

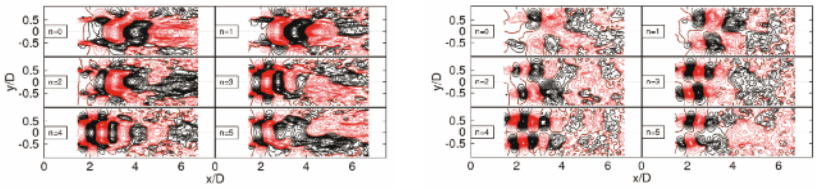


(a) (b)

**Figure 29.** Eigenfunctions associated with $\hat{\mathbf{q}}$; (a): axial velocity; (b) radial velocity

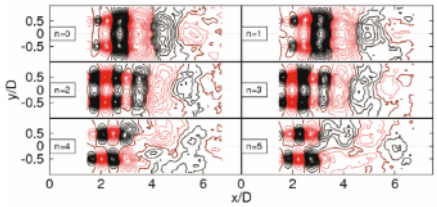


**Figure 30.** Eigenfunctions associated with $\hat{\mathbf{q}}$: pressure.

The eigenfunctions, shown in figures 29 and 30, emphasise once again the orderly, wavelike character of $\hat{\mathbf{q}}$, in terms of both the velocity and the pressure fields, over the first five or so diameters. Two characteristic space scales can be distinguished in the velocity eigenfunctions: one is of the order of the jet diameter, manifest in modes 0 and 1, representative of activity towards the end of the potential core, and a second, smaller space scale is observed, in modes 2 through 5, representative of structures further upstream in the annular mixing-layer region of the flow. The pressure eigenfunctions are all characterised by similar scales; they peak farther upstream and there appears to be a distinction between modes 0 through 3, which have reflectional symmetry with respect to the jet axis, and modes 4 and 5 which are antisymmetric. These symmetries are most likely the two-dimensional signatures of axisymmetric and helical wavepackets.

**Source mechanism analysis** We now, finally, consider the space-time characteristics of $\hat{\mathbf{q}}$ associated with high- and low-level sound emission. Comparison of the pressure signature on the centerline of the jet gives a

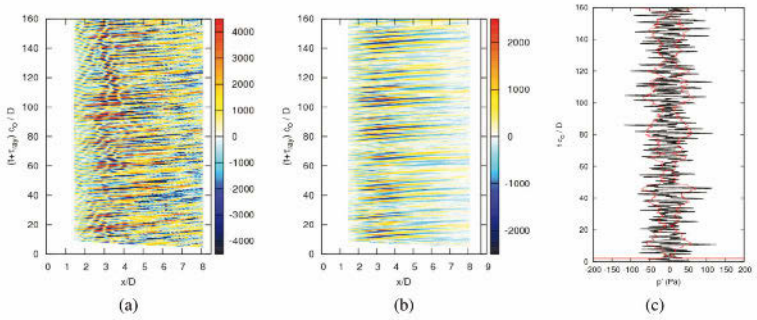


**Figure 31.** (a): $(x,t)$ structure of full pressure ($\mathbf{q}_p$) on jet centerline; (b) $(x,t)$ structure of reduced pressure ($\hat{\mathbf{q}}_p$) on jet centerline; (c): black line: acoustic pressure ($\mathbf{q}_A$) at 30°; red line: short-time Fourier series of signal. Figure (c) has been time-shifted to account for propagation times, such that events at a given time are comparable with events in (a) and (b) at the same time-coordinate.

clearest indication of how the orderly component of the flow fields behave. Figure 31 shows this quantity for the full LES solution, $\mathbf{q}_p(x_1,t)$ and the reduced flow, $\hat{\mathbf{q}}_p(x_1,t)$, and these are compared with the acoustic signature,

$\mathbf{q}_A(t)$, sampled at an angle of 30°. The latter has been time-shifted such that a direct comparison can be made with the two signals. Furthermore, the acoustic signal has been transformed by means of a short-time Fourier series and the result is shown in red. This operation provides a means by which the loud portions of the signal can be more easily identified.

Examination of the figure shows the following. While it is difficult to discern any particular relationship between the hydrodynamic centerline signature of the full flow solution and the radiated sound, analysis of the same metric of the reduced field, $\hat{\mathbf{q}}_p$, reveals a clear correspondence between the growth and decay of wavepackets (modulation of both their amplitude and axial extent is observed) and high-amplitude sound radiation. The fitting procedure applied in the previous study is repeated here using the filtered flow field, $\hat{\mathbf{q}}$, and the jittering line source *ansatz*. The result is shown in figure 32. Good agreement is found between the acoustic observable, $\mathbf{q}_A$,

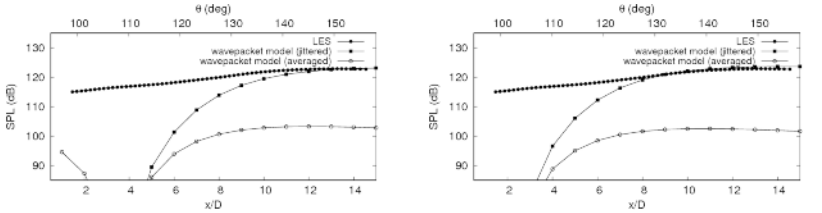


**Figure 32.** Comparison of sound field computed by Large Eddy Simulation with time-averaged and jittering wavepacket *ansatz*. (a) *ansatz* fitted with conditional field data, $\hat{\mathbf{q}}$, after radial integration; (b) *ansatz* fitted with conditiona field data, $\hat{\mathbf{q}}$ taken from mixing-layer axis.

and the modelled sound field, $\hat{\mathbf{q}}_A$, showing once again that the filtering procedure has been effective in the eduction of the sound-producing flow skeleton (kinematics).

### 4.3 Conclusions

Two case studies have been used, by way of example, in order to illustrate implementation of the analysis methodology outlined in section §3. In both cases, by following the methodology, kinematic models are constructed that mimic the sound-producing behaviour of the three different jets analysed. The quantitative accuracy is in all cases better than $1.5dB$, showing the analysis methodology—which combines the data-analysis tools

presented in section §5 with the theoretical reasoning outlined in section §3—to be effective *with regard to the kinematics of sound source mechanism identification*. For the dynamic aspect further tools are necessary; these are presented briefly in section §6.

## 5 Data analysis / reduction

The complexity of most aeroacoustic systems—being associated with high Reynolds number turbulence—means that we frequently find ourselves faced with the task of making sense of large quantities of data; such databases may be the result of numerical simulation and/or experimental measurements. Some form of data synthesis, or reduction, is necessary. The data can be considerably compressed, for example, by considering only the time-averaged values of the dependent variables, but at the loss of a large quantity of information. Other time-averaged statistical moments, such as the root mean square (2nd order moment), skewness (3rd order moment) and kurtosis (4th order moment) can be computed—further information is thereby obtained regarding the state of the system.

Between such time-averaged quantities and the full space-time structure of the system considered there lie many intermediate possibilities for compressing the data into manageable and insight-providing forms. Four techniques by which such intermediate data compression can be obtained (Fourier transform, Wavelet transform, Proper Orthogonal Decomposition and Dynamic Mode Decomposition) are presented in this section, example implementations being found in section §4. Further to these data compression/decomposition tools we also present a technique, known as Linear Stochastic Estimation, for the computation of conditional averages. This can constitute a powerful complementary approach when used in conjunction with the said data compression/decomposition tools.

The four data compression techniques discussed have the following common property: they all involve the expansion of space-time data in terms of sets of basis functions. The interest in such an operation is that the very high dimensional flow data can be broken down into a more manageable number of 'building blocks', conducive to perspicacious analysis and modelling. In the case of spectral and wavelet analyses, the basis functions are analytic and specified *a priori*; in the case of Proper Orthogonal Decomposition the basis functions are empirical and thus intrinsic to the data; in the case of Koopman modes (obtained by Dynamic Mode Decomposition), the functions are associated with the dynamics of the system, in other words they contain information regarding the temporal evolution of the system.

### 5.1 The Fourier transform

The Fourier transform is probably the best known and most commonly used data analysis tool in the domain of fluid mechanics and aeroacoustics (and indeed in engineering in general) - the Fourier power spectrum of the sound field radiated by an aeroacoustic system is the quantity that mod-

elling tools are required to reproduce; it is the quantity by which we most often endeavour to assess and understand the behaviour of the system. We recall it briefly in this section, simply so as to have it appear in juxtaposition with a number of alternative, but less commonly used, data-processing tools. We do so because three of the latter (the wavelet transform, Proper Orthogonal Decomposition, and Dynamic Mode Decomposition), as evoked above, bear certain similarities to the Fourier transform in terms of the way their result can be useful as an aid to understanding and modelling; indeed these alternative processing techniques might be best thought of as surrogate tools for assessing complex data in situations where the Fourier transform may not necessarily be the best choice.

The Fourier transform involves the expansion of a given data set in terms of analytical basis functions that are specified *a priori*; there is no flexibility in this choice. The Fourier transform and its inverse are defined as

$$\tilde{q}(f) = \int_{-\infty}^{\infty} q(a) \exp(-2\pi i a f)\, da \tag{123}$$

$$q(f) = \int_{-\infty}^{\infty} \tilde{q}(f) \exp(2\pi i a f)\, df. \tag{124}$$

When the signal $q(a)$ is periodic in the variable $a$ it can be expanded as a Fourier *series*:

$$q(a) = \frac{1}{2} A_0 + \sum_{n=1}^{\infty} A_n \cos(na) + \sum_{n=1}^{\infty} B_n \sin(na), \tag{125}$$

where

$$A_0 = \frac{1}{\pi} \int_{-\pi}^{\pi} q(a)\, da \tag{126}$$

$$A_n = \frac{1}{\pi} \int_{-\pi}^{\pi} q(a) \cos(na)\, da \tag{127}$$

$$B_n = \frac{1}{\pi} \int_{-\pi}^{\pi} q(a) \sin(na)\, da. \tag{128}$$

### 5.2 The wavelet transform

The wavelet transform provides additional flexibility on two levels when compared with the Fourier transform. (1) The transformed quantity is local in both frequency (or wavenumber) and time (or space); (2) many different kinds of basis function are available, and indeed it is possible to create new functions, provided certain mathematical constraints are satisfied.

The continuous wavelet transform of a signal $q(\alpha)$ is written:

$$\tilde{q}(s,a) = \int_{-\infty}^{\infty} q(\alpha)\psi(s, a-\alpha)d\alpha. \tag{129}$$

This amounts to the convolution of a signal of interest with a set of wavelet functions $\psi$. This set of functions is generated by dilation and translation of a basic form known as the mother wavelet: dilation is achieved by varying the scale, $s$, translation being effected by means of the variable, $a$, which could be a space or time coordinate, for example. The mother wavelet function must satisfy the mathematical constraints of admissibility and regularity; however, provided these constraints are satisfied a good deal of flexibility remains for the design of new mother wavelet functions.

The main difference between the wavelet transform and the Fourier transform is that the former allows space- or time-localised characteristics of a signal to be more clearly identified: the transformed signal is local in both space (and/or time) and scale, whereas its Fourier transformed counterpart is local only in frequency, being infinitely extended in space (and/or time).

The following are some relations between the fluctuation energy of a signal, its wavelet transform and its Fourier transform.

1. The relationship between the fluctuation energy, $E$ of the signal $q(a)$ and the wavelet transform of the signal is given by:

$$E = \int_{\mathbb{R}} |q(a)|^2 da = C_{\psi}^{-1} \int_{\mathbb{R}^+} \int_{\mathbb{R}} |\tilde{q}(s,a)|.|\tilde{q}^*(s,a)| \, \frac{ds\, da}{s^2} \tag{130}$$

   where $C_\psi$ is a constant associated with the mother wavelet function used.
2. A global wavelet energy spectrum can be defined as:

$$e_{\text{global}}(s) = \int_{\mathbb{R}} e(s,a)\, da \tag{131}$$

   where $e(s,a)$ is the energy density as a function of scale, $s$ and the space or time dimension, $a$.
3. This can also be expressed in terms of the Fourier energy spectrum $E(f) = |\hat{q}(f)|^2$:

$$e_{\text{global}}(s) = \int_{\mathbb{R}} E(f)|\hat{\psi}(sf)|^2 df \tag{132}$$

   where $\hat{\psi}(sf)$ is the Fourier transform of the wavelet. This shows that the global wavelet energy spectrum corresponds to the Fourier energy spectrum smoothed by the wavelet spectrum at each scale.

4. The total fluctuation energy of the signal can be obtained by

$$E = C_\psi^{-1} \int_{\mathbb{R}^{+*}} e_{\text{global}}(s) \frac{ds}{s} \tag{133}$$

### 5.3 Proper Orthogonal Decomposition

The Proper Orthogonal Decomposition is a data processing technique which is known by this name when used in the field of turbulence analysis, following its introduction for such usage by Lumley (1967). It can also be found referred to as Karhunen-Loève decomposition, principal component analysis (Jolliffe (1986)) and singular value decomposition (Golub and Van Loan (1996)). The presentation of POD given here follows that of Delville (1995).

Consider a flow system for which we possess the information $\mathbf{q}(\mathbf{a}, \mathbf{b})$. The vector $\mathbf{q}$ could contain, for example, the values of the three components of velocity on the four-dimensional grid, $(\mathbf{x}, t)$; in this case $\mathbf{a}$ would represent three-dimensional cartesian space, and $\mathbf{b}$ the time direction. We retain the notation $\mathbf{a}$ and $\mathbf{b}$ in order to keep the derivation as general as possible, because different variants of the POD can be derived from different specific choices of $\mathbf{a}$ and $\mathbf{b}$, and associated definitions of the inner product and averaging operations that are applied, respectively, with respect to these coordinates.

POD consists in searching for the function, $\boldsymbol{\phi}(\mathbf{a})$, that is best aligned, on average, with the field $\mathbf{q}(\mathbf{a}, \mathbf{b})$, the averaging operation being with respect to the coordinate $\mathbf{b}$.[15] Both $\mathbf{q}(\mathbf{a}, \mathbf{b})$ and $\boldsymbol{\phi}(\mathbf{a})$ are indefinitely differentiable, have compact support, and belong to the space of square integrable functions. The problem is considered in Hibert space, and so it is possible to define the inner product $(\mathbf{q}, \boldsymbol{\phi})_{\mathbf{a}}$ with respect to $\mathbf{a}$:

$$(\mathbf{q}, \phi)_{\mathbf{a}} = \int_{\mathbf{a}} \mathbf{q}(\mathbf{a}, \mathbf{b}) \boldsymbol{\phi}^*(\mathbf{a})\, d\mathbf{a} = \sum_{i=1}^{n_c} \int_{\mathbf{a}} q_i(\mathbf{a}, \mathbf{b}) \phi_i^*(\mathbf{a})\, d\mathbf{a} \tag{134}$$

where $n_c$ denotes the number of components of the vector $\mathbf{q}$ (the three components of velocity for example).

The search for the function $\boldsymbol{\phi}$ amounts to a search, over the ensemble of realisations of $\mathbf{q}$, for the $\boldsymbol{\phi}$ that most closely resembles $\mathbf{q}$ on average. This means maximising the projection $\mathbf{q}(\mathbf{a}, \mathbf{b})$ on the function $\boldsymbol{\phi}(\mathbf{a})$ with respect to the inner product defined above: we must find the function $\boldsymbol{\phi}$

[15] Note that $\mathbf{a}$ could comprise both space and time coordinates, and the averaging operation, over $\mathbf{b}$, could be, for example, a phase- or ensemble-average.

that maximises

$$\frac{< (\mathbf{q}(\mathbf{a},\mathbf{b}), \boldsymbol{\phi}(\mathbf{a}))^2 >_{\mathbf{b}}}{||\boldsymbol{\phi}(\mathbf{a})||}.^{16} \tag{135}$$

The numerator can be expressed as

$$< (\mathbf{q}, \boldsymbol{\phi})^2 > =< \int_{\mathbf{a}} \mathbf{q}(\mathbf{a},\mathbf{b}) \boldsymbol{\phi}^*(\mathbf{a})\, d\mathbf{a} \int_{\mathbf{a}} \mathbf{q}(\mathbf{a}',\mathbf{b}) \boldsymbol{\phi}^*(\mathbf{a}')\, d\mathbf{a}' >_{\mathbf{b}} \tag{136}$$

$$= \int_{\mathbf{a}} \Big( \int_{\mathbf{a}} < \mathbf{q}(\mathbf{a},\mathbf{b}) \mathbf{q}^*(\mathbf{a}',\mathbf{b}) >_{\mathbf{b}} \boldsymbol{\phi}(\mathbf{a}')\, d\mathbf{a}' \Big) \boldsymbol{\phi}^*(\mathbf{a})\, d\mathbf{a}, \tag{137}$$

the averaging being applied only to the (two-point correlations of the) data, $\mathbf{q}(\mathbf{a},\mathbf{b})$, as $\boldsymbol{\phi}$ is, by definition, independent of this direction. Denoting the two point correlation as $R_{ij}(\mathbf{a},\mathbf{a}') =< \mathbf{q}(\mathbf{a},\mathbf{b}) \mathbf{q}^*(\mathbf{a}',\mathbf{b}) >_{\mathbf{b}}$ and introducing the Hermitian operator, $A$, such that

$$A \cdot \phi_i = \sum_{j=1}^{n_c} \int_{\mathbf{a}} R_{ij}(\mathbf{a},\mathbf{a}') \phi_j(\mathbf{a}') d\mathbf{a}' \tag{138}$$

means that we can write

$$< (\mathbf{q}, \boldsymbol{\phi})^2_{\mathbf{a}} >= \sum_{i=1}^{n_c} (A \cdot \phi_i, \phi_i)_{\mathbf{a}}, \tag{139}$$

and so the POD problem comes down the maximising of

$$\frac{(A \cdot \phi_i, \phi_i)_{\mathbf{a}}}{||\boldsymbol{\phi}||^2}. \tag{140}$$

This maximisation problem corresponds to a constrained optimisation: *find $\boldsymbol{\phi}$ that maximises equation 140 subject to the constraint $||\boldsymbol{\phi}||^2 = 1$.* This side-constraint is chosen because we are only interested in the shape of the functions, $\boldsymbol{\phi}$. The optimisation problem, which can be solved using the technique of Lagrange multipliers, or by variational analysis, leads to the following eigenvalue problem

$$A \cdot \phi_i = \lambda \phi_i, \tag{141}$$

or, in integral form

$$\sum_{j=1}^{n_c} \int_{\mathbf{a}} R_{ij}(\mathbf{a},\mathbf{a}') \phi_j(\mathbf{a}')\, d\mathbf{a}' = \lambda \phi_i(\mathbf{a}), \tag{142}$$

[16] The notation $<>_{\mathbf{b}}$ indicates that the averaging operation is with respect to the direction $\mathbf{b}$

an equation known as the Fredholm integral.

Solution of the integral eigenvalue problem is obtained by means of the theory of Hilbert-Schmidt Lovitt (1950). The details are not given here, but we recall some of the main results:

1. As with most eigenvalue problems, rather than admitting a unique solution, the equation yields a set of solutions:

$$\int_{\mathbf{a}} R_{ij}(\mathbf{a},\mathbf{a}')\phi_j^{(n)}(\mathbf{a}')\,d\mathbf{a}' = \lambda^{(n)}\phi_i^{(n)}(\mathbf{a}) \quad n = 1,2,3,... \tag{143}$$

2. The ensemble of solutions can be chosen such that the eigenfunctions are orthonormal:

$$\int_{\mathbf{a}} \phi_i^{(p)}(\mathbf{a})\phi_i^{(q)}(\mathbf{a})\,d\mathbf{a} = \delta_{pq} \tag{144}$$

3. Any field, $q_i(\mathbf{a},\mathbf{b})$, can be expanded in terms of these eigenfunctions, $\phi_i^{(n)}(\mathbf{a})$:

$$q_i(\mathbf{a},\mathbf{b}) = \sum_{n=1}^{\infty} a^{(n)}(\mathbf{b})\phi_i^{(n)}(\mathbf{a}) \tag{145}$$

where the coefficients, $a^{(n)}(\mathbf{b})$, are obtained by the projection of $q_i(\mathbf{a},\mathbf{b})$ onto $\phi_i^{(n)}(\mathbf{a})$:

$$a^{(n)}(\mathbf{b}) = \int_{\mathbf{a}} q_i(\mathbf{a},\mathbf{b})\phi_i^{(n)}(\mathbf{a})\,d\mathbf{a} \tag{146}$$

4. The series converges in a least mean square sense and the coefficients, $a^{(n)}(\mathbf{b})$, are mutually uncorrelated:

$$< a^{(n)} \cdot a^{(m)} >= \delta_{mn}\lambda^{(n)} \tag{147}$$

5. The eigenvalues are real, positive, their sum finite and they form a convergent series:

$$\lambda^{(1)} > \lambda^{(2)} > \lambda^{(3)}, ... \tag{148}$$

The most common experimental implementation of POD involves space-time velocity or pressure fields: $\mathbf{q}(\mathbf{a},\mathbf{b}) = \mathbf{u}(\mathbf{x},t) = \mathbf{u}(x,y,z,t)$ or $\mathbf{q}(\mathbf{a},\mathbf{b}) = p(\mathbf{x},t) = p(x,y,z,t)$ in which case expansion of the data in terms of the POD eigenfunctions reads

$$u_i(x,y,z,t) = \sum_{n=1}^{\infty} a^{(n)}(t)\phi_i^{(n)}(x,y,z) \tag{149}$$

or (150)

$$p(x,y,z,t) = \sum_{n=1}^{\infty} a^{(n)}(t)\phi^{(n)}(x,y,z). \tag{151}$$

The space-time structure of the measured field is thus separated into spatial (*topos*) and temporal (*chronos*) functions. Example implementations are provided in section §4.

### 5.4 Koopman modes / Dynamic mode decomposition

The *Dynamic Mode Decomposition* is a procedure for estimating the eigenvectors and eigenvalues of the *Koopman operator*. The latter provides a means by which the dynamics of a flow can be analysed, this analysis being effected through some associated observable. An assumption central to the approach is that the flow can be considered as a dynamical system evolving on a manifold $\Omega$ of dimension $N$. A manifold—the locus of points that comprise the state-space trajectory of a dynamical system—is a generalisation, to the non-linear case, of the eigenspace associated with the linear instability of dynamical system in the vicinity of a fixed point : while in a linearised system eigenvectors denote the directions in which that system will move, exponentially, either to or from a fixed point (or equilibrium point), in the non-linear context the manifold amounts to a continuation of these eigenvectors, which continually change direction as the system evolves non-linearly.

This section provides an introduction to both the Koopman operator and the dynamic mode decomposition. The exposition combines elements taken from Rowley et al. (2009), Schmid (2010) and Pastur (2011).

**The Koopman operator** Let $X$ be a point on $\Omega$, corresponding to the state of the system at some given time, and let $f_t$ be a propagator (frequently referred to as a 'flow' or a 'map' in dynamical systems or control theory textbooks) that evolves, propagates, or maps, the flow from one time-step to the next; i.e. from $X(t_0) \in \Omega$ to $X(t_0 + t) \in \Omega$: [17]

$$X(t_0 + t) = f_t\{X(t_0)\}. \tag{152}$$

In an experiment we never have access to the full flow state; at best we may have access to the velocity field on a two-dimensional spatial section (from a PIV measurement for example), with restricted temporal resolution, or single-point information with higher temporal resolution (from a hot-wire, Laser Doppler Velocimeter or microphone for instance). Such an incomplete sample of the flow can be referred to as an *observable*. We denote this observation by means of a function, $q(X)$, which gives us the observable

[17] In the case of fluid flow the propagator is the right hand side of the Navier Stokes equations; i.e. the dynamic law governing the time evolution of the fluid flow.

corresponding to the full state $X$. $q$ belongs to a Hilbert space, $\mathcal{H}$, and so we can define the norm:

$$||q|| = \sqrt{(q,q)_\Omega} = \sqrt{\int_\Omega |q|^2 \, d\Omega} < \infty. \tag{153}$$

The *Koopman operator*, $U_t$, acts in $\mathcal{H}$, such that:

$$U_t\{q(X)\} = q(f_t\{X\}). \tag{154}$$

In other words, the Koopman operator is a map that describes the evolution of the *observable*, $q$ (which is a function of the full flow state $X$), from one time-step to the next. The non-linear dynamics associated with the evolution of the full flow leaves its signature in the evolution of the observable; the essence of Koopman/DMD analysis is here: by considering the evolution of the observable we seek to gain insight regarding the nature of the evolution law that underpins the dynamics of the full flow.

The Koopman operator has the following important property. Let $\phi_j$ and $\lambda_j$ be, respectively, eigenfunctions and associated eigenvalues of $U_t$.[18] If we denote by $X_k$ the state of the system at some time $k\Delta t$ after an initial time $t_0$: $X_k \equiv X(t_0 + k\Delta t)$, then:

$$\begin{aligned} q(X_{k+1}) = U\{q(X_k)\} &= U\left\{\sum_{j\geq 1} \phi_j(X_k)\nu_j\right\} \\ &= \sum_{j\geq 1} U\{\phi_j(X_k)\nu_j\} = \sum_{j\geq 1} \lambda_j \phi_j(X_k)\nu_j \end{aligned} \tag{155}$$

The first equality simply corresponds to the definition of the Koopman operator—it evolves the observable, $q$, from its value when the system is in the state $X_k$ to its value when the system is in the state $X_{k+1}$. In the second equality the observable, $q$, has been expanded in terms of the eigenfunctions of the Koopman operator (chosen here as a suitable set of basis functions); $\nu_j$ are the associated expansion coefficients, obtained by projecting the observable, $q$, onto the eigenfunctions, $\phi_j$. In the third equality the Koopman operator has simply been moved inside the summation, while in the fourth, as $\phi_j$ are eigenfunctions of $U$, $U\{\phi_j\}$ can be written as $\lambda_j\phi_j$.

$\nu_j$ are the Koopman modes (sometimes referred to as Koopman coefficients, or dynamic modes), $\lambda_j$ the Koopman eigenvalues and $\phi_j$ the Koopman eigenfunctions. The Dynamic Mode Decomposition constitutes a

[18] In what follows we will drop the the subscript $t$.

methodology, similar to the Arnoldi algorithm used in the solution of global stability problems, whereby these quantities can be *estimated* using *limited data sets*.

Now, as the evolution of the system from some initial state, $X_0$ to a later state $X_{k+1}$ is given by $U^k(X_0)$ (because $U(X_k) = UU(X_{k-1}) = U^3(X_{k-2}) = ...$), the state of the observable, $q(X_{k+1})$, can be expressed in terms of the state at some initial time, $X_0$, as:

$$q(X_{k+1}) = \sum_{j \geq 1} \lambda_j^k \phi_j(X_0) \nu_j. \tag{156}$$

This equation shows that any value of the observable, $q$, can be deduced from knowledge of the projection of the initial condition $q(X_0)$ onto the eigenfunctions, $\phi_j$, of the Koopman operator, provided the eigenvalues, $\lambda_j$ are known; this property is important in what follows. Furthermore, if the dynamics considered evolve on a non-degenerated attractor—the dynamics continue to evolve on the manifold, $\Omega$—then the Koopman operator, $U$, is a unit operator: the eigenvalues lie on the unit circle and the eigenvectors, $\phi_j$, are orthogonal.

**Krylov sub-space** Consider the following set of successive snapshots of data:

$$Q_0^{N-1} = \{q(X_0), q(X_1), q(X_2), ..., q(X_{N-1})\}, \tag{157}$$

the sub- and super-scripts on $Q$ indicate the first and last snapshots. Expressed in terms of the Koopman operator this reads:

$$Q_0^{N-1} = \{q(X_0), U\{q(X_0)\}, U^2\{q(X_0)\}, ..., U^{N-1}\{q(X_0)\}\}, \tag{158}$$

which is an $N^{th}$-order Krylov subspace. And we know that the Koopman operator applied to this subspace gives:

$$U\left\{Q_0^{N-1}\right\} = Q_1^N : \tag{159}$$

the action of the Koopman operator is inherently contained in $Q_1^N$.

To this point the observable has been considered a single-point scalar; however, the generalisation to multi-valued observables (for example a velocity field obtained from PIV) is straightforward. In this case the $\nu_j$ are multi-valued and complex.

**Dynamic mode decomposition** DMD is one possible technique, based on what is known as a companion Matrix, by which the eigenvalues and eigenvectors of $U$ can be estimated; the technique is similar to that used

for the computation of global modes from the Hessenberg matrix using the Arnoldi method.

In what follows we will consider multi-valued observables, represented by the vector $\mathbf{q}(\mathbf{x}, t_k)$. A Krylov subspace is first constructed from sampled data, where the time-step is small enough to resolve all of the dynamics:

$$Q_0^{N-1} = \{\mathbf{q}_0, \mathbf{q}_1, \mathbf{q}_2, ..., \mathbf{q}_{N-1}\}. \tag{160}$$

The indices correspond to the successive times, $t_0, t_1, t_2, ...t_{N-1}$. The assumption underpinning the companion matrix approach is that the first $N$ fields (where $N < M$, M being the dimension of the observable $\mathbf{q}$, i.e. the number of spatial points in the snapshot) are sufficient to describe any later realisation of the field $\mathbf{q}$; thus, the $N^{th}$ snapshot can be expressed as a linear combination of all previous snapshots:

$$\mathbf{q}_N = c_0\mathbf{q}_0 + c_1\mathbf{q}_1 + c_2\mathbf{q}_2 + ... + c_{N-1}\mathbf{q}_{N-1}, \tag{161}$$

or

$$\mathbf{q}_N = Q_0^{N-1}\mathbf{c}, \tag{162}$$

where $\mathbf{c} = (c_0, c_1, c_2, ..., c_{N-1})^T$ and the superscript $T$ denotes hermitian transpose. From equation 158 we know that

$$U\left\{Q_0^{N-1}\right\} = Q_1^N, \tag{163}$$

i.e. application of the Koopman operator to the Krylov subspace propagates all of the fields by one time-step. In light of this observation, and equation 162, equation 163 can be written as

$$UQ_0^{N-1} = Q_1^N = Q_0^{N-1}C + \mathbf{r}^T\mathbf{e}_N, \tag{164}$$

where $C$ is the companion matrix. $\boldsymbol{e}_N = (0\,, 0\,, \ldots\,, 1)^\dagger \in \mathbb{R}^{N+1}$ and $\boldsymbol{r}$ is a residual vector, orthogonal to the Krylov subspace $V_0^{N-1}$. The residual goes to zero when condition 162 is satisfied.

The following example will help illustrate this. Consider that we have the data:

$$Q_1^4 = \begin{bmatrix} q_{11} & q_{12} & q_{13} & q_{14} \\ q_{21} & q_{22} & q_{23} & q_{24} \\ q_{31} & q_{32} & q_{33} & q_{34} \end{bmatrix}$$

where the first and second indices on the matrix entries denote spatial and temporal coordinates, respectively: each column is a snapshot. We know that the Koopman operator, $U$, will map from $Q_1^3$ to $Q_2^4$:

$$\begin{bmatrix} U_{11} & U_{12} & U_{13} \\ U_{21} & U_{22} & U_{23} \\ U_{31} & U_{32} & U_{33} \end{bmatrix} \begin{bmatrix} q_{11} & q_{12} & q_{13} \\ q_{21} & q_{22} & q_{23} \\ q_{31} & q_{32} & q_{33} \end{bmatrix} = \begin{bmatrix} q_{12} & q_{13} & q_{14} \\ q_{22} & q_{23} & q_{24} \\ q_{32} & q_{33} & q_{34} \end{bmatrix}.$$

But, we are also making the assumption that $\mathbf{q}_{i4}$ can be expressed as a linear combination of $\mathbf{q}_{i1}$, $\mathbf{q}_{i2}$ and $\mathbf{q}_{i3}$:

$$\begin{bmatrix} q_{14} \\ q_{24} \\ q_{34} \end{bmatrix} \approx \begin{bmatrix} c_1 q_{11} + c_2 q_{21} + c_3 q_{31} \\ c_1 q_{12} + c_2 q_{22} + c_3 q_{32} \\ c_1 q_{13} + c_2 q_{23} + c_3 q_{33} \end{bmatrix}.$$

Substituting into the previous equation gives,

$$\begin{bmatrix} U_{11} & U_{12} & U_{13} \\ U_{21} & U_{22} & U_{23} \\ U_{31} & U_{32} & U_{33} \end{bmatrix} \begin{bmatrix} q_{11} & q_{12} & q_{13} \\ q_{21} & q_{22} & q_{23} \\ q_{31} & q_{32} & q_{33} \end{bmatrix} \approx \begin{bmatrix} q_{12} & q_{13} & (c_1 q_{11} + c_2 q_{12} + c_3 q_{13}) \\ q_{22} & q_{23} & (c_1 q_{21} + c_2 q_{22} + c_3 q_{23}) \\ q_{32} & q_{33} & (c_1 q_{31} + c_2 q_{32} + c_3 q_{33}) \end{bmatrix},$$

which is the same as

$$\begin{bmatrix} U_{11} & U_{12} & U_{13} \\ U_{21} & U_{22} & U_{23} \\ U_{31} & U_{32} & U_{33} \end{bmatrix} \begin{bmatrix} q_{11} & q_{12} & q_{13} \\ q_{21} & q_{22} & q_{23} \\ q_{31} & q_{32} & q_{33} \end{bmatrix} \approx \begin{bmatrix} q_{11} & q_{12} & q_{13} \\ q_{21} & q_{22} & q_{23} \\ q_{31} & q_{32} & q_{33} \end{bmatrix} \begin{bmatrix} 0 & 0 & c_1 \\ 1 & 0 & c_2 \\ 0 & 1 & c_3 \end{bmatrix}.$$

In the more general case, the companion matrix takes the form:

$$C = \begin{pmatrix} 0 & \dots & \dots & 0 & c_0 \\ 1 & 0 & & \vdots & c_1 \\ 0 & 1 & \ddots & \vdots & c_2 \\ \vdots & \ddots & \ddots & 0 & \vdots \\ 0 & \dots & 0 & 1 & c_{N-1} \end{pmatrix}. \tag{165}$$

DMD consists in computing the eigenmodes of the companion matrix, which are then considered as approximations of the eigenmodes of the Koopman operator (when the residual is zero the correspondence is exact). The matrix $C$ has dimension $N \times N$, and its unknown elements, $c_j$, can be computed by minimising the norm

$$\mathbf{c}_{opt} = \min_{\mathbf{c}} \left\| \mathbf{q}_N - \sum_{j=1}^{N-1} c_j \mathbf{q}_j \right\|_2.$$

Having computed the eigenvalues and eigenvectors of the companion matrix we are finally in a position to write

$$\tilde{\mathbf{q}}_k = \sum_{j=1}^{N} \lambda_j^{k-1} \phi_j(X_0) \boldsymbol{\nu}_j. \tag{166}$$

The initial conditions $\phi_j(X_0)$ are obtained by projecting the initial field, $\mathbf{q}_0$, on to the $\boldsymbol{\nu}_j$. The eigenfunctions, $\phi_j$, are Fourier modes, $\phi_j = \exp(i\omega_j t)$ if the dynamics are periodic.

### 5.5 Conditional analysis techniques: Stochastic estimation

The following exposition is based on that of Adrian (1996). Consider some variable, $\mathbf{q}$, which is unknown, and another vector quantity $\mathbf{E} = E_i$, $i = 1..N$ which is somehow related to $\mathbf{q}$. We are interested in identifying the functional relationship, $\mathbf{q} = g(\mathbf{E})$, which provides some approximation of $\mathbf{q}$ in terms of $\mathbf{E}$. This kind of estimation of one variable in terms of another is known as stochastic estimation and is widely used in information theory (Papoulis (1984)). When such a relationship cannot be usefully derived from first principals, we frequently revert to statistics: the *joint* probability density between $\mathbf{q}$ and $\mathbf{E}$ is:

$$f_{\mathbf{q},\mathbf{E}} d\psi d\phi = \text{Prob}\{\psi \leq \mathbf{q} < \psi + d\psi \text{ and } \phi \leq \mathbf{E} < \phi + d\phi\}; \tag{167}$$

the *conditional* probability density of $\mathbf{q}$ given $\mathbf{E}$ is

$$f_{\mathbf{q}|\mathbf{E}}(\psi|\phi) = \frac{f_{\mathbf{q},\mathbf{E}}(\psi,\phi)}{f_{\mathbf{E}}(\phi)}. \tag{168}$$

Three estimates of $\mathbf{q}$ given $\mathbf{E}$ are: (1) the *maximum likelihood estimate*, defined as the most probable value of $\mathbf{q}$ given $\mathbf{E}$, i.e. the value at which $f_{\mathbf{q}|\mathbf{E}}$ is a maximum; (2) the *conditional average* of $\mathbf{q}$ given $\mathbf{E}$, given by the centroid of the *conditional probability*

$$< \mathbf{q}|\mathbf{E} >= \int \psi f_{\mathbf{q}|\mathbf{E}}(\psi|\phi) d\psi; \tag{169}$$

and, (3) the *mean square estimate*, i.e. the estimate $\hat{\mathbf{q}} = f(\mathbf{E})$ that minimises $< |\mathbf{q} - f(\mathbf{E})|^2 >$. It can be shown that the best mean square estimate of $\mathbf{q}$ given $\mathbf{E}$ is the conditional average $< \mathbf{q}|\mathbf{E} >$. In other words, $< |\mathbf{q} - f(\mathbf{E})|^2 >$ is a minimum when $f(\mathbf{E}) =< \mathbf{q}|\mathbf{E} >$.

In this section we outline a technique by which the conditional average can be *estimated*; in other words we wish to estimate the best estimate: $\hat{\mathbf{q}} \approx< \mathbf{q}|\mathbf{E} >$. The conditional average is approximated by means of a truncated Taylor series expansion about $\mathbf{E} = 0$:

$$\hat{\mathbf{q}} \approx< \mathbf{q}|\mathbf{E} >\equiv f(\mathbf{E}) \equiv f(0) + \frac{\partial f}{\partial \mathbf{E}}\frac{\mathbf{E}}{1!} + \frac{\partial^2 f}{\partial \mathbf{E}^2}\frac{\mathbf{E}^2}{2!} + \frac{\partial^3 f}{\partial \mathbf{E}^3}\frac{\mathbf{E}^3}{3!} + ... \tag{170}$$

As we do not know the function $f(\mathbf{E})$ we cannot evaluate the derivatives $\frac{\partial^n f}{\partial \mathbf{E}^n}$ and so these are unknowns of the problem. So, considering that the

mean value is zero, ($f(0) = 0$), the expansion can be written

$$\hat{\mathbf{q}} \approx < \mathbf{q}|\mathbf{E} > \equiv f(\mathbf{E}) \equiv A\mathbf{E} + B\mathbf{E}^2 + C\mathbf{E}^3 + ... \tag{171}$$

and we are required to determine the value of the coefficients $A$, $B$, $C$,... When truncation is performed after the linear term this expression is known as *Linear stochastic estimation*, when the quadratic term is included we speak of *quadratic stochastic estimation*, and so on...

Let us now see how to calculate the coefficients, $A$, in the case where truncation is performed after the linear term. We have

$$\hat{\mathbf{q}} \approx A\mathbf{E}, \tag{172}$$

and we would like to obtain a best estimate for $< \mathbf{q}|\mathbf{E} >$; i.e. we need to minimise the error

$$e = < |< \mathbf{q}|\mathbf{E} > -\hat{\mathbf{q}}|^2 > \tag{173}$$

$$= < | < \mathbf{q}|\mathbf{E} > -A\mathbf{E}|^2 >, \tag{174}$$

we therefore require the solution to

$$\frac{\partial e}{\partial A} = 2 < - < \mathbf{q}|\mathbf{E} > \mathbf{E} > +2A < \mathbf{E}\mathbf{E} >= 0, \tag{175}$$

which is given by

$$A = \frac{<< \mathbf{q}|\mathbf{E} > \mathbf{E} >}{< \mathbf{E}\mathbf{E} >} \tag{176}$$

$$= \frac{<< \mathbf{q}\mathbf{E}|\mathbf{E} >>}{< \mathbf{E}\mathbf{E} >} \tag{177}$$

$$= \frac{< \mathbf{q}\mathbf{E} >}{< \mathbf{E}\mathbf{E} >}, \tag{178}$$

where $\mathbf{E}$ has been brought inside the conditional average on account of its being constant with respect to the latter, and, in the final step, the conditional average has been performed over all values of $\mathbf{E}$, reducing the conditional average $<< \mathbf{q}\mathbf{E}|\mathbf{E} >>$ to the conventional average $< \mathbf{q}\mathbf{E} >$.

So, the linear stochastic estimate of $\mathbf{q}$ given some related event $\mathbf{E}$, which provides a best approximation to the conditional average $< \mathbf{q}|\mathbf{E} >$, is:

$$\hat{\mathbf{q}} = \frac{< \mathbf{q}\mathbf{E} >}{< \mathbf{E}\mathbf{E} >}\mathbf{E}. \tag{179}$$

This shows the close relationship between the conditional average and the correlation function $< \mathbf{q}\mathbf{E} >$. In the context of aeroacoustics, where $\mathbf{E}$ is the

radiated acoustic pressure and $\mathbf{q}$ the turbulence velocity, such correlations can be shown to provide an approximation to the integral solution of the acoustic analogy (Lee and Ribner (1972)). An example implementation of this technique is provided in section §4.

# 6 Reduced Order Modelling

## 6.1 Introduction

It was shown in section §4 how the analysis tools presented in section §5 can provide a useful means by which the analysis methodology outlined in section §3 can help guide kinematic modelling. However, the final goal, as evoked in the introduction, is to understand and model the dynamic law associated with sound production, as it is only then that one can really claim to have identified source mechanisms.

In this section we provide a very brief introduction to reduced order modelling. For a more complete treatment the reader is encouraged to refer to Noack et al. (2011).

## 6.2 Two approaches for reduced order dynamical modelling

The governing dynamic law of the full flow system is:

$$\mathcal{N}\mathbf{q} = 0. \tag{180}$$

The objective of reduced order modelling, the final stage of the analysis methodology outlined in section §3, is to construct a simplified dynamic law governing the evolution of a simplified kinematic field, $\hat{\mathbf{q}}$:

$$\hat{\mathcal{N}}\hat{\mathbf{q}} = 0. \tag{181}$$

Two reduced-order dynamic modelling strategies will be outlined here. The first is useful when relatively complete space-time data is available, from a numerical simulation for example, the second being useful in an experimental context, where more limited data is available. In both cases the objective is to write down an Ordinary Differential Equation that mimics either the dynamics of the Navier Stokes operator, or of some reduced subspace of the system.

This can be achieved once the flow has been expanded in terms of a set of orthogonal basis functions, which can be obtained, for example, by means of POD:[19]

$$\hat{\mathbf{q}}(\mathbf{x}, t) = \sum_{n=1}^{N} a_i(t)\boldsymbol{\phi}(\mathbf{x}). \tag{182}$$

The temporal evolution of the flow is here contained in $a_i(t)$, and so it is via these, the *topos*, that we can attempt to write down a simplified

[19] See section §5 for details.

evolution equation, in the form of an ODE:

$$\frac{da_i}{dt} = L_{ij}a_j + Q_{ijk}a_j a_k, \tag{183}$$

which mimics both linear and non-linear aspects of the dynamics, via, respectively, the first and second terms on the right hand side. The goal is to compute the coefficients, $L_{ij}$ and $Q_{ijk}$, that best reproduce the (known) temporal structure of $a_i(t)$; we then have a simplified dynamic model for the flow (or flow sub-space) considered.

The difference between the two said approaches is in the way that the coefficients $L_{ij}$ and $Q_{ijk}$ are computed.

**Galerkin projection** In this approach, the Navier Stokes equations are projected onto the basis functions, $\boldsymbol{\phi}(\mathbf{x})$, giving, directly

$$\frac{da_i}{dt} = \nu L_{ij}a_j + (Q^c_{ijk} + Q^p_{ijk})a_j a_k \tag{184}$$

where

$$L_{ij} = (\phi_i, \Delta\phi_j) = \int_{\mathbf{x}} \phi_i \Delta\phi_j d\mathbf{x} \tag{185}$$

$$Q^c_{ijk} = (\phi_i, \nabla\cdot(\phi_j \otimes \phi_k)) = \int_{\mathbf{x}} \phi_i \nabla\cdot(\phi_j \otimes \phi_k) d\mathbf{x} \tag{186}$$

$$Q^p_{ijk} = (\phi_i, \phi^p_{jk}) = \int_{\mathbf{x}} \phi_i \phi^p_{jk} d\mathbf{x}. \tag{187}$$

$$\tag{188}$$

$Q^c_{ijk}$ is here associated with the non-linear convection term of the Navier-Stokes equations, $Q^p_{ijk}$ is associated with the pressure term[20], while $L_{ij}$ is associated with viscous and linear convection terms.

**Polynomial identification** This technique, proposed by Perret et al. (2006) is useful when only limited experimental data is available. The polynomial form

$$\frac{da_i}{dt} = L_{ij}a_j + Q_{ijk}a_j a_k \tag{189}$$

is chosen as a suitable generic dynamic *ansatz*; then, knowing the values of $a_i$, we have a linear system of equations with unknowns, $L_{ij}$ and $Q_{ijk}$. By solving this linear system, the coefficients can be identified.

[20] see Noack et al. (2011) for details

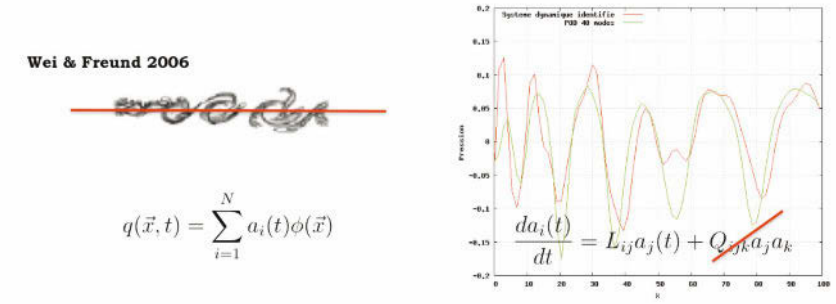


**Figure 33.** Left: instantaneous image of DNS of 2-D mixing-layer of Wei and Freund (2006): pressure fluctuations are sampled along the red line, and this field is then decomposed using POD; Right: green line shows a truncated representation of the DNS solution for the spatial structure of the pressure field on the red line at some given instant in time, while the red line shows the structure predicted by the simplified dynamic model given by the ODE—the quadratic term has been neglected in this example.

### 6.3 Example

Figure 33 shows an example implementation of the polynomial identification technique. The DNS computation of a two-dimensional shear-layer, performed by Wei & Freund, is used. The pressure field is sample along the red line shown on the left of the figure. This sampled pressure field is then decomposed using Proper Orthogonal Decomposition, allowing it to be represented in terms of a set of temporal functions, $a_i(t)$, and spatial functions, $\phi(x)$. Using the polynomial identification technique, truncated to only include the linear term, the coefficients, $L_{ij}$ are determined . The ODE is then integrated in time and the result compared with a truncated representation (using 40 POD modes, a number found sufficient to reproduce the full DNS field with good accuracy) of the original pressure field.

The integrated ODE, a snapshot of which is shown in figure 33, was found to follow the DNS very closely for about three convective time units. After this the two solutions begin to differ, although the simplified dynamic model continues to behave in a qualitatively similar manner to the DNS.

## Bibliography

G. K. Batchelor. *The theory of homogeneous turbulence*. Cambridge University Press, 1953. ISBN 0521041171.

GK Batchelor and AE Gill. Analysis of the stability of axisymmetric jets. *Journal of Fluid Mechanics*, 14(04):529–551, 1962. ISSN 1469-7645.

KA Bishop, JE Williams, and W. Smith. On the noise sources of the unsuppressed high-speed jet. *Journal of Fluid Mechanics*, 50(01):21–31, 1971. ISSN 1469-7645.

D. J. Bodony and S. K. Lele. On using large-eddy simulation for the prediction of noise from cold and heated turbulent jets. *Physics of Fluids*, 17(8):085103, 2005.

C. Bogey, C. Bailly, and D. Juvé. Noise investigation of a high subsonic, moderate Reynolds number jet using a compressible large eddy simulation. *Theoretical and Computational Fluid Dynamics*, 16(4):273–297, 2003. ISSN 0935-4964.

G. L. Brown and A. Roshko. On density effects and large structure in turbulent mixing layers. *Journal of Fluid Mechanics*, 64(4):775–816, 1974.

B.J. Cantwell. Organized motion in turbulent flow. *Annual Review of Fluid Mechanics*, 13(1):457–515, 1981. ISSN 0066-4189.

A. V. G. Cavalieri, G. Daviller, P. Comte, P. Jordan, G. Tadmor, and Y. Gervais. Using LES to explore sound-source mechanisms in jets. In *IUTAM Symposium on Computational Aero-Acoustics for Aircraft Noise Prediction*, Southampton, UK, March 29-31 2010a.

A. V. G. Cavalieri, P. Jordan, A. Agarwal, and Y. Gervais. Jittering wavepacket models for subsonic jet noise. In *AIAA Paper 2010-3957, 16th AIAA/CEAS Aeroacoustics Conference and Exhibit*, Stockholm, Sweden, June 7-9 2010b.

A. V. G. Cavalieri, P. Jordan, A. Agarwal, and Y. Gervais. Jittering wavepacket models for subsonic jet noise. *Journal of Sound and Vibration*, accepted for publication, 2011a.

A. V. G. Cavalieri, Jordan P., Y. Gervais, and T. Colonius. Axisymmetric superdirectivity in subsonic jets. In *AIAA Paper 2011-NNNN, 17th AIAA/CEAS Aeroacoustics Conference and Exhibit*, Portland, USA, June 7-9 2011b.

Y.Y. Chan. Spatial waves in turbulent jets. *Physics of Fluids*, 17:46, 1974.

B.T. Chu and L.S.G. Kovásznay. Non-linear interactions in a viscous heat-conducting compressible gas. *Journal of Fluid Mechanics*, 3(05):494–514, 1958. ISSN 1469-7645.

T. Colonius, A. Samanta, and K. Gudmundsson. Parabolized stability equation models of large-scale jet mixing noise. *Procedia Engineering*, 6: 64–73, 2010. ISSN 1877-7058.

D. G. Crighton. Basic principles of aerodynamic noise generation. *Progress in Aerospace Sciences*, 16(1):31–96, 1975.

D. G. Crighton and M. Gaster. Stability of slowly diverging jet flow. *Journal of Fluid Mechanics*, 77(2):397–413, 1976. ISSN 0022-1120.

D. G. Crighton and P. Huerre. Shear-layer pressure fluctuations and superdirective acoustic sources. *Journal of Fluid Mechanics*, 220:355–368, 1990.

S. C. Crow. Acoustic gain of a turbulent jet. *Phys. Soc. Meeting, Univ. Colorado, Boulder*, 6(paper IE), 1972.

S. C. Crow and F. H. Champagne. Orderly structure in jet turbulence. *Journal of Fluid Mechanics*, 48(3):547–591, 1971.

J. Delville. *La decomposition orthogonale aux valeurs propres et l'analyse de l'organisation tridimensionelle des ecoulements turbulents cisailles libres.* PhD thesis, Universite de Poitiers, 1995.

P.E. Dimotakis and G.L. Brown. The mixing layer at high Reynolds number: large-structure dynamics and entrainment. *Journal of Fluid Mechanics*, 78(03):535–560, 1976. ISSN 1469-7645.

J. E. Ffowcs Williams and A. J. Kempton. The noise from the large-scale structure of a jet. *Journal of Fluid Mechanics*, 84(4):673–694, 1978. ISSN 0022-1120.

J. B. Freund. Noise sources in a low-Reynolds-number turbulent jet at Mach 0.9. *Journal of Fluid Mechanics*, 438:277–305, 2001.

HV Fuchs. Space correlations of the fluctuating pressure in subsonic turbulent jets. *Journal of Sound and Vibration*, 23(1):77–99, 1972. ISSN 0022-460X.

W. K. George, P. D. Beuther, and R. E. A. Arndt. Pressure spectra in turbulent free shear flows. *Journal of Fluid Mechanics*, 148:155–191, 1984. ISSN 0022-1120.

M. E. Goldstein. A generalized acoustic analogy. *Journal of Fluid Mechanics*, 488:315–333, 2003.

M. E. Goldstein. On identifying the true sources of aerodynamic sound. *Journal of Fluid Mechanics*, 526:337–347, 2005. ISSN 0022-1120.

G.H. Golub and C.F. Van Loan. *Matrix computations*. Johns Hopkins Univ Pr, 1996. ISBN 0801854148.

L. Graftieaux, M. Michard, and N. Grosjean. Combining PIV, POD and vortex identification algorithms for the study of unsteady turbulent swirling flows. *Measurement Science and Technology*, 12:1422, 2001.

A. Hussain and K. Zaman. The preferred mode of the axisymmetric jet. *Journal of fluid mechanics*, 110(-1):39–71, 1981. ISSN 1469-7645.

IT Jolliffe. Principal component analysis., 1986.

F. Kerhervé, P. Jordan, C. Bogey, and D. Juvé. Jet turbulence characteristics associated with downstream and sideline sound emission. In *AIAA Paper 2010-3964, 16th AIAA/CEAS Aeroacoustics Conference and Exhibit*, Stockholm, USA, June 2010.

H.K. Lee and HS Ribner. Direct correlation of noise and flow of a jet. *The Journal of the Acoustical Society of America*, 52:1280, 1972.

L. Lesshafft, P. Huerre, and P. Sagaut. Aerodynamic sound generation by global modes in hot jets. *Journal of Fluid Mechanics*, 647:473–489, 2010. ISSN 0022-1120.

M. J. Lighthill. On sound generated aerodynamically. I. General theory. *Proceedings of the Royal Society of London. Series A, Mathematical and Physical Sciences*, pages 564–587, 1952.

G. M. Lilley. On the noise from jets. *AGARD CP-131*, pages 13–1, 1974.

W.V. Lovitt. *Linear integral equations*. Dover Publications, 1950.

JL Lumley. The structure of inhomogeneous turbulent flows. *Atmospheric turbulence and radio wave propagation*, pages 166–178, 1967.

R. Mankbadi and JTC Liu. Sound generated aerodynamically revisited: large-scale structures in a turbulent jet as a source of sound. *Philosophical Transactions of the Royal Society of London. Series A, Mathematical and Physical Sciences*, 311(1516):183–217, 1984. ISSN 0080-4614.

A. Michalke. A wave model for sound generation in circular jets. Technical report, Deutsche Luft- und Raumfahrt, November 1970. URL `http://elib.dlr.de/63062/`.

A. Michalke. Instabilitat eines Kompressiblen Runden Freistrahls unter Berucksichtigung des Einflusses der Strahlgrenzschichtdicke. *Z. Flugwiss*, 19:319–328; English translation: NASA TM 75190, 1977, 1971.

A. Michalke. On the effect of spatial source coherence on the radiation of jet noise. *Journal of Sound and Vibration*, 55(3):377–394, 1977. ISSN 0022-460X.

A. Michalke and H. V. Fuchs. On turbulence and noise of an axisymmetric shear flow. *Journal of Fluid Mechanics*, 70:179–205, 1975.

A. Michalke and A. Timme. On the inviscid instability of certain two-dimensional vortex-type flows. *Journal of Fluid Mechanics*, 29(04):647–666, 1967. ISSN 1469-7645.

U. Michel. The role of source interference in jet noise. In *15th AIAA/CEAS Aeroacoustics Conference(30th Aeroacoustics Conference)*, pages 1–15, 2009.

E. Mollo-Christensen. Measurements of near field pressure of subsonic jets. Technical report, ADVISORY GROUP FOR AERONAUTICAL RESEARCH AND DEVELOPMENT PARIS (FRANCE), 1963.

E. Mollo-Christensen. Jet noise and shear flow instability seen from an experimenter's viewpoint(Similarity laws for jet noise and shear flow instability as suggested by experiments). *Journal of Applied Mechanics*, 34:1–7, 1967.

E. Mollo-Christensen and R. Narasimha. Sound emission from jets at high subsonic velocities. *Journal of Fluid Mechanics*, 8(01):49–60, 1960. ISSN 1469-7645.

C. J. Moore. The role of shear-layer instability waves in jet exhaust noise. *Journal of Fluid Mechanics*, 80(2):321–367, 1977.

B.R. Noack, M. Morzynski, and G. Tadmor. *Reduced-Order Modelling for Flow Control. CISM Courses and Lectures 528*. Springer-Verlag Berlin (in press), 2011.

L. Pastur. personal communication, 2011.

L. Perret, E. Collin, and J. Delville. Polynomial identification of POD based low-order dynamical system. *Journal of Turbulence*, 7(17):1–15, 2006.

O.M. Phillips. On the generation of sound by supersonic turbulent shear layers. *Journal of Fluid Mechanics*, 9(1):1–28, 1960. ISSN 0022-1120.

C.W. Rowley, I. Mezić, S. Bagheri, P. Schlatter, and D.S. Henningson. Spectral analysis of nonlinear flows. *Journal of Fluid Mechanics*, 641(-1): 115–127, 2009. ISSN 1469-7645.

A. Samanta, J. B. Freund, M. Wei, and S. K. Lele. Robustness of acoustic analogies for predicting mixing-layer noise. *AIAA Journal*, 44(11):2780–2786, 2006.

P.J. Schmid. Dynamic mode decomposition of numerical and experimental data. *Journal of Fluid Mechanics*, 656:5–28, 2010. ISSN 0022-1120.

S. Sinayoko, A. Agarwal, and Z. Hu. Flow decomposition and aerodynamic sound generation. *Journal of Fluid Mechanics*, 668:335–350, 2011. ISSN 1469-7645.

T. Suzuki and T. Colonius. Instability waves in a subsonic round jet detected using a near-field phased microphone array. *Journal of Fluid Mechanics*, 565:197–226, 2006.

C. K. W. Tam and P. J. Morris. The radiation of sound by the instability waves of a compressible plane turbulent shear layer. *Journal of Fluid Mechanics*, 98(2):349–381, 1980. ISSN 0022-1120.

C.K.W. Tam and D.E. Burton. Sound generated by instability waves of supersonic flows. Part 2. Axisymmetric jets. *Journal of Fluid Mechanics*, 138(-1):273–295, 1984. ISSN 1469-7645.

C. E. Tinney and P. Jordan. The near pressure field of co-axial subsonic jets. *Journal of Fluid Mechanics*, 611:175–204, 2008.

M. Wei and J. B. Freund. A noise-controlled free shear flow. *Journal of Fluid Mechanics*, 546:123–152, 2006.

# Broadband Noise from Lifting Surfaces Analytical Modeling and Experimental Validation

Michel Roger
Ecole Centrale de Lyon

**Abstract**

The chapter is dedicated to the noise radiated by thin airfoils in either disturbed or homogeneous flows. This includes noise produced by impingement of upstream turbulence onto a leading edge, self-noise caused by boundary-layer turbulence scattering at the trailing edge and noise due to the formation of a vortex street in the near wake. Analytical modeling is proposed in the frequency domain, based on linearized theories of unsteady aerodynamics. The same mathematical background referred to as Schwarzschild's technique is used for all mechanisms in order that the predicted trends can be compared. In a first step the analysis is focused on the derivation of the induced lift fluctuations, acting as the sources of sound according to Ffowcs Williams & Hawkings' analogy. The radiation properties of isolated aerodynamic wave-numbers in the sources are discussed in a second step. Next a statistical declination of the formalism is introduced, relating the source statistics to the PSD of the acoustic pressure in the far field. Finally the statistical models are assessed against experimental data.

## 1 Introduction

### 1.1 Methodology and Context

Rotating blades, wings with high-lift devices and other so-called lifting surfaces (splitter plates, spoilers...) embedded in a flow generate aerodynamic sound by various declinations of vortex dynamics. Some of them have been introduced in chapter 2. If random disturbances are carried from upstream in the oncoming flow, they are rapidly distorted around the leading edge of the surface. This produces what is often called interaction or impingement noise. It is not intrinsic to the surface but rather characteristic of the incident flow, even though the surface shape may have a large influence

R. Camussi (Ed.), *Noise Sources in Turbulent Shear Flows: Fundamentals and Applications*, CISM International Centre for Mechanical Sciences, DOI 10.1007/978-3-7091-1458-2_5,

on the produced noise. In absence of oncoming disturbances, the surface generates its own vortex dynamics through the formation of boundary layers or the onset of vortex shedding, because of the effect of viscosity. The associated acoustic signature is called self-noise because it is more intrinsic to the incriminated surface. Most applications involve airfoil-like lifting surfaces, defined by their chord and span lengths and some cross-section design. Interaction noise and self-noise include span-wise distributed sources concentrated at the leading edge or the trailing edge, and localized sources at span ends (tips of blades, flap side-edges of high-lift devices...).

In all cases the prediction of the broadband noise is made a considerable task by the random character of the flow. The corresponding mechanisms can be addressed either numerically or analytically. Typically a numerical approach, based on the recent know-how in Computational Aero-Acoustics for a direct simulation or based on hybrid techniques, can be understood as a demanding extension (more than just a special case) of Computational Fluid Dynamics. An analytical approach is conceptually different. It is dedicated to an isolated, previously identified mechanism and needs drastic simplifications and assumptions on the flow features and/or on the geometry. The general equations are linearized and the initial problem is generally interpreted as a wave-scattering problem. This major difference makes both approaches different jobs and what can be expected from one or the other one cannot fit with the same ambitions. The numerical techniques are aimed at understanding the tiniest details of the sound generating mechanism and describing or reproducing it as accurately as possible. This is achieved at the price of heavy, time-consuming computations. Some of them are not tractable yet for the Reynolds and Mach numbers of interest, making the field still open for further progress. Conversely the analytical investigations are aimed at providing approximate but very fast and cheep results. The previously required recognition of a mechanism makes the solution clearly expressed as a function of the main parameters of the flow, thus the solution itself is easily used to get information on the scaling laws and the underlying physics. This is very useful for preliminary design in engineering context. Within the scope of hybrid approaches, an analytical prediction model can also be used to deduce the far-field sound by post-processing an already available simulation of the flow. It is clear that both approaches remain necessary in any case, and for the both of them significant improvements and new achievements are made every year in the community of aeroacoustics. On the one hand, numerical techniques become more and more attractive and tractable. On the other hand, analytical techniques can still be extended and thus have not yet reached their limitations. The present chapter is dealing more specially with flows developing on airfoils placed

in either disturbed or clean streams. It is focused on analytical prediction methods and their experimental validation.

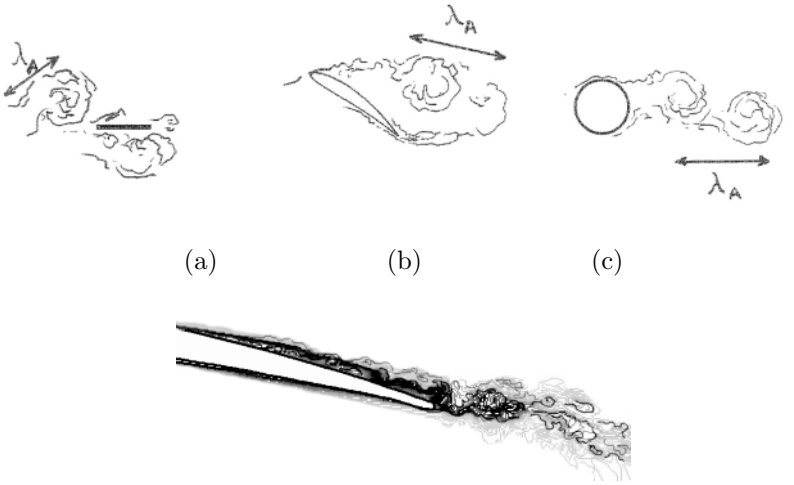


**Figure 1.** Top: large-scale unsteady fluid motions around bodies. (a): splitter plate in turbulence; (b): stalled airfoil, (c): vortex shedding behind a cylinder. Bottom: turbulent boundary layer upstream of an airfoil trailing-edge, as example of small-scale motion.

### 1.2 Importance of Characteristic Scales

Whenever the dimensions of a solid body immersed in a disturbed flow are smaller than or of the same order of magnitude as some aerodynamic wavelength $\lambda_A$, the characteristic period of the experienced aerodynamic force variations on the body $\lambda_A/U_0$ is not small with respect to the traveling time of fluid particles over the body, say $L/U_0$. In such conditions, the body responds as a whole to the disturbances, which can be defined as aerodynamic compactness in the sense that the non-dimensional aerodynamic wavenumber $2\,\pi\,/\lambda_A$ is small. This also ensures that the body is acoustically compact because the acoustic wavelength $\lambda = \lambda_A/M_0$ exceeds the body size, especially at low and moderate Mach numbers. Typical large-scale motions for which this asymptotic behavior makes sense are illustrated in Fig.1-top. They are the turbulence impingement on a flat body at low frequency (case

(a)), the stall regime of an airfoil for which a large recirculating bubble forms (case (b)) and the shedding of vortices in the near wake of a cylinder (case (c)). In contrast the flow patterns of Fig. 1-bottom responsible for the emission of trailing-edge noise correspond to much smaller scales which involve more subtle mechanisms. Typically for the narrow-band vortex-shedding sound of a cylinder in a flow, any cross-section of the cylinder is equivalent to a point dipole as stated in chapter 2. A relevant model based on the definition of an unsteady lift coefficient has been proposed by Goldstein (1976). The same would hold for any bluff body, introducing adequate global aerodynamic coefficients able to provide a description of the equivalent dipoles. A finer description in terms of distributed wall-pressure fluctuations will be needed for the configuration of Fig. 1-bottom, as shown later on.

In the present chapter the general framework introduced in Fig. 1 is reduced to span-wise distributed sources of broadband noise for relatively thin airfoils. Two mechanisms clearly dominate in most situations, namely interaction with upstream turbulence and boundary-layer turbulence scattering at the trailing-edge. The both of them are different declinations of the same basic process: sound is generated as the inertia of a vortical pattern is modified by its interaction with a singularity on a solid surface. The first mechanism, referred to as turbulence-impingement noise or leading-edge noise, involves the breakdown of oncoming vortices on the airfoil and, as such, corresponds to equivalent acoustic sources concentrated at the leading edge (Fig. 1-d of chapter 2). Nevertheless the trailing edge is involved as well in the response of the airfoil, at least as far as the scales in the incident flow are not negligibly small when compared to the chord length. A basis for the modeling will be the use of unsteady aerodynamic theories presented in the next section. Trailing-edge noise involves a modification of the incident vortices due to the secondary vorticity shed in the wake as a consequence of the Kutta condition; the corresponding acoustic sources concentrate at the trailing edge. In each case, sound radiation is associated with a sudden change in the boundary conditions applied to convected vortical patterns. In the case of a blunted trailing edge or when the boundary layer thickness is small enough with respect to the physical trailing-edge thickness, von Kármán vortex shedding takes place in the near wake, similar to case (c) of Fig. 1 but at smaller scale (Fig. 1-c of chapter 2). The shed vortices induce pressure fluctuations on the surface close to the trailing edge, again producing vortex-shedding sound. This mechanism is considered different from trailing-edge noise and will be addressed separately.

The general methodology described in the next sections relies first on linearized unsteady aerodynamic theories to get an approximate description of the equivalent acoustic sources. Because the addressed mechanisms

involve thin airfoils in subsonic Mach number flows, on the one hand, and because only non-accelerated motion is considered, the aerodynamic noise is essentially unsteady-loading noise. The noise itself is deduced in a second step using the acoustic analogy.

## 2 Unsteady Aerodynamics

### 2.1 Preliminaries

A lifting surface embedded in a disturbed flow experiences time variations of both lift and drag forces. These variations are sources of sound according to the acoustic analogy. For airfoil-like designed bodies with attached flows considered later on, lift variations are much larger than drag forces, therefore the latter are neglected and the unsteady problem is addressed based on non-viscous flow arguments. Random incident velocity disturbances cause time variations of both the magnitude and the angle of attack of the relative velocity vector experienced by the airfoil. These variations induce a total instantaneous force $F(t)$, or at a more precise level the corresponding local instantaneous lift forces distributed over the surface, noted $\ell(t)$. When calculating the noise from the airfoil according to Ffowcs Williams & Hawkings' equation, the major difficulty to deal with is the evaluation of this force field with enough accuracy. In the fluid-dynamics community, the mean value of $F(t)$ or $\ell(t)$, referred to as steady loading, is primarily addressed because only the steady-state is directly related to the aerodynamic efficiency the surface must ensure. Typically the airfoil is designed for a desired value of the mean lift coefficient $C_L$, as a function of the angle of attack $\alpha$. The fluctuations of $F(t)$ or $\ell(t)$ around the mean, essentially responsible for the noise, are much more difficult to quantify, and depend on external conditions not intrinsic to the surface design. The fluctuations bring no benefit to the aerodynamic efficiency and are only an undesirable source of noise (or vibration, even though vibrations are not addressed here). So any reduction of the unsteadiness, if possible, is a good deal from the acoustical point of view and does not essentially suffer from efficiency constraints.

### 2.2 Basic Assumptions - Thin-Airfoil Linearized Theory

For the mathematical statement dedicated to analytical investigations, is defined as unsteady aerodynamics any lift variation on an airfoil due to a variation in the oncoming flow (speed or angle of incidence), for which the Kutta condition of no flow around the trailing edge has to be fulfilled. Such a mechanism involves the entire airfoil section. The theoretical determina-

tion of $\ell(t)$ would be certainly a considerable task, were the exact solution sought for each practical flow field of interest, because of the variety encountered in both airfoil shapes and surrounding flow conditions. But acoustic calculations benefit from the favorable effect of the logarithmic dB-scale, and often only require a consistent approximation of $\ell(t)$ in most cases of interest (rotating blades, high-lift devices). For subsonic thin airfoils with small camber and angle of incidence, referred to as slightly loaded airfoils, and small velocity fluctuations, the linearized unsteady aerodynamic theory described below provides helpful approximate solutions. In contrast for highly cambered, thick blades, such as the ones encountered in turbine blade rows, the linearized approach is not relevant, and a numerical analysis is required.

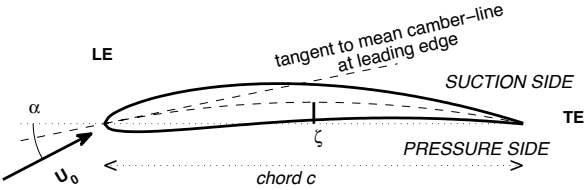


**Figure 2.** General airfoil definition. $\alpha$ and $\zeta$ are the angle of attack and the maximum camber displacement, respectively.

Before listing the assumptions of the linearized thin-airfoil theory, let us perform first a rapid analysis in the two-dimensional framework of Fig. 2. $U_0$ is the mean flow velocity, at an angle of attack $\alpha$ with respect to the chord line. Consider the velocity fluctuation vector $\mathbf{u} = (u, w)$ superimposed on the mean flow and defined in absence of airfoil. $u$ is the variation of velocity magnitude along the average flow direction and $w$ the variation of angle of attack.

A first insight into unsteady aerodynamics is provided by perturbing the steady-state equation relating the lift force per unit span $F_0$ to the relative velocity $U_0$:

$$F_0 \;=\; C_L \, c \, \frac{1}{2} \, \rho_0 \, U_0^2 \,, \tag{1}$$

where $C_L$ is the lift coefficient, function of the angle of attack $\alpha$ , and $c$ the chord length (Fig. 2). Small variations of the angle of attack and of the magnitude of the velocity vector then lead to the differential

$$dF \;=\; C_L\, c\, \rho_0\, U_0\, u + \frac{\partial C_L}{\partial \alpha}\, \frac{1}{2}\, c\, \rho_0\, U_0\, w\,.$$

This is a quasi-steady approximation because eq.(1) is assumed to hold also for transient flow conditions. For weakly loaded airfoils it can be assumed that $C_L \ll 1$ ; furthermore $\partial C_L/\partial \alpha = 2\,\pi$ for a Joukowski airfoil. It is concluded that whenever the incident velocity disturbances $w$ and $u$ have the same order of magnitude, the component $w$ is responsible for the major part of the unsteady loads. The assumptions are better justified for moderately cambered airfoils or lifting surfaces. Intuitively, blowing on a flat plate parallel to its surface and varying the flow speed is not expected to induce lift variations, whereas slightly changing the angle of attack produces significant ones. In contrast, variations of the flow speed $U_0$ at constant angle of attack on a highly cambered surface are known to also generate large lift fluctuations, as suggested by the vertical efforts exerted on an umbrella in a varying wind. As a consequence, only the fluctuations of angle of attack are generally considered in linearized unsteady aerodynamic theories applied to slightly cambered airfoils. Highly cambered airfoils are not considered here; they would require numerical investigation.

Obviously the direct proportionality and the immediate response of the airfoil expressed in eq.(1) are abusive. Indeed by virtue of the Kutta condition, vorticity is continuously shed in the wake as a result of any inflow variation. The evacuation of the shed vorticity in the flow requires a finite time, which results in some delay of the force variation. The quasi-steady approximation is just the asymptotic form of a needed more general description; it is valid for very slow variations or for large flow patterns with respect to the dimensions of a body in a flow (see Fig. 1-a again). Part of the broadband noise from low-speed fans is predicted based on similar arguments by Sharland (1964) and Fukano *et al* (1977).

Anyway, as shown by the pioneering work by von Kármán & Sears (1938), cited by Goldstein (1976), small thickness, camber and angle of incidence only determine the steady lift, but have no significant effect on the unsteady loads. This fundamental decoupling of the unsteady aerodynamic behavior from the mean loading has very important implications. Typically it means that lift fluctuations can be determined independently of the airfoil design by just solving the problem of the response of a thin flat

plate embedded at zero incidence in a parallel mean flow carrying normal velocity disturbances. This will be called Sears' problem in this course.

The general approach for solving Sears' problem in two or three dimensions is described now. First of all, the incident disturbances are assumed frozen, which means that their decaying time is large in comparison with a characteristic traveling time along the chord length. They are rotational in essence but the additional disturbance induced by the airfoil can be described as a potential field, apart from the wake; the part of this field which propagates away from the airfoil is precisely the acoustic motion. Secondly the solution is derived in the frequency domain because the time delay produced by the Kutta condition must be compared to the characteristic period of the variations of angle of attack. The procedure is as follows.

1 - The oncoming velocity disturbance normal to the airfoil surface (upwash) is Fourier-analyzed. Each Fourier component defines a transverse sinusoidal gust in the sense of unsteady aerodynamics. A gust is characterized by the chord-wise aerodynamic wave number $k_1$ and, because of the convection speed $U_0$ , induces forces on the airfoil at the corresponding angular frequency $\omega = k_1 U_0$ . A spanwise aerodynamic wavenumber $k_2$ is also introduced when the theory is extended in three dimensions (Fig.5 ).

2 - At a given value of $\omega$ or $k_1$ , the Fourier coefficient $\tilde{F}(k_1)$ of the total unsteady lift force is determined by some unsteady aerodynamic theory in terms of the transverse fluctuation amplitude $\tilde{w}(k_1)$ . In order to connect the formal result eq.(1), it is written:

$$\tilde{F}(k_1) \;=\; \pi\, \rho_0\, U_0\, \tilde{w}\, c\, T\,,$$

where $T$ is some aerodynamic transfer function introduced for physical consistency to account for the phase shift between the lift variations and the variations of angle of attack. More precisely the local distribution of fluctuating lift along the chord line, say $\tilde{\ell}(k_1, y_1)$ where $y_1$ is the chord-wise coordinate, may be of interest. For acoustic purposes, the integrated lift is enough if the chord length is acoustically compact, but the distributed local lift is needed if it is not.

The phase shift results in an inclined hysteresis response curve in the plane $(\alpha, C_L)$ (Fig. 3). Instead of following the steady-state curve, the operating point of the airfoil follows that hysteresis loop, centered around the mean-value point. The amplitude of the lift variations is well smaller than what the quasi-steady approximation would predict. The figure also suggests that oncoming disturbances can prevent the airfoil from stall. Indeed wind-tunnel experiments and simulations on oscillating airfoils have confirmed this point.

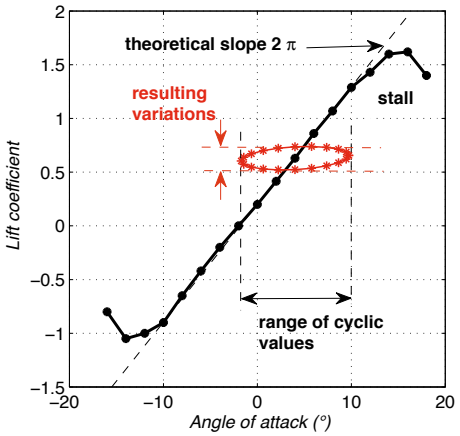


**Figure 3.** Typical aerodynamic lift coefficient curve of an airfoil (steady state) and illustration of the unsteady aerodynamic response to cyclic variations of the angle of attack.

3 - The contribution of the gust to the far-field sound is derived, based on the acoustic analogy.

In this procedure the key step is the relationship between the incident velocity disturbances, assumed known, and the associated lift variations, still to be determined. A minimum review of available theories achieving this step is given below. It must be kept in mind that in practice information about velocity disturbances is generally of easier access than information about the wall pressure on a body.

### 2.3 The Two-dimensional Incompressible Gust

The simplest physically consistent theory is two-dimensional Sears' theory assuming incompressible flow (see for instance Goldstein (1976)). Though it only addresses parallel gusts, it is presented for historical interest and because it already contains major physical features which will also be included in more sophisticated approaches. The local instantaneous lift fluctuation per unit span is distributed as:

$$\ell^S(k_1, y_1, t) \;=\; 2\,\rho_0\,U_0\,\tilde{w}(k_1^*)\,\sqrt{\frac{1-y_1^*}{1+y_1^*}}\,S^*(k_1^*)\,e^{-i\,\omega\,t}\,, \qquad (2)$$

where $y_1^* = 2\,y_1/c$ is the non-dimensional chord-wise coordinate with refer-

ence at mid chord and $k_1^* = k_1\, c/2$ the non-dimensional aerodynamic wave number of the incident fluctuation in the chord-wise direction. The theory applies to a given wave number and requires a Fourier analysis of the incident fluctuations. $S^*$ is Sears' function, expressed with Bessel functions as

$$S^*(k_1^*) \;=\; \frac{2}{\pi\, k_1^*}\; \left([J_0(k_1^*) - Y_1(k_1^*)] - i\; [J_1(k_1^*) + Y_0(k_1^*)]\right)^{-1}\;.$$

Integrating eq. (2) along the chord line leads to the total unsteady lift force per unit span for the wave number $k_1^*$ of the incident gust

$$\tilde{F}(k_1, t) \;=\; \tilde{F}(k_1)\, e^{-i\,\omega\, t} \;=\; \pi\, \rho_0\, c\, U_0\, \tilde{w}(k_1^*)\, S^*(k_1^*)\, e^{-i\,\omega\, t}\,.$$

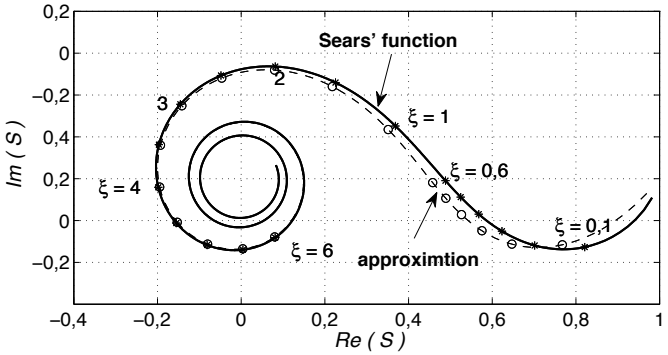


**Figure 4.** Sears' function (solid line) and its approximation (dashed line).

This result gives sense to the intuitively introduced transfer function $T$ of section 2.2. Equation (2) shows that the lift fluctuations concentrate at the leading edge and decay to zero at the trailing edge. The center of action of the total fluctuating lift force is at the quarter-chord point. Sears' function is plotted in Fig. 4. It does not depart so much from the approximation

$$\bar{S}^*(k_1^*) \;=\; \frac{1}{\sqrt{1 + 2\,\pi\, k_1^*}}\, e^{\;i\, k_1^*\, \left[1 \,-\, \dfrac{\pi^2}{2\,(1\,+\,2\,\pi\, k_1^*)}\right]}\,.$$

The amplitude of Sears' function decays as frequency increases. In that sense higher-frequency fluctuations correspond to lower aerodynamic efficiency.

Assuming incompressibility means that the sound speed is considered infinite in view of the time and velocity scales involved in the aerodynamic processes. This is acceptable if the time taken for the airfoil response to incident disturbances remains much smaller than the periods of oscillations. If the response to an event occurring at the leading edge involves transmission of information down to the trailing edge plus back-transmission upstream to the leading edge accounting for the effect of the Kutta condition, the condition reads

$$\frac{2c}{c_0\beta^2} \ll \frac{\lambda_A}{U_0}\,,$$

with $\beta^2 = 1 - M_0^2$, $M_0 = U_0/c_0$. In other words, since $\lambda_A = 2\pi/k_1$,

$$\frac{M_0 k_1^*}{\beta^2} = \frac{kc}{2\,\beta^2} \ll \frac{\pi}{2}\,.$$

The incompressible Sears and von Kármán's solution is therefore only valid if the chord is compact and if the Mach number is sufficiently small. As a result the effect of compressibility is important not only at high Mach number but also at high frequencies (Homicz & George (1974)). In many cases of interest the aforementioned condition is not fulfilled and a compressible solution is needed.

### 2.4 The Compressible Gust - Schwarzschild's Technique

Compressible alternatives to von Kármán & Sears' theory have been proposed and reviewed for instance by Goldstein (1976). The approach proposed by Amiet (1976) is selected here for its formal simplicity and the wide possibilities of extensions it offers, discussed later on. In particular the solution will be easily extended in a three-dimensional context. At low frequencies it reduces to a compressibility correction of the incompressible theory, described in the references. The correction is not addressed here because it remains quite close to original Sears' solution for compact airfoils. Of more interest is the case of non-compact airfoil chords and related high frequencies, for which the solution is detailed below.

Sears' problem is considered now in a three-dimensional space, thus introducing oblique gusts. A gust is defined by two aerodynamic wavenumbers $k_1$ and $k_2$ in the streamwise (chordwise) and spanwise directions respectively

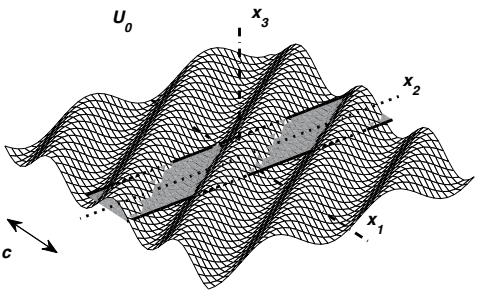


**Figure 5.** Two-dimensional gust for generalized Sears' problem statement.

by the upwash $\tilde{w}(k_1, k_2)\, e^{i\,(k_1\,x_2 + k_2\,x_2 - \omega\,t)}$ (Fig. 5). For convenience, the notation $(y_1, y_2, y_3)$ is devoted later on to the source point (with $y_3 = 0$) and $(x_1, x_2, x_3)$ to the observation point or any field point. When evaluating the unsteady lift the airfoil is assumed of infinite span, as also featured in the figure, so that the potential is factorized as $\phi(x_1, x_2, t)\, e^{i\,(k_2\,x_2 - \omega\,t)}$ in accordance with the excitation by the gust. This leads to the modified convected Helmholtz equation, equivalent form of the linearized Euler and continuity equations

$$\beta^2\,\frac{\partial^2\phi}{\partial x_1^2} \,+\, \frac{\partial^2\phi}{\partial x_3^2} \,+\, 2\,i\,k\,M_0\,\frac{\partial\phi}{\partial x_1} \,+\, (k^2 - k_2^2)\,\phi \,=\, 0$$

to be solved with the rigidity condition on the surface of the airfoil and a Kutta condition in the wake. This equation is reduced to the ordinary Helmholtz equation by a change of variables referred to as Ribner's transformation:

$$\Phi \,=\, e^{i\,M_0\,\mu\,x_1^*}\,\phi\,, \qquad \mu \,=\, \frac{k_1^*\,M_0}{\beta^2}\,, \qquad x_1^* \,=\, \frac{2\,x_1}{c}\,, \qquad x_3^* \,=\, \frac{2\,\beta\,x_1}{c}$$

leading to

$$\frac{\partial^2\Phi}{\partial x_1^{*\,2}} \,+\, \frac{\partial^2\Phi}{\partial x_3^{*\,2}} \,+\, \mu^2\,\left(1 - \frac{1}{\Theta^2}\right)\,\Phi \,=\, 0\,, \tag{3}$$

where Graham's parameter $\Theta = M_0\,k_1^*/(\beta\,k_2^*)$ has been introduced for convenience. When $\Theta$ is smaller than 1 the gust is said sub-critical and the

equation is elliptic. The disturbance potential attenuates as an evanescent wave away from the airfoil leading edge. When $\Theta$ is larger than 1 the gust is supercritical and the potential radiates to the far field as sound. This is why the interest is often limited to supercritical gusts as the only contributing ones in the sound field. But this is true only in the limit of infinite or arbitrary large span and if the problem is addressed to directly derive the sound. In the following two-step approach the equation is solved first to derive the induced unsteady lift, which is the trace of the sound on the airfoil. The sound itself is calculated afterwards from its trace by taking into account the source distribution over the actual span, and this truncation makes the sub-critical gusts contribute as well. In other words the sources are evaluated ignoring the span-end effect. It is worth noting that sub-critical and supercritical gusts correspond to subsonic and supersonic phase speeds of their trace along the leading edge with respect to the incident mean flow, respectively, as pointed out by Amiet (1975).

The aeroacoustic response of the airfoil is now interpreted as a wave scattering problem. The approach is outlined as a reference that can be applied in many more complicated configurations. The focus is first on the induced lift and the acoustic field will be addressed in the next section, essentially because the complete mathematical problem has no analytical solution. Furthermore even the finite-chord strip representing the airfoil cannot be handled exactly from this standpoint. The solution proposed by Amiet (1976) is to consider separately the contributions of the leading edge and of the trailing edge within the scope of an iterative procedure called Schwarzschild's technique (see Landahl (1961)). The theoretical background is Schwarzschild's theorem, stated as follows. Let $\psi$ be a scalar field solution of the Helmholtz equation

$$\frac{\partial^2 \psi}{\partial x_1'^2} + \frac{\partial^2 \psi}{\partial x_3'^2} + k^2 \psi = 0$$

with the boundary conditions:

$$\psi(x_1, 0) = F(x_1) \qquad x_1 \geq 0\,,$$

$$\frac{\partial \psi}{\partial x_3}(x_1, 0) = 0 \qquad x_1 < 0\,,$$

where $F$ is a known function. Then for $x_1 < 0$ , the solution on $x_3 = 0$ reads

$$\psi(x_1, 0) = \frac{1}{\pi} \int_0^\infty \sqrt{\frac{-x_1}{\xi}}\, \frac{e^{i\,\mu\,(\xi - x_1)}}{\xi - x_1}\, F(\xi)\, d\xi\,. \tag{4}$$

This theorem is inherited from electromagnetism (the complex conjugate can need being taken depending on the choice of convention for the time Fourier transform). It produces closed-form solutions provided that the integral can be calculated analytically, which is always the case when dealing with gusts defined by complex exponentials.

Only the principle is explained here. For the application the airfoil is first assumed semi-infinite by removing the trailing edge to infinity downstream. A zero-order disturbance potential is introduced that exactly cancels the incident gust upwash not only on the airfoil surface but also everywhere on $x_3 = 0$. This potential is balanced upstream of the leading-edge by a first-order contribution for which the transformed potential $\Phi_1$ is solution of a Schwarzschild's problem. Indeed $\Phi_1$ is prescribed upstream of the leading edge and its normal derivative must be zero on the extended airfoil surface. Once determined, it is transformed back to get the effective potential $\phi_1$, and the pressure jump $\ell = \Delta p_1 = 2\,p_1$ is deduced by the relationship in the presence of flow

$$p = -\rho_0\,U_0\,\left[\frac{\partial\phi}{\partial x_1} - i\,k_1\,\phi\right].$$

This first iteration alone is wrong because the actual airfoil chord is not infinite. Therefore a trailing-edge correction is introduced, calculated as if now the leading edge was removed to infinity upstream. The difference is that the disturbance pressure is used to write down another Schwarzschild's problem, because the Kutta condition states that this pressure must be zero in the wake and have a zero normal derivative on the airfoil surface (the details, not given here, again involve changes of variables to move the origin of coordinates from the leading edge to the trailing edge). In principle higher-order iterations could be performed but the first two are enough in practice, as pointed out by Amiet (1976). Details can be found in the referenced papers. In the present three-dimensional context, the full solution for the distributed unsteady lift of supercritical oblique gusts including main leading-edge impingement and trailing-edge back-scattering reads (Mish & Devenport (2000), Roger (2010))

$$\tilde{\ell}(y_1, y_2) = \ell(y_1, y_2, t)\,e^{i\,\omega\,t} = \frac{2\,\rho_0\,U_0\,\tilde{w}\,e^{i\,\pi/4}}{\sqrt{2\,\pi\,(k_1^* + \beta^2\kappa)}}\,e^{i\,k_2^*\,y_2^*}$$

$$\times\left\{1 - \sqrt{\frac{2}{1+y_1^*}} - (1-i)\,E\,[2\,\kappa\,(1-y_1^*)]\right\}\,e^{-i\,(M_0\,\mu-\kappa)\,(1+y_1^*)},$$

introducing the non-dimensional chordwise coordinate $y_1^*$ with origin at the

center chord, and the notation $\kappa = \mu\sqrt{1-1/\Theta^2} = \sqrt{\mu^2 - k_2^{*\,2}/\beta^2}$. $E$ is the function introduced by Amiet and involving Fresnel integrals

$$E(\xi) = \int_0^\infty \frac{e^{i\,t}}{\sqrt{2\,\pi\,t}}\,dt\,.$$

The same expression for the unsteady lift and more generally for Schwarzschild's eq. (4) or the complex conjugates are found in the literature depending on the definition of Fourier transforms; remind that in the present document time dependence is assumed as $e^{-i\,\omega\,t}$.

For sub-critical gusts $\kappa$ is replaced by $i\,\kappa'$ with $\kappa' = \sqrt{(k_2^{*\,2}/\beta^2) - \mu^2}$ and the term involving the function $(1-i)\,E$ by the error function erf ($[2\,\kappa'(1-y_1^*)]^{1/2}$). All gusts involve the integrable inverse square-root singularity at the leading edge already pointed out by Sears's solution, but the unsteady lift of sub-critical gusts decreases much faster farther downstream. This is emphasized in Fig. 6, where the chord-wise distribution of the unsteady lift amplitude on a flat-plate airfoil is plotted for various oblique gusts contributing to the same frequency, thus various angles triggered by different values of $k_2$. Despite the physical drop at the trailing edge imposed by the Kutta condition, the lift induced by supercritical gusts contaminates more significantly the aft part of the airfoil.

Including sub-critical gusts in the modeling and paying attention to the sub- or supercritical duality of sinusoidal gusts is important for practical applications. Typically analytical studies of rotating blade broadband noise rely on a strip-theory approach: a blade is split into segments, each of which is assimilated to a rectangular airfoil of small aspect ratio, in order to account for span-wise varying conditions. If a two-dimensional response of each segment is assumed for simplicity, only parallel gusts are abusively selected, supercritical by definition. If the actual excitation by oncoming disturbances tends to produce sub-critical conditions, substantial errors are expected.

In its original two-dimensional declination for parallel gusts ($k_2 = 0$) the compressible high-frequency solution holds whenever $\mu = k\,c/(2\,\beta^2) > \pi/4$ or whenever $c/\beta^2 > \lambda/4$. Very low frequencies are possibly addressed by the technique but would *a priori* require a larger number of iterations, not compatible anymore with the derivation of closed-form solutions. Classical Sears' solution could provide a good alternative for gust-impingement at a leading edge at low frequencies, used together with Graham's similarity rules (see Graham (1970)). The mathematical limitation must be transposed to the parameter $\kappa$ instead of $\mu$ in the general case, leading to possible concern for values of $k_2$ approaching the transition between sub-critical and supercritical gusts. A palliative interpolation between both regimes can be

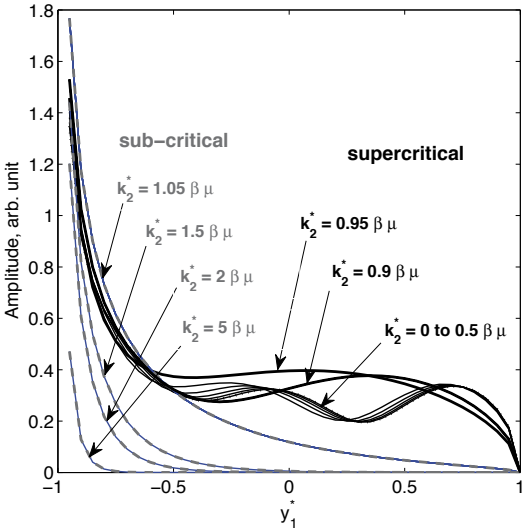


**Figure 6.** Typical chord-wise distribution of unsteady lift amplitude for various oblique gusts in both sub-critical and supercritical ranges. $kc = 2\,\pi$, $M_0 = 0.3$.

applied instead as proposed by Roger & Moreau (2005) for the similar case encountered in trailing-edge noise modeling.

### 2.5 Radiation Integrals of Oblique Gusts

The trace determined by Schwarzschild's technique provides the pressure jump along the airfoil, acting as the equivalent source distribution. The acoustic field is calculated now from the sources by a classical radiation integral. This is equivalent to resorting to Ffowcs Williams & Hawkings' acoustic analogy. The sources are exactly the dipole contribution of the analogy, recognized as dominant at subsonic Mach numbers. Since the problem is solved in a non-compact and compressible context, the solution implicitly accounts for the auto-diffraction by the surface. But if the formalism is to be applied to rotating blades, mutual diffraction between adjacent blades, if any, is not accounted for, because Amiet-Schwarzschild's approach provides isolated-airfoil response functions. For non-overlapping blades or low-solidity fans within the scope of a strip-theory approach, this other simplification is fully acceptable. Oppositely high blade counts typi-

cal of some turbomachines would in principle require the implementation of cascade response functions, much more expensive and time-consuming, not addressed here.

The far-field radiation for a single gust is expressed in a reference frame attached to the airfoil as

$$\tilde{p}(\mathbf{x},\omega) \;=\; -\,\frac{i\,k\,c\,\rho_0\,x_3}{2\,S_0^2}\,U_0\,\tilde{w}\,L\,\frac{\sin[\,L\,(k_2^*-k^*\,x_2/S_0)/c]}{L\,(k_2^*-k^*\,x_2/S_0)/c}\,I\,,$$

with $k^* = kc/2$, where the sine-cardinal function $\sin\xi/\xi$ represents the span-wise radiation integral and where the non-dimensional chord-wise radiation integral (or aeroacoustic transfer function) $I$ is introduced as

$$I\,(\mathbf{x},k_1,k_2) \;=\; \int_{-1}^{1}\frac{\ell(y_1^*,y_2^*)\,e^{-i\,k_2^*\,y_2^*}}{2\,\pi\,\rho_0\,\tilde{w}}\,e^{i\,\mu\,(M_0-x_1/S_0)\,y_1^*}\,dy_1^*\,.$$

In the expressions $(x_1,x_2,x_3)$ stand for observer's coordinates with origin at the center of the airfoil, respectively in the stream-wise, span-wise and normal directions. $S_0 = [x_1^2+\beta^2\,(x_2^2+x_3^2)]^{1/2}$ is a corrected distance accounting for sound convection by the surrounding flow. It is close to the geometrical distance $R$ only if $M_0$ is small. $L$ is the span. The sine-cardinal function accounts for the span-wise interference associated with the wavenumber $k_2$. The function $I$ has different expressions for the sub-critical and supercritical gusts, including leading-edge and trailing-edge contributions: $I = I_1 + I_2$. For supercritical gusts it reads (Roger (2010))

$$I_1 \;=\; -\,\frac{1}{\pi}\,\sqrt{\frac{2}{(k_1^*+\beta^2\,\kappa)\,\Theta_4}}\,e^{-i\,\Theta_2}\,E\,[2\,\Theta_4]\;, \tag{5}$$

$$I_2 \;=\; \frac{e^{-i\,\Theta_2}}{\pi\,\sqrt{2\,\pi\,(k_1^*+\beta^2\,\kappa)\,\Theta_4}} \tag{6}$$

$$\times\,\left\{i\,(1-e^{2\,i\,\Theta_4})\;-\;(1+i)\,\left[E(4\,\kappa)\;-\;e^{2\,i\,\Theta_4}\,\sqrt{\frac{2\,\kappa}{\Theta_3}}\,E\,[2\,\Theta_3]\right]\right\}\;,$$

with $\Theta_2 = \mu\,(M_0 - x_1/S_0) - \pi/4$, $\Theta_3 = \kappa + \mu\,x_1/S_0$, $\Theta_4 = \kappa - \mu\,x_1/S_0$.

For sub-critical gusts the expressions follow as

$$I_1 \;=\; -\,\frac{1}{\pi}\,\sqrt{\frac{2}{(k_1^*+i\,\beta^2\,\bar{\kappa}')\,\Theta_4'}}\,e^{-i\,\Theta_2}\,E\,[2\,\Theta_4']\;, \tag{7}$$

$$I_2 \;=\; \frac{-\,e^{-i\,\Theta_2}}{i\,\pi\,\sqrt{2\,\pi\,(k_1^*+i\,\beta^2\,\bar{\kappa}')\,\Theta_4'}} \tag{8}$$

$$\times \left\{ 1 - e^{2\,i\,\Theta'_4} - erf(\sqrt{4\,\kappa'}) + 2\,e^{2\,i\,\Theta'_4} \sqrt{\frac{\kappa'}{\Theta'_3}}\, E\,[2\,\Theta'_3] \right\} ,$$

with $\Theta'_4 = i\,\kappa' - \mu\,x_1/S_0$, $\Theta'_3 = i\,\kappa' + \mu\,x_1/S_0$.

For the sake of robustness the Fresnel integrals and related functions are better implemented using the following relationship with the complex error function of complex argument

$$ES\,(z) = \frac{E(z)}{\sqrt{z}} = \frac{1+i}{2}\,\frac{\Phi^{(0)}(\sqrt{-i\,z})}{\sqrt{z}}\,, \qquad \Phi^{(0)}(Z) = \frac{2}{\sqrt{\pi}} \int_0^Z e^{-u^2}\,du$$

and the algorithm

$$\frac{\Phi^{(0)}(\sqrt{-i\,z})}{\sqrt{z}} = 2\,\frac{e^{-i\,\pi/4}}{\sqrt{\pi}} \sum_{n=0}^{\infty} \frac{(i\,z)^n}{(2n+1)\,n\,!}\,.$$

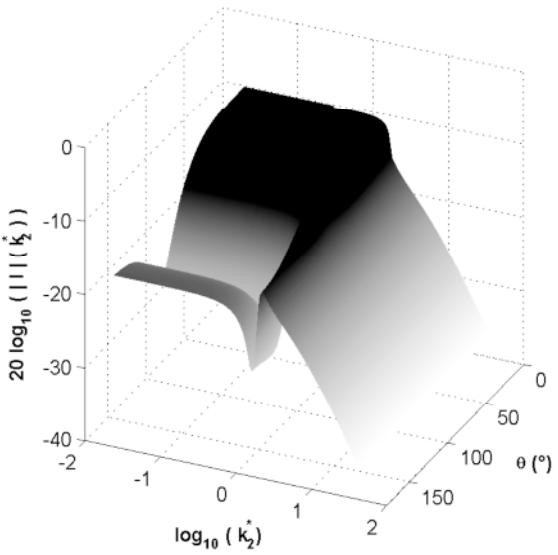


**Figure 7.** Chord-wise radiation-integral amplitude $|I|$ as a function of observation angle with respect to chord line and span-wise wavenumber. $\mu = 2\,\pi$, $M_0 = 0.3$, $x_2 = 0$.

The amplitude of the radiation integral $I$ is plotted in decibels and in logarithmic $k_2^*$-scale in Fig. 7 for an arbitrary set of parameters, as a function of observation angle with respect to the chord-wise direction. The plot emphasizes a rapid drop for large values of $k_2^*$, and a plateau for small values at fixed angle. Note that interpolation has been performed between the supercritical and sub-critical ranges to smoothen the response surface at the singular value $k_2^* = \beta\,\mu$, for which the two-step Schwarzschild's procedure breaks down because the effective frequency parameter $\kappa$ is exactly zero. At some angles the dip in the supercritical range *a priori* makes the sub-critical gusts more significant contributors. This dip is caused by cancellations which result from chord-wise non compactness. At lower frequencies (typically $\mu < \pi/4$) the plateau would extend nearly constant whatever the observation angle could be. In contrast at even higher frequencies, multiple dips would be found.

The complete directivity pattern of a single oblique gust results from the combination of this radiation integral with the additional sine-cardinal function, on the one hand, and the factor $x_3/S_0$ which accounts for the dipole character of the lift fluctuations, on the other hand. For non-compact chords and supercritical gusts it exhibits multiple inclined lobes. Another sample result with different parameters is plotted in Fig. 8. The four lobes result from chord-wise non-compactness associated with the relatively high reduced frequency. They are inclined away from the mid-span plane because of the obliqueness of the gust, as first pointed out by Amiet (1975). The radiation would be preferentially in the mid-span plane for a parallel gust. The larger the aspect ratio $L/c$, the thinner the lobes. In the limit of infinite aspect ratio, a single oblique angle would be selected. As frequency increases, not only the number of lobes increases but the radiation also takes place with more pronounced beaming downstream. In the limit of arbitrary large frequencies, as shown later on, the diagram would become cardioid-like with a maximum downstream; this is a typical feature of the half-plane Green's function already identified in chapter 2. In contrast to supercritical gusts, sub-critical ones cannot produce multiple radiation lobes nor oblique focusing.

Globally the chord-wise radiation integral behaves like a low-wavenumber filter. The sine-cardinal factor acts as a band-pass filter centered on the wavenumber $k_2^* = k^* x_2/S_0$ which gets progressively thinner as the aspect ratio increases. The wider it is, the more likely the sub-critical gusts contribute. More precisely if the observer gets closer to the mid-span plane, the sub-critical gusts bring a poor contribution. In this case the parallel and nearly-parallel gusts are responsible for the major sound. As $x_2/S_0$ increases the sine-cardinal filter shifts towards larger values of $k_2$ and gives more im-

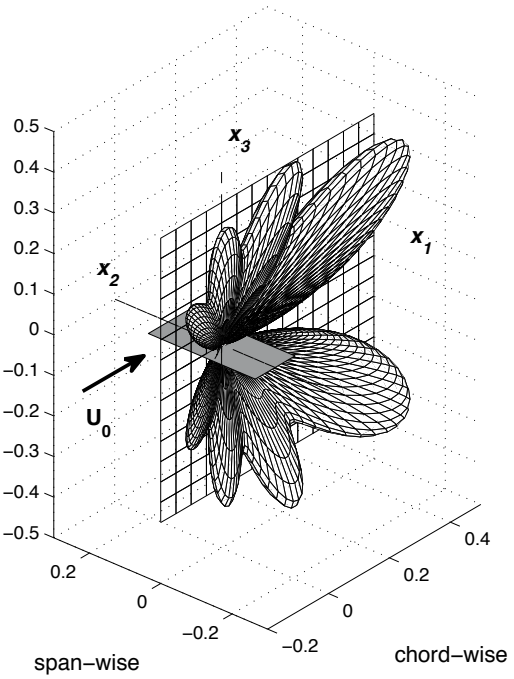


**Figure 8.** Typical directivity diagram of an oblique supercritical gust. $kc = 12.57$, $\mu = 6.3$, $M_0 = 0.05$, $k_2^* = -1.26$, $L/c = 2$. Arbitrary units.

portance to sub-critical gusts. But in the same time extreme observer positions close to the airfoil plane along the span correspond to vanishing values of $x_3$ for which the dipole directivity factor makes the contribution smaller and smaller. This is why, again, sub-critical gusts are often discarded for simplicity. Yet in view of the three-dimensional plot of Fig. 7 their relative contribution can be significant if the sound must be evaluated for all possible observer locations and for all configurations. This is precisely what is needed in rotating blade noise studies.

Because the present discussion is a question of gust obliqueness combined with convection Mach number, it will also hold in the subsequent analysis of trailing-edge noise, based on the same mathematical background.

### 2.6 Extensions

One of the most striking aspects of aforementioned Amiet-Schwarzschild's technique is its wide range of extension capabilities. First it is applied later on to derive formulas for trailing-edge noise and vortex-shedding noise; secondly it has also been used to account for realistic features departing from the restrictive assumption of a rectangular airfoil the edges of which are perpendicular to the mean flow. The former advantage makes the analytical models of the three mechanisms addressed in this chapter quantitatively comparable, because they are built on the same basis. The latter allows introducing more physics in the models, thus offering more practical interest. But it is beyond the scope of the present document. Only indicative examples of reported works that are expected to enlarge turbulence-impingement noise modeling are listed below as an open door towards further extensions.

1 - *Impingement of disturbances on a swept edge.* Because the span-wise extent of the airfoil is assumed infinite for the sake of determining the induced lift, sweep, defined as a possible arbitrary angle between the leading edge and the flow direction, is simply accounted for by performing a change of variables and introducing Cartesian coordinates along and normal to the edges, thus oblique with respect to the flow direction. First derivations of the lift distribution $\tilde{\ell}$ are reported by Adamczyk (1974), based on the Wiener-Hopf technique. Equivalent solutions are obtained with Schwarzschild's technique, and lead to extended expressions of the radiation integrals, as shown by Roger & Carazo (2010). Essentially the effect of sweep is to shift the threshold between supercritical and sub-critical gusts by changing the relative edge-to wavefront angle and the associated span-wise phase speeds of the interaction.

2 - *Effect of varying chord length.* Fan design usually involves span-wise variations of all geometrical parameters of a blade. Therefore any blade segment in a strip-theory approach can have different chords at both ends, or equivalently non-parallel leading and trailing edges. This again can be included in Amiet-Schwarzschild's approach, provided that some approximation is accepted. Indeed both edges are treated separately as edges of half-planes. Once the dominant leading-edge scattering is determined by the first iteration in the same way as for a rectangular airfoil, a change of variables is performed in order to project the solution $\tilde{\ell}_1$ in a new set of coordinates aligned with the trailing edge. The procedure, detailed by Roger & Carazo (2010), requires a splitting of $\tilde{\ell}_1$ into trailing-edge aligned secondary gusts, which is only valuable for segments of moderate aspect-ratio.

3 - *Unsteady response of a blade tip.* Because the highest relative flow speeds on rotating blades are encountered at the tip, the effect of the blade

termination upon the unsteady aerodynamic response is a key issue, especially if the oncoming disturbances concentrate to precisely impinge near the tip. Again Schwarzschild's technique provides a way to include the tip effect in the analysis. Detailed derivations are also described by Roger & Carazo (2010), for the tip of a rectangular unswept airfoil. The principle is as follows. The unsteady lift determined ignoring the tip is first continued by zero away from the airfoil surface and expanded in Fourier components. For each component the lift is forced to zero beyond the tip by adding a correction which is solution of another Schwarzschild's problem, now in the span-wise direction instead of the original stream-wise statement. The inverse Fourier transform is finally performed numerically to get the corrected response. Application to blade-tip vortex interaction noise modeling is proposed by Roger & Schram (2012).

4 - *Different convection and free-stream velocities.* In some analytical reductions of practical problems, oncoming disturbances can need being assumed with a convection or phase speed that differs from the free-stream velocity involved in the far-field radiation. For instance, this would be the case for the turbulence generated in the flap cove of a wing with deployed high-lift devices and impinging on the flap leading edge. Though seldom addressed this extension is quite straightforward. It is not discussed here because similar statements are mentioned in the next sections for trailing-edge noise and vortex-shedding noise modeling.

## 3 Unsteady Aerodynamics for Trailing-Edge Scattering

Most attached flows over well designed airfoils with a more or less sharp trailing edge belong the regime illustrated in Fig. 9. Turbulence carried in the boundary layers radiates sound because it is rapidly re-organized around the trailing-edge. Analytical sound predictions require a special mathematical statement. They are better derived starting from the incident wall-pressure field corresponding to the boundary-layer turbulence, since the Kutta condition is expressed in terms of a pressure release. In that sense the convection speed $U_c$ of Fig. 9 refers to the wall-pressure trace of the incident vortex dynamics rather than to the incriminated velocity field. The sound-generating mechanism is addressed by the generic configuration of hydrodynamic pressure patterns convected past the edge of a thin rigid plate, sketched in Fig. 10.

More precisely the wall-pressure field is again Fourier-analyzed and expressed as a combination of pressure gusts, and the airfoil response deduced for each gust. This suggests that few differences arise in the modeling with

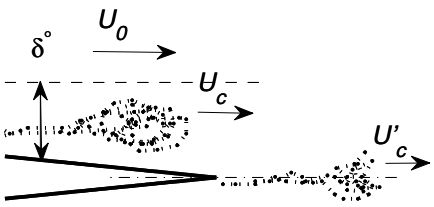


**Figure 9.** Pure trailing-edge noise configuration. The secondary convection speed $U_c'$ in the wake introduced by Howe (1978) is not used in the present modeling approach.

respect to the previous mechanism, except that what was done with the velocity or the velocity potential is now repeated with the disturbance pressure. It must be noted however that different models have been proposed in the literature (see for instance Howe (1978) and Blake (1986)). They are not detailed here.

The incident forcing by a wall-pressure gust of amplitude, say $P_0$ is considered for one side only, that most often is the suction side of a loaded airfoil. The proper way of imposing a Kutta condition remains a matter of controversy when resorting to simplified models expected to reproduce real-life flows. A full Kutta condition on the pressure jump is most often considered. The scattered pressure field around the edge involves contributions in phase opposition on each side of the plate, so that the pressure jump is continuous and zero. Another choice is to assume that an incident vortical pattern in the boundary layer tends to follow its path in the wake. According to this interpretation discussed by Moreau & Roger (2009), the disturbance pressure remains continuous and zero around the edge instead of the pressure jump, and a counter-pressure of amplitude $P_0$ is distributed on each side of the airfoil. A factor 2 makes the difference between both assumptions, and the effect will be 6 dB more in the far-field noise with the second one, for the same incident turbulence. Apart from that, the procedure will be declined in the same way. According to authors' experience with a set of airfoils tested at low speeds, the condition of zero pressure around the edge produces the best agreement with measured data; further-

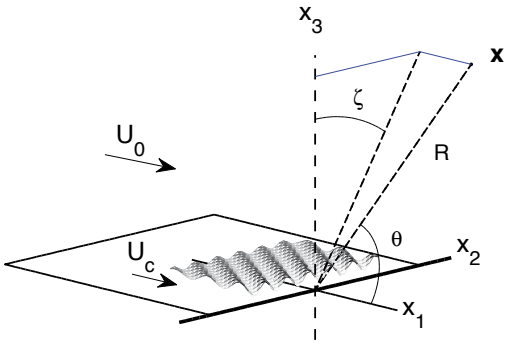


**Figure 10.** Reference frame for trailing-edge noise modeling, and schematic view of a wall-pressure gust. Radiation angles mentioned for completeness. $\theta$ is used in asymptotic formulations of section 6.1.

more it ensures that Amiet's formulation coincides with asymptotic Howe's theory at very high non-dimensional frequencies (Moreau & Roger (2009)).

In the derivations the origin of coordinates is taken at trailing-edge midpoint according to the sketch of Fig. 10. Pressure gusts are defined in a first step as if there were neither scattering nor edge. Though turbulence in a boundary layer is not homogeneous in the stream-wise direction, it is assumed almost homogeneous over the small extent just upstream of the edge where the dominant vortex dynamics takes place. More rigorously a gust should be given a growing amplitude, which would be equivalent to adding an imaginary part to the stream-wise wavenumber. Accepting the simplification, a gust of wall-pressure $P_0$ is then forced to zero at the trailing edge by adding a counter-pressure $P_1$ in phase opposition on both sides of the airfoil (this ensures continuity of the pressure in a close vicinity of the edge). If the airfoil leading edge is removed to infinity, $P_1$ is solution of a Schwarzschild's problem since it has to exactly cancel $P_0$ in the wake and have a zero normal derivative upstream. The corresponding induced lift does not satisfy the condition of zero potential upstream of the airfoil leading edge. In the original formulation proposed by Amiet (1976-b), this is not considered a drawback because trailing-edge noise generally involves

small-scale turbulence and relatively high frequencies for which the induced counter-pressure decreases rapidly away from the edge. For low-frequency needs, a leading-edge back-scattering correction can be derived by going back to the disturbance potential and performing another application of Schwarzschild's theorem (Roger & Moreau (2005)). The back-scattering correction is not negligible but is is only significant in limited cases. As such it is not detailed here. In contrast the duality of supercritical and sub-critical gusts still makes sense in the three-dimensional formulation of trailing-edge noise. The induced lift of supercritical gusts is $\tilde{\ell} = \tilde{\ell}_1 + \tilde{\ell}_2$, with the dominant contribution $\tilde{\ell} \simeq \tilde{\ell}_1$ given as

$$\tilde{\ell}_1(y_1^*, , y_2^*) \;=\; 2\, e^{i\,(a\,k_1^*\,y_1^* + k_2^*\,y_2^*)}\;\left[(1-i)\,E\;(-\;[a\,k_1^* + \kappa + M_0\,\mu]\;y_1^*) - 1\right]\,, \tag{9}$$

where $a = U_0/U_c$ is the ratio of the free-stream velocity to the averaged convection speed of the incident boundary-layer wall-pressure disturbances.

For sub-critical gusts, the expression reads

$$\tilde{\ell}_1(y_1^*, y_2^*) \;=\; 2\, e^{i\,(a\,k_1^*\,y_1^* + k_2^*\,y_2^*)}\;\left[1 - \Phi^{(0)}\;\left(-\;[i\,(a\,k_1^* + i\,\kappa' + M_0\,\mu)\,y_1^*]^{1/2}\right)\right] \tag{10}$$

with the same other notations as in previous section.

It is worth noting that the model assumptions remain questionable, probably because the physical processes highly depend on the flow features and airfoil design in the vicinity of the trailing edge. Reducing the airfoil to a flat plate of zero thickness and assuming locally homogeneous turbulence is a concern if the actual shape is not much thinner than the boundary-layers, as in the case of quite thick beveled edges. In particular, the meaning and the hypothesis of a full or partial Kutta condition, as well as questions about the coupled incident and scattered wall pressures have been examined by some authors (Howe (1978), Zhou & Joseph (2007)). This variability of small-scale motions in boundary-layers explains both the difficulty of defining universal scaling laws, addressed in section 6.1, and the either successful or disappointing comparisons of model predictions with measurements. It must be also kept in mind that trailing-edge noise modeling is addressed for a single incriminated boundary layer. Most often this one is the suction-side boundary layer of a loaded airfoil; if the pressure-side boundary layer is also turbulent, the model must be considered twice with different parameters, assuming uncoupled sides. Outdoor measurements of the trailing-edge noise of wind-turbine blades reported by Oerlemans & Mendez-Lopez (2005) exhibit spectral features involving both sides of the blades: logically the high-frequency range is attributed to the thinner boundary layers of the

pressure sides whereas the low-and-middle frequency range is attributed to the thicker suction-side boundary layers.

Chord-wise radiation integrals (aeroacoustic transfer functions) are also derived from the unsteady lift distributions, following the same methodology as in section 2.5. The expression initially proposed by Amiet (1976-b) for parallel gusts has been readdressed by Roger & Moreau (2005) to account for three-dimensionality. For supercritical gusts the result reads

$$I_1 \;=\; \frac{e^{-2i\,C}}{i\,C}\;\left\{(1-i)\,e^{2i\,C}\,\sqrt{\frac{B}{B-C}}\,E\left[2\,(B-C)\right]-(1-i)\,E\left[2B\right]+1\right\}, \tag{11}$$

with $B = a\,k_1^* + M_0\,\mu + \kappa$, $C = a\,k_1^* + \mu\,(M_0 - x_1/S_0)$. Again for numerical issues it is better implemented using the function $ES$. For sub-critical gusts the radiation integral is found as

$$I_1' \;=\; \frac{e^{-2i\,C}}{i\,C}\;\left\{(1-i)\,e^{2i\,C}\,\sqrt{2B'}ES\;\left[2\,(B'-C)\right]\;-\Phi^{(0)}\left(\left[-2\,i\,B'\right]^{1/2}\right)+1\right\} \tag{12}$$

with $B' = a\,k_1^* + i\,\kappa' + M_0\,\mu$ .

Because trailing-edge scattering and turbulence impingement involve vortex dynamics close to an edge, the associated radiation properties have some similarities. Typically, isolated oblique supercritical wall-pressure gusts force trailing-edge noise in oblique directions, in the same way as illustrated in Fig. 8 for turbulence-impingement noise but with lobes now pointing preferentially upstream.

## 4 Vortex-Shedding Noise - The Reversed Sears' Problem

Vortex-shedding noise is referred to in this chapter as the generation of sound by the formation of structured vortices, such as a von Kármán street, downstream of a blunted airfoil trailing edge. The mechanism differs from aforementioned trailing-edge noise produced by vortical patterns already present upstream in the developing boundary layers (note that yet some authors use the same terminology). As stated by Brooks & Hodgson (1981), the occurrence or not of structured vortex shedding is a matter of compared values of the physical thickness of the trailing edge $h$ and of the boundary layer displacement thickness $\delta_1$. Typically the vortex street cannot develop if $h/\delta_1 < 0.3$. Vortex shedding is known to radiate narrow-band noise

around the Strouhal frequency $f_0 = 0.2\,U_0/h$. In contrast trailing-edge noise is either broadband or tonal depending whether the boundary layers are turbulent or laminar-unstable. Vortex-shedding sound in fan technology can be difficult to recognize because the different values of the characteristic flow speed along the span of a blade result in a broader frequency range.


(a) (b)

**Figure 11.** Model von Kármán vortex street in the wake of a thick plate (a) and associated reversed Sears' problem (b) from Roger *et al* (2006). Pure vortex-shedding configuration.

Imposing a Kutta condition in the present generic model would make no sense because both experiments and numerical simulations show evidence of lift fluctuations concentrating at the trailing edge with phase opposition between both sides. This symmetry with what happens at a leading edge impinged by upstream disturbances and referred to as Sears' problem in section 2 suggests that a similar mathematical statement is also relevant. This is why the configuration is interpreted as a reversed Sears' problem by Roger *et al* (2006) (note that another modeling approach has been proposed by Blake (1986)). This is simply made by reversing the flow direction in Fig.2-a and assuming that the leading edge becomes the trailing edge and *vice versa*. The wake oscillation defines an upwash $w$ which is convected downstream and has to be canceled farther upstream on the airfoil surface. When applied to the vortex-shedding noise from a thick plate, a refinement must be introduced to account for a convection speed $U_c$ of the upwash lower than the external flow speed $U_0$ (Fig. 11). Again using Schwarzschild's technique, the dominant first iteration for the induced lift is obtained as

$$\tilde{\ell}(y_1^*) \;=\; -\,2\,\rho_0\,w\,U_0\,(1-i)\,e^{i\,a\,k_1^*\,y_1^*} \tag{13}$$

$$\times \left\{ \frac{\Theta'_1}{K_1^*} \frac{e^{-i\,\Theta'_1\,y_1^*}}{\sqrt{-\,2\,\pi\,\Theta'_1\,y_1^*}} - i\,\frac{(a-1)\,k_1^*}{K_1^*}\,E\,[-\Theta'_1\,y_1^*] \right\},$$

with $\Theta'_1 = ak_1^* + \mu\,(1+M_0)$, $K_1^* = a\,k_1^*\,[1-M_0^2\,(1-1/a)^2]^{1/2}$, $ak_1^* \simeq 0.2\,\pi\,c/h$. Since vortex shedding is known to have quite a large spanwise correlation length, between 5 and 7 trailing-edge thicknesses $h$, and because the observer is generally in the mid-span plane in validation experiments, the solution is derived only for two-dimensional gusts. The result reduces to the main term of parallel-gust impingement onto a leading edge as the convection speed is set equal to $U_0$ and as the Mach number and chord-wise coordinates are given the opposite sign. The mathematical expression is defined up to $-\infty$ upstream, but the unsteady loads concentrate at the trailing edge and negligible values are expected at the leading edge. Only the loads distributed over the actual plate surface are taken into account for the acoustic calculations.

The normalized radiation integral of a gust at angular frequency $\omega$ is derived in a way similar to preceding cases. It is found as

$$I_1^{VK} = -\frac{(1-i)}{\pi\,K_1^*} \left\{ \sqrt{\frac{\Theta'_1}{\Theta'_1-\Theta'_2}}\,E\,[2\,(\Theta'_1-\Theta'_2)] \right. \tag{14}$$

$$\left. \times \left(1 - \frac{(a-1)\,k_1^*}{\Theta'_2}\right) + (a-1)\,k_1^*\,\frac{e^{-2\,i\,\Theta'_2}}{\Theta'_2}\,E\,[2\,\Theta'_1] \right\},$$

with

$$\Theta'_2 = a\,k_1^* - \mu\left(\frac{x_1}{S_0} - M_0\right).$$

## 5 Application to Airfoil Broadband Noise Modeling

The equivalent source distributions derived analytically in previous sections are now used for a statistical description of the far-field noise. For tonal noise predictions, they would be applied directly. It must be noted that the theoretical background of Amiet's theory and equivalent formulations ignore the aerodynamic wavenumber of the incident disturbances in the direction normal to the airfoil plane, say $k_3$. This together with the flat-plate assumption is considered enough for most broadband noise modeling purposes. More sophisticated and fully three-dimensional approaches

are possible, but they are beyond the scope of the course and most often not tractable anymore by analytical methods.

### 5.1 Statistical Turbulence-Interaction Noise Model

Once the radiation integral corresponding to a single gust is obtained from the distributed unsteady lift analytically, the power spectral density (PSD) of the far-field sound pressure $S_{pp}$ is related to the statistics of the upstream turbulent velocity field *via* spectral turbulent models used as input data. The complete formulation for a rectangular airfoil reads

$$S_{pp}(\mathbf{x},\omega) \;=\; \left(\frac{k\,\rho_0\,c\,x_3}{2\,S_0^2}\right)^2 \pi\,U_0\,\frac{L}{2}\int_{-\infty}^{\infty}\left[\,\Phi_{ww}\left(\frac{\omega}{U_0},k_2\right)\right.$$

$$\left.\times\left|I\left(x_1,\frac{\omega}{U_0},k_2\right)\right|^2\;\frac{\sin^2\left[\left(\dfrac{k\,x_2}{S_0}-k_2\right)\dfrac{L}{2}\right]}{\pi\,\dfrac{L}{2}\left(\dfrac{k\,x_2}{S_0}-k_2\right)^2}\,\right]dk_2\,, \tag{15}$$

where $\Phi_{ww}$ is the two-dimensional wave-number spectrum of the turbulent velocity component normal to the airfoil. The full expression is required for short-span airfoils, most often encountered in rotating blade applications. For large-span airfoils, typically high-lift flaps such that the aspect ratio $L/c \to \infty$, an approximate expression follows from the equivalence of the sine-cardinal function with Dirac's delta function, as

$$S_{pp}(\mathbf{x},\omega) \;=\; \left(\frac{\rho_0\,k\,c\,x_3}{2\,S_0^2}\right)^2 \pi\,U_0\,\frac{L}{2}\,\Phi_{ww}\left(k_1,\frac{k\,x_2}{S_0}\right)\left|I\left(x_1,k_1,\frac{k\,x_2}{S_0}\right)\right|^2 . \tag{16}$$

This approximation selects the specific wavenumber $k_2 = k\,x_2/S_0$ and perfectly focuses the radiation in the corresponding oblique direction.

When using eq.( 15) or eq.( 16) the minimum relevancy for $\Phi_{ww}$ is ensured by assuming homogeneous and isotropic turbulence, described by analytical models such as Liepmann's or von Kármán's. This reduces the statistical inputs to two parameters, the root mean square value of the velocity fluctuations $w_{rms}$ and the integral length scale $\Lambda$. Expressions for $\Phi_{ww}$ can be found in the standard literature on turbulent flows (Hinze (1975)). For assessment in the mid-span plane, the quantity $\Phi_{ww}$ is related to the frequency spectrum $S_{ww}(\omega)$ and the correlation length $\ell_y(\omega)$ by the relationship $\Phi_{ww} = U_0\,S_{ww}\,\ell_y/\pi$ with, respectively for the von Kármán's

and Liepmann's models,

$$S_{ww}(\omega) \;=\; \frac{w_{rms}^2\,\Lambda}{6\,\pi\,U_0}\,\frac{3+8\left(\dfrac{k_1}{k_e}\right)^2}{\left[1+\left(\dfrac{k_1}{k_e}\right)^2\right]^{11/6}}\,, \qquad k_e \;=\; \frac{\sqrt{\pi}}{\Lambda}\,\frac{\Gamma(5/6)}{\Gamma(1/3)}\,,$$

$$\ell_y(\omega) \;=\; \frac{8\,\Lambda}{3}\left(\frac{\Gamma(1/3)}{\Gamma(5/6)}\right)^2 \frac{\left(\dfrac{k_1}{k_e}\right)^2}{\left[3+8\left(\dfrac{k_1}{k_e}\right)^2\right]\sqrt{1+\left(\dfrac{k_1}{k_e}\right)^2}}$$

and

$$S_{ww}(\omega) \;=\; \frac{w_{rms}^2\,\Lambda}{2\,\pi\,U_0}\,\frac{1+3\,k_1^2\Lambda^2}{\left(1+k_1^2\Lambda^2\right)^2}\,, \qquad \ell_y(\omega) \;=\; \frac{3\,\pi\,\Lambda}{2\,\sqrt{1+k_1^2\Lambda^2}}\,\frac{k_1^2\Lambda^2}{1+3\,k_1^2\Lambda^2}\,.$$

It is worth noting that the wall pressure field does not enter the formulation directly though it is the equivalent source of the sound according to the acoustic analogy. In fact resorting to unsteady aerodynamic theories displaces the needed input data from lift fluctuations to incident velocity fluctuations. In this interpretation the airfoil acts as a converter of velocity disturbances into acoustic pressure waves.

The statistics of the upwash component is not of easy access in experiments because it requires using for instance cross-wire two-dimensional anemometry. Single hot-wire anemometry is more tractable but it provides only the power spectral density of the stream-wise velocity component $S_{uu}$. The information on $S_{ww}$ can be reconstructed from $S_{uu}$ by fitting the parameters $(u_{rms}, \Lambda)$ of one of the aforementioned turbulence models on the measurements, with $w_{rms} = u_{rms}$. This is done typically in the experiments mentioned in the next section, in which airfoils are tested in grid-generated turbulence. Model expressions for $S_{uu}$ according to von Kármán and Liepmann are respectively given as (Hinze (1975))

$$S_{uu}(\omega) \;=\; \frac{\dfrac{u_{rms}^2\,\Lambda}{\pi\,U_0}}{\left[1+\left(\dfrac{k_1}{k_e}\right)^2\right]^{5/6}}\,, \qquad S_{uu}(\omega) \;=\; \frac{u_{rms}^2\,\Lambda}{\pi\,U_0}\,\frac{1}{1+k_1^2\,\Lambda^2}\,.$$

A typical check against hot-wire measured spectra is reported in Fig. 12. The measurements are made in the presence of a turbulence grid placed upstream of the nozzle contraction in an open-jet wind tunnel, at different speeds. The distance to the grid is too short for obtaining ideal homogeneous and isotropic turbulence but ensures a higher fluctuating level. The agreement is not perfect but well satisfactory enough for acoustic applications. By the way the collapse in non-dimensional variables confirms that grid-generated turbulence is a self-similar flow. For a better consistency a correction can been applied to force the model spectral envelope to decrease at the highest frequencies towards the Kolmogorov scale, if these frequencies effectively contribute to the sound.

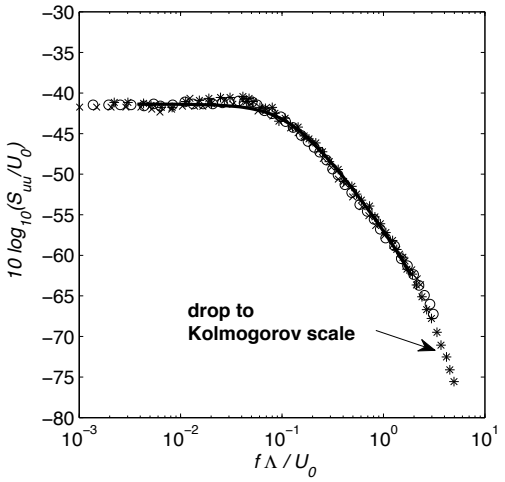


**Figure 12.** Stream-wise velocity spectra at the exit of a convergent nozzle measured by hot-wire anemometry. Flow speed 20 m/s ($*$), 30 m/s ($o$), 40 m/s ($\times$). Cont. line: von Kármán model including high-frequency correction.

If turbulence parameters must be estimated from RANS simulations, they are related to the turbulent kinetic energy $\bar{K}$ and the dissipation $\bar{\varepsilon}$ as

$$w_{rms}^2 = \frac{2}{3}\bar{K}\,, \qquad \Lambda \simeq \frac{(2\bar{K}/3)^{3/2}}{\bar{\varepsilon}}\,.$$

Reliability issues remain when non-homogeneous turbulence is addressed or when the local turbulence parameters vary over distances which are not

large when compared to the airfoil chord. For instance, the predictions of turbulence-impingement noise of a ring-airfoil placed in the mixing layer of a round jet reported by Roger (2010) are based on measured $S_{uu}$ turbulent spectra. For a ring of same diameter as the jet, the predictions compare very well with the measurements, because turbulence in the middle of the jet shear layers is quite close to homogeneity. In contrast the disagreement observed with smaller or larger rings is attributed to significant departure from homogeneous and isotropic turbulence away from the center shear layer. In another context, the complex flows developing over high-lift devices of aircraft wings such as deployed flaps also exhibit strong variations in the vicinity of the flap leading edge; applying the methodology in such a case becomes questionable.

### 5.2 Trailing-Edge Noise Model

The corresponding PSD of the far-field sound reads

$$S_{pp}(\mathbf{x},\omega) \;=\; \left(\frac{k\,x_3\,L\,c}{4\,\pi\,S_0^2}\right)^2 \;\frac{2}{c}\;\int_{-\infty}^{\infty} \Pi_0(\frac{\omega}{U_c},k_2^*) \tag{17}$$

$$\times\;\frac{\sin^2\left\{\dfrac{L}{c}\,(k_2^*-k^*\dfrac{x_2}{S_0})\right\}}{\left\{\dfrac{L}{c}\,(k_2^*-k^*\dfrac{x_2}{S_0})\right\}^2}\;\left|I(\frac{\omega\,c}{2\,U_c},k_2^*)\right|^2\;dk_2^*\,.$$

It is written here in non-dimensional variables, introducing the wavenumber spectrum of the wall-pressure fluctuations

$$\Pi_0(\frac{\omega}{U_c},k_2^*) \;=\; \frac{1}{\pi}\,\Phi_{pp}(\omega)\,\ell_y(k_2^*,\omega)\,,$$

where $\Phi_{pp}(\omega)$ is the wall-pressure PSD induced closely upstream of the trailing edge by the incident turbulence only (ignoring contamination by the Kutta condition) and $\ell_y(k_2^*,\omega)$ is the correlation length defined from the coherence function between two span-wise locations $\eta_2$ apart from each other as

$$\ell_y(k_2^*,\omega) \;=\; \int_0^{\infty} \sqrt{\gamma^2(\eta_2,\omega)}\,\cos(k_2\,\eta_2)\,d\eta_2\,.$$

The associated long-span approximation reads

$$S_{pp}(\mathbf{x},\omega) \;=\; \left(\frac{k\,x_3 c}{2\,\pi\,S_0^2}\right)^2\;\pi\,\frac{L}{2}\;\left|I(\frac{\omega\,c}{2\,U_c},k^*\frac{x_2}{S_0})\right|^2\;\Pi_0(\frac{\omega}{U_c},k^*\frac{x_2}{S_0})\,. \tag{18}$$

The key practical issue is to get a relevant information on $\Phi_{pp}(\omega)$ and $\ell_y(k_2^*, \omega)$. Very different flow conditions are encountered in engineering applications, corresponding to different wall-pressure statistics: attached turbulent boundary layers with more or less pronounced adverse pressure gradients, intermittently separated flows, re-attached flows after leading-edge separation and so on (in principle separated flows are out of the scope of usual trailing-edge noise modeling, except if the trace of the turbulence in terms of wall pressure still exhibits a phase convection speed in the streamwise direction). The source information is reconstructed in experimental studies by interpolation from measurements on a cluster of wall-pressure sensors. Span-wise distributed sensors are needed to give partial access to the correlation length, and chord-wise sensors are needed to evaluate the convection speed $U_c$ involved in the transfer function $I$. When small-scale mock-ups are tested in wind tunnels, the size of the sensors causes resolution issues that limit the relevance of the measurements; furthermore very thin areas such as the vicinity of the trailing edge are difficult to implement. This makes eq. (17) and eq. (18) more difficult to feed with reliable input data when compared to the equivalent expressions for turbulence-impingement noise.

Caution is required if Computational Fluid Dynamics is used to simulate the flow. At moderate Mach numbers, incompressible LES is the minimum required computational effort, but it may be not affordable. A possible alternative is resorting to RANS (Reynolds-Averaged Navier-Stokes) computations to infer the inner and/or outer scales of the boundary layers, and reconstructing the quantities $\Phi_{pp}$ and $\ell_y$ *via* empirical laws previously tuned on experimental data bases. This approach still needs being comforted, facing the wide variety of possible flows encountered in rotating blade technology. Furthermore wall-pressure fluctuations are caused by turbulent patterns developing at different heights in the boundary layer and traveling at different convection speeds. Larger and faster eddies are farther away from the wall whereas smaller and slower ones are convected at shortest distance. In the same time larger or smaller eddies define lower or higher frequencies at same convection speed. This intricate mechanisms make the wall-pressure statistics difficult to analyze. Schematically arbitrary low frequencies can be produced by small-scale turbulence convected at very low speed. But eddy size is limited by boundary layer thickness, so that the correlation length is expected to drop at vanishing frequencies.

Wall pressure statistics is addressed more specifically in chapter 6. Complementary considerations are presented in the present section for trailing-edge noise applications. Wall-pressure spectra $\Phi_{pp}$ measured beneath boundary layers over flat plates and/or curved airfoil surfaces with more or less

pronounced stream-wise pressure gradients are first reported in Fig. 13 in dimensionless variables taking the displacement thickness as parameter. For finite-chord airfoils the measurement has been performed close to the trailing edge. Developed turbulence over a flat plate with zero pressure gradient (small dots) often taken as reference is found to produce the lowest fluctuations. In contrast an adverse pressure gradient causes a significant increase, more especially at lower frequencies, up to 10 or 20 dB. This has been observed by many investigators, on both large plates and airfoils, and certainly depends on many parameters, such as curvature and gradient strength. More especially leading-edge separation followed by reattachment is found to produce the highest levels, with a wide low-frequency bump. This flow regime is typical of thin or roughly designed leading-edges in fan-noise technology, for which off-design conditions can be encountered.

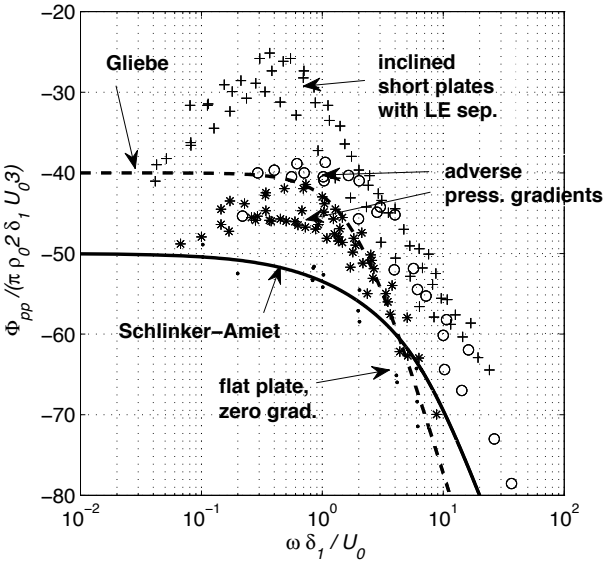


**Figure 13.** Wall-pressure spectra measured beneath turbulent boundary layers, with or without pressure gradient, made dimensionless by outer variables, from Keith *et al* (1992) and ECL flat-plate data. External-variable models plotted for comparison.

Model wall-pressure spectra can be built up based on boundary-layer parameters. A review dedicated to aeronautical fan-noise applications has

been proposed for instance by Gliebe *et al* (2000). Substantial differences might be expected for low-speed cooling fans. First reported attempts for the definition of universal statistical models are based on the use of outer boundary-layer variables to scale the wall-pressure spectrum, as

$$\Psi_{pp}(\omega) \,=\, \frac{\Phi_{pp}(\omega)}{\rho_0^2\,\delta_1\,U_0^3} \qquad or \qquad \Psi_{pp}(f) \,=\, \frac{\Phi_{pp}(f)}{\pi\,\rho_0^2\,\delta_1\,U_0^3}, \qquad \omega = 2\,\pi\,f > 0\,,$$

where the second form is directly expressed in terms of frequency. Schlinker-Amiet's model reads

$$\Psi_{pp}(\omega) \,=\, 10^{-5}\,\left(1 + \tilde{\omega} \,+ 0.217\,\tilde{\omega}^2 \,+ 0.00562\,\tilde{\omega}^4\right)^{-1}, \qquad \tilde{\omega} \,=\, \omega\,\delta_1/U_0$$

and Gliebe's *et al* model

$$\Psi_{pp}(\omega) \,=\, 10^{-4}\,\left(1 + \tilde{a}\,\tilde{\omega}^2\right)^{-5/2}\,,$$

where $\tilde{a}$ is 0.5 in the reference, and is better replaced by a smaller value, here 0.3 to fit with the low-Mach number results of Fig. 13. Both provide constant values at vanishing frequencies, abusive in view of some measurements, and asymptotic high-frequency trends like $\omega^{-4}$ and $\omega^{-5}$. The former and the latter hold for zero and adverse pressure gradients, respectively. The alternative Chase-Howe model based on inner variables (not plotted here) is expressed as

$$\bar{\Psi}_{pp} \,=\, \frac{\Phi_{pp}\,U_0}{\delta_1\,\tau_p^2} \,=\, \tilde{\omega}^2\,\left(\tilde{\omega}^2 + 0.0144\right)^{-3/2}\,,$$

where $\tau_p$ is the wall-shear stress. It is known to yield better high-frequency collapse and reproduces some low-frequency decrease. In counterpart the wall-shear stress is of more difficult access for practical applications. The large scatter of data in Fig. 13 suggests that model predictions could be very sensitive to the pressure gradient associated with aerodynamic loading. Yet this gradient does not enter explicitly the definition of aforementioned models. An improved model including the pressure gradient and based on mixed variables has been proposed very recently by Rozenberg *et al* (2012). The assessment on extended sets of experimental data still requires further investigation.

The correlation length is another matter of concern for sound predictions. For developed turbulence in boundary layers with zero pressure gradient,

Corcos' model is often used. The corresponding expression reads

$$\ell_y(k_2^*, \omega) \;=\; \frac{\omega/(b_c U_c)}{k_2^2 + \omega^2/(b_c U_c)^2}\,,$$

where $b_c$ is a constant, and essentially states that the correlation is inversely proportional to frequency (at least for parallel gusts $k_2 = 0$). This property is not physically consistent at very low frequencies. Indeed low frequencies naturally correspond to large scales and scales larger than the boundary layer thickness cannot be found.

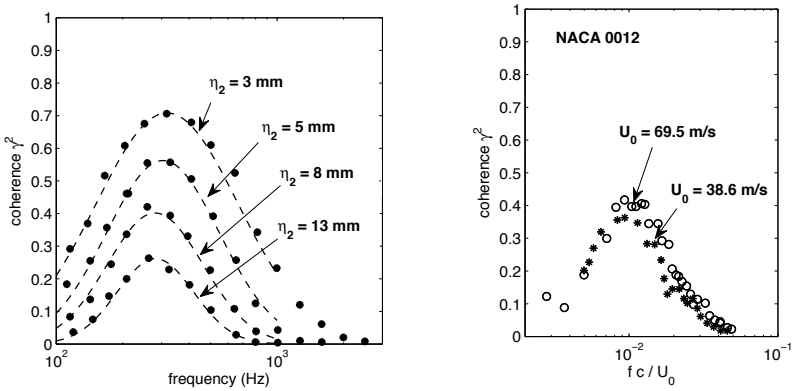


**Figure 14.** Evidence of a log-normal distribution of the span-wise coherence as a function of frequency. Left: measured data on a thin, moderately cambered rotating blade, from Rozenberg *et al* (2008). Right: reference data of Brooks & Hodgson (1981).

Evidence of a relevant Gaussian distribution of the coherence as a function of frequency on a logarithmic scale is reported in Fig. 14. The left-hand side plot refers to wall-pressure measurements directly made on the blades of a low-speed axial fan, from Rozenberg *et al* (2008). They are compared to a theoretical fit that obeys the log-normal law

$$\gamma^2(f) \;=\; \frac{A^2}{\sigma\sqrt{2\,\pi}\,f}\, e^{-[\ln f - \ln f_0]^2\,/(2\,\sigma^2)}$$

in which the parameters $A$, $f_0$, $\sigma$ appear as functions of the span-wise separation. Only retaining the variations of $A$ as dominant makes the same

qualitative variations expected for the correlation length. A similar behavior is reported by Roger & Moreau (2004) about the development of a rapidly growing boundary layer close to the trailing edge of a Controlled-Diffusion airfoil, in a flow regime identified as 'distributed vortex shedding' (see Fig. 22-d later on). In such a case, believed representative of many airfoils in real applications, the mean flow remains attached but vortical patterns are progressively shed along the suction side in the aft part of the airfoil. In fact Corcos' model fails at very low frequencies but often provides a consistent estimate of the coherence or of the correlation length at middle-and high frequencies. If the low-frequency range is not accessible as in some wind-tunnel airfoil testing setups because of installation effects or background noise issues, this model remains acceptable provided that turbulence in the vicinity of the trailing-edge is close to homogeneity. Other coherence measurements performed at two different speeds by Brooks & Hodgson (1981) on a NACA-0012 airfoil are shown on the right-hand side plot of Fig. 14. The log-normal frequency distribution is confirmed, with some similarity according to a Strouhal-number scaling.

Other data recently reported by Fischer (2012) also exhibit the drop of the coherence and of the correlation length at low frequencies, for airfoils dedicated to wind-turbine applications. Typical correlation lengths as determined by Rozenberg and Fischer are plotted in Fig. 15, in the upper and lower plots respectively. Bump-shaped distributions expected from the log-normal profiles are found. The data of Fig. 15-a refers to clustered wall-pressure probes mounted in the tip region of a blade and close to mid-span, for two stagger angles of the blades triggering different flow regimes. The physical behavior is the same but the involved characteristic scales are different. In Fig. 15-b, the NACA 64-618 airfoil is tested at different flow speeds. The frequency is scaled by the Reynolds number, proportionally to some Strouhal number, and the correlation length by the square root of the Reynolds number, quite arbitrarily. Classical laws for boundary layers do not make a perfect collapse expected this way, because the transition occurs at different locations on the airfoil suction side at different flow speeds. Anyway the results suggest that modeling the correlation is achievable but still remains an open issue. Other reported variations of $\ell_y$ with the angle of attack suggest that again the pressure gradient should enter the scaling parameters. Physical considerations lead to accept that the correlation length $\ell_y$ must be proportional to boundary-layer thickness.

The non-dimensional plot of Fig. 16 attempts in pointing evidence of such a proportionality, but the reported data exhibit significant scatter. Determinations of both $\ell_y$ and $\delta_1$ suffer from uncertainties because of either numerical or experimental resolution issues. The average theoretical

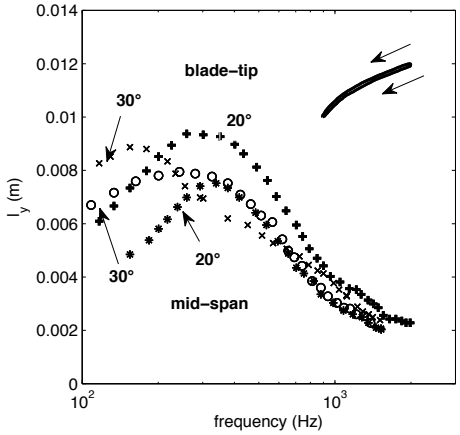


(a)

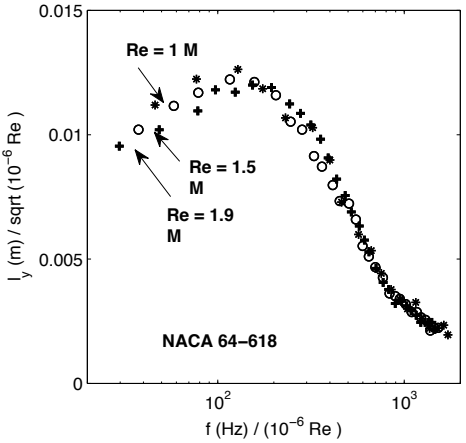


(b)

**Figure 15.** Span-wise correlations lengths as deduced from coherence measurements on airfoils. (a): ECL rotating-blade results, from Rozenberg *et al* (2008), blade section shown in the upper right; (b) scaled airfoil data from Fischer (2012).

fit proposed by Guédel *et al* (2011) and another fit deduced from the log-normal model assuming variations of $A$ only with the span-wise separation

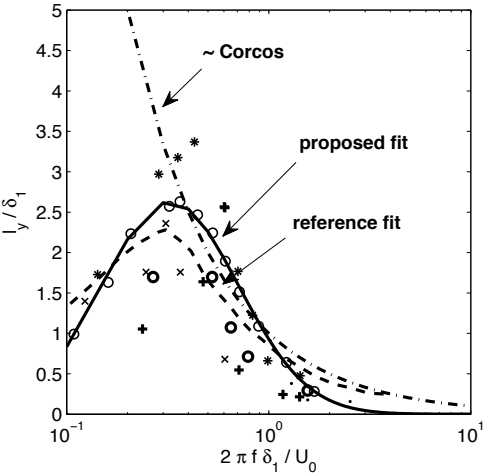


**Figure 16.** Correlation length reference data from Guédel *et al* (2011), and various theoretical fits.

are added on the figure. Both are acceptable assumptions for acoustic predictions in terms of decibels. In contrast Corcos-like fitting is not, at low frequencies. Extrapolated values at high frequencies for which measurements cannot be achieved lead to significant differences. At $2\,\pi\,f\,\delta_1/U_0 = 4$ in Fig. 16 the new proposed fit produces 12 dB less than the other two, therefore the choice of theoretical model becomes crucial.

### 5.3 Vortex-Shedding Noise Model

For vortex-shedding noise the far-field pressure PSD reads

$$S_{pp}(\mathbf{x},\omega) \;=\; \left(\frac{\rho_0\,k\,c\,x_3\,U_0}{2\,S_0^2}\right)^2 \frac{L}{2}\,S_{ww}(\omega)\,l_y(\omega)\,\left|I_1^{VK}\right|^2 \tag{19}$$

and only refers to the narrow-band spectral signature. The expression looks very similar to the one of turbulence-impingement noise because the mathematical statement also relies on velocity disturbances as the origin of sound. Here $S_{ww}$ is the PSD of the upwash velocity $w$ in the near wake and $l_y$ the corresponding span-wise correlation length. It must be noted that the quantity $S_{ww}$ refers to a disturbance field which is not homogeneous in the direction normal to the wake, therefore the definition of input data for the formulation is questionable. The obvious choice is taking the information

on the wake center-line where it is at its maximum. Moreover the formation of von Kármán vortices at the back edge of a body requires a finite stream-wise distance which influences the induced loads. The situation is clear in the case of a rectangular trailing-edge for which the flow detaches from the corners, taken below as example. Two sets of data obtained from different methods and referring to different Reynolds numbers of the flow over a flat plate a zero incidence are compared in Fig. 17. The power spectral density of the upswash is evaluated at twice the plate thickness $h$ downstream and assumed representative of the forcing quantity. It is deduced from incompressible LES performed over a limited span-wise extent for the low-Reynolds number case, and directly measured by hot-wire anemometry in the large-Reynolds number case. For the latter a slight frequency shift has been applied to account for some confinement effect in the experiment. A very good collapse is obtained by plotting the reduced PSD $S_{ww}/U_0$ as a function of the Strouhal number $fh/U_0$. This allows proposing a model exponential fit in logarithmic frequency scale, to be used as input data.

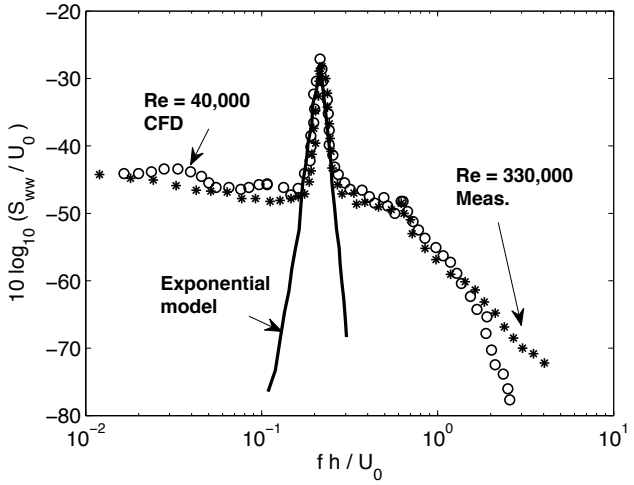


**Figure 17.** Upwash velocity spectra in the near wake of a flat plate as predicted by LES at low $Re_h$ of 4,000 (from Roger *et al* (2006)) and as measured at high $Re_h$ of 330,000 (unpublished ECL data, French Program SAMBA).

The associated correlation length has been assessed in the experiment from wall-pressure measurements closely upstream of the trailing edge, as-

suming that it is the same here and in the near wake by virtue of the continuity of the flow. It is quite large at the vortex-shedding frequency and drops rapidly besides. A consistent model fitted on measured data for the coherence has been found as

$$\gamma^2 \;=\; e^{-(\zeta/\Lambda_0)^2}\, e^{-a\,|\omega-\omega_0|}$$

where $a$ is some constant, around $0.012\,/(2\,\pi)$ at the Reynolds number of 4,000 based on the trailing-edge thickness. The corresponding correlation length reads $\ell_y(\omega) \;=\; \sqrt{\pi/2}\,\Lambda(\omega)$, with $\Lambda \;=\; \Lambda_0\, e^{-a\,|\omega-\omega_0|}$ and $\Lambda_0 \;\simeq\; 7\,h$.

Because the scaling of Fig. 17 is perfect with regard to the differences of dimensional parameters, it is considered reliable. However it holds only for zero angle of attack and a rectangular trailing edge. Other shapes such as beveled edges would possibly exhibit different features.

## 6 Scaling Laws and Experimental Validations

### 6.1 Scaling Laws and Asymptotic Trends

Scaling laws in aeroacoustics are often used as empirical prediction means. They can be obtained either from experimental data bases or from theoretical arguments. In the first case, the point is that the laws may fail when applied to configurations not covered by the original data base. The theoretical background is more reliable. Scaling laws are discussed in this section for turbulence-interaction noise and trailing-edge noise, from the aforementioned analytical models. They are based on the very important assumption that the flows are self-similar. This is very often so in practice because unsteady flows exhibit higher frequencies and levels with increasing mean-flow speeds. Typically the frequency is proportional to the mean flow speed $U_0$ and can be made dimensionless by introducing a Strouhal number $St \;=\; f\,l/U_0$ based on a relevant length scale $l$. Depending on the configuration, the fluctuating velocity amplitudes can be also proportional to the mean flow speed, or not (especially for three-dimensional flows, highly Reynolds-number dependent flows...). Therefore the PSD of the acoustic pressure is divided by $U_0^n$ where the exponent $n$ is to be determined. Aforementioned analytical models state that the acoustic intensity is proportional to the mean square value of the forcing disturbance, $w_{rms}^2$ or $P_{rms}^2$, to its span-wise correlation length $\ell_y$ and to the span-wise extent of the edge $L$. The derivations assume that the ratio $\ell_y/L$ is small. Furthermore the incident disturbances must have the properties of homogeneous and stationary random processes. Examples will be given in the next section.

The asymptotic high-frequency trend for turbulence-impingement noise is derived by only retaining the first term $I_1$ of the radiation integral, since the trailing-edge correction gets smaller and smaller. For $kc = 2\,M_0\,k_1^* \to \infty$ and accounting for the developments of Fresnel integrals (Abramowitz & Stegun (1970)), some algebra leads to

$$\frac{S_{pp}}{\Phi_{ww}} \simeq \frac{\rho_0^2\,U_0\,L\,M_0}{\pi\,R_e^2}\,\frac{\cos^2(\theta_e/2)}{(1+M_0\,\cos\theta_e)^3}$$

with $S_0 = R_e\,(1+M_0\,\cos\theta_e)$. The result is expressed in emission coordinates with respect to the surrounding flow for the sake of a better physical insight, and $\theta_e$ is the observation angle from the streamwise direction (see chapter 2 for definitions). In the limit of small Mach numbers $M_0^2 \to 0$, a cardioid directivity pattern is found. The sound goes to zero upstream at small angles close to the airfoil plane and is maximum downstream. For the low-frequency limit, Amiet's formalism must be replaced by Sears' theory and the radiation integral reads $|I| = |S(k_1^*/\beta^2)|/\beta$. Small values of $kc$ and reasonable values of $M_0$ make the function get close to 1, so that now the ratio becomes

$$\frac{S_{pp}}{\Phi_{ww}} \simeq \frac{\rho_0^2\,U_0\,\pi\,L\,M_0}{8\,\beta^2\,R_e^2}\,(kc)^2\,\frac{\sin^2\theta_e}{(1+M_0\,\cos\theta_e)^4}\,.$$

The radiation is that of a compact dipole in motion, zero in the plane of the airfoil and maximum in the normal direction. Except that it is not specified in the mid-span plane, the general case illustrated by the sample results of Figs. 7 and 8 is between the two asymptotic regimes. Apart from the change in the directivity, the exponent of convective amplification is also found to go from 4 to 3 from low to high frequencies because of increased non-compactness.

A similar analysis for trailing-edge noise only makes sense for the high-frequency limit. In this case, introducing the convection Mach number $M_c = U_c/c_0$ yields the result

$$\frac{S_{pp}}{\Phi_{pp}\,\ell_y} \simeq \frac{L\,M_c\,\sin^2(\theta_e/2)}{\pi^2\,R_e^2\,(1+M_0\,\cos\theta_e)}\,\frac{1-(M_0-M_c)}{[1+(M_0-M_c)\,\cos\theta_e]^2}$$

in which the last factor has a secondary importance, especially for low-Mach number applications. The opposite cardioid trend to leading-edge noise is found, no sound being radiated downstream and a maximum radiation upstream. Both results are in accordance with what is expected from the half-plane Green's function for a distant observer and a source located close

to the edge. In the limit of high frequencies, what happens at one edge radiates as if the complementary edge was removed to infinity. Trailing-edge noise radiates preferentially upstream and turbulence-impingement noise preferentially downstream.

Even though different in essence, both vortex-shedding noise and trailing-edge noise have common features because the underlying vortex dynamics responsible for sound radiation takes place in the very vicinity of the trailing edge in terms of emitted wavelengths. As a result if the radiation is interpreted as quadrupole sound according to Lighthill's analogy it tends to obey the asymptotic half-plane Green's function and produce a cardioid pattern. The present statements using Schwarzschild's technique adopt Ffowcs Williams & Hawkings' interpretation and directly address the equivalent distributed dipoles the radiation of which is defined by the free-space Green's function. Again it is verified that both interpretations provide the same result.

### 6.2 Turbulence-Impingement Noise Results

The figure 18 reproduces turbulence-impingement sound spectra for a NACA-0012 airfoil embedded in grid-generated turbulence, as reported by Paterson & Amiet (1976). The airfoil is mounted between end-plates at the nozzle of an open-jet anechoic wind tunnel and the noise is measured in the mid-span plane. Model predictions are superimposed on the sound spectra for different flow speeds. The agreement is found very good at the highest speed whereas the sound is clearly overestimated at the lowest flow speeds. The same experimental protocol repeated on a smaller set-up with a thinner airfoil of maximum thickness 3% at three flow speeds provides the results reported next in Fig. 19. Obviously the overall sound level and frequencies both increase with increasing flow speeds but humps and dips are seen always at the same frequencies, at Helmholtz numbers close to $2\,\pi$ and $4\,\pi$. The dips are attributed to interference fringes caused by chord-wise non-compactness and therefore do not depend on the flow speed (at least at the low Mach numbers investigated). They correspond to the same pattern illustrated in Fig. 7. A similar dip is observed in Fig. 18. But unlike the ones of the NACA-0012, the model predictions based on the same analytical formulation are now found very close to the measurements despite the low flow speeds. This difference is attributed to the thinner airfoil design, 3% against 12%. Various authors recognized that thick rounded leading edges have a reduced response to oncoming turbulence at sufficiently high frequencies. This is especially prominent for some cross-sections of wind-turbine blades,

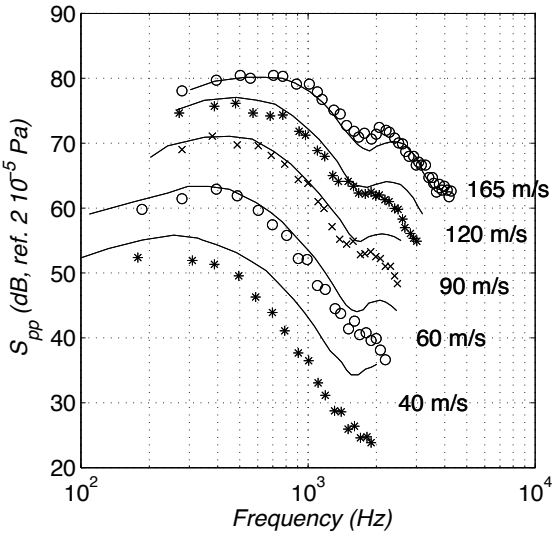


**Figure 18.** Turbulence-impingement noise spectra of a NACA-0012 airfoil from Paterson & Amiet (1976). Grid-generated turbulence, observer at 90° in the mid-span plane. $c = 23$ cm.

the relative thickness of which reaches 15% or 18%. The reduction occurs intuitively when the incident turbulent eddies are smaller than the airfoil leading-edge thickness or curvature radius. Such small eddies are deviated by the mean streamlines instead of being scattered at the edge. If Amiet's theory is assumed to hold for vanishing thickness or at least as long as the characteristic lengths of the turbulence exceed the thickness at the leading edge, comparing the response of different airfoils to the same incident turbulence provides a way to quantify the reduction due to thickness effect.

Data gathered from various investigators are found to collapse reasonably, at least over an extended range of parameters, provided that they are plotted in a corrected form to account for the variety of experimental conditions, as shown in Fig.20 reproduced from Roger & Moreau (2010). The reduction is divided by the ratio $(e/c)\,/\,(e/c)_{ref}$ and plotted as a function of the variable $f\xi/U_0$ where $\xi = (\Lambda/c)_{ref}\,/\,(\Lambda/c)$, the index *ref* standing for the NACA-0012 airfoil in the experiment of Paterson & Amiet (1976) taken as reference.

The amount of reduction in dB is almost proportional to thickness and to

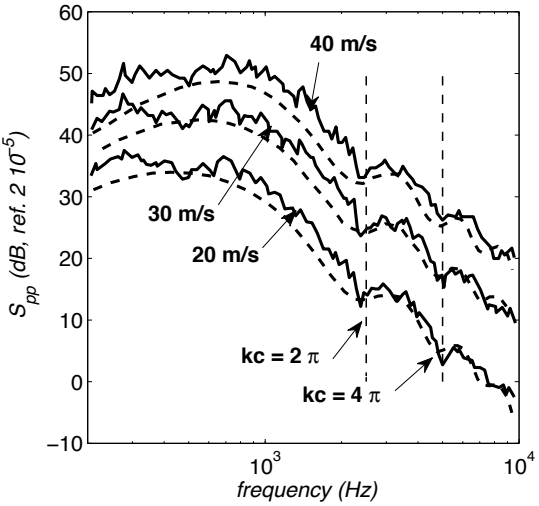


**Figure 19.** Turbulence-impingement noise spectra of a thin cambered airfoil (ECL, relative thickness 3%). Grid-generated turbulence, observer at 90° in the mid-span plane. $c = 13.6$ cm. Predictions (dashed) versus experiment (cont.).

frequency. The reduction also depends on the experimental set-up, mainly the grid-mesh size used to generate the turbulent field. The reasonable collapse of the figure can be used to empirically correct analytical predictions based on a thin-airfoil assumption.

Globally, turbulence-interaction noise at any subsonic Mach number is well predicted by Amiet's analytical model for velocity disturbance rates of less than 10%, relative thicknesses of a couple of percent, and moderate cambers. The mean load, or equivalently the actual angle of attack neglected in the linearized theories of unsteady aerodynamics, has no noticeable effect for a thin and slightly cambered airfoil over a large range of realistic values, provided that the oncoming turbulence is nearly homogeneous and isotropic. Recent developments also indicate that the precise design of an airfoil is more sensitive when the incident turbulence departs from ideal homogeneity and isotropy (Staubs *et al* (2008)).

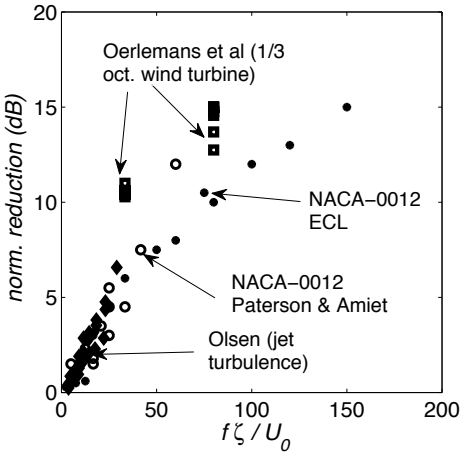


**Figure 20.** Dimensionless plot of thickness-induced noise reduction for thick airfoils in incident turbulence, according to various investigators. Oerleman's and Olsen's results reviewed by Roger & Moreau (2010).

### 6.3 Strouhal-Number Versus Helmholtz-Number Scaling

For self-similar flows the properties of which do not essentially vary with the Reynolds number, the amplitude and the frequencies of velocity fluctuations are both proportional to the mean flow speed. The spectral shape of the far-field sound extends wider for higher speeds, with increased levels. The flow statistics involved in the forcing source terms is expected to scale according to the Strouhal number $St = fc/U_0$. As a result, plotting the reduced PSD $S_{pp}\, U_0^{-(n-1)}$ as a function of the Strouhal number and ignoring non-compactness interferences must produce a perfect collapse of the curves, if the overall (frequency-integrated) acoustic intensity scales like $U_0^n$. This property should be used systematically to scale broadband noise data in aeroacoustics. In the same time higher frequencies triggered by higher flow speeds make the airfoil chord less compact, and departure from the self-similarity is expected in the sound signature from the onset of interference fringes. Apart from this, any geometrical environment of a flow is characterized by resonant frequencies which do not essentially depend on flow speed. It can be guessed that resonance and interference features, in particular related to chord-wise non-compactness, rather depend on the Helmholtz number $He = kc$. Indeed plotting the PSD as a function of frequency or

Helmholtz number preserves the non-compactness dips and humps at the same places but cannot produce a collapse over the entire frequency range. Plotting as a function of the Strouhal number provides a better overall collapse except that the dips are now at different Strouhal numbers for different speeds. Yet the Strouhal-number scaling is more physically consistent when tracking scaling laws of sound-generating mechanisms.

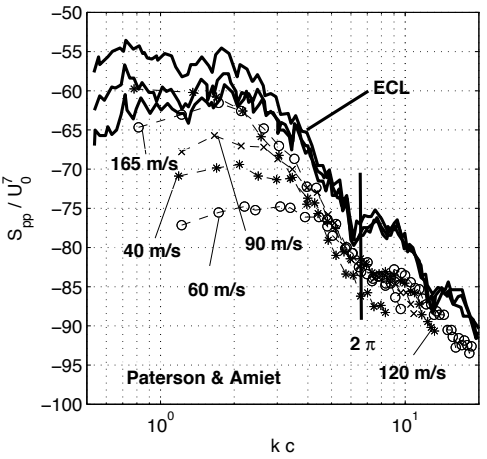


**Figure 21.** Helmholtz-number scaling of turbulence-airfoil interaction noise. Symbols stand for the NACA-0012 of Paterson & Amiet (1976) and thick lines for the thin cambered airfoil tested at ECL. Grid-generated turbulence, observer at 90° in the mid-span plane.

The sample results collected in Fig. 21 are taken again from Paterson & Amiet (1976) and the ECL data for a thin cambered airfoil (Figs. 18 and 19). A good collapse is achieved by plotting $S_{pp}/U_0^7$ as a function of the Helmholtz number $kc$, if the plot is aimed at emphasizing the humps and the dips attributed to non-compactness. Yet unacceptable scatter is found at lower frequencies. The first dip occurs quite close to the value $kc = 2\,\pi$ for which the acoustic wavelength is equal to the chord length, which is somewhat expected for an observer at 90°. The slight frequency shift of the dip between both sets of data is attributed to the different geometrical design. The sound levels also differ because of different experimental conditions and because of the thickness effect of the NACA-0012. This simple example illustrates that aerodynamic noise in the presence of solid surfaces

combines intricate flow and geometry effects. The duality $He$-versus-$St$ has been identified in many applications, for instance by Neise & Barsikow (1982) who discussed the acoustic similarity laws of low-speed fans.

### 6.4 Trailing-Edge Noise Results

Trailing-edge noise results for an industrial Controlled-Diffusion (CD) airfoil tested at low-Mach number are presented and discussed in this section as illustration of the methodology. The experimental protocol is the same as for turbulence-impingement noise. The airfoil is instrumented by clustered remote-microphone probes so that the wall-pressure statistics ($\Phi_{pp}$ and $\ell_y$) close to the trailing edge is measured directly (Roger & Moreau (2004)). This provides information on the sound sources. The far-field sound is also measured in the mid-span plane. Both wall-pressure spectra and acoustic spectra are compared in Fig. 22. Different flow regimes are obtained by setting different geometrical angles of attack, all with attached and stable laminar boundary layers on the pressure side. The acoustic spectra are artificially shifted up in order to make the comparison of spectral envelopes easier.

In case (a) a laminar unstable boundary layer develops on the suction side, with the expected Tollmien-Schlichting (TS) instability waves. The main bump and its distortion harmonics feature the range of unstable frequencies. Because the unsteady motion is coherent, both source and sound spectra exhibit additional tones resulting from acoustic back-reaction. Case (b) corresponds to a turbulent boundary layer triggered by a small leading-edge separation bubble. This regime is characterized by quite high fluctuating levels at low frequencies. In case (c) the flow remains attached but the boundary layer rapidly grows upstream of the trailing edge due to the formation of large vortical patterns in the aft part of the airfoil. This regime is referred to as 'distributed vortex shedding' by Roger & Moreau (2004). In each case the overall similarity of source and sound spectra confirms the cause-to-effect relationship. The level differences illustrate the ratio $S_{pp}/\Phi_{pp}$ and emphasize the variations of radiation efficiency with flow regime and/or frequency, essentially attributed to the span-wise correlations length $\ell_y$. TS waves are the most efficient in the frequency range of the bump, because they are associated with quite large values of $\ell_y$. Case (b) has the minimum efficiency, nearly frequency-independent. In contrast case (c) is more efficient below 1 kHz, because the span-wise coherence takes quite high values as reported in the reference paper.

Sound predictions in dimensional variables achieved by the analytical model of section 5.2 taking the measured wall-pressure statistics as input

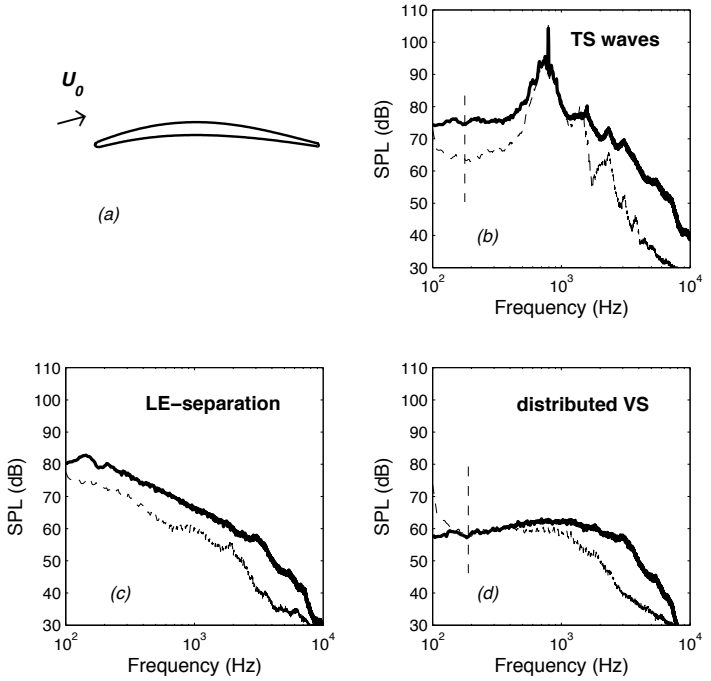


**Figure 22.** Compared wall-pressure (thick lines) and far-field sound (thin dotted) spectra for a CD airfoil at different flow regimes. Sound measured in the mid-span plane, normal to chord length. (a) airfoil cross-section. (b) Tollmien-Schlichting waves (laminar boundary layer). (c) leading-edge separation. (d) distributed vortex shedding. Acoustic spectra scaled by $R^2/(Lc)$ and shifted up by 30 dB. Frequencies below the vertical dashed lines are not reliable because of background-noise issues.

data are compared with measurements in Fig. 23, for the same three aforementioned regimes (Moreau & Roger (2009)). The upper plot refers to the onset of TS waves. The tones of Fig. 22-b resulting from amplification by acoustic feedback have been removed from the spectrum because the statistical model only addresses direct sound production from random disturbances. The remaining hump-like part corresponding to the primary

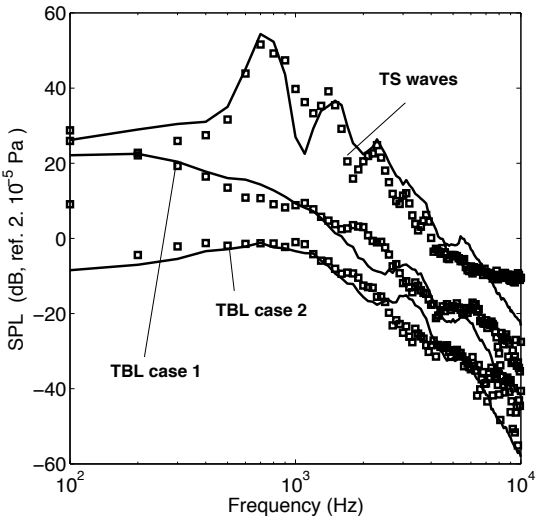


**Figure 23.** Predicted versus measured trailing-edge noise spectra of a thin cambered airfoil, from Moreau & Roger (2009). The three sets of data are vertically shifted from each other by 10 dB for clarity.

TS wave radiation with no feedback is reproduced accurately because the span-wise coherence can be measured over an extended frequency range. The other plots are shifted by -10 dB (case 1, Fig. 22-c) and -20 dB (case 2, Fig. 22-d) for clarity. In these cases the much weaker span-wise coherence at high frequencies is not accessible. Therefore it is as far as possible deduced from the measurements and continued by fitted theoretical trends; Corcos' model is used in case 1 and an *ad hoc* model proposed by Roger & Moreau (2004) is used in case 2. Bumps in the predicted spectra around 3 kHz and 5.5 kHz as well as dips around 2 kHz and 4.5 kHz are attributed to chord-wise non compactness (airfoil chord 13 cm). They do not clearly appear or they are shifted in the measurements, possibly because of camber effects and additional sound scattering by the nozzle lips in the experiment. Anyway the good overall agreement reported in Fig. 23 shows that the predictions are reliable when fed with directly measured input data. Similar results for a flat plate are found in next section.

### 6.5 Vortex-Shedding Noise Results

Vortex-shedding sound is a less documented topic. Indicative results and modeling attempts are mentioned in this section, for a flat plate with rectangular trailing-edge. Complementary elements are found in the book by Blake (1986). Typical far-field sound spectra are first plotted in Fig. 24 for an inclined flat plate tested in an open-jet anechoic wind tunnel. Because the flow is deflected by the mean lift acting on the plate, precise values of the geometrical angle of attack are indicative. Only the qualitative features of the flow and the related acoustic signature make sense, described here for increasing values of the angle from $\alpha_1 = 0$ to a maximum value $\alpha_4$. Even higher values would correspond to stall. The relative thickness of the plate is 3%. At zero angle of attack, a large peak is heard at the expected Strouhal number of 0.2 built on the plate thickness $h$. As the angle increases that peak reduces whereas a wide hump grows at lower frequencies. The higher the angle of attack, the lower and wider the associated frequency range. The bump is attributed to trailing-edge noise; indeed the flow separates at the leading edge and reattaches on the suction side of the plate, triggering a turbulent boundary layer, similar to the case of the CD airfoil, Fig. 22-c. The drop of the peak is caused by a loss of coherence and a progressive deactivation of the vortex shedding by increasing upstream disturbances. The frequency shift is attributed to different local flow accelerations at different angles of attack. It is concluded that both vortex-shedding sound and trailing-edge noise can coexist if the frequency range of the latter does not cover the one of the former. Yet competition obviously takes place.

The same plate of 3% thickness tested on a different nozzle produces the results of Fig. 25, taken from Chang *et al* (2006) and Roger & Moreau (2010) for illustrating the accompanying prediction methodology. In the first configuration at zero angle of attack, vortex shedding is well structured and not significantly influenced by disturbances developing upstream in the boundary layers. The associated sound can be predicted with eq. (19). The needed upwash spectrum is provided by the model calibrated in Fig. 17. The agreement is perfect in this case, dealing with the narrow-band signature only.

The procedure has been repeated for the geometrical angle of attack of 5°. In this case vortex shedding is disturbed by a higher turbulence level in the boundary layers and again the emergence of the peak is reduced as already emphasized in Fig. 24. Because of computational cost issues the numerical simulations ignored the flow-deflection effect in the experiment and some uncertainty results in the definition of the input data. An empirical spectral shape has been again defined anyway and the effect of the uncertainty assessed by the upper and lower estimates of the acoustic signature

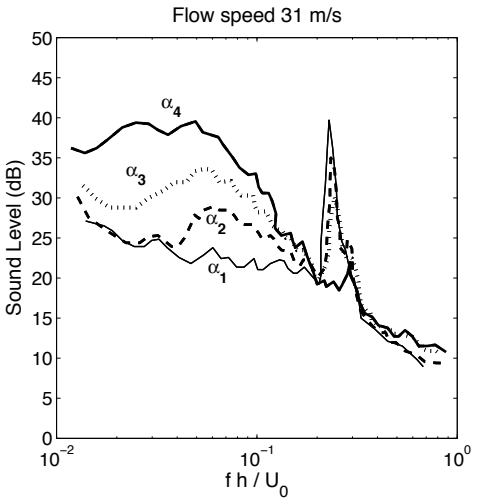


**Figure 24.** Sound spectra of a flat plate of 10 cm chord length inclined in a flow, as function of angle of attack. Combined trailing-edge noise and vortex-shedding noise. ECL data.

in Fig. 25. For completeness, the trailing-edge noise prediction achieved with the model of section 5.2 fed with measured wall-pressure statistics is reported, again showing a satisfactory agreement.

The flat-plate test-case illustrates a hybrid application in which input data are partly measured and partly provided by Computational Fluid Dynamics. The good overall agreement achieved here is in favor of the physical consistency of the reversed Sears' problem. However the practical application is made tricky by the non-homogeneity of the velocity in the near wake.

## 7 Concluding Remarks

The analytical approach declined in the chapter for various broadband-noise mechanisms can be understood as a post-processing technique to be associated with some flow description. It is found reliable for thin and moderately cambered airfoils provided that aerodynamic input data are available. The latter appear as the crucial point of the method. When they are provided by unsteady flow computations, the models can be applied as an alternative till full numerical methods including the prediction of the sound field can be applied at reasonable cost. The analytical method also suffers

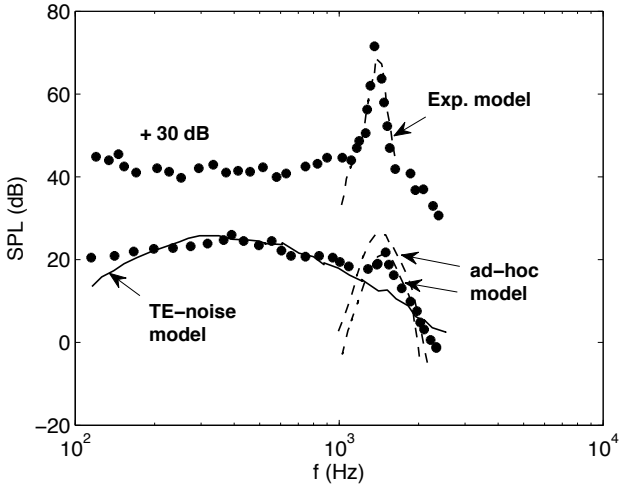


**Figure 25.** Measured sound spectra of the flat plate at the Reynolds number of 4,000 at 0° and 5° angles of attack, versus vortex-shedding sound predictions. From Roger & Moreau (2010).

from limitations inherent to the necessary assumptions. The limitations are the best motivation for further developments and improvements. Among other topics, connections between the wall-pressure statistics and the mean-flow parameters in the boundary layers with adverse pressure gradients still need being elucidated for trailing-edge noise predictions. For turbulence-impingement noise, the effect of departures from homogeneity are not fully understood either. Finally, for all investigated mechanisms, including three-dimensional effects related to blade geometry in turbomachines is required to accurately cover engineering applications.

## Bibliography

M. Abramowitz & I.A. Stegun, *Tables of Integrals, Series and Products*, Dover, NY, 1970

J.J. Adamczyk, *The Passage of an Infinite Swept Airfoil Through an Oblique Gust*, NASA CR 2395, 1974

R.K. Amiet (1975), *Acoustic Radiation From an Airfoil in a Turbulent Stream*, J. Sound Vib. vol. 41(4), p. 407-420

R.K. Amiet (1976), *High Frequency Thin-Airfoil Theory for Subsonic Flow*, AIAA Journal vol. 14(8), p. 1076-1082

R.K. Amiet, *Effect of the Incident Surface Pressure Field on Noise Due to Turbulent Flow Past a Trailing Edge*, Journal of Sound and Vibration, vol. 57(2), pp. 305–306, 1978.

W.K. Blake, *Mechanics of flow-induced sound and vibration*, Academic Press, Orlando, 1986.

T.F Brooks & T.H. Hodgson *Trailing Edge Noise Prediction from Measured Surface Pressures*, J. Sound & Vib., vol. 78(1), pp. 69-117, 1981.

K. W. Chang, J. H. Seo, Y. J. Moon & M. Roger, *Prediction of Flat Plate Self Noise*, 12th AIAA/CEAS Aeroacoustics Conference, paper 2006-2513, Cambridge MA, 2006.

J.E. Ffowcs Williams & D.L. Hawkings, *Sound generated by turbulence and surfaces in arbitrary motion*, Phil. Trans. Roy. Soc., A 264, 1969.

T. Fukano, Y. Kodama & Y. Senoo, *Noise generated by low pressure axial flow fans, I: Modeling of the turbulent noise*, J. Sound & Vib., vol. 50(1), pp. 63-74, 1977.

A. Guédel, M. Robitu, N. Descharmes, D. Amor & J. Guillard, *Prediction of the blade trailing-edge noise of an axial flow fan*, ASME Turbo Expo 2011, paper GT2011-45256, Vancouver, 2011.

A. Fischer, *Experimental characterization of airfoil boundary layers for improvement of aeroacoustic and aerodynamic modeling*, Thesis DTU, 2012

P. Gliebe, R. Mani, H. Shin, B. Mitchell, G. Ashford, S. Salamah & S. Connell, *Aeroacoustic prediction codes*, NASA-CR 2000-210244, 2000.

M.E. Goldstein, *Aeroacoustics*, McGraw-Hill, NY, 1976.

I.S. Gradshteyn & I.M. Ryszik (1980), *Tables of Integrals, series and products*, Academic Press, New York 1980.

J.M.R. Graham, *Similarity rules for thin aerofoils in non-stationary subsonic flows*, J. Fluid Mech. vol.43(4), p. 753-766

J.0. Hinze, *Turbulence*, McGraw-Hill, New-York 1975

G.F. Homicz & A.R. George, *Broadband and discrete frequency radiation from subsonic rotors*, J. Sound & Vib., 36 (2), pp. 151-177, 1974.

M.S. Howe, *A Review of the Theory of Trailing-Edge Noise*, Journal of Sound and Vibration, vol. 61(3), 1978, pp. 437–465, 1978.

W. L. Keith, D. A. Hurdis & B. M. Abraham, *A comparison of turbulent boundary layer wall-pressure spectra*, ASME Journal of Fluids Engineering, vol. 114(3), pp. 338347, 1992.

M. Landahl, *Unsteady Transonic Flow*, Pergamon Press, New York, 1961.

P. F. Mish & W. J. Devenport, *An experimental investigation of unsteady surface pressure on an airfoil in turbulence - Part 1: effects of mean loading*, J. Sound Vib., vol. 296 (3), pp. 417–446, 2006.

S. Moreau & M. Roger, *Back-scattering correction and further extensions of Amiets trailing-edge noise model. Part II: Application*, J. Sound Vib., vol. 323, pp. 397-425, 2009.

W. Neise & B. Barsikow, *Acoustic Similarity Laws for fans*, ASME TRans, vol. 104, pp. 162-168, 1982

S. Oerlemans & Beatriz Mendez-Lopez, *Acoustic Array Measurements on a Full Scale Wind Turbine*, $11^{th}$ AIAA/CEAS Aeroacoustics Conference, paper 2005-2963, Monterey CA, 2005.

R.W. Paterson & R.K. Amiet, *Acoustic Radiation and Surface Pressure Characteristics of an Airfoil Due to Incident Turbulence*, NASA CR-2733, 1976.

M. Roger, *On broadband jet-ring interaction noise and aerofoil turbulence-interaction noise predictions*, J. Fluid Mech. Vol. 653, pp. 337-364, 2010.

M. Roger & A. Carazo *Blade-Geometry Considerations in Analytical Gust-Airfoil Interaction Noise Models*, 16th AIAA/CEAS Aeroacoustics Conference, Stockholm, Sweden, AIAA Paper 2010-3799, 2010.

M. Roger & S. Moreau, *Broadband Self-Noise from Loaded Fan Blades*, AIAA J. vol. 42 (3), pp. 536-544, 2004.

M. Roger & S. Moreau, *Back-scattering correction and further extensions of Amiet's trailing-edge noise model; part I: theory*, J. Sound & Vib. vol. 286, pp. 477-506, 2005.

M. Roger & S. Moreau, *Extensions and limitations of analytical airfoil broadband noise models*, Int. J. of Aeroacoustics, vol. 9(3), pp.273-305, 2010.

M. Roger & C. Schram, *Analytical modeling of the tonal noise from open rotors due to tip vortices*, ISROMAC-14, Honolulu, 2012

M. Roger, S. Moreau & A. Guédel, *Vortex-Shedding Noise and Potential-Interaction Noise modeling by a Reversed Sears' Problem*, 12th AIAA/CEAS Aeroacoustics Conference, paper 2006-2607, Cambridge, MA, 2006.

Y. Rozenberg, M. Roger & S. Moreau, *Rotating Blade Trailing-Edge Noise: Experimental Validation of Analytical Model*, AIAA J., vol. 48(5), pp. 951-962, 2010.

Y. Rozenberg, G. Robert & S. Moreau, *Wall Pressure Spectral Model Including the Adverse Pressure Gradient Effects: Application to the Prediction of Trailing-Edge Noise*, to be published in AIAA J., 2012

I.J. Sharland, *Sources of noise in axial flow fans* J. Sound & Vib. vol.1, pp. 302-322, 1964.

J.K Staubs, W.J. Devenport & S.A.L. Glegg, *Sound radiation from a series of airfoils immersed in grid-generated turbulence*, 14th AIAA/CEAS Aeroacoustics Conference, paper 2008-3018, Vancouver 2008.

T. von Kármán & W.R. Sears, *Airfoil Theory for Non-Uniform Motion*, J. Aero. Sci. vol.5, p. 379-390, 1938.

Q. Zhou & P. Joseph, *A frequency domain numerical method for airfoil broadband self-noise prediction* J. Sound & Vib. vol.299, pp. 504-519, 2007.

# Boundary layer noise
# Part 1: generation mechanisms

Roberto Camussi, and Alessandro Di Marco
Universitá Roma Tre,
Dipartimento di Ingegneria Meccanica e Industriale,
Via della Vasca Navale 79, 00146, Roma, Italy

**Abstract** Boundary layer noise concerns the generation of acoustic waves as an effect of the interaction of a fluid with a moving surface. Several issues are related to the noise generation mechanisms in such a configuration. In the present description we focalize mainly onto the case of an infinite flat plate and two main distinct situations are considered. The first one deals with the prediction of the far field noise as accomplished from the classical integral theories, and the main formulations, including Curle's approach, are briefly reviewed. A novel approach based on the computation of the surface transpiration velocity is also presented. The second aspect concerns the interior noise problem and it is treated from the view point of the fluid dynamic effects rather than from that of the structural dynamics. Attention is focused on the statistical properties of the wall pressure fluctuations and a review of the most effective theoretical models predicting statistical quantities is given. The discussion is completed by a short review of the pressure behavior in realistic situations, including the separated boundary layers in incompressible and compressible conditions and the effect of shock waves at transonic Mach numbers.

## 1 Introduction

Aerodynamic noise from a turbulent boundary layer is a fundamental topic in flow-induced noise and is of interest for both fundamental studies and applied research. The action of the pressure fluctuations indeed provides the driving force to excite surface vibrations and produce acoustic radiation. Many engineering problems are connected with this topic. Fatigue loading on panels of an aircraft fuselage and the vibrational generation of acoustic radiation into an aircraft cabin enclosed by the boundary surface,

R. Camussi (Ed.), *Noise Sources in Turbulent Shear Flows: Fundamentals and Applications*, CISM International Centre for Mechanical Sciences, DOI 10.1007/978-3-7091-1458-2_6,

are two examples among many. Generally speaking, in high speed transport technology, the understanding of the physical mechanisms underlying the generation of pressure fluctuations at the wall, has received increasing attention in view of the use of lightweight and flexible structures. In the field of aerospace launch vehicles design, this problem is of great relevance since vibrations induced in the interior can cause costly damages to the payload while panel vibrations of the external surface must be avoided to prevent fatigue problems and structural damages. In the context of marine transportation, this topic has become quite important in the case e.g. of high-speed ships for passenger transportation where requirements of on board comfort have to be satisfied. This concern has become of great importance for ground transportation as well, notably for high speed trains design. In this case, the effect of pressure fluctuations induced by flow separations (e.g. due to the pantograph cavity) becomes the dominant noise producing mechanism, this situation being of relevance in the automotive industry in general, since large flow separations are unavoidable on cars.

The vibration of a panel induced by a random pressure load leads to acoustic radiation into the flow as well. Also this problem is of relevance for many engineering applications including, for example, the generation of noise from piping systems or the transmission of pressure waves by underwater vehicles, the so–called acoustic–signature.

Due to its importance, since the early 1960s, researchers have been studying this subject using different approaches including experimental investigations, numerical simulations and theoretical speculations.

When a solid surface is overflown by a turbulent boundary layer, several relevant mechanisms contributing to the generation of sound waves, can be identified. To simplify the description, consider the case of a panel subject to a flow on one side. The pressure field on the surface flow side consists of the sum of the turbulence pressures which would be observed on a rigid wall and the acoustic pressures which would be generated by the plane motion in the absence of turbulence. At a first approximation, these two effects can be studied separately. This idea represents the so-called *w*eak coupling approximation and can be derived from an acoustic analogy analysis of the problem [see e.g. Dowling (1983) and Howe (1992)]. The hypothesis that the basic turbulence structure is unaffected by the acoustic motions is indeed the basis of the acoustic analogies and can be accepted if the acoustic velocities are small in comparison with the turbulence velocities. This position, even though not always satisfied, has become accepted as a standard method even at supersonic flow speed [see also Graham (1997)]. The main reason for this is that fully coupled computations are, at present, prohibitive for any length scale of practical relevance even with the most

powerful computer resources. On the other hand, the engineering design still nowadays requires simple models which allows fast understanding and rapid computations.

In view of such considerations, in the following discussions the wall can be considered as a rigid plate and the panel vibrations considered apart.

The problem of the boundary layer noise can then be treated considering two different aspects, namely the so-called *community* noise and the *interior* noise. The first term applies to the effect of the acoustic waves generated by the wall turbulence and evolving in the far field from the flow side of the surface. The second one pertains with the transmission of noise at the side of the surface in still air. In both cases, the attempt to predict the noise emission is based on the correct representation, in a statistical sense, of the random load acting on the surface. For this reason, most of the discussions that follow are concerned with the clarification of the properties of the wall pressure field and the predictability of its main statistical properties. In Figure 1 an overall view of the mechanisms generating sound waves including the definitions adopted therein is reported. Figure 2 evidences the topics faced in the present chapter. The problem related to the interior noise is treated in more details in the second part of this chapter where the theoretical background regarding the noise transmission trough solid structures is presented.

## 2 The community noise problem

With the term 'Community noise' we mean the far field noise generated at the flow side of a plate moving in a still fluid. Even though very difficult, several theoretical studies have been carried out with the aim of predicting the features of the pressure field radiated by a plane turbulent boundary layer. This topic was first investigated by Curle (1955) and Powell (1960a) using Lighthill's analogy [Lighthill (1952)]. In the following, the integral formulations underlying those original approaches are briefly reviewed along with order of magnitude considerations to establish the importance of the radiative effects.

### 2.1 Integral formulations

The prediction of the propagation of acoustic waves in the far-field can be attained through an acoustic analogy approach and the search for a solution of the propagation equation derived therein. The reference theory is that of Lighthill (1952) that is based on the rearrangement of the Navier-Stokes equations to form an exact, inhomogeneous, wave equation, whose

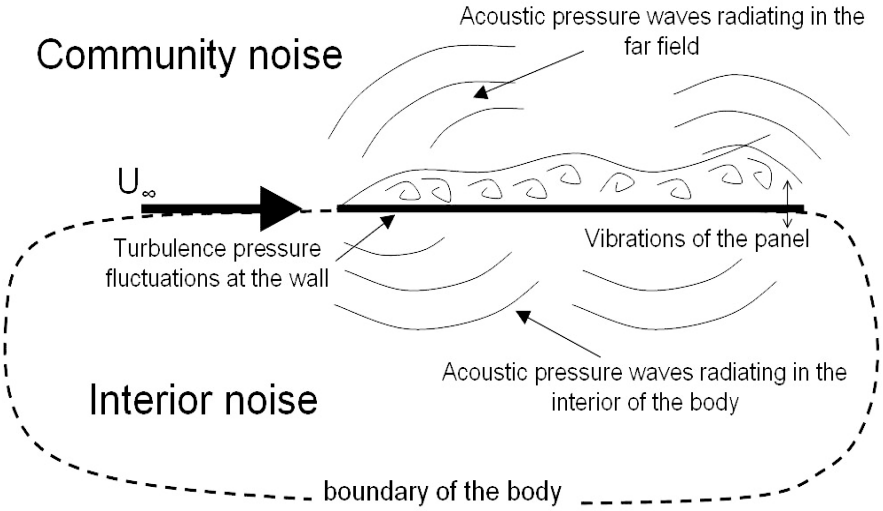


**Figure 1.** A scheme of the overall mechanisms generating sound waves from a turbulent boundary layer overflowing an elastic flat plate.

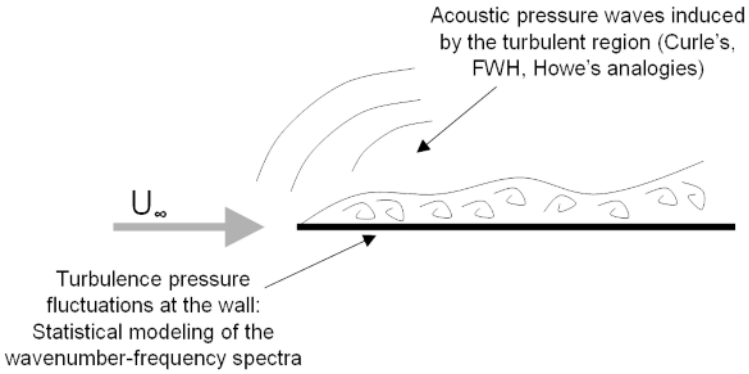


**Figure 2.** A scheme of the theoretical problems faced in the present chapter.

source terms are significant in the neighborhood of vortical regions of the flow. As pointed out above, the sound is supposed to be a sufficiently small component of the whole motion that its effect on the main flow can be neglected. This hypothesis can be accepted in low Mach number ($M$) flows as well as in the absence of resonating systems and multiphase flows.

Detailed discussion about such an approach, elucidating also the applicability limits, are given in other chapters of the present book. Here we limit ourselves to recall the final form of Lighthill's equation that can be written as:

$$\frac{\partial^2 \rho}{\partial t^2} - c^2 \nabla^2 \rho = \frac{\partial^2 T_{ij}}{\partial x_i \partial x_j} \tag{1}$$

where $T_{ij}$ represents the Lighthill stress tensor that, neglecting the viscous terms, is denoted as follows:

$$T_{ij} = \rho u_i u_j + (p - \rho c^2)\delta_{ij} \tag{2}$$

Here, $c$ is the speed of sound, $\rho$ and $p$ are density and pressure perturbations, $\mathbf{u}$ the fluid velocity, $\mathbf{x}$ the spatial coordinate and $t$ the time. This equation is valid within and without a source region. Where linear acoustics is valid, the acoustic pressure can be found from the relation $p = c^2\rho$.

In the presence of solid boundaries, an integral solution of Eq. 1 is based on the introduction of a closed control surface $S$ that may coincide with the surface of a moving body or mark a convenient interface between fluid regions of widely differing mean properties. When $S$ coincides with the solid boundary, the solution of the equation is carried out by imposing suitable boundary conditions on it. The oldest strategy proposed to solve the propagation equation relies on the use of a proper Green's function obtained as a solution of Eq. 1 when the source term is replaced by the impulse point source. The most general representation of this kind is due to Ffowcs Williams & Hawkings (1969), and is applicable to a control surface in arbitrary motion. This equation is obtained by deriving a wave type equation similar to that by Lighthill for a region made up of two subregions bounded by the control surface $S$. The region inside $S$ contains fluid and/or solid boundaries, the region outside contains only fluid.

Without entering into the details, the integral form of the Ffowcs Williams and Hawkings equation can be obtained again making use of the free space Green's function, leading to the outgoing wave solution. To the purpose of the present discussion, we can consider the case of a stationary control surface, leading the FWH equation to reduce to a simpler formula [see also

Howe (1998)] that was given previously by Curle (1955) and that we report in the following[1]:

$$p(\mathbf{x},t) = \frac{\partial^2}{\partial x_i \partial x_j}\int_V T_{ij}\frac{d^3\mathbf{y}}{4\pi\,|\mathbf{x}-\mathbf{y}|} - \frac{\partial}{\partial x_i}\int\int_S (\rho u_i u_j + p\delta_{ij} - \sigma_{ij})\frac{dS_j(\mathbf{y})}{4\pi\,|\mathbf{x}-\mathbf{y}|} + \frac{\partial}{\partial t}\int\int_S (\rho u_j)\frac{dS_j(\mathbf{y})}{4\pi\,|\mathbf{x}-\mathbf{y}|} \tag{3}$$

As indicated by Howe (1998), Curle's equation written for a rigid surface can be used to determine the order of magnitude of the sound generated by an acoustically compact body within a turbulent flow (e.g. a cylinder or an airfoil moving in an incompressible flow). This analysis applies also for non-compact bodies when turbulence interacts with compact structural elements, such as surface discontinuities, edges, corners.

The contribution from the quadrupole volume integral in Eq. 3 to the acoustic power $\Pi$ radiated in the far field, can be estimated to be

$$\Pi \propto v^3\, M^5 \tag{4}$$

The quadrupole effect predicted by Eq. 4 is the same as in the absence of the body (it is the famous Lighthill's 'eight power' law). On the other hand, at low $M$, the total power radiated by the dipole term (the first surface integral of equation 3) can be estimated to be:

$$\Pi \propto v^3\, M^3 \tag{5}$$

thus exceeding the quadrupole power by a factor $\sim 1/M^2 >> 1$. The conclusion is that at low $M$ the dipole term is largely dominant. This is the reason why surfaces with disconuities (such as sharp edges, steps, cavities) are much more noisy than smooth walls.

A different conclusion can be driven in the case of non-compact structures, that is, for objects whose size is not small compared to the acoustic wavelength, as is the case of an infinite rigid plate. Curle's approach can again be used, and the presence of the infinite surface can be taken into account by introducing image vortices [Powell (1960b)]. Powell suggests

[1] The notation evidencing the retarded time is not reported for clarity. Interested readers can find a more detailed presentation of this equation and of its theoretical framework in Chapters 1 and 2.

to use a Green's function that is basically obtained by superimposing the free-space $G$ with its image. In this way Powell shows that the pressure exerted on a plane boundary is the result of reflections of the quadrupole generators of the flow itself. In other words it is demonstrated that the surface integral is not a true dipole source but it represents the effect of image quadrupoles. Therefore, as concluded by Howe [Howe (1998)], the apparently strong contribution from the surface pressure dipoles actually reduces to a term of quadrupole strength, thus much less efficient, at low $M$, in terms of radiated pressure power. In the airframe noise context, if the effect of panel vibrations is not accounted for, it is reasonable to ignore the pure quadrupole radiation from the boundary layers, in comparison with that from edges and other inhomogeinities, such as wing trailing edge, flap side-edges, undercarriage gears and cavities. This is proven even for aircraft of large dimensions. As an example, the noise from the fuselage is expected to be more than 10dB below the level of the trailing edge noise.

However [Hubbard (1991)] the far field acoustic radiation due to panel vibrations might be a significant source of airframe noise in real (full-scale) aircraft. Furthermore [Howe (1998)] the presence of roughness breaks the Powell cancellation mechanism thus leading the dipole contribution to become relevant.

It should be pointed out that some recent numerical experiments [Hu, Morfey & Sandham (2002), Hu, Morfey & Sandham (2003) and Shariff & Wang (2005)] have focused on the role of the wall shear stress, rather than pressure, as sound source. They have shown that unsteady shear stresses can be an efficient sound source of dipole type that can be dominant at low Mach numbers and at very low frequencies.

We refer the reader to classical textbooks [such as Howe (1998)] and to the notes of the other authors included in this book, for further details on the integral approaches.

### 2.2 Prediction of the far field pressure spectrum: a novel approach

In a recent paper Morino, Leotardi & Camussi (2010) proposed a novel approach for estimating the far field pressure Power Spectrum (PSD) by the knowledge of the PSD of the pressure on the boundary surface, provided that the region where the flow is rotational and/or nonlinear is adequately thin. In order to accomplish this, the PSD of the pressure at any given point (either in the field or on the boundary) is evaluated in terms of the Power Spectral Density (PSD) of the transpiration velocity over the boundary surface. This contribution is denoted as given by *equivalent sources* $\chi_B$.

The approach briefly described therein is based upon a formulation that falls within the general class of potential–vorticity decompositions for the velocity field of the type

$$\mathbf{v} = \nabla\varphi + \mathbf{w}, \tag{6}$$

where $\mathbf{w}$ is any particular solution of the equation

$$\nabla \times \mathbf{w} = \zeta. \tag{7}$$

with $\zeta := \nabla \times v$ denoting the vorticity field.

The decomposition given in Eq. 6 is valid for any vector field and Eq. 7 is a necessary and sufficient condition for the validity of Eq. 6. Here, we assume $\mathbf{w}$ to be defined so as to have

$$\mathbf{w} = 0 \tag{8}$$

outside of the vortical region, $V_\zeta$, which is defined as the region where the vorticity $\zeta$ is not negligible.

For incompressible flows, the continuity equation reads

$$\nabla \cdot \mathbf{v} = 0 \tag{9}$$

Combining with $\mathbf{v} = \nabla\varphi + \mathbf{w}$, one obtains

$$\nabla^2\varphi = \sigma, \quad \text{where} \quad \sigma = -\nabla \cdot \mathbf{w} \tag{10}$$

In order to complete the problem, the boundary conditions have to be considered. For viscous flows, the boundary condition over $S_B$ is the no–slip condition:

$$\mathbf{v} = \mathbf{v}_B \qquad \big(\mathbf{x} \in S_B\big) \tag{11}$$

For simplicity, we introduce an additional boundary condition

$$\mathbf{w} \cdot \mathbf{n} = 0 \qquad \big(\mathbf{x} \in S_B\big) \tag{12}$$

Similarly, on the wake mid–surface $S_W$, we impose

$$\Delta\big(\mathbf{w} \cdot \mathbf{n}\big) = 0 \qquad \big(\mathbf{x} \in S_W\big) \tag{13}$$

Combining Eqs. 6, 11 and 12, we have, on the body surface $S_B$,

$$\frac{\partial\varphi}{\partial n} = \chi, \qquad \text{where} \quad \chi := \mathbf{v}_B \cdot \mathbf{n} \qquad \big(\mathbf{x} \in S_B\big) \tag{14}$$

Similarly, combining Eqs. 6 and 13, we have, on the wake mid–surface $S_W$,

$$\Delta\left(\frac{\partial\varphi}{\partial n}\right) = 0 \qquad \left(\mathbf{x} \in S_W\right) \tag{15}$$

In addition, in a frame of reference connected with the undisturbed air, we have

$$\varphi = O\left(\|\mathbf{x}\|^{-1}\right), \qquad \text{at infinity.} \tag{16}$$

Finally, at the trailing edge, we have (from the Joukowski smooth–flow assumption, akin to quasi–potential flows)

$$\lim_{\mathbf{x}_W \to \mathbf{x}_{TE}} \Delta\varphi(\mathbf{x}_W) = \lim_{\mathbf{x}_2 \to \mathbf{x}_{TE}} \varphi(\mathbf{x}_2) - \lim_{\mathbf{x}_1 \to \mathbf{x}_{TE}} \varphi(\mathbf{x}_1), \tag{17}$$

where 1 and 2 here denote the sides of the wing surface corresponding to the sides 1 and 2 of the wake mid–surface, respectively.

Using Eqs. 15 and 16, the boundary integral representation for the Poisson's equation, Eq. 10, is:

$$\begin{aligned} E(\mathbf{x},t)\,\varphi(\mathbf{x},t) = & \oint_{S_B}\left(\frac{\partial\varphi}{\partial n}\,G - \varphi\,\frac{\partial G}{\partial n}\right) dS(\mathbf{y}) \\ & - \int_{S_W} \Delta\varphi\,\frac{\partial G}{\partial n}\,dS(\mathbf{y}) + \int_{V_\zeta} \sigma\,G\,dV(\mathbf{y}) \end{aligned} \tag{18}$$

where $G = -1/4\pi\|\mathbf{x}-\mathbf{y}\|$. If the vortical region, $V_\zeta$ (boundary layer and wake), is sufficiently thin, we can 'compress' the volume integral into a source layer over $S_B$ and $S_W$, to yield

$$\begin{aligned} E(\mathbf{x},t)\,\varphi(\mathbf{x},t) = & \oint_{S_B}\left((\chi+\chi_B)\,G - \varphi\,\frac{\partial G}{\partial n}\right) dS(\mathbf{y}) \\ & + \int_{S_W}\left(\chi_W\,G - \Delta\varphi\,\frac{\partial G}{\partial n}\right) dS(\mathbf{y}) \end{aligned} \tag{19}$$

Equation 19 is the *key* to the approach presented here since it allows one to evaluate $\varphi$ anywhere in the field, if $\varphi$ and $\chi+\chi_B$ over $S_B$, as well as $\Delta\varphi$ and $\chi_W$ over $S_W$ are known.

The linearized Bernoulli's theorem reads:

$$p - p_\infty = -\rho\left(\dot{\varphi} + U_\infty\frac{\partial\varphi}{\partial x}\right) \tag{20}$$

The numerical formulation of the above equations can be determined both in the physical and in the Fourier domain but it is not reported here for

the sake of brevity. We just point out that, after discretization using piece–wise constant approximation and Fourier transform, the following linear relationship can be achieved:

$$\hat{p}_F = H\,\hat{p}_B. \tag{21}$$

the symbol $\hat{\cdot}$ denotes the Fourier transform of the discretized counterpart of the pressure and the equation represents the desired relationship between the field pressure (subscript $F$) and the boundary pressure (subscript $B$).

By using classical Wiener-Khintchine relationships, the above equation can be expressed in terms of the PSD matrix $S_v$. Thus, using Eq. 21, we have

$$S_{p_F} = H^*\,S_{p_B}\,H^T \tag{22}$$

which is the desired relationship between the PSD matrix $S_{p_F}$ of the pressure at $N_V$ arbitrary points in the region $\Re^3\backslash W$ and the PSD matrix $S_{p_B}$ of the pressure at $N_B$ points on $S_B$.

The expression in Eq. 22 allows one to evaluate the field–pressure PSD from the boundary–pressure PSD, thereby providing a link between two sets of experimental data (PSD of field pressure and PSD of surface pressure), often considered independent.

## 3 The wall pressure statistics

The random forces resulting from pressure fluctuations in the turbulent boundary layer over structural surfaces cause vibration. This surface motion becomes a source of noise which must be considered in the design of a vehicle. Therefore, the development of methods aimed at predicting interior noise levels, pressure fluctuations, and structural loading has become important in the design for instance of commercial aircraft, payload–carrying aerospace launchers, high speed trains. As pointed out by Graham (1996), in order to take into account this aspect in the design phase, there is a need for simple models capable of enhancing our physical understanding of the noise generation process and to provide relatively simple predictive formula to be utilized in the design process.

The methods of modeling and predicting sound and vibrations from a structure subject to a random pressure load, presume that the forcing function for the surface has been estimated. It can be shown [see e.g. Blake (1986) and Graham (1997)] that the excitation term is directly related to the boundary layer wavenumber-frequency spectrum that, therefore, has become the subject of many investigations. In the present discussion, we

do not enter into the details of the structural aspects, but we limit ourselves to reviewing the main features concerning the wavenumber-frequency spectrum analysis, modeling and prediction.

### 3.1 Relevant properties of the turbulent boundary layer

A short review of the main parameters characterizing the turbulent boundary layer and used for the scaling of the wall pressure spectra is given in the following. Extensive discussions can be found in several textbooks [see e.g. Schlichting (1979)]; therefore we limit ourselves to reviewing some relevant parameters that influence the overall statistical properties of the wall pressure fluctuations field.

At the wall, the boundary layer exerts a shear stress $\tau_w$, and there is a strong connection between this shearing and the behavior of the flow in the immediate vicinity of the wall. As the distance from the wall increases, the influence of the wall shear on the fluid motion diminishes and the flow properties may be described in terms of the local free stream velocity $U_\infty$ and the thickness of the boundary layer $\delta$, this symbol denoting the so-called Blasius thickness. In this region, the flow behavior is usually called $wake-like$. Thus, depending upon the distance from the wall, two important flow regions can be identified. A layer close to the wall, where the velocity depends upon the fluid viscosity and the local wall shear, and an outer layer, where the velocity depends on the external properties of the flow (i.e. $U_\infty$, $\delta$ and the upstream history of the layer). In the near wall region, the velocity increases linearly for increasing distance from the wall. In the outer layer the velocity defect evolves according to the well–known logarithmic law. Of course, due to the turbulent nature of the velocity field, the two regions boundaries can be defined only statistically.

In the linear region, the velocity gradient is independent of the distance from the wall. This assumption yields the following relationship:

$$U_1 = \frac{\tau_w y}{\mu} \tag{23}$$

where the subscript 1 denote the velocity component on the streamwise ($x$) direction and $\mu$ is the dynamic viscosity of the fluid.

In the logarithmic region the turbulence activity is the greatest and the velocity gradients are proportional to the distance from the wall. This gives rise to the logarithmic velocity profile described by the following equation:

$$\frac{U_1}{U_\tau} = \frac{1}{k} \ln\left(\frac{yU_\tau}{\nu}\right) + B \tag{24}$$

where $\ln(\cdot)$ is the natural logarithm of $\cdot$. The quantity $U_\tau$ is called the friction velocity and it is defined as

$$U_\tau = \sqrt{\frac{\tau_w}{\rho}} \tag{25}$$

being $\rho$ the fluid density at ambient temperature. The coefficient $k$ in Eq. 24 is the so–called Von Kàrmàn constant, equal to approximately 0.4 for any type of wall. $B$ is a coefficient that depends only on the degree of surface roughness. The notation commonly used to represent the dimensionless quantities, is the following:

$$U^+ = \frac{U_1}{U_\tau}, \;\; y^+ = \frac{yU_\tau}{\nu} \tag{26}$$

In Figure 3 a simplified scheme of the turbulent boundary layer is reported for completeness.

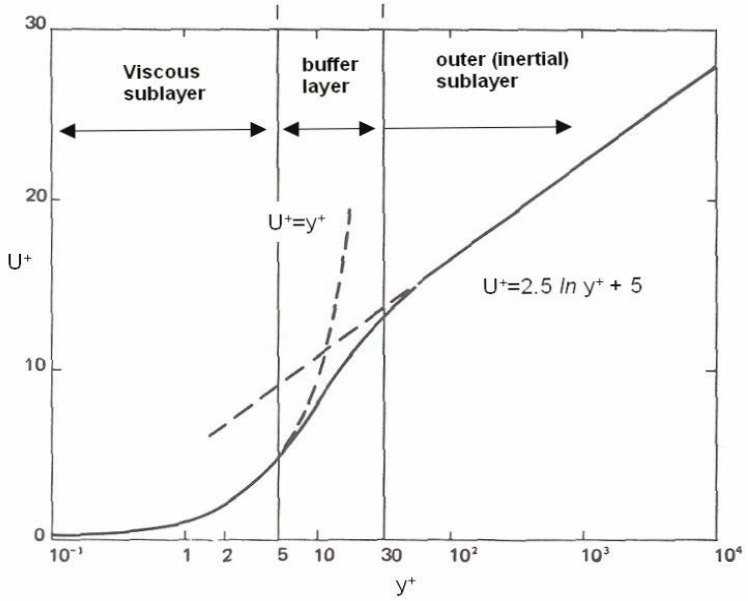


**Figure 3.** A scheme of the main parts of a turbulent boundary layer

Throughout the major portion of the fully developed turbulent boundary layer, the mean velocity profile over both smooth and rough walls satisfies

a defect law of the following form:

$$\frac{U_e - U_1}{U_\tau} = \frac{1}{k} \ln\left(\frac{y}{\delta}\right) + 1.38\left[2 - W\left(\frac{y}{\delta}\right)\right] \tag{27}$$

where $U_e$ is the external velocity, outside the boundary layer. The function $W(y/\delta)$ has been introduced by Coles (1956) and it is given by:

$$W\left(\frac{y}{\delta}\right) = 1 + \sin\left[\left(\frac{y}{\delta} - \frac{1}{2}\right)\pi\right] \tag{28}$$

It is well know that the definition of the Blasius thickness $\delta$ is not suitable for turbulent boundary layers. It is better to introduce more objective definitions. Very briefly we remind the definition of displacement thickness $\delta^*$ based on a mass balance in the boundary layer and given by the following expression:

$$\delta^* = \int_0^\infty \left[\frac{U_e - U_1(y)}{U_e}\right] dy \tag{29}$$

Of course also $\delta^*$ is an *outer* scale because its magnitude is of the order of the depth of the viscous sublayer. Typically, $\delta^*$ is approximately equal to a fraction of $\delta$, from 1/8 to 1/5, depending on the surface roughness and the pressure gradient. Similarly, another length scale can be defined on the basis of the momentum balance. It is called the momentum thickness $\theta$ and it is given by the following expression:

$$\theta = \int_0^\infty \frac{U_1(y)}{U_e}\left[\frac{U_e - U_1(y)}{U_e}\right] dy \tag{30}$$

The ratio of the two length scales is called the shape factor:

$$H = \frac{\delta^*}{\theta} \tag{31}$$

According to the laws of the wall described above, it is possible to determine explicit relationships among set of boundary layer thickness and the friction factor. We refer to more specific textbooks for the details [e.g. Schlichting (1979)].

By integrating along $y$, between 0 and $\delta$, the momentum balance equation written on $x$, it is possible to determine an equation relating integral quantities characterizing the turbulent boundary layer. This relationship, often denoted as the Von Kàrmàn integral equation, reads:

$$\frac{C_f}{2} = \frac{d\theta}{dx} - \frac{\theta}{2}\left(\frac{2+H}{\frac{1}{2}\rho U_\infty^2}\right)\frac{dP}{dx} \tag{32}$$

$C_f$ is the wall friction coefficient, given by:

$$C_f = \frac{\tau_w}{\frac{1}{2}\rho U_\infty^2} \tag{33}$$

Equation 32 gives the growth of the boundary layer in terms of $\theta$ as a function of the local wall shear stress coefficient and the static pressure gradient.

For a given Reynolds number $Re_x = xU_\infty/\nu$ it is possible to determine the momentum thickness by using empirical relationships. A commonly used expression, valid for smooth infinite flat plates, is the following:

$$C_f = 0.0592\ Re_x^{-\frac{1}{5}} \ \text{ for } \ Re_x \geq 10^8 \tag{34}$$

combining with Eq. 32, one obtains:

$$\frac{\theta}{x} = 0.037\ Re_x^{-\frac{1}{5}} \tag{35}$$

This equation is valid provided that

$$\frac{C_f}{\theta} \ \gg \ -(2+H)\frac{C_p}{dx} \tag{36}$$

being $C_p$ the static pressure coefficient.

Empirical relationships are used also to determine the inner properties of the turbulent boundary layer once the outer scales are known either experimentally or numerically. In this case, by the knowledge of $\theta$, it is possible to empirically determine $C_f$ and then $U_\tau$. This approach is of common use since the estimation of $U_\tau$ by the direct measurement or computation of $\tau_w$ might be very difficult in practice.

We finally remind that the velocity profile at high Reynolds numbers can be described by a power law of the following form [Schlichting (1979)]:

$$\frac{U_1}{U_\tau} = \left(\frac{y_1}{\delta}\right)^{\frac{1}{n}} \tag{37}$$

where typically $n \sim 7$ for smooth walls and 4 for rough walls. By considering the thickness definitions, the following relations are obtained:

$$\frac{\delta^*}{\delta} = \frac{1}{n+1} \tag{38}$$

and

$$\frac{\delta^*}{\theta} = \frac{n+2}{n} \tag{39}$$

For $n = 7$ it is obtained $\delta^*/\delta = 1/8$. Also Eqs. 37, 38 and 39 can be used for a qualitative estimation of the boundary layer integral properties.

### 3.2 Statistical properties of the wall pressure spectrum: correlations and wavenumber–frequency spectra

According to the 'weak coupling approximation' introduced above, in the present approach we consider a boundary layer developing on an infinitely extended rigid flat plate in a low Mach number flow without mean pressure gradients. In this framework, taking into account that the boundary layer thickness increases slowly in the streamwise direction, it is possible to consider the pressure field statistically homogeneous on the plane of the plate and statistically stationary in time. The homogeneous plane is described by the Cartesian axes that, for the sake of clarity, are defined as $x_1$, $x_2$, being $x_1$ aligned with the free stream velocity. The frame of reference adopted is depicted in Figure 4.

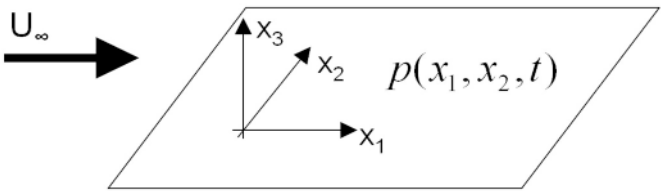


**Figure 4.** Frame of reference adopted to describe the statistics of pressure fluctuations.

Considering the fluctuating component of the pressure field $p(x_1, x_2, t)$, the space time correlation can be written as:

$$R_{pp}(\xi_1, \xi_2, \tau) = \frac{1}{\sigma_p^2} E[p(x_1, x_2, t)p(x_1 + \xi_1, x_2 + \xi_2, t + \tau)] \tag{40}$$

where $\sigma_p^2$ is the pressure variance and the symbol $E[\cdot]$ denotes the expected value. When the ergodic hypothesis holds, time averages can be used. This is an important hypothesis when pointwise pressure measurements are performed. In this case the pressure is a function of time only and the cross-correlation is given by a much simpler expression:

$$R_{pp}(\tau) = \frac{1}{\sigma_p^2} < p(t)p(t + \tau) >_t \tag{41}$$

where the symbol $< \cdot >_t$ now denotes the time average. Taking the Fourier transform of Eqs. 40 and 41 one obtain the wavenumber-frequency spectrum $\Phi_P(k_1, k_2, \omega)$ and the frequency spectrum $\Phi_p(\omega)$. In this notation $\omega$ is

the radian frequency and $k_1$, $k_2$ are the components of a two dimensional wavevector. By taking the frequency Fourier transform of Eq. 40 it is possible to obtain the cross-spectrum $\Gamma_p(\xi_1, \xi_2, \omega)$ that is defined in the space–frequency domain. The experimental determination not being very difficult, $\Gamma_p$ represents a key ingredient for the theoretical models that are presented below.

In the framework of the statistical modeling, a relevant role is played by the phase velocity $\omega/k$, being $k$ the magnitude of the wavevector, whose magnitude spans from the order of the flow speed to sonic or supersonic values.

### 3.3 The wave–number frequency spectrum

In this section the main characteristics of the wall pressure spectrum are briefly reviewed. First, the scaling properties of the frequency spectra are discussed taking into account the most relevant experimental investigations conducted in the last 50 years. Then, illustrative examples of statistical models of the wavenumber-frequency spectrum are revised starting from the early Corcos' idea up to the most recent developments.

**Scaling of the frequency spectra** Due to the complex structure of the turbulent boundary layer, it is not possible to obtain a single scaling that leads to a satisfactory collapse of experimental or numerical frequency spectra $\Phi_P(\omega)$. As will be clarified below, it is possible to normalize the spectra using inner or outer variables, and a universal collapse can be obtained in various regions of the pressure spectra separately [see, among many, the early work by Willmarth (1975) and the papers by Keith, Hurdis & Abraham (1992), Farabee & Caserella (1991) and Goody *et al.* (1998)]. This is due to the fact that the wall pressure is influenced by velocity fluctuations from all parts of the boundary layer and because the convection velocity depends strongly upon the distance from the wall, as a result of the non-uniform mean velocity distribution.

For an incompressible flow, the wall pressure can be written in the form of a Poisson's equation,

$$\nabla^2 \, p(\vec{x}, t) \;=\; q(\vec{x}, t) \tag{42}$$

where $q(\vec{x}, t)$ represents the source terms. As suggested by Farabee & Caserella (1991), the analysis of the solution of the above equation in the Fourier domain, shows that the contributions to the high-frequency portion of the spectrum has mainly to be attributed to turbulence activity located in the near wall region while contributions to the lower-frequency portion

can originate from activities throughout the boundary layer. Following this physical picture, and the conjectures suggested by Bradshaw (1967) and Bull (1979), it is possible to divide $\Phi_p(\omega)$ into three main regions, depending on the frequency magnitude. At low frequencies, $\Phi_p(\omega)$ scales on outer layer variables; at high frequencies, $\Phi_p(\omega)$ is influenced by the fluid viscosity and thus it scales on inner variables; at intermediate frequencies, the shape of the spectrum is scale independent and an universal power law decay of the type $\omega^{-1}$ is expected.

Measurements of the cross-spectral densities [e.g. Bull (1967) and Farabee & Caserella (1991)] confirm that the pressure field can be divided into two distinct families, one associated with the motion in the outer layer and the other with motion in the inner layer. This separation occurs at the frequency where the auto-spectrum exhibit its maximum value. This frequency separates the non-universal from the universal scaling regimes of the frequency spectrum.

More precisely, in the low frequency region, different outer scalings have been identified. Keith, Hurdis & Abraham (1992) suggests to scale the frequency using $U$ (the free stream velocity) and $\delta^*$, whereas the amplitude of the pressure spectrum can be scaled through the free stream based dynamic pressure $q$. Other authors [including Farabee & Caserella (1991)] recommend a more effective scaling using $\tau_w$ instead of $q$. They suggest to scale the frequency upon $U/\delta$ and the dimensionless spectrum to be of the form $\Phi_P(\omega)U/\tau_w^2\delta$.

In the high frequency region, there is a more general consensus on the most effective scaling that is achieved through the variables $U_\tau$, $\nu$ and $\tau_w$. This implies that the dimensionless frequency is $\omega\nu/U_\tau^2$ and the dimensionless spectrum should be $\Phi_P(\omega)U_\tau^2/\tau_w^2$.

The universal region can be interpreted as an overlap of the two regions described above. In this part of the spectrum it is assumed $\omega\Phi_P(\omega)U/\tau_w^2 =$ constant, thus leading to the $\omega^{-1}$ scaling. A precise definition of the amplitude of the frequencies bounding the universal region can be found in Bull (1979) and Farabee & Caserella (1991).

An additional range at very low frequencies has been also identified by some authors. Farabee & Caserella (1991) determine this region at $\omega\delta^*/U \leq 0.03$ and they collapsed the spectrum using the normalization $\Phi_P(\omega)U/q^2\delta^*$. In the very low frequency region they observed the spectrum to scale as $\omega^2$. This form of scaling is in agreement with the prediction given by the Kraichnan-Phillips theorem [Kraichnan (1956) and Phillips (1956)] which suggests that the wavenumber spectrum should scale like $k^2$ as $k \to 0$. According to the theoretical developments of e.g. Lilley & Hodgson (1960), this conclusion can be extended to the frequency spectrum under the hy-

pothesis of low Mach number flow conditions.

In Figure 5 a scheme summarizing the expected scalings is reported.

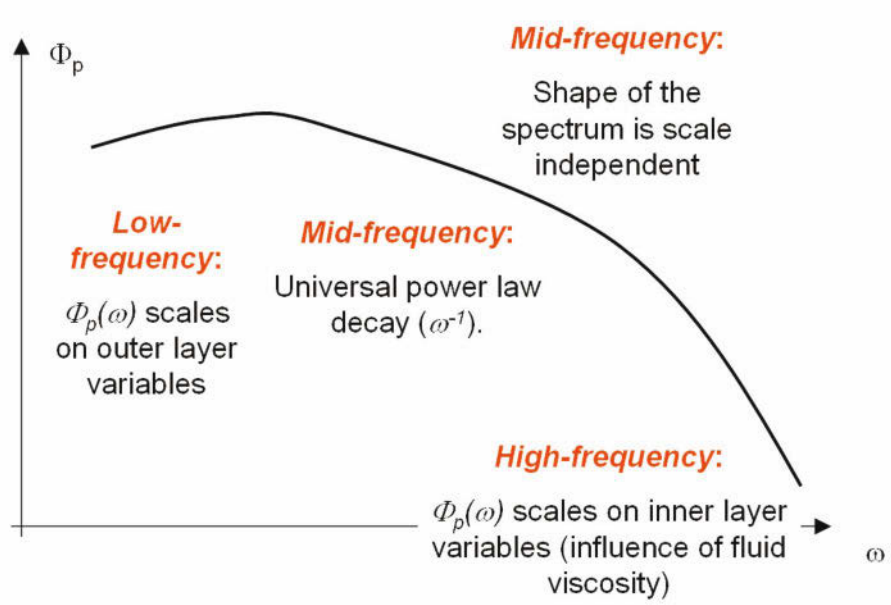


**Figure 5.** Sketch clarifying the expected scaling regions of a typical wall pressure auto–spectrum.

We refer to the literature [in particular Farabee & Caserella (1991) and Bull (1996)] for further discussions on the above topics and considerations about the scaling of the pressure variance.

**Modeling the wavenumber-frequency spectrum** According to the above discussion, several models have been proposed in the literature to reproduce the shape of the frequency auto-spectrum using suitable fits of experimental data. Here we only cite some of them as illustrative examples of common approaches. We refer to the literature for comprehensive reviews.

An early and widely used model was proposed by Corcos (1964). He gives the following representation of the frequency auto-spectrum:

$$\Phi_p(\omega) = \begin{cases} C & \text{for } \omega \leq \frac{U_e}{\delta^*} \\ C\frac{U_e}{\omega\delta^*} & \text{for } \omega > \frac{U}{\delta^*} \end{cases} \tag{43}$$

The quantity $C$ is a dimensionless constant and $U$ is the external velocity. Note that for $\omega > \frac{U_c}{\delta^*}$ the model correctly predicts the power law decay of the spectrum of the form $\omega^{-1}$.

An example, among many, explaining the way the Corcos' early model has been successively modified, is given by Cousin (1999). This more general approach leads to the following expression:

$$\Phi_p(\omega) = \begin{cases} 2.14 \times 10^{-5} B & \text{for } \omega\delta^*/U_e \leq 0.25 \\ 7.56 \times 10^{-6} B \left(\omega\delta^*/U\right)^{-0.75} & \text{for } 0.25 < \omega\delta^*/U_e \leq 3.5 \\ 1.27 \times 10^{-4} B \left(\omega\delta^*/U\right)^{-3} & \text{for } \omega\delta^*/U_e > 3.5 \end{cases} \quad (44)$$

where $B = q^2\delta^*/U$.

Other formulations worth mentioning are those by Efimtsov (1986) and Chase (1987, 1991). We refer to the literature for the details.

As pointed out above, the knowledge of the frequency spectrum is not sufficient to determine the modal excitation term of a plate subject to the turbulence induced pressure filed. This quantity is directly related to the shape of the complete wavenumber-frequency spectrum of the wall pressure field. The knowledge of $\Phi_P(k_1, k_2, \omega)$ is therefore fundamental to compute the response of a surface panel subject to the action of the random pressure load.

As pointed out by Bull (1996), the highest spectral levels of the pressure fluctuations are associated to the mean flow convection and, in the wavenumber spectrum, are centered on a wavenumber $k_1 = \omega/U_c$, $k_1$ along the free stream velocity. This part of the spectrum is often referred to as the convective ridge. For $k_1 \ll \omega/U_c$ the spectrum is expected to be independent of the wavenumber. Another important aspect is related to the so-called sonic wavenumber $k_0 = \omega/c$. According to Blake (1986), for $k = k_0$ an apparent singularity is present in the spectrum. However, in real flows, the wavenumber-frequency spectrum is expected to have a local finite peak in the vicinity of $k_0$. These are among the main features that an analytical model attempting to predict the $\Phi_p(k_1, k_2, \omega)$ shape, have to reproduce correctly.

One of the most reliable model developed in literature is again the early approach proposed by Corcos (1964) and based on the Fourier transform of a curve fit of measured narrow band pressure correlations. According to extensive experimental measurements [namely Willmarth (1975) and Bull (1967)], the cross-spectral density $\Gamma_p(\xi_1, \xi_2, \omega)$ can be represented as:

$$\Gamma_p(\xi_1, \xi_2, \omega) = \Phi_p(\omega)\, A(\omega\xi_1/U_c)\, B(\omega\xi_2/U_c)\, e^{i\omega\xi_1/U_c} \quad (45)$$

where

$$A(\omega\xi_1/U_c) = e^{-\alpha_1|\omega\xi_1|/U_c} \text{ and } B(\omega\xi_2/U_c) = e^{-\alpha_2|\omega\xi_2|/U_c}$$

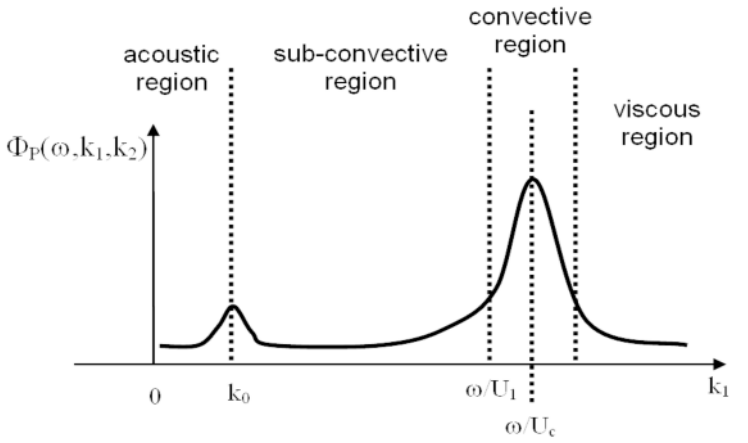


**Figure 6.** A scheme representing the wavenumber-frequency spectrum as a function of wavenumber, at constant frequency (scheme adapted from Blake (1986)).

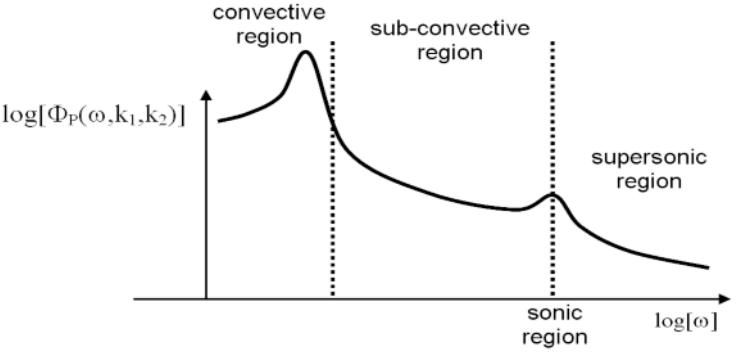


**Figure 7.** A scheme representing the wavenumber-frequency spectrum as a function of frequency, at constant wavenumber (scheme adapted from Blake (1986)).

whereas $U_c$ is the convection velocity and $\alpha_1$ and $\alpha_2$ are parameters chosen to yield the best agreement with experiments. Various values are given in the literature. The typical range of the values is $\alpha_1 = 0.11 \div 0.12$ and $\alpha_2 = 0.7 \div 1.2$ for smooth rigid walls.

Unfortunately, only few experimental or numerical data concerning direct measurements of the wavenumber–frequency spectrum are available in the literature [Abraham (1998), Choi & Moin (1990), Panton & Robert (1994), Farabee & Geib (1991), Hwang & Maidanik (1990), Manoha (1996)]. However, it appears evident that a big spread is present in the low wavenumber range and that the Corcos model overpredicts levels at wavenumbers below the convective peak. This point is crucial for many applications, in particular in the case of underwater and surface marine vehicles and for aeronautical structures above the aerodynamic coincidence frequency [see also Ciappi *et al.* (2009)]. Later workers used analytical or quasi analytical approaches, or revised versions of the Corcos approach, in attempts to describe this region more accurately [see e.g. Graham (1997) for details].

Most of the models proposed continued to follow the philosophy of the Corcos approach that can be generalized as follows. A first common feature of those empirical models is the separation of variables approach to represent the correlation function dependence on the streamwise separation $\xi_1$ and the crossflow separation $\xi_2$. This is known as the 'multiplication hypothesis' in which the coherence of the cross-spectral density for an arbitrary separation direction is formed by the product of the cross-spectral densities for streamwise and spanwise separations, respectively. The axisymmetry of the geometry and of the flow is usually not explicit in those formulations but it is accounted for through the adjustable coefficients. According to the Corcos idea given in Eq. 45, most of the models suggest to take exponential decaying form of the functions $A$ and $B$,

$$A(\omega, \xi_1) = e^{-\frac{|\xi_1|}{L_1(\omega)}} \text{ and } B(\omega, \xi_2) = e^{-\frac{|\xi_2|}{L_2(\omega)}} \tag{46}$$

where $L_1$ and $L_2$ are the so-called coherence lengths in the streamwise and spanwise direction respectively.

The main advantage of adopting the expression given in Eqs. 45 and 46 is that the auto-spectrum part is decoupled from the cross-spectrum part. That implies that any choice for modeling the function $\Phi_p(\omega)$, as those described above, can be addressed independently of any choice for representing the functions $L_1$ and $L_2$.

As for auto-spectra, Cousin modified the Corcos model yielding the fol-

lowing expressions of the coherence lengths:

$$\begin{aligned} L_1 &= \frac{U_c}{\omega\alpha_1}\left\{1+\left(\frac{U_c}{\omega b_M \delta}\right)^2\right\}^{-1/2} \\ L_2 &= \frac{U_c}{\omega\alpha_2}\left\{1+\left(\frac{U_c}{\omega b_T \delta}\right)^2\right\}^{-1/2} \end{aligned} \tag{47}$$

where $U_c = 0.75U$, $b_M = 0.756$, $b_T = 0.378$. $\alpha_1 = 0.115$ for smooth walls and 0.32 for rough walls, whereas $\alpha_2 = 0.32$ in all cases.

A similar model, not reported here for brevity, has been proposed by Cockburn & Robertson (1974). Wu & Maestrello (1995) proposed a model where the flow is assumed semi-frozen and decaying in space and time at a constant velocity $U_c$. After performing a comprehensive set of experimental results of wind tunnel testing, they defined an ensemble average of the cross correlation for the pressure fluctuation due to the turbulent boundary layer in which the effects of the Reynolds number and the boundary layer thickness were included.

Other models proposed by Chase (1980), Efimtsov (1982), Ffowcs Williams (1982), Chase (1987) and Smol'yakov & Tkachenko (1991) are compared in Graham (1997) and a plot reporting the spectra predicted by different models is given in Figure 8. It is shown that even at the convective peak, a relevant scattering among the model predictions is evident. Even larger scattering is observed in the estimation of the radiated sound as reported in the same paper.

The best model for high speed aircraft is, according to Graham, the one which provides an accurate description of the convective peak. Efimtsov's model, an extension of Corcos model, is cited as a suitable candidate. For the sake of completeness, we report in the following the Efimtsov idea:

$$\begin{aligned} L_1 &= \delta\left[\left(\frac{a_1 St_\tau}{U_c/U_\tau}\right)^2 + \frac{a_2^2}{St_\tau^2+(a_2/a_3)^2}\right]^{-1/2} && \text{for} \quad 0.41 < M < 2.1 \\ L_2 &= \delta\left[\left(\frac{a_4 St_\tau}{U_c/U_\tau}\right)^2 + \frac{a_5^2}{St_\tau^2+(a_5/a_6)^2}\right]^{-1/2} && \text{for} \quad M < 0.75 \\ L_2 &= \delta\left[\left(\frac{a_4 St_\tau}{U_c/U_\tau}\right)^2 + a_7^2\right]^{-1/2} && \text{for} \quad M > 0.9 \end{aligned} \tag{48}$$

In this model $U_c = 0.75U_e$ and $St_\tau = \omega\delta/U_\tau$ is a Strouhal number defined on the friction velocity. Averaged values of the empirical constants are $a_1 = 0.1$, $a_2 = 72.8$, $a_3 = 1.54$, $a_4 = 0.77$, $a_5 = 548$, $a_6 = 13.5$, $a_7 = 5.66$. It can be shown that at high frequencies, these expressions correspond to a Corcos model with $\alpha_1 = 0.1$ and $\alpha_2 = 0.7$. Even though the number of

empirical constants is relevant, the model is extensively used thanks to the introduction of the Mach number as a relevant parameter.

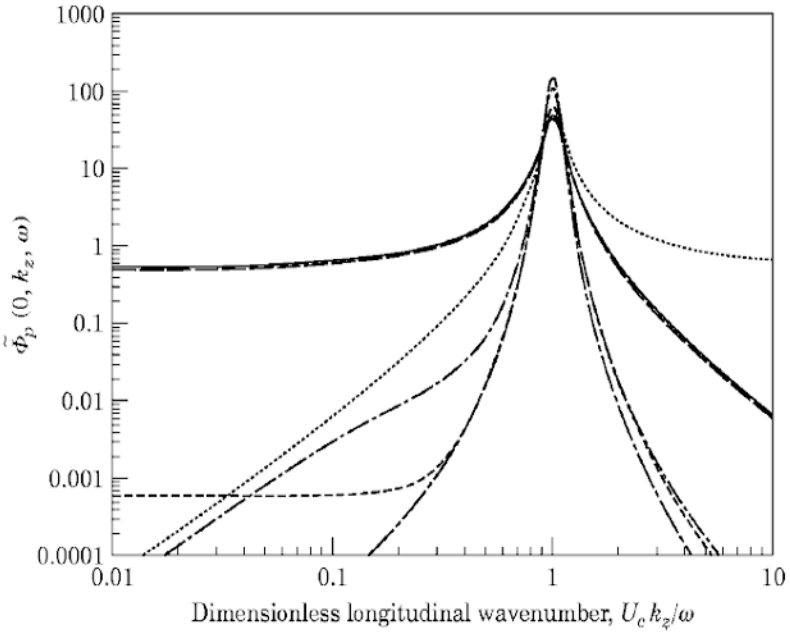


**Figure 8.** Wavenumber frequency spectra computed at a fixed frequency as reported in Graham (1997). The spectra are computed as functions of the longitudinal wavenumber non-dimensionalized on the convective wavenumber $\omega/U_C$ (courtesy of JSV).

More recently, Singer (1996a) and Singer (1996b) performed a Large-Eddy Simulation (LES) of a turbulent boundary layer at relatively high Reynolds number and proposed a model that overcomes the 'multiplication hypothesis' that is the basis of all the models based on the Corcos' philosophy. His approach is based on an accurate fit of the two-dimensional coherence and therefore is particularly efficient for the determination of the off-axis coherences.

To the best of our knowledge, the most recent model proposed in literature is the one presented by Finneveden *et al.* (2005). They suggested a modified version of the Corcos and of the Chase model, thus going back to the 'multiplication hypothesis'. They demonstrated that it is possible

to find for both models a complete set of free parameters that provide a fair agreement with experimental data. The key point was to modify the Corcos model by introducing a frequency and flow speed dependence in the parameters and to introduce two new parameters in the Chase model to better fit the spanwise coherence to measurements.

### 3.4 Coherent structures and wall pressure fluctuations

As pointed out above, it is possible to establish a connection between the wall pressure wavenumber spectra and physical quantities describing the turbulent boundary layer. In particular, the high wavenumber components should be attributed to fluid dynamic structures in the near wall region while the low wavenumber domain is influenced by the large scale structures in the outer layer. However, the detailed features of organized events that occur in the boundary layer are lost by the unconditional averaging techniques used in obtaining spectral estimates of the pressure field. This is an important issue from the practical viewpoint since a deeper knowledge of the fluid dynamic structures underlying the observed pressure properties may be helpful to address suitable control strategies aimed at manipulating the flow structures and modifying the wall pressure behavior.

Numerical simulations of simplified configurations attempted to clarify the connection between wall pressure fields and near wall vortical structures whose topology was selected a-priori according to classical conceptual models of the turbulent boundary layer. For example, Dhanak & Dowling (1995) and Dhanak, Dowling & Si (1997), following the conceptual model of the boundary layer proposed by Orlandi & Jimenez (1994), were able to clarify the effect of near wall quasi-streamwise structures upon the wall pressure field. More recently, Ahn, Graham & Rizzi (2004) and Ahn, Graham & Rizzi (2010) reproduced correlations and spectra at the wall. In order to estimate the wall pressure distribution, they reproduced hairpin vortex dynamics on the basis of the so called attached eddy model proposed by Perry & Chong (1982).

Only a few experiments have been focused on these aspects, since the correlation between wall pressure and coherent structures is rather difficult to interpret due to the chaotic nature of the pressure field. Among the existing studies, the work by Johansson, Her & Haritonidis (1987) can be mentioned: they carried out simultaneous pressure–velocity measurements and suggested physical mechanisms for the underlying generation of positive or negative pressure peaks at the wall. However, they did not clarify the connection between the educed structures and the wall pressure spectral quantities.

In a recent paper, Camussi, Robert & Jacob (2008) applied non conventional time-frequency post-processing tools to analyze wall pressure experimental data. The application of multi-variate wavelet transform permitted them to establish a connection between sweep/ejections events and large pressure coherence. More specifically, using a conditional sampling technique, they observed that averaged pressure signatures due to hydrodynamic effects were composed of a large negative pressure drop coupled to a weaker positive bump. This behavior was ascribed to accelerated-decelerated motions within the turbulent boundary layer.

The presence of a positive pressure bump coupled with a stronger negative pressure drop was also observed by Dhanak & Dowling (1995) who simulated numerically the pressure field induced at the wall by streamwise vortices. Similarly, in an experiment performed by Johansson, Her & Haritonidis (1987) negative–positive pressure jumps were also observed and were identified as $burst-sweep$ events. The conditional results of Johansson, Her & Haritonidis (1987) were obtained by correlating pressure negative peaks with velocity events found in the buffer region of the boundary layer through the so–called VITA technique [see e.g. Blackwelder & Kaplan (1976)].

Analogous conclusions were driven by Jayasundera, Casarella & Russell (1996) through the investigation of experimental wall pressure and inflow velocity data and the application of coherent structures identification techniques. They showed that the organized structures present within the turbulent boundary layer contain both ejection and sweep motions inducing positive and negative pressure events respectively.

More recently, Kim, Choi & Sung (2002) attempted to correlate the wall pressure fluctuations with the streamwise vortices of a numerically simulated turbulent boundary layer. They suggest that the high negative wall pressure fluctuations are due to outward motion in the vicinity of the wall correlated to the presence of streamwise vortices.

### 3.5 Effect of adverse pressure gradient and separation

An overall effect of adverse pressure gradients onto the wall pressure field statistics is an increase of the wall pressure fluctuations and a reduction of the convection velocity. This behavior was first observed by Schloemer (1967) through an experimental study devoted to the investigation of the influence of a mild adverse pressure gradient on wall pressure fluctuations. Owing to changes in the streamwise turbulent intensity, Schloemer also noticed an increase in the wall pressure spectral densities at low-frequencies (in outer scaling), whereas little effect was observed in the high-frequency range. This result has been later confirmed [see e.g. Lim (1971)] and seems

to suggest that the pressure gradient influences the outer layer region which, as described above, is directly correlated to the mid and low frequency range of the wall pressure frequency spectra.

Na & Moin (1998) performed a Direct Numerical Simulation (DNS) of a turbulent boundary layer developing over a flat plate, under both mild and strong imposed adverse pressure gradient. In the latter case (involving extensive separation) the frequency spectra in the separation bubble were found to exhibit a $\omega^{-4}$ decay, whereas a $\omega^{-2}$ behavior at high frequencies was observed for the spectra downstream of the reattachment position. The analysis of two-point correlations of wall pressure fluctuations also revealed strong coherence in the spanwise direction, that was attributed to the occurrence of large two-dimensional roller-type vortical structures. These authors also showed that the presence of flow separations, re-circulations and re-attachments lead to the generation of wall pressure fluctuations whose overall level might be significantly larger (up to 30dB) than that observed in equilibrium turbulent boundary layer with no separations.

Measurements of surface pressure fluctuations for a separated turbulent boundary layer under adverse pressure gradient were reported by Simpson, Ghodbane & McGrath (1987). Those authors found that pressure fluctuations increase monotonically through the adverse pressure gradient region, and showed that the maximum turbulent shear stress in the wall-normal direction can be used as a scaling variable since it yields good collapse of the normalized spectra at various streamwise stations.

Several studies have been conducted to characterize the fluid dynamic structure of flows whose separation is induced by a surface discontinuity. Detailed results have been obtained for several geometries, including backward facing steps [see Simpson (1989), and the literature cited therein for a comprehensive review in the field], sharp edges [as in Kiya, Sasaki & Arie (1982), Kiya & Sasaki (1985), and Hudy, Naguib & Humphreys (2003)], inclined surfaces [e.g. Song, DeGraaff & Eaton (2000)] and surface bumps [e.g. Kim & Sung (2006)]. Most of these studies have shown that the wall pressure fluctuations are driven by a low frequency excitation linked to the expansion and contraction of the separation bubble, a phenomenon usually designated as flapping motion. Besides, the vortical structures within the shear layer have been identified as the source of higher frequency peaks normally observed close to the reattachment position.

Stüer, Gyr & Kinzelbach (1999) analyzed the separation bubble upstream of a Forward Facing Step (FFS) in laminar flow conditions through flow visualizations and particle tracking velocimetry measurements. They demonstrated that the laminar re-circulating region upstream of the step is an open separation bubble characterized by spanwise quasi-periodic un-

steadiness. The flow topology and the pressure field upstream and downstream of an FFS at much higher Reynolds numbers have been recently studied by Largeau & Moriniere (2007). The effect of the relevant length-scales has been underlined in this work and the influence of the flapping motion upon the pressure field at the reattachment point has been demonstrated by means of pressure-velocity cross-correlations obtained from simultaneous wall microphones and hot wire anemometry measurements. Fourier pressure spectra upstream and downstream of a FFS have been presented also by Efimtzov *et al.* (1999) who showed that the region downstream of the step is the most significant in terms of pressure level. On the other hand, Leclercq *et al.* (2001) considered the acoustic field induced by a forward-backward step sequence and suggested that the most effective region in terms of noise emission is located just upstream of the FFS. The experimental results reported in Leclercq *et al.* (2001) have been successfully reproduced in a large eddy simulation performed by the same group, Addad *et al.* (2003). It was confirmed that the largest acoustic source is located in the separated region upstream of the wall discontinuity. Camussi, Guj & Ragni (2006) and Camussi *et al.* (2006) measured the pressure fluctuations at the wall of a shallow cavity representing a backward-forward step sequence. The authors again showed that the region close to the FFS is the most effective in terms of wall pressure fluctuations level even though the origin of the observed acoustic field was not clarified. In a recent study of the incompressible flow past a forward-facing step, Camussi *et al.* (2008) also observed the increase of energy at low-frequencies and a decrease at higher ones.

A flow separation can be induced also by the effect of a shockwave interacting with the boundary layer, a situation that can typically be encountered in transonic flow conditions. The prediction of pressure fluctuations in the transonic regime is particularly important in the vibro-acoustic design of aerospace launch vehicles. As a matter of fact, vibrations induced in the interior of the vehicle can exceed design specifications, and cause payload damage, as well as structural damage due to fatigue problems.

The presence of a shockwave and the consequent separation, causes an adverse pressure gradient that modifies significantly the boundary layer dynamics and causes substantial modification of the wall pressure signature. The Mach number effect in attached boundary layers has been taken into account in a few literature models [see e.g. the one proposed by Efimtsov (1982) and cited above]. On the other hand, the effect of the shockwave induced separation on the wavenumber-frequency spectrum is the subject of quite a few literature papers. We remind the numerical studies conducted by Pirozzoli and co-workers [Pirozzoli, Bernardini & Grasso (2010)

and Bernardini, Pirozzoli & Grasso (2011)] based on a DNS approach used to simulate the shockwave induced separation on a flat plate at a transonic Mach number ($M = 1.3$). They show that the shape of the frequency wall pressure spectra is qualitatively modified by the interaction with the shock wave. In the region with zero pressure gradient, the shape of the spectra is similar to that observed in low-speed boundary layers. When the pressure gradient is relevant, the low-frequency components of the spectrum are enhanced while the higher ones are attenuated. This observation is in agreement with results obtained in low-speed boundary layers in adverse pressure gradient and it is the signature of the greater importance of large-scale, low-frequency dynamics past the interacting shock, with respect to the fine scale effects. According to observations in low speed flows upstream an FFS by Camussi *et al.* (2008), in the separated region downstream of the shock, a self-similar structure of the pressure spectra is observed exhibiting the -7/3 inertial scaling at intermediate frequencies and a -5 decay law at high frequencies.

Similar scalings were observed in transonic and supersonic flow conditions by Camussi *et al.* (2007). They analyzed the statistics of the wall pressure fluctuations on a scaled model of an aerospace launcher that has been investigated in transonic and supersonic wind tunnels. Even though qualitatively, the -1 and -7/3 scalings were documented at several stations along the surface of the model.

The determination of a general predictive model for the wavenumber–frequency spectrum in the presence of shockwaves is however still far and, to the authors' opinion, this topic merits to be the task for future extensive research.

### 3.6 Concluding remarks

A brief overview of the studies made in the field of boundary layer noise in the last 60 years, has been reported, with particular emphasis on the interior noise problem and the mechanisms underlying the generation of the wall pressure fluctuations responsible for the panel vibrations and the transmission of noise.

The problem of the acoustic radiation due to the interaction of a turbulent boundary layer with a solid surface, has been treated only qualitatively. The prediction of the far field noise can be achieved by integral formulations and the main feature outlined in the present notes consisted in an order of magnitude estimation of the terms representing the far field pressure solution. The practical consequences of those results have been discussed in the framework of the airframe noise problem.

More emphasis has been given on the description of the wall pressure statistics mainly in terms of their spectral content estimated in the Fourier domain. The scaling parameters of the frequency spectra have been discussed in connection with the properties of the near wall and the outer–layer regions of the turbulent boundary layer. The main properties of the wavenumber-frequency spectra have been also reviewed and discussed along with the main statistical models proposed in literature to predict the auto– and cross–spectra behaviors.

More practical aspects have been treated by considering the case of separated flows and the complex behavior arising by the interaction of the boundary layer with shockwaves.

## Bibliography

B.M. Abraham, *Direct measurements of the turbulent boundary layer wall pressure wavenumber–frequency spectra*, Journal of Fluids Engineering 120, pages 29–39, 1998.

Y. Addad, D. Laurence, C. Talotte and M.C. Jacob, *Large eddy simulation of a forward-backward facing step for acoustic source identification*, International Journal of Heat and Fluid Flow 24, pages 562–571, 2003.

B-K. Ahn, W.R. Graham and S.A. Rizzi, *Modelling unsteady wall pressures beneath turbolent boundary layers*, 10th CEAS/AIAA Aeroacoustics Conference, 10-12 May 2004, Manchester, UK, 2004.

B-K. Ahn, W.R. Graham and S.A. Rizzi, *A structure-based model for turbulent-boundary-layer wall pressures*, Journal of Fluid Mechanics 650, pages 443–478, 2010.

R.F. Blackwelder and R.E. Kaplan, *On the wall structure of the turbulent boundary layer*, Journal of Fluid Mechanics 76, pages 89–112, 1976.

W.K. Blake, Mechanics of flow-induced sound and vibration. Volume II: Complex flow-structure interactions, Academic Press, 1986.

P. Bradshaw, *'Inactive' motion and pressure fluctuations in turbulent boundary layers*, Journal of Fluid Mechanics 30, pages 241-258, 1967.

M.K. Bull, *Wall pressure fluctuations associated with subsonic turbulent boundary layer flow*, Journal of Fluid Mechanics 28, pages 719–754, 1967.

M.K. Bull, *On the form of the wall-pressure spectrum in a turbulent boundary layer in relation to noise generation by boundary layer-surface interactions*, Mechanics of Sound Generation in Flows, IUTAM Conference, Springer-Verlag, Berlin, pages 210–216, 1979.

M.K. Bull, *Wall-pressure fluctuations beneath turbulent boundary layers: some reflections of forty years of research*, Journal of Sound and Vibration 190(3), pages 299–315, 1996.

R. Camussi, G. Guj and A. Ragni, *Wall pressure fluctuations induced by turbulent boundary layers over surface discontinuities*, Journal of Sound and Vibration 294, pages 177–204, 2006.

R. Camussi, G. Guj, A. Di Marco and A. Ragni, *Propagation of wall pressure perturbations in a large aspect-ratio shallow cavity*, Experiments in Fluids 40, pages 612–621, 2006.

R. Camussi, G. Guj, B. Imperatore, A. Pizzicaroli and D. Perigo, *Wall pressure fluctuations induced by transonic boundary layers on a launcher model*, Aerospace Science and Technology 11, pages 349–359, 2007.

R. Camussi, G. Robert and M.C. Jacob, *Cross–wavelet analysis of wall pressure fluctuations beneath incompressible turbulent boundary layers*, Journal of Fluid Mechanics 617, pages 11–30, 2008.

R. Camussi, M. Felli, F. Pereira, G. Aloisio and A. Di Marco, *Statistical properties of wall pressure fluctuations over a forward-facing step*, Physics of Fluids 20, pages 075113-1 – 075113-13, 2008.

D. Chase, *Modelling the wavevector-frequency spectrum of turbulent boundary layer wall pressure*, Journal of Sound and Vibration 70, pages 29–67, 1980.

D.M. Chase, *The character of the turbulent wall pressure spectrum at subconvective wavenumbers and a suggested comprehensive model*, Journal of Sound and Vibration 112, pages 125–147, 1987.

D.M. Chase, *Fluctuations in wall-shear stress and pressure at low streamwise wavenumbers in turbulent boundary-layer flow*, Journal of Fluid Mechanics 225, pages 545–556, 1991.

H. Choi and P. Moin *On the space–time characteristics of wall pressure fluctuations*, Physics of Fluids A 2, pages 1450–1460, 1990.

E. Ciappi, F. Mangionesi, S. De Rosa and F. Franco, *Hydrodynamic and hydroelastic analyses of a plate excited by the turbulent boundary layer*, Journal of Fluids and Structures 258, pages 321–342, 2009.

J.A. Cockburn and J.E. Robertson, *Vibration response of spacecraft shrouds to in-flight fluctuating pressures*, Journal of Sound and Vibration 33, pages 399–425, 1974.

D. Coles, *The law of the wake in the turbulent boundary layer*, Journal of Fluid Mechanics 1, pages 191-226, 1956.

G.M. Corcos, *The structure of the turbulent pressure field in boundary-layer flows*, Journal of Fluid Mechanics 18(3), pages 353–378, 1964.

G. Cousin, *Sound from TBL induced vibrations*, PhD Thesis, KTH Marcus Wallenberg Laboratory for Sound and Vibration Research, Stockholm, 1999.

N. Curle, *The influence of solid boundaries upon aerodynamic sound*, Proceedings of the Royal Society of London A231, pages 505–514, 1955.

M.R. Dhanak and A.P. Dowling, *On the pressure fluctuations induced by coherent cortex motion near a surface*, Proc. 26th AIAA Fluid Dynamics Conference, June 1995, Paper No. 95-2240, 1995.

M.R. Dhanak, A.P. Dowling and C. Si, *Coherent vortex model for surface pressure fluctuations induced by the wall region of a turbulent boundary layer*, Physics of Fluids A 9, pages 2716–2731, 1997.

A.P. Dowling, *Flow-acoustic interaction near a flexible wall*, Journal of Fluid Mechanics 128, pages 181–198, 1983.

B.M. Efimtsov, *Characteristics of the field of turbulent wall pressure fluctuations at large Reynolds numbers*, Soviet Physics - Acoustics 28, pages 289–292, 1982.

B.M. Efimtsov, *Vibrations of a cylindrical panel in a field of turbulent pressure fluctuations*, Soviet Physics - Acoustics 32(4), pages 336–337, 1986.

M. Efimtsov, N.M. Kozlov, S.V. Kravchenko and A.O. Anderson, *Wall pressure fluctuation spectra at small forward-facing step*, Proceedings of the Fifth AIAA/CEAS Aeroacoustics Conference, Bellevue WA, AIAA Paper No. 99-1964, 1999.

T. M. Farabee and M. J. Casarella, *Spectral features of wall pressure fluctuations beneath turbulent boundary layers*, Physics of Fluids A 3(10), pages 2410–2420, 1991.

T.M. Farabee and F.E. Geib, *Measurements of boundary layer pressure fluctuations at low wavenumbers on smooth and rough walls*, ASME Symposium on Flow Noise Modelling, Measurement and Control, NCA-vol. 11, FED-vol. 130, pages 55–68, 1991.

J.E. Ffowcs Williams, *Boundary-layer pressures and the Corcos model: a development to incorporate low wavenumber constraints*, Journal of Fluid Mechanics 125, pages 9–25, 1982.

J.E. Ffowcs Williams and D.L. Hawkings, *Sound Generated by Turbulence and Surfaces in Arbitrary Motion*, Philosophical Transactions of the Royal Society A264, pages 321–342, 1969.

S. Finnveden, F. Birgersson, U. Ross and T. Kremer, *A model of wall pressure correlation for prediction of turbulence–induced vibration*, Journal of Fluids and Structures 20, pages 1127-1143, 2005.

M.C. Goody, R.L. Simpson, M. Engel, C.J. Chesnakas and W.J. Devenport, *Mean velocity and pressure and velocity spectral measurements within a separated flow around a prolate spheroid at incidence*, AIAA Paper 98-0630, 1998.

W.R. Graham, *Boundary layer induced noise in aircraft. Part I: The flat plate model*, Journal of Sound and Vibration 192, pages 101–120, 1996.

W.R. Graham, *A comparison of models for the wavenumber-frequency spectrum of turbolent boundary layer pressures*, Journal of Sound and Vibration 206(4), pages 541–565, 1997.

M.S. Howe, *The wall-pressure spectrum in turbulent flow over a randomly inhomogeneous elastic solid*, Journal of the Acoustical Society of America 91(1), pages 91–98, 1992.

M.S. Howe, Acoustics of Fluid: Structure Interactions, Cambridge University Press, London, 1998.

Z. Hu, C.L. Morfey and N.D. Sandham, *Aeroacoustics of wall-bounded turbulent flows*, AIAA Journal 40, pages 465–473, 2002.

Z. Hu, C.L. Morfey and N.D. Sandham, *Sound radiation in turbulent channel flows*, Journal of Fluid Mechanics 475, pages 269–302, 2003.

H. Hubbard, *Aerodynamic noise and the plane boundary*, Aeroacoustics of flight vehicles: theory and practice, volume 1: noise sources (D. Crighton: 'Airframe noise', pp. 391-447), NASA RP-1258, 1991.

M. Hudy, A.M. Naguib and W.M. Humphreys Jr., *Wall-pressure array measurements beneath a separating/reattaching flow region*, Physics of Fluids 15, pages 706–717, 2003.

Y.F. Hwang and G. Maidanik, *A wavenumber analysis of the coupling of a structural mode and flow turbulence*, Journal of Sound and Vibration 142, pages 135–152, 1990.

S. Jayasundera, M.J. Casarella and S.J. Russell, *Identification of coherent motions using wall-pressure signatures*, Tech. Rep. 19960918-036, Catholic Univ. of America, Washington DC, 1996.

A.V. Johansson, J.-Y. Her and J.H. Haritonidis, *On the generation of high-amplitude wall-pressure peaks in turbulent boundary layers and spots*, Journal of Fluid Mechanics 175, pages 119–142, 1987.

W.L. Keith, D.A. Hurdis and B.M. Abraham, *A comparison of turbulent boundary layer wall-pressure spectra*, Journal of Fluids Engineering 114, pages 338–347, 1992.

J. Kim, J.-I. Choi and H.J. Sung, *Relationship between wall pressure fluctuations and streamwise vortices in a turbulent boundary layer*, Physics of Fluids 14, pages 898–901, 2002.

J. Kim and H.J. Sung, *Wall pressure fluctuations and flow induced noise in a turbulent boundary layer over a bump*, Journal of Fluid Mechanics 558, pages 79–102, 2006.

A. Kiya, K. Sasaki and M. Arie, *Discrete-vortex simulation of a turbulent separation bubble*, Journal of Fluid Mechanics 120, pages 219–244, 1983.

A. Kiya and K. Sasaki, *Structure of large-scale vortices and unsteady reverse flow in the reattaching zone of a turbulent separation bubble*, Journal of Fluid Mechanics 154, pages 463–491, 1985.

R.H. Kraichnan, *Pressure fluctuations in turbulent flow over a flat plate*, The Journal of the Acoustical Society of America 28, pages 278–390, 1956.

J. Largeau and V. Moriniere, *Wall pressure fluctuations and topology in separated flows over a forward-facing step*, Experiments in Fluids 42(1), pages 21–40, 2007.

D.J.J. Leclercq, M.C. Jacob, A. Louisot and C. Talotte, *Forward–backward facing step pair: Aerodynamic flow, wall pressure and acoustic characterization*, Proceedings of the Seventh AIAA/CEAS Aeroacoustics Conference, Maastricht, The Netherland, AIAA Paper No. 2001-1249, 2001.

M.J. Lighthill, *On sound generated aerodinamically. Part I: General Theory*, Proceedings of the Royal Society of London A211, pages 564–587, 1952.

G.M. Lilley and T.H. Hodgson, *On surface pressure fluctuations in turbulent boundary layers*, AGARD Report No. 276, 1960.

K.B. Lim, *A study of pressure fluctuations in turbulent shear flows under the effects of mean pressure gradients*, PhD thesis, Department of Mechanical Engineering, University of Adelaide, 1971.

E. Manoha, *The wavenumber-frequency spectrum of the wall pressure fluctuations beneath a turbulent boundary layer*, Proceedings of AIAA/CEAS Aeroacoustics Conf., May 6-8, State College, PA, AIAA paper 96-1758, 1996.

L. Morino, C. Leotardi and R. Camussi, *Power spectral density transfer function from boundary-pressure to field-pressure*, Proc. 16th AIAA/CEAS Aeroacoustics Conference, Stockholm (Swe), AIAA paper 2010–3993, 2010.

Y. Na and P. Moin, *The structure of wall-pressure fluctuations in turbulent boundary layers with adverse pressure gradient and separation*, Journal of Fluid Mechanics 377, pages 347–373, 1998.

P. Orlandi and J. Jimenez, *On the generation of turbulent wall friction*, Physics of Fluids 6, pages 634–641, 1994.

R.L. Panton and G. Robert, *The wavenumber-phase velocity representation for the turbulent wall-pressure spectrum*, Journal of Fluid Engineering 116, page 447, 1994.

A.E. Perry and M.S. Chong, *On the mechanism of wall turbulence*, Journal of Fluid Mechanics 119, pages 173–217, 1982.

O.M. Phillips, *On the aerodynamic surface sound from a plane turbulent boundary layer*, Proceedings of the Royal Society of London, Series A, Vol. 234, pages 327–335, 1956.

S. Pirozzoli, M. Bernardini and F. Grasso, *Direct numerical simulation of transonic shock/boundary layer interaction under conditions of incipient separation*, Journal of Fluid Mechanics 657, pages 361–393, 2010.

M. Bernardini, S. Pirozzoli and F. Grasso, *The wall pressure signature of transonic shock/boundary layer interaction*, Journal of Fluid Mechanics 671, pages 288–312, 2011.

A. Powell, *The influence of solid boundaries upon aerodynamic sound*, Proceedings of the Royal Society of London A231, pages 962–990, 1960.

A. Powell, *Aerodynamic noise and the plane boundary*, Journal of the Acoustical Society of America 32, pages 982–990, 1960.

H. Schlichting, Boundary-Layer Theory, McGraw-Hill, New York, 1979.

H.H. Schloemer, *Effects of pressure gradient on turbulent-boundary-layer wall-pressure fluctuations*, Journal of the Acoustical Society of America 42(1), pages 93–113, 1967.

K. Shariff and M. Wang, *A numerical experiment to determine whether surface shear-stress fluctuations are a true sound source*, Physics of Fluids 17, pages 107105-1–107105-11, 2005.

R.L. Simpson, M. Ghodbane and B.E. McGrath, *Surface pressure fluctuations in a separating turbulent boundary layer*, Journal of Fluid Mechanics 177, pages 167–186, 1987.

R.L. Simpson *Turbulent boundary-layer separation*, Annual Review of Fluid Mechanics 21, pages 205–234, 1989.

B.A. Singer, *Turbulent wall-pressure fluctuations: new model for off-axis cross-spectral density*, NASA Contractor Report 198297, 1996.

B.A. Singer, *Large-eddy simulation of turbulent wall-pressure fluctuations*, NASA Contractor Report 198276, NASA, 1996.

A.V. Smol'yakov and V.M. Tkachenko, *Model of a field of pseudosonic turbulent wall pressures and experimental data*, Soviet Physics - Acoustics 37(6), pages 627–631, 1991.

S. Song, D.B. DeGraaff and J.K. Eaton, *Experimental study of a separating, reattaching, and redeveloping flow over a smoothly contoured ramp*, International Journal of Heat and Fluid Flow 21, pages 512–519, 2000.

H. Stüer, A. Gyr and W. Kinzelbach, *Laminar separation on a forward facing step*, European Journal of Mechanics B/Fluids 18, pages 675–692, 1999.

W.W. Willmarth, *Pressure fluctuations beneath turbulent boundary layers*, Annual Review of Fluid Mechanics 7, pages 13-38, 1975.

S.F. Wu and L. Maestrello, *Responses of finite baffled plate to turbulent flow excitations*, AIAA Journal 33, pages 13–19, 1995.

# 7 Boundary Layer Noise – Part 2: Interior Noise Radiation and Control

Paolo Gardonio

Dipartimento di Ingegneria Elettrica Gestionale e Meccanica
Università degli Studi di Udine, Via delle Scienze 208, Udine, Italy

**Abstract** This chapter is focused on the interior noise caused by a Turbulent Boundary Layer (TBL) relative fluid flow over the flexible thin walls of an enclosure. This is a typical interior noise problem encountered in surface and air passenger transportation vehicles. When such vehicles travel at high speed, the airflow around the skin develops into a TBL. This phenomenon produces large pressure fluctuations that effectively excite the skin panels of the vehicle, which, in turn, radiate noise into the interior.

The formulation for the coupled structural–acoustic response to a TBL pressure field is first introduced for a general model problem given by a cylindrical cavity bounded by a thin flexible wall, which is immerged in a convected fluid that has developed a TBL. Structural vibration and sound radiation effects are expressed in terms of the Power Spectral Densities (PSD) of the wall flexural kinetic energy and cavity acoustic potential energy.

A reduced model problem is then analysed in detail by examining a small section of the enclosure flexible wall and assuming a heavily damped interior. In this case a simplified model is used, which considers a rigidly baffled flat panel with unbounded fluid domains on the two sides. The panel is excited on the exterior side by the pressure field generated by a TBL fluid flow and radiates sound on the interior side. To facilitate the analysis, the PSDs of the panel flexural kinetic energy and interior sound power radiation produced by the TBL pressure field are contrasted with those produced by harmonic acoustic plane waves, by a stochastic acoustic diffuse field and by the so called "rain on the roof" stochastic excitation.

The chapter is then completed with two sections illustrating the principal effects produced by mass, stiffness and damping passive treatments and structural–acoustic active systems on the panel. The first active system consists of an array of decentralised feedback loops with point sensor and actuator transducers while the second active system is composed by a single channel feedback loop with distributed sensor and actuator transducers.

R. Camussi (Ed.), *Noise Sources in Turbulent Shear Flows: Fundamentals and Applications*, CISM International Centre for Mechanical Sciences, DOI 10.1007/978-3-7091-1458-2_7,

## 1. Flexural Response and Interior Sound Radiation of a Closed Shell Excited by a TBL Pressure Field

This section introduces a general formulation for the interior noise in a cavity bounded by a flexible wall, which is excited by the space and time stochastic pressure field exerted by a "Turbulent Boundary Layer" (TBL) relative fluid flow (for brevity, the fact that the fluid flow is relative to the wall structure will not be specified in the remaining part of this chapter). A coupled structural–acoustic formulation is presented considering a cylindrical cavity of finite length bounded by a thin flexible wall, which is assumed to be simply–supported at the two ends. As illustrated in Figure 1, the cylindrical flexible wall is connected to rigid extensions acting as baffles and is immerged in an unbounded fluid. The fluid is convected in axial direction and produces a fully developed TBL over the wall. Although this model problem can be used to study a limited number of practical systems, it provides general indications of the principal mechanisms characterising the TBL excitation, response and radiation phenomena of the complex enclosures that are encountered in surface and air passenger transportation vehicles (Mixson and Wilby 1995; Thompson and Dixon 2004).

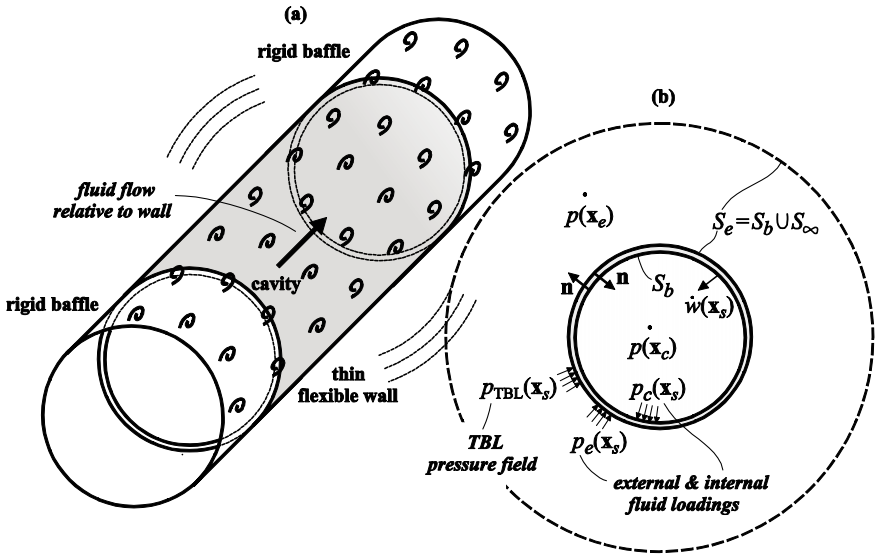


**Figure 1.** (a) Cylindrical wall with rigid extensions immerged in a convected fluid that has developed a turbulent boundary layer in axial direction. (b) Notation for the exterior and interior fluid domains.

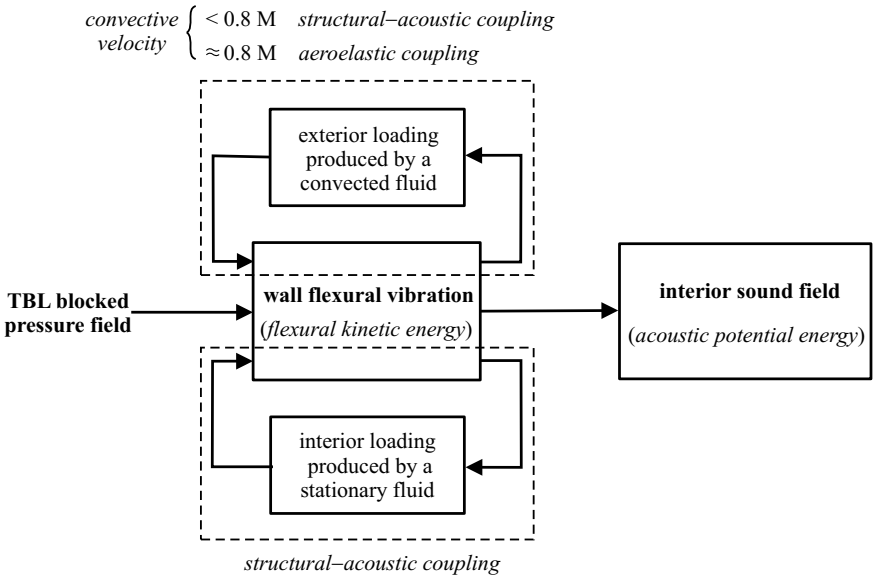


**Figure 2.** Block diagram for the interior noise caused by a TBL fluid flow over the flexible thin wall of an enclosure

As schematically depicted in Figure 2, the interior sound radiation is produced by the flexural vibration of the enclosing wall, which depends on the resulting pressure fields acting on the inner and outer faces of the wall. The pressure field on the inner face is due to the interior sound field, which, in turn, depends on the flexural vibration of the enclosing wall itself. Normally, at low audio frequencies, the interior sound is characterised by standing wave fields due to the low order acoustic natural modes of the enclosure. Alternatively, at higher frequencies the interior sound field becomes increasingly diffuse since, at each frequency, the acoustic response of the enclosure results from the overlap of multiple acoustic modes whose number grows with the cube of frequency (Morse and Ingard 1968; Pierce 1989; Nelson and Elliott 1992; Fahy and Gardonio 2007). Usually the transition from standing wave to diffuse sound field is specified in terms of the "modal overlap" factor, which depends on the "modal density" and damping properties of the cavity (Cremer et al. 1988). At low frequencies where the acoustic response of the enclosure and the vibration response of the shell structure are characterised by distinct resonant modes, the interior fluid loading effect is normally formulated in terms of modal coupling

factors (Dowell and Voss 1962; Pretlove 1966; Fahy 1969; Guy and Bhattacharya 1973). Alternatively, at higher frequencies such that the acoustic and structural responses are controlled by the overalp of multiple modes, the fluid loading is modelled in average terms through coupling factors for "statistical energy analysis" models (Lyon and DeJong 1995; Craik 1996; Keane and Price 1997; Langley and Fahy 2004; Fahy and Gardonio 2007). In general, the interior of surface and air transportation vehicles is filled with air, i.e. a lightweight compressible fluid. As further detailed in Section 1.5, in this case the interior fluid loading primarily produces a damping action.

The pressure field on the outer face of the wall structure is characterised by two contributions: first, the pressure field produced by the TBL fluid flow over the flexible wall and second the acoustic pressure field due to the exterior sound radiation produced by the vibration of the flexible wall itself. As discussed in Chaper 6 of this book, the TBL fluid flow produces a stochastic pressure field over the external surface of the wall, which, in general, is also influenced by the flexural vibration of the wall (Graham 1997; Maury et al. 2002a). However, in this chapter, the so called "blocked pressure" field is considered, which corresponds to the pressure developed beneath a boundary layer on a hard wall. In this case the pressure generated by the TBL fluid flow is not affected by the flexural vibration of the wall and it is twice the pressure that a nominally identical turbulent fluid flow would generate in absence of the wall. This assumption is valid when the TBL is fully developed and the acoustic near field particle velocities produced by flexural vibration of the wall are small in comparison with the turbulence particle velocities (Graham 1997; Maury et al. 2002a). This type of approximation has been found valid in a wide range of cases as detailed in the following references, for example (Davies 1971; Efimtsov and Shubin 1977; Efimtsov 1986; Bano et al. 1992). A fully coupled model would require a rather complex formulation, using the Lighthill stress tensor to describe the boundary layer sources (Dowling and Ffowcs Williams 1983). The outward sound radiation due to the wall flexural vibration also produces a pressure field over the surface of the shell structure. In general, the exterior of surface and air transportation vehicles is characterised by air (i.e. lightweight compressible fluid), which, as will be shown in Section 1.5, for low flow speeds, tends to produce a damping fluid loading effect arising from the sound radiation into a fully or partially unbounded field (Junger and Feit 1986; Fahy and Gardonio 2007). However, the cruise speed of aircraft for passenger transportation approaches rather high values, around 0.8 Mach. In this case the flexible skin structure efficiently couples with the fluid dynamic response and gives rise to the so called "aeroelastic coupling" (Dowell 1975; Abrahams 1983; Lyle and Dowell 1994; Atalla and Nicolas 1995; Clark and Frampton 1997; Frampton and Clark 1997; Frampton 2005; Xin and Lu 2010). Clark and Frampton (Clark and

Frampton 1997; Frampton and Clark 1997; Frampton 2005) have shown that, for high flow speeds around 0.8 Mach, the convected fluid produces damping and increasingly higher mass impedance effects on the structure that tend to reduce the amplitude and to move to lower frequencies the resonance peaks that characterise the low–frequency spectrum of the flexural response of the enclosing wall structure. The aeroelastic response of shell structures is a rather complex non–linear phenomenon that involves strong coupling effects between low order flexural modes of the wall panels via the dynamics of the mean flow. Eventually, for very large flow velocities that exceed the speed of sound, this coupling effect may lead to limit cycle modal vibrations and thus to flutter instability conditions (Dowell 1975). Of course, flutter is of no concern for the skin panels of modern aircraft. Nevertheless, for high flow speeds approaching 0.8 Mach, the dynamic coupling between the panels and the fluid has a relevant effect on the response of the shell structure and interior sound radiation. The scope of this chapter is to introduce the principal characteristics of interior sound radiation produced by TBL disturbances. Thus, although the model problem considered in this section also refers to fast moving air transportation vehicles, to keep the analysis simple, the proposed formulation does not take into account aeroelastic coupling. However it considers the fluid loading effect arising from sound radiation into a stationary fluid, which can be assumed valid for flow velocities below 0.8 Mach. This formulation provides a good basis for the understanding of the physical mechanisms characterising the coupling of structural modes via the exterior fluid loading. In general, a high velocity mean flow tends to emphasise these coupling effects so that, even with lightweight compressible fluids, strong couplings between low order modes of the wall structure may emerge (Clark and Frampton 1997; Frampton and Clark 1997; Frampton 2005). In summary the model presented in this chapter considers the flexural response and interior sound radiation of a closed shell structure, which is excited by the blocked pressure field exerted by a TBL fluid flow and is influenced by the acoustic loading effects exerted by the interior and exterior fluids.

Much of the analytical work on the structural–acoustic response to TBL fluid flow excitation is organised around two types of models: the first is based on space–frequency domain formulations (Dyer 1959; Mead and Richards 1968; Crocker 1969; Davies 1971; Robert 1984; Blake 1986; Masson 1991; Bano et al. 1992; Filippi and Mazzoni 1994; Thomas and Nelson 1995; Durant et al. 2000), while the second is based on wavenumber–frequency domain formulations (Aupperle and Lambert 1973; Blake 1986; Hwang and Maidanik 1990; Strawderman 1990; Graham 1996; Borisyuk and Grinchenko 1997; Graham 1997; Han et al. 1999; Maury et al. 2002a). The first modelling approach uses the space–frequency spectra of the pressure fields exerted by the internal and

external fluids and by the TBL fluid flow, which, as discussed in Chapter 6, was introduced by Corcos (Corcos 1963a; Corcos 1963b; Corcos 1967). The second is instead based on the wavenumber–frequency spectra of the pressure fields exerted by the internal and external fluids and by the TBL fluid flow. As discussed in Chapter 6, over the past three decades a selection of analytical or quasi–analytical models have been proposed in the attempt of describing the spectrum of TBL pressure fields both at convective and sub–convective wavenumbers (Chase 1980; Efimtsov 1982; Ffowcs Williams 1982; Chase 1987; Smol'yakov and Tkachenko 1991; Bull 1995; Graham 1997). Maury et al. (2002a) have analysed the principal characteristics of the space–frequency and wavenumber–frequency formulations in a consistent framework and have highlighted how the two formulations are related by spatial Fourier transforms.

As seen for the interior sound field, in general, at low audio frequencies the response of the wall structure is also characterised by a low modal overlap. Thus the expression of the flexural vibration field can be expanded into a series of modal terms with reference to the *in vacuo* natural modes of the structure. In this case both formulations in the space and wavenumber domains lead to double series modal expressions for the structural response and sound radiation, which include the self and mutual admittance functions for the modal excitation exerted by the TBL pressure field, the self and mutual fluid loading impedance functions and the self and mutual sound radiation efficiencies (Davies 1971; Blake 1986). With the space–frequency domain formulation, the modal excitation, fluid loading and sound radiation effects are derived from integral expressions in a bounded space domain. Alternatively, for the wavenumber–frequency domain formulation, these terms are derived from integral expressions in the unbounded wavenumber domain. Although the two approaches provide equivalent results, the formulation in the space–frequency domain is more intuitive to derive since it refers to spatial coordinates (Blake 1986; Thomas and Nelson 1995; Maury et al. 2002a). Nevertheless, with the wavenumber–frequency domain formulation, the expressions for the modal excitation, fluid loading and sound radiation effects are transformed into wavenumber spectra. Thus the response of the structure can be viewed as the result of filtering phenomena between the wavenumber spectra of the modal excitation, the interior and exterior modal fluid loading and the interior modal sound radiation (Blake 1986; Hwang and Maidanik 1990; Graham 1997). This provides direct insight on the physics of the excitation, fluid loading and interior sound radiation phenomena under study, although working in the wavenumbers domain requires some practice. Both types of approaches are based on double integrations, which, in general, cannot be solved analytically and thus involve numerical derivation using, for example, the Gaussian quadrature. The wavenumber approach offers some advantages when the geometry of the structure can be defined in terms of a single coordinate

with reference to systems of orthogonal coordinates in which the structural vibration field, the interior sound pressure field and the exterior sound and TBL pressure fields are separable. In this case, the wavenumber integral expressions can be derived analytically in closed form (Junger and Feit 1986; Fahy and Gardonio 2007). On the other hand the spatial approach can be easily implemented when the vibration response of complex structures and the interior and exterior sound fields are derived with approximated methods such as the structural and acoustic "Finite Element Method" (FEM) and the acoustic "Boundary Element Method" (BEM) (Filippi and Mazzoni 1994). At high audio frequencies the structural response and the interior sound field increasingly become complex, since multiple resonant modes contribute to both the vibration and sound fields at each frequency. Thus alternative formulations based on energy functions are employed such as the "Statistical Energy Analysis" (SEA) method. This chapter considers only the modal formulation, which for simple model problems, such as the cylindrical enclosure considered in this section or the baffled panel considered in the following sections, provides realistic results also at high audio frequencies.

In summary this section introduces the space–frequency domain formulation for the structural–acoustic response to TBL fluid flow excitations. Also, it briefly discusses the derivation of the modal excitation functions in the wavenumber–frequency domain. The reader interested to know more about "full" wavenumber–frequency domain formulations is referred to the review papers by (Graham 1997; Maury et al. 2002a) and to the monograph chapters written by (Blake 1986). The space–frequency domain formulation presented here is built around the description of the interior and exterior sound fields and the modal representation of the distributed flexural vibration of thin shells. In general, the interior and exterior sound fields can be derived with the so called "direct boundary integral formulation", which uses acoustic Green functions (Morse and Ingard 1968; Blake 1986; Junger and Feit 1986; Pierce 1989; Nelson and Elliott 1992; Fahy and Gardonio 2007). For the exterior fluid domain, this equation provides the resultant sound field produced by a distribution of acoustic sources and by the radiation and scattering effects of a flexible body (or multiple bodies) of arbitrary shape. Alternatively, for the interior fluid domain, it provides the resultant sound field produced inside the enclosure by a distribution of interior acoustic sources and by the radiation and reflection effects of the enclosure flexible walls. The effects produced by the surface of the body or enclosure are normally classified in terms of three different boundary conditions that prescribe a) the velocity distribution normal to the boundary surface (Neumann or natural boundary condition), b) the sound pressure acting on the boundary surface (Dirichlet or essential boundary condition) and c) the specific acoustic impedance normal to the boundary surface (mixed boundary condition)

(Ciskowski and Brebbia 1991; Desmet 1998; Wu 2000; Gaul et al. 2003). In general, when the boundary surface is defined by a flexible structure, the boundary conditions for both the exterior and interior noise problems are expressed in terms of the acoustic particle velocity distributions normal to the boundary surface, which are considered compatible with the transverse vibration velocity of the flexible wall. Thus they are treated as Neumann boundary conditions. The boundary integral formulation involves a surface integration that can be solved in closed form only for few regular shapes (e.g. cylinders and spheres). For more realistic irregular boundary surfaces, approximated numerical methods are employed such as the acoustic "Boundary Element Method" (BEM) or the acoustic "Finite Element Method" (FEM) (Wu 2000; Fahy and Gardonio 2007). Although the two methods can be used for both interior and exterior sound problems, normally the BEM method is used for the exterior sound radiation/scattering problem, while the FEM method is employed for the interior sound radiation/reflection problem.

For simple wall structures either formed by a single span shell or an assembly of plate and shell panels, the flexural response can be derived analytically from the inhomogeneous equations of motion for closed shells or flat and curved panels. The flexural response is derived in terms of structural Green functions, which, are usually expressed as admittance or mobility functions (Gardonio and Brennan 2002; Gardonio and Brennan 2004). Also in this case, for distributed pressure field excitations, the expression for the response assumes an integral form over the surface of the structure. In general, only for very few simple structures, such as for example cylinders or flat and curved rectangular panels, the flexural response can be derived analytically. In practice, the body of surface and air vehicles are rather complex structures. Thus, as for the acoustic problem, approximated numerical methods are normally employed such as the structural FEM (Fahy and Gardonio 2007). When the analysis is limited to low audio frequencies, the problem is often simplified by considering a simple closed wall structure (e.g. a cylinder or a folded box) where the stiffening and mass effects of the reinforcing ribs are smeared over the surface of the structure. Alternatively, at mid and high audio frequencies, the response of different sections of the enclosure wall can be considered weakly coupled to each other and thus the problem can be split into the analysis of the structural–acoustic response of single span flat panels and curved shells.

As schematically shown in Figure 2, the coupled structural–acoustic analysis presented in this section is derived by combining the acoustic responses of the interior and exterior sound fields and the structural response of the flexible wall. The flexural response of the wall produced by the TBL pressure field and by the feedback effects exerted by sound pressure fields over the internal and external surfaces of the wall is derived from the structural equation of motion. The sound

pressure over the internal and external surfaces are derived from the direct boundary integral equations for the interior and exterior sound fields calculated on the boundary surface. The structural equation of motion and the direct boundary integral equations are then combined into a system of equations in the unknown sound pressure and particle velocity fields over the boundary surface. The resulting sound pressure and particle velocity fields are then used again in the direct boundary integral equation for the interior sound field to derive the noise radiation inside the enclosure.

To effectively establish the interior sound radiation and global flexural response of a cavity bounded by flexible walls, it is convenient to express the two phenomena in terms of energy functions, which embrace in a single term the spatially distributed nature of the sound and flexural vibration fields in the cavity and enclosing wall respectively (Nelson and Elliott 1992; Gardonio 2012). Moreover, the stochastic nature of the disturbance pressure field exerted by the TBL fluid flow on the external side of the flexible wall, makes indispensable to express these energy functions in terms of concepts and formulations for random processes. Thus, a particular formulation is introduced in Section 1.6, which is inspired to a similar study proposed by (Gardonio et al. 2012) and refers to the formulations for stationary stochastic processes given in (Crandall and Mark 1963; Newland 1975; Bendat and Piersol 2000).

### 1.1 Direct boundary integral equation for exterior and interior sound fields

Assuming the system is linear, the exterior and interior sound fields of the model problem shown in Figure 1 can be expressed as the superposition of the *boundary sound fields* generated by the scattering/reflection and radiation effects of the flexible wall and the *direct sound fields* generated by acoustic sources located respectively outside and inside the cavity. Both terms can be derived starting from the following inhomogeneous acoustic wave equation (Dowling and Ffowcs Williams 1983)

$$\nabla^2 p(\mathbf{x},t) - \frac{1}{c_0^2}\frac{\partial^2 p(\mathbf{x},t)}{\partial t^2} = \nabla \cdot \mathbf{f}(\mathbf{x},t) - \rho\frac{\partial q(\mathbf{x},t)}{\partial t} \tag{1}$$

that takes into account the effects produced by acoustic monopole and dipole sources. In fact, the excitation terms $\rho\partial q(\mathbf{x},t)/\partial t$ and $\nabla \cdot \mathbf{f}(\mathbf{x},t)$ represent a kinematic (volumetric) monopole source and a kinetic (force) dipole source respectively. More precisely $q(\mathbf{x},t)$ is the rate of volume flow per unit volume produced by the monopole source and $\mathbf{f}(\mathbf{x},t)$ is a vector with the fluctuating forces produced by the dipole source. In this equation $c_0$ is the speed of sound, $\rho$ is the mass density of the fluid and the vector $\mathbf{x}$ identifies the position in the

exterior or interior fluid domains. Also $\nabla^2 p(\mathbf{x},t)$ is the Laplacian of $p(\mathbf{x},t)$ and $\nabla \cdot \mathbf{f}(\mathbf{x},t)$ is the divergence of $\mathbf{f}(\mathbf{x},t)$. Assuming time–harmonic dependence, the wave equation can be rewritten in the following form (Morse and Ingard 1968; Nelson and Elliott 1992)

$$\nabla^2 p(\mathbf{x},\omega) + k^2 p(\mathbf{x},\omega) = -Q(\mathbf{x},\omega) \quad , \tag{2}$$

where $k = \omega / c_0$ is the acoustic wavenumber and the volumetric monopole and force dipole sources are merged in the term $Q(\mathbf{x},\omega) = j\rho\omega q(\mathbf{x},\omega) - \nabla \cdot \mathbf{f}(\mathbf{x},\omega)$. Also $p(\mathbf{x},\omega)$, $Q(\mathbf{x},\omega)$, $q(\mathbf{x},\omega)$, $\nabla \cdot \mathbf{f}(\mathbf{x},\omega)$ are the frequency dependent complex amplitudes of the co-respective time–domain functions assuming the time–harmonic dependence is given in the exponential form $\exp(j\omega t)$, where $\omega$ is the circular frequency. The remaining part of this formulation will be expressed in the frequency domain and, for brevity, the frequency dependence of the complex amplitudes will not be displayed. The solution of Eq. (2) is derived in terms of acoustic Green functions $G(\mathbf{x} \mid \mathbf{x}', \omega)$, which are chosen according to the problem under study and satisfy the following inhomogeneous differential equation (Morse and Ingard 1968; Nelson and Elliott 1992)

$$\nabla^2 G(\mathbf{x} \mid \mathbf{x}') + k^2 G(\mathbf{x} \mid \mathbf{x}') = -\delta(\mathbf{x} - \mathbf{x}') \quad , \tag{3}$$

where $\delta(\mathbf{x} - \mathbf{x}')$ is the three-dimensional Dirac delta function, which defines a point monopole source in $\mathbf{x}'$ (Nelson and Elliott 1992). Thus, the Green function describes the spatial dependence of the complex pressure field at $\mathbf{x}$ produced by a harmonic point monopole source at $\mathbf{x}'$. Eq. (2) is then solved by multiplying it by $G(\mathbf{x} \mid \mathbf{x}')$ and subtracting to the resulting equation Eq. (3) multiplied by $p(\mathbf{x})$. The resulting equation is then integrated in the acoustic volume $V$, which yields

$$p(\mathbf{x}') = \int_V \left( G(\mathbf{x} \mid \mathbf{x}') \nabla^2 p(\mathbf{x}) - p(\mathbf{x}) \nabla^2 G(\mathbf{x} \mid \mathbf{x}') \right) dV + \int_V Q(\mathbf{x}) G(\mathbf{x} \mid \mathbf{x}') dV \quad . \tag{4}$$

The Green's theorem given in the form $\int_V \left( f\nabla^2 g - g\nabla^2 f \right) dV = \int_S \left( f\nabla g - g\nabla f \right) \cdot \mathbf{n}\, dS$ and the reciprocity property $G(\mathbf{x} \mid \mathbf{x}') = G(\mathbf{x}' \mid \mathbf{x})$ are then used to transform the first volume integral into an integral over the boundary surface $S$ of the acoustic volume $V$. As a result, the following "direct boundary integral equation" is derived

$$c(\mathbf{x}') p(\mathbf{x}') = \int_S \left( G(\mathbf{x}' \mid \mathbf{x}) \nabla p(\mathbf{x}) \cdot \mathbf{n} - p(\mathbf{x}) \nabla G(\mathbf{x}' \mid \mathbf{x}) \cdot \mathbf{n} \right) dS + \int_V G(\mathbf{x}' \mid \mathbf{x}) Q(\mathbf{x}) dV \quad , \tag{5}$$

where

$$c(\mathbf{x}') = \begin{cases} -1 & \mathbf{x}' \text{ in V} \\ -1/2 & \mathbf{x}' \text{ in S} \\ 0 & \mathbf{x}' \text{ outside V} \end{cases} \tag{6}$$

and $\mathbf{n}$ is a unit vector with direction orthogonal to the boundary surface $S$ (note that, as shown in Figure 1, $\mathbf{n}$ has opposite directions for the exterior and interior domains).

In order to solve Eq. (5) it is necessary to define the pressure and pressure gradient on the boundary surface, i.e. for $\mathbf{x} \in S$. For a well–posed boundary–value problem, only one of the two sets of boundary conditions can be defined *a priori*. However, also the other set can be derived from the direct boundary integral equation by co–locating the point $\mathbf{x}'$ on the boundary surface itself. Thus the derivation of the scattered/reflected or radiated sound fields by a flexible object or an enclosure is carried out in two steps based on the same integral equation. Although at first sight this may appear as a mere repetition of the same integration, the implementation of the first step is not trivial since the surface integral becomes singular when the point $\mathbf{x}'$ is co–located on the boundary surface. Nevertheless this singularity is weak, and the surface integral converges in the regular sense (Wu 2000). There is also a second difficulty to be considered, that is, for exterior problems, the surface integral in Eq. (5) may not have a unique solution at certain characteristic frequencies. The reader is referred to specialised monographs that show how this problem is normally overcome with the so called CHIEF method (Wu 2000).

Besides the boundary conditions, a suitable Green function $G(\mathbf{x}' \mid \mathbf{x})$ must be defined to implement the direct boundary integral Eq. (5). In principle there is a vast selection of functions that can be used to solve a given problem, since the only requirement is that they satisfy both Eq. (3) and the principle of reciprocity (Nelson and Elliott 1992). Nevertheless exterior and interior sound fields are normally handled with two specific types of functions that are described below.

### 1.2 Green function for the exterior sound field

As shown in Figure 1, a particular boundary surface is chosen for the exterior sound field, which is composed by the external surface $S_b$ of the flexible wall and by the surface $S_\infty$ of an imaginary sphere centred in the radiating object and with radius that tends to infinity. In this way the Sommerfeld radiation condition at infinity (Sommerfeld 1949) can be assumed, which imposes that only waves travelling outwards from a source are allowed and that the pressure tends to zero at infinite distance from the source. Assuming the system of reference is located

at the centre of the radiating object, this physical condition can be expressed mathematically with the following equation:

$$\lim_{|\mathbf{x}_e|\to\infty} |\mathbf{x}_e| \left( \frac{\partial p(\mathbf{x}_e)}{\partial |\mathbf{x}_e|} + jkp(\mathbf{x}_e) \right) = 0 \ , \tag{7}$$

where the vector $\mathbf{x}_e$ identifies a point in the exterior sound field. In this case, it can be shown that the surface integral over $S_\infty$ in Eq. (5) goes to zero. Also, for free–field sound radiation, the Green function takes the simple form

$$g(\mathbf{x}_e \,|\, \mathbf{x}'_e) = \frac{e^{-jk|\mathbf{x}_e - \mathbf{x}'_e|}}{4\pi |\mathbf{x}_e - \mathbf{x}'_e|} \ , \tag{8}$$

which is known as the *free space Green function* (Morse and Ingard 1968; Nelson and Elliott 1992). For the specific problem considered in this chapter where there is no external acoustic source distribution, i.e. $Q(\mathbf{x}_e)$, and the velocity distribution normal to the boundary surface is prescribed as compatible with the transverse vibration velocity of the flexible wall, the direct boundary integral equation derived above can be re-formulated as follows

$$c(\mathbf{x}_e)\, p(\mathbf{x}_e) = \int_{S_b} \left( \frac{\partial g(\mathbf{x}_e \,|\, \mathbf{x}_s)}{\partial n} p(\mathbf{x}_s) - g(\mathbf{x}_e \,|\, \mathbf{x}_s) \frac{\partial p(\mathbf{x}_s)}{\partial n} \right) dS_b \ , \tag{9}$$

where the vector $\mathbf{x}_s$ identifies a point on the surface of the enclosure wall and $\partial g(\mathbf{x}_e \,|\, \mathbf{x}_s)/\partial n$ and $\partial p(\mathbf{x}_e)/\partial n$ are the directional derivatives[1] of $g(\mathbf{x}_e \,|\, \mathbf{x}_s)$ and $p(\mathbf{x}_e)$ along the normal $n$ to the boundary surface $S_b$ (Junger and Feit 1986). Equation (9) gives the sound pressure radiated by a vibrating body, provided the sound pressure in $S_b$ and its derivative along the normal to the surface $S_b$ are known. According to the fluid momentum equation, the sound pressure derivative $\partial p(\mathbf{x}_s)/\partial n$ and the sound particle velocity $\dot{v}_n(\mathbf{x}_s)$ along the normal to the boundary surface are related by the momentum equation $\partial p(\mathbf{x}_s)/\partial n + j\omega\rho \dot{v}_n(\mathbf{x}_s) = 0$ (Morse and Ingard 1968; Pierce 1989; Fahy and Gardonio 2007). Thus Eq. (9) can be rewritten in the following form

$$c(\mathbf{x}_e)\, p(\mathbf{x}_e) = \int_{S_b} \left( \frac{\partial g(\mathbf{x}_e \,|\, \mathbf{x}_s)}{\partial n} p(\mathbf{x}_s) + j\omega\rho g(\mathbf{x}_e \,|\, \mathbf{x}_s) \dot{v}_n(\mathbf{x}_s) \right) dS_b \ , \tag{10}$$

[1] $\nabla \cdot \mathbf{n} = \frac{\partial}{\partial n}$ (Junger and Feit 1986).

which, in literature, is known as the *Helmholtz integral equation* (Junger and Feit 1986; Wu 2000). Since the sound particle velocity $\dot{v}_n(\mathbf{x}_s)$ is compatible with the transverse velocity of the structure $\dot{w}(\mathbf{x}_s)$, the sound pressure over the boundary surface $p(\mathbf{x}_s)$ can be readily derived by coupling the structural wave equation with the Helmholtz integral Eq. (10) calculated in $\mathbf{x}_e = \mathbf{x}_s$ assuming $c(\mathbf{x}_s) = -1/2$ and setting[2] $\dot{v}_n(\mathbf{x}_s) = -\dot{w}(\mathbf{x}_s)$. The radiated sound field can then be derived yet again from the Helmholtz integral equation setting $c(\mathbf{x}_e) = -1$. Nevertheless, for the noise problem considered in this section, this first step is sufficient to provide the external sound pressure fluid loading effect on the flexible wall. A phenomenological analysis of Eq. (10) indicates that the sound pressure $p(\mathbf{x}'_s)$ at a given point $\mathbf{x}'_s$ of the boundary surface of a flexible body is given by the surface integral of the superposition of the sound pressure generated by the vibration of the body, via the term $j\omega\rho\, g(\mathbf{x}'_s \mid \mathbf{x}_s)\dot{w}(\mathbf{x}_s)$, and the sound pressure generated by the scattering effect of the body, via the term $\frac{\partial g(\mathbf{x}'_s,\mathbf{x}_s)}{\partial n} p(\mathbf{x}_s)$.

In general, for arbitrary geometries of the flexible body, the surface pressure distribution necessary to solve the Helmholtz integral equation must be derived by solving Eq. (10) numerically (Wu 2000). Analytical approximate solutions can be derived in the short– and long–wavelength limits (Junger and Feit 1986; Koopmann 1997). For instance, analytical solutions can be derived either for very small sound radiating objects compared to the acoustic wavelength or when the acoustic wavelength is smaller than both the radius of curvature of the sound radiating object and the portions of the sound radiating object that vibrate in phase. Also, analytical exact solution can be derived for specific geometries of the sound radiating object so that a special class of acoustic Green functions, $\hat{G}_e(\mathbf{x}_e \mid \mathbf{x}_s)$, can be defined. These functions satisfy the Neumann boundary condition on the surface of the sound radiating object, i.e. $\frac{\partial}{\partial n}\hat{G}_e(\mathbf{x}_e \mid \mathbf{x}_s)\Big|_{\mathbf{x}_e=\mathbf{x}_s} = 0$ (Junger and Feit 1986; Koopmann 1997). As a result, only the velocity normal to the boundary surface is required to derive Eq. (10). According to the nomenclature in (Kellogg 1953), these functions are referred to as the *Green functions of the second kind*. Alternatively other authors identify them as *Neumann functions* (Garabedian 1964). The $\frac{\partial}{\partial n}\hat{G}_e(\mathbf{x}_e \mid \mathbf{x}_s)\Big|_{\mathbf{x}_e=\mathbf{x}_s} = 0$ condition can be straightforwardly imposed when the shape of the radiating body is such that it

[2] Note that, as shown in shown in Figure 1b, the standard notation used for the Helmholtz integral equation is used where the vector **n** points away from the acoustic domain, thus $\dot{v}_n(\mathbf{x}_s) = -\dot{w}(\mathbf{x}_s)$.

can be defined in terms of a single coordinate with reference to systems of orthogonal coordinates in which the acoustic wave equation is separable (e.g. rectangular, cylindrical and spherical coordinates) (Junger and Feit 1986). In this case the second kind Green function can be formulated analytically and the simplified form of the Helmholtz integral equation

$$c(\mathbf{x}_e)p(\mathbf{x}_e) = j\omega\rho\int_{S_b}\hat{G}_e(\mathbf{x}_e \mid \mathbf{x}_s)\dot{v}_n(\mathbf{x}_s)dS_b \tag{11}$$

can be used to derive the radiated sound field directly from the boundary particle velocity $\dot{v}_n(\mathbf{x}_s)$, that is the transverse velocity of the structure $\dot{w}(\mathbf{x}_s)$. From a physical point of view, in contrast to the free space Green function, this function includes the scattering effect that would have the wall if assumed to be rigid (Junger and Feit 1986; Koopmann 1997).

It is interesting to note that in the special case where the flexible body is an infinitely extended flat plate, the scattering of sound is such that the first term equals the second term in Eq. (10). Thus, using the expression for the free space Green function given in Eq. (8) and recalling that $\dot{v}_n(\mathbf{x}_s) = -\dot{w}(\mathbf{x}_s)$, the radiated sound pressure can be readily derived with the following integral

$$p(\mathbf{x}_e) = \frac{j\omega\rho}{2\pi}\int_{S_b}\dot{w}(\mathbf{x}_s)\frac{e^{-jk|\mathbf{x}_e-\mathbf{x}_s|}}{|\mathbf{x}_e-\mathbf{x}_s|}dS_b \quad . \tag{12}$$

This integral expression in known as the *Rayleigh integral* for the radiated sound pressure by an infinitely extended flat surface with transverse velocity $\dot{w}(\mathbf{x}_s)$ (Fahy and Gardonio 2007). Thus the free space Green function can be considered as a second kind Green function for the sound radiation problem of an infinitely extended flat surface.

Since this section is focused on the coupled structural–acoustic response of a cylindrical enclosure, the second kind Green function for the baffled cylinder vibrating surface shown in Figure 1 is briefly recalled. In the literature this Green function is derived by applying space–Fourier transforms to the homogeneous counterpart of Eq. (3) formulated in cylindrical coordinates $z,\theta,r$ (Morse and Ingard 1968; Junger and Feit 1986). More specifically, since the cylindrical geometry imposes a periodicity along the circumferential direction, a Fourier series is applied along the circumferential direction, such that $p(z,\theta,r) = \sum_{m_2=-\infty}^{+\infty} p_{m_2}(z,r)e^{jm_2\theta}$, and a space–Fourier transform[3] is applied along the

[3] Space–Fourier transforms are normally referred to as wavenumber transforms (Junger and Feit 1986; Fahy Gardonio 2007).

axial direction, which is given by $\tilde{p}_{m_2}(k_z, r) = \int_{-\infty}^{+\infty} p_{m_2}(z, r) e^{-jk_z z} dz$, where the acoustic wave number is expressed as $k^2 = k_r^2 + k_z^2$ and $m_2 = 0, 1, 2, \ldots$ is the index for the Fourier series expansion in circumferential direction. In this way, the homogeneous counterpart of the partial differential Eq. (3) is transformed into a series expansion of Bessel's differential equations in the unknown $\tilde{p}_{m_2}(k_z, r)$ functions. This series expansion is satisfied when each Bessel's differential equation is set to zero. The solution of this set of equations can be found analytically in terms of Hankel functions. This formulation leads to a series expression whose terms are function of the axial wavenumber. Thus to obtain the Green function in the spatial coordinates, an inverse space–Fourier transform is implemented with reference to the axial wavenumber, which leads to the following expression (Morse and Ingard 1968; Stephanishen 1981; Lesueur 1988; Millard 1997)

$$\hat{G}_e(\mathbf{x}_e \mid \mathbf{x}_s) = -\frac{1}{4\pi^2} \sum_{m_2=0}^{\infty} \varepsilon_{m_2} \cos\left[m_2(\theta_e - \theta_s)\right] \int_{-\infty}^{+\infty} \frac{H_{m_2}^{(1)}(k_r r_e)}{k_r R \, H_{m_2}^{(1)'}(k_r R)} e^{jk_z |z_e - z_s|} dk_z \quad , \tag{13}$$

where the position vectors $\mathbf{x}_e$ and $\mathbf{x}_s$ are defined in cylindrical coordinates $z, \theta, r$, and $m_2 = 0, 1, 2, \ldots$ Here $R$ is the radius of the cylinder, $H_{m_2}^{(1)}(\ldots)$ is the first kind Hankel function of order $m_2$ and $\varepsilon_{m_2=0} = 1$, $\varepsilon_{m_2>0} = 2$ is the Neumann factor. A comprehensive introduction to the wave number transform approach for the solution of wave equations can be found in the monographs by (Morse and Ingard 1968; Junger and Feit 1986; Millard 1997). Since the Green function in Eq. (13) satisfies Neumann's boundary condition such that $\frac{\partial}{\partial n} \hat{G}_e(\mathbf{x}_e \mid \mathbf{x}_s)\Big|_{\mathbf{x}_e = \mathbf{x}_s} = 0$, the integral expression in Eq. (10) reduces to Eq. (11). From the physical point of view this result follows from the fact that the Green function of Eq. (13) already includes the scattering effects that are produced by the cylinder.

### 1.3 Green function for the interior sound field

In general, the Green function for enclosed sound fields can be expressed with a series expansion in terms of $n = 1, 2, \ldots$ acoustic natural modes of the cavity $\psi_n(\mathbf{x}_c)$ and complex modal amplitudes $a_n(\mathbf{x}'_c)$ due to a point monopole source of unit amplitude (Morse and Ingard 1968; Pierce 1989; Nelson and Elliott 1992; Koopmann 1997), that is:

$$G_c(\mathbf{x}_c \mid \mathbf{x}'_c) = \sum_{n=1}^{\infty} \psi_n(\mathbf{x}_c) a_n(\mathbf{x}'_c) \quad . \tag{14}$$

Here the vectors $\mathbf{x}_c$ and $\mathbf{x}'_c$ identify the positions of the sound pressure and point monopole source in the enclosure. The natural modes are chosen to form a complete set of functions so that any pressure field in the cavity can be derived from their linear combination. As seen for the exterior sound field, in order to avoid the two steps numerical solution of the boundary integral Eq. (5), the series expansion for the Green function in Eq. (14) is chosen to satisfy Neumann's boundary condition such that $\frac{\partial}{\partial n}\hat{G}_c(\mathbf{x}_c \mid \mathbf{x}_s)\Big|_{\mathbf{x}_c=\mathbf{x}_s} = 0$ over the boundary surface of the enclosure (Morse and Ingard 1968; Pierce 1989; Nelson and Elliott 1992; Koopmann 1997). From the physical point of view, this condition corresponds to rigidly walled boundary conditions. Thus the natural mode shapes used in Eq. (14) are chosen assuming the cavity is rigidly walled. The complex modal amplitudes $a_n$ are derived by substituting Eq. (14) into Eq. (3), which is then multiplied by the $\bar{n}$–th mode and integrated over the volume of the cylindrical cavity. As a result, considering the orthonormality property of the natural modes, the following set of uncoupled ordinary equations in the unknown modal amplitudes $a_n(\mathbf{x}'_c)$ are derived

$$V\left(\omega_{a,n}^2 - \omega^2\right)a_n = c_0^2 q_n \qquad n = 1, 2, \ldots, \infty \ . \tag{15}$$

These equations are derived assuming the natural modes of the cavity $\psi_n(\mathbf{x}_c)$ are normalised in such a way as $\int_V \psi_n^2(\mathbf{x}_c) = V$, where $V$ is the volume of the cavity. Also $\omega_{a,n}$ is the *n*–th natural frequency for the rigidly walled cavity and $q_n$ are the modal excitation terms, which, using the "sifting" property of the three–dimensional Dirac delta function, are derived as follows

$$q_n = \int_V \psi_n(\mathbf{x}_c)\delta(\mathbf{x}_c - \mathbf{x}'_c)dV = \psi_n(\mathbf{x}'_c) \ . \tag{16}$$

Thus, the Neumann Green function for the interior sound field is given by:

$$\hat{G}_c(\mathbf{x}_c \mid \mathbf{x}'_c) = c_0^2 \sum_{n=1}^{\infty} \frac{\psi_n(\mathbf{x}_c)\psi_n(\mathbf{x}'_c)}{V\left(\omega_{a,n}^2 - \omega^2\right)} \ . \tag{17}$$

The sound absorption effects produced by internal fittings in transportation vehicles (floor, seats, wall finishing/trim layers, etc.) generate a damping action, which, for light damping, is normally taken into account in terms of modal damping so that Eq. (17) becomes (Morse and Ingard 1968; Nelson and Elliott 1992):

$$\hat{G}_c(\mathbf{x}_c \mid \mathbf{x}'_c) = c_0^2 \sum_{n=1}^{\infty} \frac{\psi_n(\mathbf{x}_c)\psi_n(\mathbf{x}'_c)}{V\left(\omega_{a,n}^2 - \omega^2 + j2\zeta_{a,n}\omega_{a,n}\omega\right)} \quad , \tag{18}$$

where $\zeta_{a,n}$ is the acoustic modal damping. The details for the derivation of this expression can be found in Morse and Ingard (1968) and Nelson and Elliott (1992). In conclusion, assuming there are no interior acoustic sources $Q(\mathbf{x}_c)$ and assuming the Neumann Green function (18) is employed, also for the interior sound field the boundary integral equation (5) reduces to:

$$c(\mathbf{x}_c)\, p(\mathbf{x}_c) = j\rho\omega \int_{S_b} \hat{G}_c(\mathbf{x}_c \mid \mathbf{x}_s)\dot{v}_n(\mathbf{x}_s)\, dS_b \quad , \tag{19}$$

where $\dot{v}_n(\mathbf{x}_s)$ is the sound particle velocity in direction normal to the boundary surface.

When the enclosing wall has regular geometry it is possible to derive the natural frequencies $\omega_{a,n}$ and natural modes $\psi_n(\mathbf{x}_c)$ in terms of simple analytic expressions. For instance, for the cylindrical enclosure shown in Figure 1, the natural frequencies and natural modes, assuming rigid wall boundary conditions, are given by (Blevins 2001):

$$\omega_{a,n} = c_0 \left( \frac{n_1^2 \pi^2}{L^2} + \frac{\lambda_{n_2,n_3}^2}{R^2} \right)^{\frac{1}{2}} \tag{20}$$

and

$$\begin{aligned} \psi_n^s(z,\phi,r) &= \cos\left(\tfrac{n_1 \pi z}{L}\right)\cos(n_2\theta) J_{n_2}\left(\lambda_{n_2,n_3}\tfrac{r}{R}\right) \\ \psi_n^a(z,\phi,r) &= \cos\left(\tfrac{n_1 \pi z}{L}\right)\sin(n_2\theta) J_{n_2}\left(\lambda_{n_2,n_3}\tfrac{r}{R}\right) . \end{aligned} \tag{21a,b}$$

These equations are given in cylindrical coordinates $z$ , $\theta$ , $r$ so that $n_1 = 0,1,2,\ldots$ $n_2 = 0,1,2,\ldots$ $n_3 = 0,1,2,\ldots$ are the modal indices in axial, circumferential and radial directions for the $n$-th acoustic natural frequency and mode. Also, $J_{n_2}(\cdots)$ is the first kind Bessel function of order $n_2$ and the term $\lambda_{n_2,n_3}$ is derived from the equation $J'_{n_2}(\lambda_{n_2,n_3}) = 0$ . Finally $R$ and $L$ are the radius and the length of the cylindrical cavity respectively. Since the mode shapes show a periodicity in circumferential direction, in order to represent a generic sound pressure distribution, two mode components oriented orthogonally in circumferential direction must be employed in Eqs. (17) and (18). For instance, in this formulation the symmetric cosine and anti–symmetric sine functions given in

Eqs. (21a,b) are used, which are denoted by the superscripts *s* and *a* respectively. Thus, to take into account the contributions of both symmetric and anti–symmetric mode shapes, the Green function of Eq. (18) must be modified as follows:

$$\hat{G}_c(\mathbf{x}_c \mid \mathbf{x}'_c) = c_0^2 \sum_{\substack{n=1 \\ \alpha=s,a}}^{\infty} \frac{\psi_n^{\alpha}(\mathbf{x}_c)\psi_n^{\alpha}(\mathbf{x}'_c)}{\overline{V}_n\left(\omega_{a,n}^2 - \omega^2 + j2\zeta_{a,n}\omega_{a,n}\omega\right)} \quad , \tag{22}$$

where for each mode index $n$, the summation is carried out considering symmetric ($\alpha = s$) and antisymmetric ($\alpha = a$) mode shapes. In this case, since the natural modes given by Eqs. (21a) and (21b) are not volume–normalised, the denominator includes the term $\overline{V}_n = V\varepsilon_{n1}J_{n_2-1}^2(\lambda_{n_2,n_3})$, where $\varepsilon_{n_1} = 1/2$ when $n_1 = 0$ and $\varepsilon_{n_1} = 1/4$ when $n_1 > 0$. As discussed for the exterior sound problem, for cavities with complex geometries, either FEM or BEM numerical methods can be used to formulate an eigenvalue–eigenvector problem from which the approximate natural frequencies and natural modes are derived (Wu 2000; Fahy and Gardonio 2007).

### 1.4 Derivation of the structural response

In general, the transverse vibration of a flexible thin shell structure is governed by three inhomogeneous equations of motion, which can be written in the following form (Soedel 1993; Markus 1998):

$$\begin{aligned} &L_1(u,v,w,\mathbf{x}_s,t) - m_s\,\partial^2 u(\mathbf{x}_s,\mathrm{t})/\partial \mathrm{t}^2 = -f_z(\mathbf{x}_s,t) \\ &L_2(u,v,w,\mathbf{x}_s,t) - m_s\,\partial^2 v(\mathbf{x}_s,\mathrm{t})/\partial \mathrm{t}^2 = -f_\theta(\mathbf{x}_s,t) \\ &L_3(u,v,w,\mathbf{x}_s,t) - m_s\,\partial^2 w(\mathbf{x}_s,\mathrm{t})/\partial \mathrm{t}^2 = -f_r(\mathbf{x}_s,t) \quad . \end{aligned} \tag{23a-c}$$

Here $L_i(u,v,w,\mathbf{x}_s,\mathrm{t})$ are differential operators for the theory used to describe the equations of motion of the shell structure. Also $u,v,w$ and $f_z, f_\theta, f_r$ are the displacements and forces per unit surface along the three axis used to describe the geometry of the shell (in this section, the notation for cylindrical coordinates is used). Finally $m_s$ is the mass per unit surface of the shell structure and the vector $\mathbf{x}_s$ defines a generic point on the shell structure. Normally, for thin shell structures, the response is derived from the so-called classical theory of thin shells established by Love. This theory assumes the shell is thin compared to the radii of curvature and the deflections are reasonably small. Also it neglects the effects produced by shear deflections and rotary inertia. After Love's work, several refinement theories have been proposed for specific classes of shells, which are discussed in specialised texts such as, for example, those in references

(Graff 1975; Cremer et al. 1988; Leissa 1993; Soedel 1993; Markus 1998; Reddy 2006). Assuming time-harmonic motion, Eqs. (23a-c) become

$$\begin{aligned} L_1(u,v,w,\mathbf{x}_s,\omega) + \omega^2 m_s u(\mathbf{x}_s,\omega) &= -f_z(\mathbf{x}_s,\omega) \\ L_2(u,v,w,\mathbf{x}_s,\omega) + \omega^2 m_s v(\mathbf{x}_s,\omega) &= -f_\theta(\mathbf{x}_s,\omega) \\ L_3(u,v,w,\mathbf{x}_s,\omega) + \omega^2 m_s w(\mathbf{x}_s,\omega) &= -f_r(\mathbf{x}_s,\omega) \quad , \end{aligned} \tag{24a-c}$$

where, in this case, $u,v,w$ and $f_z, f_\theta, f_r$ are the frequency dependent complex amplitudes of the co-respective time-domain functions assuming the time-harmonic dependence is expressed in the complex exponential form $\exp(j\omega t)$. Also in this case, for brevity, the frequency dependence of the complex amplitudes will not be displayed in the remaining part of the formulation. In general, for curved shell structures, the three equations of motion are coupled (Soedel 1993; Markus 1998).

The solution of Eqs. (24a-c) can be expressed with the following set of three series expansions in the $m = 1, 2, \ldots$ structural natural modes of the shell, (Morse and Ingard 1968):

$$\begin{aligned} u(\mathbf{x}_s) &= \sum_{m=1}^{\infty} \phi_{z,m}(\mathbf{x}_s) b_{z,m} \\ v(\mathbf{x}_s) &= \sum_{m=1}^{\infty} \phi_{\theta,m}(\mathbf{x}_s) b_{\theta,m} \\ w(\mathbf{x}_s) &= \sum_{m=1}^{\infty} \phi_{r,m}(\mathbf{x}_s) b_{r,m} \quad . \end{aligned} \tag{25a-c}$$

Here $\phi_{z,m}, \phi_{\theta,m}, \phi_{r,m}$ and $b_{z,m}, b_{\theta,m}, b_{r,m}$ are the components of the *m*-th natural mode and the co-respective complex modal responses along the axis used to describe the geometry of the shell (the combination of the three functions $\phi_{z,m}, \phi_{\theta,m}, \phi_{r,m}$ constitute a natural mode).

Considering the model problem studied in this chapter, the free vibration of in vacuo cylindrical structures is characterised by three families of natural modes: the *axial modes* that are dominated by longitudinal vibrations, the *torsional modes* that are controlled by circumferential vibrations and the *flexural modes* that are governed by radial vibrations (Junger and Feit 1986). Thus for each mode number there are three natural frequencies relative to the axial, circumferential and radial natural modes. Usually the lowest one corresponds to the predominantly radial (i.e. flexural) natural mode (Markus 1998). Moreover, for circular cylinders, these mode shapes show a periodicity in circumferential direction. Thus, in order to represent a generic vibration field, two mode components oriented orthogonally in circumferential direction must be used in

Eqs. (25a-c). Normally a symmetric cosine and an anti–symmetric sine function are employed. A comprehensive account on the derivation of natural frequencies and natural modes of thin cylinders can be found in (Junger and Feit 1986; Soedel 1993; Markus 1998). For the specific structural–acoustic problem considered in this section, the coupling of the interior/exterior sound and TBL pressure fields with the structure occurs predominantly via radial, i.e. flexural, response of the structure. Thus, the formulation for the structural vibration can be simplified by neglecting the axial and torsional natural modes and using simplified expressions for the flexural natural frequencies as described by (Junger and Feit 1986; Soedel 1993). For instance, for the simply supported circular cylindrical shell model problem of Figure 1, the derivation of the response in radial direction can be expressed with the following series expansion (Soedel 1993):

$$w(\mathbf{x}_s) = \sum_{\substack{m=1 \\ \alpha=s,a}}^{\infty} \phi_{r,m}^{\alpha}(\mathbf{x}_s) b_{r,m}^{\alpha} \quad , \tag{26}$$

where, for each mode index $m$, the summation is carried out considering symmetric ($\alpha = s$) and antisymmetric ($\alpha = a$) radial mode shapes. Also the natural frequencies and co-respective symmetric and anti–symmetric radial mode shapes are given by (Soedel 1993):

$$\omega_{s,m} = \sqrt{\frac{E_s}{\rho_s R^2}} \sqrt{\frac{(m_1 \pi R/L)^4}{\left[(m_1 \pi R/L)^2 + m_2^2\right]^2} + \frac{(h/R)^2}{12(1-\nu_s^2)} \left[ \left( \frac{m_1 \pi R}{L} \right)^2 + m_2^2 \right]^2} \quad , \tag{27}$$

$$\phi_{r,m}^{s}(\mathbf{x}_s) = \sin(\tfrac{m_1 \pi}{L}) \cos(m_2 \theta) \quad , \quad \phi_{r,m}^{a}(\mathbf{x}_s) = \sin(\tfrac{m_1 \pi}{L}) \sin(m_2 \theta) \quad , \tag{28a,b}$$

where $\rho_s$, $E_s$, $\nu_s$ are respectively the mass density, Young's modulus of elasticity and Poisson ratio of the material and $R$, $L$, $h$ are respectively the radius, length and thickness of the cylinder. These equations are given in cylindrical coordinates $z, \theta, r$ so that $m_1 = 1, 2, 3, \ldots$ and $m_2 = 0, 1, 2, \ldots$ are the modal indices in axial and circumferential directions for the *m*-th structural natural mode. The first term under the square root of Eq. (27) is controlled by the membrane stiffness of the cylinder and tends to reduce to zero for increasing circumferential mode orders $m_2$. Alternatively, the second term under the square root of Eq. (27) is controlled by the bending stiffness of the cylinder and becomes progressively important for increasing circumferential mode orders $m_2$.

The unknown complex modal amplitudes $b_{r,m}^{s}$ and $b_{r,m}^{a}$ can be derived by substituting Eq. (26) into Eq. (24c). The resulting equation is then multiplied by

a $\overline{m}$ –th mode and integrated over the surface of the cylinder so that, using the orthormality property of the natural modes and assuming the natural modes are mass normalised, the following set of uncoupled ordinary equations is obtained:

$$M\left(\omega_{s,m}^2 - \omega^2\right) b_{r,m}^{\alpha} = f_{r,m}^{\alpha} \qquad m = 1, 2, \ldots, \infty \qquad \alpha = s, a \quad , \tag{29}$$

where $M$ is the mass of the shell. Thus for each mode order $m$ , two equations are defined with respect to the symmetric and anti–symmetric complex modal amplitudes $b_{r,m}^{s}$ and $b_{r,m}^{a}$ . Also, $f_{r,m}^{\alpha}$ is the *m*–th modal excitation term for either the symmetric or anti–symmetric mode shape, which, for the specific case of radial excitation only, is given by (Soedel 1993):

$$f_{r,m}^{\alpha} = \int_{S_b} \phi_{r,m}^{\alpha}(\mathbf{x}_s') f_r(\mathbf{x}_s') dS_b \quad . \tag{30}$$

Thus, according to Eqs. (26) and (29), the velocity response in radial direction of the cylinder can be expressed with the following modal summation

$$\dot{w}(\mathbf{x}_s) = j\omega \sum_{\substack{m=1 \\ \alpha=s,a}}^{\infty} \frac{\phi_{r,m}^{\alpha}(\mathbf{x}_s) f_{r,m}^{\alpha}}{M\left(\omega_{s,m}^2 - \omega^2\right)} \quad . \tag{31}$$

In general, analytical expressions for the natural frequencies and natural modes can be derived only for regular shapes such as, for example, circular cylinder closed shells or flat and curved shells panels. When the problem at hand involves complex wall structures, the Finite Element Method (FEM) numerical technique is normally employed (Fahy and Gardonio 2007).

The energy dissipation in the structure is normally modelled with a hysteretic damping model (Cremer et al. 1988), which, leads to a complex stiffness in modal coordinates so that the Eq. (31) becomes

$$\dot{w}(\mathbf{x}_s) = j\omega \sum_{\substack{m=1 \\ \alpha=s,a}}^{\infty} \frac{\phi_{r,m}^{\alpha}(\mathbf{x}_s) f_{r,m}^{\alpha}}{M\left(\omega_{s,m}^2 (1 + j\eta) - \omega^2\right)} \quad , \tag{32}$$

where $\eta$ is the loss factor. The interaction between a structure and the surrounding fluid also produce energy dissipation. For slender structures this effect is normally modelled in terms of viscous damping without carrying out a coupled structural–acoustic analysis. In particular, the so called Rayleigh damping model is used, so that the damping can be modelled in terms of viscous damping coefficients in modal coordinates. Alternatively, for structures with extended surfaces such as the cylinder problem considered in this section, the true dissipation effects are modelled with a coupled structural–acoustic analysis, which is presented in the forthcoming section.

### 1.5 Derivation of the coupled structural–acoustic response

In general, for the structural–acoustic problem at hand, the shell structure is excited only by transverse force distributions. For instance, for the cylindrical wall of the model problem shown in Figure 1, the excitation vector is characterised only by forces in radial direction. More specifically, the transverse force excitation per unit surface $f_r(\mathbf{x}'_s)$ is composed by three terms: the pressure field $p_{TBL}(\mathbf{x}'_s,t)$ produced by the TBL fluid flow and the fluid loading pressure fields $p_e(\mathbf{x}'_s,t)$, $p_c(\mathbf{x}'_s,t)$ exerted by the external and internal fluids.

As discussed in the opening part of this section, the pressure field produced by the TBL fluid flow is assumed independent from the flexural vibration of the cylindrical shell. In this case the excitation is specified in terms of the blocked pressure. Comprehensive overviews of the models for the excitation spectra that have been proposed since the early work by Corcos (1963a); (Corcos 1963b) can be found in Bull (1995); Graham (1997) and in Chapter 6 of this book. In this respect, it is important to emphasize that, despite the growing evidence that the model proposed by Corcos (Corcos 1963a; Corcos 1963b; Corcos 1967) over predicts the excitation levels at wavenumbers below the convective coincidence range (Martin and Leehey 1977; Blake 1986; Leehey 1988), it is still widely used to predict the response and interior sound radiation in high speed transportation vehicles such as aircraft. This is because, for high flow speeds, the convective coincidence range tends to coincide with the wavenumbers of the low order natural modes of the shell structure controlling the response and interior sound radiation phenomena (Graham 1997; Cousin 1999; Maury et al. 2002b). Nevertheless it is important to highlight that situations exist where the contribution in the sub–convective wavenumber region may be significant (Hwang and Maidanik 1990; Graham 1997).

The external and internal fluid loadings are instead derived considering the feedback effects produced by the flexible wall sound radiation into the external and internal fluids. As anticipated at the beginning of this section, this is a reasonable model for the fluid loadings produced by the air in the interior and exterior of a vehicle that travels at low speed. For aircraft vehicles traveling at very high speed approaching 0.8 Mach at cruise condition, a proper *aeroelastic* formulation would be necessary to correctly predict the exterior fluid loading (Frampton 2005). Nonetheless, the structural–acoustic model presented here provides a good foundation for the understanding of the physical mechanisms characterising the coupling of structural modes via the internal and external fluids. In this respect, a complete set of graphs with the spectra of the self and mutual fluid loading impedance functions is introduced at the end of this subsection, which provide direct indications on the damping–, mass– and

stiffness–like physical effects produced between the modes of the shell via the fluid loading.

In summary, the excitation exerted by the TBL fluid flow on the wall structure is expressed in terms of the blocked TBL pressure $p_{TBL}(\mathbf{x}'_s)$, which is twice the pressure that a nominally identical flow would produce if the wall was removed (Howe 1998). Also, the exterior and interior sound pressure fields, $p_e(\mathbf{x}'_s,t)$ and $p_c(\mathbf{x}'_s,t)$, are derived from the first step "collocation analysis" of the boundary integral in Eq. (5). As discussed above, if there are no distributions of acoustic sources in the exterior and interior fluid domains, the boundary integral expression (5) reduces to Eq. (11) and Eq. (19) when both the exterior and interior sound fields are described with Neumann Green functions. For instance, assuming that the acoustic particle velocity on the boundary surface of the model problem shown in Figure 1 coincides with the radial velocity of the cylinder, i.e. $\dot{v}_n(\mathbf{x}_s) \equiv \dot{w}(\mathbf{x}_s)$, the radial force per unit surface is given by[4]

$$\begin{aligned} f_r(\mathbf{x}'_s) &= p_{TBL}(\mathbf{x}'_s) + p_e(\mathbf{x}'_s) - p_c(\mathbf{x}'_s) \\ &= p_{TBL}(\mathbf{x}'_s) - 2\int_{S_b} j\omega\rho\hat{G}_e(\mathbf{x}'_s \mid \mathbf{x}_s)\dot{w}(\mathbf{x}_s)dS_b - 2\int_{S_b} j\omega\rho\hat{G}_c(\mathbf{x}'_s \mid \mathbf{x}_s)\dot{w}(\mathbf{x}_s)dS_b \end{aligned} \quad . \tag{33}$$

Since the natural modes used to derive the structural response are characterised by the symmetric and anti–symmetric functions given in Eqs. (28a,b), the modal excitation terms defined in Eq. (30) are expressed as follows

$$\begin{aligned} f^{\alpha}_{r,m} = \int_{S_b} \phi^{\alpha}_{r,m}(\mathbf{x}'_s) p_{TBL}(\mathbf{x}'_s) dS_b - 2\int_{S_b} \phi^{\alpha}_{r,m}(\mathbf{x}'_s) \int_{S_b} j\omega\rho\hat{G}_e(\mathbf{x}'_s \mid \mathbf{x}_s)\dot{w}(\mathbf{x}_s)dS_b dS_b \\ - 2\int_{S_b} \phi^{\alpha}_{r,m}(\mathbf{x}'_s) \int_{S_b} j\omega\rho\hat{G}_c(\mathbf{x}'_s \mid \mathbf{x}_s)\dot{w}(\mathbf{x}_s)dS_b dS_b \end{aligned} \quad . \tag{34}$$

Here, the two Green functions $\hat{G}_e$ and $\hat{G}_c$ are given by Eqs. (13) and (22) respectively. Thus, considering the orthonormal properties of the trigonometric functions that describe the structural and acoustic mode shapes and the Green functions for the external fluid domain, simplified analytical expressions can be derived for the three integrals in the equation above. In particular, the first integral is expressed in terms of TBL modal excitations while, considering the modal expansion for the radial displacement given by Eq. (26), the other two integrals are expressed in the form of modal impedances. Thus it follows that:

$$f^{\alpha}_{r,m} = f^{\alpha}_{TBL,m} - j\omega \sum_{\substack{\bar{m}=1 \\ \alpha=s,a}}^{\infty} Z^{\alpha}_{e,m\bar{m}} b^{\alpha}_{r,m} - j\omega \sum_{\substack{\bar{m}=1 \\ \alpha=s,a}}^{\infty} Z^{\alpha}_{c,m\bar{m}} b^{\alpha}_{r,m} \quad . \tag{35}$$

[4] According to the notation in Figure 1b: $\dot{v}_n(\mathbf{x}_e = \mathbf{x}_s) = -\dot{w}(\mathbf{x}_s)$ and $\dot{v}_n(\mathbf{x}_c = \mathbf{x}_s) = \dot{w}(\mathbf{x}_s)$.

Here the TBL modal excitations are given by

$$f^{\alpha}_{TBL,m} = \int_{S_b} \phi^{\alpha}_{r,m}(\mathbf{x}'_s) p_{TBL}(\mathbf{x}'_s) dS_b \quad . \tag{36}$$

Also, the modal impedance terms due to the interaction between the modal vibration of the cylinder wall and exterior fluid are given by (Junger and Feit 1986; Lesueur 1988)

$$Z^{\alpha}_{e,m\bar{m}} = \frac{4S_b}{\pi L \varepsilon_{m_2}} k_{m_1} k_{\bar{m}_1} \int_{-\infty}^{+\infty} \frac{N_{m_1,\bar{m}_1}(k_z) z_{m_2}(k_z)}{\left(k_z^2 - k_{m_1}^2\right)\left(k_z^2 - k_{\bar{m}_1}^2\right)} dk_z \quad , \tag{37}$$

where $N_{m_1,\bar{m}_1}(k_z) = \frac{1}{2}\cos^2(\frac{k_z L}{2})$ when $m_1$ and $\bar{m}_1$ are odd while $N_{m_1,\bar{m}_1}(k_z) = \frac{1}{2}\sin^2(\frac{k_z L}{2})$ when $m_1$ and $\bar{m}_1$ are even. In addition $k_{m_1} = \frac{m_1 \pi}{L}$, $k_{\bar{m}_1} = \frac{\bar{m}_1 \pi}{L}$ and $\varepsilon_{m_2=0} = 1$, $\varepsilon_{m_2>0} = 2$ is the Neumann factor. Finally (Junger and Feit 1986; Lesueur 1988)

$$z_{m_2}(k_z) = j\rho c_0 \frac{k\, H^{(1)}_{m_2}[(k^2 - k_z^2)^{1/2} R]}{(k^2 - k_z^2)^{1/2} H^{(1)'}_{m_2}[(k^2 - k_z^2)^{1/2} R]} \tag{38}$$

is an impedance function per unit surface, where, as introduced in Section 1.2, $k^2 = k_r^2 + k_z^2$ and $H^{(1)}_{m_2}(...)$ is the first kind Hankel function of order $m_2$. Since the flexural natural modes of the cylinder are orthogonal to each other, no coupling exists, i.e. $Z^{\alpha}_{e,m\bar{m}} = 0$, when $m_1 + \bar{m}_1$ is odd or when $m_2 \neq \bar{m}_2$. Finally, the modal impedance terms due to the interaction between the cylinder wall and interior fluid are given by

$$Z^{\alpha}_{c,m\bar{m}} = 2j\omega\rho c_0^2 \sum_{n=1}^{\infty} \frac{C^{\alpha}_{mn} C^{\alpha}_{\bar{m}n}}{\bar{V}\left(\omega^2_{a,n} - \omega^2 + j2\zeta_{a,n}\omega_{a,n}\omega\right)} \quad , \tag{39}$$

where the mode coupling terms are given by (Gardonio et al. 2001)

$$C^{\alpha}_{mn} = \int_{S_b} \phi^{\alpha}_{r,m}(\mathbf{x}_s) \psi^{\alpha}_{n}(\mathbf{x}_s) dS_b = \frac{S_b}{\varepsilon^{\alpha}_{n_2} \pi} \frac{m_1}{n_1^2 - m_1^2} [(-1)^{(n_1^2 + m_1^2)} - 1] J_{n_2}(\lambda_{n_2,n_3}) \quad , \tag{40}$$

with $\varepsilon^{s}_{n_2} = 1$ when $n_2 = 0$ and $\varepsilon^{s}_{n_2} = 2$ when $n_2 \neq 0$ and with $\varepsilon^{a}_{n_2} = 2$ for all $n_2$. Also in this case, the orthonormal properties of the trigonometric functions in the natural modes leads to no coupling, i.e. $Z^{\alpha}_{c,m\bar{m}} = 0$, between modes with $m_1 = n_1, n_1 \pm 2, n_1 \pm 4, \ldots$ or $\bar{m}_1 = n_1, n_1 \pm 2, n_1 \pm 4, \ldots$ and $m_2 \neq n_2$ or $\bar{m}_2 \neq n_2$.

Substitution of Eq. (35) into Eq. (29) gives the following set of coupled modal equations

$$M\left(\omega_{s,m}^2-\omega^2\right)b_{r,m}^{\alpha}=f_{TBL,m}^{\alpha}-j\omega\sum_{\substack{\overline{m}=1\\ \alpha=s,a}}^{\infty}Z_{e,m\overline{m}}^{\alpha}b_{r,\overline{m}}^{\alpha}-j\omega\sum_{\substack{\overline{m}=1\\ \alpha=s,a}}^{\infty}Z_{c,m\overline{m}}^{\alpha}b_{r,\overline{m}}^{\alpha} \qquad m=1,2,\ldots,\infty \qquad \alpha=s,a \tag{41}$$

To simplify the remaining part of the formulation, these equations are arranged in the following matrix expression

$$\left[-\omega^2\mathbf{M}+j\omega\mathbf{Z}+\mathbf{K}\right]\mathbf{b}_r=\mathbf{f}_{TBL}\ , \tag{42}$$

where the elements of the diagonal mass and stiffness matrices are given by $\mathbf{M}_{mm}^{\alpha}=M$ and $\mathbf{K}_{mm}^{\alpha}=M\omega_{s,m}^2$ respectively. Also, the elements of the modal excitation and modal response vectors are given by $\mathbf{f}_{TBL,m}^{\alpha}=f_{TBL,m}^{\alpha}$ and $\mathbf{b}_{r,m}^{\alpha}=b_{r,m}^{\alpha}$ respectively. Finally the complex terms in the sparse impedance matrix are given by $\mathbf{Z}_{m\overline{m}}^{\alpha}=\left(Z_{e,m\overline{m}}^{\alpha}+Z_{c,m\overline{m}}^{\alpha}\right)$. The diagonal *self impedance* terms provide the exterior and interior fluid loading effects on a given mode $m=(m_1,m_2)$ exerted by the modal velocity of the same mode $m=(m_1,m_2)$. Alternatively the off-diagonal *mutual impedance* terms (often called *cross impedances*) give the exterior and interior fluid loading effects on a given mode $m=(m_1,m_2)$ generated by the modal velocity of another mode $\overline{m}=(\overline{m}_1,\overline{m}_2)$.

Before continuing with the final part of this formulation for the interior sound radiation, the physical effects due to the fluid loadings produced by the external and internal air fluids are studied in detail for a cylindrical enclosure with aspect ratio $R/L=0.3$. To facilitate the analysis, the spectra with the real and imaginary parts of the self and mutual impedances given in Eqs. (37) and (39) are presented. The fluid loading effects are then analysed recalling that a) a real positive impedance indicates a damping–like effect, i.e. $Z_{damping}=c$; b) an imaginary positive impedance proportional to frequency denotes a mass–like effect, i.e. $Z_{mass}=j\omega m$; and c) a imaginary negative impedance inversely proportional to frequency indicates a stiffness–like effect, i.e. $Z_{stiffness}=-jk/\omega$ (here $c$, $m$, $k$, represent the damping, mass and stiffness factors respectively). Figure 3 shows the spectra of the real (left–hand side plots) and imaginary (right–hand side plots) parts of normalised self modal impedances of a cylinder immerged in air. The three rows of graphs show the self modal impedances with circumferential mode numbers $m_2=0,1,2$. The left–hand side plots shows that the spectra of the real parts are always positive. This indicates that the fluid produces a resistive effect on each mode, thus it absorbs energy from the modal vibrations of the cylinder. In general, at low frequencies, all spectra set off from

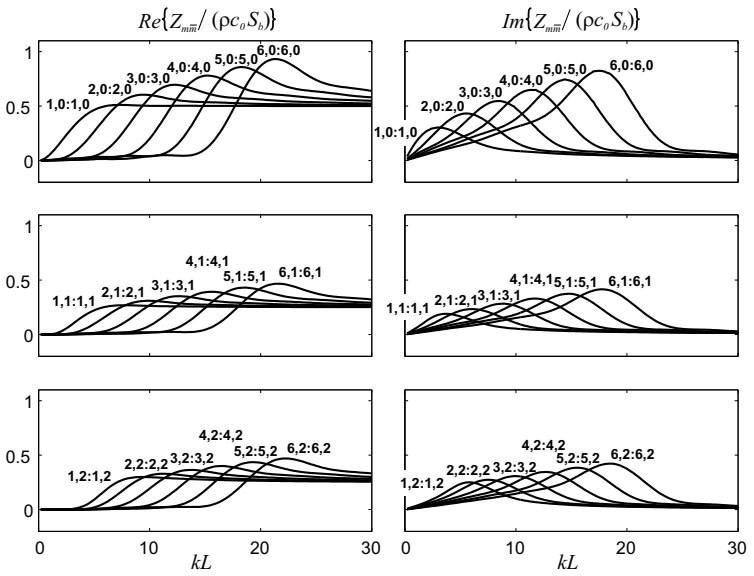


**Figure 3.** Self external fluid loading impedances on a baffled cylinder with $R/L$=0.3.

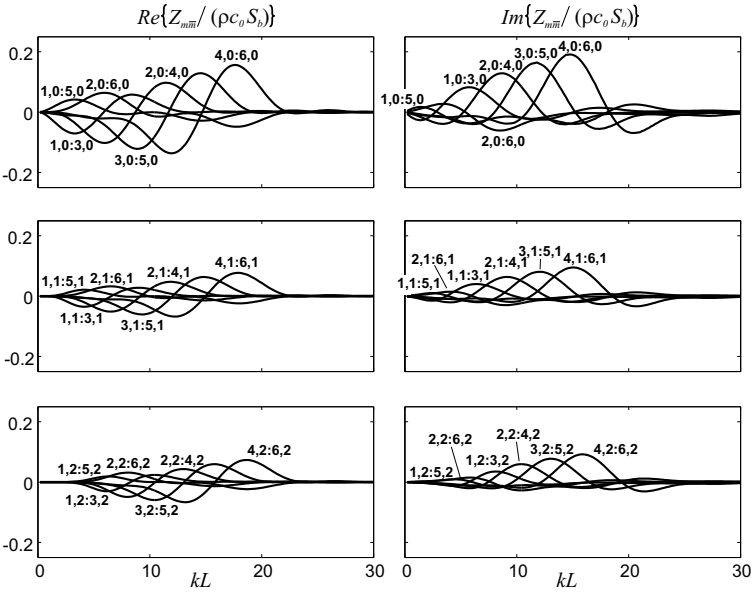


**Figure 4.** Mutual external fluid loading impedances on a baffled cylinder with $R/L$=0.3.

very small values close to zero and then rapidly rise up to a maximum value in correspondence of specific critical frequencies $\omega_{cr,mm}$. Above these critical frequencies, the resistive effects rapidly fall and then level to constant values of 0.5 for the breathing modes with $m_2 = 0$ and 0.25 for the other modes with $m_2 > 0$. Thus, in general, the self modal loading exerted by the external fluid produces large resistive effects at high frequencies starting from about the modal critical frequencies where the resistive effect is maximum. Also, the resistive effects produced by breathing modes are double than those of modes with higher circumferential mode orders. Finally the critical frequencies rise together with the axial mode orders $m_1 = \overline{m}_1$. Moving to the right–hand side plots, it is noted that also the spectra for the imaginary parts are always positive, which indicates that the fluid also produces a mass effect on each mode. In general, all spectra grow rapidly from zero and reach a maximum value at frequencies slightly lower than the modal critical frequency $\omega_{cr,mm}$. Then, for higher frequencies, they rapidly fall to zero. Thus, in general, the self modal loading exerted by the external fluid produces mass effects up to the critical frequencies. Also, the peak mass effects produced by breathing modes are double than those of modes with higher circumferential mode orders.

Figure 4 shows the spectra of the real part (left–hand side plots) and imaginary part (right–hand side plots) of normalised mutual modal impedances with circumferential mode numbers $m_2 = 0, 1, 2$. The two columns of graphs show that in this case the real and the imaginary parts assume both positive and negative values. This indicates that the fluid tends to transfer energy between pairs of modes. In general, the spectra for both the real and imaginary parts start from zero and then depict a waved contour that peaks at frequencies below the upper critical frequency of the two modes and then rapidly fade to zero. Thus, in general, the mutual fluid loading effect transfers energy from one mode to another around the upper critical frequencies $\omega_{cr,mm}$ of the two modes. Plots in Figure 4 highlight that this effect is larger for breeding modes with $m_2 = 0$ and progressively becomes smaller as the circumferential mode order grows. In general, as can be noted by contrasting the graphs in Figures 3 and 4, for light fluids the energy transfer between pairs of modes is much smaller than the energy absorption exerted on single modes (Guyader and Laulagnet 1994). For this reason, the effect of the mutual impedances is often neglected for light fluids, such as air for example, so that the set of equations (41) becomes uncoupled. To conclude this analysis, it is important to note that, according to Eq. (37) and (38), the modal impedance terms relative to the external fluid loading are proportional to the specific acoustic impedance of the fluid $\rho c_0$.

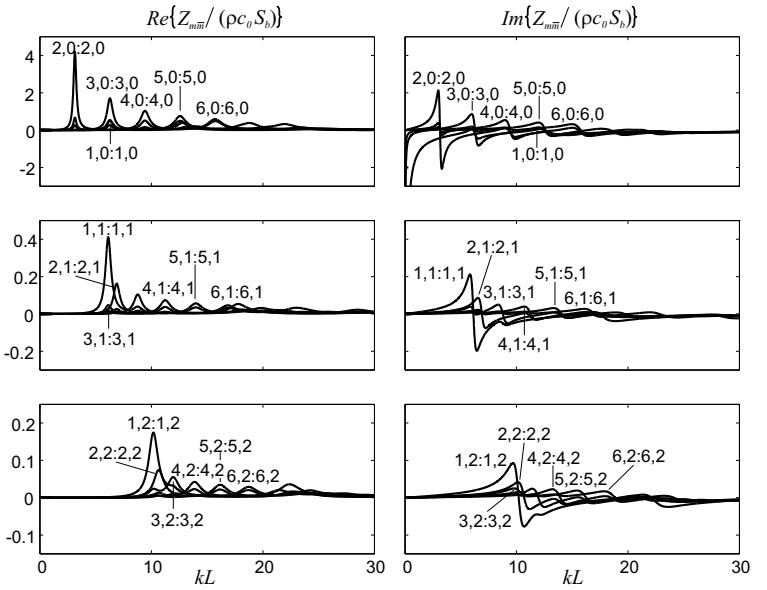


**Figure 5.** Self internal fluid loading impedances for a cylinder with $R/L$=0.3.

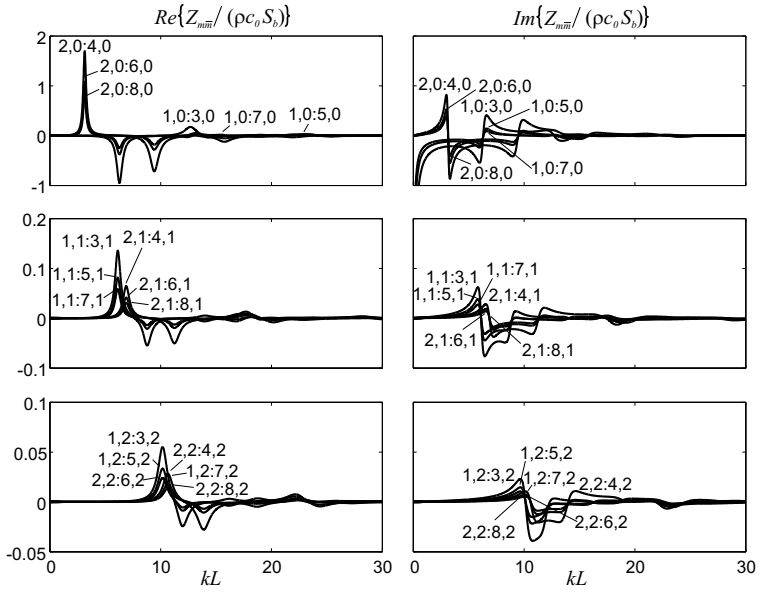


**Figure 6.** Mutual internal fluid loading impedances for a cylinder with $R/L$=0.3.

Thus the energy absorption and transfer effects, as well as the mass effects described above, become increasingly important for heavy fluids (e.g. water). Normally, for light fluids, such as air, the mutual fluid loading effects and the self mass fluid loading effects are neglected. Also, the self resistive effects are described in terms of a viscous damping ratio, which is often considered constant and equal for all modes, although it should follow the typical spectra shown in the left–hand side plots of Figure 3.

The modal impedance effects produced by the interior fluid is now analysed assuming the cylinder is filled with air and has aspect ratio $R/L=0.3$. Figure 5 shows the spectra of the real (left–hand side plots) and imaginary (right–hand side plots) parts of the normalised self modal impedances with circumferential mode numbers $m_2=0,1,2$. The left–hand side plots show that the spectra of the real parts are positive and are characterised by peaks occurring at the resonance frequencies relative to acoustic modes that are efficiently coupled with the structural mode that specifies the modal impedance term. The right–hand side plots show that the spectra of the imaginary parts jump from positive to negative values in correspondence of these resonances. Thus, the interior fluid produces a combination of stiffness, dissipative and mass effects on single structural modes, which is typical of enclosed sound fields with resonant behaviour (Kinsler et al. 2000). More specifically the stiffness effect is produced at frequencies below resonance while the mass effect is generated at frequencies above resonance. Also, the dissipative effect becomes significant at frequencies around resonance. On average, the magnitude of the impedances for breathing modes with circumferential mode order $m_2=0$ is one order of magnitude greater than that of modes with higher circumferential mode orders. Also, for a given circumferential mode order, the magnitude of the resonance peaks tends to decrease as the axial mode number $m_1$ rises. Finally, the modal impedances of breathing modes are characterised by a low frequency stiffness behaviour, which is due to the elastic reaction offered by the fluid in the cavity to the volumetric modal vibration.

Figure 6 shows the real part (left–hand side plots) and the imaginary part (right–hand side plots) of the normalised mutual modal impedances with circumferential mode numbers $m_2=0,1,2$. The left–hand side plots show that the spectra for the real parts of the mutual modal impedances are also characterised by peaks occurring at the resonance frequencies due to the acoustic modes that are efficiently coupled with the structural mode that specifies the modal impedances. However, in this case, the peaks assume either positive or negative values. As found for the self impedances, the right–hand side plots show that the spectra for the imaginary parts are characterised by a discontinuity in correspondence of the resonance frequencies where the co–respective real part

peaks. However, in this case the jumps can be either from negative to positive values or from positive to negative values. Thus, the interior fluid produces a combination of stiffness, dissipative and mass effects also between pairs of structural modes, although the order of the stiffness and mass effects is inverted for certain pairs of structural modes. This phenomenon is indicative of an energy transfer between pairs of modes. Similarly to the self impedance functions shown in Figure 5, the average magnitude of the impedances for breathing modes with circumferential mode order $m_2 = 0$ is much larger than that of modes with higher circumferential mode orders. Also, for a given circumferential mode order, the average magnitude tends to decrease as the axial mode number $m_1$ rises. Finally, as seen for the modal impedances produced by the external fluid, Eqs. (39) and (40) indicate that the modal impedance is proportional to the specific acoustic impedance of the fluid $\rho c_0$. Thus the energy absorption and transfer effects as well as the mass effects become increasingly important for heavy fluids, e.g. water. In general, for light fluids such as air, the mutual fluid loading is neglected and the self fluid loading is assumed purely dissipative. In this way, as seen for the modal impedances exerted by the exterior fluid, the self dissipative effects are described in terms of a viscous damping ratio, which is often considered constant and equal for all modes, although it should comply with the typical spectra shown in the left–hand side plots of Figure 5.

### 1.6 Interior noise radiation and vibration of the shell structure

To effectively establish the interior sound radiation and global flexural response of the enclosing flexible wall, it is convenient to express the two phenomena in terms of energy functions, which embrace in a single term the spatially distributed characteristics of the sound and flexural vibration fields. Moreover, the stochastic nature of the disturbance pressure field exerted by the TBL fluid flow necessarily leads to the expression of these energy functions in terms of concepts and formulations for random processes. Thus a particular formulation is presented below, which refers to a similar study proposed by (Gardonio et al. 2012) and considers the formulation for stationary stochastic processes given in (Bendat and Piersol 2000).

The overall sound radiation to the interior of a cavity can be established in terms of the time-averaged total acoustic potential energy $\overline{E}_p$, which can be expressed as follows (Nelson and Elliott 1992):

$$\overline{E}_p = \lim_{T\to\infty} \frac{1}{T} \int_{-T/2}^{+T/2} \frac{1}{2\rho c_0^2} \int_V p(\mathbf{x}_c, t)^2 \, dV \, dt \quad , \tag{43}$$

where the instantaneous total acoustic potential energy is given by $E_p(t)=\frac{1}{2\rho c_0^2}\int_V p(\mathbf{x}_c,t)^2 dV$. For stationary and ergodic processes, such as the interior sound radiation induced by the pressure field due to a fully developed TBL, this quantity can be derived in terms of a "Power Spectral Density" (PSD) function of the total acoustic potential energy $S_{Ep}(\omega)$

$$\overline{E}_p = \frac{1}{2\pi}\int_{-\infty}^{+\infty} S_{Ep}(\omega)d\omega \ . \tag{44}$$

Normally, in acoustics, rather than considering the averaged function, the corresponding frequency spectrum is studied, which can be plotted graphically and provides a deeper insight on the physics of the sound radiation phenomenon under study. According to (Bendat and Piersol 2000), the PSD of the total potential energy $S_{Ep}(\omega)$ can be derived starting from the following expression:

$$S_{Ep}(\omega)=\frac{1}{2\rho c_0^2}\int_V \lim_{T\to\infty}\mathrm{E}\left[\frac{1}{T}p^*(\mathbf{x}_c,\omega)p(\mathbf{x}_c,\omega)\right]dV \ , \tag{45}$$

where the superscript * indicates the complex conjugate, $\mathrm{E}[\ldots]$ denotes the expectation operator. The interior pressure can be derived from Eq. (19) with $\dot{v}_n(\mathbf{x}_s)=\dot{w}(\mathbf{x}_s)$, where $\hat{G}_c(\mathbf{x}_c\,|\,\mathbf{x}_s)$ is given by Eq. (22) and $\dot{w}(\mathbf{x}_s)$ is derived from Eq. (26), so that

$$p(\mathbf{x}_c)=-j\rho\omega c_0^2\sum_{\substack{n=1\\ \alpha=s,a}}^{\infty}\frac{\psi_n^{\alpha}(\mathbf{x}_c)}{\overline{V}\left(\omega_{a,n}^2-\omega^2+j2\zeta_{a,n}\omega_{a,n}\omega\right)}\int_{S_b}\psi_n^{\alpha}(\mathbf{x}_s)\,j\omega\sum_{\substack{m=1\\ \alpha=s,a}}^{\infty}\phi_{r,m}^{\alpha}(\mathbf{x}_s)b_{r,m}^{\alpha}dS_b \ . \tag{46}$$

Thus, after some mathematical manipulations, the PSD of the total acoustic potential energy can be expressed with the following matrix relation

$$S_{Ep}=\frac{V}{2\rho c_0^2}\omega^2\mathrm{Tr}\left[\mathbf{S}_{\mathbf{qq}}(\omega)\right] \ , \tag{47}$$

where $\mathrm{Tr}[\ldots]$ is the trace of the matrix $\mathbf{S}_{\mathbf{qq}}$ with the self and mutual PSDs of the acoustic modal responses, which is given by

$$\mathbf{S}_{\mathbf{qq}}(\omega)=\lim_{T\to\infty}\mathrm{E}\left[\frac{1}{T}\mathbf{q}(\omega)\mathbf{q}^H(\omega)\right]=\mathbf{Q}(\omega)\mathbf{Y}(\omega)\mathbf{S}_{\mathbf{pp}}(\omega)\mathbf{Y}^H(\omega)\mathbf{Q}^H(\omega) \ . \tag{48}$$

Here $\mathbf{Y}=\left[-\omega^2\mathbf{M}+j\omega\mathbf{Z}+\mathbf{K}\right]^{-1}$ is the structural modal admittance matrix that can be derived from Eq. (42). Also, $\mathbf{Q}$ is the acoustic modal impedance matrix whose elements are given by

$$\mathbf{Q}_{nm}^{\alpha} = \frac{\omega\rho c_0^2 C_{mn}^{\alpha}}{\overline{V}\left[2\zeta_{a,n}\omega_{a,n}\omega + j(\omega_{a,n}^2 - \omega^2)\right]} \quad . \tag{49}$$

Finally, the elements of the $\mathbf{S_{pp}}(\omega)$ matrix with the modal excitations PSDs are given by

$$\begin{aligned}\mathbf{S}_{\mathbf{pp},m\bar{m}}(\omega) &= \lim_{T\to\infty} \mathrm{E}\left[\frac{1}{T}\int_{S_b}\int_{S_b'} \phi_m^{\alpha}(\mathbf{x}_s) p_{TBL}^*(\mathbf{x}_s,\omega) p_{TBL}(\mathbf{x}_s',\omega)\phi_{\bar{m}}^{\alpha}(\mathbf{x}_s')dS_b dS_b'\right] \\ &= \int_{S_b}\int_{S_b'} \phi_m^{\alpha}(\mathbf{x}_s) S_{TBL}(\mathbf{x}_s,\mathbf{x}_s',\omega)\phi_{\bar{m}}^{\alpha}(\mathbf{x}_s')dS_b dS_b' \quad ,\end{aligned} \tag{50}$$

where $S_{TBL}(\mathbf{x}_s,\mathbf{x}_s',\omega)$ is the spatial cross spectral density of the TBL blocked pressure field between points $\mathbf{x}_s = (x,y)$ and $\mathbf{x}_s' = (x',y')$:

$$S_{TBL}(\mathbf{x}_s,\mathbf{x}_s',\omega) = \lim_{T\to\infty} \mathrm{E}\left[\frac{1}{T} p^*(\mathbf{x}_s,\omega) p(\mathbf{x}_s',\omega)\right] \quad . \tag{51}$$

Chapter 6 of this book presents an overview of the models and formulations for the spectral density of the pressure field produced by a TBL fluid flow on a rigid wall. Additional review material can be found in references (Blake 1986; Leehey 1988; Bull 1995; Graham 1997; Howe 1998; Cousin 1999; Maury et al. 2002b; Hwang et al. 2009).

The analysis of the sound radiation to the interior is often contrasted with the flexural response of the shell enclosure, which can also be represented in terms of a single function. In fact, the overall flexural vibration of the shell can be established in terms of the time-averaged total flexural kinetic energy $\overline{E}_k$, which can be expressed as follows:

$$\overline{E}_k = \lim_{T\to\infty} \frac{1}{T} \int_{-T/2}^{+T/2} \tfrac{1}{2}\int_{S_b} \rho_s h \dot{w}(\mathbf{x}_s,t)^2 dS_b \, dt \quad , \tag{52}$$

where the instantaneous total flexural kinetic energy is given by $E_k(t) = \frac{1}{2}\int_{S_b} \rho_s h \dot{w}(\mathbf{x}_s,t)^2 dS_b$. As seen with the interior sound radiation, for stationary and ergodic processes this quantity can be derived in terms of the PSD functions of the total kinetic energy $S_{Ek}(\omega)$:

$$\overline{E}_k = \frac{1}{2\pi}\int_{-\infty}^{+\infty} S_{Ek}(\omega) d\omega \quad , \tag{53}$$

where

$$S_{Ek} = \frac{1}{2}\int_S \rho_s h \lim_{T\to\infty} \mathrm{E}\left[\frac{1}{T}\dot{w}^*(\mathbf{x}_s,\omega)\dot{w}(\mathbf{x}_s,\omega)\right] dS_b \quad . \tag{54}$$

Also, in this case, the orthonormality property of the structural natural modes leads to the following simple matrix expression

$$S_{Ek} = \frac{1}{2} M\omega^2 \mathrm{Tr}\left[\mathbf{S}_{\mathbf{bb}}(\omega)\right] , \tag{55}$$

where the matrix $\mathbf{S}_{\mathbf{bb}}(\omega)$ with the self and mutual PSDs of the structural modal responses is given by:

$$\mathbf{S}_{\mathbf{bb}}(\omega) = \lim_{T\to\infty} \mathrm{E}\left[\frac{1}{T}\mathbf{b}(\omega)\mathbf{b}^H(\omega)\right] = \mathbf{Y}(\omega)\mathbf{S}_{\mathbf{pp}}(\omega)\mathbf{Y}^H(\omega) \quad . \tag{56}$$

As discussed at the beginning of this section, the space–frequency domains formulation presented above can also be developed in the wavenumber–frequency domain. For instance, as discussed in Chapter 6, the spatial cross spectral density of the excitation field can be expressed in terms of the wavenumber spectral density function $S_{TBL}(\mathbf{k},\omega)$ by means of inverse space–Fourier transform such that:

$$S_{TBL}(\mathbf{x}_s,\mathbf{x}'_s,\omega) = \frac{1}{(2\pi)^2}\int_{-\infty-\infty}^{+\infty+\infty} S_{TBL}(\mathbf{k},\omega) e^{j\mathbf{k}(\mathbf{x}-\mathbf{x}')} d^2\mathbf{k} \quad , \tag{57}$$

where the vector $\mathbf{k}$ contains the wavenumber components in the stream-wise and cross-wise directions of the fluid flow. Substitution of this expression into Eq. (50) leads to the following expression for the elements of the matrix with the modal excitations PSDs

$$\begin{aligned} \mathbf{S}_{\mathbf{pp},m\bar{m}}(\omega) &= \int_{S_b}\int_{S'_b} \phi_m^\alpha(\mathbf{x}_s)\, \frac{1}{(2\pi)^2}\int_{-\infty-\infty}^{+\infty+\infty} S_{TBL}(\mathbf{k},\omega) e^{j\mathbf{k}(\mathbf{x}-\mathbf{x}')} d^2\mathbf{k}\ \ \phi_{\bar{m}}^\alpha(\mathbf{x}'_s) dS_b dS'_b \\ &= \frac{1}{(2\pi)^2}\int_{-\infty-\infty}^{+\infty+\infty} \phi_m^\alpha(\mathbf{k}) S_{TBL}(\mathbf{k},\omega) \phi_{\bar{m}}^\alpha(\mathbf{k})^* d^2\mathbf{k} \end{aligned} \quad , \tag{58}$$

where the *shape functions* $\phi_m^\alpha(\mathbf{k},\omega)$ are given by the space–Fourier transforms of the natural modes:

$$\phi_m^\alpha(\mathbf{k}) = \int_{S_b} \phi_m^\alpha(\mathbf{x}_s) e^{-j\mathbf{k}\mathbf{x}} dS_b \quad . \tag{59}$$

Here the integration is restricted to the surface of the structure $S_b$ since $\phi_m^\alpha(\mathbf{x}_s) = 0$ for $\mathbf{x}_s \notin S_b$. Eq. (58) highlights how the wavenumber approach leads

to a formulation where the frequency–dependent modal excitation produced by the TBL fluid flow, $\mathbf{S}_{\mathbf{pp},m\bar{m}}(\omega)$, is given by the unbounded integral in the wavenumber domain of the product of the wavenumber spectral density function for the excitation field $S_{TBL}(\mathbf{k},\omega)$ and the wavenumber spectrum of the natural modes $\phi^{\alpha}_{\bar{m}}(\mathbf{k},\omega)$, i.e. the shape functions. Thus it can be interpreted as the result of a filtering effect between the wavenumber spectrum of the excitation field and the wavenumber spectrum of the natural modes.

The spatial Fourier transform approach can be extended also to the early part of the formulation presented above for the derivation of the total potential energy PSD, $S_{Ep}(\omega)$, and total kinetic energy PSD $S_{Ek}(\omega)$. In this case, as shown by Mazzoni (2003) and Maury et al. (2002a), the PSD functions are derived from the wavenumber integrals of the products of wavenumber spectra for the TBL excitation, the modal shapes and the structural–acoustic modal response functions. With this "full wavenumber" approach, the structural response and interior sound radiation are thus derived as the product of wavenumber spectra for the excitation, modal couplings and structural and acoustic responses, each producing a specific filtering effect. This appears to be a very interesting and appealing approach for studying the response of a system, although some practice is required to produce accurate analyses.

## 2. Sound Radiation by a Baffled Panel Subject to TBL Exciation

The formulation presented in the section above has provided a general modelling framework for the structural–acoustic coupled response of a closed shell, which is excited by the pressure field exerted by the TBL fluid flow. A simplified model problem is now considered in order to identify the principal properties of the interior sound radiation generated by a flexible wall subject to a TBL pressure field. As schematically shown in Figure 7, the model problem considered here comprises a thin flat rectangular panel, which is baffled and immerged in an unbounded fluid. The panel is excited by a TBL pressure field on the outer side and radiates sound to the inner side. The panel is considered to be immerged in air, in which case, based on the considerations presented in Section 1.5, the so called "weakly coupled response" is derived by neglecting the fluid loading effects on both sides of the panel. This type of model provides the principal features for the sound radiation to the interior of a large and heavily damped enclosure produced by a section of the enclosure wall.

For this type of problem, the interior sound radiation is expressed in terms of the time-averaged total radiated sound power $\overline{P}_r$, which can be derived with the following formula:

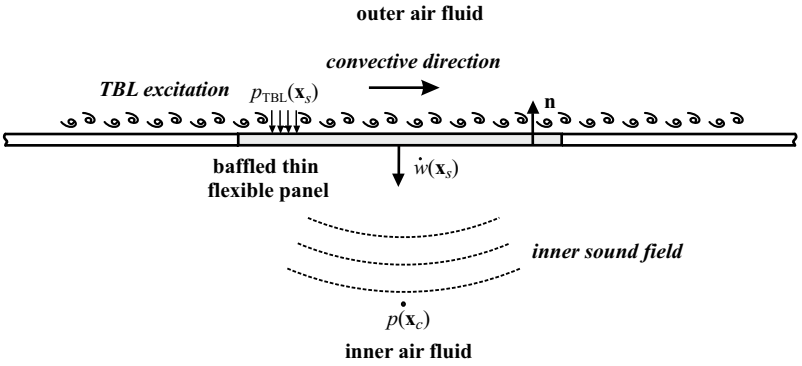


**Figure 7.** Model problem composed of a baffled flexible panel, which is excited by a TBL pressure field on the outer side and radiates sound on the inner side.

$$\overline{P}_r = \lim_{T\to\infty} \frac{1}{T} \int_{-T/2}^{+T/2} \int_{S_b} \dot{w}(\mathbf{x}_s,t)\, p(\mathbf{x}_s,t) dS_b\, dt \ . \tag{60}$$

Here the spatial integral is for the instantaneous total radiated sound power $P_r(t) = \int_{S_b} \dot{w}(\mathbf{x}_s,t) p(\mathbf{x}_s,t) dS_b$ (Fahy and Gardonio 2007). As discussed in the previous section, assuming the process is stationary and ergodic, this quantity can be derived with the following relation:

$$\overline{P}_r = \frac{1}{2\pi} \int_{-\infty}^{+\infty} S_{\mathrm{Pr}}(\omega) d\omega \ , \tag{61}$$

where the PSD function of the total radiated sound power $S_{\mathrm{Pr}}(\omega)$ is given by (Gardonio et al. 2012):

$$S_{\mathrm{Pr}} = \frac{1}{2} \int_{S_b} \lim_{T\to\infty} \mathrm{E}\left[ \frac{1}{T} \dot{w}^*(\mathbf{x}_s,\omega)\, p(\mathbf{x}_s,\omega) \right] dS_b \ . \tag{62}$$

The complex velocity $\dot{w}(\mathbf{x}_s,\omega)$ can be derived from the modal expansion of the transverse displacement, which is given by Eq. (25c). Also, as discussed in

Section 1.2, the sound pressure over the surface of the panel can be derived from the Rayleigh integral given in Eq. (12) assuming[5] $\dot{v}_n(\mathbf{x}_s) = -\dot{w}(\mathbf{x}_s)$, so that

$$p(\mathbf{x}_s) = \frac{j\omega\rho}{2\pi}\int_{S_b} \dot{w}(\mathbf{x}'_s)\frac{e^{-jk|\mathbf{x}'_s-\mathbf{x}_s|}}{|\mathbf{x}'_s-\mathbf{x}_s|}dS_b \quad . \tag{63}$$

Substituting this equation into Eq. (62) and considering the modal expansion for the panel velocity derived from Eq. (25c), after some mathematical manipulations, the following expression is derived for the radiated sound power PSD

$$S_{\mathrm{Pr}} = \frac{1}{2}\omega^2 \mathrm{Tr}\left[\mathbf{A}(\omega)\mathbf{S}_{\mathbf{bb}}(\omega)\right] \tag{64}$$

where $\mathbf{A}(\omega)$ is the *power transfer matrix* that defines the sound power radiated by single modes (diagonal terms) and pairs of modes (off diagonal terms). For a flat rectangular panel the power transfer matrix is given by (Fahy and Gardonio 2007)

$$\mathbf{A}(\omega) = \frac{\omega\rho}{4\pi}\int_{S_b}\int_{S'_b} \boldsymbol{\varphi}_r^T(\mathbf{x}_s)\frac{\sin kd}{kd}\boldsymbol{\varphi}_r(\mathbf{x}_s)dS_b dS'_b \quad , \tag{65}$$

where $d = |\mathbf{x}_s - \mathbf{x}'_s|$ is the distance between point $\mathbf{x}_s$ and point $\mathbf{x}'_s$. Also, the matrix $\mathbf{S}_{\mathbf{bb}}(\omega)$ with the self and mutual PSDs of the modal responses is given by

$$\mathbf{S}_{\mathbf{bb}}(\omega) = \lim_{T\to\infty}\mathrm{E}\left[\frac{1}{T}\mathbf{b}(\omega)\mathbf{b}^H(\omega)\right] = \mathbf{Y}(\omega)\mathbf{S}_{\mathbf{pp}}(\omega)\mathbf{Y}^H(\omega) \quad , \tag{66}$$

where the structural modal admittance matrix $\mathbf{Y}$ is obtained from the modal equations of motion of the plate structure. More specifically, as seen for the cylinder structure, the unknown complex modal amplitudes $b_{r,m}$ are derived by substituting Eq. (25c) into Eq. (24c) with the differential operator $L_3(\ldots)$ for flexural vibration of thin flat plates (Graff 1975; Cremer et al. 1988; Reddy 2006). The resulting equation is then multiplied by a $\overline{m}$ –th mode and integrated over the surface of the plate so that, using the orthonormality property of the natural modes and assuming hysteretic structural damping, the following set of uncoupled ordinary equations is obtained:

$$M_p\left(\omega_{s,m}^2(1+j\eta)-\omega^2\right)b_{r,m} = f_{r,m} \quad , \tag{67}$$

[5] Also for this system, as shown in shown in Figure 7, the standard notation used for the Helmholtz integral equation is used where the vector **n** points away from the acoustic domain, thus $\dot{v}_n(\mathbf{x}_s) = -\dot{w}(\mathbf{x}_s)$.

where $M_p$ is the mass of the panel and $f_{r,m}$ is the *m*–th modal excitation term, which is given by

$$f_{r,m} = \int_{S_b} f_r(\mathbf{x}'_s)\phi_{r,m}(\mathbf{x}'_s)dS_s \quad . \tag{68}$$

For a flat rectangular thin panel, the natural frequencies and natural modes are given by:

$$\omega_{s,m} = \sqrt{\frac{B_p}{m_p}}\left[\left(\frac{m_1\pi}{l_{xp}}\right)^2 + \left(\frac{m_2\pi}{l_{yp}}\right)^2\right], \quad \phi_m(\mathbf{x}_s) = 2\sin\left(\frac{m_1\pi x}{l_{xp}}\right)\sin\left(\frac{m_2\pi y}{l_{yp}}\right) \tag{69a,b}$$

where $m_p = \rho_p h_p$, $M_p = \rho_p h_p l_{xp} l_{yp}$ and $B_p = E_p h_p^3 / \left[12(1-\nu_p^2)\right]$, assuming $\rho_p$, $E_p$ and $\nu_p$ are respectively the density, Young's modulus of elasticity and Poisson's ratio for the material of the plate. Finally, $m_1$, $m_2$ are the indices in the *x* and *y* directions for the *m*-th mode. As seen in Section 1.5, the set of Eqs. (67), can be casted in the following matrix expression

$$\left[-\omega^2\mathbf{M} + \mathbf{K}(1+j\eta)\right]\mathbf{b}_r = \mathbf{f}_r \quad , \tag{70}$$

where the diagonal elements of the mass and stiffness matrices are given by $\mathbf{M}_{mm} = M_p$ and $\mathbf{K}_{mm} = M_p\omega_{s,m}^2$ respectively and the elements in the modal response and excitation vectors are given by $\mathbf{b}_{r,m} = b_{r,m}$ and $\mathbf{f}_{r,m} = f_{r,m}$ respectively. Thus, the structural modal admittance matrix is given by $\mathbf{Y} = \left[-\omega^2\mathbf{M} + \mathbf{K}(1+j\eta)\right]^{-1}$. In summary, for the simplified model problem considered in this section, the flexural response and interior sound radiation are studied using Eqs. (55) and (64) respectively. The modal amplitudes are derived by substituting Eq. (25c) into Eq. (24c), which, for a flat plate structure, is uncoupled from Eqs. (24a,b) for the in–plane vibration (Soedel 1993). According to Eq. (55) the spatially averaged response of the structure depends on the squared modal responses, which, in turn, depend on the coupling between the distributed excitation field and the natural modes. As illustrated in more detail in the following subsection, the TBL pressure field efficiently couples with all modes. In contrast, for example, a plane acoustic wave incident at a given angle with the normal axis to the plate, tends to couple efficiently with the so called *volumetric modes* which are characterised by a non–zero spatially averaged displacement and thus have both mode orders odd. Eq. (64) shows that the radiated sound power PSD depends on the squared modal amplitudes weighted by the diagonal terms of the matrix $\mathbf{A}(\omega)$ and on the products of pairs of modal amplitudes weighted by the appropriate off-diagonal terms of the matrix $\mathbf{A}(\omega)$.

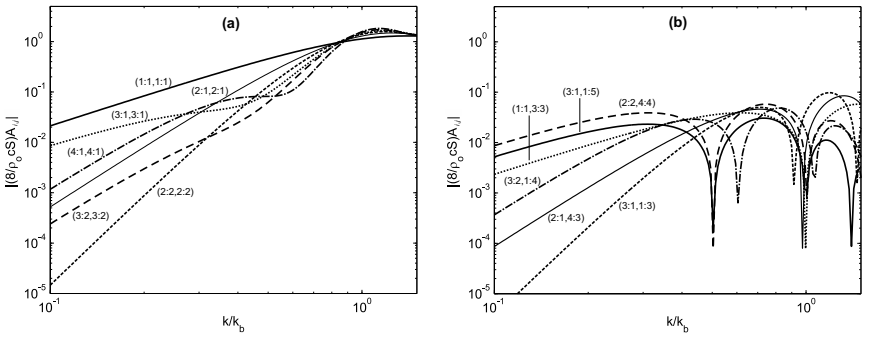


**Figure 8.** Self (a) and mutual (b) radiation efficiencies of the rectangular panel natural modes.

In other words, sound radiation occurs both via self radiation effects of each mode and the cross radiation effects of pairs of modes. Figure 8 shows both the diagonal (plot a) and off-diagonal (plot b) elements of the matrix $\mathbf{A}(\omega)$ for the panel considered in the next subsection with reference to the ratio between the acoustic and flexural wave numbers $k/k_b$. Plot (a) indicates that, at low frequencies such that $k<k_b$ (i.e. for subsonic flexural waves such that $c_b<c$, where $c_b=\sqrt{\omega}\left(B_p/m_p\right)^{1/4}$), the self radiation effect of each mode is rather weak and tends to increase with frequency until it reaches the maximum value around $k/k_b=1$ (i.e. for sonic flexural waves with $c_b=c$). Volumetric modes characterised by both odd mode orders tend to radiate sound more efficiently than other modes. Also, the radiation efficiency tends to decrease as the mode orders raise. For frequencies such that $k>k_b$ (i.e. for supersonic flexural waves with $c_b>c$) all modes become efficient radiators of sound. Plot (b) shows that the mutual radiation effects are comparatively smaller than the self radiation effects, particularly at higher frequencies such that $k>0.5k_b$. Also, the curves in the graph are characterised by sharp dips around certain values of the ratio $k/k_b$, which are due to the fact that the off diagonal terms in matrix $\mathbf{A}(\omega)$ alternate between positive and negative values and thus their moduli go to zero at certain values of the ratio $k/k_b$ (Fahy and Gardonio 2007). This interesting finding indicates that for certain frequency bands, the mutual sound radiation effect of pairs of modes may be either positive or negative; in other words it may enhance or reduce the total sound radiation. Therefore, reducing the response due to some

specific modes could lead to reductions of sound radiation at given frequency bands, but to the enhancement of sound radiation at other frequency bands (Fuller et al. 1996).

### 2.1 Physics of TBL sound radiation by a baffled panel

In order to better understand the physics of the interior sound radiation generated by a TBL pressure field on the panel (Figure 9d), three typical sound radiation problems are considered first, which are due to the following excitation fields acting upon the panel: a) the fully correlated pressure field generated by a time–harmonic "acoustic plane wave" (APW) with grazing, 45$^o$ and normal angles of incidence (Figure 9a); b) the partially correlated pressure field generated by an "acoustic diffuse field" (ADF), which is composed by a random distribution of plane waves whose energies are equally divided over all angles of incidence (Figure 9b) and c) the fully uncorrelated pressure field due to the so called "rain on the roof" (ROR) random excitation, which is characterised by a uniform distribution of point forces totally uncorrelated between each other (Figure 9c). The panel is assumed simply supported along the perimeter and its dimensions and material properties are summarised in Table 2.1. An extended version of this analysis can be found in (Rohlfing and Gardonio 2009).

The panel response and the sound radiation produced by the ADF, ROR and TBL excitations are analysed in terms of the total kinetic energy PSD and total radiated sound power PSD, derived with the formulation presented in the

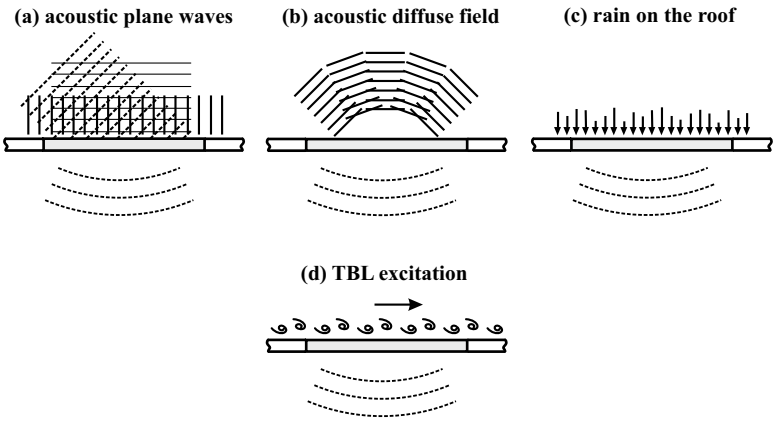


**Figure 9.** Sound radiation induced by: a) APW at grazing, normal and 45$^o$ incidence angles, b) ADF, c) ROR and d) TBL.

**Table 2.1.** Geometry and physical parameters for the panel.

| Parameter | Value |
|---|---|
| dimensions | $l_{xp} \times l_{yp} = 278 \times 247$ mm |
| thickness | $h_p = 1.6$ mm |
| mass density | $\rho_p = 2720\,\mathrm{Kg/m^3}$ |
| Young's modulus | $E_p = 7 \times 10^{10}$ N/m$^2$ |
| Poisson ratio | $\nu_p = 0.33$ |
| Structural loss factor | $\eta = 0.02$ |

previous section. For the fully correlated time–harmonic plane wave acoustic excitations, the panel response and sound radiation are instead investigated with reference to the spectra of the time–averaged total kinetic energy $\overline{E}_k(\omega)$ and time–averaged total radiated sound power $\overline{P}_r(\omega)$. These two frequency–dependent functions are derived from Eqs. (52) and (60) respectively. Thus, as discussed in (Fahy and Gardonio 2007), these two functions can be derived in terms of the complex modal responses with the following two matrix expressions:

$$\overline{E}_k(\omega) = \frac{\rho_p h_p}{4} \int_{S_b} \left| \dot{w}(\mathbf{x}_s, \omega) \right|^2 dS_b = \frac{1}{4} \omega^2 M_p \mathbf{b}_r(\omega)^H \mathbf{b}_r(\omega) \ , \tag{71}$$

$$\overline{P}_r(\omega) = \frac{1}{2} \int_{S_b} \mathrm{Re}\left[ \dot{w}(\mathbf{x}_s, \omega)^* \, p(\mathbf{x}_s, \omega) \right] dS_b = \omega^2 \mathbf{b}_r(\omega)^H \mathbf{A}(\omega) \mathbf{b}_r(\omega) \ , \tag{72}$$

where the vector $\mathbf{b}_r(\omega)$ is derived from Eq. (70). The pressure field over the surface of the panel produced by an acoustic wave with azimuthal and elevation (with reference to the normal of the plate) angles, $\phi$ and $\theta$ respectively, can be expressed as:

$$p_{APW}(\mathbf{x}'_s, t) = \mathrm{Re}\left\{ \hat{p}_{APW}(\omega) \, e^{j(\omega t - k_x x' - k_y y')} \right\} \ , \tag{73}$$

where $\hat{p}_{APW}(\omega)$ is the complex amplitude of the incident wave and $k_x = k \sin(\theta)\cos(\phi)$, $k_y = k \sin(\theta)\sin(\phi)$ are the wave number components in $x$ and $y$ directions. Thus, the incident acoustic plane wave produces a waved pressure field on the panel whose wavelength is given by $\lambda / \sin\theta$. For instance, as schematically depicted in Figure 5a, for grazing angle of incidence such that

$\theta=90^o$, the waved pressure field acting on the panel is characterised by the same wavelength as that of the incident acoustic field. When the angle of incidence turns to $\theta=45^o$, the wavelength of the pressure field acting on the panel becomes $\sqrt{2}$ times longer than that of the incident acoustic wave. Finally, if the angle of incidence is further reduced towards $\theta=0^o$ the projection of the acoustic wavelength into the plane of the plate tends to infinity and thus the pressure field is no more waved and becomes spatially uniform. Moving back to the formulation for the response and sound radiation of the plate, considering the excitation pressure field given in Eq. (73), the modal excitation terms $f_{r,m}$ in Eq. (68) result (Wang et al. 1991):

$$f_{r,m}(\omega)=2\hat{p}_{APW}(\omega)\int_S \phi_{r,m}(x,y)\,e^{-j(k_x x+k_y y)}dS=4\,\hat{p}_{APW}(\omega)\,I_{m_1}I_{m_2}l_{xp}l_{yp} \tag{74}$$

where, if $m_1\pi\neq\pm\sin\theta\cos\phi(\omega l_{xp}/c_o)$ and $m_2\pi\neq\pm\sin\theta\sin\phi(\omega l_{yp}/c_o)$,

$$I_{m_1}=\frac{m_1\pi\left[1-(-1)^{m_1}e^{-j\sin\theta\cos\phi(\omega l_{xp}/c_o)}\right]}{\left[m_1\pi\right]^2-\left[\sin\theta\cos\phi(\omega l_{xp}/c_o)\right]^2} \quad , \quad I_{m_2}=\frac{m_2\pi\left[1-(-1)^{m_2}e^{-j\sin\theta\sin\phi(\omega l_{yp}/c_o)}\right]}{\left[m_2\pi\right]^2-\left[\sin\theta\sin\phi(\omega l_{yp}/c_o)\right]^2}, \tag{75a,b}$$

and, if $m_1\pi=\pm\sin\theta\cos\phi(\omega l_{xp}/c_o)$ and $m_2\pi=\pm\sin\theta\sin\phi(\omega l_{yp}/c_o)$,

$$I_{m_1}=\frac{j}{2}sgn(\sin\theta\cos\phi) \quad , \quad I_{m_2}=\frac{j}{2}sgn(\sin\theta\sin\phi)\ . \tag{76a,b}$$

The response and sound radiation produced by the other three types of excitations are instead analysed in terms of the total kinetic energy PSD and total radiated sound power PSD derived with the formulations presented in Sections 1.6 and 2 respectively. Thus the excitations are expressed in terms of cross spectral density functions. The cross spectral density for the diffuse sound field excitation is assumed

$$S_{ADF}(\mathbf{x}_s,\mathbf{x}'_s,\omega)=\hat{S}_{ADF}(\omega)\frac{\sin kd}{kd} \tag{77}$$

where in this case $d=|\mathbf{x}_s-\mathbf{x}'_s|$ is the distance between the two points $\mathbf{x}_s$ and $\mathbf{x}'_s$ and $\hat{S}_{ADF}(\omega)$ is the PSD of the ADF excitation at any point on the panel. Thus the ADF cross spectral density function is the same in all directions and is characterised by the so called "sinc" function which is shown by the dashed line in Figure 10. For the fully uncorrelated rain on the roof excitation, the cross spectral density is assumed as

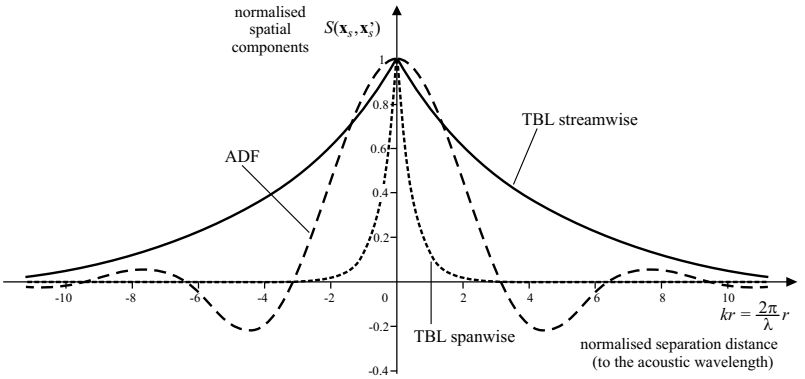


**Figure 10.** Normalised spatial components of the cross spectral density function of the TBL excitation in stream–wise (solid line) and span–wise (dotted line) directions and ADF excitation (dashed line) with reference to the separation distance *r* per unit acoustic wavelength.

$$S_{ROR}(\mathbf{x}_s, \mathbf{x}_s', \omega) = \begin{cases} 0 & \text{for } \mathbf{x}_s' \neq \mathbf{x}_s \\ \widehat{S}_{ROR}(\omega) & \text{for } \mathbf{x}_s' = \mathbf{x}_s \end{cases}, \tag{78}$$

where, in this case, $\widehat{S}_{ROR}(\omega)$ is the PSD of the ROR excitation at any point on the panel. Thus the cross spectral density is characterised by a delta function. As discussed in Chapter 6, the cross spectral density for TBL excitation is derived from the Corcos model, so that (Corcos 1963a; Corcos 1963b; Corcos 1967)

$$S_{TBL}(\mathbf{x}_s, \mathbf{x}_s', \omega) = \widehat{S}_{TBL}(\omega) e^{-|r_x|/L_x} e^{-|r_y|/L_y} e^{-j\omega r_y/U_c}, \tag{79}$$

where $\widehat{S}_{TBL}(\omega)$ is the PSD of the TBL excitation at any point on the panel, $r_x$ and $r_y$ are the *x* and *y* components of the distance between points $\mathbf{x}_s$ and $\mathbf{x}_s'$, $L_x = \alpha_x U_c/\omega$ and $L_y = \alpha_y U_c/\omega$ are the correlation lengths in *x* and *y* directions and $U_c$ is the convective velocity, which is normally derived from the relation $U_c = KU_\infty$, with $0.6 \leq K \leq 0.85$ (Cousin 1999). In this study, the convective velocity is assumed to be $U_c = 0.6U_\infty$, where the free flow velocity is taken as $U_\infty = 225\text{m/s}$. Also, as indicated in references (Maury et al. 2004; Elliott et al. 2005), the empirical parameters $\alpha_x$ and $\alpha_y$ are assumed to be 1.2 and 8

respectively. According to Eq. (79), the TBL cross spectral density function varies with direction and is characterised by two exponentially decaying functions in the stream-wise and span-wise flow directions. In the stream-wise direction, the convective effect also produces a waved profile of the cross spectral density function. The solid and dotted lines in Figure 10 show that the span-wise component decays more rapidly than that in the stream-wise direction. This is due to the fact that the correlated pressure field produced by each vortex in the turbulent fluid flow is smeared in the direction of the flow by the motion of the fluid.

The comparative analysis of the structural response and sound radiation produced by these four types of excitations will be carried out considering the spectra of the time–averaged total kinetic energy and of the time–averaged total radiated sound power produced by the APW excitations with unit amplitude, i.e. $\widehat{p}_{APW}(\omega)=1$. Also the spectra of the total kinetic energy PSD and total radiated sound power PSD produced by the ADF, ROR and TBL excitations will be considered assuming they have unit PSD, i.e. $\widetilde{S}_{ADF}(\omega)=\widetilde{S}_{RR}(\omega)=\widetilde{S}_{TBL}(\omega)=1$. In this way the specific characteristics of the structural response and sound radiation produced by the TBL pressure field are contrasted with those of the other three excitations independently from the specific energy distribution in frequency of each type of excitation.

### 2.2 APW excitation

The effects produced by the acoustic plane wave excitations are considered first. The three lines in plots (a) and (b) of Figure 11 show the spectra of the time–averaged total kinetic energy and total radiated sound power by the panel due to acoustic plane waves at grazing, $45^{o}$ and normal angles of incidence as depicted in Figure 9a. Considering first the kinetic energy plot (a), the three lines show that, at low frequency the spectra are characterised by sharp and well separated peaks due to the natural modes of the panel. The spectrum for the acoustic plane wave excitation with normal angle of incidence (dotted line) is characterised by fewer resonance peaks, as this type of wave excites only the modes with a net non–zero volumetric displacement, that is modes with both odd mode orders. At frequencies above the first resonance frequency of the panel, the mean kinetic energy spectra tend to fall with a typical 6 dB/octave slope, i.e. the so called “mass law”, which is due to the mass effect of the panel. As the frequency rises, the resonance peaks in the kinetic energy spectra progressively overlap so that the spectra show wide rounded crests spaced out by wide troughs, which are due to the clustering of many resonance peaks at given frequency bands. This effect is specific to the structure at hand and is quantified by the “modal overlap” factor

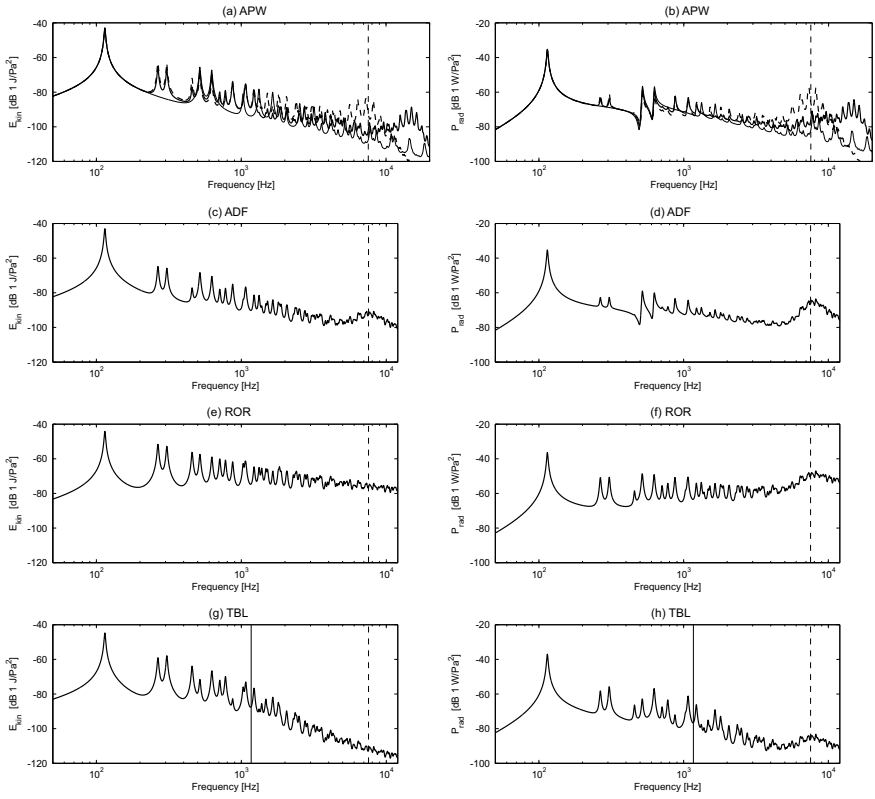


**Figure 11.** Spectra of the total kinetic energy (left–hand side plots) and total radiated sound power (right–hand side plots) per unit exciation due to (a,b) APWat grazing (dashed line) 45$^o$ (thick-solid line) and normal (faint-solid line) angles of incidence; (c,d) ADF; (e,f) ROR and (g,h) TBL pressure fields.

(Cremer et al. 1988), which gives the number of structural modes of the structure significantly excited at any one excitation frequency. For instance, the modal overlap for thin rectangular plates increases linearly with frequency and is given by

$$N_p(\omega) = \eta\omega n_p(\omega) = \eta\omega \frac{l_{xp} l_{yp}}{4\pi} \left( \frac{m_p}{B_p} \right)^{1/2} \tag{80}$$

where $n_p(\omega)$ is the plate "modal density". For the plate considered in this section the modal overlap reaches the threshold value of 1 at about 3.6 kHz. Starting from this frequency, the response of the panel at each frequency is characterised by the overlap of two or more resonant responses. For frequencies above 5 kHz, the kinetic energy spectra produced by the grazing (dashed line) and 45° (thick-solid line) acoustic plane waves show distinct wide frequency band ridges, which are characterised by multiple resonance peaks. These phenomena are generated by the so called "coincidence effect" where the projection of the acoustic wavelength into the plane of the panel equals the frequency-dependent bending wavelength, i.e. $\lambda/\sin\theta = \lambda_b$, and thus the waved pressure field produced on the plate by the incident acoustic plane wave couples effectively with the structural wave motion (Fahy and Gardonio 2007). Consequently, for frequencies close to the "acoustic coincidence frequency" $\omega_{co}$, such that $\lambda/\sin\theta = \lambda_b$, the response of the panel increases and forms the wide frequency band crests with multiple resonance peaks that can be seen in the kinetic energy spectra produced by the grazing and 45° incident acoustic waves (dashed and thick-solid lines respectively). Since for acoustic waves $\lambda = 2\pi/k$, with the wavenumber given by $k = \omega/c$, and since for thin plates $\lambda_b = 2\pi/k_b$, with the wavenumber given by $k_b = \omega/c_b = \sqrt{\omega}\left(m_p/B_p\right)^{1/4}$, the acoustic coincidence frequency can be readily derived as follows:

$$\omega_{co} = \frac{\omega_{cr}}{\sin^2\theta} \quad , \tag{81}$$

where

$$\omega_{cr} = c^2\left(\frac{m_p}{B_p}\right)^{1/2} \tag{82}$$

is the so called "critical frequency", which is highlighted with the thick-dashed vertical lines in the plots of Figure 11 and represents the smallest coincidence frequency that occurs for acoustic waves incident at grazing angle, that is $\theta = 90°$. For the panel at hand, the critical frequency occurs at about 7.54 kHz. Eq. (81) indicates that the coincidence frequency tends to infinity as $\theta \to 0$, thus as the acoustic wave approaches normal angle of incidence. Indeed the kinetic energy spectra produced by the normal acoustic plane wave excitation (faint-solid line) do not show the wide frequency band ridge found for the grazing and 45° excitations (dashed and thick-solid lines respectively). Normally, the coincidence phenomenon between flexural waves in the structure and acoustic waves in the

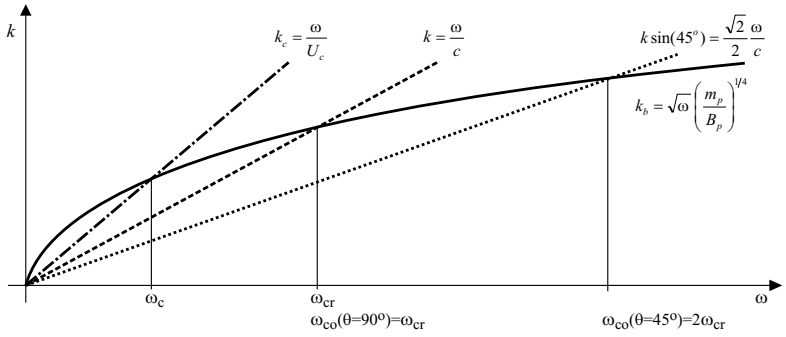


**Figure 12.** Dispersion curves relative to a) flexural waves in a thin plate (solid line), b) acoustic trace wave for grazing incidence (dashed line), c) acoustic trace wave for 45° incidence and d) convective flow (dash-dotted line).

fluid is analysed with reference to the dispersion curves for the two types of waves. For instance, Figure 12 shows that the dispersion curve for the trace of the acoustic wave at grazing angle with the panel (dashed line) intersects the dispersion curve for flexural wave propagating in the plate (solid line) exactly at the critical frequency, so that $\omega_{co}(\theta=90^o)=\omega_{cr}$. Moreover, the dispersion curve for the trace of the acoustic wave at 45° with the panel (dotted line) intersects the dispersion curve for flexural wave propagation on the thin plate (solid line) at higher frequency than the critical frequency, that is $\omega_{co}(\theta=45^o)=2\omega_{cr}$. Moving back to plot (a) of Figure 11, the dashed and thick-solid lines show that for very high frequencies above the coincidence region, the mean kinetic energy spectrum falls rapidly with a typical 18 dB/octave slope, i.e. following the so called "stiffness law", which is due to the bending stiffness effect of the panel (Fahy and Gardonio 2007).

Considering now plot (b) in Figure 11, it is noted that the spectra of the radiated sound power by the panel due to acoustic plane waves at grazing, 45° and normal angles of incidence (dashed, thick-solid, faint-solid lines respectively) are similar to those found for the kinetic energy. However, at low frequencies where the spectra of the kinetic energy are characterised by well separated resonance peaks, the co-respective spectra of the radiated sound power are characterised by fewer resonance peaks. This is because, as discussed in Section 2.1, at low frequencies such that $k/k_b < 1$, the natural modes characterised by one or both even mode orders are poor sound radiators. As a result the resonant vibration responses due to those natural modes do not turn into a high

sound radiation. For example the resonant responses due to the (1,2) and (2,1) natural modes of the panel produce the second and third sharp resonance peaks in the kinetic energy spectra and the comparatively much smaller second and third resonance peaks in the radiated sound power spectra. For frequencies above the first resonance frequency of the panel, the spectra of the mean radiated sound power tend to fall following the so called mass law, i.e. with a typical 6 dB/octave slope. As found for the kinetic energy spectra, at higher frequencies where the response of the panel at every frequency is characterised by the overlap of multiple modes the sound radiation spectra are characterised by increasingly smoother wide frequency band crests and troughs, which are generated by the resonant response of clusters of natural modes. When the frequency approaches the critical frequency at about 7.54 kHz (highlighted by the thick-dashed vertical line), in all three cases under consideration the sound radiation tends to rise. This is due to the fact that $k/k_b \approx 1$ and thus, as can be noted in Figure 8a, all modes become efficient sound radiators. In particular, when the plate is excited by the plane wave at grazing angle (dashed line), this phenomenon is magnified by the concomitant efficient acoustic excitation effect described above. Thus, the coincidence ridge in the sound radiation spectrum becomes very high. Alternatively, when the plate is excited by the plane wave with a $45^o$ angle of incidence, the spectrum is characterised by a small crest around the critical frequency, which is due to the efficient sound radiation of all modes, and then, at higher frequencies, by another comparatively bigger ridge, which is due to the efficient excitation of the waved pressure field generated on the panel by the acoustic plane wave. Finally, the radiated sound power spectrum of the plate excited by the plane wave with normal angle of incidence (faint-solid line) is characterised only by a small ridge around the critical frequency due to the efficient sound radiation of all modes.

### 2.3 ADF excitation

The effects produced by the acoustic diffuse field excitations are considered next with reference to the spectra of the total kinetic energy PSD and total radiated sound power PSD shown in plots (c) and (d) of Figure 11. At frequencies below acoustic coincidence, the spectrum of the kinetic energy is similar to that found for the $45^o$ acoustic plane wave excitation (thick-solid line in plot (a)). Thus, above the first resonance frequency of the plate, the spectrum of the kinetic energy tends to fall following the mass law with a 6 dB/octave slope. Also, the spectrum becomes increasingly smooth and characterised by wide band crests due to the overlapping of a linearly increasing number of modal responses. Around the critical frequency at about 7.54 kHz, the spectrum shows the wide frequency band ridge with multiple resonance peaks. However, this ridge is

relatively modest in comparison to that found for the grazing acoustic plane wave excitation and extends over a wider frequency band. This is because, as schematically shown in Figure 9(b), the acoustic diffuse field excitation is composed by acoustic plane waves with a uniform distribution of angles of incidence. Thus the excitation coincidence phenomenon extends to all frequencies starting from the critical frequency (highlighted by the thick-dashed vertical line) to infinity. Since the energy of the diffuse excitation field is equally divided between waves at all angles of incidence, the excitation coincidence phenomenon at every frequency, and thus for every angle of incidence, is not as strong as that for the single plane wave with a fixed angle of incidence. However, it spans over a much wider frequency range, ideally up to infinity.

In general the observations made for the spectrum for the total kinetic energy also apply to the spectrum for the total radiated sound power. In fact, for frequencies below acoustic coincidence, the radiated sound power shown in plot (d) is similar to that found for the $45^o$ acoustic plane wave excitation (solid line in plot b). Thus, at low frequencies, the spectrum of the radiated sound power PSD is characterised by a smaller number of well separated resonances since the sound radiation mechanism tends to filter out those resonances due to plate natural modes with both or one even mode orders. As the frequency rises above the fundamental resonance frequency of the plate, the spectrum of the mean radiated sound power tends to fall according to the mass law with a slope of 6 dB/octave. When the frequency reaches the critical frequency at about 7.54 kHz (highlighted by the thick-dashed vertical line), the spectrum shows a wide band ridge, which is less marked than that visible in plot (b) for the $45^o$ acoustic plane wave excitation (thick-solid line) but is much more noticeable than that found in plot (c) for the kinetic energy due to the diffuse acoustic field excitation. This phenomenon is due to the fact that, on one hand, the diffuse acoustic field distributes the energy to plane waves with all angles of incidence and thus distributes the excitation coincidence effect over all frequencies above the critical frequency and, on the other hand, the sound radiation becomes very effective around the critical frequency.

### 2.4 ROR excitation

The effects produced by the rain on the roof excitation are now analysed considering plots (e) and (f) of Figure 11. Considering first plot (e), it is noted that also in this case the spectrum of the kinetic energy is characterised by well separated resonances, which tend to become wide band crests as the frequency, and thus modal overlap effect, grows. However, contrasting this graph with the two kinetic energy graphs (a) and (c), it is clear that, when the panel is excited by a uniform distribution of uncorrelated forces, all resonant modes are efficiently

actuated. This is due to the fact that, in contrast to acoustic excitations, the rain on the roof excitation is composed by a uniform distribution of fully uncorrelated forces, which equally couples with all natural modes of the panel. Hence the amplitude of the resonance peaks in the spectrum for the kinetic energy tends to be uniform, since the coupling between the ROR excitation field and modal response of the panel does not vary from one mode to another. The relative amplitude of the resonance peaks are solely dictated by the damping effect and by the overlap with neighbouring modes. As a result, at frequencies above the fundamental resonance of the panel, the amplitudes of the resonance peaks are rather uniform and the mean spectrum falls with a 3 dB/octave rate instead of the 6 dB/octave rate found for the plane wave and diffuse acoustic excitations. Thus, as one would expect, the mean spectrum of the panel kinetic energy due to a rain on the roof excitation follows that of the squared point mobility function for the ratio between the transverse velocity and transverse force. This trend carries on also around and beyond the critical frequency at about 7.54 kHz. This is due to the fact that there are no favoured frequencies, such as the acoustic coincidence frequency, where the excitation field effectively couples with the structural response of the panel.

Moving on to the radiated sound power, comparing plot (f) with plots (b) and (d), it is noted that the spectrum of the radiated sound power generated by a rain on the roof excitation presents remarkable differences with respect to the spectra generated by an acoustic plane wave or diffuse field excitations. For instance, in contrast to what found with the acoustic excitations, at low frequencies the sound radiation is characterised by many more resonance peaks, which are due to efficiently and non efficiently radiating modes. Thus the radiated sound power is characterised by a comparatively denser distribution of resonance peaks, which, at low frequency, are well separated and then, as the frequency and modal overlap rise, become wide frequency band crests characterised by the overlap of multiple resonant modes. Moreover the level of the spectrum of the radiated sound power remains constant up to about the critical frequency where it shows the typical wide band ridge. All this is due to two concomitant effects. Firstly, as discussed above, the rain on the roof uniform distribution of uncorrelated point forces equally excites all natural modes of the panel. Secondly, as discussed in (Fahy and Gardonio 2007), in contrast with the modal sound radiation, the sound radiation produced by point forces is constant with frequencies, thus it is very effective also at frequencies well below the critical frequency. Moving back to plot (f), at higher frequencies around the critical frequency at about 7.54 kHz, the sound radiation shows the typical wide frequency band ridge with multiple resonance peaks, which is due to the fact that all structural modes effectively radiates sound.

### 2.5 TBL excitation

The response and sound radiation of the panel when it is excited by the fully developed TBL pressure field is finally studied with reference to the spectra of the total kinetic energy PSD and total sound power radiated PSD shown in plots (g) and (h) of Figure 11. At low frequencies, the spectrum of the kinetic energy PSD is similar to that for the panel excited by the uncorrelated pressure field shown in plot (e). In fact, the response is characterised by well separated sharp resonance peaks of all natural modes with either odd or even mode orders. However, in contrast to what found with the ROR excitation, in this case the amplitude of the resonance peaks is uneven. These effects are produced by two concomitant properties of the TBL excitation. On one hand, as seen for the ROR excitation, the TBL pressure field is composed by a stochastic distribution of small patches of transverse force excitations that couples efficiently with all modes of the panel. On the other hand, the convected fluid tends to smear these excitations in a waved pattern along the stram-wise direction. Thus the coupling of the waved excitation field with the resonant modes varies depending on the plate mode order in the direction of the fluid flow. At about 1.17 kHz, the spectrum of the response PSD shows a small ridge, which is due to the so called "convective coincidence" or "aerodynamic coincidence" effect. As discussed in Chapter 6, the vortexes that develop in the TBL fluid flow are conveyed in the stream-wise direction at the convective velocity $U_c$. Thus the pressure field generated over the panel is characterised by an exponentially decaying correlation function in span-wise direction and a weaved exponentially decaying correlation function in stream-wise direction, whose characteristic wave length is given by $\lambda_c = 2\pi/k_c$, where $k_c = \omega/U_c$ is the convective wave number. As a result, the panel is efficiently excited at frequencies close to the so called "convective coincidence frequency", where the wavelength of the flexural vibration in the flow direction coincides with the correlation wavelength that characterises the TBL pressure field in the stream-wise direction, i.e. $\lambda_b = \lambda_c$. This condition implies that $k_b = k_c$ and thus, considering that $k_b = \omega/c_b = \sqrt{\omega}\left(m_p/B_p\right)^{1/4}$ and $k_c = \omega/U_c$, the convective coincidence frequency can be readily derived as follows:

$$\omega_c = U_c^2 \left( \frac{m_p}{B_p} \right)^{1/2} . \tag{83}$$

This expression suggests that the convective coincidence frequency grows with the square of the convective speed $U_c$. Recalling that the convective speed is a fraction of the flow velocity, i.e. $U_c = KU_\infty$ with $0.6 \le K \le 0.85$ and comparing

Eq. (83) and Eq. (82) for the lower acoustic coincidence frequency, it is noted that

$$\frac{\omega_c}{\omega_{cr}} = K^2 \left( \frac{U_\infty}{c} \right)^2 . \tag{84}$$

Thus, even for a sonic speed of the flow, i.e. $U_\infty = c$, the convective coincidence frequency is $1.4$ to $2.8$ times smaller than the critical frequency. When the speed of the flow is lower than the speed of sound, the convective coincidence frequency becomes much smaller than the lowest acoustic coincidence frequency. Thus, for most vehicles, the convective coincidence effect is likely to occur in the low to mid audio frequency range where noise is mostly perceived as a source of annoyance and, as will be discussed in the next section, passive sound insulation treatments are less effective. Indeed, as can be noted in plot (g), the spectrum of the kinetic energy is characterised by a wide band ridge around the convective coincidence frequency that, as highlighted by the thick-solid vertical line, for the panel and flow conditions at hand, occurs around 1.17 kHz. As seen for the acoustic coincidence phenomenon, the convective coincidence can also be analysed in terms of dispersion curves for the flexural wave and for the fluid-dynamic convective effect. As an example, Figure 12 shows the dispersion curves for the plate flexural wave and for the TBL fluid flow considered in this study. The two curves intersect at $k_b = k_c$, that is at the convective critical frequency $\omega_c$.

Moving back to the analysis of plot (g), at frequencies above the convective coincidence frequency, which is highlighted by the thick-solid vertical line, the spectrum of the kinetic energy becomes increasingly smoother, since the response of the panel at each frequency is due to the overlap of an increasing larger number of modes. As a result, the spectrum is characterised by wide frequency band crests with multiple resonant modes, spaced out by wide frequency band troughs. The spectrum of the kinetic energy falls rapidly with a $12$ dB / octave slope, thus following the so called "stiffness law", since the response is controlled by the stiffness of the panel. The spectrum continues to fall rapidly even at very high frequencies around acoustic coincidence.

Considering now the sound power radiated, by contrasting plots (h) and (f), it is noted that, below and around the convective coincidence frequency, which is highlighted by the thick-solid vertical line, the spectrum of the radiated sound power generated by the TBL excitation is quite similar to that produced by the ROR excitation, although the spectrum in plot (h) shows a much uneven sequence of resonance peaks. This is due to two phenomena. Firstly, as discussed above, the convected stochastic excitation field couples with all modes but

unevenly. Secondly, at frequencies below the acoustic critical frequency, the sound radiation efficiency varies from mode to mode. As seen for the kinetic energy in plot (g), at frequencies above the convective coincidence frequency, the spectrum of the radiated sound power in plot (h) becomes increasingly smoother, since the response of the structure is given by the overlap of an increasingly larger number of modes. Similarly to the spectra obtained for acoustic excitations in plots (b) and (d), the mean value of the spectrum in plot (h) tends to fall with a 6 dB / octave slope up to higher frequencies around the acoustic coincidence frequency, where the spectrum shows the characteristic wide band ridge with multiple resonance peaks due to the enhanced sound radiation properties of all modes. At further higher frequencies, the spectrum resumes the 6 dB / octave slope.

## 3. Passive Treatments to Reduce Sound Radiation

The previous section has shown that the sound radiated to the interior of a distributed thin wall structure is a complex phenomenon that depends on the characteristics of the excitation field, the flexural response of the structure and the radiation properties of the structure. Normally, for a NVH[6] engineer it is rather difficult to work on the excitation and sound radiation aspects in a transportation vehicle, since they strongly depend on the operation conditions and interior design of the vehicle. Thus, the most common option left to reduce noise transmission to the interior is to modify the flexural response of the body of the vehicle. In general, the flexural response of a thin structure is determined by three parameters: a) the mass per unit area, b) the flexural stiffness and c) the structural or fluid damping. Normally structural energy dissipation is modelled by considering a complex modulus of elasticity $\overline{E} = E(1 + j\eta)$, where $\eta$ is the

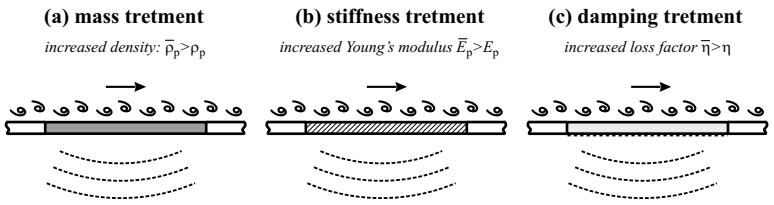


**Figure 13**. Sound radiation induced by a TBL pressure field acting on a panel with (a) mass treatment; (b) stiffness treatment and (c) damping treatment.

[6] NVH stands for Noise Vibration Harness

loss factor (Cremer et al. 1988; Fahy and Gardonio 2007). As discussed in Section 1.5, the energy dissipation arising from the fluid loading on the structure is a complex phenomenon, which however, for light fluids can be modelled in terms of modal damping ratios. In practice, the implementation of passive sound insulation treatments always produces a combination of mass, stiffness and damping effects. However, the treatment can be focused on one of the three properties and described as a mass, or stiffness, or damping treatment. Thus, as schematically depicted in Figure 13, in this section the sound radiation of the panel excited by the TBL pressure field considered in the previous section is analysed with reference to variations in turn of the density (mass-treatment), Young modulus of elasticity (stiffness treatment) and structural loss factor (damping treatment) of the panel. Figure 14 shows the spectra for the total kinetic energy PSD (left–hand side plots a, c, e) and total radiated sound power PSD (right–hand side plots b, d, f) in presence of mass (plots a, b), stiffness (plots c, d) and damping (plots e, f) treatments. The thick-solid lines in the plots show the kinetic energy and radiated sound power spectra for the reference panel considered in the previous section. The solid faint lines show the spectra when one of the three properties are varied. Also, the variations of the acoustic coincidence frequency (thick-dashed vertical line) and convective coincidence frequencies (thick-solid vertical line) are indicated by a thin-dashed vertical line and a thin-solid vertical line respectively.

The effect of increasing by a factor 2 the mass density of the panel is analysed first. Plots (a) and (b) show that the first few resonance frequencies shift to lower values. Also, the transition from a spectrum with well separated resonance frequencies to a smoother spectrum characterised by the overlap of multiple resonant modes at each frequency occurs at lower frequencies. In fact, according to Eq. (80), the modal overlap grows more rapidly with frequency as the mass density is increased. The thick-solid (for the reference panel) and faint-solid (for the heavier panel) vertical lines in the two plots highlight that the increment of mass density shifts to higher frequencies the convective coincidence effect. In particular, as can be deduced from Eq. (83), the convective coincidence frequency of the reference panel at about 1.17 kHz is increased by a factor $\sqrt{m_p'/m_p} = \sqrt{2}$ to about 1.65 kHz for the panel with double density. At higher frequencies the spectra for the reference and heavier panels become increasingly smoother. It is interesting to note that the levels of the two spectra for the kinetic energy nearly coincide while the levels of the two spectra for the radiated sound power are about $6\,\mathrm{dB}$ apart. This discrepancy between the two plots should not mislead the reader. In fact, the kinetic energy plot gives the level of the response of the panel weighted by the mass of the panel. Thus, if the spectrum of the spatially averaged squared transverse velocity PSD was plotted,

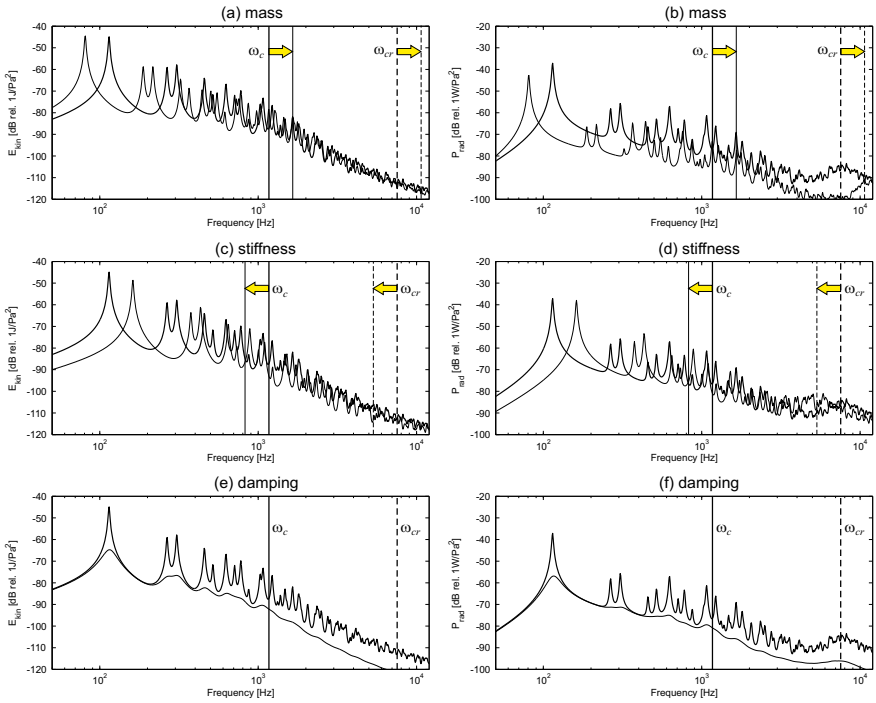


**Figure 14**. PSD of the total kinetic energy (left–hand plots) and total radiated sound power (right–hand plots) per unit turbulent boundary layer pressure field PSD. Thick solid lines reference panel; faint solid lines (a,b) panel with double mass density; (c,d) panel with double Young's modulus; (e,f) panel with ten times higher loss factor. Solid and dashed vertical lines identify the convective coincidence frequency and acoustic critical frequency for the reference panel (thick-lines) and for the panel with passive treatments (faint-lines).

when $N_p > 1$, the two spectra for the reference and heavier panel would be separated by a factor proportional to $m_p / m'_p = 1/2$, which corresponds to $-6$dB. Finally, considering the spectra for the radiated sound power PSD in plot (b), it is noted that, when the panel density is increased, the typical wide band ridge due to efficient sound radiation of all modes of the panel is shifted up in frequency. In fact, according to Eq. (82) the critical frequency for the heavier panel is increased by a factor $\sqrt{m'_p / m_p} = \sqrt{2}$ with respect to that of the reference

panel. Thus, as highlighted by the thick-dashed and thin-dashed vertical lines in plot (b), the critical frequency of the reference panel at about 7.54 kHz is shifted up to about 10.67 kHz for the heavier panel.

The effect of increasing by a factor 2 the panel material Young's modulus of the panel is considered next. Plots (c) and (d) of Figure 14 show that the increased stiffness of the panel shifts the resonance frequencies of the fundamental and low order modes of the panel to higher values. Also, the transition from a spectrum with well separated resonance frequencies to a smoother spectrum occurs at relatively higher frequencies. This is because, as can be deduced from Eq. (80), when the stiffness of the panel is increased, the modal overlap factor grows less rapidly with frequency. The thick-solid and faint-solid vertical lines in the two plots indicate that, when the stiffness of the panel is increased, the convective coincidence effect in the two spectra is shifted down from about 1.17 kHz to about 826 Hz. In fact, according to Eq. (83), the convective coincidence frequency of the stiffer panel is varied by a factor proportional to $\sqrt{B_p/B_p'} = 1/\sqrt{2}$. At higher frequencies, where $N_p > 1$ and thus the two spectra become increasingly smoother, the spectrum of the kinetic energy of the stiffer panel is about 3 dB lower than that of the reference panel, while the levels of the spectra of the radiated sound power for the reference and stiffer panel are the same. Finally, the spectra for the radiated sound power in plot (d), show that, in this case, the typical wide band ridge due to efficient sound radiation of all modes of the panel is shifted down in frequency. In fact, according to Eq. (82) the critical frequency for the stiffer panel is varied by a factor $\sqrt{B_p/B_p'} = 1/\sqrt{2}$ with respect to that of the reference panel. Thus, as highlighted by the thick-dashed and faint-dashed vertical lines in plot (d), the critical frequency of the reference panel at about 7.54 kHz is shifted down to about 5.33 kHz for the stiffer panel.

At last, the effect of increasing by a factor 10 the material loss factor of the panel is considered. According to Eqs. (82) and (83), damping has no effects on the acoustic and the convective coincidence phenomena. Thus the thick and faint solid or dashed vertical lines shown in plots (e) and (f) overlap. The two graphs also show that the damping does not shift the resonance frequencies of the lower order modes. However, as can be deduced from Eq. (80), damping has an important effect on the modal overlap factor. In particular, the doubling of the loss factor produces a doubling of the overlap factor so that the transition from a response characterised by well separated resonances to a smoother spectrum characterised by the overlap of multiple modes is shifted to lower frequencies. The spectra in plots (e) and (f) show that the increment of damping in the panel also reduces the amplitudes of the resonance peaks, due to the fundamental and

low order modes, which are still well separated from each other. Finally, the two plots show how an increase in the loss factor effectively reduces the levels of the spectra of the kinetic energy and radiated sound power as the frequency rises. For instance, when the frequency approaches the critical frequency at about 7.54 kHz, both the kinetic energy and the radiated sound power spectra have fallen by about 10 dB in contrast to the values for the reference panel.

In summary, adding mass to a partition produces two important beneficial effects: first it reduces the level of the response and sound radiation and second it moves to higher frequencies the convective and acoustic coincidence effects. This second effect is particularly important since human annoyance to noise is particularly important at mid audio frequencies, thus in the range from 1 to 4 kHz. Increasing the stiffness of the partition shifts to higher frequencies the resonances of the fundamental and lower order modes of the panel. However it has little effects on the level of the response and radiated sound power and, more importantly, it tends to shift to lower frequencies the convective and acoustic coincidence effects. This is a rather undesirable effect since it tends to compress the two coincidence phenomena towards the mid audio frequency range, which is particularly critical in terms of noise annoyance perception. Finally, increasing damping is generally beneficial although it normally affects the higher frequency portion of the spectrum where the response and sound radiation of the structure are in any case relatively low.

## 4. Active Treatments to Reduce Sound Radiation

In parallel to passive treatments, active control systems can also be added to shell structures in order to reduce their vibration and sound radiation (Maury et al. 2001; Maury et al. 2002c). The fundamental principles of active noise control dates back to the 1930' (Gardonio 2010), however it took more than 50 years before the first applications were developed. This was due to both intrinsic limitations in the speed of the electronics for the controllers and to the limited technologies available for the sensor and actuator transducers. Nevertheless, the progress in digital electronics occurred in the second half of the twentieth century has brought to the development of fast processors with high computing power that enables the implementation of multi-channel controllers, which can manage the small time delays allowed for the implementation of noise and vibration control algorithms. In parallel, new types of transducers were developed, which have brought to the conception of new control systems. For example arrays of small size piezoelectric patch actuators or thin piezoelectric films were embedded in thin plates or shells to form composite structures with active layers (Bianchi et al. 2004; Aoki et al. 2008; Gardonio et al. 2010; Gardonio 2012). Alternatively electromechanical or magnetostrictive transducers

were used to build small size proof–mass actuators that can be attached to thin structures to produce localised active effects (Preumont 2002; Preumont 2006; Gonzalez Diaz et al. 2008a; Gonzalez Diaz et al. 2008b; Gardonio and Alujevic 2010; Alujevic et al. 2011; Rohlfing et al. 2011). Such "smart structures" can be effectively used for the implementation of the so called "Active Structural Acoustic Control" (ASAC) systems for the reduction of the sound radiation by thin structures (Fuller et al. 1996; Gardonio and Elliott 2004; Gardonio and Elliott 2005b; Gardonio 2012).

In this section the basic principles of ASAC control are reviewed and then two examples of ASAC smart panels are described in more details with reference to the control of vibration and sound radiation due to a TBL excitation pressure field. Section 2 has shown that sound radiation is a rather complex phenomenon, which depends on the self and mutual radiation efficiencies between pair of modes of the structure. The fact that, as shown in Figure 8, at certain frequency bands the mutual radiation efficiencies may assume negative values indicates that the interaction between the vibration of pair of modes may lead to a "natural" reduction of the total radiation of noise. Thus, it is not so clear-cut that reducing the response of clusters of structural modes, for example of low order modes, leads to the control of the sound radiation at low frequencies. On the contrary it may bring to an increment of the sound radiation at some narrow frequency bands since the natural reduction of sound radiation between certain pairs of modes has been prevented. Several authors have studied the implementation of specific vibration control approaches aimed at the reduction of the sound radiation by structures. In this chapter the formulation proposed by Elliott and Johnson (1993) for the description of the sound radiation in terms of a new set of modes of the structure, which radiates sound independently, is considered. This is a simple and elegant formulation which directly leads to the conception of a new control paradigm where the sound radiation is reduced by controlling the vibration field of the most efficient radiation mode(s) of the structure. The formulation is based on the fact that the matrix $\mathbf{A}(\omega)$ with the self and mutual radiation efficiencies defined in Eq. (65) is normal, i.e. it is real, symmetric and positive definite. Thus the following eigenvalue-eigenvector decomposition can be implemented,

$$\mathbf{A}(\omega) = \mathbf{P}(\omega)^T \mathbf{\Omega}(\omega) \mathbf{P}(\omega) \ , \tag{85}$$

where $\mathbf{P}(\omega)$ is the $[R \times M]$ orthogonal matrix of eigenvectors and $\mathbf{\Omega}(\omega)$ is the $[R \times R]$ diagonal matrix with real and positive eigenvalues. Therefore, the expression for the radiated sound power PSD in Eq. (64) can be rewritten as follows

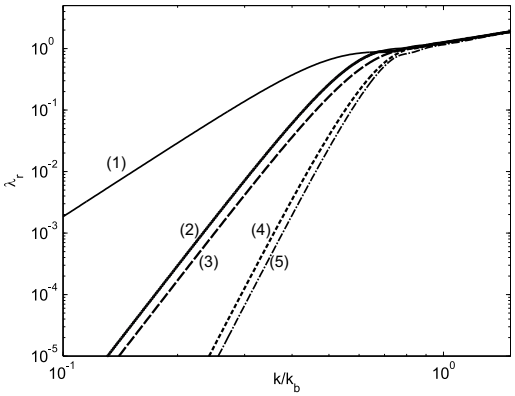


**Figure 15.** First five radiation efficiencies of the radition modes derived from the eigenvalue-eigenvector problem in Eq. (85).

$$S_{\mathrm{Pr}} = \frac{1}{2}\omega^2 \mathrm{Tr}\left[\mathbf{\Omega}(\omega)\mathbf{S}_{\mathbf{aa}}(\omega)\right] , \tag{86}$$

where $\mathbf{S}_{\mathbf{aa}}(\omega)$ is the matrix of PSDs of the transformed complex modal responses $\mathbf{a}(\omega)$ that radiate sound independently from each other

$$\mathbf{a}(\omega) = \mathbf{P}(\omega)\mathbf{b}(\omega) . \tag{87}$$

Thus, considering Eq. (66), the matrix of the new modal responses $\mathbf{S}_{\mathbf{aa}}(\omega)$ is given by

$$\mathbf{S}_{\mathbf{aa}}(\omega) = \mathbf{P}(\omega)\mathbf{Y}(\omega)\mathbf{S}_{\mathbf{pp}}(\omega)\mathbf{Y}^H(\omega)\mathbf{P}^T(\omega) . \tag{88}$$

According to Eq. (85), the diagonal matrix with the eigenvalues $\mathbf{\Omega}(\omega)$ provides the self radiation efficiencies of the new set of vibration modes, whose shapes can be reconstructed by linearly combining the natural modes of the panel with the eigenvectors. Thus the *j*-th radiation mode is given by

$$\psi_j(x,y,\omega) = \boldsymbol{\varphi}(x,y)\mathbf{P}_j^T(\omega) \tag{89}$$

where $\mathbf{P}_j(\omega)$ is the *j*-th row of the matrix $\mathbf{P}(\omega)$. This expression indicates that the radiation modes are frequency dependent. The plot in Figure 15 shows the first six eigenvalues, that is the first six radiation efficiencies, with reference to the ratio between the acoustic and flexural wave numbers $k/k_b$ in logarithmic scale.

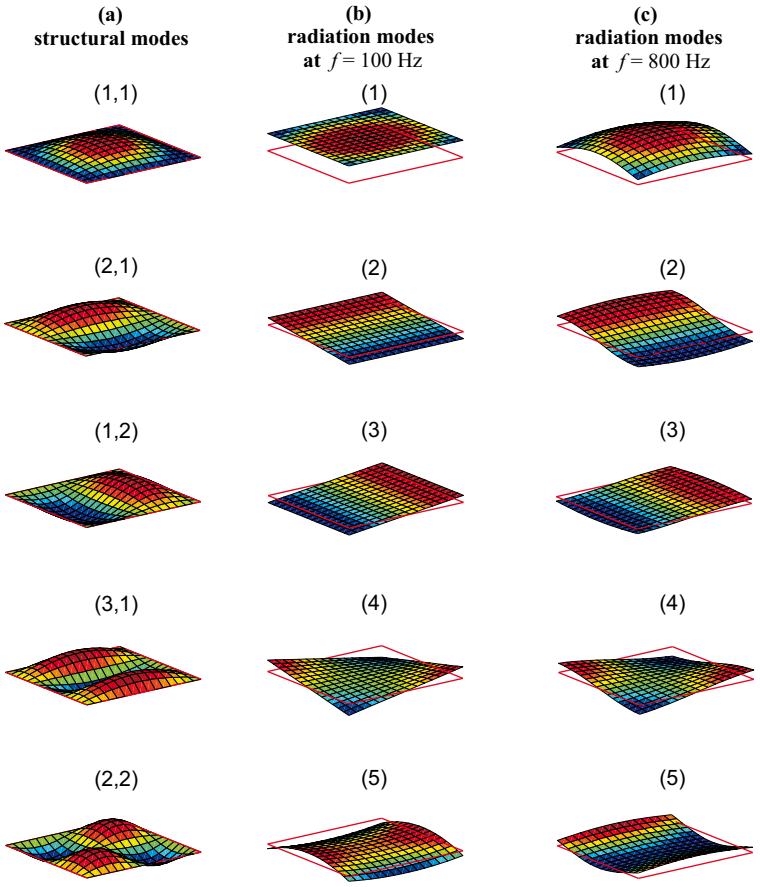


**Figure 16.** First five structural modes (column a) and radiation modes at 100 and 800 Hz (respectively columns b and c) for the panel considered in this chapter.

The graph shows that, similarly to the self radiation efficiencies of the structural modes, the radiation modes are also characterised by rather small radiation efficiencies at low frequencies, which however rise rapidly with frequency up to the critical frequency where $k = k_b$. At higher frequencies the radiation rises further but at a lower rate. At low frequencies the radiation efficiency of the second and higher order radiation modes is much lower than that of the first radiation mode. Thus it is expected that controlling the vibration field related to

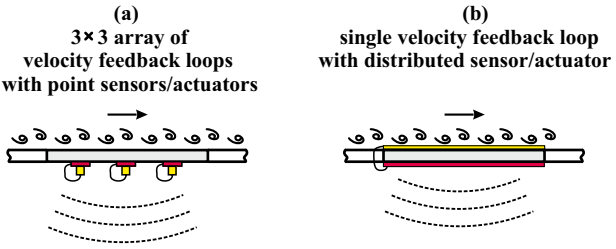


**Figure 17.** Sound radiation induced by TBL pressure field on smart panels composed of: (a) a 3x3 array of decentralised velocity feedback loops using idealised point velocity and point force sensor–actuator pairs and (b) a single velocity feedback using an idealised distributed volume velocity sensor and an idealised distributed uniform force actuator pair.

the first radiation mode should lead to a consistent reduction in the sound radiation particularly at low frequencies below the critical frequency where $k = k_b$. The graphs in Figure 16 show the first five structural modes (column a) and then the first five radiation modes at 100 and 800 Hz (respectively columns b and c) for the panel considered in this study. The first and most efficient radiation mode is therefore characterised by a volumetric shape, which tends to be rounded off along the borders as the frequency rises. This leads to the conclusion that, in order to control the vibration field of the panel associated to the first radiation mode, and thus to control the low frequency sound radiation, it is necessary to reduce the volumetric vibration of the panel. This may be achieved with an active system, which uses a distributed actuator that exerts a uniform force over the panel surface in such a way as to minimise an error signal provided by a sensor that measures the volumetric vibration of the panel. In principle, a multiple channel controller can be used, which simultaneously controls two or more radiation modes. However, this would be a rather complex system that marginally increments the control effects at low frequencies. In general, the active control of sound and vibration is based on two control architectures. When the primary disturbance to be controlled can be detected in advance, a feed-forward control architecture is implemented, which drives the control actuators in such a way as to produce a secondary acoustic or vibration field that destructively interferes with the primary disturbance field (Gardonio 2012). Alternatively, when the primary disturbance cannot be detected in advance, a feedback control architecture is used, which tends to modify the dynamic response of the system in such a way as to reduce the effect of the

primary disturbance (Gardonio 2012). Since the pressure field generated by TBL excitations is stochastic (both in time and in space domains) it is rather difficult to collect the reference signals that would allow the implementation of feed-forward control systems. Thus, feedback control systems are normally implemented to contrast the effects produced by TBL disturbances. In this chapter the two smart panels with the feedback systems shown in Figure 17 will be considered. System (a) comprises a $3\times3$ array of decentralised feedback loops composed of an idealised force actuator with a collocated velocity sensor. The second system consists of a distributed uniform force actuator with a matched volume velocity sensor that implements a single absolute velocity feedback loop. In this case the feedback loop is aimed at controlling the volumetric vibration field of the panel, which, as discussed above, is the major contributor to sound radiation. The control of both feedback loops is proportional to velocity, thus it produces a damping effect. For this reason, these control systems are often reported as "active damping systems". When the feedback loop or loops are implemented, the structural modal admittance matrix $\mathbf{Y}$ used to derive the kinetic energy PSD and radiated sound power PSDs is derived from the following modified version of Eq. (70)

$$\left[-\omega^2\mathbf{M}+\mathbf{K}(1+j\eta)+j\omega\,\mathbf{D}\right]\mathbf{b}_r=\mathbf{f}_r \quad , \tag{90}$$

thus $\mathbf{Y}=\left[-\omega^2\mathbf{M}+\mathbf{K}(1+j\eta)+j\omega\mathbf{D}\right]^{-1}$. The elements of the "active damping matrix" $\mathbf{D}$ for the system with the $3\times3$ array of feedback loops are given by

$$D_{pq}=\sum_{i=1}^{S} g_s\phi_p(\mathbf{x}_{a,i})\phi_q(\mathbf{x}_{s,i}) \quad , \tag{91}$$

where $g_s$ is the gain implemented in the feedback loops and the vectors $\mathbf{x}_{a,i}$ and $\mathbf{x}_{s,i}$ identify the positions of the *i*-th control actuator and *i*-th error sensor, which are collocated in the specific case under consideration. The elements of the "active damping matrix" $\mathbf{D}$ for the system with the distributed uniform force actuator and distributed volume velocity sensor are instead given by

$$D_{pq}=g_s\int_{S_b}\phi_p(\mathbf{x}_s)dS_b\int_{S_b}\phi_q(\mathbf{x}_s)dS_b \quad . \tag{92}$$

where $g_s$ is the gain implemented in the feedback loop. In summary the total kinetic energy PSD and total radiated sound power PSD for the smart panels with arrays of point feedback loops or with a single feedback loop using distributed transducers have been derived from Eqs. (55) and (64) with the matrix of modal response PSDs $\mathbf{S}_{\mathrm{bb}}(\omega)$ derived with Eq. (66) using the

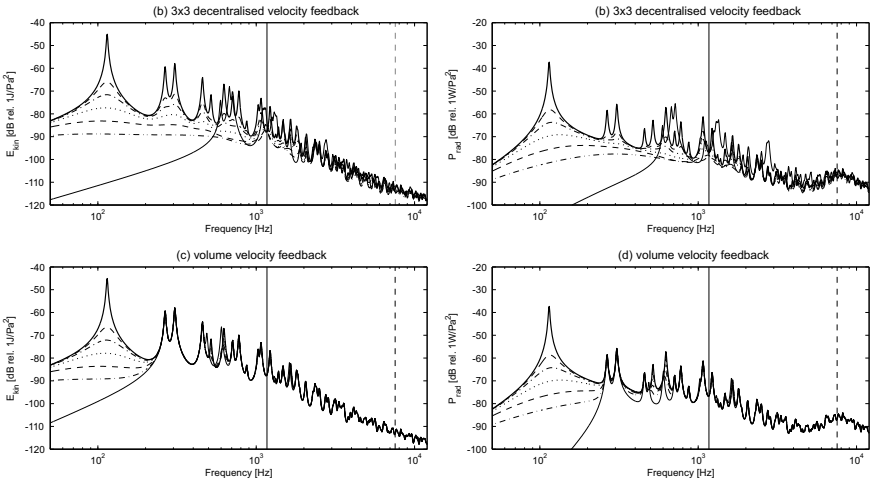


**Figure 18.** PSD of the total kinetic energy (left–hand side plots) and total radiated sound power (right–hand side plots) per unit TBL pressure field PSD. Thick solid lines reference panel. Broken and solid-faint lines in plots (a,b) reference panel with 3×3 array of point velocity feedback loops with increasing feedback gains up to the optimal value that minimises the radiated sound power. Broken and solid-faint lines in plots (c,d) reference panel with the volume velocity–uniform force feedback loop with increasing feedback gains.

following expression for the matrix of modal addmittances $\mathbf{Y}(\omega) = \left[-\omega^2\mathbf{M} + \mathbf{K}(1+j\eta) + j\omega\mathbf{D}\right]^{-1}$.

Plots (a) and (b) in Figure 18 show the spectra of the total kinetic energy PSD and total radiated sound power PSD as the control gains of the 3×3 array of velocity feedback loops are increased. The broken and solid-faint lines in the two plots indicates that, as the feedback control gains are increased, the active damping action exerted by the feedback loops smoothens the resonance peaks of the low order modes of the panel. Thus, this system can effectively reduce both the response and sound radiation at low frequencies where, as discussed in Section 3, passive treatments are less effective. The principal reason why this active system is so effective at low frequencies is because the damping effect produced by the feedback loops is proportional to the absolute transverse velocity of the panel. Thus the so called "sky-hook" active damping effect is produced (Preumont 2002), which effectively reduces the flexural response and sound radiation of the panel. In contrast, the action of a passive damping

treatment is proportional to the strain rate in the structure, which is particularly small at low frequencies where the response is controlled by the lower order modes whose shapes are shown in column (a) of Figure 16. Plots (a) and (b) show that, if the control gains are set to very large values, the response and sound radiation at mid frequencies become even larger than those of the reference panel without control system. This phenomenon is due to the fact that for very large feedback gains, control loops tend to pin the panel at the control positions (Gardonio and Elliott 2005a). Thus the loops do not absorb energy, that is they do not produce active damping anymore. They in fact introduce new boundary conditions, which lead to new set of modes with higher natural frequency. Thus the response and sound radiation of the panel become those of a new, stiffened, panel, with the natural frequencies of the fundamental and low order modes shifted to higher frequencies. As a result, the mid frequency response and sound radiation are increased with respect to those of the reference panel. In conclusion, the 3×3 array of velocity feedback loops produces a very effective sky-hook active damping action which is maximum for a given set of feedback gains. The optimal feedback gains for the minimisation of the response, and thus sound radiation, are very similar to each other (Gardonio and Elliott, 2004). Zilletti et al. (2010) have shown that these correspond to the condition of locally maximising the power absorbed by each feedback loop. This is a very interesting result since it indicates that the feedback loops can be locally tuned without the need of a global cost function to be minimised. Moreover, since the control force is proportional to velocity, the power absorbed given by the product of the control force and control velocity, is in practice proportional to the square of the control velocity. Thus the velocity control sensor signal can be used to implement both the feedback loop and the tuning algorithm necessary to set the optimal control gain.

Plots (c) and (d) in Figure 18 show the kinetic energy PSD and radiated sound power PSD as the control gain of the single feedback loop using a volume velocity distributed sensor and a uniform force distributed actuator is increased. In this case, the control system tends to smoothen the response and sound radiation of selected resonances of the panel. This is because the system can act only on those modes that have a non zero net volumetric component, that is those modes with both mode orders odd. Thus, for example, it cannot be effective on the (1,2), or (2,1) modes, which cause the second and third resonance peaks in the two spectra. However, in this case, since the control system acts on the approximated shape of the first radiation mode, the feedback effect rises indefinitely with the control gain. Thus, provided the control gain is set to large enough values, there is no need of an online tuning system of the control gain. Nevertheless, the control effect produced by this control configuration is relatively lower than that obtained with the decentralised system. It should be

highlighted that this result is peculiar to the TBL pressure field primary excitation, which, as discussed in Section 2, effectively excites both volumetric and non volumetric modes.

The short analysis presented in this section about the implementation of active systems for the reduction of vibration and sound radiation by a thin panel excited by a TBL pressure field has been focused on the physics of these control systems. No discussion has been presented on the stability and practical implementation of the feedback loops. This is a very important aspect of the systems, which however lies outside the scope of this chapter. The reader who would like to learn more on this topic is referred to specialised text and articles, as for example those in references (Fuller et al. 1996; Clark et al. 1998; Preumont 2002; Fahy and Gardonio 2007; Gardonio 2012).

## 5. Acknowledgements

The author is very grateful to Dr Jens Rohlfing and Dr Michele Zilletti for their precious help in the production of simulation graphs and the editing of the text and formulation. Also a special thank goes to Silvia for her support throughout the preparation of the chapter.

## 6. References

Abrahams, I. D. (1983). Scattering of sound by an elastic plate with flow. *Journal of Sound and Vibration* 89: 213-231.

Alujevic, N., Gardonio, P. and Frampton, K. D. (2011). Smart Double Panel for the Sound Radiation Control: Blended Velocity Feedback. *AIAA Journal* 49(6): 1123-1134.

Aoki, Y., Gardonio, P. and Elliott, S. J. (2008). Rectangular plate with velocity feedback loops using triangularly shaped piezoceramic actuators: Experimental control performance. *The Journal of the Acoustical Society of America* 123(3): 1421-1426.

Atalla, N. and Nicolas, J. (1995). A formulation for mean flow effects on sound radiation from rectangular baffled plates with arbitrary boundary conditions. *Journal of Vibration and Acoustics* 117: 22-29.

Aupperle, F. A. and Lambert, R. F. (1973). Acoustic radiation from plates excited by flow noise. *Journal of Sound and Vibration* 26(2): 223-245.

Bano, S., Marmey, R., Jourdan, L. and Guibergia, J. P. (1992). Etude théorique et expérimentale de la réponse vibro-acoustique d'une plaque couplée à une cavité en fluide lourd. *Journal d'Acoustique* 5: 99-124.

Bendat, J. S. and Piersol, A. G. (2000). *Random Data Analysis and Measurement Procedures*. New York, Jhon Wiley & Sons, Inc, Third Edition

Bianchi, E., Gardonio, P. and Elliott, S. J. (2004). Smart panel with multiple decentralized units for the control of sound transmission. Part III: control system implementation. *Journal of Sound and Vibration* 274(1–2): 215-232.

Blake, W. K. (1986). Mechanics of Flow-Induced Sound and Vibration. In Frenkiel, F. N. and Temple, G. *Applied Mathematics and Mechanics*. Volumes I and II, pp.

Blevins, R. D. (2001). *Formulas for natural frequency and mode shape*. Melbourne, Florida, USA, Krigger Publishing Company

Borisyuk, A. O. and Grinchenko, V. T. (1997). Vibration and noise generation by elastic elements excited by a turbulent flow. *Journal of Sound and Vibration* 204(2): 213-237.

Bull, M. K. (1995). Wall-pressure fluctuations beneath turbulent boundary layers: some reflections on forty years of research. *Journal of Sound and Vibration* 190(3): 299-315.

Chase, D. M. (1980). Modeling the wavevector-frequency spectrum of turbulent boundary layer wall pressure. *Journal of Sound and Vibration* 70(1): 29-67.

Chase, D. M. (1987). The character of the turbulent wall pressure spectrum at subconvective wavenumbers and a suggested comprehensive model. *Journal of Sound and Vibration* 112(1): 125-147.

Ciskowski, R. D. and Brebbia, C. A. (1991). *Boundary Element Methods in Acoustics*. Southampton, Boston, Computational Mechanics Publications (co published with Elsevier Applied Science, London)

Clark, R. L. and Frampton, K. D. (1997). Aeroelastic structural acoustic coupling: implications on the control of turbulent boundary-layer noise transmission. *Journal of the Acoustical Society of America* 102: 1639-1647.

Clark, R. L., Saunders, W. R. and Gibbs, G. P. (1998). *Adaptive Structures*. NewYork, John Wiley & Sons, 1sted

Corcos, G. M. (1963a). Resolution of Pressure in Turbulence. *The Journal of the Acoustical Society of America* 35(2): 192-199.

Corcos, G. M. (1963b). The structure of the turbulent pressure field in boundary-layer flows. *Journal of Fluid Mechanics* 18: 353-378.

Corcos, G. M. (1967). The resolution of turbulent pressures at the wall of a boundary layer. *Journal of Sound and Vibration* 6(1): 59-70.

Cousin, G. (1999). Sound from TBL induced vibrations. Technical Document No: Royal Institute of Technology, Department of Vehicle Engineering

Craik, R. J. M. (1996). *Sound transmission through buildings : using statistical energy analysis*. Aldershot, England Gower

Crandall, S. H. and Mark, W. D. (1963). *Random Vibration in Mechanical Systems*. London, Academic Presss

Cremer, L., Heckl, M. and Ungar, E. E. (1988). *Structure-Borne Sound*. Berlin, Springer-Verlag, 2nd

Crocker, M. J. (1969). The response of a supersonic transport fuselage to boundary layer and to reverberant noise. *Journal of Sound and Vibration* 9(1): 6-20.

Davies, H. G. (1971). Sound from Turbulent-Boundary-Layer-Excited Panels. *The Journal of the Acoustical Society of America* 49(3B): 878-889.

Desmet, W. (1998). A wave based prediction technique for coupled vibro-acoustic analysis. PhD thesis, Katholieke Universiteit Leuven, Leuven, Belgium

Dowell, E. H. (1975). *Aeroelasticity of Plates and Shells*. Groningen, The Netherlands, Noordhoff

Dowell, E. H. and Voss, H. M. (1962). The effect of a cavity on panel vibration. *AIAA Journal* 1(2): 476-477.

Dowling, A. P. and Ffowcs Williams, J. E. (1983). *Sound and sources of sound*. Chichester, Sussex, Ellis Horwood Ltd.

Durant, C., Robert, G., Filippi, P. J. T. and Mattei, P. O. (2000). Vibroacoustic response of a thin cylindrical shell excited by a turbulent internal flow: comparison between numerical prediction and experimentation. *Journal of Sound and Vibration* 229(5): 1115-1155.

Dyer, I. (1959). Boundary Layer Induced Flow Noise. *The Journal of the Acoustical Society of America* 31(11): 1566.

Efimtsov, B. M. (1982). Characteristics of the field of turbulent wall pressure fluctuations at large Reynolds numbers. *Soviet Physics-Acoustics* 28(4): 289-292.

Efimtsov, B. M. (1986). Vibrations of a cylindrical panel in a field of turbulent pressure fluctuations. *Soviet Physics Acoustics* 32(4): 336-337.

Efimtsov, B. M. and Shubin, S. E. (1977). Experimental study of the vibrations and sound radiation of a plate in a turbulent pressure-fluctuation field. *Soviet Physics Acoustics* 23(4): 334-337.

Elliott, S. J. and Johnson, M. E. (1993). Radiation modes and the active control of sound power. *The Journal of the Acoustical Society of America* 94(4): 2194-2204.

Elliott, S. J., Maury, C. and Gardonio, P. (2005). The synthesis of spatially correlated random pressure fields. *The Journal of the Acoustical Society of America* 117(3): 1186-1201.

Fahy, F. J. (1969). Vibration of containing structures by sound in the contained fluid. *Journal of Sound and Vibration* 10(3): 490-512.

Fahy, F. J. and Gardonio, P. (2007). *Sound and Structural Vibration*. London, Elsevier

Ffowcs Williams, J. E. (1982). Boundary-layer pressures and the Corcos model: a development to incorporate low wavenumber constraints. *Journal of Fluid Mechanics* 125: 9-25.

Filippi, P. J. T. and Mazzoni, D. (1994). Noise induced inside a cavity by an external turbulent boundary layer. In Brebbia, C. A. *Boundary Elements XVI*, Southampton-Boston: Computational Mechanics Publications, pp. 47-54.

Frampton, K. D. (2005). The effect of flow-induced coupling on sound radiation from convected fluid loaded plates. *Journal of the Acoustical Society of America* 117: 1129-1137.

Frampton, K. D. and Clark, R. L. (1997). Power flow in an aeroelastic plate backed by a reverberant cavity. *Journal of the Acoustical Society of America* 102: 1620-1627.

Fuller, C. R., Elliott, S. J. and Nelson, P. A. (1996). *Active Control of Vibration*. London, AcademicPress

Garabedian, P. R. (1964). *Partial Differential Equations*. Providence, Rhode Island, AMS Chelsea Publishing

Gardonio, P. (2010). Active Noise Control. In Blockley, R. and Shyy, W. *Encyclopedia of Aerospace Engineering*. Chichester, UK, John Wiley & Sons Ltd, pp. 3575-3588.

Gardonio, P. (2012). Composite Smart Panels for Active Control of Sound Radiation. In Nicolais, L. and Borzacchiello, A. *Encyclopedia of Composites*, John Wiley & Sons, Inc, , pp. (pages 22).

Gardonio, P. and Alujevic, N. (2010). Double panel with skyhook active damping control units for control of sound radiation. *The Journal of the Acoustical Society of America* 128(3): 1108-1117.

Gardonio, P., Aoki, Y. and Elliott, S. J. (2010). Smart panel with active damping wedges along the perimeter. *Journal of Smart Materials and Structures* 19(6): 1-15.

Gardonio, P. and Brennan, M. J. (2002). On the origins and development of mobility and impedance methods in structural dynamics. *Journal of Sound and Vibration* 249(3): 557-573.

Gardonio, P. and Brennan, M. J. (2004). Mobility and impedance methods in structural dynamics. In Fahy, F. J. and Walker, J. *Advanced Applications in Acoustics, Noise and Vibration*. London, E & FN Spon, pp. 387–388.

Gardonio, P. and Elliott, S. J. (2004). Smart panels for active structural acoustic control. *Journal of Smart Materials and Structures* 13: 1314-1336.

Gardonio, P. and Elliott, S. J. (2005a). Modal response of a beam with a sensor–actuator pair for the implementation of velocity feedback control. *Journal of Sound and Vibration* 284(1–2): 1-22.

Gardonio, P. and Elliott, S. J. (2005b). Smart panels with velocity feedback control systems using triangularly shaped strain actuators. *The Journal of the Acoustical Society of America* 117(4): 2046-2064.

Gardonio, P., Ferguson, N. S. and Fahy, F. J. (2001). A modal expansion analysis of noise transmission through circular cylindrical shell structures with blocking masses. *Journal of Sound and Vibration* 244(2): 259-297.

Gardonio, P., Miani, S., Blanchini, F., Casagrande, D. and Elliott, S. J. (2012). Plate with decentralised velocity feedback loops: Power absorption and kinetic energy considerations. *Journal of Sound and Vibration* 331(8): 1722-1741.

Gaul, L., Kogl, M. and Wagner, M. (2003). *Boundary Element Methods for Engineers and Scientists*. Berlin, Springer

Gonzalez Diaz, C., Paulitsch, C. and Gardonio, P. (2008a). Active damping control unit using a small scale proof mass electrodynamic actuator. *Journal of the Acoustical Society of America* 124(2): 886-897.

Gonzalez Diaz, C., Paulitsch, C. and Gardonio, P. (2008b). Smart panel with active damping units. Implementation of decentralized control. *The Journal of the Acoustical Society of America* 124(2): 898-910.

Graff, K. F. (1975). *Wave Motion in Elastic Solids*. New York, NY, Dover Publications.

Graham, W. R. (1996). Boundary layer induced noise in aircraft, Part I: the flat plate model. *Journal of Sound and Vibration* 192(1): 101-120.

Graham, W. R. (1997). A comparison of models for the wavenumber-frequency spectrum of turbulent boundary layer pressures. *Journal of Sound and Vibration* 206(4): 541-565.

Guy, R. W. and Bhattacharya, M. C. (1973). The transmission of sound through a cavity-backed finite plate. *Journal of Sound and Vibration* 27(2): 207-223.

Guyader, J. L. and Laulagnet, B. (1994). Structural acoustic radiation prediction: Expanding the vibratory response on a functional basis. *Applied Acoustics* 43(3): 247-269.

Han, F., Bernhard, R. J. and Mongeau, L. G. (1999). Prediction of flow-induced structural vibration and sound radiation using energy flow analysis. *Journal of Sound and Vibration* 227(4): 685-709.

Howe, M. S. (1998). *Acoustics of fluid-structure interactions* Cambridge, Cambridge University Press

Hwang, Y. F., Bonness, W. K. and Hambric, S. A. (2009). Comparison of semi-empirical models for turbulent boundary layer wall pressure spectra. *Journal of Sound and Vibration* 319(1–2): 199-217.

Hwang, Y. F. and Maidanik, G. (1990). A wavenumber analysis of the coupling of a structural mode and flow turbulence. *Journal of Sound and Vibration* 142(1): 135-152.

Junger, M. C. and Feit, D. (1986). *Structures, and their Interaction* Cambridge, Massachusetts, The MIT Press, 2nd

Keane, A. J. and Price, W. G. (1997). *Statistical Energy Analysis: An Overview, With Applications in Structural Dynamics*. Cambridge, UK, Cambridge University Press

Kellogg, O. D. (1953). *Foundations of Potential Theory*. New York, NY, Dover Publications Inc.

Kinsler, L. E., Frey, A. R., Coppens, A. B. and Sanders, J. V. (2000). *Fundamentals of Acoustics*, John Wiley & Sons, Inc., IV Edition

Koopmann, G. H. (1997). *Designing Quiet Structures, A Sound Power Minimization Approach*. London, Academic Press

Langley, R. S. and Fahy, F. J. (2004). High-Frequency Structural Vibration. In Fahy, F. J. and Walker, J. G. *Advanced Applications in Acoustics, Noise and Vibration*. London, UK, E & FN Spon, pp. 490-529.

Leehey, P. (1988). Structural excitation by a turbulent boundary layer: an overview. *Transactions ASME* 110: 220-225.

Leissa, A. (1993). *Vibrations of Shells*. New York, NY, ASA through American Institute of Physics

Lesueur, C. (1988). *Rayonnement Acoustique Des Structures*. Vol 66 Collection de la Direction des Études et Recherches d'Électricité de France. Paris, Editions Eyrolles.

Lyle, K. H. and Dowell, E. H. (1994). Acoustic Radiation Damping of Flat Rectangular Plates Subjected to Subsonic Flows. Parts I and II. *Journal of Fluids and Structures* 8(7): 711-746.

Lyon, R. H. and DeJong, R. G. (1995). *Theory and application of statistical energy analysis*. Boston, USA, Butterworth-Heinemann

Markus, S. (1998). *The mechanics of vibrations of cylindrical shells*. Oxford, Elsevier

Martin, N. C. and Leehey, P. (1977). Low wavenumber wall pressure measurements using a rectangular membrane as a spatial filter. *Journal of Sound and Vibration* 52(1): 95-120.

Masson, B. (1991). Development of a prediction method for the noise generated by a separated flow and transmitted by a flexible surface. Master Thesis, University of Southampton UK

Maury, C., Elliott, S. J. and Gardonio, P. (2004). Turbulent boundary layer simulation with an array of loudspeakers. *AIAA Journal* 42(2): 706-713.

Maury, C., Gardonio, P. and Elliott, S. J. (2001). Active control of the flow-induced noise transmitted through a panel. *AIAA Journal* 39(10): 1860-1867.

Maury, C., Gardonio, P. and Elliott, S. J. (2002a). A wavenumber approach to modelling the response of randomly excited panel, Part I: general theory. *Journal of Sound and Vibration* 252(1): 83-113.

Maury, C., Gardonio, P. and Elliott, S. J. (2002b). A wavenumber approach to modelling the response of a randomly excited panel, Part II: application to aircraft panels excited by a turbulent boundary layer. *Journal of Sound and Vibration* 252(1): 115-139.

Maury, C., Gardonio, P. and Elliott, S. J. (2002c). Model for active control of flow-induced noise transmitted through double partitions. *AIAA Journal* 40(6): 1113-1121.

Mazzoni, D. (2003). An efficient approximation for the vibro-acoustic response of a turbulent boundary layer excited panel. *Journal of Sound and Vibration* 264(4): 951-971.

Mead, D. J. and Richards, E. J. (1968). *Noise and Acoustic Fatigue in Aeronautics*. London, John Wiley & Sons, Inc.

Millard, J. (1997). Advanced time domain sensing for active structural acoustic control PhD Thesis, Blacksburg, Virginia USA

Mixson, J. S. and Wilby, J. F. (1995). Interior Noise. In Hubbard, H. H. *Aeroacoustics of Flight Vehicles, Theory and Practice*. NASA Langley Research Center, Hampton, Virginia, pp.

Morse, P. M. and Ingard, K. U. (1968). *Theoretical Acoustics*. London, McGraw–Hill

Nelson, P. A. and Elliott, S. J. (1992). *Active Control of Sound*. London, Academic Press

Newland, D. E. (1975). *An introduction to Random Vibrations and Spectral Analysis*. London, Longman

Pierce, A. D. (1989). *Acoustics: An Introduction to its Physical Principles and Applications*. Melville, NY, Acoustical Society of America

Pretlove, A. J. (1966). Forced vibrations of a rectangular panel backed by a closed rectangular cavity. *Journal of Sound and Vibration* 3(3): 252-261.

Preumont, A. (2002). *Vibration Control of Active Structures*. London, Kluwer Academic Press

Preumont, A. (2006). *Mechatronics, Dynamics of Electromechanical and Piezoelectric Systems*. Dordrecht, The Netherlands, Springer

Reddy, J. N. (2006). *Theory and Analysis of Elastic Plates and Shells*. London, CRC Press, Taylor & Francis Group

Robert, G. (1984). Modélisation et simulation du champ excitateur induit sur une structure par une couche limite turbulente. Ecole Centrale de Lyon, France

Rohlfing, J. and Gardonio, P. (2009). Homogeneous and sandwich active panels under deterministic and stochastic excitation. *The Journal of the Acoustical Society of America* 125(6): 3696-3706.

Rohlfing, J., Gardonio, P. and Thompson, D. J. (2011). Comparison of decentralized velocity feedback control for thin homogeneous and stiff sandwich panels using electrodynamic proof-mass actuators. *Journal of Sound and Vibration* 330(5): 843-867.

Smol'yakov, A. V. and Tkachenko, V. M. (1991). Model of a field of pseudosonic turbulent wall pressures and experimental data. *Soviet Physics-Acoustics* 37(6): 627-631.

Soedel, W. (1993). *Vibrations of shells and plates*. New York, Marcel Dekkerr Inc, 2nd

Sommerfeld, A. (1949). *Partial differential equations in physics*. New York, Academic Press

Stephanishen (1981). Modal coupling in the vibration of fluid–loaded cylindrical shells. *The Journal of the Acoustical Society of America* 71(4): 813-823.

Strawderman, W. A. (1990). Wavevector-frequency analysis with applications to acoustics. Technical Document No: 008-047-00408-7, Naval Underwater Systems Center

Thomas, D. R. and Nelson, P. A. (1995). Feedback control of sound radiation from a plate excited by a turbulent boundary layer. *The Journal of the Acoustical Society of America* 98(5): 2651-2662.

Thompson, D. J. and Dixon, J. (2004). Vehicle Noise. In Fahy, F. and Walker, J. *Advanced Applications in Acoustics, Noise and Vibration*. London, Spon Press Taylor & Francis Group, pp.

Wang, B.-T., Fuller, C. R. and Dimitriadis, E. K. (1991). Active control of noise transmission through rectangular plates using multiple piezoelectric or point force actuators. *The Journal of the Acoustical Society of America* 90(5): 2820-2830.

Wu, T. W. (2000). The Helmholtz integral equation, Chapter 2. In Wu, T. W. *Boundary Element Acoustics, Fundamentals and Computer Codes*. London, WIT Press, pp.

Xin, F. X. and Lu, T. J. (2010). Analytical modeling of sound transmission across finite aeroelastic panels in convected fluids. *Journal of the Acoustical Society of America* 128: 1097-1107.

Zilletti, M., Elliott, S. J. and Gardonio, P. (2010). Self-tuning control systems of decentralised velocity feedback. *Journal of Sound and Vibration* 329(14): 2738-2750.